Advances in Quantum Chemistry

Volume 52

Contents

Contributors

Numbers in parentheses indicate the pages where the authors' contributions can be found.

Ludwik Adamowicz (231), Department of Chemistry, The University of Arizona, Tucson, AZ 85721, USA, ludwik@u.arizona.edu

A. Akar (277), Department of Physics, Faculty of Arts and Sciences, Ondokuz Mayıs University, Samsun 55139, Turkey

I. Baccarelli (189), Supercomputing Consortium for University and Research, CASPUR, Via dei Tizii 6b, 00185 Rome, Italy

F. Blanco (21), Departamento de Física Atómica, Molecular y Nuclear, Universidad Complutense de Madrid, Ciudad Universitaria, 28040 Madrid, Spain

R. Cabrera-Trujillo (149), Quantum Theory Project, Departments of Physics and Chemistry, University of Florida, Gainesville, FL 32611-8435, USA

Emilie Cauët (121), Service de Chimie Quantique et Photophysique, Université Libre de Bruxelles, CP 160/09, 50 Avenue F.D. Roosevelt, B-1050 Bruxelles, Belgium

E. Deumens (149), Quantum Theory Project, Departments of Physics and Chemistry, University of Florida, Gainesville, FL 32611-8435, USA

G. García (21), Instituto de Matemáticas y Física Fundamental (IMAFF), Consejo Superior de Investigaciones Científicas (CSIC), Serrano 113-bis, 28006 Madrid, Spain

Oksana Geithner (289), Department of Medical Physics, German Cancer Research Center (DKFZ), D-69120 Heidelberg, Germany

F.A. Gianturco (189), Department of Chemistry, The University of Rome 'La Sapienza', Piazzale A. Moro 5, 00185 Rome, Italy

A. Grandi (189), Supercomputing Consortium for University and Research, CASPUR, Via dei Tizii 6b, 00185 Rome, Italy

H. Gümüş (277), Department of Physics, Faculty of Arts and Sciences, Ondokuz Mayıs University, Samsun 55139, Turkey

R. Hellhammer (149), Hahn-Meitner Institut, Glienickerstraße 100, D-14109 Berlin, Germany

Oliver Jäkel (289), Department of Medical Physics, German Cancer Research Center (DKFZ), D-69120 Heidelberg, Germany

Abraham F. Jalbout (231), Department of Chemistry, The University of Arizona, Tucson, AZ 85721, USA, ajalbout@u.arizona.edu

Xifeng Li (59), Department of Nuclear Medicine and Radiobiology, Faculty of Medicine, Université de Sherbrooke, Quebec, J1H 5N4, Canada

Jacques Liévin (121), Service de Chimie Quantique et Photophysique, Université Libre de Bruxelles, CP 160/09, 50 Avenue F.D. Roosevelt, B-1050 Bruxelles, Belgium, jlievin@ulb.ac.be

R.R. Lucchese (189), Department of Chemistry, Texas A&M University, College Station, TX 77843-3255, USA

A. Muñoz (21), Centro de Investigaciones Energéticas, Medioambientales y Tecnológicas (CIEMAT), Avenida Complutense 22, 28040 Madrid, Spain

Y. Öhrn (149), Quantum Theory Project, Departments of Physics and Chemistry, University of Florida, Gainesville, FL 32611-8435, USA

N.T. Okumuşoğlu (277), Department of Physics, Rize Faculty of Arts and Sciences, Karadeniz Technical University, Rize 53100, Turkey

J.C. Oller (21), Centro de Investigaciones Energéticas, Medioambientales y Tecnológicas (CIEMAT), Avenida Complutense 22, 28040 Madrid, Spain

Helmut Paul (289), Institut für Experimentalphysik, Atom- und Oberflächenphysik, Johannes-Kepler-Universität, Altenbergerstrasse 69, A-4040 Linz, Austria

J.M. Pérez (21), Centro de Investigaciones Energéticas, Medioambientales y Tecnológicas (CIEMAT), Avenida Complutense 22, 28040 Madrid, Spain

Z. Pešić (149), Hahn-Meitner Institut, Glienickerstraße 100, D-14109 Berlin, Germany

John R. Sabin (1), Department of Physics, University of Florida, Gainesville, FL, USA and Department of Chemistry, University of Southern Denmark, Odense, Denmark

J.R. Sabin (149), Quantum Theory Project, Departments of Physics and Chemistry, University of Florida, Gainesville, FL 32611-8435, USA

N. Sanna (189), Supercomputing Consortium for University and Research, CASPUR, Via dei Tizii 6b, 00185 Rome, Italy

Michael D. Sevilla (59), Department of Chemistry, Oakland University, Rochester, MI 48309, USA

Jack Simons (171), Chemistry Department, University of Utah, Salt Lake City, UT 84112, USA, simons@chemistry.utah.edu, http://simons.hec.utah.edu

N. Stolterfoht (149), Hahn-Meitner Institut, Glienickerstraße 100, D-14109 Berlin, Germany and Quantum Theory Project, Departments of Physics and Chemistry, University of Florida, Gainesville, FL 32611-8435, USA

Béla Sulik (253), Institute of Nuclear Research of the Hungarian Academy of Sciences, H-4001 Debrecen, Hungary, sulik@atomki.hu

Károly Tőkési (253), Institute of Nuclear Research of the Hungarian Academy of Sciences, H-4001 Debrecen, Hungary

František Tureček (89), Department of Chemistry, University of Washington, Box 351700, Bagley Hall, Seattle, WA 981195-1700, USA

Clemens von Sonntag (5), Max-Planck-Institut für Bioanorganische Chemie, Stiftstrasse 34-36, 45413 Mülheim an der Ruhr, Germany and Leibnitz-Institut für Oberflächenmodifizierung (IOM), Permoserstrasse 15, 04303 Leipzig, Germany, clemens@vonsonntag.de

Preface

This thematic issue of Advances in Quantum Chemistry is devoted to the theory of the interaction of radiation with biological systems. The subject is timely, as knowledge of the fundamental physics and chemistry of the interaction is critical to understanding problems as critical as radiation therapy of tumors and radiation protection in space. A true understanding of the interaction of radiation with a biological entity requires study of phenomena ranging over many orders of magnitude in size and time. In this volume, however, we concentrate on the individual collision processes between an ion or photon and a single biomolecule. The volume is composed of thirteen contributions from specialists in the field.

As most of the theory used in this volume is based in quantum mechanics, the size of target systems under consideration is generally small: There are calculations on nucleobases, on DNA radicals, on transient negative ions (TNI), and on the most common biomolecule—water. All are important for the understanding of the primary ion-biomolecule interactions. However, the volume does not go to larger clusters such as double strands, nor to longer timescales where the chemical phase of radiation damage becomes important.

It is very easy for a theorist to carry out complex calculations on a system thought to be both interesting and relevant to the biological problem, only to discover at some later time that the interest remains but that there is no biological relevance to the problem. To put this problem in perspective, the first paper, after a short introduction, is by an experimentalist, Clemens von Sonntag, who discusses the calculation of ion-molecule reactive collisions with particular emphasis on the types of problems where quantum calculations on biomolecules would be of use to experimentalists.

Von Sonntag's paper is followed by a series of contributions describing various aspects of radiation damage.

The first a contribution by Muñoz *et al.* concerning high accuracy quantum mechanical modeling of energy deposition by electrons in biologically important molecules. These calculations are used to determine parameters used as input to a Monte Carlo scheme to simulate energy deposition.

Radicals, and their importance to radiobiological processes are the subject of the next two papers. Li and Sevilla discuss electrons and holes produced in DNA models by ionizing radiation and the effect of these radicals on the subsequent chemical reactions of the biomolecules, while Turček addresses structures and energetics of nucleobase and carbohydrate radical reactions using density functional methods. The contribution from Cauët and Liévin focus on the DNA bases, using high level quantum mechanical methods to describe ionization potentials, interactions, and excited states.

The next contribution, authored by Stolterfoht *et al.*, treats one of the most ubiquitous processes in radiation damage studies: Namely electron capture and fragmentation of wa-

ter by swift ions. High levels of dynamical theory are used to calculate appropriate cross sections, which are compared to experimental results.

As much of the radiation damage in biological systems arises from secondary, or delta, electrons coming from ionization of water by the incoming radiation, the interaction of these electrons with biological molecules is of utmost importance in the overall understanding of radiation damage. In the next paper, Jack Simons uses high level quantum mechanical theory to discuss the formation of a transient negative ion (TNI) in a DNA fragment and the mechanism that leads to a subsequent strand break. This paper is followed by a contribution by Baccarelli *et al.*, which also deals with TNI's, but in this case, their formation from biological molecules in the gas phase. Continuing with the theme of electron attachment to biomolecules, Jalbout and Adamowicz present *ab initio* quantum mechanical studies of electron attachment to DNA base complexes. Following that paper, Sulik and Tőkési address the problem of the Fermi shuttle acceleration of secondary electrons using classical trajectory Monte Carlo methods.

The last two contributions in this volume with energy deposition or stopping power. Akar *et al.* discuss the stopping power of electrons by biological molecules, while Paul *et al.* consider the effects of stopping power on dosimetry.

All in all, we find this an informative and useful collection of papers, and we hope that you enjoy reading it as much as we enjoyed putting it together. Finally, we wish to thank all the authors for their help in producing this volume.

Erkki Brändas and John R. Sabin
Editors

Theoretical Studies of the Interaction of Radiation with Biomolecules

John R. Sabin

Department of Physics, University of Florida, Gainesville, FL, USA
and
Department of Chemistry, University of Southern Denmark, Odense, Denmark

Although the bulk of biological damage resulting from exposure to radiation comes from either single (SSB) or double (DSB) strand breaks in DNA, relatively few of these are produced by direct hits of ions or photons on DNA. Rather, because it is ubiquitous in the cell, most damage arises from decay products of the interaction of radiation with water: From δ (or secondary) electrons which can interact either directly or indirectly through water with a bio-molecule, or from $O^{\bullet}$ and $OH^{\bullet}$ free radicals. For massive ionizing radiation such as protons and alphas, this is almost entirely the case, whereas for photons, there is a larger possibility of exciting a molecule somewhat larger than water, or localized fragment of a molecule, causing electronic excitation which is followed by fragmentation or decomposition into radicals and electrons. For incident electrons, the process is similar, but here the electron can be captured into an excited state of the molecule, which then fragments into radicals and electrons. Understanding the interaction of radiation, both massive and mass-less particles, with biological targets becomes ever more important as we seek to protect healthy cells from radiation damage, and to target therapeutic radiation selectively on pathologic cells. The problem extends over many orders of magnitude in complexity, time scale, and size as the effects of the interaction of radiation with matter become more complicated: The initial reactions of radiation with molecules in the cell (the physical stage), through diffusion processes (the physical–chemical stage), to molecular dissociations and ionizations (the chemical phase), to attack and damage to DNA, to cell damage, tissue damage, organ damage, and eventually to possible death of the organism. The time scales for these processes begin with atto-seconds (the physical stage), and continue through tens of years (e.g. the Nagasaki studies [1,2]). At each stage, methods appropriate to the time and length scales must be used to investigate the phenomena and address the posited questions. Radiation protection involves scavenging the electrons and radicals before they can produce SSB's and DSB's, while therapy ideally involves irradiation only of those select cells that have damaged or mis-repaired DNA.

The overall aim of this volume is to describe cutting edge theoretical and computational methods to study individual ion/biomolecule collisions and the resulting ion tracks. Thus we intend to describe and, hopefully, understand the early steps in radiolysis of cells, leading to suggestions for possible new anti-radiation drugs and therapy protocols.

The problem of describing and explaining the effects of radiological action on biological systems is tremendous. In any such process, where there is exposure of a biological

ADVANCES IN QUANTUM CHEMISTRY, VOLUME 52
ISSN: 0065-3276 DOI: 10.1016/S0065-3276(06)52001-5

entity to radiation, be it for therapeutic or malevolent purposes, there are long chains of sequential and parallel actions, as well as possible non-linearities between initial radiogenic molecular changes and final biological effects [3–5]. The chain of events can be viewed in a hierarchical scheme beginning with the initial interaction of the radiation with a molecule in a biological sample. To wit: Initial reactions (physical phase) → diffusion (physical–chemical phase) → de-excitation and/or dissociation (chemical phase) → effects on DNA (e.g. multiple strand breaks) → effects on the cell → effects on tissue → effects on organs → and finally, effects on the organism. All of these processes must be well understood in order to deal effectively with problems such as radiation protection and radiation therapy.

There are two general ways to approach such a problem: Either top down or bottom up. Both are valid, and contribute greatly to the final understanding of the process. In this volume, most contributors take the bottom up approach, and, more particularly, apply quantum mechanical molecular scattering and electronic structure theory to the problem. Most papers thus use molecular theory to investigate various aspects of the interaction of radiation with biomolecular targets. As discussed here, calculations indicate the chances for successful inroads on the problem are good.

The interaction of radiation with molecular targets has broad and deep implications in almost all aspects of modern life. Some modern speculation involves the interaction of swift ions and/or photons (γ-radiation) with inter-stellar proto-biotic molecules to produce glycine, a precursor of life [6]. The interaction of ions and gammas can be used to treat, or cause, cancers, depending on the point of application and the nature of the radiation. Single, double, or multiple strand breaks in DNA can cause damage with resulting repair, mutation, or cell death.

One problem is that there are several sorts of radiation and particles that are of interest when one is concerned with the interaction of radiation with biological matter, and they interact with a molecule in one of two somewhat different ways. Photons interact via direct interaction and excitation of the electronic structure of the target molecule, be it water or a biomolecule. The resulting excitation can lead to ionization, decay, emission of secondary radiation, or fragmentation. Typically, in a macroscopic experiment, the energy deposition curve for photons is broad, meaning that energy is deposited along the entire track, until the beam reaches its penetration depth. Massive particles, however, deposit energy in a molecule by collision with either the electrons (the dominant mechanism) or the nucleus of the molecule. The collision typically results in electronic excitation of the target molecule, followed by ionization, decay, emission of secondary radiation, or fragmentation, as in the case of photons. In the ion case, however, the energy deposition is done predominantly at the end of the track, and the Bragg peak (the maximum in the energy deposition per unit path length) comes just before the particle comes to rest.

There are many sorts of radiation that can be investigated, the different classes of which are summarized below.

- Perhaps the most spectacular form of radiation, due to the large amount of energy that it can deposit in matter, is the highly charged, high energy heavy ion; Xe^{18+}, for example. Such ions blast through a biological sample wrecking havoc along the track. Although there may be few direct hits on biomolecules, water is ionized and fragmented abundantly, and the resulting radicals and δ-electrons cause great damage. Most ionic radiation is not so spectacular, however, and consists of the much more mundane, more common, and better understood swift protons and alphas. These particles also ionize and fragment water as well as causing damage by direct hits.

- Another form of radiation that has great significance in radiation biology is electrons. Although these particles interact with biomolecules in a very different way than do the heavy ions, they are produced in large numbers in heavy ion/water collisions in cells, and are responsible for much of the radiation damage in biological material. Electrons with kinetic energies in the eV range can be captured by molecules in a cell, resulting in transient negative ions and subsequent molecular fragmentation.
- Gammas and X-rays, in contrast to the forms mentioned above, are massless photons, and interact with a biological molecule in yet another way. These rays are highly penetrating, and can cause both ionization and fragmentation of water and the target biomolecule, but by excitation molecular electronic structure.
- A fourth type of radiation, neutrons, generally are not considered by molecular and collision theorists, as their collisions with molecules are exceedingly difficult to treat, due to their weak interaction with molecules. However, as the field develops one might expect neutrons to be studied in the future.
- Finally, there are many more exotic particles which are seldom treated, although, in many cases, there is no theoretical barrier to doing so. These include mesons such as muons, and various anti-particles such as anti-protons and positrons. We do note, however, that although not found with any great frequency in nature, many of these are easy to produce artificially and may have some use in tumor therapy and imaging. They may thus appear as subjects of study at a later time.

It would be a great step forward to be able to treat the interaction of all types of radiation with molecules on an equivalent theoretical basis. It would then be possible to make comparisons among various theories and calculations without making different assumptions and approximations for each type of radiation and energy range used. Although it is not yet possible to do this, the bare bones are available, and many of them are presented here.

It is hoped that this volume will provide a basis for understanding of the most fundamental processes that take place in radiation biology, namely a quantum mechanical description of the interaction of radiation with matter on the molecular level.

REFERENCES

[1] W. Zhang, C.R. Muirhead, N. Hunter, *J. Radiol. Prot.* **25** (2005) 393.
[2] W. Ruhm, L. Walsh, M. Chomentowski, *Rad. Env. Biophys.* **42** (2003) 119.
[3] C. von Sonntag, *The Chemical Basis for Radiation Biology*, Taylor and Francis, London, 1987.
[4] C. von Sonntag, *Free-Radical DNA Damage and its Repair—A Chemical Perspective*, Springer-Verlag, Heidelberg, 2005.
[5] T. Schlathölter, F. Alvardo, R. Hoekstra, *Nucl. Instrum. Methods B* **233** (2005) 62.
[6] Interstellar glycine search intensifies, *Chem. Eng. News* (14 February, 2005) 44.

Free-Radical-Induced DNA Damage as Approached by Quantum-Mechanical and Monte Carlo Calculations: An Overview from the Standpoint of an Experimentalist

Clemens von Sonntag

Max-Planck-Institut für Bioanorganische Chemie, Stiftstrasse 34-36, 45413 Mülheim an der Ruhr, Germany
and
Leibnitz-Institut für Oberflächenmodifizierung (IOM), Permoserstrasse 15, 04303 Leipzig, Germany
E-mail: clemens@vonsonntag.de

Abstract

The free-radical chemistry of DNA and its model systems has been widely studied by experimentalists as well as theoreticians. In the present paper, the important contributions of theory to a better understanding of this complex matter has been reviewed by an experimentalist with an emphasis on the following topics: modeling of DNA damage induced by ionizing radiation, pattern of $^{\bullet}$OH attack on DNA, ionization potentials and electron affinities of the nucleobases (reduction potentials), hole and electron transfer through DNA, tautomerization and isomerization reactions of DNA radicals, regioselectivity of $^{\bullet}$OH attack on the nucleobases, selectivity of free-radical attack at the sugar moiety, reactions of alkyl radicals, assignment of transients by quantum-chemical calculations of their electronic transitions, reduction potentials of DNA radicals, and DNA stability and repair. Some pending questions that may be tackled by theoreticians are addressed.

Contents

1. INTRODUCTION

Although most of the free-radical-induced DNA damage is repaired by the cellular repair enzymes, the remaining damage may lead to mutations (and eventually to cancer) and to

ADVANCES IN QUANTUM CHEMISTRY, VOLUME 52
ISSN: 0065-3276 DOI: 10.1016/S0065-3276(06)52002-7

reproductive cell death. The latter effect is the basis of radiotherapy, and one of the reasons for studying free-radical-induced DNA damage was the hope to improve radiotherapy by modifying DNA damage, e.g., by radiosensitizers (Adams, 1977). This, however, required a detailed knowledge of the free-radical-induced DNA damage and its repair. This and many other aspects of free-radical-induced DNA damage has let to a host of experimental data (for reviews see (von Sonntag, 1987, 2006)).

Quantum mechanical and other calculations have not only made important contributions in the interpretation of the experimental data, but in certain areas such as the relevance of clustered lesions as a function of radiation quality calculations preceded confirmation by the experiment.

The author of this review is an experimentalist with a more than limited knowledge of quantum chemistry or any other theoretical approach that has been used in the context of free-radical-induced DNA damage but highly admires the progress achieved by theoreticians. Since the ultimate goal of science is to solve the question "why?", an in-depth theoretical approach will always be the end of a chain of experiments that answered the questions "what?" (such as a product study) and "how?" (such as kinetics). The question "why?" has rarely been answered yet, but theories at their various levels of sophistication were often most helpful in assisting to answer at least the lower-level questions "what?" and "how?".

In this brief review, the considerable progress in understanding DNA free-radical chemistry using quantum mechanics and other theoretical approaches will be discussed. It is out of the area of competence of the reviewer to discuss the various methods, their strengths and their shortcomings, but a few, among the many, questions will be addressed, where theory could make major contributions to a better understanding of free-radical-induced DNA damage.

2. THE VARIOUS TYPES OF DNA DAMAGE

The backbone of DNA is made-up by 2-deoxyribose linked to the next unit by phosphate groups at the 3′- and 5′-positions. At the C1′ position, the nucleobases are bound via an *N*-glycosidic linkage.

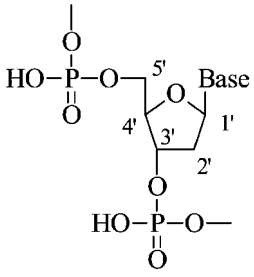

2-Deoxyribose unit

There are four nucleobases, the pyrimidines thymine (Thy, T) and cytosine (Cyt, C) and the purines adenine (Ade, A) and guanine (Gua, G). DNA forms a double helix held together by opposing AT and GC pairs that are hydrogen bridged.

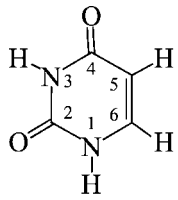

Uracil (Ura)

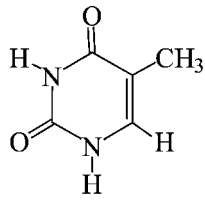

Thymine (Thy)

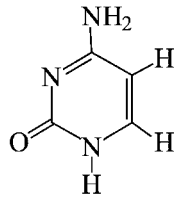

Cytosine (Cyt)

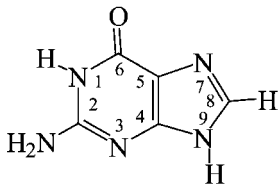

Guanine (Gua)

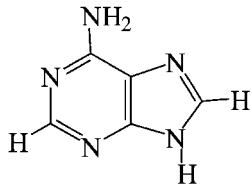

Adenine (Ade)

Free radicals may attack the nucleobases or the sugar moiety. With the nucleobases they may react by addition, oxidation (electron transfer) or H-abstraction (from the methyl group of Thy). In RNA, uracil (Ura) replaces Thy, and in many model studies Ura has been investigated rather than Thy. With the sugar moiety, only an H-abstraction is possible. The phosphate group is largely inert.

We thus may consider as DNA lesions first of all damaged bases, and as a result of a free-radical attack at the sugar moiety a single-strand break (SSB) and the release of an unaltered nucleobase. Two close-by SSBs give rise to a double-strand break (DSB). The free-radical chemistry of DNA being quite complex, a single attacking radical may lead to neighboring lesions (tandem lesion), and higher-order lesions (clustered damage) are also conceivable, notably with ionizing radiation (see below).

3. DNA DAMAGE BY IONIZING RADIATION—GENERAL ASPECTS AND MODELING

Recalling the importance of radiotherapy and the impact it has made to study free-radical-induced DNA damage, some aspects of the interaction of ionizing radiation with matter must be mentioned here very briefly. Charged particles such as high-energy electrons ionize the matter (M), whereby a radical cation ($M^{\bullet+}$) and two electrons of lower energy are formed [reaction (1)]. The latter may cause further ionizations. The radical cation may also retain some excess energy.

$$e^-_{\text{high-energy}} + M \rightarrow M^{\bullet+} + 2e^-_{\text{lower-energy}} \tag{1}$$

High-energy photons loose their energy by the Compton effect [reaction (2)] or the photo effect [reaction (3)].

$$h\nu + M \rightarrow M^{\bullet+} + e^-_{\text{high-energy}} + h\nu' \tag{2}$$

$$h\nu + M \rightarrow M^{\bullet+} + e^-_{\text{high-energy}} \tag{3}$$

The high-energy electrons may cause further ionizations. Eventually they are thermalized and become solvated [reaction (4)].

$$e^-_{\text{thermalized}} + nH_2O \rightarrow e^-_{aq} \tag{4}$$

Electrons that retain not enough energy to ionize matter but are not yet solvated are called epithermal or subexcitation electrons. They are only very short-lived, but despite of this they may undergo reactions with DNA that require an excess energy that solvated electrons cannot provide. While DNA strand breakage by e^-_{aq} is not observed in dilute aqueous solution (von Sonntag, 1987), an interaction of epithermal electrons with the phosphate group leads to strand breakage.

DFT calculations show that these reactions are exoenergetic but require an activation energy (Li *et al.*, 2003); for quantum-mechanical calculations see (Berdys *et al.*, 2004a); for base radical anions serving as a relay see (Berdys *et al.*, 2004b). It has been envisaged that low-energy-electrons could induce this reaction in competition to other reactions such as thermalization/solvation [reaction (4)] and addition to the bases (for reviews on the reactions of low-energy electrons in their reactions with DNA see (Sanche, 2002a, 2002b). Reactions (5)–(7) have been indeed observed under certain conditions (Becker *et al.*, 2003). Subexcitation electrons (< 3 eV) may also release Thy from DNA (Abdoul-Carine *et al.*, 2004).

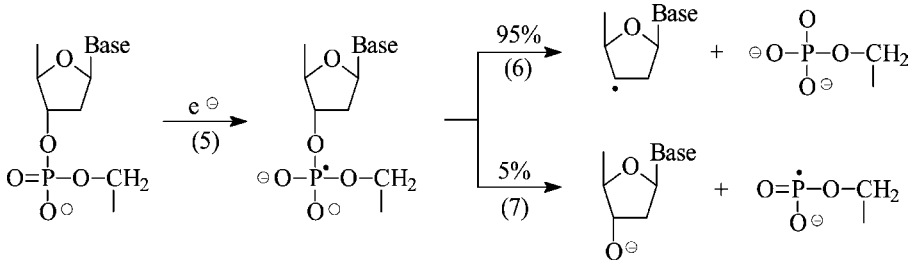

Cells consist to about 70% of water, and thus the radiolysis of water [reaction (8)] is of a major importance.

$$H_2O + \text{ionizing radiation} \rightarrow {}^{\bullet}OH, e^-_{aq}, H^{\bullet}, H_2, H_2O_2, H^+ \tag{8}$$

The radicals $^{\bullet}OH$, e^-_{aq} and $H^{\bullet}$ are highly reactive, and in a cellular environment their diffusion length is only very short. For this reason, DNA damage is only caused by those water radicals that are created in the very neighborhood of DNA. This effect has been termed 'indirect effect'. In model studies, this effect can be mimicked by irradiating DNA in aqueous solution, and it is mainly reaction (10) that is of consequence.

$$^{\bullet}H/(e^-_{aq} + H^+) + DNA \rightarrow DNA(^{\bullet}H) \tag{9}$$

$$DNA + {}^{\bullet}OH \rightarrow DNA(^{\bullet}OH). \tag{10}$$

For cellular DNA damage, there is a second source, the 'direct effect'. Here, the energy of the ionizing radiation is absorbed by DNA itself leading to DNA radical cations ($DNA^{\bullet+}$) and electronically excited DNA (DNA*) [reactions (11) and (12)].

$$DNA + \text{ionizing radiation} \rightarrow DNA^{\bullet+} + e^- \tag{11}$$

$$DNA + \text{ionizing radiation} \rightarrow DNA^* \tag{12}$$

It is not easy to disentangle contributions by the 'direct effect' and the 'indirect effect' experimentally, and it is hoped that theoretical approaches of the various kinds (cf. (Friedland *et al.*, 1999, 2003; Bernhardt *et al.*, 2003, 2004; Valota *et al.*, 2003)) will provide a better estimate of the 'indirect effect' than the 60–70% that have been obtained by •OH-scavenging experiments (von Sonntag, 2006).

With sparsely ionizing radiation such as γ-rays, the energy of ionizing radiation is deposited in packages, called spurs, of 100 eV on average. With densely ionizing radiation such as α-particles, these spurs overlap and form a 'track'. The relative biological efficiency (RBE) of densely ionizing radiations is markedly higher than that of sparsely ionizing radiation. In a mammalian cell, about 700 8-oxo-adenines (a typical single-base lesions), 1000 single-strand breaks (SSBs), 40 double-strand breaks (DSBs) and 150 DNA-protein cross-links are formed per 1 Gy that cause 0.2–0.8 lethal events (Ward, 1988; Goodhead, 1994). This has led to the conclusion that in most cases such relatively 'simple' lesions are successfully repaired by the repair enzymes. Thus, much more complex lesions (clustered lesions) are responsible for lethality. This concept of clustered lesions is compatible with an increase of RBE on going from sparsely to densely ionizing radiation. Here, modeling of tracks of ionizing radiation and their interaction with DNA was essential in a better understanding of the RBE and the development of the concept of clustered lesions (Charlton *et al.*, 1989; Nikjoo *et al.*, 1989, 1994, 1997). These calculations triggered a number of experiments that support this concept (Gulston *et al.*, 2004, 2002). It is noteworthy that the anticancer drugs bleomycin and neocarzinostatin, both based on free-radical-induced DNA damage (for a quantum-chemical study concerning mechanistic aspects of bleomycin functioning see (Neese *et al.*, 2000), are capable of producing DSBs and most likely also higher-level clustered lesions (von Sonntag, 2006).

Monte Carlo-type calculations have now been advanced to such a high level that the interaction of a ionizing particle track through the nucleus of a cell can be simulated to an extent that together with suitable assumptions provide information that are still very difficult to measure experimentally. Thus, also here, theoreticians lead the way into a new area of research. For sharpening his analytical tools, the analytical chemist/biochemist must know what he should look for, and here the theoreticians lead the way. Below, there will be examples, where it is the other way round, that is, there are many high-quality experimental data that still await an adequate theoretical interpretation.

4. PATTERN OF •OH ATTACK ON DNA

Since the structure of DNA is sequence-dependent (leading to variations in the minor groove width and other structural parameters), the nucleobases and the various hydrogens of the sugar moiety are differently exposed to an attack by •OH. Moreover, the various nucleobases have different rate constants (cross-sections) in their reaction with •OH. Thus, •OH-attack on the various H-atoms of the sugar moiety must vary along the DNA chain. As a consequence, the probability of effects related to H-abstraction of certain hydrogens such as the production of frank SSBs varies from base pair to base pair. A model, called RADACK (RADiation attACK) that allows to calculate the probability of reaction of sugar and nucleobases with •OH, based on the structures of DNA or DNA-ligand complexes obtained by NMR, crystallography or molecular modelling has been developed (Begusova

et al., 1999, 2000a, 2000b, 2001a, 2001b, 2005; Michalik *et al.*, 1995a, 1995b, 1995c; Sy *et al.*, 2001, 1997; Tartier *et al.*, 1994, 1998). It is also capable of predicting the pattern single-strand breakage of large DNA sections and the protection of DNA sections by a bound protein such as the lactose suppressor (Begusova *et al.*, 2001a). Recently, the model was expanded to proteins and allows to calculate the probability of damage at each residue of a (free or DNA bound) protein of known structure (Gillard *et al.*, 2004; Begusova *et al.*, 2005). Because of its high predictive potentials, this program can support, on the basis of the experimental SSB patterns, one or another of different structures proposed by NMR or crystallography for a DNA-protein. It would be interesting to see, whether it has the potential to be further developed, for example, into predicting preferential sites of DNA-protein cross-links. As to the mechanism of this lesion, our knowledge is still rather limited (von Sonntag, 2006). But experimental data (once available), when introduced into the RADACK model, would lead to most valuable information.

5. IONIZATION POTENTIALS AND ELECTRON AFFINITIES OF THE NUCLEOBASES (REDUCTION POTENTIALS)

For many aspects of the free-radical chemistry of DNA, the ionization potentials and electron affinities of the nucleobases (reduction potentials) play a dominant role. The accurate experimental determination of the reduction potentials of the nucleobases at pH 7 in an aqueous environment [$E^7(N^{\bullet+}/N)$ and $E^7(N/N^{\bullet-})$] is not possible for all nucleobases or fraught with a considerable error. Moreover, this property changes substantially on going from the free nucleobase (nucleoside/nucleotide) to DNA. Here, the environment of the nucleobase plays a dramatic role (see below). It is, therefore, highly desirable to arrive at such values by quantum-mechanical calculations. The reduction potentials of the nucleobases and related compounds have recently been calculated (Baik *et al.*, 2001). This study shows that quantum-mechanical calculations are now at a level that they can be used with advantage to predict the reduction potential of a given compound (here: altered nucleobases) without having it synthesized laboriously.

In the study of the electron affinity of Thy it became apparent that the choice of the level of theory is most important (Li *et al.*, 2002a, 2002b, 2002c). At the highest level that was available at that time or was feasible with respect to computing time the deviation of the computed value from the experimental one was 0.3 V. This is quite good, but not good enough for the prediction of exact reduction potentials, where an uncertainty of much less than 0.1 V is required. Thus, further improvements of theory and programs are urgently needed. In this context, it may be of interest that calculations based on Gaussian 98 yielded values closer to the experimental one than, at the same level of theory, Gaussian 03 (Naumov and von Sonntag, 2006).

6. HOLE AND ELECTRON TRANSFER THROUGH DNA

Among the DNA constituents, G has the lowest ionization potential. This is further reduced, when two or three Gs are next to one another (GG; GGG). Quantum mechanical calculations indicate that this effect is dramatic, and a gain of 0.7 eV on going from $G^{\bullet+}$

to $GG^{\bullet+}$ has been calculated (Saito *et al.*, 1998). The 5′-G is the preferred cleavage site in a GG trap, and in the GGG trap it is either the 5′-G or the middle G depending on the nucleobases neighboring the trap (for references see (Davis *et al.*, 2000)). This aspect has also been addressed by quantum-mechanical calculations (Voityuk *et al.*, 2000). Hole transfer from one-electron oxidized DNA constituents such as $T^{\bullet+}$, $C^{\bullet+}$, $A^{\bullet+}$, the radical cations formed in the course of DNA strand breakage (upon $^{\bullet}OH$ attack at C4′ (Dizdaroglu *et al.*, 1975)), and one-electron oxidants tethered to or reacting with DNA can not only occur to a neighboring G leading to $G^{\bullet+}$ but also over a large distance. Even $G^{\bullet+}$ can undergo hole transfer to, e.g., a GGG site forming predominantly $GG^{\bullet+}G$. In Chapter 12 of (von Sonntag, 2006), experimental details are reviewed. In the area of free-radical-induced DNA damage, hole transfer through DNA has been most widely and most successfully studied by quantum mechanics (Jortner *et al.*, 1998; Turro and Barton, 1998; Mujica *et al.*, 1999; Bixon *et al.*, 1999; Grozema *et al.*, 1999, 2000, Ye *et al.*, 1999; Berlin *et al.*, 2000, 2001a, 2001b, 2002, 2004; Conwell and Rakhmanova, 2000; Giese and Spichty, 2000; Schlag *et al.*, 2000; Bixon and Jortner, 2001, 2002; Olofsson and Larsson, 2001; Treadway *et al.*, 2002; Senthilkumar *et al.*, 2005). The reviewer is not in the position to discuss the various approaches in adequate detail and refers to the literature.

In the context of hole transfer one has to consider that the radical cations, notably $G^{\bullet+}$, also react with water and by proton transfer in competition. This question has been addressed by quantum chemical calculations (Reynisson and Steenken, 2002a, 2002b, 2002c).

For electron transfer through DNA there are not as detailed theoretical studies available as for hole transfer (Wagenknecht, 2003). This is very surprising, since a biologically most important process, the enzymatic repair of pyrimidine dimers (the major UV-induced DNA damage), may occur by electron transfer through the base stack (Schwögler *et al.*, 2000). The sequence of electron affinities of the nucleobases have been calculated at Thy > Cyt > Ade > Gua (Li *et al.*, 2002a); for the effect of base pairing see Li *et al.*, (2001, 2002b), Richardson *et al.* (2003).

7. TAUTOMERIZATION AND ISOMERIZATION REACTIONS OF DNA RADICALS

The intermediates that are formed upon free-radical attack on DNA or its constituents are again free radicals, and thus they may be characterized by EPR if sufficiently long-lived. Quantum-mechanical calculations of their hyperfine coupling constants has now become an indispensable tool (Close *et al.*, 2000; Close, 2003; Geimer *et al.*, 2000; Naumov *et al.*, 2000, 2001, 2003; Naumov and Beckert, 2002). Often, a number of radicals may be formed in a given reaction, and then the high predictive power of such calculations allows one to exclude certain potential intermediates. When deprotonation/reprotonation (at another site) reactions are fast compared to the radical lifetime, only the final (thermodynamically most stable) radical may be detected by conventional EPR. In favorable cases such as the fast protonation of the Thy radical anion at oxygen (not detected by EPR) followed by a slow protonation at C(6) (detected by EPR) [reactions (13) and (14)], pulse radiolysis may provide the missing information (Deeble *et al.*, 1985).

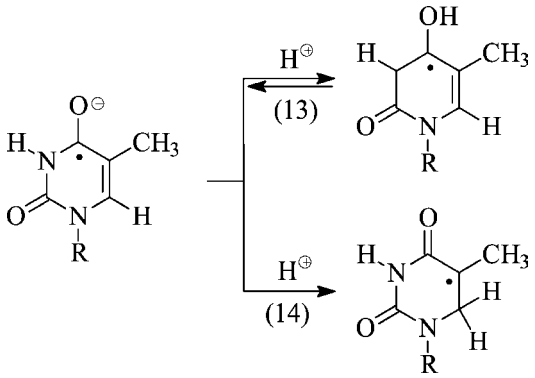

However in another case, the $SO_4^{\bullet -}$-induced oxidation of dCyd, pulse radiolysis data did not provide enough information to ascertain the tautomerization reaction (15).

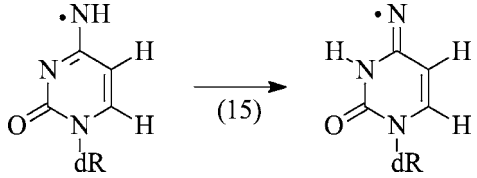

Yet, the EPR spectrum was that characteristic that its assignment by quantum-mechanical calculations was without doubt (Naumov *et al.*, 2001). In all these reactions, the first species (not detected by conventional EPR) is formed for kinetic reasons, and the final one (detected by EPR) is the thermodynamically favored one. The energetics of these transformations are also accessible by quantum-chemical calculations as is the acid-catalyzed rearrangement of the Thy C5 •OH-adduct (kinetically favored; see below) into the thermodynamically favored C6 •OH-adduct [reaction (16)] (Naumov and von Sonntag, 2006).

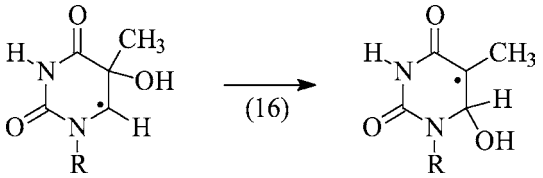

For the dGuo radical (•G, formed upon deprotonation of the dGuo radical cation, $G^{\bullet +}$) two isomers can be written, •G(N1) and •G(N2).

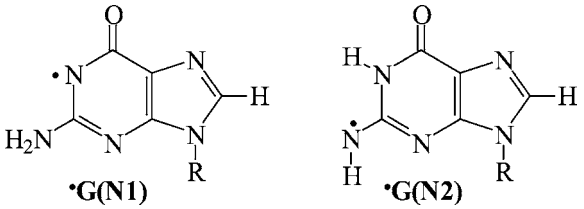

The radical observed in γ-irradiated single-crystals is the •G(N2) radical (Hole *et al.*, 1987, 1989, 1992a, 1992b; Close *et al.*, 1985; Nelson *et al.*, 1988), and as a recombination product in the photoexcitation of a ruthenium complex in the presence of dGMP (Jaquet *et al.*, 1995), while •G(N1) has been assumed to dominate in aqueous solution (Steenken,

1989). In the gas phase, •G(N2) has been calculated as the stable species (Mundy *et al.*, 2002; von Sonntag, 2006); an energy-richer rotamer (local minimum) seems to have been calculated by (Wetmore *et al.*, 1898). Quantum-mechanical calculations now show that the energy difference between these two tautomers is only small and that due to the much higher dipole moment of •G(N1) as compared to that of •G(N3) (von Sonntag, 2006), the former dominates in a high dielectric constant environment such as water, while the latter is thermodynamically favored in an environment of low to medium dielectric constant such as the single-crystal.

8. REGIOSELECTIVITY OF •OH ATTACK ON THE NUCLEOBASES

Hydroxyl radicals are highly electrophilic (Anbar *et al.*, 1966). With nucleosides, they react preferentially by adding to C–C and C–N double bonds, while H-abstraction from the sugar moiety and the methyl group in Thy is of lesser importance (von Sonntag, 2006) despite the high HO–H binding energy. In general, •OH undergoes electron transfer only very reluctantly (von Sonntag, 2006), although the reduction potential at pH 7 is $E^7 = 1.9$ V (Wardman, 1989). In principle, this would allow the one-electron oxidation of all nucleobases, but this reaction does not take place for kinetic reasons. These principal features have to be taken into account when addressing the reaction of •OH with the nucleobases.

The rate of reaction of •OH with the nucleobases is close to diffusion-controlled. Yet in the pyrimidines, there is a high regioselectivity towards an attack at C5 [reaction (17)] (Fujita and Steenken, 1981; Hazra and Steenken, 1983), despite the fact that the radical resulting from an attack at C6 [reaction (19)] is the thermodynamically favored one. This has been explained by the electrophilic nature of the •OH radical that seeks the site of highest electron density, here C5.

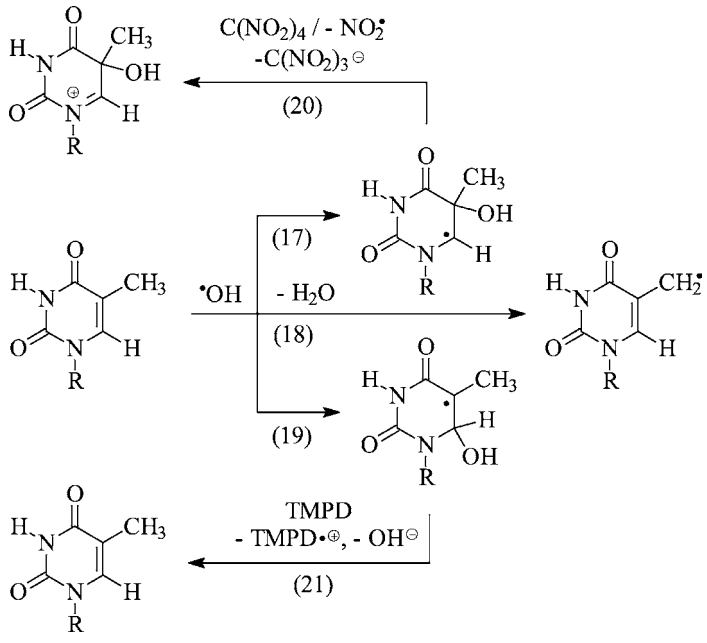

The concept of the "site of highest electron density" as the main determinant for the observed regioselectivity breaks down, when the purines are studied, and it seems that in the purine series the Mulliken charge is of an even higher importance (von Sonntag, 2006). For a better understanding of the phenomenon of regioselectivity, more refined quantum mechanical calculations would be most welcome.

The $^{\bullet}$OH reactions with the nucleobases are a typical example that kinetics may override thermodynamics. An addition to the C–C double bond [cf. reaction (17) and (19)] has been calculated at $\Delta G = -62.6\,\mathrm{kJ\,mol^{-1}}$ and $\Delta G = -85.5\,\mathrm{kJ\,mol^{-1}}$, respectively, while an H-abstraction at methyl [reaction (18)] is with $\Delta G = -117.2\,\mathrm{kJ\,mol^{-1}}$ much more exothermic (Wu *et al.*, 2004). Yet, the latter reaction only occurs at about 10% (Fujita and Steenken, 1981). Another example is Gua where it has been calculated that $^{\bullet}$OH would preferentially abstract a hydrogen giving rise to the guanyl radical, $^{\bullet}$G (Mundy *et al.*, 2002). In aqueous solution, however, this reaction does not occur at all, and the thermodynamically less favorable $^{\bullet}$OH adducts are formed instead (von Sonntag, 2006). Another example of kinetics overrunning thermodynamics may be found in the reaction of thiols with alkyl radicals. Due to quantum-mechanical calculations, this reaction is now fairly well understood (Reid *et al.*, 2002; Reid *et al.*, 2003). From this, it follows that in quantum-chemical calculations of the mechanism of the formation and reactions of DNA radicals one should not be guided exclusively by thermodynamical considerations.

9. SELECTIVITY OF FREE-RADICAL ATTACK AT THE SUGAR MOIETY

There is always a competition between a free-radical attack at the bases and at the sugar moiety. This internal competition has been addressed in a recent computational study (Bluett and Green, 2006). The bond dissociation energy (BDE) of the hydrogen atoms in the 2-deoxyribose moiety varies considerably (Miaskiewicz and Osman, 1994). According to a quantum-chemical calculation on 2′-deoxyguanosine, the C–H BDE increases in the sequence C1′–H < C4′–H < C3′–H < C5′–H < C2′–H (Steenken *et al.*, 2001). This is certainly one if not the major reason why intramolecular H-transfer reactions involving a base radical and the C2′–H are observed in the polyribonucleotide poly(U) (Deeble *et al.*, 1986) but not in DNA. In poly(U), the C2′–H is weakened by 10–20 $\mathrm{kJ\,mol^{-1}}$ due to the neighboring OH. For such an H-transfer to occur within DNA, a radical as highly reactive as the uracilyl radical [BDE(vinylic C–H) = $465\,\mathrm{kJ\,mol^{-1}}$; (Berkowitz *et al.*, 1994)] is required. The allylic C–H [BDE(allylic C–H) = $367\,\mathrm{kJ\,mol^{-1}}$; (Berkowitz *et al.*, 1994)] is weaker by about $16\,\mathrm{kJ\,mol^{-1}}$ than the C1′–H (Naumov and von Sonntag, 2006), and attack of poorly H-abstracting radicals such as peroxyl radicals [BDE(hydroperoxidic O–H) = $366\,\mathrm{kJ\,mol^{-1}}$ (Golden *et al.*, 1990)] seem to react with the methyl group of thymine rather than with the C1′–H (Martini and Termini, 1997). Moreover, there are recent data on the formation of C1′ oxidation products in DNA (Roginskaya *et al.*, 2005). The reported yields are that high that they cannot be explained on the basis of an $^{\bullet}$OH attack at this position only (note that in B-DNA the C1′–H is difficult to access by freely diffusing radicals (Miaskiewicz and Osman, 1994; Sy *et al.*, 1997; Begusova *et al.*, 2001b). There is certainly more work required to understand such H-transfer reactions. They are likely involved in the formation of clustered lesions, and this makes them that interesting. Quantum chemistry could be leading here.

There is yet another type of H-abstraction that is not at all understood at present. The famous, well-known since decades (Keck *et al.*, 1966; Keck, 1968; Raleigh *et al.*, 1976; Mariaggi *et al.*, 1976; Raleigh and Blackburn, 1978; Haromy *et al.*, 1980; Berger and Cadet, 1983; Raleigh and Fuciarelli, 1985; von Sonntag, 1994), purine-8,5-cyclonucleosides/tides require at one stage a C5′ radical which is commonly assumed to be generated by H-abstraction by $^{\bullet}$OH. However, the (strongly pH-dependent) yields are much too high to allow this reaction to be the dominant one (von Sonntag, 2006). Base radicals must hence be involved in this H-abstraction. But to make the interpretation more difficult, the C5′–H is not the most likely one to be abstracted on thermodynamical grounds (BDE; see above). This H-transfer seems to require a complex of a purine nucleoside/tide radical and a purine nucleoside/tide wherefrom the H-transfer occurs that specifically. Here, quite elaborate quantum-mechanical calculations could be of help. As it stands, it is not foreseen how to tackle this problem experimentally.

10. REACTIONS OF ALKYL RADICALS

In contrast to $^{\bullet}$OH and H$^{\bullet}$ that are electrophilic, alkyl radicals are nucleophilic. In their reactions with the pyrimidines they add preferentially at C6 (Schuchmann *et al.*, 1986). Likewise, they react with purines faster when the purines are protonated (Aravindakumar *et al.*, 1994). Such reactions involving protein-derived radicals could be of importance in DNA–protein cross-linking, but the sugar-derived radicals and the nucleobase $^{\bullet}$OH-adduct radicals and the allylic Thy radical are also alkyl-type radicals. Indeed, tandem lesions involving the latter have already been detected (Box *et al.*, 2000; Bellon *et al.*, 2002; Hong and Greenberg, 2005; Hong *et al.*, 2006). Sugar-derived radicals are also alkyl-type radicals, and their addition to a neighboring nucleobase results in the formation of cyclonucleotides (von Sonntag, 2006). Recent DFT calculations provide free-energy barriers and reaction free energies of such reactions (Zhang and Erikson, 2006). Addition of a sugar radical to a nucleobase at some distance within the same or the other strand would result in a intramolecular DNA–DNA cross-link in the form of a small loop. Such a lesion has not yet detected (looked for). It is usually considered unlikely, because DNA is typically seen as a rigid rod. Here, simulations that take the flexibility of DNA into account could be most helpful to indicate the loop sizes that one would be concerned with here. Whether such reactions would take place *in vivo* where most of the DNA is covered by proteins, would be the next question.

11. REDUCTION POTENTIALS OF DNA RADICALS

Our knowledge of the position of $^{\bullet}$OH attack on pyrimidines and purines is largely based on the redox properties of the resulting radicals. For example, an $^{\bullet}$OH attack at C6 of the pyrimidines leads to an oxidizing radical [monitored by an oxidation of N, N, N', N'-tetramethylphenylenediamine; reaction (21)], while an attack at C5 produces a reducing radical (monitored by a reduction of tetranitromethane, reaction (20)] (Fujita and Steenken, 1981; Hazra and Steenken, 1983).

In the purine series, the situation is much more complex (Steenken, 1989, von Sonntag, 2006). The purine radical cations (A$^{\bullet+}$ and G$^{\bullet+}$) and the corresponding conjugate

bases ($A^{\bullet}$ and $G^{\bullet}$) are the most strongly oxidizing radicals in the purine series (they may be formed by strong one-electron oxidants such as $SO_4^{\bullet-}$ and Tl^{2+} and upon water elimination of some of the $^{\bullet}OH$ adduct radicals) (von Sonntag, 2006). They are the only oxidizing nucleobase radicals for which reduction potentials have been determined with some accuracy [$E^7(\text{Ado}^{\bullet+}/\text{Ado}) = 1.59$ V, $E^7(\text{Guo}^{\bullet+}/\text{Guo}) = 1.29$; $pK_a(\text{dAdo}^{\bullet+}) < 1$, $pK_a(\text{dGuo}^{\bullet+}) = 3.9$] (Steenken and Jovanovic, 1997). The most strongly reducing radicals are the pyrimidine radical anions [$E^7(\text{Thy}/\text{Thd}^{\bullet-}) = -1.2$ V, $E^7(\text{Cyd}/\text{Cyd}^{\bullet-}) = -1.15$ V; the pK_a value of the conjugate acid of $\text{Thd}^{\bullet-}$ is near 7, that of the conjugate acid of $\text{Cyd}^{\bullet-}$ is > 13] (von Sonntag, 2006). It would be interest to have also the reduction potentials of the pyrimidine and purine $^{\bullet}OH$ adduct radicals. There are no experimental data on such species; they have only been grouped as 'reducing', 'oxidizing' and 'neither reducing nor oxidizing' (von Sonntag, 2006). In reduction processes, the proton-coupled electron transfer (PT–ET) that lower the overall free energy is a common phenomenon (Rehm and Weller, 1970; Atherton and Harriman, 1993); for a theoretical treatment see (Cho and Shin, 2000, and references cited therein). In the case of $^{\bullet}OH$ adduct radicals, one also may speculate, whether electron transfer could be coupled with the loss of OH^-. The parent pyrimidine/purine would then be formed without an electron adduct as an intermediate. Potential alternatives are exemplified in reactions (22)–(27).

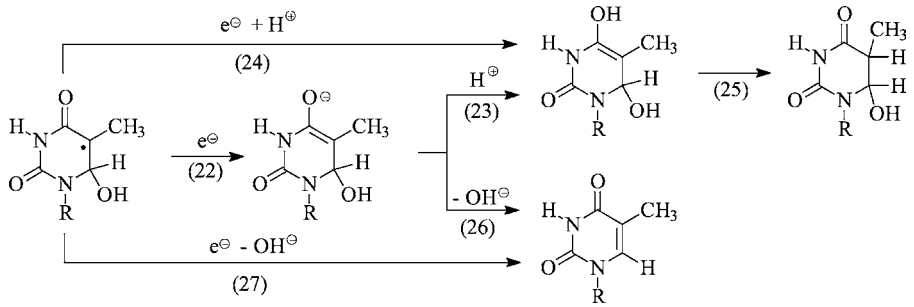

Reaction (22) is a simple electron transfer (ET) leading to the enolate that subsequently can be protonated to the enol [reaction (23)], while reaction (24) is a PT–ET process that leads directly to the enol. The enol is not stable and can ketonize [reaction (25)]. The enolate may also eliminate OH^- giving rise to the parent pyrimidine [reaction (26)]. The same product would be formed if in an ET coupled with an elimination of OH^- [reaction (27)]. Experimentally, it would be difficult to distinguish between reaction (27) and reaction (22) followed by (26), but quantum-mechanical calculations could possibly falsify/support the feasibility of reaction (27). The free energy that would have to be associated with the reduction of this radical will certainly depend on the route that is taken.

12. ASSIGNMENT OF TRANSIENTS BY QUANTUM-CHEMICAL CALCULATIONS OF THEIR ELECTRONIC TRANSITIONS

In pulse radiolysis and laser flash photolysis experiments, transients that absorb in the UV and sometimes also in the visible are the basis for an interpretation of the reaction kinetics and the reaction products. There are often more than one transient formed side by side. It would be highly desirable to assign such transients to a given chemical species on the basis of the quantum-chemical calculation of their electronic transitions. The early

attempt to do this for the •OH and H• adducts of the pyrimidines (Krauss and Osman, 1993) failed to give an acceptable agreement with the experiment (Deeble *et al.*, 1985; Deeble and von Sonntag, 1985). The reason for this was the low level of theory and the limited computer facilities available at that time. Yet, we have learned a lot from these studies despite their shortcomings. This also holds for the calculations of the optical transitions (Krauss and Osman, 1994) of vinyl peroxyl radicals that absorb in the visible. Such a species is formed in the reaction of O_2 with the uracilyl radical, an important species in the free-radical chemistry of 5-bromo- and 5-iodouracil [reaction (28)–(30); for DFT calculations see Li *et al.* (2002c)].

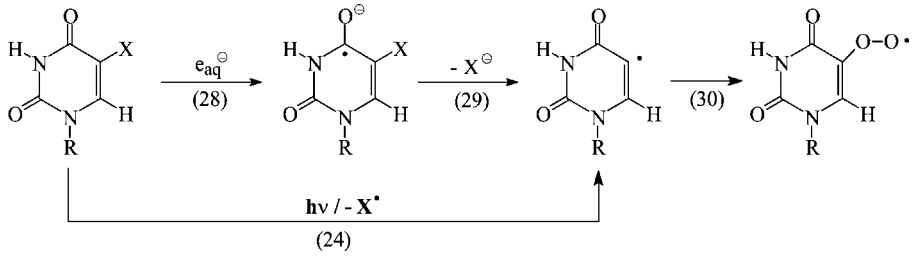

The quality of the quantum-chemical chemical calculations has changed remarkably recently. The calculations of the UV spectrum and oscillator strength of isocytosine (an intermediate observed upon pulse radiolysis of Cyt) as compared to its thermodynamically favored isomer Cyt [reactions (31) and (32)] gave reasonable agreement with the experiment (Schuchmann *et al.*, 2005).

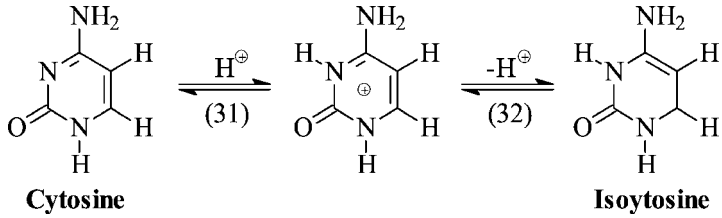

This is a closed shell species, and thus the good agreement is not too surprising. Yet when the earlier calculations on the electronic transitions of the vinylperoxyl radicals and related species were resumed using a higher-level theory, agreement with the experiments improved considerably (Naumov and von Sonntag, 2005). Further refinements are highly desirable to make quantum-mechanical calculations a general tool for the assignment of free-radical intermediates.

13. DNA STABILITY AND REPAIR

When a nucleobase has been altered or eliminated (apyrimidinic/apurinic, AP, site), hydrogen bonding between the opposing bases is impaired and the local melting temperature reduced (for the striking effect of an AP site see (Bales *et al.*, 2002). The alterations, including bulging due to partial melting, that are induced must be the target for a damage recognition by the repair enzymes. It will be a great step towards the understanding of repair processes if such target–enzyme interactions could be addressed by, necessarily sophisticated, calculations. A very first step in this direction has been done a decade

ago by calculating the structure if thymine glycol and dihydrothymine embedded in DNA (Miaskiewicz *et al.*, 1993).

REFERENCES

Abdoul-Carine, H., Gohlke, S., Fischbach, E., Scheike, J., Illenberger, E., 2004. *Chem. Phys. Lett.* **387**, 267.

Adams, G.E., 1977. In: Becker, F.F. (Ed.), *Radiotherapy, Surgery, and Immunotherapy*. Plenum Press, New York, p. 181.

Anbar, M., Meyerstein, D., Neta, P., 1966. *J. Phys. Chem.* **70**, 2660.

Aravindakumar, C.T., Mohan, H., Mudaliar, M., Rao, B.S.M., Mittal, J.P., Schuchmann, M.N., von Sonntag, C., 1994. *Int. J. Radiat. Biol.* **66**, 351.

Atherton, S.J., Harriman, A., 1993. *J. Am. Chem. Soc.* **115**, 1816.

Baik, M.-H., Silverman, J.S., Yang, I.V., Ropp, P.A., Szalay, V.A., Yang, W., Thorp, H.H., 2001. *J. Phys. Chem. B* **105**, 6437.

Bales, B.C., Pitié, M., Meunier, B., Greenberg, M.M., 2002. *J. Am. Chem. Soc.* **124**, 9062.

Becker, D., Bryant-Friedrich, A., Trzasko, C.-A., Sevilla, M.D., 2003. *Radiat. Res.* **160**, 174.

Begusova, M., Eon, S., Sy, D., Culard, F., Charlier, M., Spotheim-Maurizot, M., 2001a. *Int. J. Radiat. Biol.* **77**, 645.

Begusova, M., Gillard, N., Sy, D., Castaing, B., Charlier, M., Spotheim-Maurizot, M., 2005. *Radiat. Phys. Chem.* **72**, 265.

Begusova, M., Spotheim-Maurizot, M., Michalik, V., Charlier, M., 2000a. *Int. J. Radiat. Biol.* **76**, 1.

Begusova, M., Spotheim-Maurizot, M., Sy, D., Michalik, V., Charlier, M., 2001b. *J. Biomol. Struc. Dyn.* **19**, 141.

Begusova, M., Sy, D., Charlier, M., Spotheim-Maurizot, M., 2000b. *Int. J. Radiat. Biol.* **76**, 1063.

Begusova, M., Tartier, L., Syt, D., Spotheim-Maurizot, M., Michalik, V., Charlier, M., 1999. *Int. J. Radiat. Biol.* **75**, 913.

Bellon, S., Ravanat, J.-L., Gasparutto, D., Cadet, J., 2002. *Chem. Res. Toxicol.* **15**, 598.

Berdys, J., Anusiewicz, I., Skurski, P., Simons, J., 2004a. *J. Am. Chem. Soc.* **126**, 6441.

Berdys, J., Anusiewicz, I., Skurski, P., Simons, J., 2004b. *J. Phys. Chem. A* **108**, 2999.

Berger, M., Cadet, J., 1983. *Chem. Lett.* **12**, 435.

Berkowitz, J., Ellison, G.B., Gutman, D., 1994. *J. Phys. Chem.* **98**, 2744.

Berlin, Y.A., Burin, A.L., Ratner, M.A., 2000. *J. Phys. Chem. A* **104**, 443.

Berlin, Y.A., Burin, A.L., Ratner, M.A., 2001a. *J. Am. Chem. Soc.* **123**, 260.

Berlin, Y.A., Burin, A.L., Ratner, M.A., 2002. *Chem. Phys.* **275**, 61.

Berlin, Y.A., Burin, A.L., Siebbeles, L.D.A., Ratner, M.A., 2001b. *J. Phys. Chem. A* **105**, 5666.

Berlin, Y.A., Kurnikov, I.V., Beratan, D., Ratner, M.A., Burin, A.L., 2004. *Top. Curr. Chem.* **237**, 1.

Bernhardt, P., Friedland, W., Paretzke, H.G., 2004. *Radiat. Environ. Biophys.* **43**, 77.

Bernhardt, Ph., Friedland, W., Jacob, P., Paretzke, H.G., 2003. *Int. J. Mass Spectrom.* **223–224**, 579.

Bixon, M., Giese, B., Wessely, S., Langenbacher, T., Michel-Beyerle, M.E., Jortner, J., 1999. *Proc. Natl. Acad. Sci. USA* **96**, 11713.

Bixon, M., Jortner, J., 2001. *J. Phys. Chem. A* **105**, 10322.

Bixon, M., Jortner, J., 2002. *Chem. Phys.* **281**, 393.

Bluett, V., Green, N.J.B., 2006. *J. Phys. Chem. A* **110**, 4736.

Box, H.C., Patrzyc, H.B., Dawidzik, J.B., Wallace, J.C., Freund, H.G., Iijima, H., Budzinski, E.E., 2000. *Radiat. Res.* **153**, 442.

Charlton, D.E., Nikjoo, H., Humm, J.L., 1989. *Int. J. Radiat. Biol.* **56**, 1.

Cho, S.-I., Shin, S., 2000. *J. Mol. Struct. (Theochem)* **499**, 1.

Close, D.M., 2003. In: Leszczynski, J. (Ed.), *Computational Chemistry, Reviews of Current Trends*, vol. 8. World Scientific, Singapore, p. 209.

Close, D.M., Eriksson, L.A., Hole, E.O., Sagstuen, E., Nelson, W.H., 2000. *J. Phys. Chem. B* **104**, 9343.

Close, D.M., Sagstuen, E., Nelson, W.H., 1985. *J. Chem. Phys.* **82**, 4386.

Conwell, E.M., Rakhmanova, S.V., 2000. *Proc. Natl. Acad. Sci. USA* **97**, 4556.

Davis, W.B., Naydenova, I., Haselsberger, R., Ogrodnik, A., Giese, B., Michel-Beyerle, M.E., 2000. *Angew. Chem. Int. Ed.* **39**, 3649.

Deeble, D.J., Das, S., von Sonntag, C., 1985. *J. Phys. Chem.* **89**, 5784.

Deeble, D.J., Schulz, D., von Sonntag, C., 1986. *Int. J. Radiat. Biol.* **49**, 915.
Deeble, D.J., von Sonntag, C., 1985. *Z. Naturforsch.* **40c**, 925.
Dizdaroglu, M., von Sonntag, C., Schulte-Frohlinde, D., 1975. *J. Am. Chem. Soc.* **97**, 2277.
Friedland, W., Jacob, P., Bernhardt, P., Paretzke, H.G., Dingfelder, M., 2003. *Radiat. Res.* **159**, 401.
Friedland, W., Jacob, P., Paretzke, H.G., Merzagora, M., Ottolenghi, A., 1999. *Radiat. Environ. Biophys.* **38**, 39.
Fujita, S., Steenken, S., 1981. *J. Am. Chem. Soc.* **103**, 2540.
Geimer, J., Hildenbrand, K., Naumov, S., Beckert, D., 2000. *Phys. Chem. Chem. Phys.* **2**, 4199.
Giese, B., Spichty, M., 2000. *Chem. Phys. Chem.* **1**, 195.
Gillard, N., Begusova, M., Castaing, B., Spotheim-Mauizot, M., 2004. *Radiat. Res.* **162**, 566.
Golden, D.M., Bierbaum, V.M., Howard, C.J., 1990. *J. Phys. Chem.* **94**, 5413.
Goodhead, D.T., 1994. *Int. J. Radiat. Biol.* **65**, 7.
Grozema, F.C., Berlin, Y.A., Siebbeles, L.D.A., 1999. *Int. J. Quantum Chem.* **75**, 1009.
Grozema, F.C., Berlin, Y.A., Siebbeles, L.D.A., 2000. *J. Am. Chem. Soc.* **122**, 10903.
Gulston, M., de Lara, C., Jenner, T., Davis, E., O'Neill, P., 2004. *Nucleic Acids Res.* **32**, 1602.
Gulston, M., Fulford, J., Jenner, T., de Lara, C., O'Neill, P., 2002. *Nucleic Acids Res* **30**, 3664.
Haromy, T.P., Raleigh, J., Sundaralingam, M., 1980. *Biochemistry* **19**, 1718.
Hazra, D.K., Steenken, S., 1983. *J. Am. Chem. Soc.* **105**, 4380.
Hole, E.O., Nelson, W.H., Close, D.M., Sagstuen, E., 1987. *J. Chem. Phys.* **86**, 5218.
Hole, E.O., Nelson, W.H., Sagstuen, E., Close, D.M., 1992a. *Radiat. Res.* **129**, 119.
Hole, E.O., Sagstuen, E., Nelson, W.H., Close, D.M., 1989. *Free Radical Res. Commun.* **6**, 87.
Hole, E.O., Sagstuen, E., Nelson, W.H., Close, D.M., 1992b. *Radiat. Res.* **129**, 1.
Hong I.S., Ding H., Greenberg M.M., 2006. *J. Am. Chem. Soc.*, in press.
Hong I.S., Greenberg M.M., 2005. *J. Am. Chem. Soc.*, in press.
Jaquet, L., Kelly, J.M., Kirsch-De Mesmaeker, A., 1995. *J. Chem. Soc., Chem. Commun.*, 913.
Jortner, J., Bixon, M., Langenbacher, T., Michel-Beyerle, M.E., 1998. *Proc. Natl. Acad. Sci. USA* **95**, 12759.
Keck, K., 1968. *Z. Naturforsch.* **23b**, 1034.
Keck, K., Hagen, U., Friebolin, H., 1966. *Naturwiss.* **53**, 304.
Krauss, M., Osman, R., 1993. *J. Phys. Chem.* **97**, 13515.
Krauss, M., Osman, R., 1994. *J. Phys. Chem.* **99**, 11387.
Li, X., Sevilla, M.D., Sanche, L., 2003. *J. Am. Chem. Soc.* **125**, 13668.
Li, X., Cai, Z., Sevilla, M.D., 2001. *J. Phys. Chem. A* **105**, 10115.
Li, X., Cai, Z., Sevilla, M.D., 2002a. *J. Phys. Chem. A* **106**, 1596.
Li, X., Cai, Z., Sevilla, M.D., 2002b. *J. Phys. Chem. A* **106**, 9354.
Li, X., Sanche, L., Sevilla, M.D., 2002c. *J. Phys. Chem. A* **106**, 11248.
Mariaggi, N., Cadet, J., Teoule, R., 1976. *Tetrahedron* **32**, 2385.
Martini, M., Termini, J., 1997. *Chem. Res. Toxicol.* **10**, 234.
Miaskiewicz, K., Miller, J., Osman, R., 1993. *Int. J. Radiat. Biol.* **63**, 677.
Miaskiewicz, K., Osman, R., 1994. *J. Am. Chem. Soc.* **116**, 232.
Michalik, V., Spotheim-Maurizot, M., Charlier, M., 1995a. *Nucl. Instrum. Methods Phys. Res. B* **105**, 328.
Michalik, V., Spotheim-Maurizot, M., Charlier, M., 1995b. *J. Biomol. Struc. Dyn.* **13**, 565.
Michalik, V., Tartier, L., Spotheim-Maurizot, M., Charlier, M., 1995c. In: Fuciarelli, A.F., Zimbrick, J.D. (Eds.), *Radiation Damage in DNA/Function Relationships in Early Times*. Battelle Press Columbus, Richland, p. 19.
Mujica, V., Nitzan, A., Mao, Y., Davis, W., Kemp, M., Roitberg, A., Ratner, M.A., 1999. In: Jortner, J., Bixon, M. (Eds.), *Electron Transfer: From Isolated Molecules to Biomolecules. Part Two, Advances in Chemical Physics Series*, vol. 107. Wiley, New York, p. 403.
Mundy, C.J., Colvin, M.E., Quong, A.A., 2002. *J. Phys. Chem. A* **106**, 10063.
Naumov, S., Barthel, A., Reinhold, J., Dietz, F., Geimer, J., Beckert, D., 2000. *Phys. Chem. Chem. Phys.* **2**, 4207.
Naumov, S., Beckert, D., 2002. *Phys. Chem. Chem. Phys.* **4**, 45.
Naumov, S., Hildenbrand, K., von Sonntag, C., 2001. *J. Chem. Soc., Perkin Trans.* **2**, 1648.
Naumov, S., Reinhold, J., Beckert, D., 2003. *Phys. Chem. Chem. Phys.* **5**, 64.
Naumov, S., von Sonntag, C., 2005. *J. Phys. Org. Chem.* **18**, 586.
Naumov S., von Sonntag C., 2006. Unpublished results.
Neese, F., Zaleski, J.M., Zaleski, K.L., Solomon, E.I., 2000. *J. Am. Chem. Soc.* **122**, 11703.
Nelson, W.H., Hole, E.O., Sagstuen, E., Close, D.M., 1988. *Int. J. Radiat. Biol.* **54**, 963.
Nikjoo, H., Goodhead, D.T., Charlton, D.E., Paretzke, H.G., 1989. *Phys. Med. Biol.* **34**, 691.
Nikjoo, H., O'Neill, P., Goodhead, D.T., Terrisol, M., 1997. *Int. J. Radiat. Biol.* **71**, 467.

Nikjoo, H., O'Neill, P., Terrissol, M., Goohead, D.T., 1994. *Int. J. Radiat. Biol.* **66**, 453.
Olofsson, J., Larsson, S., 2001. *J. Phys. Chem. B* **105**, 10389.
Raleigh, J.A., Blackburn, B.J., 1978. *Biochem. Biophys. Res. Commun.* **83**, 1061.
Raleigh, J.A., Fuciarelli, A.F., 1985. *Radiat. Res.* **102**, 165.
Raleigh, J.A., Kremers, W., Whitehouse, R., 1976. *Radiat. Res.* **65**, 414.
Rehm, D., Weller, A., 1970. *Isr. J. Chem.* **8**, 259.
Reid, D.L., Armstrong, D.A., Rauk, A., von Sonntag, C., 2003. *Phys. Chem. Chem. Phys.* **5**, 3994.
Reid, D.L., Shustov, G.V., Armstrong, D.A., Rauk, A., Schuchmann, M.N., Akhlaq, M.S., von Sonntag, C., 2002. *Phys. Chem. Chem. Phys.* **4**, 2965.
Reynisson, J., Steenken, S., 2002a. *Phys. Chem. Chem. Phys.* **4**, 527.
Reynisson, J., Steenken, S., 2002b. *Phys. Chem. Chem. Phys.* **4**, 5353.
Reynisson, J., Steenken, S., 2002c. *Phys. Chem. Chem. Phys.* **4**, 5346.
Richardson, N.A., Wesolowski, S.S., Schaefer III, H.F., 2003. *J. Phys. Chem. B* **107**, 848.
Roginskaya, M., Bernhard, A.W., Marion, R.T., Razskazovskiy, Y., 2005. *Radiat. Res.* **193**, 85.
Saito, I., Nakamura, T., Nakatani, K., Yoshioka, Y., Yamaguchi, K., Sugiyama, H., 1998. *J. Am. Chem. Soc.* **120**, 12868.
Sanche, L., 2002a. *Radiat. Protect. Dosim.* **99**, 1.
Sanche, L., 2002b. *Mass Spectrom. Rev.* **21**, 349.
Schlag, E.W., Yang, D.-Y., Sheu, S.-Y., Selzle, H.L., Rentzepis, P.M., 2000. *Proc. Natl. Acad. Sci. USA* **97**, 9849.
Schuchmann, H.-P., Wagner, R., von Sonntag, C., 1986. *Int. J. Radiat. Biol.* **50**, 1051.
Schuchmann, M.N., Naumov, S., Schuchmann, H.-P., von Sonntag, J., von Sonntag, C., 2005. *Radiat. Phys. Chem.* **72**, 243.
Schwögler, A., Burgdorf, L.T., Carrel, T., 2000. *Angew. Chem. Int. Ed.* **39**, 3918.
Senthilkumar, K., Grozema, F.C., Guerra, C.F., Bickelhaupt, F.M., Lewis, F.D., Berlin, Y.A., Ratner, M.A., Siebbeles, L.D.A., 2005. *J. Am. Chem. Soc.* **127**, 14894.
Steenken, S., 1989. *Chem. Rev.* **89**, 503.
Steenken, S., Jovanovic, S.V., 1997. *J. Am. Chem. Soc.* **119**, 617.
Steenken, S., Jovanovic, S.V., Candeias, L.P., Reynisson, J., 2001. *Chem. Eur. J.* **7**, 2829.
Sy, D., Flouzat, C., Eon, S., Charlier, M., Spotheim-Maurizot, M., 2001. Theor. *Chem. Acc.* **106**, 137.
Sy, D., Savoye, C., Begusova, M., Michalik, V., Charlier, M., Spotheim-Maurizot, M., 1997. *Int. J. Radiat. Biol.* **72**, 147.
Tartier, L., Michalik, V., Spotheim-Maurizot, M., Rahmouni, A.R., Sabattier, R., Charlier, M., 1994. *Nucleic Acids Res.* **22**, 5565.
Tartier, L., Spotheim-Maurizot, M., Charlier, M., 1998. *Int. J. Radiat. Biol.* **73**, 45.
Treadway, C.R., Hill, M.G., Barton, J.K., 2002. *Chem. Phys.* **281**, 409.
Turro, N.J., Barton, J.K., 1998. *J. Biol. Inorg. Chem.* **3**, 201.
Valota, A., Ballarini, F., Friedland, W., Jacob, P., Ottolenghi, A., Paretzke, H.G., 2003. *Int. J. Radiat. Biol.* **79**, 643.
Voityuk, A.A., Jortner, J., Bixon, M., Rösch, N., 2000. *Chem. Phys. Lett.* **324**, 430.
von Sonntag, C., 1987. *The Chemical Basis of Radiation Biology*. Taylor and Francis, London.
von Sonntag, C., 1994. *Int. J. Radiat. Biol.* **66**, 485.
von Sonntag, C., 2006. *Free-Radical-Induced DNA Damage and Its Repair. A Chemical Perspective*. Springer-Verlag, Berlin.
Wagenknecht, H.-A., 2003. *Angew. Chem. Int. Ed.* **42**, 2454.
Ward, J.F., 1988. *Progr. Nucleic Acid Res. Molecular Biol.* **35**, 95.
Wardman, P., 1989. *J. Phys. Chem. Ref. Data* **18**, 1637.
Wetmore, S.D., Boyd, R.J., Eriksson, L.A., 1898. *J. Phys. Chem. B* **102**, 9332.
Wu, Y., Mundy, C.J., Colvin, M.E., Car, R., 2004. *J. Phys. Chem. A* **108**, 2922.
Ye, Y.-J., Chen, R.-S., Martinez, A., Otto, P., Ladik, J., 1999. *Solid State Commun.* **112**, 139.
Zhang, R.B., Erikson, L.A., 2006. *Chem. Phys. Lett.* **417**, 303.

Energy Deposition Models at the Molecular Level in Biological Systems

A. Muñoz[1], F. Blanco[2], J.C. Oller[1], J.M. Pérez[1] and G. García[3]

[1]*Centro de Investigaciones Energéticas, Medioambientales y Tecnológicas (CIEMAT), Avenida Complutense 22, 28040 Madrid, Spain*
[2]*Departamento de Física Atómica, Molecular y Nuclear, Universidad Complutense de Madrid, Ciudad Universitaria, 28040 Madrid, Spain*
[3]*Instituto de Matemáticas y Física Fundamental (IMAFF), Consejo Superior de Investigaciones Científicas (CSIC), Serrano 113-bis, 28006 Madrid, Spain*

Abstract

In this study we have developed a model to describe the electron interaction of intermediate and high energy electrons (10–10000 eV) with some molecules of biological interest. Differential and integral electron scattering cross sections have been calculated with an optical potential method following an independent atom representation. Important improvement related to relativistic corrections, many-body effects, local velocity considerations and a screening correction procedure which take into account the overlapping of the constituent atoms in the molecule have been introduced to improve the accuracy and applicability of the method for a high variety of molecular targets. The accuracy of these calculations has been checked by comparison with total electron scattering cross section data we have measured in a transmission beam experiment with experimental errors within 5%. Finally, we have developed a Monte Carlo simulation program, based on the general tools of GEANT4, which uses as input parameters our calculated cross sectional data and the energy loss distribution functions based on the experimental energy loss spectra. This simulation procedure allows energy deposition models at the molecular level that could be very useful in biological and medical applications when microscopic energy deposition patterns are required.

Contents

ADVANCES IN QUANTUM CHEMISTRY, VOLUME 52
ISSN: 0065-3276 DOI: 10.1016/S0065-3276(06)52003-9

1. INTRODUCTION

Important applications related to biology and medicine are requiring an increasing degree of detail in how radiation transfers the energy to the medium and its consequences in terms of induced damage. Traditional dosimetry gives a macroscopic description by means of the absorbed dose, i.e. the total energy absorbed per unit mass. In general, for bulk materials the radiation damage is proportional to the dose and therefore it is used as reference parameter in most applications connected with radiation protection and radiotherapy. When higher spatial resolution is needed, for example to irradiate only some parts of the cell keeping out of the radiation field the rest, we can try to apply the concept of dose to a microscopic volume entering in the domain of the microdosimetry. We are considering in this case a microscopic target but the reference parameter is the absorbed dose again. Increasing the level of detail in the interaction process we should need to distinguish, at the molecular level, which part of the biological material, DNA for example, could be damaged by the radiation. This point of view could be referred as nanodosimetry or, more properly, a description of the radiation interaction with matter at the molecular level. At this level, the absorbed dose is not a relevant parameter but a detailed description of the different processes that can take place and the energy transferred, as well as the properties of the secondary particles that can be produced. The relevant parameters to describe processes and energies involved in molecular interactions with radiation particles are the corresponding cross sections. These represent the probability per unit of incident and target particle that a given process takes place. High energy photons can ionise molecules extracting electrons from their inner shells being therefore highly energetic processes, but the direct produced damage can be insignificant in these cases, hence transferring damage capacity to the generated secondary electron. On the other hand, low energy electrons, with energies even below the ionisation limit, can induce molecular dissociations via internal excitation leading to dissociative states of the system and producing therefore a relevant damage with no significant energy balance. Recent studies showed that below the electronic excitation threshold, low energy electrons can damage biological molecules via dissociative electron attachment [1–6]. A similar behaviour has been recently described for the low energy electrons produced by high energy ion beams used in radiotherapy [7].

These considerations motivated this study whose main objective is to develop an energy deposition model for radiation particles, mainly electrons and photons, interacting

with molecular targets. Since ionising radiation produces secondary electrons which are the main responsible of the energy deposition pattern and the radiation damage, we will be mainly devoted to the study of the electron interactions with molecules of biological interest over a wide energy range, initially from 10 to 10000 eV. When large biological molecules interacting with electrons at these intermediate and high energies are considered, the problem wont be tackled if some initial simplification are not taken into account. First of all we have studied atoms (Ne, Ar, Kr, Xe) and small molecules (N_2, O_2, CH_4, CO_2) which are the constituents of gas mixtures used to fill radiation detectors, as air [8] and tissue equivalent gases [9]. After a reasonable description of the electron transport and interactions in these gases we will propose a method to generalise the result to larger biological molecules as DNA bases and combinations of them to form some nucleotides.

The method proposed here is a combination of theory and experiment to obtain a reliable set of cross section data for the most relevant processes at the considered energy range. These cross sectional data will be finally introduced in a Monte Carlo simulation program [10] to obtain single particle tracks and an interaction map providing the energy transfer pattern. In a first approach to the problem, the most relevant input parameters are the total electron scattering cross sections which define the mean free path in the simulations and they are the sum of all the possible processes, the differential and integral elastic and inelastic cross section which define the direction of scattered electrons and if any amount of energy is deposited in the medium and finally the energy loss spectra to provide the transferred energy through inelastic collisions.

Finally, we will generalise our calculation procedure to larger molecules, from the individual DNA bases to some complex of nucleotides constituting DNA fragments.

2. CROSS SECTIONAL DATA

2.1. Calculations

As mentioned above, the primary particles in the applications that prompted this study are mainly electrons and photons. In the energy range considered here, 10–10000 eV, photons interacts, nearly 100%, ionising the target via photoelectric effect, producing a secondary electron with almost the same energy of the primary photon except for its binding energy. Calculated photoelectric interaction data are available for most of target of interest [11], being their reliability confirmed by experiments and simulations. Therefore we will focus our calculations on the electron scattering by molecules at intermediate and high energies.

The number of open channels in a molecular system colliding with electrons of these energies is so high that a complete theoretical description would be impossible and therefore some approximations will be needed. The crudest approximation is the Born–Bethe theory [12] which considers only the asymptotic aspects of the problem. Although this approximation has been extensively used to obtain radiation parameters, as the stopping power [13], we have shown [14] that it overestimates the total electron scattering cross sections from molecules, even at 5000 eV, and especially the elastic part.

Due to the difficulties involved in their reliable measurement or calculation, accurate data on cross sections for electron scattering by most molecules are very scarce. Many works have been devoted to combine experimental results with theoretical calculations, obtaining elastic and inelastic integral cross sections for electron scattering by molecules and

atoms in a wide energy range. These have realised the importance of approximate ab initio procedures of reasonable accuracy for evaluating elastic as well as inelastic processes. While semiempirical treatments can be great when fitting previous experimental values, they become of dubious accuracy for extrapolating unknown values. Also semiempirical treatments become almost useless when data on a new molecule is needed, or as a guide for the critical analysis of dubious experimental data.

We will consider here an ab initio treatment which is based for atoms on an approximate central potential, and whose extension to molecules relies on the well-known Independent Atom Model (IAM) [15]. In this treatment the inelastic contributions for the atoms are included by means of an ab initio absorption potential based on the "quasi-free" [16,17] approximation which will be described in Section 2.1.3.

Firstly, we will illustrate the above procedure when it applies to atoms. Then we will consider molecules, by means of the IAM approximation. Finally, introducing some appropriate screening corrections, we will show how the IAM procedure can be extended from the smallest molecules to larger ones. Finally we will show how the basic ideas underlying the IAM procedure can be extended for the treatment of the largest macro-molecules.

2.1.1. Calculation of atomic cross sections

As is well known, calculations ignoring inelastic processes [18] do not allow determination of total cross sections but provide with good (somewhat overestimated) differential and integrated elastic values. In these cases a complete description of the collision is not obtained and absorption contributions must be estimated separately.

Unfortunately most available ab initio treatments including inelastic contributions have a restricted range of applicability or become complicated when applied to situations of practical interest. As a consequence, for a long time, most treatments for complex atoms or molecules have been of semiempirical nature, resulting of limited confidence in the absence of experimental data.

Available non-empirical treatments can be clasified in three main groups. A first one comprises those usually denominated "weak coupling methods". This includes the First Born Approximation (FBA), Distorted Wave methods (DW) and First-Order Many-Body Theory (FOMBT). These [19] are techniques of relatively simple application, at the expense of modest results and usually only applicable in a reduced range of electron energies.

A second group includes what are usually known as "close coupling methods". These [20] usually provide excellent results (specially at low energies) at the expense of considerable computation needs. Also the complexity of the treatment grows with the number of involved electrons. Some recent variants (CCC-convergent close coupling, RMPS-R matrix with pseudo-states) provide improved results but have been seldom beyond H and He atoms.

The last group comprises those treatments based on the use of optical potentials obtained from different approximations. These include those obtained form the second order Born one, the Eikonal one, the use of dispersion relations from the atomic polarisation, and the statistical treatment of the atom. While most of these are usually limited to large (above 500 eV) electron energies or become complicated for large atoms, one of them known as "the quasifree model" has proved some outstanding properties that will deserve our attention here.

Based on an statistical treatment of the atom, the "quasi-free" model optical potential, is a non-empirical one originally proposed by Staszewska, Schwenke, Thirumalai, Truhlar

and Goldberger [16,17,21]. We will describe here in some detail this model potential, as it has proved to be useful in providing with differential elastic, as well as total elastic and inelastic electron–atom cross sections. While being not perfect, to our knowledge, this procedure is unique in combining an acceptable precision, a reasonable simplicity (almost independent on the involved atoms) and allows covering of a very large energy range (1 eV to 10 keV).

There are numerous calculations based on this model [22–26] but, due to some deficiencies of the original formulation, for a long time many authors used semi-empirical variants for it. Nevertheless, it has been shown [27–31] that, when it is properly amended, the model results a non-empirical valuable tool.

2.1.2. Calculation of total and differential elastic cross sections

We will revise here the method used for the atomic calculations. This is the very well-known one [32] where phase shifts are obtained from the solution of the corresponding Schrödinger dispersion equation, under a central model potential. For our purposes the electron-atom interaction is represented by the approximate optical potential.

$$V_{\text{opt}}(r) = V_s(r) + V_e(r) + V_p(r) + i\,V_a(r). \tag{1}$$

Here $V_s(r)$ is the electrostatic potential calculated by using the charge density deduced from Hartree–Fock [33] atomic wave functions. The $V_e(r)$ term is the exchange potential, arising from the indistinguishability between incident and target electrons. A relatively simple and accurate expression for it can be the semiclassical energy-dependent formula derived by Riley and Truhlar [34]. The $V_p(r)$ term (target polarization potential) accounts for the interaction between the polarized atom and the incident electron. A practical form can be the one given by Zhan *et al.* in Ref. [35]:

$$V_p(r) = \frac{\alpha}{2(r^2 + r_{\text{co}}^2)^2}$$

where α is the atomic polarizability and r_{co} is chosen there to ensure $V_p(r)$ approaches in the near-target region the value proposed by Perdew and Zunger in Ref. [36]. Finally $V_a(r)$ is the absorption potential considered in each case.

In order to obtain the l_{th} complex partial wave phase shift δ_l, the scattering equation for the $u_l(r)$ radial wavefunctions should be numerically integrated by means of an adaptive-step-size fourth order Runge–Kutta algorithm [37] based on the variable-phase technique [32]. Once the corresponding δ_l phase shifts are obtained for the above potential, the elastic differential $d\sigma/d\Omega$ and total absorption $\sigma_{\text{tot}}(E)$ cross sections result from their well-known partialwave and optical theorem expressions

$$f(\theta) = \frac{1}{2ik}\sum_{l=0}^{l_{\max}}(2l+1)\left(e^{2i\delta_l} - 1\right)P_l(\cos\theta), \tag{2}$$

$$\frac{d\sigma}{d\Omega} = \left|f(\theta)\right|^2, \tag{3}$$

$$\sigma_{\text{el}}(E) = \frac{4\pi}{k^2}\sum_{l=0}^{l_{\max}}(2l+1)\sin^2\delta_l, \tag{4}$$

$$\sigma_{\text{tot}}(E) = \frac{4\pi}{k}\,\text{Im}(f_{\theta=0}). \tag{5}$$

The $l_{\max}$ limit in (2) was chosen in each case to ensure a convergence of the calculations within 1%, and phase shifts corresponding to l values above $l = 60$ were extrapolated by the usual effective-range formula [23].

2.1.3. The quasi-free absorption model for atoms

In 1983 Staszewska *et al.* [16] derived a non-empirical expression for the imaginary part of the optical potential for electron–atom scattering by using a method suggested by Goldberger [21] for an analogous problem in nuclear physics. In this model the inelastic interaction of the incident electron with the target (atom or molecule) arises from its dispersion by the target electrons. While the two-body e–e-elastic collisions are calculated as if the target electrons were free, the target properties enter as boundary conditions for the binary collisions: Spatial and momentum density distributions, and Pauli-principle restrictions on the allowed final states for colliding electrons. This was called the quasi-free scattering model. It included an energy-gap parameter (Δ) representing the energy electronic excitation threshold of the target.

Although the resulting model potential gives reasonably good results in some cases [16], it presents severe limitations that have been partially corrected with empirical modifications. Several modifications of this kind were suggested [17] by their authors, but the most widely used has been the substitution in the different expressions of the threshold energy by an average excitation energy [22–25]. With this modification the agreement with the experiment is improved, but the method loses its ab initio nature. In addition, as will be discussed, the original deviation of the model presented some deficiencies for which a semiempirical correction would not be reasonable.

As is well known, when calculating the spatial distribution of a quantum particle by means of the corresponding Schrödinger equation, absorption processes can be easily treated by the inclusion of an imaginary part in the corresponding interaction potential. In fact, a local imaginary potential iV_a corresponds to an $-2V_a$ absorption per unit time [35].

If we denote by $\bar{\sigma}$ the effective collision cross section for an electron traversing a $\rho(r)$ electron charge density, the interaction rate per time unit (absorption rate from the elastic channel) can be estimated as $\rho(r)u\bar{\sigma}(r, E)$, and so a $V_a(r, E) = -\frac{1}{2}\rho(r)u\bar{\sigma}(r, E)$ imaginary potential can be used in order to account for the inelastic processes. There $u(r, E) = \sqrt{2(E - V(r))}$ stands for the velocity corresponding to the local kinetic energy $E - V(r)$ of an scattered electron, and obtaining the explicit form means calculating the effective $\bar{\sigma}$ cross section for an electron traversing the $\rho(r)$ electron gas for which a Fermi velocity distribution is assumed.

The effective cross section is evaluated [16,17,27] by integrating the binary electron-electron differential cross section ($d\sigma/d\Omega$) over all the final states allowed for the scattered electrons (p', k') and averaging over the target electron momentum distribution. This Fermi momentum distribution can be given as

$$N(\mathbf{k}, k_F) = \begin{cases} N_k \equiv 3/(4\pi k_F^3) & \text{for } k \leqslant k_F, \\ 0 & \text{for } k > k_F, \end{cases} \tag{6}$$

where $k_F(\rho(r)) = [3\pi^2\rho(r)]^{1/3}$ is the Fermi momentum, and results available just from the atomic charge density.

The resulting expression for the $\bar{\sigma}$ effective cross section reads:

$$\bar{\sigma} = \frac{1}{u} \int d\mathbf{k}\, N(k, k_F)|\mathbf{u} - \mathbf{k}| \int d\hat{p}_f \frac{d\sigma_b}{d\Omega_{p_f}} \Theta(k', p', k_F). \tag{7}$$

The expression given in Ref. [16] for the Pauli-blocking factor was

$$\Theta(k', p', k_F) = H\big((p')^2 - k_F^2\big) H\big((k')^2 - k_F^2 - 2\Delta\big), \tag{8}$$

where $H(x)$ is the Heaviside [16,17] unit-step function and Δ is the above mentioned threshold energy corresponding to the energy gap between the target ground state and the lowest excited electronic state. This Pauli-blocking factor restrict the processes included in (7) to those where (after the interaction) the incident electron can escape (energy above the Fermi sea level) and the target electron has been promoted out of the Δ "valence band". It must be noted that the Δ parameter represents a gap up to the first unoccupied atomic level.

As known, the correct expression for the differential cross section $(d\sigma_b/d\Omega)$ of two non-polarized electrons in centre of mass is the Mott one [15] given by:

$$\frac{d\sigma_M(\theta)}{d\Omega} = \frac{1}{v_r^4}\left(\frac{1}{\sin^4\theta/2} + \frac{1}{\cos^4\theta/2} - \frac{\Phi}{\sin^2\theta/2\cos^2\theta/2}\right), \tag{9}$$

where v_r is the relative velocity of the colliding particles and $\Phi \to 1$ for $v_r \geqslant 1$. However, the complicated angular and energy dependence of this formula does not allow its use in Eq. (7) to obtain manageable expressions, and a simpler $d\sigma_b/d\Omega$ approximate expression must be used.

Comparing with the classical Rutherford value for the Coulomb interaction between identical particles,

$$\frac{d\sigma_R(\theta)}{d\Omega} = \frac{1}{v_r^4}\left(\frac{1}{\sin^4\theta/2} + \frac{1}{\cos^4\theta/2}\right), \tag{10}$$

the absence of the quantum interference term in (9) is the only difference. Assuming the Pauli blocking restrictions can exclude much of the near forward scattering, and taking into account that for $\theta = \pi/2$ dispersion the effect of the interference term is only to reduce a factor of 2 the differential cross section, in Ref. [16] the following "sideways" approximation was proposed

$$\frac{d\sigma_b}{d\Omega} \approx \frac{1}{2}\frac{d\sigma_R}{d\Omega}. \tag{11}$$

However, this sideways approximation fails at medium and high energies where near forward processes become more important.

Taking into account that the main contribution of the quantum interference term in (9) occurs around $\theta = \pi/2$ where $(\sin^2\frac{\theta}{2}\cos^2\frac{\theta}{2})^{-1} \approx 4$, a new corrected Rutherford formula for the differential cross section $(d\sigma_{\mathrm{CR}}/d\Omega)$ was proposed in [27] as

$$\begin{aligned}\frac{d\sigma_b(\theta)}{d\Omega} &\approx \frac{d\sigma_{\mathrm{CR}}(\theta)}{d\Omega} \equiv \frac{1}{v_r^4}\left(\frac{1}{\sin^4\theta/2} + \frac{1}{\cos^4\theta/2} - 4\right) \\ &= \frac{d\sigma_R(\theta)}{d\Omega} - \frac{1}{2}\frac{d\sigma_R(\theta = \pi/2)}{d\Omega}.\end{aligned} \tag{12}$$

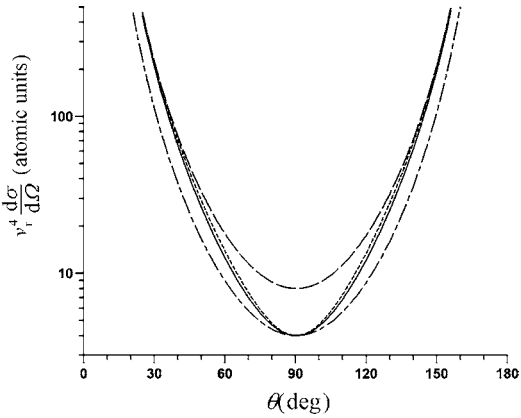

Fig. 1. Comparison of the angular dependence of the Mott e–e-differential cross section for $\phi = 1$ (continuous line) with different approximations: Rutherford expression (dashed line), sideways approximation from Ref. [16] (dot-dashed line), and corrected-Rutherford approximation from this work (dotted line).

The differential cross sections given by (9), (10), (11) and (12) are shown in Fig. 1 as a function of the scattering angle. As can be seen in this figure the "corrected Rutherford" formula (11) reproduces to a good approximation the Mott expression (9) while being much simpler.

By introducing in (6) the simplified cross section given by (11), we obtain two terms for the average electron–electron cross section,

$$\bar{\sigma} = \bar{\sigma}_R + \bar{\sigma}_C \tag{13}$$

and so the final expression for the model potential results also separable in two terms

$$V^a(\mathbf{r}, E) = -\frac{1}{2}\rho(\mathbf{r})u(\mathbf{r}, E)[\bar{\sigma}_R + \bar{\sigma}_C] \equiv V_R^a + V_C^a, \tag{14}$$

the V_R^a one arising from the Rutherford contribution, and the V_C^a one arising from the correcting term.

After a tedious calculation detailed in [16,17,27], the two 3-dimension integrals in (7) can be explicitly evaluated, for both V_C^a and V_R^a terms.

The resulting expression for V_R^a reads:

$$V_R^a = \frac{-2u}{15\pi p^2} H\big(p^2 - k_F^2 - 2\Delta\big)\left[\frac{5k_F^3}{2\Delta} - \frac{k_F^3(5p^2 - 3k_F^2)}{(p^2 - k_F^2)^2} + H(\delta)\frac{2\delta^{5/2}p^5}{(p^2 - k_F^2)^2}\right], \tag{15}$$

where p is the electron incident momentum, and

$$\delta(r, E) = 2\big(k_F^2 + \Delta\big)/p^2 - 1.$$

The above expression from [27] is a $\frac{1}{2}$ factor smaller than the original one found in [16], both due to the correction of a detected errata and to the improved approximation used for the $d\sigma_b/d\Omega$ term. The explicit form of the V_C^a term obtained in [27] will be not presented here because, as indicated in [27,28], this is a very small contribution that can be safely ignored in most situations.

2.1.4. Improvements on the original quasi-free absorption model

As described in [28,29], the absorption potential introduced in previous section requires some corrections in order to improve its foundations, accuracy and range of applicability. We will comment these only briefly here.

Electron indistinguishability The first non-desirable aspect of the original model is the different treatment given to the two colliding electrons inside the atom, which is incompatible with their indistinguishability.

Effectively, the form

$$\Theta(k', p', k_F) = H\big((p')^2 - k_F^2\big)H\big((k')^2 - k_F^2 - 2\Delta\big) \tag{16}$$

for the Fermi-blocking factor is clearly in conflict with the electron indistinguishability and results in some difficulties with the interpretation of the exchange contribution in the Rutherford e–e-dispersion.

The most natural solution for both difficulties [28] is the use of symmetric Pauli-blocking conditions in a form that can also maintain the Δ value for the threshold

$$\Theta(k', p', k_F) = H\big((p')^2 - k_F^2 - \Delta\big)H\big((k')^2 - k_F^2 - \Delta\big). \tag{17}$$

Energy conservation restrictions It must be noted that, after accelerating in the atomic potential V, low-energy incident electrons can gain very high energies and then, satisfying the Pauli restrictions of the model, they are allowed to remove even very tightly bound internal atomic electrons. While such a process can be allowed "from the point of view" of the interacting electrons, it clearly means an energy conservation violation for the whole electron–atom system. This situation produces [27] absurdly large values of the total inelastic cross section at low incident energies, and was repaired in the first version of the model by using the electron incident velocity instead of the local one in the $\bar{\sigma}$ expression. This situation can be better solved by incorporating into the model an energy-conservation boundary condition (similar to the two other Pauli blocking conditions of the model).

This is the obvious one: If the kinetic energy of the incident electron is lower than the binding energy of the target electron, the inelastic interaction is not allowed. An explicit formulation of this restriction requires some estimation of the "local binding energy" for target electrons. While for weakly bound external electrons this can be the threshold energy of the model, for internal electrons a good estimate could be the binding potential (the average potential seen by each atomic electron arising from the nucleus plus the remaining $Z - 1$ electrons).

Therefore the adopted correction is the inclusion of a new factor $H(E_{\text{in}} - \Delta + V_b)$, where H is the usual "Heaviside" step function and

$$V_b(r) = V(r)\frac{Z-1}{Z} - \frac{1}{r}$$

is an estimation of the potential due to $Z - 1$ electrons plus the nucleus.

Relativistic corrections The convenience of including relativistic corrections in the Schrödinger equation for the incident electron does not arise from the range of incident energies that will be considered here (up to a few keV). Relativistic effects arise from

the larger energies an incident electron acquires inside a heavy atom, where very strong potentials are present.

The numerical results for He to Xe noble gases [29] show that relativistic corrections have no effect on the calculated total cross sections. Only Kr and Xe differential cross sections are affected for large angles (and in the case of Kr only at 200 eV or lower energies).

The procedure adopted in considering relativistic effects for the incident electron can just involve the usual corrections [33] in the wave equation, resulting in the use of an effective g_l wave function and potential [18]. In this way the treatment remains very simple but, except for ignoring the difference between δ_l and δ_{-l-1}, the treatment follows the one given by Fink *et al.* [18]. In fact it can be shown that, by omitting the absorption potential, the results are quite close to Fink *et al.* pure relativistic ones.

Even while relativistic corrections for the incident electron are only of small importance here, they are usually included in all calculations, as once they are implemented in the numerical procedures, they result in no extra work.

Many-body and screening effects inside the atom Contrary to the small relativistic corrections, many-body effects, not taken into account by the original model, are very important even for a relatively small atom like Ne. Since a detailed treatment of these effects is not currently available, the needed corrections can be included, at least in an approximate way, as follows.

First of all, the imaginary absorption potential in the inner region is reduced in the same proportion that the arriving electron flux is reduced by absorption at external layers. The basic idea is to avoid the absorption, in the inside region, that fraction of the flux already absorbed in the external regions. This was treated in [29] by using a C_{scr} screening coefficient:

$$V^a_{\mathrm{cor}}(r) = V^a(r) \cdot C_{\mathrm{scr}}(r) \tag{18}$$

with

$$C_{\mathrm{scr}}(r) = \exp \int_r^\infty \frac{V^a(t)}{u(t)} \frac{2t\,dt}{\sqrt{t^2 - r^2}}. \tag{19}$$

Another questionable assumption of the original model, also related to many-body processes, is to consider the probability of interacting with Z electrons as Z times the probability of interacting with one electron: If inside a region of size λ^3 ($\lambda = 2\pi/u$ the local wavelength of the incident electron) there were present more than one target electron, it would not be physically reasonable to consider interaction with each of them as independent of the others (even if target electrons are considered to behave as independent of each other).

The corresponding correction results by substitution of the original $\rho(r)$ electron density by an effective $\rho_{\mathrm{eff}}(r)$ one:

$$\rho_{\mathrm{ef}} = \rho_{\mathrm{sat}}\left(1 - e^{-\rho/\rho_{\mathrm{sat}}}\right) \tag{20}$$

where

$$\rho_{\mathrm{sat}} = \frac{u^3}{(2\pi)^3}. \tag{21}$$

It must be noted that applying the above two approximate corrections does not mean correcting twice for the same effect: While the first is related to the probability for the incident electron to reach the position r, the second is related to the probability of interacting with a target electron at r once arriving there. Both corrections deal with complementary manifestations of the many-body situation.

Determination of the Δ parameter It must be remembered that the effective cross section $\bar{\sigma}$ arises from integration of the binary electron–electron differential one $d\sigma_b/d\Omega$ over all the continuum final states (p', k') energetically allowed for the scattered electrons ($p'^2/2 > k_F^2/2 + \Delta$ and $k'^2/2 > k_F^2/2 + \Delta$). This means the Δ parameter represents the threshold energy for continuum states: Only ionisation processes are taken into account, excitation to discrete levels being ignored by the model.

Using for Δ any value under the ionisation potential can be understood as a desirable attempt to include in the model some contribution from excitation to discrete bound states, but requires some discussion for the appropriate value: The original proposal for Δ [16] was the energy gap between the ground state and the first discrete level. Unfortunately this value is unacceptable for most atoms because it is so small (for example 0.002 eV for a Carbon atom) that nonsense σ values would result.

Probably the most judicious choice for the Δ parameter should require a careful discussion for each particular system. Nevertheless, taking into account that the contribution of optically forbidden transitions to the excitation cross section is usually very small compared to the contribution of those optically allowed, a reasonable general assumption is taking Δ as *the gap between the ground state and the first level optically allowed from the ground one* (first resonant level).

Detailed expressions for the imaginary part of the optical potential The final expressions after the several corrections can be summarized as:

$$V^a_{\mathrm{cor}}(r) = V^a(r) \cdot C_{\mathrm{scr}}(r), \tag{22}$$

$$C_{\mathrm{scr}}(r) = \exp \int_r^\infty \frac{V^a(t)}{u(t)} \frac{2t\,dt}{\sqrt{t^2 - r^2}}, \tag{23}$$

$$V^a = \frac{-2\pi\rho_{\mathrm{ef}}}{u} H\big(E_{\mathrm{in}} + V_b(r) - \Delta\big) \times \left[\frac{1}{\Delta} - \frac{u^2 - \Delta - 3/5k_F^2}{(u^2 - k_F^2 - \Delta)^2} + H(\delta)\frac{2\delta^{5/2}u^5}{5k_F^3(u^2 - k_F^2 - \Delta)^2}\right]. \tag{24}$$

Here E_{in} stands for the incident kinetic energy, Δ is the energy gap between ground and first resonant states, $V_b(r)$ is estimated from the effective atomic potential $V(r)$ as

$$V_b(r) = V(r)\frac{Z-1}{Z} - \frac{1}{r}$$

and the following notation has been used:

$$u(r, E_{\mathrm{in}}) = \sqrt{2\big(E_{\mathrm{in}} - V(r)\big)},$$

$$\rho_{\mathrm{ef}} = \big(1 - e^{-\frac{\rho}{\rho_{\mathrm{sat}}}}\big),$$

$$\rho_{\mathrm{sat}} = u^3/(2\pi)^3,$$

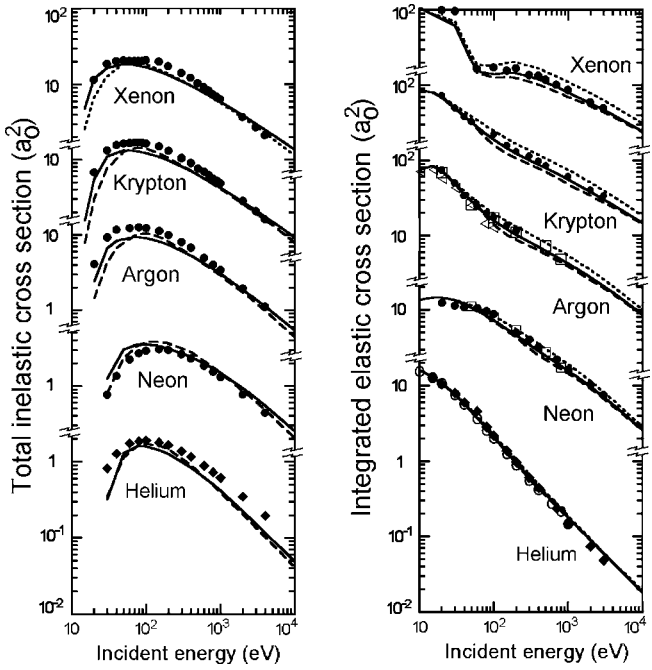

Fig. 2. (Left) Total inelastic cross sections for He to Xe. Dotted line results when using for Δ the ionization potential, ignoring excitation processes. Full lines are the results when using for Δ the energy gap between ground and first resonant level (correcting for excitation processes). (Right) Comparison for He to Xe of the calculated integral elastic cross section (curves) with some available experimental data (symbols): Solid line from the model including all corrections; dashed line (almost overlapping) without corrections; dotted line pure elastic calculation omitting the imaginary absorption potential; ◆ Ref. [87]; ● Ref. [88]; □ Ref. [89]; ○ Ref. [90]; ◁ Ref. [38]. Note the discontinuities in the axis.

$$\delta = \left(2k_F^2 + 2\Delta - u^2\right)/u^2,$$
$$k_F\left(\rho(r)\right) = \left[3\pi^2\rho(r)\right]^{1/3}.$$

Comparison with experimental data Most checks of the above model for atoms have been carried out with noble gases, due to the relative abundance of experimental data for them.

Comparison of the predicted total cross section values with experimental ones is very favourable in general, as can be seen in Fig. 2.

Differential elastic cross sections are presented in Fig. 3 for low, intermediate and high energies for which experimental data are available. The corrected results are usually higher for large angles resulting in better agreement with available experimental data. This is specially remarkable for intermediate to high energies, where they are a factor $\times 2$ to $\times 10$ larger towards experimental data. For integrated elastic cross sections, Fig. 2 also indicates that in all cases the corrected results are closer to the experimental ones.

It is very interesting to compare the results from calculations including the $iV^a(r)$ term with those obtained when ignoring it (pure elastic): The former provides with good total,

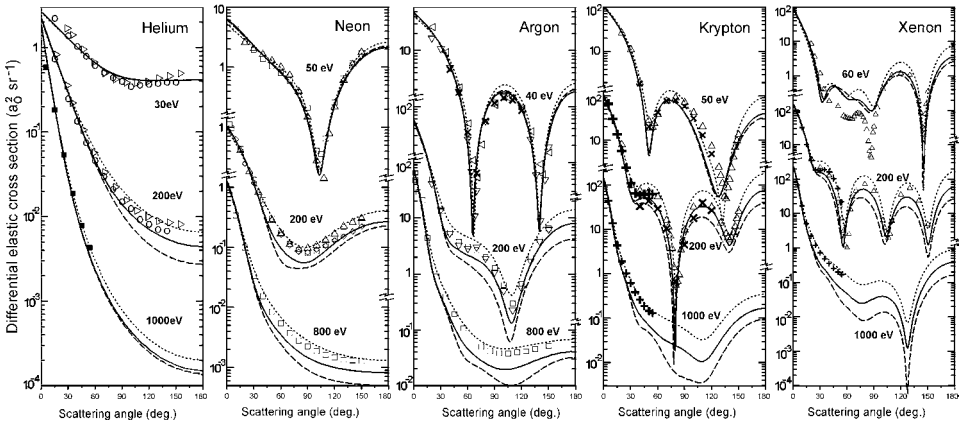

Fig. 3. Differential cross sections for He to Xe noble gases. All symbols and line styles same as Fig. 2 and also ■ Ref. [91]; ▹ Ref. [92]; △ Ref. [93]; ▽ Ref. [94]; ◇ Ref. [95]; × Ref. [96]; + Ref. [97]. Note the discontinuities in the axis.

absorption, integrated elastic and differential elastic values (these last somewhat underestimated at large energies). The second one do not allows determination of total nor absorption cross sections and somewhat overestimates differential elastic values. Thus (only for determination of differential elastic values) both calculations can be considered as complementary for the time being, as they result in useful upper and lower bounds for the experimental ones.

Some fine details as the position of the minima for differential cross sections are reasonably well reproduced. As an example, the critical points in Ar (67.5°, 35 eV) and (140°, 38 eV) are not far from the experimental [38] ones (68.5°, 41.30 eV) and (143.5°, 37.30 eV). Finally, Fig. 4 compares both experimental and theoretical $d\sigma_{\rm el}(E,\theta)/d\Omega$ values for a broad energy and angular ranges: It is a two dimensional contour level plot of these data. As this figure shows the proposed model correctly accounts for the main overall characteristics down to 10 eV energies.

2.2. Calculation of electron–molecule cross sections

2.2.1. Independent atom approximation

As indicated in the introduction, electron–molecule cross sections can be approximately deduced from those for atoms by means of the independent atom model (IAM) [23,25,15, 39,40] and the usual expression [15] for multicenter dispersion

$$F(\theta) = \sum_{\text{atoms}} f_i(\theta) e^{i\mathbf{q}\cdot\mathbf{r}_i}, \tag{25}$$

where $\mathbf{q} = \mathbf{K}_{\rm out} - \mathbf{K}_{\rm in}$ is the momentum transfer and $f_i(\theta)$ are the atomic dispersion functions. According to the optical theorem, the resulting total cross sections is then

$$\sigma_{\rm total}^{\rm molecule} = \frac{4\pi}{k} \operatorname{Im} F(\theta = 0) = \frac{4\pi}{k} \sum_{\text{atoms}} \operatorname{Im} f_i(\theta = 0) = \sum_{\text{atoms}} \sigma_{\rm total}^{\rm atom}, \tag{26}$$

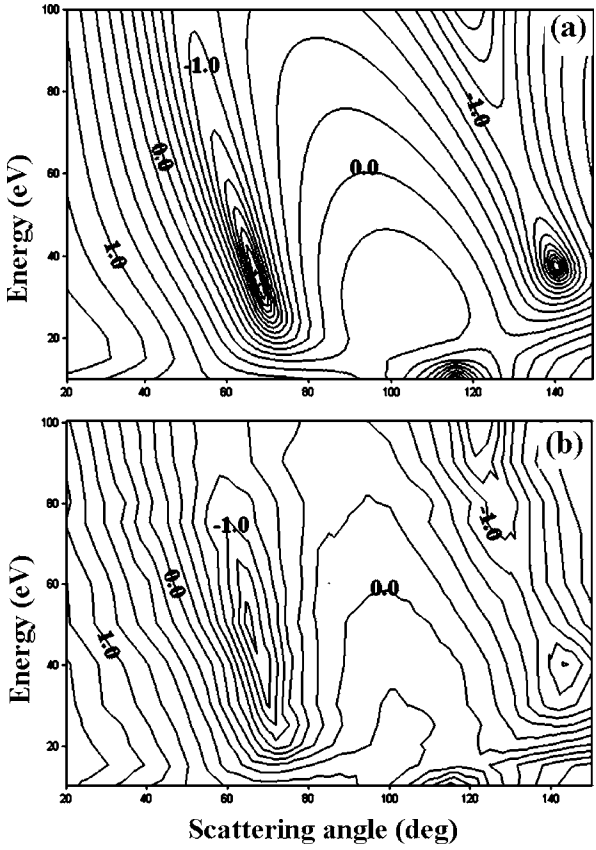

Fig. 4. Contour level plot of the function for Argon in atomic units. (a) Ab-initio proposed model. (b) Experimental, from available numerical data in Ref. [38]. Numbers correspond to the decimal logarithm of the cross section values in atomic units.

a result known [23] as the additivity rule (AR). After averaging the differential cross section $|F(\theta)|^2$ over all molecule orientations [41,42] one also obtains:

$$\frac{d\sigma^{\text{molec}}}{d\Omega} = \sum_{i,j} f_i(\theta) f_j^*(\theta) \frac{\sin qr_{ij}}{qr_{ij}}, \tag{27}$$

where $q = 2k \sin \frac{\theta}{2}$, r_{ij} is the distance between i and j atoms, and $\sin qr_{ij}/r_{ij} = 1$. Unfortunatelly (27) is not appropriate for calculation of integrated elastic values due to its poor normalisation (this is very clear for the pure elastic dispersion where $F(\theta)$ violates the optical theorem,

$$\int_{4\pi} \left|F(\theta)\right|^2 d\Omega \neq \frac{4\pi}{k} \operatorname{Im} F(\theta = 0)$$

even in the simplest case of two identical atoms). Taking into account that $\sin(qr_{ij})/qr_{ij}$ factors are usually very small except for $i = j$ where they equal 1, the above limitation can be remedied by approximating them as δ_{ij} while evaluating integral elastic values. This

results again in an *additivity rule* relation

$$\sigma^{\text{molecule}}_{\text{Integral Elastic}} = \sum_{\text{atoms}} \sigma^{\text{atom}}_{\text{Integral Elastic}}. \tag{28}$$

2.2.2. *Results and limitations of the IAM approximation*

The calculated values from (26), (27) and (28) for N_2 and CO_2 molecules are compared in Figs. 5 and 6 with available experimental or theoretical data.

As can be seen in the figures, the overall agreement between experimental and calculated values is good for differential cross sections. As with the noble gases case, the calculated values for medium to large angles trend to be lower than the experimental ones as energy

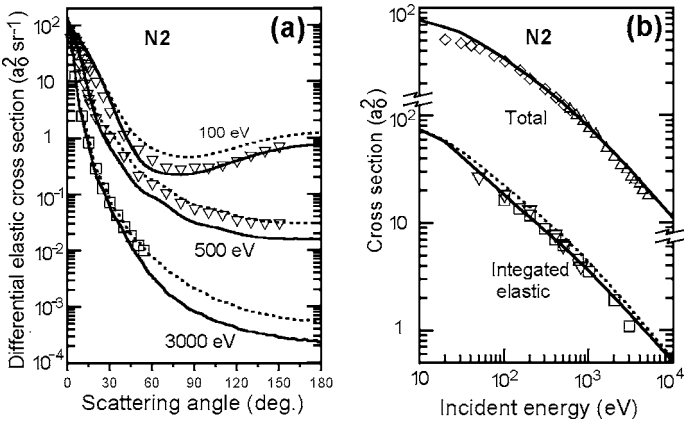

Fig. 5. Comparison for N_2 of the calculated (curves) differential elastic (a) and total (b) cross sections, with some available experimental data (symbols): Solid line from the complete model; dotted line pure elastic calculation omitting the imaginary absorption potential; dashed line from Ref. [98]; □ Ref. [91]; △ Ref. [99]; ◇ Ref. [100]; ▽ Ref. [89]. Note the discontinuities in the axis.

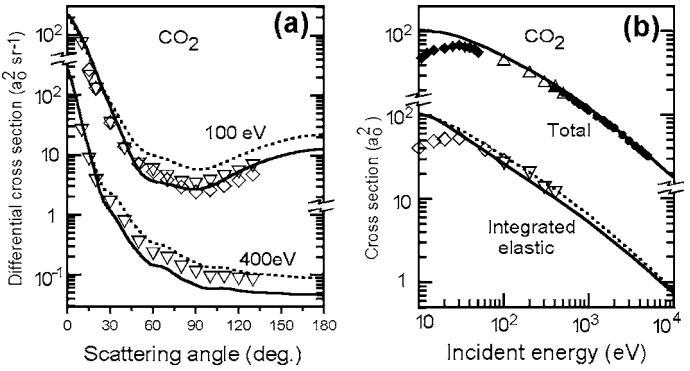

Fig. 6. Same as Fig. 5 but for CO_2 molecule, and ◆ Ref. [100]; △ Ref. [101]; ◇ Ref. [102]; ▽ Ref. [103]; ● Ref. [104]. Note the discontinuities in the axis.

increases. Same as for noble gases, the results from the corrected model are closer to the experimental data than the ones from the uncorrected one. Values resulting both when including the $iV^a(r)$ absorption term, and when omitting it (pure elastic) are shown for comparison and, same as for the atoms, they behave as upper and lower bounds for the experimental data.

The calculated total cross sections are in excellent agreement with experimental values at medium to large energies (100 eV and above). At lower energies the agreement worsens, due to the need of screening corrections that will be discussed in next section. Basically this is because low energy atomic total cross sections are very large (of the order of molecular sizes) and the used IAM expressions ignore this. This is clearer for the largest CO_2 molecule.

2.3. Screening corrections for small to medium size molecules

2.3.1. Low energy failure of IAM and the need for screening corrections

Expression (9) ignores interactions of the incident electron with more than one atom at a time and so, in spite of the good behaviour of this approximation for medium to large energies, good results for low energies are not to be expected: First because low energy atomic total cross sections as aforementioned are very large (of the order of molecular sizes) and second because low energy electrons have low "resolving power" with associated wavelengths of the order of the interatomic distances ($\lambda = 2\pi/k > 2.3$ a.u. at energies below 100 eV). Consequently the low-energy failure of the AR can be partially interpreted as arising form ignoring the mutual overlapping of nearby large atomic cross sections, and so from "counting" each electron interaction with a pair of almost overlapped atoms twice (as two independent interactions).

The main attempts to extend the AR validity to low energies include some semiempirical treatments [43,44], some geometrical ones for some specific molecular shapes [45–47] and carefull calculation of the average geometrical overlapping within a model of black spheres [48]. Although these approaches lack of generallity [43–47] or result complicated even for diatomic cases [48], their good results confirm the importance of low-energy screening effects and encouraged the search for a simple approximate correction of easy application in polyatomic situations. This was called "Screening Corrrected Aditivity Rule" (SCAR).

2.3.2. The SCAR procedure

According to the SCAR procedure [49], screening corrections for molecular total cross sections can be introduced by means of a modified additivity rule

$$\sigma^{\text{total}} = \sum_i s_i \sigma_i , \tag{29}$$

where the screening correction coefficients s_i account for the geometrical overlapping of the atoms in the molecule as seen by the incident electrons. As discussed in [49], the s_i coefficients can be obtained as a sum of (k) terms, each of them arising from k-atoms overlapping, which can be calculated in a recurrent way:

$$s_i = 1 - \frac{\varepsilon_i^{(2)}}{2!} + \frac{\varepsilon_i^{(3)}}{3!} - \frac{\varepsilon_i^{(4)}}{4!} + \cdots \pm \frac{\varepsilon_i^{(N)}}{N!}, \tag{30}$$

$$\varepsilon_i^{(1)} = 1, \tag{31}$$

$$\varepsilon_i^{(k)} \cong \frac{N-k+1}{N-1} \sum_{j(\neq i)} \frac{\sigma_j \varepsilon_j^{(k-1)}}{\alpha_{ij}} \quad (k = 2, \ldots, N). \tag{32}$$

In above expressions N stands for the number of atoms in the molecule, the j index runs over all the N atoms except the i one, r_{ij} is the distance between centres of atoms i and j and $\alpha_{ij} = \max(4\pi r_{ij}^2, \sigma_i, \sigma_j)$.

We will describe here the origin of the above expressions only for the simplet diatomic case. For a diatomic molecule (or for a general one, if one ignores multiple atom overlappings) only the $\varepsilon_i^{(2)}$ terms survive in above expressions, and then they reduce to

$$s_i = 1 - \frac{1}{2} \sum_{j(\neq i)} \frac{\sigma_j}{\alpha_{ij}}. \tag{33}$$

In that cases expression (29) can be rewritten as

$$\sigma^{\text{molecule}} = \sum_i \sigma_i - \sum_{i<j} \sigma_{ij}, \tag{34}$$

where $\sigma_{ij} = \sigma_i \sigma_j / \alpha_{ij}$ is the average overlapping of atoms i and j. This average overlapping of atom pairs is approximated by $\sigma_{ij} \cong \sigma_i \sigma_j / 4\pi r_{ij}^2$ when atoms are far enough (corresponding to the average screening of a σ_j surface due to a σ_i one distributed over a $4\pi r_{ij}^2$ area) or by $\min(\sigma_i, \sigma_j)$ when atoms are close together.

In the general case the procedure provides not only with the corrected values, but also with the s_i coefficients which can be useful in discussing to which extent each individual atom is screened or contributes to the molecular cross section.

It must be emphasised that the introduced s_i coefficients cannot be considered as fitting parameters, as expressions (30)–(32) give them in closed form as a function of i atomic total cross sections and r_{ij} interatomic distances in the molecule. Even while usually all the involved quantities are obtained ab initio using different approximations, the above procedure could be of interest to any work interested in fitting molecular cross sections as a combination of atomic ones: Expressions like (29) with s_i depending on all the atomic i and positions should be more appropriate than simple sums like expression (26).

Also it must be clarified that SCAR procedure is not expected to give good results at very low energies where the wavelength of incident electrons is smaller than interatomic distances. That difficulty is not related to the IAM approximation but to the use of expression (25). The minimum energies for its applicability can be estimated as the ones for which e-associated wavelengths are of the order of the average interatomic distances $\langle r_{ij} \rangle$, i.e. $E \geqslant 2\pi^2 / \langle r_{ij} \rangle^2$. In practice, good results are usually found for integrated elastic and total cross sections down to about $6/\langle r_{ij} \rangle^2$ a.u. ($160/\langle r_{ij} \rangle^2$ eV) incident energies. That predices the observed better behaviour at low-energies for large molecules (5 eV for Bencene, for instance).

While the above procedure deals only with total (elastic plus inelastic) cross sections, there is no inconvenience in applying the same geometrical arguments to the calculation of total elastic cross sections: Assuming a $1 - s_i$ fraction of each atom in the molecule is geometrically hidden by their neighbours, it results very plausible to consider it also contributes to the total integrated elastic cross section not with σ_i^{elast} but with $s_i \sigma_i^{\text{elast}}$. So

total elastic cross sections are evaluated as

$$\sigma^{\text{elast}} = \sum_i s_i \sigma_i^{\text{elast}}. \tag{35}$$

Calculation of molecular differential elastic cross sections requires some additional considerations. Two contributions to the observed molecular elastic cross section are to be considered: A direct one arising from single interactions, and a redispersed one arising from further dispersion of the already dispersed wave amplitudes

$$\frac{d\sigma^{\text{elast}}}{d\Omega} = \frac{d\sigma^{\text{elast}}_{\text{direct}}}{d\Omega} + \frac{d\sigma^{\text{elast}}_{\text{redisp}}}{d\Omega}, \tag{36}$$

$$\sigma^{\text{elast}} = \sigma^{\text{elast}}_{\text{direct}} + \sigma^{\text{elast}}_{\text{redisp}}. \tag{37}$$

While accurate calculation of the angular distribution for this redispersed contribution can be very difficult, some estimative values can be easily proposed by means of simplifying arguments. Let us consider in first place the following two very simple extreme treatments, depending on the angular distribution of dispersed electrons:

i. For electrons suffering appreciable deviations, after two or more dispersions very low directionality can remain, and so an isotropic distribution could be used;
ii. In case of strong forward directionality another extreme simplification would be assuming the same angular distribution for both $d\sigma^{\text{elast}}_{\text{redisp}}/d\Omega$ and $d\sigma^{\text{elast}}_{\text{direct}}/d\Omega$.

As the true angular distribution lays somewhere in between the two above extreme limits, an acceptable description results by estimating the fraction of redispersed electrons closer to each of above simplified descriptions (X_{iso} and X_{same}) and combining them accordingly:

$$d\sigma^{\text{elast}}_{\text{redisp}}/d\Omega \cong X_{\text{iso}}\, d\sigma^{\text{elast}}_{\text{redisp}}/d\Omega\big|_{\text{iso}} + X_{\text{same}} d\sigma^{\text{elast}}_{\text{redisp}}/d\Omega\big|_{\text{same}} \tag{38}$$

and so one gets

$$\frac{d\sigma^{\text{elast}}}{d\Omega} \cong X_{\text{iso}} \frac{\sigma^{\text{elast}}_{\text{redisp}}}{4\pi} + \left[1 + X_{\text{same}} \frac{\sigma^{\text{elast}}_{\text{redisp}}}{\sigma^{\text{elast}}_{\text{direct}}}\right] \frac{d\sigma^{\text{elast}}_{\text{direct}}}{d\Omega}. \tag{39}$$

A very simple criterion for estimating X_{iso} and X_{same} fractions is considering in X_{iso} group all electrons undergoing large deviations (say 90° or more) after being redispersed, an in X_{same} group the remaining ones. As the precise values of $X_{\text{iso}}/X_{\text{same}}$ weights are not critical, one can further approximate the fraction of electrons in iso/same classes as those deviating $90°/2 = 45°$ or more/less after a single dispersion. In this way one simply gets:

$$X_{\text{same}} \approx \frac{\int_0^{45°} \frac{d\sigma^{\text{elast}}_{\text{direct}}}{d\Omega} \sin\theta\, d\theta}{\int_0^{180°} \frac{d\sigma^{\text{elast}}_{\text{direct}}}{d\Omega} \sin\theta\, d\theta}, \qquad X_{\text{iso}} = 1 - X_{\text{same}}. \tag{40}$$

Numerical calculations indicate a good behaviour for this treatment in the whole expected range of energies: From the smallest $2\pi^2/\langle r_{ij}\rangle^2$ aforementioned ones, up to the largest ones where screening effects almost vanish. This will be illustrated below.

2.3.3. Some SCAR results

For differential cross sections only low energy calculations will be presented here (as SCAR procedure approaches the well-known AR one at higher incident energies). As Figs. 7, 8 and 9 show, in all cases SCAR procedure clearly results in an improvement over the AR one and, in all cases, the reduction of forward dispersion and the smoothing of the minima, due to redispersion, goes in the right direction.

For total cross sections, SCAR, AR and other theoretical values are compared with experimental ones in Fig. 8. Results are also very satisfactory in all cases. As expected from

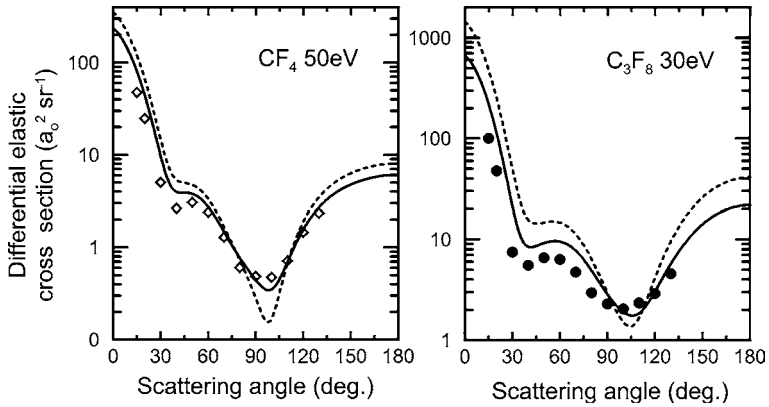

Fig. 7. Comparison for CF_4 and C_3F_8 of the calculated (curves) differential cross sections with some low-energy available experimental data (symbols): Dotted line results from the standard IAM procedure ignoring screening, while full line corresponds to the proposed screening-corrected AR (SCAR). ● Ref. [105]; ◇ Ref. [106].

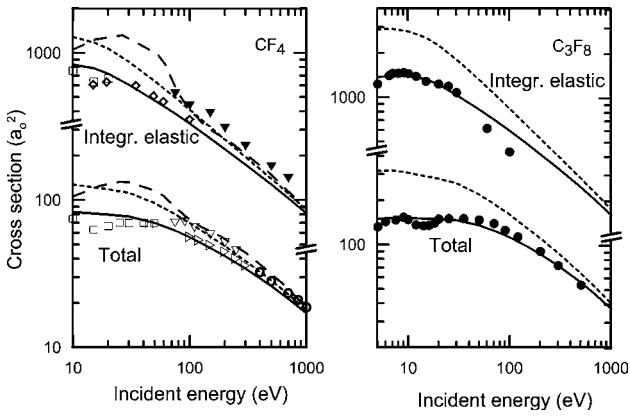

Fig. 8. Same as Fig. 7 but for total and integrated elastic cross sections up to 1 keV energy. Experimental values are ▼ Ref. [107]; □ Ref. [108]; ○ Ref. [60]; ▽ Ref. [109]; ▷ Ref. [110]. Dashed line represents theoretical values from Ref. [111] for CF_4. Note the discontinuities in the axis.

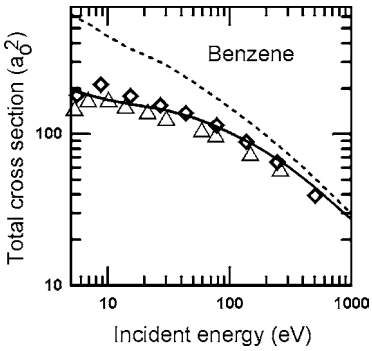

Fig. 9. Comparison for Benzene of the calculated (curves) total cross sections with some available experimental data (symbols): Dotted line results from the standard AR while full line corresponds to the SCAR. ◇ Ref. [112]; △ Ref. [113].

our introduction, for the largest molecule good results are found even at a few eV incident energies.

Even while large screening effects are only to be expected in the low-to-medium energy region, screening effects can be noticed for large molecules at energies as large as 1 keV, and are to be expected very large for macromolecules.

A very interesting merit of SCAR procedure is its simplicity and the fact that the only data required are atomic total cross sections and positions inside the molecule. As considerations on molecular symmetry become unnecessary, the procedure can be applied to arbitrary molecules. For molecules with more than two atoms, multiple-atom overlappings can be easily calculated by means of closed expressions involving a finite number of steps.

2.4. Screening corrections for macro-molecules

Let us consider the important case where a macro-molecule can be assumed as a superposition of smaller easily identifiable blocks. Very important examples of these kind of molecules are proteins (where the building blocks are amino acids) and nucleic acids (where building blocks are the bases or nucleotides).

2.4.1. The SCAR-M treatment in IMM approximation

Calculation of total cross sections While for diatomic species screening effects, due to geometrical overlapping of the different atoms, are relevant only at low energies (below 100 eV), these effects are significant at much larger energies for larger molecules [49], and they should not be ignored at any energies for macro-molecules.

While there is in principle no inconvenient in applying SCAR procedure for macromolecules, some practical difficulties arise for them. One of these is the necessity of specifying the spatial position of each atom, which can be a hard work for a really large molecule. The second one, of numerical nature, arises form the very large number of contributions that must be handled (each atom overlapping with all of the remaining atoms). A natural simplification of SCAR procedure for macromolecules will be considering their constituent

blocks as the basic units instead of atoms:

$$\sigma^{MM} = \sum_{\substack{\text{constituent} \\ \text{moleculess}}} s_i^M \sigma_i^M, \tag{41}$$

where σ^{MM} stands for the total cross section of macro-molecule and σ_i^M represents the total cross section of each of the molecules that build up the macro-molecule. Here the cross sections can be experimental values, or previously calculated ones by means of a SCAR procedure. The s_i^M coefficients correcting for the screening between the blocks are obtained from the cross section values by the usual SCAR expressions. In this case, for the position of each individual block in s_i^M calculations one can use the "center of gravity" calculated as

$$\langle \vec{r}_i^M \rangle = \sum_{\text{atom sin } M_i} \vec{r}_j^{\text{atom}} \sigma_j^{\text{atom}} \Big/ \sum_{\text{atom sin } M_i} \sigma_j^{\text{atom}}. \tag{42}$$

While the σ_i^{atom} cross sections values are energy-dependent, their similar energy behaviour makes $\langle r^M \rangle$ values almost energy-independent.

From the analogy with the atomic case, we will refer this as the Independent molecule model (IMM) and (41) as the SCAR-M procedure.

While for most cross section values one is only interested in the all-orientations average, when considering expression (41) this should be discussed. If for each of the σ_i^M values we use the all-orientations average, we are ignoring the effect of the relative orientation of de different blocks inside the macromolecule. Some sample calculations show that these effects are usually small.

Fig. 10 shows some calculations for an extreme case: a few timine rings all of them with different relative orientations. As can be appreciated, even in this extreme situation, the orientation-effects are small: around 10% at 10 eV and smaller at larger energies. Smaller effects can be expected to arise in a large macromolecule from different orientations of each constituent block.

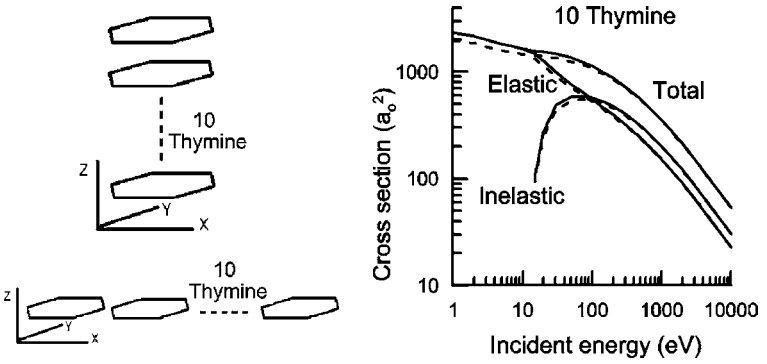

Fig. 10. An imaginary macromolecule consisting of 10 thymine rings. The continuos curves correspond to the results form the IMM treatment. The results form the detailed IAM calculation for the whole macromolecule (dotted lines) coincide with the IMM ones for the chain oriented along the z axis, and are slightly smaller (dashed lines) for the chain oriented along the x axis.

In the same figure the good behaviour of the SCAR-M treatment can be also appreciated, giving results quite close the SCAR ones in all cases.

Calculation of differential cross sections In the same way that the SCAR procedure can be extended for calculation of molecular elastic cross sections [50], we can extend the IMM approximation for evaluation of integrated elastic values. That means using also expression (41) for calculation of integrated elastic cross sections in macro-molecules. Integrated elastic values obtained in this way (SCAR-M) are very favourably compared in Fig. 10 with those obtained by an atom-by-atom treatment (SCAR).

Calculation of differential values in the SCAR approximation [50] was more complicated because one had to separately evaluate contributions to the angular distribution from those electrons that are dispersed by a single atom and those who suffer redispersion. Application of the same procedure to a SCAR-M treatment is troublesome.

This is mainly because for atoms one has spherical symmetry with their dispersion function depending only on the angle around incident direction, while for molecules the corresponding $f_i(\theta, \phi)$ depends on their relative orientation. As an all-orientations average of each molecular block $f_i(\theta, \phi)$ is not useful due to the resulting drastic cancellations, one has to content with the all-orientations average of each $|f_i(\theta, \phi)|^2$, which are just the $d\sigma_i^M/d\Omega$ values.

Under this approximation one can use an expression similar to the one used for evaluation of integrated elastic values:

$$\frac{d\sigma^{MM}}{d\Omega} = \sum_{\substack{\text{constituent}\\ \text{moleculess}}} s_i^M \frac{d\sigma_i^M}{d\Omega}. \tag{43}$$

The main limitation of this expression arises from ignoring (in the angular distribution) all interference terms between atoms belonging to different blocks inside the macromolecule. Nevertheless contribution from these terms is expected to be smaller than that from interference between atoms in each molecule (correctly accounted). This is both because they are spatially more separated, and because a large number of cancellations is to be expected for large species.

Some results from the IMM and SCAR-M approximation As Fig. 11 shows, calculations for the 10-timine unit indicates a good behaviour of expression (43), specially at large energies. At low energies the effect of the ignored interference terms can be appreciated in the absence of rapid oscillations, which are also strongly dependent on the relative orientation of the blocks.

For some applications, such as Monte Carlo simulations, the approximate results from (43) can be enough, as they correctly account for the average values, and the ignored rapid oscillations are not expected to give significant effects in a statistical treatment.

We will finally present some sample results for a real DNA fragment. This will be the well-known dodecamer complex d(CGCGAATTCGCG)2. The atomic coordinates were taken [51] form the Brookhaven Protein Databank (PDB file 1BNA), and the Hydrogen coordinates were restored by means of MolProbity software [52]. An image of the macromolecule generated by RasMol code [53] can be seen in Fig. 12 for its 760 atoms distributed in 24 nucleotides.

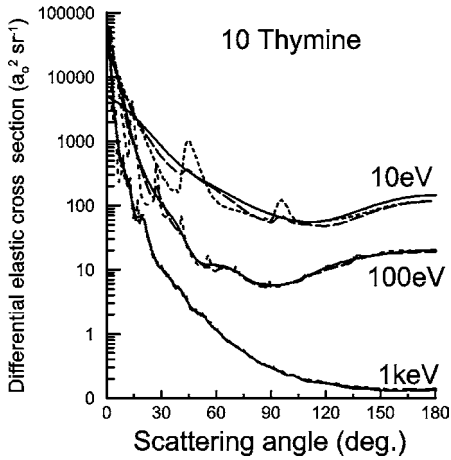

Fig. 11. Differential cross sections for the same imaginary macromolecule consisting of 10 thymine rings. Line coding is the same as used for Fig. 10.

Fig. 12. Image of the d(CGCGAATTCGCG)2 dodecamer complex form 1BNA.PDB file in the Brookhaven Protein Databank. (Hydrogen atoms were also included by MolProbity software.)

Fig. 13 presents differential elastic as well as total elastic and inelastic cross sections calculated in two different ways. The first procedure was the SCAR one under IAM approximation for the 760 individual atoms. The second procedure was the SCAR-M one under the IMM approximation for the 24 nucleotides.

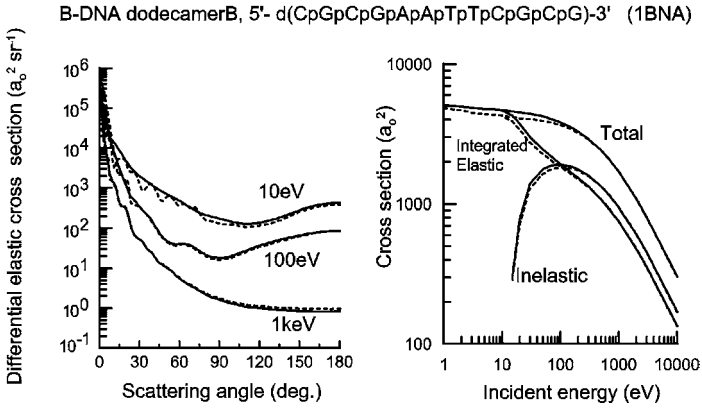

Fig. 13. Comparison of results form the SCAR-M (continuous lines) and SCAR (dashed lines) treatments for 1BNA complex. Differential elastic and total (elastic and inelastic) cross section.

As can be seen, results form both treatments are quite similar, but the SCAR-M one reduces the computation time in around a $760^2/24^2 \approx 1000$ factor respect to the SCAR one. For very large especies this reduction can become very significative, not only due to the required computation effort, but also to numerical difficulties in handling huge number of tiny contributions between each atom pair. Also a very interesting point is the possibility of calculating cross sections for very complicated molecules by means of previously calculated (or experimental) data for a few constituents, as in the case of DNA or protein structures.

2.5. Molecular gas mixtures: Electron scattering cross sections and energy loss

An important application of the model we are proposing here is to characterise the response of the radiation detectors that are commonly used for radiotherapy and radiation protection purposes. Ionisation chambers for dosimetric uses are commonly filled of air and sometimes of special gas mixtures that absorb energy as the human tissue (Tissue Equivalent Material). The method of calculation described above can be easily applied to these targets by introducing the coefficient of each component in the mixture. As far as experiments are concerned, the enormous amount of data required to represent the trajectories of electrons in the considered energy range it is impossible to comprise a complete set of experimental data. Hence approximate calculation methods as those described above are then very useful for this purpose. However, in order to estimate the accuracy of the final simulation model, some experimental validation of the calculated data should be needed. From the experimental point of view, the most accurate cross sectional data are the total electron scattering cross section. In the last decade, we have been applying a transmission beam technique to measure the total electron scattering cross sections from simple molecules with experimental errors within 3% [54–60]. Therefore, we have measured the corresponding total electron cross sections to compare the results with the sum of the calculated integral elastic and inelastic electron scattering cross sections. The result of this comparison will determine the accuracy we will assign to the theoretical data.

On the other hand, other important point in the simulation model is the decision of the energy loss by the electrons for each single collision. Its here again impossible to formulate an energy loss distribution function based on the probability distribution of all accessible excited states, both discrete and continuous. As will be shown, available simulation codes assume excitation probability distributions based on empirical considerations or in the Bethe formula [10]. As this probability function is essential for a molecular description of the electron transport we will derive it from our experimental energy loss spectra.

2.5.1. Total cross section measurements

The experimental set-up to perform total cross section measurements and energy loss spectra is based on that reported previously [61] including the recent improvements already described in Ref. [62]. A schematic draw of the experimental system is shown in Fig. 14. Only a brief description will be given here. The primary beam is produced by an emitting filament. A combination of magnetic and electrostatic fields controls the direction of the beam and reduces the energy spread to about 100 meV. The collision chamber containing the gas target has a 75 mm length tube delimited by two apertures. The entrance aperture is 0.5 mm in diameter. Different exit apertures of 1, 2 and 3 mm have been used, according to the experimental requirements. The gas pressure in the chamber is measured with an absolute capacitance gauge (MKS Baratron 127A) and it is varied up to 20 mTorr according to the experimental conditions. Electrons emerging from the collision chamber are deflected by a quadrupole electrostatic system to select the angle of analysis. The energy analyser is a hemispherical electrostatic spectrometer in combination with a retarding field. In these conditions, the energy resolution of the spectrometer is estimated to be 0.5 eV for the whole energy range considered here. Transmitted electrons through the analyser are finally detected by a channel electron multiplier operating in single pulse counting mode. Counting rates are typically of the order of 10^3 s^{-1} for total cross section measurements and up to 10^4 s^{-1} during the energy loss spectra capture. The maximum angular acceptance of the energy analyser is 1.9×10^{-5} sr. The system is differentially pumped by two turbo pumps of 70 and 250 l/s, respectively, reaching a background pressure of 10^{-8} Torr.

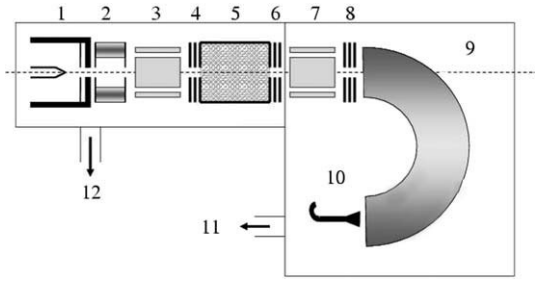

Fig. 14. Experimental apparatus: 1, electron gun. 2, transverse magnetic field. 3, 7, quadrupole electrostatic plates. 4, 6, 8, decelerating and accelerating lenses. 5, scattering chamber. 9, hemispherical electrostatic energy analyzer. 10, channel electron multiplier. 11, 12 vacuum turbo pumps.

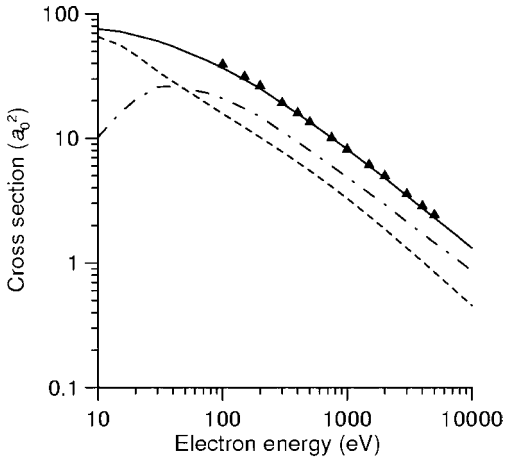

Fig. 15. Present electron scattering cross sections from methane based tissue equivalent material; ▲, total cross section measurements; —, calculated total cross sections; - -, calculated integral elastic cross sections; - · -, calculated integral inelastic cross sections.

The pressure in the electron gun and energy analyser region is kept lower than 10^{-6} Torr during the measurements.

As an example of the degree of concordance between the present theoretical and experimental data we will show a comparison for methane based tissue equivalent gaseous material (TEM). The total electron scattering cross sections from this TEM have been measured for energies between 100 and 5000 eV. The gaseous TEM target was prepared as a mixture formed by methane (64.4%), carbon dioxide (32.4%) and nitrogen (3.2%). A glass bulb is filled with each constituent gas up to a total gas pressure of 2 bar by controlling their partial gas pressures with an absolute manometer.

The experimental results are plotted in Fig. 15 in order to establish a comparison with the calculated values. The estimated experimental error of these data is set to about 5%. A detailed analysis of the main error sources can be found in Ref. [62]. The additional error induced by the composition of the target mixture has been included in the statistical uncertainties by repeating the measurements for different sample preparations with the same composition. As it is shown in Fig. 15, there is a good agreement between theoretical and experimental data. For energies above 1 keV, experimental total cross section tend to be higher than the calculated values as the energy increases, reaching a maximum discrepancy of about 10% at 5 keV. We can therefore assume an accuracy for the present calculated integral cross section of the order of 10.

2.5.2. Energy loss spectra

The same experimental system shown in Fig. 14 can be used to obtain electron energy loss spectra by swiping the energy analyser with a controlled voltage ramp. Energy loss spectra have been measured for energies between 100 and 5000 eV at different scattering angles. The scattering angles were selected by deflecting the scattered beam with a quadrupole electrostatic plate system at the exit of the collision chamber. As mentioned earlier, these spectra will be used as normalised energy loss distribution functions in the electron trajectories simulation procedure that will be discussed in Section 3.

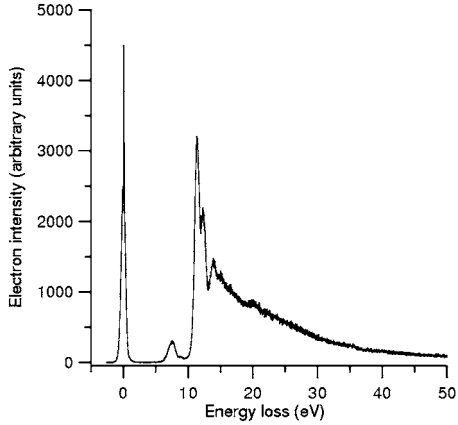

Fig. 16. Experimental energy loss spectrum for 2000 eV incident electrons and 20 mTorr of air in the collision chamber.

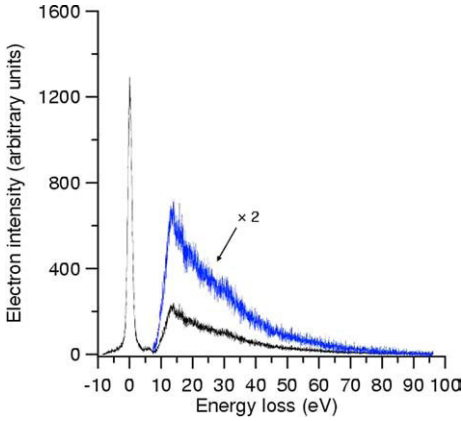

Fig. 17. Energy loss of 750 eV electrons in 10 mTorr of methane based tissue equivalent material for a scattering angle of 10 degrees.

Representative energy loss spectra of electrons in air and methane based TEM are shown in Figs. 16 and 17, respectively. As mentioned above, the energy loss distribution functions we used in the simulation procedure described in the next section are based in these experimental spectra.

3. MONTE CARLO SIMULATION

In this section we will describe a Monte Carlo code that implements the standard physics for photons in combination with new processes for electrons based directly on our experimental and calculated cross sections. From a different point of view, this Monte Carlo code can be seen as a tool to apply the knowledge gathered in new experimental low energy

electron databases to practical applications, suitable both in macroscopic and microscopic scales. Macroscopic parameters, such as energy loss profiles and averaged deposited energy, can be studied more accurately from these new models. According with the energy range of the implemented cross sections, this code can be naturally applicable to study profiles of deposition of energy in the microscopic scale, in which other codes can only extrapolate results generated from data computed to be used at higher energies and larger scales.

The code, presented in detail in [8,10] is based on the GEANT4 [63] code developed at CERN, incorporating new interaction processes for the low energy electron collisions. Since GEANT4 was specifically designed to provide the opportunity of using databases and processes different to the ones included in the distribution, its standard procedures can be replaced or complemented with new interaction processes. The main input parameters for the new implemented processes are experimental energy loss spectra and (differential and integral) cross sections of the most probable interaction processes occurring in the energy range of interest. Two scattering processes are implemented: elastic and inelastic. Ionization is treated as a probabilistic subprocess of the inelastic scattering. The original low energy processes in GEANT4 were used for the interactions of incoming photons and secondary X and gamma rays. Among the variety of targets of interest in radiological and dosimetric applications, air and tissue equivalent material (TEM) are among the most suitable. Air is commonly adopted as a reference radiological material and usually fills the ionization chambers in which some radiation detectors are based. The interest of tissue in these fields is obvious. Only data for these two materials are implemented in the current version of the code. We provide in this section a detailed description of the new processes is presented. Some representative cases of the tests performed to validate the code are also presented and comparisons with a reliable Monte Carlo code are discussed.

3.1. General description of the simulation code

The code was designed as a standard GEANT4 application program. GEANT4 provides a set of tools designed for simulating the passage of particles through matter. It was written in the C++ programming language and includes a complete set of functions such as geometry and material definition, physics modeling, particle tracking and hit process. Regarding the physics, a full range of processes are available, including electromagnetic, hadronic and optical. The energy range of application covers from 250 eV to the TeV. A complete reference to the implementation of the processes can be found in [64].

One of the most valuable features of GEANT4 is its great flexibility. The toolkit was designed specifically to add and modify standard physical processes by using new models and databases. It is possible to modify some of the implemented processes to solve a specific problem, and also to write processes completely from scratch and to operate together with existing ones. To build our code we followed the usual way in GEANT4 applications, which includes the definition of the geometry associated to the physical arrangement, the generation of primary events according to the simulated experiment, the registration of particles and physics processes involved and the event manipulation in order to render statistics and data output. Tools for geometry modelling and visualization provided in GEANT4 are more than sufficient for the needs on geometry modelling in practically any realistic application.

3.2. Standard photon physics

The so-called GEANT4 low energy electromagnetic model [65,66] was designed to extend the coverage of standard electromagnetic interactions in GEANT4 down to 250 eV. It is based on the data evaluated from the following public libraries:

- EPDL97 (Evaluated Photons Data Library) [11];
- EEDL (Evaluated Electrons Data Library) [67];
- EADL (Evaluated Atomic Data Library) [68];
- Stopping power data: Refs. [69–72];
- Binding energy values based on data of Scofield [73]

and a number of classical works for sampling final states of the particle after a Compton [74–77], Rayleigh [78,79], Pair Production [80–84] and Photoelectric [11,68] interaction. See the section for Low energy extension of electromagnetic processes in the manual [63, Chapter III, Section 11].

When low energy photons pass through matter the most probable interaction process is the photoelectric effect, and we will concentrate on this effect. In this code, the low energy extension of the photoelectric effect implemented in GEANT4 is used. Other processes have less impact on the simulation. Pair production occurs above 1.02 MeV, and is out of our scope at the current stage. Rayleigh and Compton scattering have small cross sections at 10 keV and below when compared to photoelectric effect. These three effects of secondary interest will be taken into account in future versions simply by declaring their corresponding GEANT4 classes.

3.3. New electron interaction processes

3.3.1. Implementation of new processes in GEANT4

A new set of processes were constructed for tracking the electrons, based on experimental cross sections at energies from 10 eV to 10 keV. In the current version, two main processes are considered: elastic and inelastic scattering. Once an inelastic process occurred, ionization process was also considered. The transition from a standard GEANT4 code is done by declaring new processes for electrons in the GEANT4 class physics. The new processes for electrons are declared by making use of the function `AddDiscreteProcess` of the particle manager. In a conventional GEANT4 code using low energy electromagnetic processes the classes considered for declaring the permitted electron processes (multiple scattering, ionization and bremsstrahlung) are:

- `G4MultipleScattering`
- `G4LowEnergyIonisation`, and
- `G4LowEnergyBremsstrahlung`.

In our approach, these classes are ruled out. Processes of two new classes, the new elastic and inelastic scattering processes, are added to the list constructed by the process manager for electrons. The classes associated with these two new processes are created as inherited classes of the class `G4VdiscreteProcess`, strictly following all GEANT4 procedures for the following tasks:

i. Cross section data input. The functions `SetPhysicsTableBining` and `BuildPhysicsTable` are used for this purpose.
ii. Cross section data handling, performed by making use of the following functions: `ComputeCrossSectionPerMolecule`, `GetMeanFreePath`, `ComputeMeanFreePath` and `GetMicroscopicCrossSection`.
iii. Modification of the energy and momentum of the particle, computing the deposited energy, change of direction and generation of secondary particles (function `PostStepDoIt`).
iv. Other actions, such as the ones carried out by the functions `IsApplicable` or `PrintInfoDefinition`.

The new processes are treated as discrete processes. GEANT4 standard interaction processes implements both discrete and continuous approaches for electron energy loss. These have not been designed to be compatible with other GEANT4 processes for electrons. As a matter of fact, a potential user has to select either the standard GEANT4 multiple scattering, ionization and bremsstrahlung processes for electrons, or the new package of processes, without having the possibility of mixing "conventional" and "new proposed" ones.

The simulation of elastic and inelastic scattering of electrons passing through air was implemented by making use of integral and differential cross sections obtained from experimental data and theoretical calculations, as reported in Section 2. The energy lost by an electron in an inelastic scattering process was sampled by making use of a probability distribution function based on normalized experimental energy loss spectra. As simplification, one single energy loss spectrum is considered in the simulation for the whole energy range. The energy lost by an electron in an inelastic scattering process was sampled by making use of a probability distribution function (the normalized experimental energy loss spectra).

Both elastic and inelastic scattering new processes were implemented in the `C++` programming language by adapting inherited classes of existing classes in GEANT4 for discrete processes. When a single collision takes place, the program must decide whether it is elastic or inelastic by assessing the related cross section data. When an inelastic process occurs, a secondary electron can be ejected by an ionization process. Accurate ionization cross section data have been taken from the experimental results. In this energy range, the ionization probability can be considered as a constant for each material constituent within the inelastic processes.

Once the total cross sections are properly introduced for each new process, by making use of the GEANT4 functions for creating cross section tables, the mean free path corresponding to electrons for each process is computed and processed directly by GEANT4, as a procedure transparent to the new processes.

It has been shown [56] that experimental cross sections used in this code have been obtained at conditions in which multiscattering processes are negligible. These cross sections can be used to model the elastic and inelastic scattering of an electron in air, no matter where it originated. They can be used without any limitations to track primary electrons, or secondary ones, generated by inelastic scattering (supposing that their energies lie within the energy range of the implemented cross section data tables). They can therefore be used to track scattering of electrons in air, independently of its pressure, as long as the gas can be considered as ideal, an approach used in GEANT4 for relating pressure, temperature,

density and number of molecules per mol. This is also valid for the case of the tissue equivalent gas used in this simulation

3.3.2. Elastic scattering

When an elastic interaction takes place the electron undergoes a change in its direction. We have assumed no energy loss because, according to the relationship between the electron and atom mass, a few thousandths of eV are lost in the worst case.

The change in the electron direction is calculated according to an angular probability distribution function derived from the differential elastic cross section which was previously calculated. In order to decide the angle of the emerging scattered electron, the energy range was divided into 22 bins.

Differential elastic cross sections at a representative energy for each of the 22 bins have been used to compute the normalized distribution functions for the scattering angles.

3.3.3. Inelastic scattering

Energy loss and scattered direction In inelastic collisions the electron losses part of its energy. The amount of energy lost is sampled from databases obtained from experimental measurements. In this way, the simulation provides an energy loss profile compatible with experimental data. The agreement between experimental loss spectrum and simulated energy loss results was previously demonstrated [8] to be lower than 0.1%. In this version, the differential cross sections for elastic scattering have also been used for modeling the scattered electron direction in the inelastic process.

Ionization process Ionization was considered as a subprocess of the inelastic scattering. This approach appears to be a natural one because the ionized electron takes its energy from the incident electron in an inelastic collision.

The complete algorithm to treat an inelastic interaction, in its current implementation, could be stated as follows:

i. Given the kinetic energy K of the incident electron, GEANT4 samples whether an inelastic interaction occurs and the interaction position, taking into account the electron mean free path in the media and cross sections for the declared processes at this energy.
ii. The energy W that the electron will lose is sampled by Monte Carlo techniques, according to the energy loss spectrum in the interval from 0 to K.
iii. The scattered electron continues with a kinetic energy $K-W$ in a direction sampled according to the differential cross section corresponding to the incident energy.
iv. A new sampling determines whether an ionization process will occur or not. As commented above, a simple uniform distribution function is used. If no ionization has to be considered, then the whole energy W left by the primary electron is deposited in the medium.
v. If ionization occurs, then an energy U equal to the ionization energy of the atom the electron has stroked is deposited in the medium. GEANT4 provides standard functions to locate the particular atom of the medium where the interaction has taken place. The secondary electron then will carry a kinetic energy $W-U$, and its direction is computed using a simplified model: Conservation of momentum and energy is supposed.

3.4. Benchmarking

3.4.1. Validation tests

Some tests were performed in order to check the consistency of the simulation output within the framework of the model considered. One representative test performed was related with the intensity of a transmitted electron beam passing through a volume, acting as collision chamber, filled with air at different pressures. A perfectly collimated monochromatic beam focused at the analyzer was simulated. Energy of the electrons was fixed at 5 keV, and all particles not deflected by the gas molecules were detected and accounted for in the analyzer. The relative intensity of the beam was computed as the ratio between electrons passing through the gas without undergoing any interaction per unit time, I, and the electrons emitted by the source per unit time, I_0. To avoid multiple scattering and to make sure that single interactions were absolutely dominant in the simulated experiment, only low pressure values were used. As expected, the relative transmitted intensity of the electron beam showed an exponential relationship with the gas pressure. An estimate of the total interaction cross section for 5 keV electrons in air can be derived from the slope of the linear fit. The obtained value corresponded to $4.33a_0^2$. As a comparison, the expected total cross section for 5 keV electrons scattering in air can be calculated as $4.30a_0^2$, which is in agreement with the value obtained from simulation.

3.4.2. Comparison with Penelope

In the last few years, Penelope [85] has become one of the Monte Carlo simulation codes widely used in the domain of low energies. We have used it as a reference in our modeling of photon physics, and for contrasting results from our simulations. Penelope has been designed to cover the whole physics involved in the passage of particles through matter, down to 100 eV. This includes the implementation of up-to-date models and algorithms related to processes, particle tracking and interaction cross sections at this range of energies. This section shows that agreement between both approximations are achieved in macroscopic estimates and total cross sections, while differences appear in the microscopic energy deposition distributions and differential cross sections. This is just the expected result, according to the models used by Penelope and our simulation code.

Energy loss distribution The energy lost by a 5 keV electron beam passing through layers of air and TEM at several pressure values was evaluated both with the code presented in this paper and Penelope-2003. The layer was sufficiently thin to guarantee just one interaction per incident electron, avoiding multiple scattering which could blur the comparison of the results. Normalized energy loss histograms are plotted in Fig. 18.

Results were rather insensitive to the pressure values of the gas layer. As expected, the results provided by Penelope in the low energy range are far from accurate. According with its model, it just provides a discrete approach to the continuum energy loss spectrum. The simplified model used in Penelope is based on single energy depositions, as a consequence of adopting the model from Liljequist [86], describing the shell excitation as a single delta oscillator. It can be confirmed in Fig. 18 that only these single energy channels are representative, together with their multiples.

In the interpretation of results presented in Fig. 18 it must be taken into account that the width of energy bins in the Penslab module of Penelope code was reduced from 20 eV

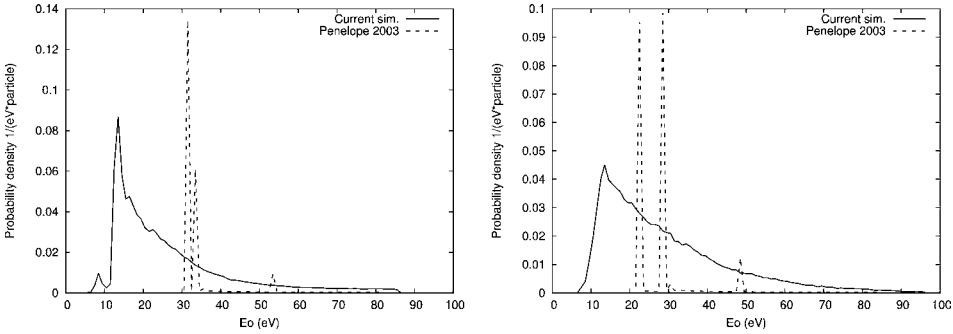

Fig. 18. Energy loss histograms (normalized) for electrons interactions in air (left) and TEM (right) from 10 to 100 eV. Thin dashed lines correspond to Penelope, solid lines to the presented code.

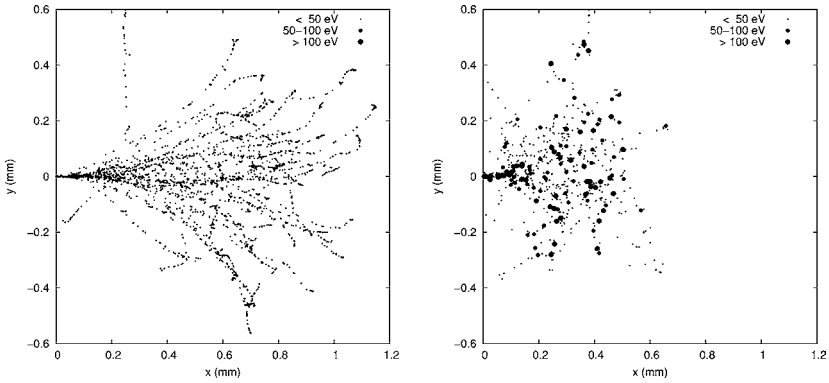

Fig. 19. Energy loss profile for 5 keV electrons interactions in air at 1 atmosphere. (Left) Results from the presented code. (Right) Results from Penelope.

(original value) down to 1 eV, in order to provide higher energy resolution. This parameter is also relevant in the estimate of the average deposited energy. While in our code it is 31.9 eV in air and 38.9 in TEM, the value calculated from Penelope data are 38.7 eV in air and 47.0 eV in TEM.

Energy deposition profile In Figs. 19 and 20 we present graphic results of interaction profiles obtained for a simulation of an electron collision experiment. In this case, a beam of 5 keV electrons impinging air (Fig. 19) and TEM (Fig. 20) at a pressure of 1 atmosphere was simulated. Energy depositions are represented in a size scale depending on the deposited energy value. Results obtained with our code are shown on the left, and on the right results with Penelope for conditions as similar as technically possible.

There are significant differences between the profiles of trajectories provided by both simulation codes. The penetration of electrons in air given by our code seems to be larger than in Penelope, and trajectories are less curled. Both facts may be considered a consequence of differential cross sections used. On the other hand, in our code a greater amount

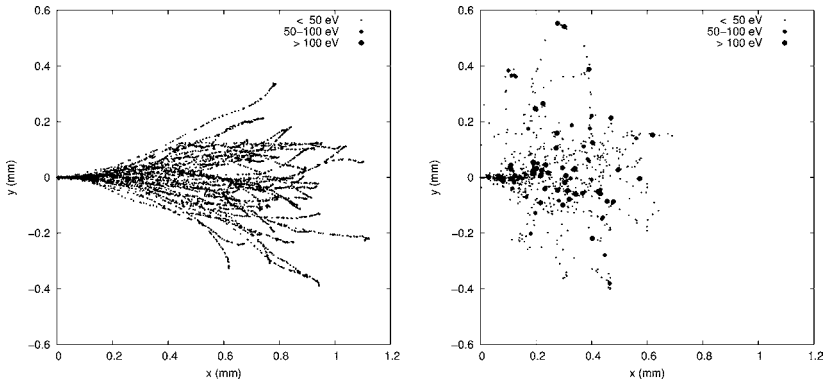

Fig. 20. Energy loss profile for 5 keV electrons interactions in TEM-gas at 1 atmosphere. (Left) Results from the presented code. (Right) Results from Penelope.

of low energy deposition points can be observed, while Penelope shows fewer number of deposition points, but with larger amount of deposited energy. This is caused by the 100 eV threshold value for electrons used in Penelope. Thus, we simulated electron cascades and energy depositions with more detail than Penelope.

At this stage, these differences can only be interpreted from a qualitative point of view. It must be taken into account that simplifications such as the use of identical differential cross sections for elastic and inelastic scattering or a gross binning for the differential cross sections affect the results of our code. On the other hand, current version of our simulation code includes reliable (below 10% error) differential cross section values only for electrons with energies above 100 eV.

4. CONCLUSIONS

The study of radiation, and particularly electrons, interactions with materials of biological interest at intermediate and high energies presents difficulties related with the high variety of possible processes and the complexity of their constituting molecules. In this context, realistic approximations, validated by experimental results, are needed. Electron–atom and electron–molecule cross sections can be calculated ab initio by relatively simple methods, with reasonable accuracy. For large molecules screening corrections are essential, especially for large ones. For the largest macro-molecules an approximated treatment considering smaller units can considerably simplify calculations. Sample calculations indicate good results for total cross sections, while differential values are somewhat less accurate. One of the most interesting points is the possibility of calculating cross sections for very complicated molecules by means of previously calculated (or experimental) data for a few constituents, as in the case of DNA or protein structures.

The degree of accuracy of calculated data can be checked through a comparison with the total electron scattering cross section obtained with a transmission beam technique. This method provides accurate values, within 5%, giving also information about the distribution of the energy loss by the electrons after the interaction.

Finally, we have developed a Monte Carlo simulation program, based on the general tools of GEANT 4, which uses as input parameters our calculated cross sectional data and the energy loss distribution functions based on the experimental energy loss spectra. This simulation procedure allows energy deposition models at the molecular level that could be very useful in biological and medical applications when microscopic energy deposition patterns are required.

REFERENCES

[1] B. Boudaiffa, P. Cloutier, D. Hunting, M.A. Huels, L. Sanche, *Science* **287** (2000) 1658.
[2] B. Boudaiffa, P. Cloutier, D. Hunting, M.A. Huels, L. Sanche, *Radiat. Res.* **157** (2002) 227.
[3] S. Gohlke, A. Rosa, E. Illenberger, F. Brüning, M.A. Huels, *J. Chem. Phys.* **116** (2002) 10164.
[4] M.A. Huels, B. Boudaiffa, P. Cloutier, D. Hunting, L. Sanche, *J. Am. Chem. Soc.* **125** (2003) 4467.
[5] X. Pan, P. Cloutier, D. Hunting, L. Sanche, *Phys. Rev. Lett.* **90** (2003) 208102.
[6] L. Sanche, *Eur. Phys. J. D* **35** (2005) 367.
[7] Z. Deng, I. Bald, E. Illenberger, A. Huells, *Phys. Rev. Lett.* **95** (2005) 153201.
[8] A. Roldán, J.M. Pérez, A. Williart, F. Blanco, G. García, *J. Appl. Phys.* **95** (2004) 5865.
[9] J.C. Oller, A. Muñoz, J.M. Pérez, F. Blanco, P. Limão-Vieira, G. García, *Chem. Phys. Lett.* (2005), submitted for publication.
[10] A. Muñoz, J.M. Pérez, G. García, F. Blanco, *Nucl. Instrum. Methods A* **536** (2005) 176.
[11] D. Cullen, J.H. Hubbell, L. Kissel, *EPDL97*: *The Evaluated Photon Data Library*, 1997 version, UCRL-50400, vol. 6, rev. 5.
[12] M. Inokuti, *Rev. Mod. Phys.* **43** (1971) 297.
[13] *International Commission on Radiation Units and Measurements*, ICRU Report No. 37, Bethesda, MD, 1984.
[14] G. García, F. Manero, *Phys. Rev. A* **53** (1996) 250.
[15] N.F. Mott, H.S.W. Massey, *The Theory of Atomic Collisions*, third ed., Oxford Univ. Press, 1965.
[16] G. Staszewska, D.W. Schwenke, D. Thirumalai, D.G. Truhlar, *Phys. Rev. A* **28** (1983) 2740;
G. Staszewska, D.W. Schwenke, D. Thirumalai, D.G. Truhlar, *J. Phys. B* **16** (1983) L281.
[17] G. Staszewska, D.W. Schwenke, D.G. Truhlar, *Phys. Rev. A* **29** (1984) 3078.
[18] D. Gregory, M. Fink, *At. Data Nucl. Data Tables* **14** (1974) 39;
M. Fink, A. Yates, *At. Data* **1** (1970) 385.
[19] I.I. Sobelman, L.A. Vainshtein, E.A. Yukov, *Excitation of Atoms and Broadening of Spectral Lines, Springer Series in Chemical Physics*, vol. 7, Springer-Verlag, 1981.
[20] Dz. Belkic, *Principles of Quantum Scattering Theory*, Series in Atomic and Molecular Physics, IOP, 2004.
[21] M.L. Goldberger, *Phys. Rev.* **74** (1948) 1269.
[22] A. Jain, B. Etemadi, K.R. Karim, *Phys. Scr.* **41** (1990) 321.
[23] Y. Jiang, J. Sun, L. Wan, *Phys. Rev. A* **52** (1995) 398.
[24] D. Raj, S. Tomar, *J. Phys. B* **30** (1997) 1989.
[25] S.P. Khare, D. Raj, P. Sinha, *J. Phys. B* **27** (1994) 2569.
[26] K.N. Joshipura, P.M. Patel, *Z. Phys. D* **29** (1994) 269.
[27] F. Blanco, G. García, *Phys. Lett. A* **255** (1999) 147.
[28] F. Blanco, G. García, *Phys. Lett. A* **295** (2002) 178.
[29] F. Blanco, G. García, *Phys. Rev. A* **67** (2003) 022701.
[30] F. Blanco, G. García, *Phys. Lett. A* **317** (2003) 458.
[31] F. Blanco, G. García, *Phys. Lett. A* **330** (2004) 230.
[32] F. Calogero, *Variable Phase Approach to Potential Scattering*, Academic Press, New York, 1967.
[33] R.D. Cowan, *The Theory of Atomic Structure and Spectra*, University of California Press, London, 1981.
[34] M.E. Riley, D.G. Truhlar, *J. Chem. Phys.* **63** (1975) 2182.
[35] X.Z. Zhang, J.F. Sun, Y.F. Liu, *J. Phys. B* **25** (1992) 1893.
[36] J. Perdew, Zunger, *Phys. Rev. B* **23** (1981) 5048.
[37] H. William, *Numerical Recipes in Fortran*, second ed., Cambridge Univ. Press, 1994.
[38] R. Panajotovic, D. Filipovic, B. Marinkovic, V. Pejcev, M. Kurepa, L. Vuskovic, *J. Phys. B* **30** (1997) 5877.

[39] H.S. Massey, *Electronic and Ionic Impact Phenomena*, vol. 2, Clarendon, Oxford, 1969.
[40] D. Raj, *J. Phys. B* **24** (1991) L431.
[41] Y. Jiang, J. Sun, L. Wan, *Phys. Lett. A* **231** (1997) 231.
[42] K.N. Ioshipura, P.M. Patel, *J. Phys. B* **29** (1996) 3925.
[43] J. Sun, Y. Jiang, L. Wan, *Phys. Lett. A* **195** (1994) 81;
Y. Liu, J. Sun, *Phys. Lett. A* **222** (1996) 233.
[44] G.P. Karwasz, A. Piazza, R.S. Brusa, A. Zecca, *Phys. Rev. A* **59** (1999) 1341.
[45] K.N. Joshipura, P.M. Patel, *Z. Phys. D* **29** (1994) 269.
[46] Y. Jiang, J. Sun, L. Wan, *J. Phys. B* **30** (1997) 5025.
[47] Y. Jiang, J. Sun, L. Wan, *Phys. Lett. A* **237** (1997) 53.
[48] A. Zecca, R. Melissa, R. Brusa, G. Karwasz, *Phys. Lett. A* **257** (1999) 75.
[49] F. Blanco, G. García, *Phys. Lett. A* **317** (2003) 458.
[50] F. Blanco, G. García, *Phys. Lett. A* **330** (2004) 230.
[51] Brookhaven Protein Databank (PDB file 1bna), http://pdb.ccdc.cam.ac.uk/pdb/.
[52] MolProbity software at http://kinemage.biochem.duke.edu/molprobity/index.html.
[53] RasMol visualization software at http://www.umass.edu/microbio/rasmol/index2.htm.
[54] G. García, F. Manero, *Phys. Rev. A* **53** (1996) 250.
[55] G. García, F. Manero, *J. Phys. B* **29** (1996) 4017.
[56] G. García, M. Roteta, F. Manero, *Chem. Phys. Lett.* **264** (1997) 589.
[57] G. García, F. Manero, *Phys. Rev. A* **57** (1998) 1069.
[58] G. García, F. Blanco, A. Williart, *Chem. Phys. Lett.* **335** (2001) 227.
[59] J.L. de Pablos, P.A. Kendall, P. Tegeder, A. Williart, F. Blanco, G. García, N.J. Mason, *J. Phys. B* **35** (2002) 865.
[60] F. Manero, F. Blanco, G. García, *Phys. Rev. A* **66** (2002) 032713.
[61] A. Williart, P.A. Kendall, F. Blanco, P. Tegeder, G. García, N.J. Mason, *Chem. Phys. Lett.* **375** (2003) 39.
[62] P. Limão-Vieira, F. Blanco, J.C. Oller, A. Muñoz, J.M. Pérez, M. Vinodkumar, G. García, N.J. Mason, *Phys. Rev. A* **71** (2005) 032720.
[63] S. Agostinelli, *et al.*, *Nucl. Instrum. Methods Phys. Res. A* **506** (2003) 250.
[64] *GEANT4 Physics Reference Manual. Low energy Extensions*, available at GEANT4 web page http://wwwasd.web.cern.ch/wwwasd/geant4/geant4.html.
[65] J. Apostolakis, *et al., GEANT4 Low Energy Electromagnetic Models for Electrons and Photons*, CERN-OPEN-99-034, 19 August 1999.
[66] J. Apostolakis, *et al., Low-Energy Extensions of GEANT4 Electromagnetic Processes*, Proc. of Space Radiation Environment Workshop, ESA-ESTEC, Noordwijk, The Netherlands, November 1999.
[67] S.T. Perkins, D.E. Cullen, S.M. Seltzer, *Tables and Graphs of Electron-Interaction Cross-Sections from 10 eV to 100 GeV Derived from the LLNL Evaluated Electron Data Library (EEDL)*, $Z = 1$–100, UCRL-50400, vol. 31.
[68] S.T. Perkins, D.E. Cullen, M.H. Chen, J.H. Hubbell, J. Rathkopf, J. Scofield, *Tables and Graphs of Atomic Subshell and Relaxation Data Derived from the LLNL Evaluated Atomic Data Library (EADL)*, $Z = 1$–100, UCRL-50400, vol. 30.
[69] H.H. Andersen, J.F. Ziegler, *The Stopping and Ranges of Ions in Matter*, vol. 3, Pergamon, 1977.
[70] J.F. Ziegler, *The Stopping and Ranges of Ions in Matter*, vol. 4, Pergamon, 1977.
[71] J.F. Ziegler, J.P. Biersack, U. Littmark, *The Stopping and Ranges of Ions in Solids*, vol. 1, Pergamon, 1985.
[72] A. Allisy, *et al.*, Stopping Powers and Ranges for Protons and Alpha Particles, ICRU Report 49, 1993.
[73] J.H. Scofield, in: B. Crasemann (Ed.), *Radiative Transitions in Atomic Inner-Shell Processes*, Academic Press, New York, 1975, pp. 265–292.
[74] Summary of existing information on the incoherent scattering of photons particularly on the validity of the use of the incoherent scattering function, *Radiat. Phys. Chem.* **50** (1997) 113.
[75] D.E. Cullen, *Nucl. Instrum. Methods Phys. Res. B* **101** (1995) 499.
[76] J. Stepanek, New photon, positron and electron interaction data for geant in energy range from 1 eV to 10 TeV, in preparation.
[77] W. Heitler, *The Quantum Theory of Radiation*, Clarendon, Oxford, 1954.
[78] J.H. Hubbell, *et al.*, *J. Phys. Chem. Ref. Data* **8** (1979) 69.
[79] D.E. Cullen, *Nucl. Instrum. Methods Phys. Res. B* **101** (1995) 499.
[80] L. Urban, in: R. Brun *et al., Geant. Detector Description and Simulation Tool*, CERN Program Library, Section Phys/211, 1993.

[81] R. Ford, W. Nelson, SLAC-210, UC-32, 1978.
[82] J.C. Butcher, H. Messel, *Nucl. Phys.* **20** (1960) 15.
[83] H. Messel, D. Crawford, *Electron–Photon Shower Distribution*, Pergamon, Oxford, 1970.
[84] Y.S. Tsai, *Rev. Mod. Phys.* **46** (1974) 815;
Y.S. Tsai, *Rev. Mod. Phys.* **49** (1977) 421.
[85] F. Salvat, J.M. Fernández-Varea, J. Sempau, PENELOPE. A Code System for Monte Carlo Simulation of Electron and Photon Transport, OECD-Nuclear Energy Agency, 2003.
[86] D. Liljequist, *J. Phys. D* **16** (1987) 1567.
[87] F.J. de Heer, R.H.J. Jansen, *J. Phys. B* **10** (1977) 374.
[88] F.J. de Heer, R.H.J. Jansen, W. van der Kaay, *J. Phys. B* **12** (1979) 979.
[89] R.D. DuBois, M.E. Rudd, *J. Phys. B* **9** (1976) 2657.
[90] D.F. Register, S. Trajmar, S.K. Srivastava, *Phys. Rev. A* **21** (1980) 1134.
[91] R.H.J. Jansen, F.J. de Heer, H.J. Luyken, B. van Wingerden, H.J. Blaauw, *J. Phys. B* **9** (1976) 185.
[92] T.W. Shyn, *Phys. Rev. A* **22** (1980) 916.
[93] J.F. Williams, A. Crowe, *J. Phys. B* **8** (1975) 2233.
[94] J.F. Williams, B.A. Willis, *J. Phys. B* **8** (1975) 1670.
[95] S.C. Gupta, J.A. Rees, *J. Phys. B* **8** (1975) 417.
[96] D. Cvejanovic, A. Crowe, *J. Phys. B* **30** (1997) 2873.
[97] R.H.J. Jansen, F.J. de Heer, *J. Phys. B* **9** (1976) 213.
[98] A. Jain, K.L. Baluja, *Phys. Rev. A* **45** (1992) 202.
[99] G. García, A. Perez, J. Campos, *Phys. Rev. A* **38** (1988) 654.
[100] K.R. Hoffman, M.S. Dababneh, Y.-F. Hseih, W.E. Kauppila, V. Pol, J.H. Smart, T.S. Stein, *Phys. Rev. A* **25** (1982) 1393.
[101] Ch.K. Kwan, Y.-F. Heish, W.E. Kauppila, S.J. Smith, T.S. Stein, M.N. Uddin, M.S. Dababneh, *Phys. Rev. A* **27** (1983) 1328.
[102] H. Tanaka, T. Ishikawa, T. Masai, T. Sagara, L. Boestaen, M. Takekawa, Y. Itikawa, M. Kimura, *Phys. Rev. A* **57** (1998) 1798.
[103] I. Iga, M.G.P. Homem, K.T. Mazon, M.-T. Lee, *J. Phys. B* **32** (1999) 4373.
[104] G. García, F. Manero, *Phys. Rev. A* **33** (1996) 250.
[105] H. Tanaka, Y. Tachibana, M. Kitajima, O. Sueoka, H. Takaki, A. Amada, M. Kimura, *Phys. Rev. A* **59** (1999) 2006.
[106] L. Boesten, H. Tanaka, A. Kobayashi, M.A. Dillon, M.A. Kimura, *J. Phys. B* **25** (1992) 1607.
[107] T. Sakae, S. Sumiyoshi, E. Murakami, Y. Matsumoto, K. Ishibashi, A. Katase, *J. Phys. B* **22** (1989) 1385.
[108] R.K. Jones, *J. Chem. Phys.* **84** (1986) 813.
[109] A. Zecca, G.P. Karwasz, R.S. Brusa, *Phys. Rev. A* **46** (1992) 3877.
[110] O. Sueoka, S. Mori, A. Hamada, *J. Phys. B* **27** (1994) 1453.
[111] K.L. Baluja, A. Jain, V. Di Martino, F.A. Gianturco, *Europhys. Lett.* **17** (1992) 139.
[112] P. Mozejko, G. Kasperski, Cz. Szmytkowski, G.P. Karwasz, R.S. Brusa, A. Zecca, *Chem. Phys. Lett.* **257** (1996) 309.
[113] O. Sueoka, *J. Phys. B* **21** (1988) L631.

DFT Treatment of Radiation Produced Radicals in DNA Model Systems

Xifeng Li[1,*] and Michael D. Sevilla[2]

[1] *Department of Nuclear Medicine and Radiobiology, Faculty of Medicine, Université de Sherbrooke, Quebec, J1H 5N4, Canada*
[2] *Department of Chemistry, Oakland University, Rochester, MI 48309, USA*

Contents

1. INTRODUCTION

The initial events in ionizing radiation damage to DNA are critically important to the subsequent biochemical and ultimately biology effects [1,2]. Ionizing radiation's primary initial effect is the production of DNA holes and ejected electrons. During the process of thermalization, these energetic electrons are known to promote dissociative electron attachment reactions that fragment molecular bonds [3,4]. After thermalization electrons add to the most electron affinic components of DNA, the DNA bases [5,6]. Since all valence electrons have approximately equal probability for ionization, radiation produced holes are produced randomly throughout DNA. Holes produced on the DNA bases yield the DNA base cation radicals which are known to undergo hole transfer through stacked bases to the base of lowest ionization energy, guanine [1,5,6]. Trapped electrons undergo electron transfer to bases of highest electron affinity, thymine and cytosine [5,7]. Holes on the sugar phosphate backbone undergo two competitive reactions: 1. deprotonation of the sugar cation radical to form neutral sugar radicals and 2. hole transfer to the nearest DNA base [1,8]. Since sugar radicals in DNA subsequently result in strand breaks they are considered the most hazardous of initial DNA lesions.

As can be seen from this brief overview of radiation events in DNA, these initial events involve fundamental physical and chemical processes that are amenable to treatment by high level ab initio molecular orbital theories. Thus much effort along these lines has been

* Current address: Patheon, Inc., 865 York Mills Road, Toronto, Ontario, Canada M3B 1Y5.

ADVANCES IN QUANTUM CHEMISTRY, VOLUME 52
ISSN: 0065-3276 DOI: 10.1016/S0065-3276(06)52004-0

made over the past decade and substantial understandings of the chemical processes post radiation have been obtained. There have been several reviews of earlier efforts along these lines [9,10]. These initial reviews clearly states the problems that need to be considered in a treatment of initial radiation damage and many of these have been taken up in the intervening period. In this review we consider our own recent work and the allied work of others in the areas of: 1. DNA base electron affinities and ionization energies [11]. 2. The effect of base pairing and inter base proton transfer on these properties [12,13]. 3. Low energy electron attachment reactions to DNA bases resulting in hydrogen atoms [14,15]. 4. Low energy electron attachment reactions to halouracils resulting in halide ions [16,17]. 5. Low energy electron attachment reactions to DNA resulting in DNA strand cleavage in model deoxyribose phosphate systems [18]. 6. The energetics of electron induced base release in deoxyribonucleosides.

2. ELECTRON AFFINITIES OF DNA BASES (VALENCE AND DIFFUSE STATES) [11]

The electron affinities of the fundamental informational units of DNA, the DNA bases, are of importance to the understanding of DNA radiation damage as well as excess electron transfer through DNA [1,9,19–28]. There are numerous reports [13,29–42], both experimental and theoretical, concerning the electron affinities (EAs) and ionization potentials (IPs) of the DNA/RNA bases. However the values of adiabatic EAs are found to lack the self-consistency of those reported for the IPs [13,33,35] (see Table 1). The greatest disagreement in values is for guanine, which has experimental and theoretical values of adiabatic EA reported from −0.7 [35] to +1.5 eV [39]. Theoretical efforts by Wesolowski *et al.* [33] and Vera and Pierini [34] suggest the higher value is not reasonable, while values from −0.7 to 0 eV still remain in the literature. In this review we present evidence that values closer to the lower number are the most likely.

Table 1. Electron affinities (eV) reported

	Vertical						Adiabatic				
Type	Exp.[a]		Theory				Exp.		Theory		
Refs.	[29]	[30]	[35][b]	[29][c]	[32,34][d]	[11][e]	[42][f]	[40,41][g]	[33] DFT[h]	[11] DFT[i]	[17] CBS-Q[j]
G	−0.74[k]	–	−1.23	−1.19	(−0.4)[m]	−1.25	–		(0.07)[m]	−0.75	
A	−0.54	−0.45	−0.74	−0.79	−0.74	−0.80	–		(−0.17)[m]	−0.35	
C	−0.32	−0.55	−0.40	−0.52	−0.55	−0.63	(0.13)		−0.02	−0.05	−0.13
T	−0.29	0	−0.32	−0.36	−0.30	−0.28	(0.12)	ca.0	0.16	0.15	−0.06
U	−0.22	–	−0.19	−0.22	−0.27	−0.32	(0.15)	ca.0	0.19	0.20	0.002

[a] Electron transmission spectroscopy results; [b] Scaled ab initio HF at MP2/6-31+G(D); [c] Scaled ab initio results; [d] DFT (B3LYP/6-311+G(2df, p)); [e] B3LYP /D95V+(D) except for G which is estimated from trends; [f] Estimated from experiment by extrapolation of data for hydrated bases; [g] Estimated from stable valence anion complexes, e.g., U(Ar)$^-$; [h] DFT /B3LYP/TZ2P++, Ref. [32] gives similar results at B3LYP/6-311+G(2df, p) level; [i] Best estimates from DFT basis set dependence study (vide infra). Thymine from Ref. [17]; [j] CBS-Q results; [k] Estimate of keto tautomer from enol tautomer experimental value (−0.46 eV) plus calculated difference in energy between keto and enol tautomers (0.28 eV) Ref. [29]; [m] These values are for diffuse states mixed with valence states and are not reliable for valence states.

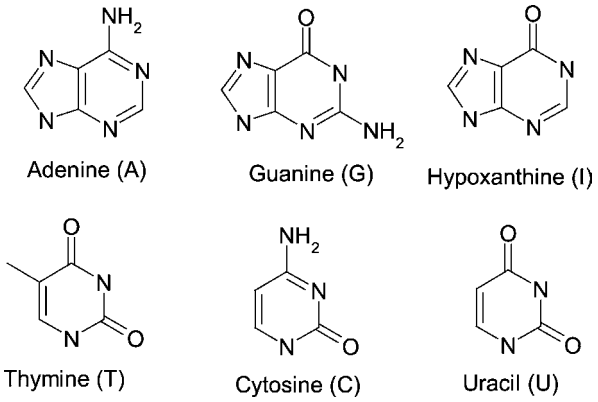

Fig. 1. Structures and names of DNA/RNA bases and hypoxanthine. Reprinted with permission from *J. Phys. Chem.* (Ref. [11]).

Structures of DNA/RNA bases, and hypoxanthine, are shown in Fig. 1.

The major difficulty in obtaining accurate valence electron affinities theoretically is not limited to DNA bases but includes all molecules with negative electron affinities [34,43–45].[1] All theoretical calculations for negative electron affinities can be problematic. Only stable bound states are readily accessible to DFT or HF theories, and for molecules with negative valence electron affinities, no stable bound state exists, other than dipole-bound or continuum states. For this reason excess electrons are energetically driven to leave the molecular structure to either become trapped nearby in a dipole-bound state or to be lost to the continuum. Nevertheless, experiments employing electron transmission spectroscopy (ETS) [34,46,47] are able to experimentally measure negative electron affinities, i.e., those molecular states that exist above the zero of energy in the continuum (see Table 1) [11,17]. Since negative electron affinities are experimentally available, a number of "practical" methods for dealing with negative electron affinities theoretically have been proposed and used in the literature [11,17]. The chief one is the use of small basis sets that confine the electron to the molecular framework and produce reasonable estimates of the relative (but not absolute) valence electron affinities [33,48,49]. We note that in solution the diffuse states are energetically unfavorable, for example, valence anion radicals of several pyrimidine DNA bases have been observed in the gas phase when even one molecule of water is bound [41,42]. Further, we note that in aqueous media all DNA base anions have been observed experimentally by electron spin resonance as valence π-anion radicals [23–25].

Recently Vera and Pierini [34] have used standard DFT methods and compared these results with experimentally measured values of the vertical valence electron affinities of 30 compounds and found excellent results. Thus from these results the DFT pre-

[1] Difficulties in the application of DFT to anion radicals have been pointed out [36,37,44]. However, recent comparisons to experimental values of EA suggest [34] good estimates of EAs can be obtained for relative large molecular anions as long as the system remains in valence states.

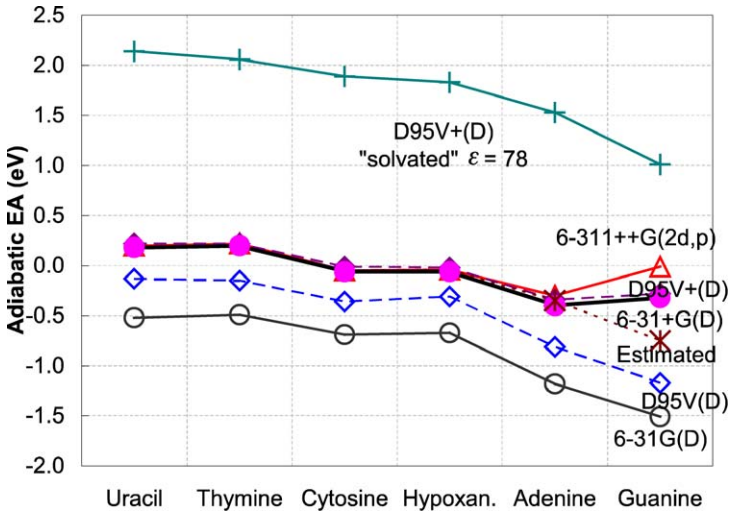

Fig. 2. Trends in DNA base adiabatic EAs with basis set size. Reprinted with permission from *J. Phys. Chem.* (Ref. [11]).

dictions of vertical electron affinities in Table 1 are expected to be accurate to within ±0.2 eV.

Li *et al.* investigated the cause of diversity in the reported EA values for DNA bases, by performing a series of DFT (B3LYP functional) calculations using basis sets of differing size [11]. By displaying these EA values obtained by each basis set as a trend line, the basis set effect can be compared visually (see Fig. 2 for the adiabatic EA trend). The resulting best values for adiabatic and vertical electron affinities are summarized in Table 1.

Without diffuse functions, the gas phase EA trend lines of the 6-31G(D), D95V(D) basis sets are very similar. The trend lines obtained with the three larger basis sets with diffuse functions, 6-31+G(d), D95V+(d) and 6-311++G(2d, p), nearly overlap each other for U, T, C and I, and are displaced to higher EA values while echoing the trend of the smaller basis sets. With these three larger basis sets containing diffuse functions, the EA values drift slightly for A, and dramatically for G, away from the relative trends of EA values obtained using smaller basis set (Fig. 2). At the largest basis sets the EA for G becomes close to zero. Under solvation, however, the diffuse function in the basis set gives the same trend line as found for the compact basis sets. Solvation raises all values of the EA by about 2 eV, to positive values of at least 1 eV, where the DFT results are expected to be more reliable. It is reasonable to expect the relative EA values to be very similar either in the gas phase or under solvation. The gas phase EA values for A and G, obtained with the three larger basis sets, thus become open to question.

Examining the spin density and SOMO surfaces, it was found that with the inclusion of diffuse functions in basis sets, these surfaces change substantially for guanine anion radical at DFT levels with the B3LYP functional (Fig. 3). With diffuse functions the “dipole bound” state is dominant rather than the valence state. The SOMO surfaces and unpaired spin distributions of the relaxed anions of A, T, C, U and I, remain nearly unchanged

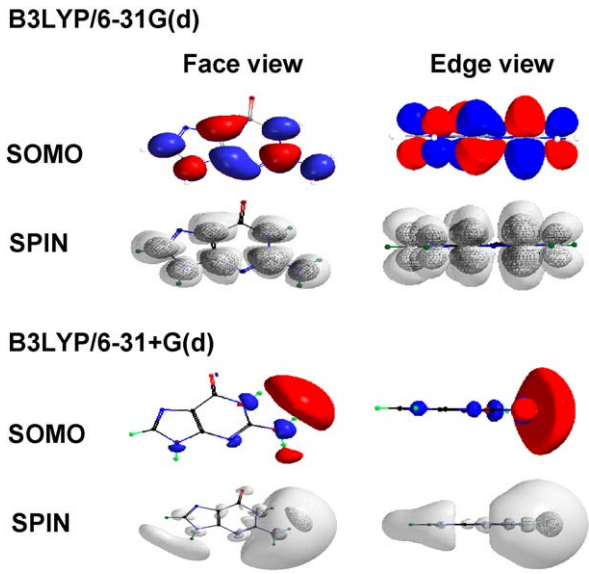

Fig. 3. SOMO surfaces and Spin density distributions of guanine anion radical. The 6-31G(D) basis set represents valence-bound anions. The 6-31+G(D) basis set clearly has large contributions from diffuse functions and no longer is representative of the valence state.

through the four basis sets: 6-31G(D), 6-31+G(D), D95V(D) and D95V+(D). No significant diffuse state contributions are found for these molecules at these basis sets (Fig. 4).

The zero-point energy difference (ΔZPE) between the neutral and its anion is a good indicator of the degree of molecular–electron interaction. The zero-point vibrational energy will be affected by the excess electron to the extent that the electron causes reorganization in the molecular framework. In the extreme case that the electron is lost in continuum, there will be no change in the ZPE contribution before and after addition of the electron. As can be seen, while the ΔZPE remains constant for the bases U, T, C and I, it decreases for G and A as the basis set size increases (Table 2). The excess electron causes little change in vibrational structure in guanine or adenine, when described with the largest basis sets that provide extra active space for the electron. Thus these calculations are clearly dominated by the diffuse "dipole bound" and continuum states.

The results of Li *et al.* [11] are compared to other calculations and experiment in Table 1. Li *et al.* carefully excluded diffuse states that arise for only G and A and estimated their vertical and adiabatic EAs. In these cases the smaller basis sets, confining the excess electron to the molecule, allow for reasonable estimates of relative valence electron affinities excluding dipole bound states and suggest the order of both the adiabatic and vertical valence electron affinities to be U $\approx$ T $>$ C $\approx$ I $>$ A $>$ G with G nearly 1 eV less electron affinic than U. The values calculated for the vertical EAs are in good agreement with each other and with experiment for U and T and reasonable agreement for C and A. As mentioned the recent theoretical results from Vera and Pierini [34] suggest the DFT values are good predictions of experimental vertical EAs. However, for G in its keto form no experimental result is available and an estimate derived from the enol form compares poorly

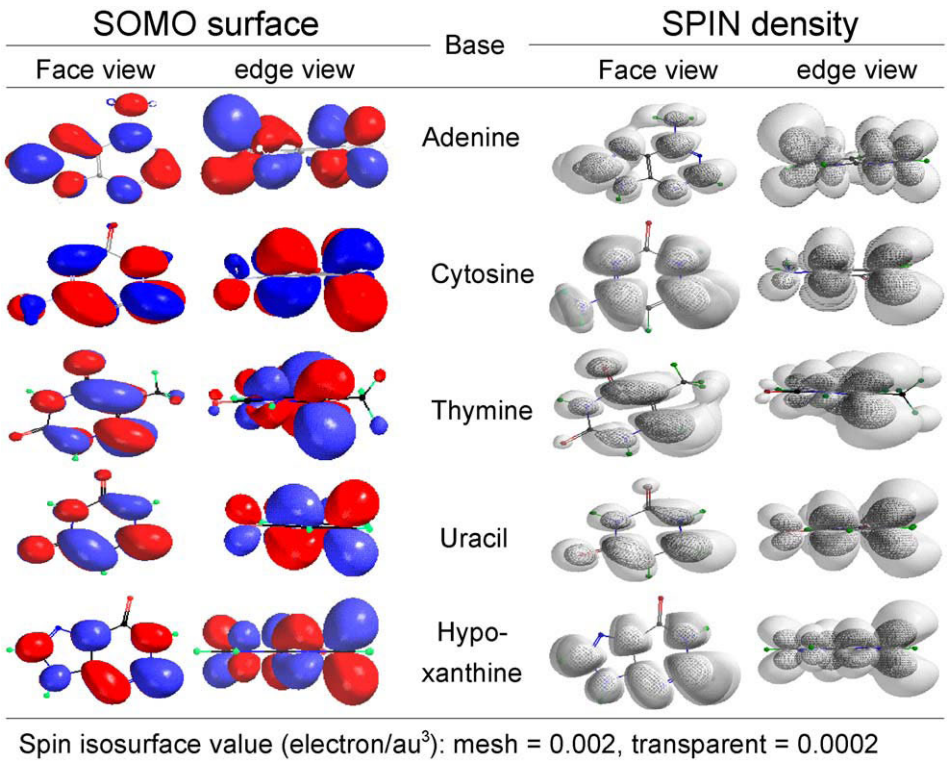

Fig. 4. SOMO surfaces and Spin density distributions of valence DNA base anion radicals (adenine, cytosine, thymine, uracil, and hypoxanthine), obtained at the B3LYP/D95V+(d) level. Reprinted with permission from *J. Phys. Chem.* (Ref. [11]).

Table 2. ΔZPE in gas phase [ZPE neutral–ZPE anion] (eV)

Basis set	U	T	C	I	A	G
6-31G(D)	0.17	0.17	0.10	0.20	0.20	0.27
D95V(D)	0.16	0.16	0.09	0.20	0.19	0.26
6-31+G(D)	0.17	0.16	0.10	0.20	0.12	0.06
D95V+(D)	0.17	0.16	0.09	0.20	0.12	0.06
6-311++G(2d, p)	0.17	0.17	0.10	0.21	0.03	0.04

with the estimates from various approaches (Table 1). Both vertical and adiabatic EAs of G have been reported as near zero [32,33], but in these report calculations the electron is in a diffuse state and do not described the valence state which is predicted to be less stable (of lower EA). It is clear from both experimental and theoretical results that the vertical EA of G is quite negative (Table 1).

The adiabatic EAs of U and T are known from experiment to be in the range 0 to 0.15 eV. DFT theory agrees with the higher values and CBS-Q calculations favor values near zero. This is a small uncertainty that should be settled with additional experiments and improvements in theory. However the uncertainty for the purines A and G is much greater. A and G clearly have negative adiabatic electron affinities which DFT theory suggests to be ca. -0.35 eV and -0.75 eV, respectively and of course their vertical electron affinities are more negative, i.e., -0.74 eV (A) [34] and -1.25 eV (G). Experiment suggests the theoretical vertical values somewhat too low. However, both theory and experiment agree that the vertical EA for G and A are so negative that nuclear relaxation will not raise the adiabatic EAs to positive values. Of course these virtual states (i.e. negative electron affinities) for A and G in the gas phase become relevant to biology when they become bound states in solvated systems.

3. EFFECT OF BASE PAIRING AND PROTON TRANSFER [12,13]

The electronic properties of the DNA base pairs are important to the understanding of excess charge (electron & hole) transfer within double stranded DNA [7]. Adiabatic Electron Affinities (AEA), Vertical Electron Affinities (VEA) and Vertical Electron Detachment Energy (VEDE) are the most important properties of base pairs that affect excess electron transfer through neighboring base pairs. On the other hand, Adiabatic Ionization Energy (AIE), Vertical Ionization Energy (VIE) and Vertical Electron Attachment Energy (VEAE) are the properties affecting hole transfer across base pairs. Intra-base pair proton transfer, which occurs in the GC base pair cation and anion radicals, can alter these properties and thus change the energetics of charge transfer.

3.1. EAs and IPs of the base pairs

Structures of the base pairs studied are shown in Fig. 5. The electron affinities and ionization potentials of the four base pairs, AT, AU, GC and IC, are calculated at DFT B3LYP level, in couple with the 6-31+G(d) basis set. The results are compiled in Table 3, which shows that the adiabatic EAs (with ZPE correction) of the four base pairs are AT (0.30 eV), AU (0.32 eV), IC (0.42 eV) and GC (0.49 eV). The EA of AT is the smallest and is about 0.19 eV less than GC, it's competitor for the electron in DNA. As might be expected the AT anion's vertical electron detachment energy (VEDE) is also the smallest among the four base pairs. An energetic cycle for formation of base pair anionic radical is visualized in Fig. 6. This data indicates that the energetic depth of the trap for an excess electron by a base pair as measured by the adiabatic EA is in the order of AT $<$ AU $<$ IC $<$ GC. In DNA, base stacking and local conditions will alter this ordering of trapping well depth to some extend [9,50]. However, based on the energetic cycle (Fig. 6), it can be concluded that the AT base pair has the shallowest trap and provides the most favorable route for electron transfer. This conclusion is supported by previous experimental observations that electron transfer rates were higher in polydAdT that in polydGdC [51].

Colson *et al.* [52] computed the base pair electron affinities of GC and AT at the HF level with the 6-31+G(d)//321G basis set and scaled them to experiment by an additive correction constant [27,35] which resulted in values of 0.6 eV for GC and 0.3 eV for AT;

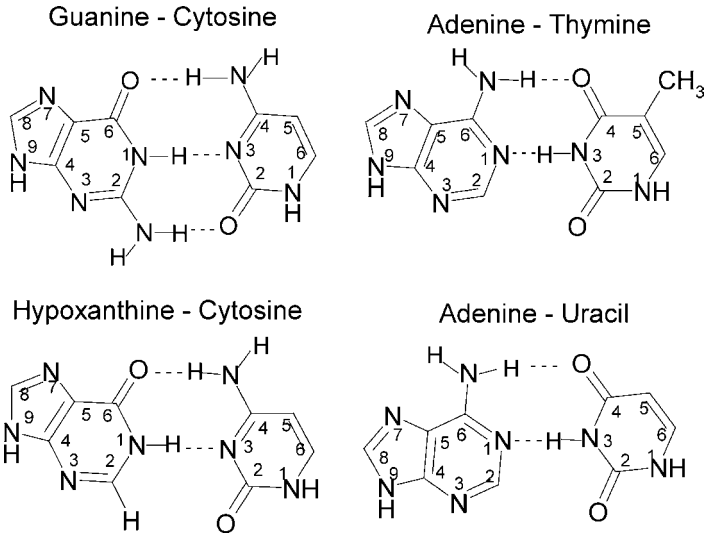

Fig. 5. Structures of base pairs. Reprinted with permission from *J. Phys. Chem.* (Ref. [12]). © 2002 American Chemical Society.

Table 3. Electron affinities and ionization potentials of base pairs at B3LYP 6-31+G(d)//6-31+G(d)

Electron affinities					
Base pair	Adiabatic EA		VEA		VEDE
	ZPE corrected		Uncorrected		
AT	0.30		−0.16		0.60
AU	0.32		−0.13		0.93
GC	0.49		−0.15		1.16
IC	0.42		−0.19		1.06
Ionization potentials					
Base pair	Adiabatic IP		VIP		VEAE[a]
	ZPE corrected		Uncorrected		
AT	7.68	7.45[a]	7.80	7.74[a]	7.43
AU	7.68	–	7.91	–	7.38
GC	6.90	6.71[a]	7.23	7.16[a]	6.53
IC	7.63	–	7.94	–	7.28

[a] Results by Hutter and Clark [53] at DFT b3lyp/D95* //UHF/6-31G*. From a linear correlation to experimental IP values for single bases these authors found a relationship that suggested their IP values should be increased by ca. 0.3 eV. Bertran *et al.* [54] give estimates of 7.79 and 6.96 eV for AIP's of AT and GC.

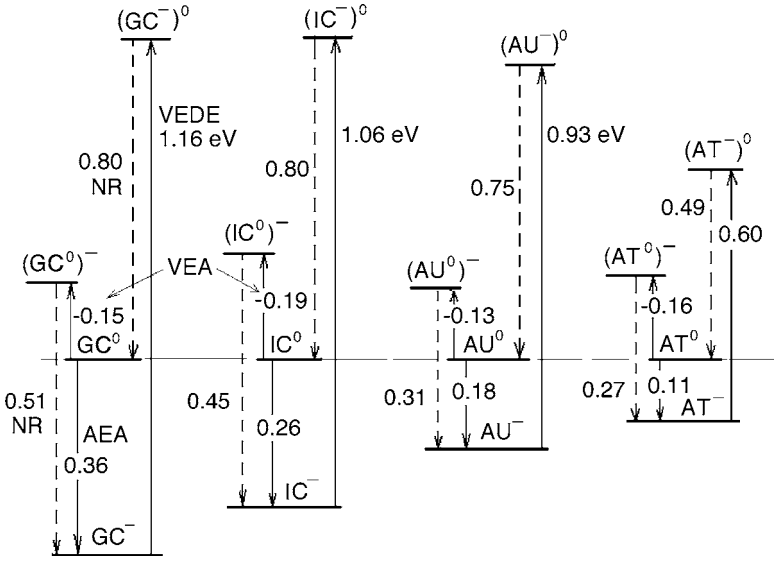

Fig. 6. Energetic cycles for electron addition to various base pairs. Reprinted with permission from *J. Phys. Chem.* (Ref. [12]).

these corrected values are in good agreement with those in Table 3 (0.5 eV and 0.3 eV, respectively). The level of theory employed in the present work suggests our calculated values likely to be within 0.2 eV of experiment when available [11].

The adiabatic ionization potentials, with ZPE-correction, of the base pairs are found to be AT (7.68 eV), AU (7.68 eV), IC (7.63 eV), and GC (6.90 eV), respectively. For comparison, the results by Hutter and Clark [53] at DFT b3lyp/D95*//UHF /6-31G* show the same trend, and after a linear correlation to experimental IP values the IP values should be increased by ca. 0.3 eV to 7.79 eV for AT and 7.08 eV for GC. Bertran *et al.* [54] estimated the AIP's at 7.79 and 6.96 eV for AT and GC, which are in good agreement with the extrapolated values of Hutter and Clark and our calculated values.

Figure 7 shows the energetics of ionization and electron hole recombination for each of the base pairs under consideration and thus visually compares the energy cost of hole transfer. The hole therefore is preferentially stabilized on GC in DNA and the barriers to hole transfer from one base pair to another can be estimated by the relative ionization potentials. Thus, the energy barriers for hole transfer through a base pair is in the following order GC $<$ AT $\approx$ AU $\approx$ IC. Once the hole stabilizes on a base pair, the nuclear relaxation energy provides an additional energetic barrier to its transfer to neighboring base pairs (see Table 1, Fig. 7). The nuclear relaxation energies after hole formation in a base pair are found to be: AT (0.10 eV), AU (0.21 eV), IC (0.26 eV), and GC (0.34 eV); and the relaxation energies after recombination of the electron and the relaxed base pair cation are AT (0.27 eV), AU (0.32 eV), IC (0.40 eV), and GC (0.36 eV). The reorganization energy (λ) for an adiabatic ET process in which a hole begins on a base pair and ends on a base pair of the same type, are: AT (0.37 eV), AU (0.53 eV), IC (0.66 eV), and GC (0.70 eV), which are the sum of the two relaxation energies [55].

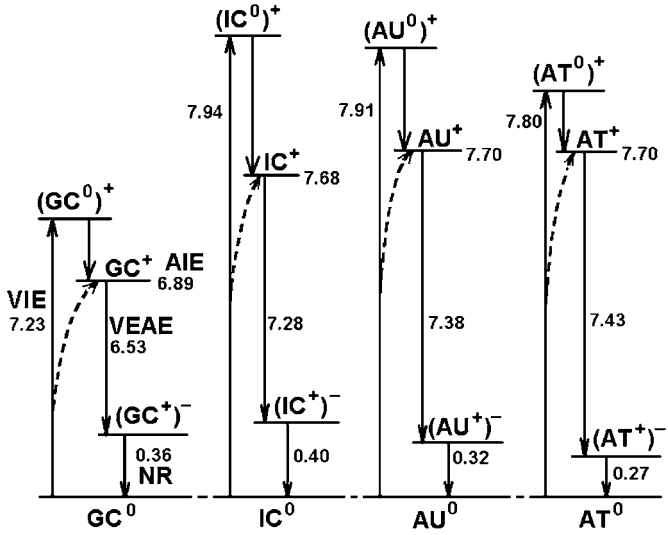

Fig. 7. Energetic cycles for the formation of base pair cation radicals. Reprinted with permission from *J. Phys. Chem.* (Ref. [12]).

The small relaxation energy of AT suggests that hole transfer through stretches of stacked AT's would be less hindered by reorganization energy. Recent results from Giese and coworkers [56] suggest such a rapid transfer through stacked AT sequences. And results by Sartor *et al.* suggests a remarkably slow fall off in rates of transfer as multiple AT stacks increased in length [57].

The base pairing energies are defined as the difference in the energy between the fully optimized base pair and the sum of the individual energies of the two optimized bases. Table 4 lists the base pairing energies calculated for various base pairs. The calculated values reported in this work and others [52,54] clearly show that ion radical formation results in significantly stronger base pairing energies. These predictions may now be quantitatively tested by experiments on base pairs in the gas phase.

3.2. Proton transfer within base pair

Employing density functional theory with B3LYP functionals and the 6-31+G(D) basis set, the transition structures have been found and the potential surface determined by IRC following for the proton transfer processes in GC and IC base pair anion radicals and cation radicals. Figure 8 shows the energy profiles and the base-base distance (monitored with their closest N–N distance) during the proton transfer process for the four base pair ions. With the transition structures found, the activation energies, ΔH, ΔG, and equilibrium constants for each of the proton-transfer process were calculated and are given in Table 5. Based on these thermodynamic data, it was concluded that proton transfer is strongly favored in IC for both anion and cation radicals, favorable in $GC^{-\bullet}$, and slightly unfavorable in $GC^{+\bullet}$ radical. The fact that no substantial activation barriers were found for both anion

Table 4. DFT calculated (B3LYP/6-31+G(d)) energetics of base pairing[a,b]

Neutral pairing energies	ΔE	ΔH	ΔG	ΔS
$G^0 + C^0 \rightarrow GC^0$	−22.9	−23.5 (−24.0)	−12.5 (−12.6)	−36.8
$I^0 + C^0 \rightarrow IC^0$	−17.0	−17.61	−6.84	−36.1
$A^0 + T^0 \rightarrow AT^0$	−10.7	−11.3 (−10.9)	−1.7 (0.3)	−32.2
$A^0 + U^0 \rightarrow AU^0$	−10.1	−10.71	−0.40	−34.6
Anion pairing				
$G^0 + C^- \rightarrow GC^-$	−36.2	−36.78	−25.01	−39.5
$G^0 + C^- \rightarrow GC^-$ (PT)[c]	−39.1	−39.67	−28.12	−38.7
$I^0 + C^- \rightarrow IC^-$	−28.35	−28.95	−17.80	−37.4
$I^0 + C^- \rightarrow IC^-$ (PT)[c]	−34.9	−35.51	−25.10	−34.9
$A^0 + T^- \rightarrow AT^-$	−12.85	−13.44	−4.96	−28.4
$A^0 + U^- \rightarrow AU^-$	−12.8	−13.36	−4.35	−30.2
Cation pairing				
$G^+ + C^0 \rightarrow GC^+$	−40.5	−41.1 (−43.0)	−28.69 (−30.0)	−41.6
$G^+ + C^0 \rightarrow GC^+$ (PT)[c]	−39.1	−39.7 (−41.7)	−27.3 (−28.7)	−41.6
$I^+ + C^0 \rightarrow IC^+$	−33.8	−34.4	−23.3	−37.2
$I^+ + C^0 \rightarrow IC^+$ (PT)[c]	−38.9	−39.45	−28.4	−37.1
$A^+ + T^0 \rightarrow AT^+$	−20.6	−21.2 (−21.7)	−10.1 (−10.5)	−37.0
$A^+ + T^0 \rightarrow AT^+$ (PT)[b,c]		(−21.3)	(−9.1)	(−40.9)
$A^+ + U^0 \rightarrow AU^+$	−19.5	−20.1	−9.0	−37.2

[a] ΔE, ΔH, and ΔG are in kcal/mol. ΔS values are in cal/mol/K. All values are ZPE corrected and thermodynamic corrections to 298.15 K, 1.0 atm. [b] Values in parenthesis are BSSE corrected at B3LYP 6-31G** from Bertran *et al.* [54]. [c] These values are calculated for the base pair cation and anion radicals after proton transfer from N1 on guanine to N3 on cytosine or N1 on hypoxanthine to N3 of cytosine [13]. Proton transfer is not expected in the AT or AU anion radical base pairs [13,26,52,58] but theory suggests that transfer from the amine group on A to oxygen on T is likely in the AT cation radical [54].

and cation radicals of IC suggest their initial structures are unstable to immediate proton-transfer after formation of the radicals.

Structural change during proton transfer in each of the four radicals investigated is character by a substantial contraction of the inter-base spacing in the base pair, i.e., the two base rings move about 0.3 Å together in transition region and relax to normal distance after transfer complete (see Fig. 9 for an example). This suggests that oscillatory motions of DNA can greatly promote proton transfer, providing a mechanism for the phonon assisted proton–electron transfer processes along the DNA strand [59,60].

The proton transfer from G to C [26,58–62] or A to T [61] within the base pair cation radicals may hinder hole transfer across base pairs. Studies [26,58–62] suggest that proton transfer is not complete and is reversible in ds DNA for both the AT and GC cation radicals. Thus proton transfer should have only a moderate impact on hole transfer. However, proton transfer in GC and IC will have a far greater impact on the excess electron

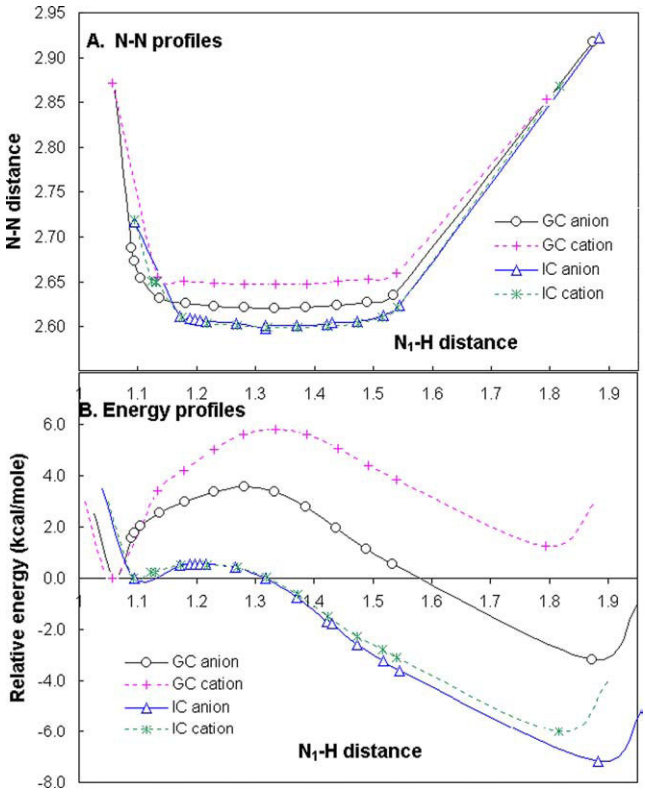

Fig. 8. (A) N_1–N_3 distance (N_1 on guanine or hypoxanthine and N_3 on cytosine) profiles. (B) Energy (uncorrected for ZPE) profiles as the guanine (or hypoxanthine) N_1–H distance increases. For each species, the energies are compared to that on initial structure. Reprinted with permission from *J. Phys. Chem.* (Ref. [13]).

transfer. For both case of GC and IC anion radicals, proton transfer are quite energetically favorable and will provide additional barriers to electron transfer of 3 and 7 kcal/mol for GC and IC, respectively [62]. The reported lower rates of electron transfer in IC and GC polynucleotides [51] provide good experimental support.

4. ELECTRON INDUCED DEHALOGENATION REACTIONS OF HALOURACILS AND EFFECT OF BASE PAIRING [14,15]

Interactions of low energy electrons (LEE) with halouracils are of particular interest since these molecules, when incorporated in cellular DNA, are known to have radio-sensitization properties, which have potential applications in radiation therapy [63–65]. In these molecules attachment of a low energy electron results in an unstable anion which dissociates into the halide anion and the very reactive neutral uracilyl radical [14,66].

Table 5. Proton transfer activation energies, enthalpy and free energy changes calculated at B3LYP/6-31+G(d), with ZPE correction (kcal/mol, 298 K)

Structure	Activation energy		ΔH	ΔG	$k_{\text{equilibrium}}$
	Forward	Backward			
GC anion	0.84	3.73	−2.89	−3.11	1.9E+02
GC cation	2.96	1.58	1.38	1.38	9.7E−02
IC anion	−1.80	4.76	−6.56	−7.30	2.2E+05
IC cation	−1.70	3.37	−5.07	−5.10	5.4E+03

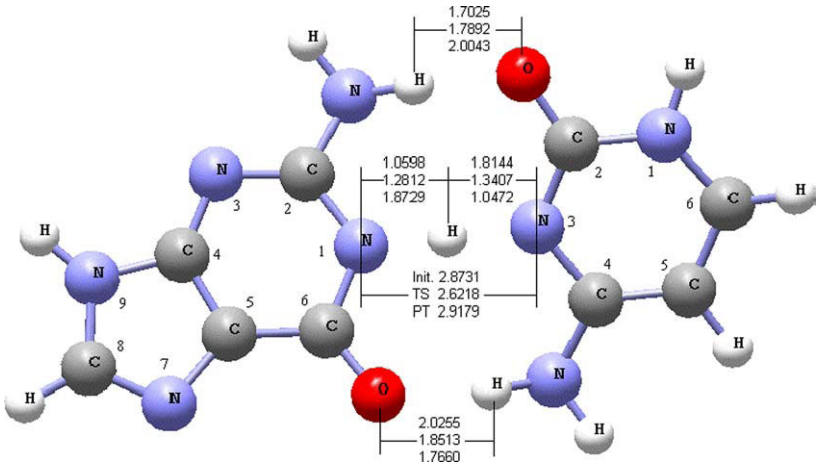

Fig. 9. Key atom-pair distances (Å) in the initial, transition state (TS) and proton-transferred (PT) structures of GC anion radical. In each group of data, the upper value is for the initial structure, the middle for the TS and the lower for the PT structure. Reprinted with permission from *J. Phys. Chem.* (Ref. [13]).

The energetics of the dehalogenation upon attachment of low energy electrons to single halouracils (5-XU) or to adenine-halouracil base pairs (A5XU, where X represents a halogen atom), were investigated by use of density functional theory [14,15]. Structures of single 5-bromouracil and its base pair with adenine are shown in Fig. 10. Electron affinities of halouracils and base pairs, anionic potential energy surface for C–X bond dissociation as well as the excess charge distribution and spin density were obtained.

As expected single halouracils are found to have adiabatic electron affinities (AEA) substantially higher than that of uracil [14]. However, unexpectedly it is found that base pairing with adenine slightly decreases the electron affinities of the halouracils (Table 6) [15]. This is contrast to natural DNA bases that base pairing substantially increases their EAs. For example, base pairing increases the EA's from 0.18 eV for U to 0.32 eV in AU, from 0.20 eV for T to 0.30 eV in AT and from −0.06 eV for C to 0.49 eV in GC. The substantial increase in EA for GC is associated with the fact G has one net donor hydrogen involved in the hy-

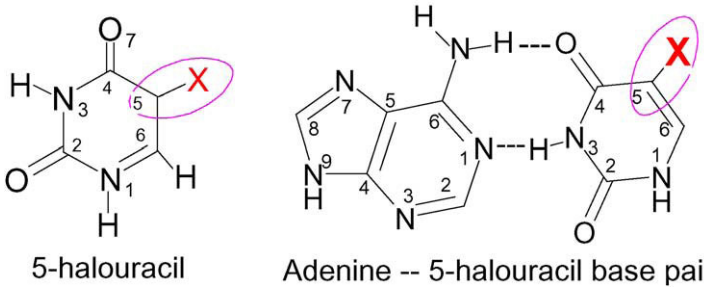

Fig. 10. Structures of 5-halouracil and corresponding adenine-halouracil base pair. X represent Br, Cl, F, H or yl (radical). Abbreviations: 5BrU, 5ClU, 5FU, U and 5ylU (single halouracils); and A5BrU, A5ClU, A5FU, AU and A5ylU (base pairs). Reprinted with permission from *J. Am. Chem. Soc.* (Ref. [15]).

Table 6. Electron affinities (eV) of halouracils (5XU)[a] and base pairs with adenine B3LYP/6-31+G(d)

	Single	bp	X = Br	Cl	F	H	5-yl[b]	ZPE correction[c]
AEA (gas)	5XU		0.63	0.60	0.48	0.18	2.34	Yes
			0.51	0.49	0.37	0.066	2.30	No
		A5XU	0.59	0.56	0.47	0.32	2.36	Yes
			0.57	0.55	0.45	0.18	2.32	No
VEA	5XU		0.11	0.06	−0.15	−0.35	1.89	No
		A5XU	0.18	0.15	−0.10	−0.13	1.79	
AEA[d] (solvated)	5XU		2.44	2.26	2.21	2.02	4.47	No
		A5XU	2.20	2.36	2.30	1.92	3.95	
VDE	5XU		1.21	1.20	1.14	0.76	2.74	No
		A5XU	1.33	1.33	1.27	0.93	2.87	

[a] Values for unpaired halouracils were taken from Ref. [14]. Note that the VEA for 5FU and uracil reported in Ref. [14] should be negative and are correct as shown in this table. [b] A5ylU = AUracil-5-yl radical. [c] Zero point energy corrections. [d] H_2O, $\varepsilon = 78$.

drogen bonding to C, contributing to an increase of ca. 0.5 eV in the electron affinity [52]. Note that in every case the captured electron resides on the pyrimidine base. Base pairing does not reduce the reactive nature of the A5ylU radical (where X = 5-yl, the uracil C_5 is a radical site), which still has a very high electron affinity comparable to the reactive U-5-yl radical.

The EAs for bases and base pairs can be used to estimate the driving force for electron capture at the halouracils in ss-DNA and ds-DNA. In double stranded DNA the electron

is initially trapped at the GC base pair; thus our simplified model for the driving force for electron capture at the halouracil in ds DNA is the difference in EA between GC (0.49 eV) and A5BrU (0.59 eV). This amounts to only 0.1 eV for ds-DNA. However, in single strand DNA the most likely electron capture site is T (EA = 0.20 eV) or less likely C (EA = −0.06 eV) [11]. Thus the difference in the EAs between T and 5-BrU is 0.43 eV and between C and BrU is 0.69 eV [11,14]. Thus on base pairing a significant reduction in driving force of at least 0.4 eV is found for electron capture at the halouracil after an initial attachment on T or C. While base stacking and solvation tend to alter the energetics, the differences in driving forces are large and are not likely to alter the large reduction in driving force found here on going from ss-DNA to ds-DNA. As a result, the competitiveness of halouracils in base pairs for excess electrons is significantly reduced relative to non-base-paired halouracils. We project that the probability of capture of a low energy electron by 5XU is decreased when based paired to A, and thus the radio-sensitivity of halouracils are likely to be reduced in double strand DNA.

The potential energy surfaces (PES) of the halouracil radical anions shows several thermally accessible low-lying electronic states: a planar π^* state, a dissociative planar σ^* state and a non-planar π^*-type mixed state that connects the two planar states [14,67]. An example of 5-bromouracil with such complex PES is shown in Fig. 11. Adiabatic dehalogenation of halouracil radical anions follow the non-planar mixed state PES (Fig. 11). For the A5XU base pair radical anions, only the non-planar mixed state PESs along the C–X bond were calculated. Fig. 12 compares the potential energies surfaces found on extension

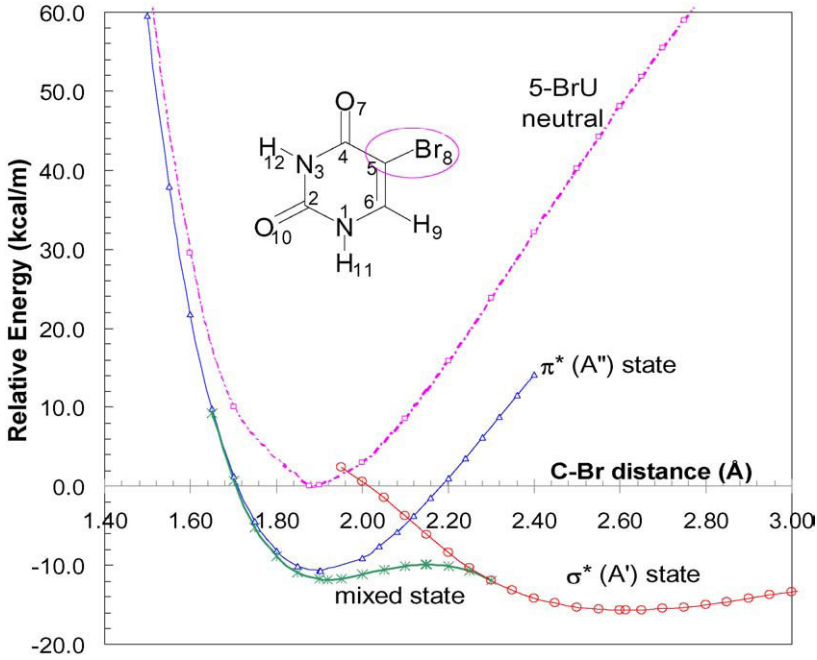

Fig. 11. A typical potential energy surface of 5-halouracil (5-bromouracil). Reprinted with permission from *J. Phys. Chem.* (Ref. [14]).

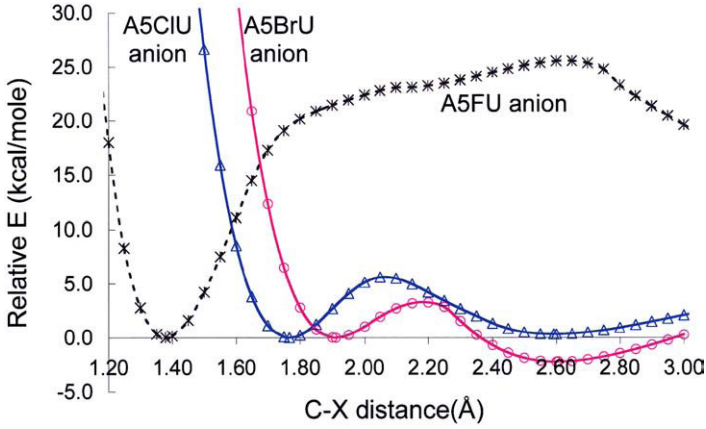

Fig. 12. Potential energy surfaces of adenine-halouracil anions along the C–X bond, calculated at B3LYP/6-31+G(d) level. The energy (without ZPE correction) is relative to that of each optimized anion. Reprinted with permission from *J. Am. Chem. Soc.* (Ref. [15]). © 2003 American Chemical Society.

Table 7. Energetics of dehalogenation from halouracil radical anions: Effect of base pairing with adenine (kcal/mol)

	Single	Paired	X = Br	Cl	F	ZPE correction
Activation energy	5XU		1.88	3.99	20.80	No
		A5XU	3.29	5.62	25.6	
ΔH	5XU		−2.98	−0.98	20.82	Yes
		A5XU	−0.95	1.27	–	
ΔG	5XU		−3.80	−2.32	19.01	Yes
		A5XU	−1.52	−0.28	–	

of the C–X (X = Br, Cl or F) bond of A5XU anions. For convenience, the energies of optimized anions are used as references for each PES. The potential energy surfaces along the C_5–X bond (Fig. 12) suggest an additional reduction in the effectiveness of sensitization of halouracils to low-energy electrons once in pair with adenine, i.e., slightly higher activation barriers and smaller ΔH and ΔG are found for dehalogenation reactions of Br- and Cl-uracil anions in the base pairs than for single halouracils (Table 7).

Detachment of hydrogen from C_5 of uracil anion radical leads to formation of the U-yl$^-$ and a H atom; however, for haloruracils (BrU and ClU) as single bases or base paired with adenine, the halogen departs as a halide ion and the uracil-5-yl radical is formed. This is clearly a result of the fact that the uracilyl radical has an electron affinity greater than the hydrogen atom but less than the halogen atoms. For FU the departing fluoride ion has a large proton affinity and leaves with a proton from the N_1 nitrogen. In the base

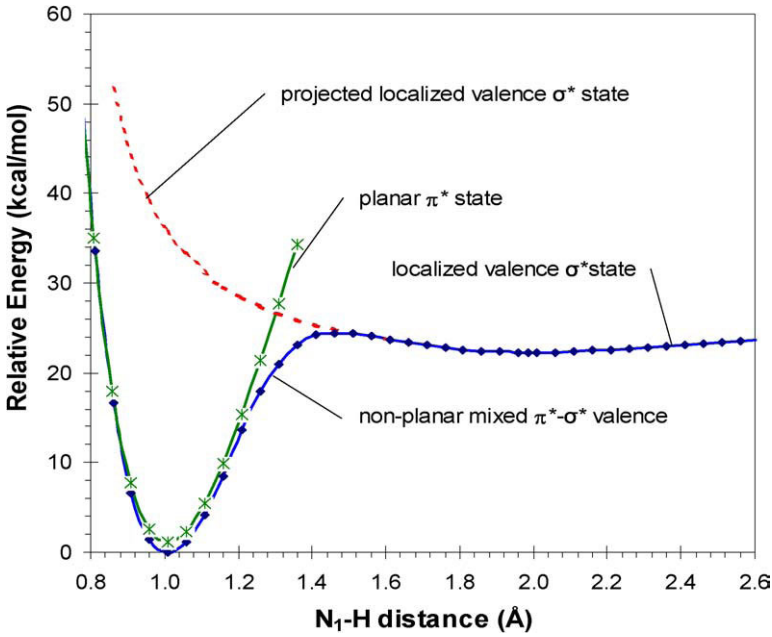

Fig. 13. Uracil anion radical PESs along N_1–H coordinate, calculated at B3LYP/6-31+G(d) level. Showing the planar valence π^* state in which symmetry is conserved during the calculation. On molecular relaxation a mainly π^* state is found at short distances and at long distances crosses to a σ^* state. Reprinted with permission from *J. Phys. Chem.* (Ref. [16]).

paired A5XU radical anions, over 90% of negative charge and 100% spin density fall on the halouracils (XU) rather than on adenine (A).

The considerably higher electron reactivity with non-base-paired halouracils compared to those within ds DNA, indicates that during cell division and replication, when DNA must be at times in the single strand form, DNA containing halouracils may be much more vulnerable to excess electron attack. This was recently shown experimentally [68]. This result may be of significance to the development of new clinical modalities in radiotherapy.

5. HYDROGEN ATOM LOSS IN PYRIMIDINE DNA BASES [16,17]

The interaction of low energy electrons (LEEs) with pyrimidine DNA bases have been shown by experiment to induce hydrogen atom loss via a "dissociative electron attachment" mechanism. Thus dissociation of hydrogen atoms from N–H and C–H bonds in DNA bases may be a key step in low energy electron (LEE) induced base damages of DNA and RNA. Subsequent reactions of the resulted H atoms and the base radical fragment could lead to permanent DNA damage such as strand breaks.

Studies of electron induced bond cleavage in thymine, cytosine or uracil have been investigated theoretically [16,17] and experimentally [69–71]. Similar to the halouracils in

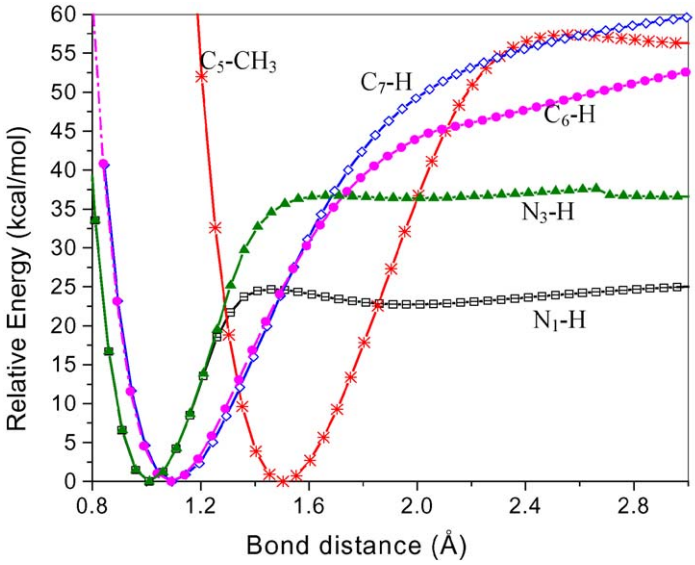

Fig. 14. The adiabatic potential energy surfaces of the *thymine anion radical* along each N–H or C–H coordinate, calculated at the B3LYP/6-31+G(d) level. Energy relative to that of optimized anion in equilibrium state. The zero point energy is not included. Reprinted with permission from *J. Phys. Chem.* (Ref. [17]).

Table 8. Comparison of ΔE for bond cleavage in pyrimidine anion radicals calculated at the CBS-Q and DFT levels (kcal/mol)

Position	Theory	Uracil	Thymine	Cytosine
N_1	CBS-Q	19.5	20.5	27.5
	DFT	21.5	20.5	27.3
C_6	CBS-Q	51.4	50.4	51.8
	DFT	52.3	52.8	51.7

the previous section, π^* and σ^* states were found for uracil, as well as for thymine and cytosine. For example, Fig. 13 shows PESs along the N_1–H bond in uracil anion: The surface at the energy minima at short distances is dominated by a delocalized π^* state which has no significant effect on the N–H or C–H bond strength; at longer distances cross over to a truly antibonding and localized σ^* state occurs. Electron attaches to the uracil is initially in a near pure π^* valence state which intersects with an antibonding σ^* state on bond extension. Fig. 14 show PESs for various bond fragmentations in thymine anion radical (see Refs. [16] and [17] for the surfaces of uracil and cytosine, respectively).

Table 8 lists the energy, ΔE, for bond dissociation calculated by DFT B3LYP/aug-cc-pVDZ//6-31+G(d) and by a complete basis set method (CBS-Q) for dissociation of the N_1–H and C_6–H bonds in uracil, thymine and cytosine anion radicals. The dissociation

Table 9. ΔE at infinite separation: Base$^-$ $\rightarrow$ (Base–H)$^-$ + H[a] (kcal/mol)

DFT (B3LYP)	Position				
	N1	N3	C5	C6	
Uracil$^-$ ΔE	21.5	33.9	66.3	52.3	
	N1	N3	C6	C7	C_5–CH_3[b]
Thymine$^-$ ΔE	20.5	33.1	52.8	64.4	53.4
Thymine^{0c} ΔE	92.2	115.9	110.3	85.9	104.5
	N1	C5	C6	amino N–H	C_4–NH_2
Cytosine$^-$ ΔE	27.3	60.1	51.7	30.5	72.1
Cytosine^{0c} ΔE	97.4	112.8	108.2	100.2	101.5

[a] All calculations done for the gas phase and $T = 298$ K. [b] $T^- \rightarrow (T\text{–}CH_3)^- + {}^\bullet CH_3$ and C_4–$NH_2 \rightarrow (C_4)^- + {}^\bullet NH_2$. [c] Directly calculated bond dissociation energies for neutral base.

leads to formation of an H atom and a DNA base fragment anion. The good agreement between the CBS-Q method and DFT methods suggest these values are good estimates of these bond energies.

In Table 9 the DFT bond energies for various bond dissociations are given for both the anion radical and neutral species.

Overall these studies of the potential energy surfaces (PES) and energetics of hydrogen atom loss processes in DNA bases yield the following conclusions:

(1) On electron attachment a very significant reduction in the bond energy occurs, for example for N–H the anion radical bond energy is 70 to 80 kcal/mol lower than the neutral parent. N–H bonds are more vulnerable than C–H bonds towards excess electron induced fragmentation (see Table 9).

(2) Anion radicals of Thymine and Uracil have very similar PES, along both N_1–H and C_6–H, and their N_1–H PES lie below that of cytosine's anion at extended bond distances. This may be the major reason why the cross section of the cytosine dehydrogenated anionic fragment (C–H)$^-$ is much lower than that of thymine (T–H)$^-$ and uracil (U–H)$^-$ [69].

(3) For thymine, cytosine and uracil anion radicals in valence π^* states as the N–H or C–H bond are stretched to longer distances, the radicals shifts to an antibonding σ^* state followed by cleavage to form the H deleted base fragment anion and hydrogen atom. For N–H bond PES, this shift from π^* to the antibonding σ^* states, occurs at around 1.4 Å, while for C–H bond the shift occurs near 1.6 Å.

(4) While the DNA bases themselves have low to near zero EAs, all H-deleted fragments of thymine, cytosine and uracil have high electron affinities, which effectively reduces the energy cost of fragmenting the N–H or C–H bond in the anion radicals (see Table 10). Further, the electron affinities of the nitrogen-center fragments are substantially higher than those of the carbon-center fragments. For this reason, it is expected that LEE-induced hydrogen atom lost from these pyrimidine bases will be mostly from N–H bonds, which has been confirmed by experiment.

Table 10. Electron affinities of the bases and their H-deleted radicals (eV)[a]

Method Thermal correction		B3LYP/6-31+G(d) +ZPE	CBS-Q 298 K
Thymine		0.15	−0.059
	N_1(T)[b]	3.22	3.27
	N_3(T)	3.71	4.00[c]
	C_6(T)	2.61	2.68
	C_7(T)[d]	1.08	0.99
Cytosine		−0.055	−0.13
	N_1(C)	2.90	3.58
	C_5(C)	2.21	2.34
	C_6(C)	2.33	2.44
	N_7(C)[d]	2.96	3.23
	C_4(C)[e]	1.13	1.27
Uracil [16]		0.20	0.002
	N_1(U)	3.46	3.49
	N_3(U)	3.78	4.16
	C_5(U)	2.34	2.38
	C_6(U)	2.67	2.68

[a] All the anions radicals treated are valence anions. [b] Parent base indicated in parenthesis. [c] CBS-Lq is used instead of CBS-Q since the latter failed. [d] Fragment resulting from H atom loss from the methyl group for thymine and amino group for cytosine. [e] Fragment from loss of the complete C_4 amino group.

6. ELECTRON INDUCED DNA STRAND BREAKS [18]

DNA strand breaks are considered to be the most potentially lethal form of cellular damage caused by ionizing radiation. The recent surprising discovery that DNA strand breaks can be induced by low energy secondary electrons sparked an interest by several workers to elucidate the mechanism. Experimental data suggests that the energy threshold for induction of DNA strand breaks by LEEs may be below 0.5 eV [72]. Strand breaks caused by LEEs are of particularly interest since such electrons are produced in very large quantity (4×10^4 per MeV energy deposited) [73] along all the tracks of ionizing radiation, with an energy distribution lying mainly below 15 eV.

For this purpose, Li *et al.* constructed a model that consists of two deoxyribose (sugar) rings connected by a phosphate [18]. In the model, the sites of bases on the sugar are replaced by amino groups, and the 3′- or 5′-ends are terminated with hydrogen, no counter ion such as Na^+ or structural water is included. The model is divided into a high layer that is treated at the B3LYP/6-31+G(d) level for the critical bond cleavage atoms and a low layer treated by AM1 method. Figure 15 illustrates the two possible routes of C–O bond breaking at the 3′ or 5′ that will lead to DNA strand breaks.

While the potential energy surfaces (PESs) of the neutral structure are in typical Morse potential shape with substantial bond energies, the PESs of the anion model show that dissociation at both 3′ or 5′ C–O sites is highly favorable thermodynamically (Fig. 16).

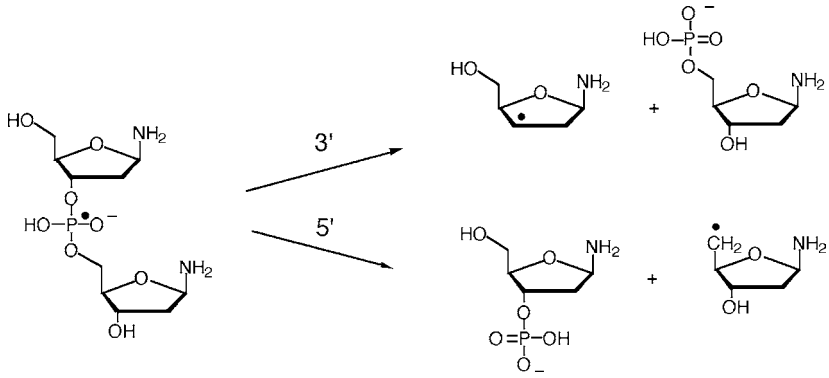

Fig. 15. Sugar-phosphate-sugar model representing a section of DNA backbone. Electron induced bond dissociations at 3′ and 5′ end of the model are investigated. Reprinted with permission from *J. Am. Chem. Soc.* (Ref. [18]).

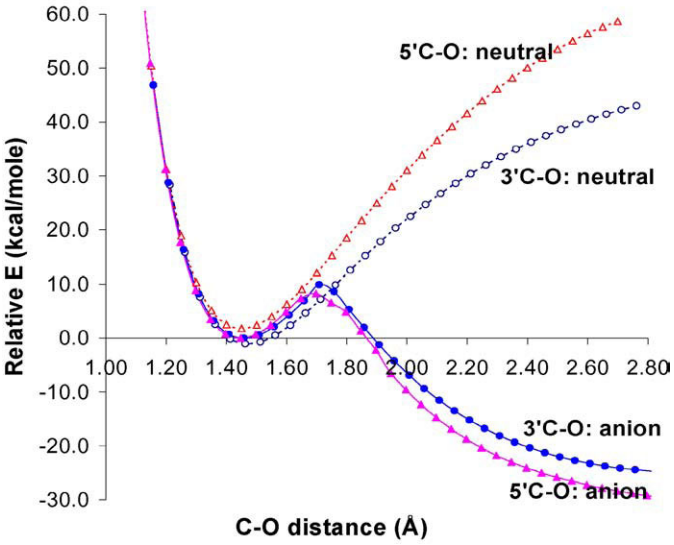

Fig. 16. Adiabatic potential energy surfaces for 3′C–O and 5′C–O bond rupture, 6-31+(G). All energies are relative to the energies of the anion radical at equilibrium. At short distances, the anion and neutral surfaces are nearly identical owing to the dipole bound nature of the initial anion. Reprinted with permission from *J. Am. Chem. Soc.* (Ref. [18]).

Bond cleavage at 3′ or 5′ C–O sites after addition of an electron is possible with a ca. 10 kcal/mol activation barrier. The energetics of bond cleavage and solvating effects are detailed in Table 11.

Table 11. ΔE (kcal/mol) for the electron induced cleavage process of the model obtained by ONIOM and full DFT calculations [18]

	ONIOM	B3LYP/6-31+G(d)
3′C–O	−36.09[a]	−37.17 (−44.64)[b]
5′C–O	−32.41[a]	−37.75 (−44.19)[b]

[a] ONIOM calculations. [b] Values in parenthesis are for solvation using PCM model, water as solvent, $\varepsilon = 78$.

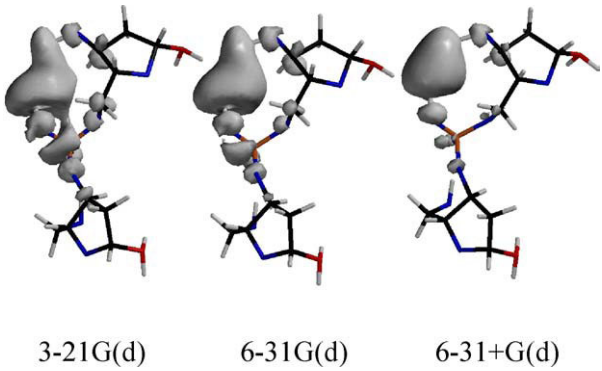

Fig. 17. Spin density distribution at several basis sets for the sugar-phosphate-sugar model of the DNA backbone. At even small basis sets the electron is largely in a diffuse state. For the 6-31+G(d) spin distribution the electron is clearly trapped in the dipolar field of two OH groups.

Our paper [18] did not describe the nature of the anion radical species and this work was questioned in recent work [74–76]. We have gone back and investigated the distribution of the excess spin in the anion radical. In Fig. 17 we show results found at various basis sets. At each basis set it is clear that the excess electron is not a valence anion but an electron held in the dipole field of the OH groups in the sugar phosphate backbone, i.e., dipole bound. The electron is held with only a small positive EA so the initial surface of the anion and that of the neutral are nearly identical. Only on stretching the C–O bonds to 1.8 Å is the electron captured in a σ^* antibonding state. An approximate treatment of this problem by Simons and co-workers [74,75] investigated the neutral, excited π^* and σ^* surfaces and suggests a low energy electron could initially be trapped in an excited π^* state and cross over to the σ^* surface which is dissociative (see Ref. [74]). Other very recent efforts by Schaefer and coworker [76] provide addition evidence for the exothermic nature of the bond cleavage process.

It is clear from our work that a LEE induced vibrational excitation in the C–O bond sufficient to extend it to 1.8 Å would effectively capture the electron in the σ^* surface.

The environment of DNA, such as the bases, structural water and counter ions will of course influence the overall energetics. Preliminary results show that solvation of the systems will augment the large exothermic energy release on strand breaking (Table 11). In aqueous solutions, LEEs will undergo energy degradation and become solvated. However,

recent measurement [77] of DEA within the sugar-phosphate unit of DNA suggests that transient anions formed at energies even up to 10 eV, have lifetimes sufficiently long to dissociate before autoionization or electron transfer. Even though the bases have a deeper energy well than that of the backbone, electron transfer from these transient anions (i.e. electron autodetachment) to the bases is not necessarily favored, because the anion states may be more strongly correlated to energy levels that are both spatially proximate and energetically close [78]. Moreover, as the C–O bond extends the electron affinity of the backbone eventually becomes higher than that of the bases (at ca. 1.8 Å) [79]. Since the minimum energy needed for the anion to surmount the activation barrier is only ~ 0.5 eV, the findings of this work suggest that direct damage by low energy electrons before solvation is a clear possibility even in solution.

We note that the radicals associated with cleavage of the 3′C–O and P–O bonds have been reported in ESR experiments [80,81] on DNA irradiated at low temperatures, and the mechanism of these radicals formation was attributed to LEEs. The experimental evidence provides solid support for LEE-induced DNA strand breaks proposed in this work.

7. ENERGETICS OF BASE RELEASE IN NUCLEOSIDE ANION RADICALS [89]

Radiation induced base release is a well-known process which has been attributed to formation of sugar radicals followed by the loss of an unaltered DNA base during chemical rearrangement [82–85]. Recently the glycosidic bond cleavage of nucleosides by low energy electrons (LEEs) have been reported. For example it was found that 15 eV electrons can induce thymidine to decompose into thymine and sugar fragments with the initial quantum yield of conversion to thymine estimated to be 3.2×10^{-2} per incident electron [86]. Electrons with lower energy (< 3 eV) were also found to be able to induce efficient dissociation of thymidine into the sugar and thymine moieties [87]. These experimental results call for theoretical investigations of the glycosidic bond strength in deoxyribonucleosides (dA, dG, dC and dT) before and after electron attachment.

Calculations show that the N_1–H is the weakest bond in thymine toward LEE cleavage [17]. Further it was predicted that in nucleosides and even in DNA, the N_1 glycosidic bond to the deoxyribose would be a weak link and highly vulnerable to LEE-induced bond fragmentation. One theoretical report has addressed LEE induced base release for dT and dC which reports the energetics of the process [88]. Recently new work has been reported that focuses on the detailed potential energy surfaces for the cleavage of the glycosidic bond (i.e., the C_1'–N link in the nucleosides between the base and deoxyribose C1′), before and after electron attachment [89]. Structures of the nucleoside molecules, deoxycytidine (dC), thymidine (dT), and deoxyadenosine, both with (dA1) and without (dA2) internal H-bonding, are shown in Fig. 18.

DFT calculations show that an excess electron effectively weakens the C_1'–N bond strength in nucleosides by 61–75 kcal/mol in the gas phase and 76–83 kcal/mol in the solvated environment. Table 12 collects the bond dissociation energy (BDE), ΔH and ΔG for homolytic dissociation of the neutral nucleoside C_1'–N bonds and heterolytic dissociation of the nucleoside anion radicals C_1'–N bonds. It can be seen that electron-induced fragmentation of the C_1'–N bond in the gas phase is exergonic for dA ($\Delta G = -14$ kcal/mol) and for dT ($\Delta G = -6$ kcal/mol) and is endergonic ($\Delta G = +1$ kcal/mol) only for dC. In the gas

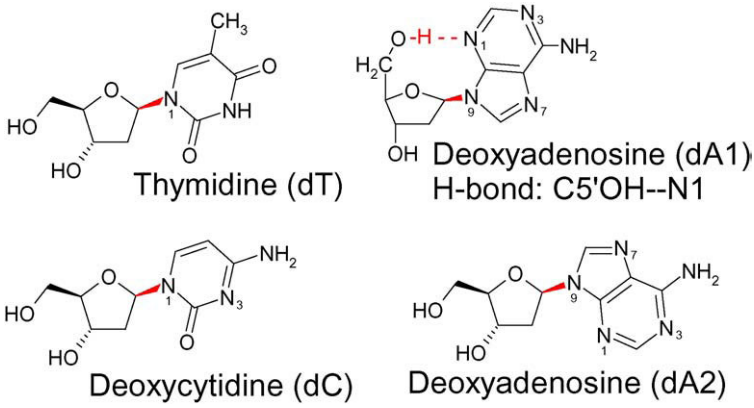

Fig. 18. Structures and names of the selected molecules. An internally H-bonded structure of dA is also included for illustrative purpose. Reprinted with permission from *Radiat. Res.* (Ref. [89]).

phase all the anionic nucleosides are found to be in valence states, except dG, which shows diffuse state contributions and therefore is not reported. Solvation is found to increase exergonic nature by an additional 20 kcal making the fragmentation both exothermic and exergonic for all nucleoside anion radicals. Thus C_1'–N bond breaking in nucleoside anion radicals is found to be thermodynamically favorable in both the gas phase and under solvation.

Figure 19 shows the adiabatic potential energy surfaces (PESs) on extension of the C_1'–N bonds of the dA2, dT and dC anions. At equilibrium, the C_1'–N bond distances of these three anions are all around 1.45 Å. As the C_1'–N bonds are stretched, the relative energies increase and reach the maxima at ca. 1.9 Å, then decrease as the bonds stretched further.

Calculated based on the energy of the transition structure or estimated from the PES, the activation barriers for the C_1'–N bond breaking process were found to be ca. 20 kcal/mol in every case examined (Table 13). This suggests that a 1 eV electron would induce spontaneous cleavage of the bond, and that stabilized anion radicals on the DNA strand would undergo base release with only a modest rate at room temperature. Recent experimental reports that show base release in thymidine (dT) for LEEs of only 1 eV (23 kcal) are in good agreement with the activation energy we find [86,87].

The PES of dA2 are characterized by sharp maxima at around 1.85 Å, suggesting quick conversion from the π^* bonding state to the dissociative σ^* antibonding state. Over the maximum in the PES of dA2 a smooth decent is found towards bond rupture. The PES of dA1 shows a near identical profile to dA2; thus internal H-bonding between C_5'OH and N_1 does not significantly alter the energy profile for fragmentation of the C_1'–N bond.

The HOMO and spin distribution contours indicate that before relaxation (*vertical anions*) the electron is in a mixed valence–diffuse state and after molecular relaxation, valence π^* states are found for anion radicals of dC, dT, dA [89]. Figure 20 shows the profiles of total charge and spin on the base portion vs the C_1'–N bonds distance. As the C_1'–N bond extends to 1.9 to 2.0 Å the valence π^* state crosses the antibonding σ^* dissociative state in which the excess electron drops into the rupturing C_1'–N bond creating a negative nitrogen

Table 12. C1′–N bond dissociation energies calculated at B3LYP/6-31+G(d), in kcal/mol and at 298 K for various deoxynucleosides [89]

	Neutral BDE: Base–R → Base$^{\bullet}$ + R$^{\bullet}$			Anion radical BDE: Base–R^{-} → Base^{-} + R$^{\bullet}$			LEE effect[c]
Gas phase	nBDE[a]	ΔH	ΔG	aBDE[b]	ΔH	ΔG	nBDE–aBDE
dT	71.22	71.81	56.41	7.08	7.68	−6.49	64.14
dC	75.91	76.50	61.59	14.88	15.47	0.86	61.03
dA1[d]	79.95	80.54	64.95	4.75	5.34	−8.81	75.20
dA2[d]	74.65	75.25	60.78	−0.48	0.11	−14.27	75.13
Solvated[e]							
dT	66.08	66.68	51.76	−9.93	−9.34	−24.18	76.01
dC	69.90	70.50	55.02	−7.35	−6.75	−21.86	77.25
dA1[d]	68.78	69.38	54.42	−10.25	−9.66	−24.81	79.03
dA2[d]	67.51	68.10	54.81	−15.96	−15.36	−28.56	83.47

[a] Zero point energy and thermal energy corrected. [b] All anion radicals are in their valence states. [c] The difference in the N–C_1' bond energy between the nucleoside neutral and anion radical is given by nBDE–aBDE. Note that nBDE–aBDE = EA (Base radical fragment)–EA (nucleoside). [d] With (dA1) and without (dA2) H-bonding $C_5'OH$–N_1. [e] Optimized using CPCM solvation model.

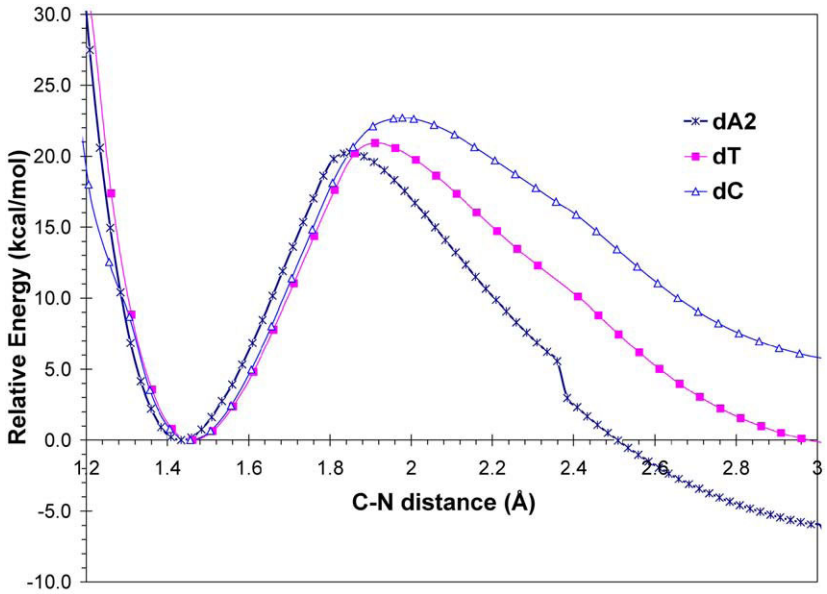

Fig. 19. Anionic N_1–C potential energy surfaces (PESs) of deoxyadenosine (dA2), thymidine (dT) and deoxycytidine (dC). Structure dA1 has a similar profile to dA2. Reprinted with permission from *Radiat. Res.* (Ref. [89]).

Table 13. Activation energies in gas phase (kcal/mol), B3LYP/6-31+G(d) [89]

Transition state anion	Activation energy[a]	C'_1–N distance (Å)
dT	19.2	1.91
dC	22.7	1.98
dA1	20.3	1.85
dA2[b]	19.5	1.84

[a] Without ZPE corrections. [b] Estimated from PES.

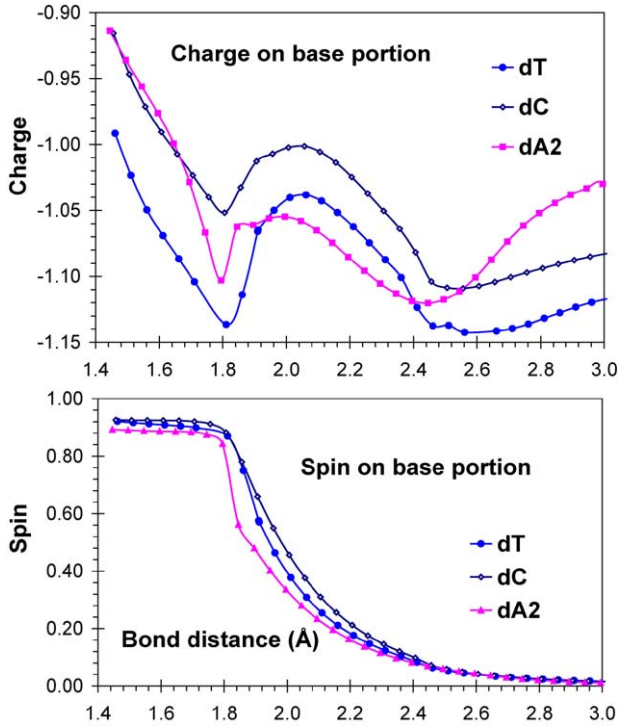

Fig. 20. Profile of charge & spin fraction on the base portion, as C'_1–N–C bond stretching for anions of dT, dC, dA. Method: B3LYP/6-31+G(d). Reprinted with permission from *Radiat. Res.* (Ref. [89]).

site on the DNA base and a free radical at C'_1 on the deoxyribose fragment, as shown below for thymidine radical anion:

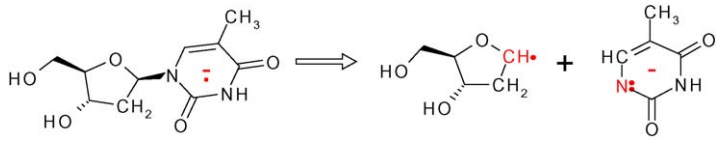

Table 14. Gas phase and solvated adiabatic electron affinities (AEA)[a] of all species involved, calculated at B3LYP/6-31+G(d) level (eV) [89]

Molecule	Gas	Solvated[b]	*Fragments*	Gas	Solvated[b]
dT	0.45	1.90	DeoxyRibose ($^{\bullet}C_1'$)	0.50[c]	2.50
dC	0.33	1.81	$^{\bullet}N_1$(T)	3.23	5.20
dA1[d]	−0.038	1.74	$^{\bullet}N_1$(C)	2.97	5.16
dA2	−0.035	1.55	$^{\bullet}N_9$(A)	3.22	5.17

[a] AEAs are ZPE corrected and thermodynamically corrected to 298 K. [b] In aqueous solvated environment, calculated using CPCM model. [c] Internal H-bonding in C_1' anion: C_5'OH–O (sugar ring) = 1.99 Å. [d] Internal H-bond between C_5'OH and N_1 (dA1).

Table 14 lists the adiabatic EA of all molecules and the relevant fragments in the gas phase and in solvated environment. The adiabatic EAs of the intact nucleosides are small: dT has the highest EA (0.45 eV) and dA1 has the smallest valence adiabatic EA (−0.038 eV) and are strongly affected by internal hydrogen bonding. The EA values suggest that the probability of thermal electron capture by any nucleosides is highest for dT followed by dC. On the other hand, the EAs of the base radical fragments are over 2.5 eV and are all localized valence states with the spin at the C1′ site.

For the pyrimidines (dT and dC), the EA values are in excellent agreement with those reported [90]. However, the EA value for dA reported by Richardson *et al.* [90], is slightly higher. The optimized equilibrium anion of dA has an interesting H-bonding between H (sugar O5′) and C8 of adenine similar to dA2 in our work. For the relaxd molecule anions (geometry optimized), their SOMO and spin contours clearly indicate the character of valence state [89].

In summary, electron attachment quite effectively weakens the strength of the C_1'–N bond and to the point that the bond-cleavage process is exergonic for all cases in solvated systems. The potential energy surface (PES) along the C_1'–N bond shows an activation barrier of ca. 20 kcal/mol for all nucleosides. As the C_1'–N bond is ruptured, the base fragment retains the charge because of its much higher electron affinity than the deoxyribose C_1' radical.

REFERENCES

[1] D. Becker, M.D. Sevilla, The chemical consequences of radiation damage to DNA in: J. Lett (Ed.), *Advances in Radiation Biology*, vol. 17, Academic Press, 1993, pp. 121–180.
[2] M.D. Sevilla, D. Becker, ESR studies of radiation damage to DNA and related biomolecules, in: *Royal Society of Chemistry Specialist Periodical Report, Electron Spin Resonance*, vol. 19, 2004, pp. 243–278, Chapter 6.
[3] L. Sanche, Nanoscopic aspects of radiobiological damage: Fragmentation induced by secondary low-energy electrons, *Mass Spectrom. Rev.* **21** (5) (2003) 349–369.
[4] B. Boudaiffa, P. Cloutier, D. Hunting, M.A. Huels, L. Sanche, *Science* **287** (2000) 1658.
[5] M. Yan, D. Becker, S. Summerfield, P. Renke, M.D. Sevilla, *J. Phys. Chem.* **96** (1992) 1983.
[6] W. Wang, D. Becker, M. Sevilla, *Radiat. Res.* **135** (1993) 146.
[7] Z. Cai, M.D. Sevilla, Studies of excess electron and hole transfer in DNA at low temperatures, in: G. Shuster (Ed.), *Topics in Current Chemistry 237: Long Range Transfer in DNA II*, Springer-Verlag, 2004, pp. 103–128.

[8] S.G. Swarts, D. Becker, M.D. Sevilla, K.J. Wheeler, *Radiat. Res.* **145** (1996) 304.
[9] A.O. Colson, M.D. Sevilla, *Inter. J. Radiat. Biol.* **67** (1995) 627.
[10] A.O. Colson, M.D. Sevilla, Application of molecular orbital theory to the elucidation of radical processes induced by radiation damage to DNA, in: J. Lesczycyski (Ed.), *Computational Molecular Biology*, *Theoretical and Computational Chemistry*, vol. 8, 1999, pp. 245–277.
[11] X. Li, Z. Cai, M.D. Sevilla, *J. Phys. Chem. A* **106** (2002) 1596.
[12] X. Li, Z. Cai, M.D. Sevilla, *J. Phys. Chem. A* **106** (2002) 9345.
[13] X. Li, Z. Cai, M.D. Sevilla, *J. Phys. Chem. B* **105** (2001) 10115.
[14] X. Li, L. Sanche, M.D. Sevilla, *J. Phys. Chem. A* **106** (2002) 11248.
[15] X. Li, M.D. Sevilla, L. Sanche, *J. Am. Chem. Soc.* **125** (2003) 8916.
[16] X. Li, L. Sanche, M.D. Sevilla, *J. Phys. Chem. B* **108** (2004) 5472.
[17] X. Li, M.D. Sevilla, L. Sanche, *J. Phys. Chem. B* **108** (2004) 19013.
[18] X. Li, M.D. Sevilla, L. Sanche, *J. Am. Chem. Soc.* **125** (2003) 13668.
[19] Z. Cai, M.D. Sevilla, *J. Phys. Chem. B* **104** (2000) 6942.
[20] Z. Cai, Z. Gu, M.D. Sevilla, *J. Phys. Chem. B* **104** (2000) 10406.
[21] Z. Cai, Z. Gu, M.D. Sevilla, *J. Phys. Chem. B* **105** (2001) 6031.
[22] D. Becker, M.D. Sevilla, *Electron Paramagnetic Resonance*, The Royal Society of Chemistry, Cambridge, 1998, 79 p.
[23] W. Wang, M. Yan, D. Becker, M.D. Sevilla, *Radiat. Res.* **137** (1993) 2.
[24] W. Wang, M.D. Sevilla, *Radiat. Res.* **138** (1994) 9.
[25] M.D. Sevilla, P. Mohan, *Internat. J. Radiat. Biol.* **25** (1974) 635.
[26] S. Steenken, *Biol. Chem.* **378** (1997) 1293.
[27] M.D. Sevilla, B. Besler, A.O. Colson, *J. Phys. Chem.* **98** (1994) 2215.
[28] A.A. Voityuk, M.E. Michel-Beyerle, N. Rosch, *Chem. Phys. Lett.* **342** (2001) 231.
[29] K. Aflatooni, G.A. Gallup, P.D. Burrow, *J. Phys. Chem. A* **102** (1998) 6205.
[30] V. Periquet, A. Moreau, S. Carles, J.P. Schermann, C. Desfrançois, *J. Electron. Spectrosc. Relat Phenom.* **106** (2000) 141.
[31] C. Desfrançois, V. Periquet, Y. Bouteiller, J.P. Schermann, *J. Phys. Chem. A* **102** (1998) 1274.
[32] S.D. Wetmore, R.J. Boyd, L.A. Eriksson, *Chem. Phys. Lett.* **322** (2000) 129.
[33] S.S. Wesolowski, M.L. Leininger, P.N. Pentchew, H.F. Schaefer III, *J. Am. Chem. Soc.* **123** (2001) 4023.
[34] D.M.A. Vera, A.B. Pierini, *Phys. Chem. Chem. Phys.* **6** (2004) 2899.
[35] M.D. Sevilla, B. Besler, A.O. Colson, *J. Phys. Chem.* **99** (1995) 1060.
[36] C. Desfrançois, H. Abdoul-Carime, J.P. Schermann, *J. Chem. Phys.* **104** (1996) 7792.
[37] G.H. Roehrig, N.A. Oyler, L. Adamowicz, *J. Phys. Chem.* **99** (1995) 14285.
[38] N.A. Oyler, L. Adamowicz, *J. Phys. Chem.* **97** (1993) 11122.
[39] E.C.M. Chen, E.S. Chen, *J. Phys. Chem. B* **104** (2000) 7835.
[40] J.H. Hendricks, S.A. Lyapustina, H.L. de Clercq, K.H. Bowen, *J. Chem. Phys.* **108** (1998) 8.
[41] J.H. Hendricks, S.A. Lyapustina, H.L. de Clercq, J.T. Snodgrass, K.H. Bowen, *J. Chem. Phys.* **104** (1996) 7788.
[42] J. Schiedt, R. Weinkauf, D.M. Neumark, E.W. Schlag, *Chem. Phys.* **239** (1998) 511.
[43] J.M. Galbraith, H.F. Schaefer III, *J. Chem. Phys.* **105** (1996) 862.
[44] N. Rösch, S.B. Trickey, *J. Chem. Phys.* **106** (1997) 8940.
[45] L.A. Cole, J.P. Perdew, *Phys. Rev. A* **25** (1982) 1265.
[46] L. Sanche, G.J. Schulz, *Phys. Rev. A* **5** (1972) 1672.
[47] K.D. Jordan, P.D. Burrow, *Chem. Rev.* **87** (1987) 557.
[48] M.F. Falcetta, K.D. Jordan, *J. Phys. Chem.* **94** (1990) 5666.
[49] M.F. Falcetta, Y. Choi, K.D. Jordan, *J. Phys. Chem. A* **104** (2000) 9605.
[50] I.K. Yanson, A.B. Teplitsky, L.F. Sukhodub, *Biopolymers* **18** (1979) 1149.
[51] Z. Cai, X. Li, M.D. Sevilla, *J. Phys. Chem. B* **106** (2002) 2755.
[52] A.O. Colson, B. Besler, M.D. Sevilla, *J. Phys. Chem.* **96** (1992) 9787.
[53] M. Hutter, T. Clark, *J. Am. Chem. Soc.* **118** (1996) 7574.
[54] J. Bertran, A. Oliva, L. Rodriquez-Santiago, M. Sodupe, *J. Am. Chem. Soc.* **120** (1998) 8159.
[55] G.D. Reid, D.J. Whittaker, J.A. Day, D.A. Turton, V. Kayser, J.M. Kelly, G.S. Beddard, *J. Am. Chem. Soc.* **124** (2002) 5518.
[56] B. Giese, J. Amaudrut, A. Kohler, M.A.W.S. Sportmann, *Nature* **412** (2001) 318.
[57] V. Sartor, E. Boone, G.B. Schuster, *J. Phys. Chem. A* **105** (2001) 11057.

[58] S. Steenken, *Chem. Rev.* **89** (1989) 503.
[59] B.G. Schuster, *Acc. Chem. Res.* **33** (2000) 253.
[60] P.T. Henderson, D. Jones, G. Hampikian, Y. Kan, G.B. Schuster, *Proc. Natl. Acad. Sci.* **96** (1999) 8353.
[61] A.O. Colson, B. Besler, D.M. Close, M.D. Sevilla, *J. Phys. Chem.* **96** (1992) 661.
[62] J. Taylor, I. Eliezer, M.D. Sevilla, *J. Phys. Chem. B* **105** (2001) 1614.
[63] S. Zamenhof, R. DeGiovanni, S. Greer, *Nature* **181** (1959) 827.
[64] T.S. Lawrence, M.A. Davis, J. Maybaum, P.L. Stetson, W.D. Ensminger, *Radiat. Res.* **123** (1990) 192.
[65] D.J. Buchholz, K.J. Lepek, T.A. Rich, D. Murray, *Int. J. Radiat. Oncol.* **32** (1995) 1053.
[66] H. Abdoul-Carime, M.A. Huels, E. Illenberger, L. Sanche, *J. Am. Chem. Soc.* **123** (2001) 5354.
[67] T. Sommerfeld, *Chem. Phys. Chem.* **2** (2001) 677.
[68] S. Cecchini, S. Giroud, M.A. Huels, L. Sanche, D.J. Hunting, *Radiat. Res.* **162** (2005) 604.
[69] G. Hanel, B. Gstir, S. Denifl, P. Scheier, M. Probst, B. Farizon, M. Farizon, E. Illenberger, T.D. Märk, *Phys. Rev. Lett.* **90** (2003) 188104;
S. Denifl, S. Ptasińska, M. Cingel, S. Matejcik, P. Scheier, T.D. Märk, *Chem. Phys. Lett.* **377** (2003) 74.
[70] R. Abouaf, J. Pommier, H. Dunet, *Int. J. Mass. Spectrom.* **226** (2003) 397.
[71] S. Ptasińska, S. Denifl, P. Scheier, T.D. Märk, *J. Chem. Phys.* **120** (2004) 8505.
[72] F. Martin, P.D. Burrow, Z. Cai, P. Cloutier, D. Hunting, L. Sanche, *Phys. Rev. Lett.* **93** (2004) 068101.
[73] J.A. LaVerne, S.M. Pimblott, *Radiat. Res.* **141** (1995) 208.
[74] J. Berdys, P. Skurski, J. Simons, *J. Phys. Chem. B* **108** (2004) 5800.
[75] I. Anusiewicz, M. Sobczyk, J. Berdys-Kochanska, P. Skurski, J. Simons, *J. Phys. Chem. A* **109** (2005) 484.
[76] J. Gu, Y. Xie, H.F. Schaefer III, *J. Am. Chem. Soc.* **128** (2006) 1250.
[77] X. Pan, P. Cloutier, D. Hunting, L. Sanche, *Phys. Rev. Lett.* **90** (2003) 208102.
[78] L. Sanche, *Surf. Sci.* **451** (2000) 82.
[79] R. Barrios, P. Skurski, J. Simons, *J. Phys. Chem. B* **106** (2002) 7991.
[80] D. Becker, Y. Razskazovskii, M. Callaghan, M.D. Sevilla, *Radiat. Res.* **146** (1996) 361.
[81] D. Becker, A. Bryant-Friedrich, C. A Trasko, M.D. Sevilla, *Radiat. Res.* **160** (2003) 174.
[82] S.G. Swarts, M.D. Sevilla, D. Becker, C.J. Tokar, K.T. Wheeler, *Radiat. Res.* **129** (1992) 333.
[83] Y. Razskazovskiy, M.F. Debije, W.A. Bernhard, *Radiat. Res.* **153** (2000) 436.
[84] E.S. Henle, R. Roots, W.R. Holley, A. Chatterjee, *Radiat. Res.* **143** (1995) 144.
[85] J.R. Wagner, C. Decarroz, M. Berger, J. Cadet, *J. Am. Chem. Soc.* **121** (1999) 4101.
[86] Y. Zheng, P. Cloutier, D.J. Hunting, J.R. Wagner, L. Sanche, *J. Am. Chem. Soc.* **126** (2004) 1002.
[87] H. Abdoul-Carime, S. Gohlke, E. Fischbach, J. Scheike, E. Illenberger, *Chem. Phys. Lett.* **387** (2004) 267.
[88] J. Gu, Y. Xie, H.F. Schaefer III, *J. Am. Chem. Soc.* **127** (2005) 1053.
[89] X. Li, L. Sanche, M.D. Sevilla, *Radiat. Res.* **165** (2006) 721.
[90] N. Richardson, J. Gu, S. Wang, Y. Xie, H.F. Schaefer III, *J. Am. Chem. Soc.* **126** (2004) 4404.

Computational Studies of Radicals Relevant to Nucleic Acid Damage

František Tureček

Department of Chemistry, University of Washington, Box 351700, Bagley Hall, Seattle, WA 981195-1700, USA

Abstract

Computational methods using ab initio and density functional theory have been employed to characterize transient intermediates of DNA and RNA damage. Hyperfine coupling constants and atomic spin densities have been obtained for adenine, guanine, cytosine, thymine, uracil, some of their derivatives, as well as nucleoside models, that were compared with experimental spectroscopic data from radiolysis. Ionization energies and redox potentials can be reliably calculated at high levels of theory and used to evaluate the energetics of charge and proton transfer reactions of nucleobase ions with solvent, amino acids, carbohydrates, and other molecules that are likely to participate in DNA damage. The structures, energetics, and kinetics of nucleobase and carbohydrate radical reactions have been addressed by computations and utilized to guide experiments and aid in experimental data interpretation.

Contents

1. INTRODUCTION

The structure units that compose DNA are attacked by energetic particles (photons, electrons, small radicals, etc.) that cause chemical changes referred to as DNA damage. DNA damage can have severe consequences for the DNA functioning and is therefore of significant importance for most life forms. The processes leading to DNA damage are usually discerned depending on the type of the primary interaction with the damage-causing agent

ADVANCES IN QUANTUM CHEMISTRY, VOLUME 52
ISSN: 0065-3276 DOI: 10.1016/S0065-3276(06)52005-2

[1,2]. Direct processes encompass ionization by electron removal (equation (1)) [3] or capture (equation (2)) [4] that produce reactive DNA ion-radicals.

$$\mathrm{DNA} \rightarrow \mathrm{DNA}^{+\bullet} + e^{-}, \tag{1}$$

$$\mathrm{DNA} + e^{-} \rightarrow \mathrm{DNA}^{-\bullet}. \tag{2}$$

Indirect processes involve attack on DNA by reactive products of solvent radiolysis, e.g., addition of $\mathrm{OH}^{\bullet}$ and $\mathrm{H}^{\bullet}$ (equations (3) and (4)), and hydrogen atom abstraction with $\mathrm{OH}^{\bullet}$ (equation (5)) forming

$$\mathrm{DNA} + \mathrm{OH}^{\bullet} \rightarrow [\mathrm{DNA} + \mathrm{OH}]^{\bullet}, \tag{3}$$

$$\mathrm{DNA} + \mathrm{H}^{\bullet} \rightarrow [\mathrm{DNA} + \mathrm{H}]^{\bullet}, \tag{4}$$

$$\mathrm{DNA} + \mathrm{OH}^{\bullet} \rightarrow [\mathrm{DNA} - \mathrm{H}]^{\bullet} + \mathrm{H_2O}, \tag{5}$$

neutral intermediates. DNA cation-radicals and anion-radicals can undergo a variety of consecutive reactions, both unimolecular and bimolecular, resulting in electron or proton transfer. The latter reactions are shown in equations (6) and (7) where the solvent, dissolved ions, peptides, or proteins capable of reacting with DNA ion radicals can be the requisite Brønsted bases and acids.

$$\mathrm{DNA}^{+\bullet} + \mathrm{base} \rightarrow [\mathrm{DNA} - \mathrm{H}]^{\bullet} + \mathrm{baseH}^{+}, \tag{6}$$

$$\mathrm{DNA}^{-\bullet} + \mathrm{acid} \rightarrow [\mathrm{DNA} + \mathrm{H}]^{\bullet} + (\mathrm{acid} - \mathrm{H})^{-}. \tag{7}$$

Of particular interest to DNA damage are highly reactive *radicals* formed by reactions (1)–(7) that are short lived and can dissociate or propagate chemical damage from the initial site either along the DNA strands or to the surrounding chromatin protein.

DNA damage has been studied extensively since the early 1960's and a wealth of experimental data have been accumulated for nucleobases, nucleosides, oligonucleotides, and model compounds [1–3]. Because of the open-shell nature of the intermediates, electron paramagnetic resonance (EPR) spectroscopy has been the main experimental tool in DNA damage studies. Fast chemical processes following radiolysis have been studied by time-resolved UV–VIS spectroscopy, typically on the microsecond time scale [3]. With the advent of quantum chemical computational methods, there has been increasing interest in complementing the experimental spectroscopic data with information on the structure, electronic properties, and energetics of DNA radicals. Computational studies of DNA and RNA radicals have so far dealt mainly with structural building blocks, such as nucleobases, base pairs, ribose or 2-deoxyribose, and nucleosides [5,6]. On one hand, this approach provides invaluable data on the intrinsic properties of isolated DNA radicals, referring to the gas phase or solution, that are currently unavailable by experiment. On the other hand, by neglecting chemical reactions of radical intermediates within DNA or with surrounding molecules and ions, it provides only a partial picture of DNA damage. Recent progress in the computational approach to DNA damage also resulted in studies that addressed the reactivity of DNA-related radicals from the point of view of reaction energetics and kinetics.

2. COMPUTATIONAL METHODS

The fact that many intermediates in the DNA damage process are open-shell species sets some requirements for the computational methods to be used for their characterization. Reliable geometries for local potential energy minima can be obtained by density functional

theory (DFT) [7] methods that include electron exchange and correlation terms. Perhaps the most popular of these has been the B3LYP hybrid [8–10] that belongs to the so-called adiabatic connection methods [11]. B3LYP includes, in a self-consistent way, Hartree–Fock exchange energy (E_x^{HF}), Becke's gradient correction to exchange (ΔE_x^{B}), local spin density terms for correlation (E_c^{LSD}) and exchange (E_x^{LSD}), and the Lee–Yang–Parr correlation potential ($\Delta E_c^{\mathrm{LYP}}$) [12] that were mixed with three parameters a_{x0}, a_{x1}, and a_c and optimized on the Gaussian 1 set of atoms and molecules (equation (8)) [13]

$$E_{xc}^{\mathrm{B3LYP}} = a_{x0}E_x^{\mathrm{LSD}} + (1 - a_{x0})E_x^{\mathrm{HF}} + a_{x1}\Delta E_x^{\mathrm{B}} + E_c^{\mathrm{LSD}} + a_c\Delta E_c^{\mathrm{LYP}}. \tag{8}$$

Although B3LYP has been tested on a set of mostly closed shell molecules, it has been found to perform well on a number of open-shell systems, as far as local energy minima were concerned. Geometries optimized with B3LYP are often equivalent to those calculated by perturbational methods (e.g. second-order Møller–Plesset, MP2) but are available at a substantially lower computational cost. The main advantage of B3LYP and other DFT methods is that they scale with roughly $N^{2.7-3}$ [7], whereas MP2 scales with O^2N^3, where O is the number of the occupied orbitals and N is the number of the basis functions [14]. DFT methods also provide good quality harmonic vibrational frequencies [15], and are fairly insensitive to contamination by higher spin states, e.g., quartet states for radicals. In the last two attributes DFT outperforms MP2-based methods that require large memory for frequency calculations and are prone to spin contamination. The latter deficiency can be mitigated by using wave functions in the restricted open-shell format (ROHF/ROMP2), as suggested for a series of simple radicals [16]. Because DFT relies on optimization of electron density, the DFT-based methods also provide accurate electron and spin distributions that are used for calculations of dipole moments, excitation energies, and hyperfine coupling constants for EPR spectra [17,18].

DFT methods have also been applied to locate transition states and provide activation energies for radical reactions. The general applicability of B3LYP in this area is yet to be assessed for several reasons, the most critical of which is the lack of reference experimental data for reactions in the gas phase. Experimental activation energies are available for relatively small systems that may not be readily extrapolated to be representative of the reactions of DNA-related radicals. From the limited computational studies reported so far, it appears that DFT can provide reasonable transition state geometries that can serve as the first approximation for further refinement (see below). Radical reactions involving bond dissociations and rearrangements have been found to be handled adequately with B3LYP for several systems. By contrast, B3LYP treatments of radical additions sometimes show false energy minima along the reaction coordinate and the calculated activation energies are often underestimated [19,20].

These deficiencies have led to attempts to improve DFT methods while maintaining their above-mentioned basic assets. Lynch *et al.* [21] suggested and tested a different mix of functionals using the Perdew–Wang 1-parameter model (termed MPW1K) [22] that was calibrated, using the 6-31+G(d, p) basis set, on a set of 20 reactions with known activation energies, and showed improved performance when compared to B3LYP [21]. Another approach relied on the observation that the relative energies calculated by B3LYP and MP2 calculations often err to a similar extent but in an opposite sense [23]. This was also reported by Rassolov, Ratner, and Pople in an unrelated study of the correlation energy in the dissociation of H_2, which was found to be overestimated by B3LYP and underestimated by MP2 [24]. Reliance on error cancellation forms the basis of the B3-MP2

method in which single-point energies calculated with B3LYP and MP2 (after spin projection [25], PMP2) are averaged and used to obtain corrected relative, dissociation, and transition state energies. Adequate basis sets of triple zeta quality that are furnished with polarization and diffuse functions, e.g., 6-311+(2d, p), 6-311++(2d, p), 6-311++G(3df, 2p), or aug-cc-pVTZ, are recommended for B3-PMP2 calculations, as permitted by the size of the molecular system under study [26–29]. The B3-PMP2 scheme has been tested against high-level correlated methods, e.g., coupled clusters with single, double, and disconnected triple excitations, CCSD(T) [30,31], and found to provide transition state energies within 4–5 kJ mol^{-1}. For a few polyatomic radical systems where experimental activation energies were known, B3-PMP2 was found to outperform CCSD(T) by providing accurate transition state energies [29]. Good results were also obtained for mapping potential energy surfaces along minimum energy reaction paths, where B3-PMP2 and CCSD(T) showed practically identical results in locating the transition state [32]. In spite of encouraging success in this area, obtaining reliable transition state geometries and accurate activation energies remains a non-routine exercise and requires multi prong approach where two or more methods dealing with dynamic electron correlation, e.g., DFT, MP2, and CCSD, are employed, and the results are compared for consistency and convergence. Multi-determinant methods, e.g., the complete active space self-consistent field (CASSCF) calculations [33,34] or configuration interaction, may be necessary in difficult cases where the wave function cannot be adequately described by a single Slater determinant [35].

In the following text, the computational studies of DNA damage will be sorted out by the nature of the chemical system. Nucleobase cation radicals will be treated first, followed by nucleobase radicals and their derivatives. Carbohydrate radicals, relevant to damage at 2-deoxyribose, will be treated last. Nucleobase anion radicals produced by capture of low-energy electrons have attracted much interest lately [36,37]. This topic has been exhaustively covered in a very recent review [38], and thus will not be dealt with in the present report.

3. NUCLEOBASE CATION RADICALS

Cation radicals are considered to be the primary intermediates of DNA damage proceeding by the direct mechanisms. While the properties of cation-radicals derived from oligonucleotides have been studied experimentally [3], computational studies have so far focused on smaller systems, primarily the four DNA nucleobases, adenine (A), guanine (G), cytosine (C) and thymine (T), and the RNA nucleobase uracil (U). In relation to experimental data, the computational studies have addressed four topics. (1) Structures and hyperfine proton–electron coupling constants have been studied computationally for adenine, guanine, cytosine, and thymine and compared to previous experimental data obtained by electron paramagnetic resonance (EPR) spectroscopy. (2) Ionization energies of gas-phase nucleobases have been calculated and compared to the data obtained by photoelectron spectroscopy and threshold photoionization measurements. (3) Electrochemical redox potentials have been calculated from the first principles and compared to experimental data. (4) Finally, structures and dissociation energies were studied computationally for adenine, and cytosine cation-radicals to interpret the formation and dissociations of gas-phase ions, as studied by tandem mass spectrometry.

Table 1. Selected bond lengths calculated for gaseous cytosine and adenine molecules and cation radicals[a]

	Neutral		Cation-radical	
	B1LYP[b]	B3LYP[c]	B1LYP[b]	B3LYP[c]
Cytosine				
$N_{(1)}$–$C_{(2)}$	1.429	1.427	1.415	1.420
$C_{(2)}$–$N_{(3)}$	1.371	1.371	1.344	1.347
$N_{(3)}$–$C_{(4)}$	1.314	1.321	1.348	1.350
$C_{(4)}$–$C_{(5)}$	1.441	1.442	1.432	1.437
$C_{(5)}$–$C_{(6)}$	1.355	1.361	1.383	1.389
$C_{(6)}$–$N_{(1)}$	1.353	1.356	1.333	1.335
$C_{(2)}$–$O_{(7)}$	1.211	1.224	1.236	1.243
$C_{(4)}$–$N_{(8)}$	1.360	1.361	1.328	1.332
Adenine				
$N_{(1)}$–$C_{(2)}$	1.341	1.341	1.312	1.318
$C_{(2)}$–$N_{(3)}$	1.333	1.334	1.381	1.383
$N_{(3)}$–$C_{(4)}$	1.336	1.336	1.298	1.304
$C_{(4)}$–$C_{(5)}$	1.395	1.397	1.430	1.433
$C_{(5)}$–$C_{(6)}$	1.409	1.409	1.435	1.437
$C_{(6)}$–$N_{(1)}$	1.341	1.342	1.355	1.359
$C_{(4)}$–$N_{(9)}$	1.376	1.377	1.386	1.388
$C_{(5)}$–$N_{(7)}$	1.384	1.384	1.336	1.340
$N_{(7)}$–$C_{(8)}$	1.306	1.308	1.343	1.348
$C_{(8)}$–$N_{(9)}$	1.379	1.380	1.352	1.355
$C_{(6)}$–$N_{(10)}$	1.350	1.353	1.320	1.325

[a] Bond lengths in angstroms. [b] Optimized with the 6-311G(d, p) basis set [39]. [c] Optimized with the 6-31+G(d, p) basis set [35].

3.1. Gas-phase structures and energetics

Improta *et al.* [39] reported a study of cation-radicals of the four DNA nucleobases using a single parameter DFT functional, called B1LYP [40], and the 6-311G(d, p) basis set. The optimized geometries of the cation-radicals show differences when compared to those of the neutral molecules in the gas phase [39]. This is illustrated for cytosine and adenine as representatives of pyrimidine and purine bases (Table 1). Note that B1LYP and B3LYP give very similar bond lengths for both gas-phase molecules and cation-radicals. The ring bonds in the cytosine cation-radical show alternating expansions and contractions that are indicative of changes in the corresponding bond orders upon ionization. This can be qualitatively visualized by the canonical valence bond structures that also illustrate the increased spin density on the $O_{(2)}$ oxygen atom obtained from NBO population analysis (Fig. 1). The calculated NBO atomic spin densities in the adenine cation-radical point to $N_{(10)}$, $N_{(3)}$, $C_{(5)}$, and $C_{(8)}$ as the major localization sites, consistent with the valence-bond

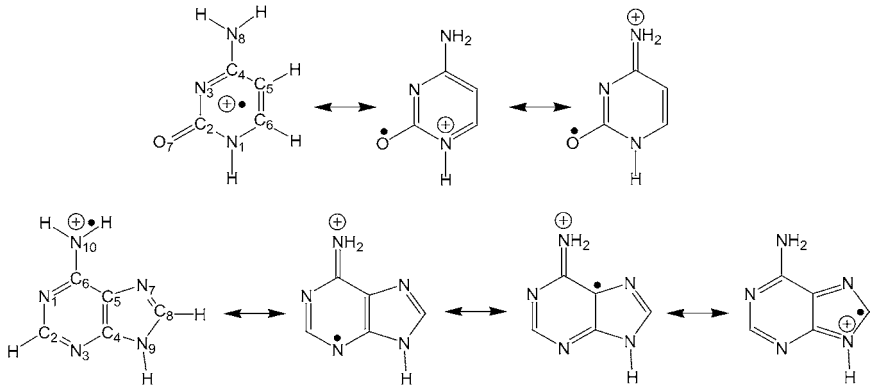

Fig. 1. Valence-bond structures of cytosine and adenine cation radicals.

Table 2. Ionization energies for DNA nucleobases[a]

	MP2/[b] 6-31+G(d, p)		B1LYP/ 6-311G(d, p)		B3LYP/[b] 6-311+G(2df, p)		CCSD(T)/[c] 6-311++G(3df, 2p)		B3-PMP2/[d] 6-311++G(3df, 2p)		Exp.	
	IE_a	IE_v	IE_a	IE_v	IE_a	IE_v	IE_a	IE_v	IE_a	IE_v	IE_a[e]	IE_v[f]
Adenine	8.18	8.58	7.95	8.16	7.91		8.25		8.28	8.43	8.26	8.44
Guanine	7.66	8.04	7.52	7.89	7.64						7.77	8.24
Cytosine[g]	8.74	8.82	8.47	8.62	8.57		8.71		8.71	8.79	8.68	8.94
Thymine	8.85	10.33	8.66	8.90	8.74						8.87	9.14
Uracil					9.21[h]		9.24[i]		9.32[i]		9.2[j]	9.34[k]

[a] In units of electron volt (eV). [b] Ref. [43]. [c] Extrapolated from the linear formula: E[CCSD(T)/6-311++G(3df, 2p)] $\approx$ E[CCSD(T)/6-31G(d, p)] + E[PMP2/6-311++G(3df, 2p)] − E[PMP2/6-31G(d, p)]. [d] From the formula: E[B3-PMP2/6-311++G(3df, 2p)] = 0.5{E[PMP2/6-311++G(3df, 2p)] + E[B3LYP/6-311++G(3df, 2p)]}. [e] From threshold photoionization measurements [47]. [f] From photoelectron spectra [48,49]. [g] Canonical 2-oxo-tautomer. [h] Calculations with the 6-311+G(2d, p) basis set Ref. [50]. [i] Calculations with the 6-311+G(3df, 2p) basis set Ref. [50]. [j] From Ref. [51]. [k] From Ref. [52].

representation in Fig. 1. The other change in structure upon ionization is the planarization of the amino groups in both cytosine and adenine cation-radicals [35].

The electronic structure of the DNA nucleobase cation-radicals has been discussed in terms of the molecular orbital model. Most studies agree that the odd-electron in the cation-radicals is delocalized in a π-type orbital whose nodal properties correlate with the alternating C–C and C–N bond lengths. Changes from a bonding π-orbital overlap between the neighboring atoms in the neutral molecule to an anti-bonding one in the cation-radical results in a bond lengthening and vice versa [35,39].

Gas-phase ionization energies were calculated for the DNA nucleobases and uracil at several levels of theory and compared with experimental data (Table 2). The calculated adiabatic ionization energies (IE_a) agree fairly well with the experimental values and correctly reproduce the order of ionization energies as IE (guanine) < IE (adenine) < IE (cytosine) < IE (thymine) < IE (uracil) (Table 2). Excellent quantitative agreement is obtained from high-level calculations using CCSD(T) or B3-PMP2 with large basis sets

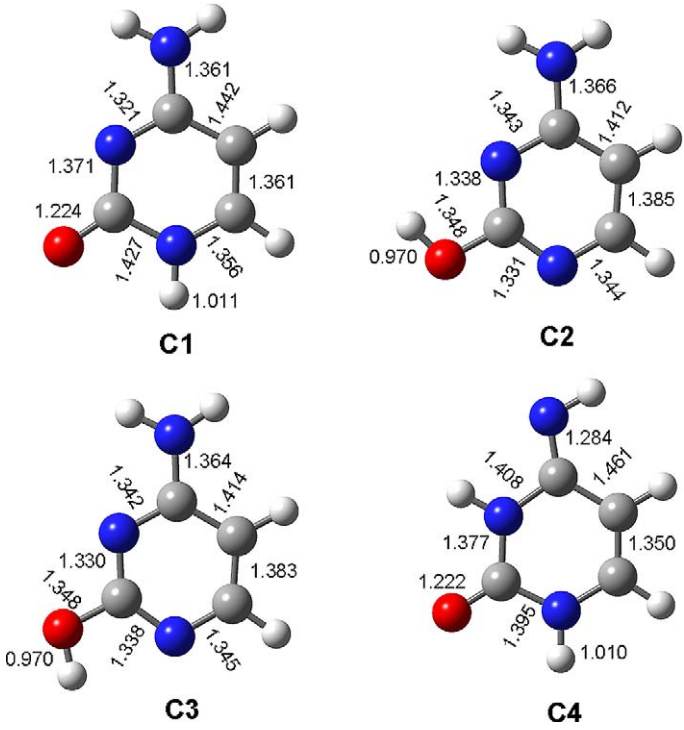

Fig. 2. B3LYP/6-31+G(d, p) optimized structures of cytosine tautomers in the gas phase.

and including zero-point vibrational energy corrections. At these levels of theory, the calculated IE_a are indistinguishable from the experimental values within the measurement uncertainty (±0.03–0.05 eV). A further, more rigorous, test of the accuracy of the computed IE_a would require more accurate experimental methods, e.g., zero electron kinetic energy (ZEKE) spectroscopy [41,42]. Other comparisons of the previously calculated IE with experimental and tabulated values can be found in Refs. [43,44].

Cytosine represents an interesting case where calculations provide additional insight into the ionization energetics. Cytosine is known to exist as a mixture of at least 4 tautomers (**C1**–**C4**, Fig. 2) in the gas-phase [45] of which the canonical 2-oxo-tautomer (**C1**) is a minor component, amounting to 13–32% at 298 K [46]. These tautomers are not distinguished in experimental measurements of ionization energies, and the corresponding bands in the photoelectron spectra or the onsets in the photoionization measurements overlap. Interestingly, the IE_a of **C1**–**C4** are calculated by CCSD(T)/6-311++G(3df, 2p) to be rather similar, e.g., 8.71, 8.62, 8.64, and 8.58 eV for **C1**, **C2**, **C3**, and **C4**, respectively [46]. The somewhat greater IE_a of the canonical tautomer **C1** increases the destabilization of its cation-radical ($\mathbf{C1}^{+\bullet}$) against the other cation-radical tautomers. Particularly interesting is the stabilization of the cation-radical of the $N-1$-imino tautomer $\mathbf{C5}^{+\bullet}$ which becomes the global minimum of the set (Table 3).

The canonical tautomer of the adenine cation-radical was calculated to be the most stable structure when compared to several isomers and is presumed to be the dominant species in both the gas phase and aqueous solution [35].

Table 3. Relative energies of tautomers of neutral cytosine and cytosine cation radicals

Species	B3LYP/ 6-31+G(d, p)		B3-PMP2/ 6-311++G(3df, 2p)		CCSD(T)/ 6-311++G(3df, 2p)	
	Neutral	Ion	Neutral	Ion	Neutral	Ion
C1	0	0	0	0	0	0
C2	6	−1.5	4	−4	0.7	−8
C3	3	−3	1	−7	−2	−9
C4	8	6	7	−0.3	2	−1.3
C5	29	−4	30	−7	31	−11

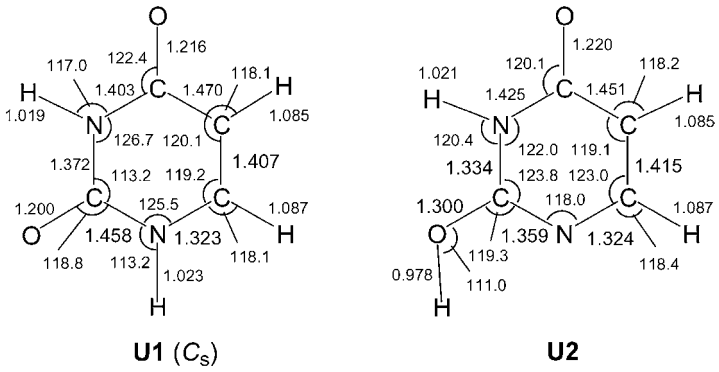

Fig. 3. B3LYP/6-31+G(d, p) optimized structures of uracil cation-radical tautomers in the gas phase.

The canonical form of the uracil cation-radical (**U1**, Fig. 3) is the most stable tautomer out of the 10 structures studied [50]. However, ion **U1** is only 8–10 kJ mol^{-1} more stable than the enol-form **U2** that can coexist with **U1** as a minor tautomer at equilibrium. The gas-phase acidity of **U1** has been evaluated using B3-PMP2 and QCISD(T) calculations with the 6-311+G(3df, 2p) basis set [50]. According to those, $N_{(1)}$ is the most acidic position in **U1** ($\Delta H_{ac,298} = 829$ kJ mol^{-1}), followed by $C_{(6)}$ (879 kJ mol^{-1}), $C_{(5)}$ (906 kJ mol^{-1}), and $N_{(3)}$ (922 kJ mol^{-1}). Even the most stable (U–H)$^{\bullet}$ radical from uracil (**U3**) has been calculated to exothermically abstract the SH hydrogen atom from CH_3SH, the OH hydrogen atom from phenol, and the α-hydrogen atom from glycine-*N*-methyl amide with $\Delta H_{rxn} = -67$, -55, and -95 kJ mol^{-1}, respectively, while restoring uracil in the process. Reactions of the other uracil (U–H)$^{\bullet}$ radicals were of course still more exothermic. It was concluded that deprotonation of **U1** and related uridine cation-radicals in RNA can form highly reactive radicals that can propagate the damage to the surrounding protein by reactions with susceptible amino acid residues, such as cysteine, tyrosine, and glycine. At the same time, peptides containing those residues can serve as repair agents by restoring the nucleobase by hydrogen atom transfer.

3.2. Solution studies

While the gas phase represents a convenient reference medium for the comparison of the calculated and experimental properties of nucleobases, DNA damage occurs in a hydrated condensed phase where solvation plays a significant role. With the advent, development, and refinement of theoretical models of solvation it became feasible to carry out calculations of enthalpies and free energies to include the surrounding solvent. The most common approach is to use a polarizable continuum model (PCM) in which the species of interest is placed in a cavity in a polarizable dielectric and its structure and energy is calculated in a self-consistent fashion by Hartree–Fock or DFT procedures that include electrostatic and van der Waals corrections to the total energy. Several PCM models have been developed [53–55] and included in quantum chemistry program packages, such as Gaussian 03 [56]. The usual approach is to express the reaction free energy in solution as a combination of the gas-phase term, $\Delta G_{\mathrm{rxn},298}(\mathrm{g})$, that was obtained at a high-level of theory, and the change in solvation free energies during the reaction, ΔG_{solv} (equations (9), (10)):

$$\Delta G_{\mathrm{rxn},298}(\mathrm{solv}) = \Delta G_{\mathrm{rxn},298}(\mathrm{g}) + \Delta G_{\mathrm{solv}}, \tag{9}$$

$$\Delta G_{\mathrm{solv}} = \Sigma G_{\mathrm{solv}}(\mathrm{products}) - \Sigma G_{\mathrm{solv}}(\mathrm{reactants}). \tag{10}$$

For example, deprotonation of the adenine cation-radical in water has been studied computationally with the aim to identify the energetically most favorable product. Scheme 1 shows $N_{(9)}$–H to be the most acidic proton of $pK_a \approx 3.2$, followed by the anti-oriented proton of the amino group of $pK_a \approx 3.3$. In the absence of $N_{(9)}$–H, as in adenosine and DNA where the $N_{(9)}$ position is occupied with deoxyribose, ionization of adenosine at physiological pH is expected to be followed by fast deprotonation forming the N_{10} aminyl radical. The latter is a highly reactive species of considerable hydrogen atom affinity, e.g., $\Delta H_{\mathrm{rxn},0}(\mathrm{g}) = -415\ \mathrm{kJ\,mol^{-1}}$ and $\Delta G_{\mathrm{rxn},298}(\mathrm{w}) = -383\ \mathrm{kJ\,mol^{-1}}$ for the recombination reaction that reforms the adenine moiety (Scheme 2). This recombination energy exceeds the $\Delta G_{\mathrm{rxn},298}(\mathrm{w})$ for hydrogen atom abstractions from the $C_{(1)}$, $C_{(3)}$,

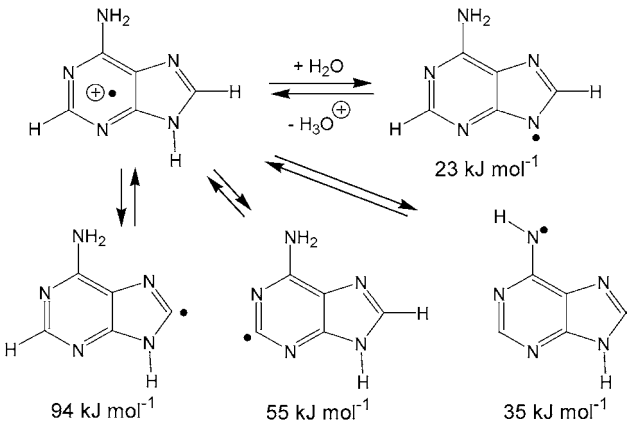

Scheme 1. Free energies ($\mathrm{kJ\,mol^{-1}}$) for proton transfer reactions from the adenine cation-radical to water in solution.

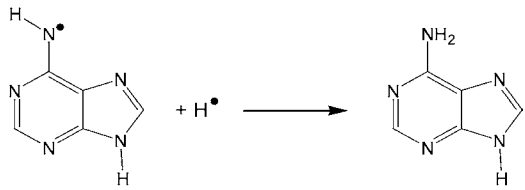

Scheme 2. Recombination of an adenine-N_{10} radical with a hydrogen atom.

$C_{(4)}$, and $C_{(5)}$ in 2-deoxyribofuranose [57], indicating exoergic hydrogen atom transfer to the adenyl radical. H-atom abstraction from $C_{(3)}$ and $C_{(5)}$ in deoxyribose is presumed to play an important role in DNA strand breaks. Hence the reaction sequence: adenine → [adenine]$^{+\bullet}$ → adenine-*N*-10-yl radical → deoxyribose-3-yl radical is revealed by first-principles calculations to be an energetically plausible pathway for damage propagation from the ionized nucleobase to the sugar-phosphate backbone to cause strand breaks.

Significant progress has also been made in calculations of electrochemical properties of nucleobases, namely, standard redox potentials. Llano and Eriksson [58] derived thermodynamic equations for the free energy change in redox reactions (equations (11), (12)) according to equation (13):

$$\mathrm{Ox(aq)} + e^- = \mathrm{Red(aq)}, \tag{11}$$

$$\mathrm{Nucleobase}^{+\bullet} + e^- \rightarrow \mathrm{Nucleobase}, \tag{12}$$

$$\Delta G^0 = \mu^{0,\mathrm{aq}}(\mathrm{Red}) - \mu^{0,\mathrm{aq}}(\mathrm{Ox}) - \mu^{0,\mathrm{SHE}}(e^-), \tag{13}$$

where $\mu^{0,\mathrm{aq}}(\mathrm{Red})$ and $\mu^{0,\mathrm{aq}}(\mathrm{Ox})$ are the standard chemical potentials of the redox couple and $\mu^{0,\mathrm{SHE}}(e^-)$ is the electron potential in the reference Pt electrode at 298 K and 1 atm (−4.34 eV).

The change in the standard potentials for the redox pair is calculated from the free energy of the gas phase electron recombination and the solvation free energies, analogously to equation (9). Equation (13) then allows one to calculate the redox potential referenced against the standard hydrogen electrode. Equation (13) can further be extended with the chemical potential of proton to include proton-coupled electron transfer processes as well [59]. Formal reduction potentials at pH 7 have been calculated for cation-radicals of adenine, guanine, cytosine and thymine as 1.59, 1.12, 2.07, and 1.96 V, in a reasonable agreement with experimental data [60].

4. NUCLEOBASE RADICALS

Computational studies of nucleobase radicals have addressed both the static properties of these transient intermediates (equilibrium geometries, relative energies, spin densities, and hyperfine coupling constants), and dynamic properties including the structures, electronic properties, and energies of transition states and dissociation or isomerization products.

Wetmore, Boyd and Eriksson reported several comprehensive studies of the relative energies, spin densities, and hyperfine coupling constants of nucleobase radicals using DFT methods. Geometries were optimized with B3LYP/6-31G(d, p) and hyperfine coupling

constants were obtained with the Perdew–Wang PWP86 functional and the 6-311G(2d, p) basis set [61]. It was noted that the PWP86 functional provides more accurate hyperfine coupling constants than does B3LYP [62]. Neutral radicals of the $(Base+H)^{\bullet}$, $(Base-H)^{\bullet}$, and $(Base + OH)^{\bullet}$ type, cation-radicals, and anion radicals were addressed.

4.1. Thymine

With thymine and 1-methylthymine, the most stable $(T + H)^{\bullet}$ radicals correspond to hydrogen atom adducts to $C_{(6)}$ followed by adducts to $C_{(5)}$ ($+12$ kJ mol^{-1}), $O_{(4)}$ ($+53$ kJ mol^{-1}), and $O_{(2)}$ ($+118$ kJ mol^{-1}) [61]. The isotropic hyperfine coupling constants calculated for the optimized geometries of the gas-phase $C_{(5)}$ adduct showed good agreement with the data reported from an ENDOR study, while a difference was found for the $O_{(4)}$–H coupling in the less stable $O_{(4)}$ adduct that was also claimed to be observed upon radiolysis in a crystal [63]. The difference was ascribed to possibly different rotational geometries about the O–H bond in the gas-phase and crystal structures [61]. The most stable $(T - H)^{\bullet}$ radical formed from thymine corresponds to H atom abstraction from the $C_{(5)}$ methyl group. The calculated hyperfine coupling constants for this radical were found to agree well with the experimental data measured in several laboratories [63–66]. The computational study of potential radiation products from thymine also concluded that there was no evidence for the presence of thymine anion-radicals, as claimed in another experimental study [64].

4.2. Cytosine

A related computational study of cytosine [67] identified a $(C + H)^{\bullet}$ adduct as being due to H atom attachment to $N_{(3)}$. This is also the most stable of $(C + H)^{\bullet}$ radicals in the gas phase. In contrast, other radical species, e.g., $(C - H)^{\bullet}$ from H atom abstraction at $N_{(1)}$, that were claimed to be detected by EPR in a previous radiolytic study [68] were found to have hyperfine coupling constants that did not match the experimental spectra. Wetmore *et al.* speculated on the formation of the $N_{(3)}$ $(C + H)^{\bullet}$ adduct and suggested possible mechanisms [67] that then were debated in the literature [69–71]. For another study of magnetic properties of cytosine radicals, see Ref. [72].

Hydrogen atom additions to cytosine, 1-methylcytosine, and microhydrated cytosine were addressed by another computational study that used B3LYP/6-31+G(d, p) for geometry optimization and B3-PMP2 and CCSD(T) single-point calculations to obtain relative, transition-state, dissociation, and association energies [73]. The goal of this computational study was to analyze conflicting data reported on the basis of radiolysis studies using EPR. Whereas most previous radiolysis studies had reported transient radicals formed by H atom addition to $C_{(5)}$ and $C_{(6)}$ in cytosine as its major radiolytic products [74–82], the work of Sagstuen *et al.* [68] suggested formation of a $N_{(1)}$–H adduct, and another report by Symons and coworkers considered the formation of adducts at $N_{(3)}$ and the NH_2 group [83].

The calculated relative enthalpies of 12 cytosine $(C + H)^{\bullet}$ radicals are shown in Table 4 [73]. The $N_{(3)}$ H adduct (**CR1**, Fig. 4) is the most stable species in the gas phase. The optimized structure shows a pyramidal NH_2 group that is rotated by 61 degrees out of the ring plane to avoid repulsive interaction with the $N_{(3)}$–H atom. $N_{(3)}$ is also pyramidized, so that the $N_{(3)}$–H bond is tilted 15 degrees out of the ring plane. Hydrogen atoms adducts

Table 4. Relative energies of cytosine radicals

	Relative energy[a]					
	B3LYP 6-31+G(d, p)	B3-MP2[b] 6-311++G(3df, 2p)				CCSD(T)[c] 6-311++G(3df, 2p)
Radical	ΔH_0(g)[d]	ΔH_0(g)[d]	ΔH_{298}(g)[e]	ΔG_{298}(g)[f]	ΔG_{298}(w)[g]	ΔH_0(g)[d]
CR1	0	0	0	0	0	0
CR2	31	36	35	34	7	31
CR3	37	44	43	39	−1	43
CR4	54	51	51	53	59	–
CR5	49	52	–	–	–	–
CR6	46	56	56	60	48	–
CR7	61	60	–	–	–	–
CR8	66	71	–	–	–	–
CR9	70	75	74	76	60	–
CR10	142	155	–	–	–	–
CR11	177	203	–	–	–	–
CR12	162	162	161	162	78	–

[a] In units of kJ mol^{-1}. All relative energies include ZPVE corrections. [b] From spin-projected MP2 energies. [c] From a linear extrapolation: E[CCSD(T)/6-311++G(3df, 2p)] ≈ E[CCSD(T)/6-31G(d, p)] + E[PMP2/6-311++G(3df, 2p)] − E[PMP2/6-31++G(d, p)]. [d] Gas-phase relative enthalpies at 0 K. [e] Gas-phase relative enthalpies at 298 K. [f] Gas-phase relative free energies at 298 K. [g] Relative free energies in water.

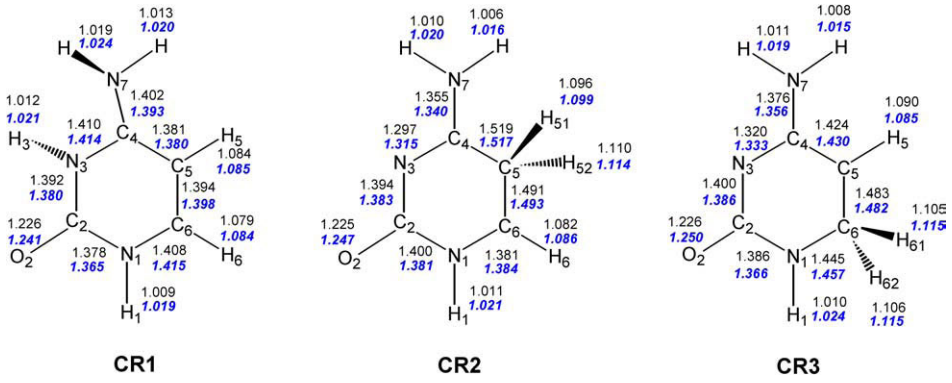

Fig. 4. B3LYP/6-31+G(d, p) optimized structures of cytosine radicals **CR1**–**CR3**. Bond lengths are in angstroms. Roman numerals are for gas phase structures, bold (blue in the web version) numerals are for structures optimized by PCM in the water dielectric.

to $C_{(5)}$ (**CR2**) and $C_{(6)}$ (**CR3**) are destabilized against **CR1** by 31 and 43 kJ mol^{-1}, respectively. Hydrogen atom adducts to the other stable cytosine tautomers (**CR4**–**CR9**) are still less stable (Fig. 5), as are the adducts to $C_{(4)}$ (**CR10**), $C_{(2)}$ (**CR11**) and the NH_2 group (**CR12**) (Fig. 6). Interestingly, the free energy differences among the cytosine radicals are

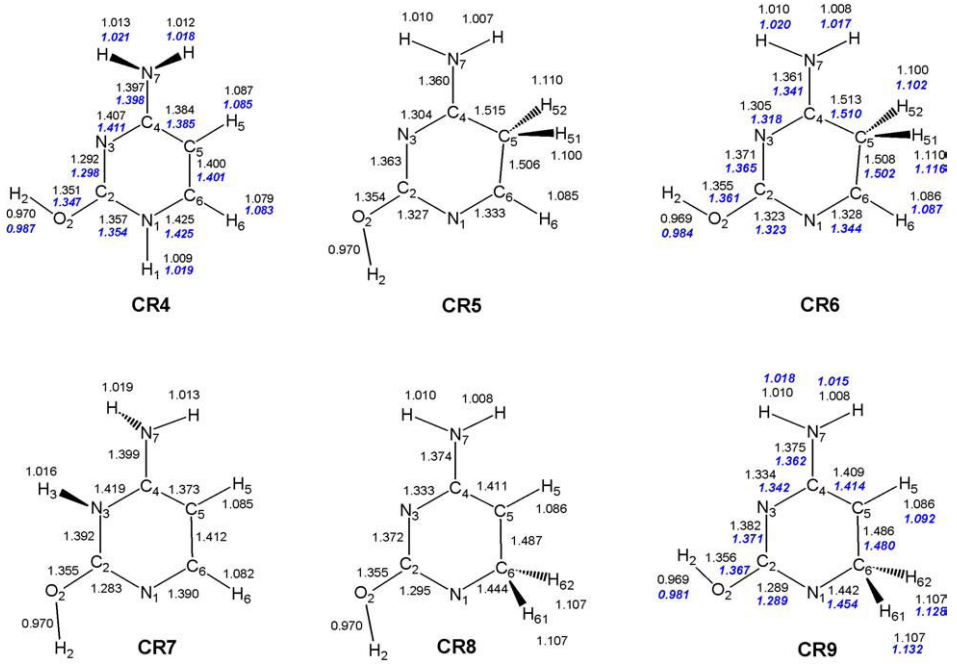

Fig. 5. B3LYP/6-31+G(d, p) optimized structures of cytosine radicals **CR4**–**CR9** in the gas phase. Bond lengths are in angstroms.

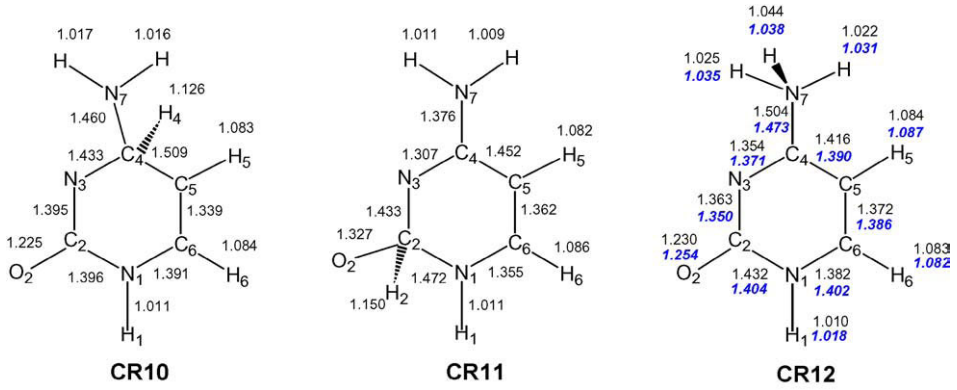

Fig. 6. B3LYP/6-31+G(d, p) optimized structures of cytosine radicals **CR10**–**CR12** in the gas phase. Description as in Fig. 5.

greatly diminished by solvation effects in water, where **CR1** and **CR3** are practically isoenergetic and **CR2** is only 7 kJ mol^{-1} less stable than **CR1**. A very similar trend was found for hydrogen atom adducts to 1-methyl cytosine, where the $N_{(3)}$ adduct is most stable in the gas phase, whereas it and the adduct to $C_{(6)}$ are practically isoenergetic in aqueous solution [73].

Table 5. Reaction enthalpies and activation energies for H-atom additions to cytosine, 1-methyl cytosine, and cytosine-water clusters

	Relative energy[a,b]		
	$N_{(3)}$	$C_{(5)}$	$C_{(6)}$
Cytosine-$N_{(1)}$-H			
$\Delta H_{0,add}$	−131 (−72)[c]	−95 (−64)[c]	−87 (−73)[c]
$E_{TS,add}$	17.6	13.5	22.8
Cytosine-$N_{(1)}$-methyl			
$\Delta H_{0,add}$	−128 (−66)[c]	−92 (−60)[c]	−84 (−65)[c]
$E_{TS,add}$	17.0	12.2	20.8
Cytosine-$N_{(1)}$-H. . .OH_2			
$\Delta H_{0,add}$	−123	−89	−83
$E_{TS,add}$	19.5	15.0	24.0
Cytosine-$N_{(8)}$-H. . .OH_2			
$\Delta H_{0,add}$	−114	−95	−89
$E_{TS,add}$	27.4	14.9	23.9
Cytosine-$N_{(1)}$-H, $N_{(8)}$-H. . .$2OH_2$			
$\Delta H_{0,add}$	−106	−88	−74
$E_{TS,add}$	28.2	15.2	24.0

[a] All energies are in units of kJ mol^{-1}. [b] From B3-PMP2/6-311++G(3df, 2p) energies and B3LYP/6-31+G(d, p) zero-point corrections. [c] Including PCM solvation energies in a water dielectric.

Hydrogen atom additions to cytosine were found to be highly exothermic in both the gas phase and water. Table 5 shows that solvation by water favors neutral cytosine against the hydrogen atom adducts, which decreases the exothermicity of H atom additions in water compared to those occurring in the gas phase [73]. The activation energies for H atom additions favor $C_{(5)}$ as the most reactive site in gas-phase cytosine, 1-methylcytosine, and microsolvated cytosine-water clusters. The activation energies inversely correlate with the electron density in the cytosine nucleus, indicating that the H atom attacking $C_{(5)}$ behaves as an electrophile. A similar correlation was found by QCISD(T)/6-311+G(3df, 2p) calculations for H atom additions to 4-aminopyrimidine which can be viewed as a deoxycytosine derivative [84]. Transition state theory calculations gave rate constants for H atom additions to $C_{(5)}$ on the order of 10^{10} mol^{-1} cm^3 s^{-1} at 298 K that were 6–39 fold greater than those for the other reactive positions, $N_{(3)}$ and $C_{(6)}$. This result was in qualitative agreement with most radiolysis data that showed **CR2** to be the major $(C + H)^{\bullet}$ product [74–78]. Solvation by water increases the activation energy of addition to $N_{(3)}$, such that it becomes slower than the addition to $C_{(6)}$. This appears to be mainly a steric effect, as $N_{(3)}$ is involved in hydrogen bonding to the solvent, and the proximate water molecule hinders approach of the H atom. It may be noted that neutral H-atom adducts to $N_{(3)}$ and $C_{(5)}$ in 1-methylcytosine were generated in the gas phase in a chemically specific manner by femtosecond electron transfer and found to be distinct species that were characterized by neutralization–reionization mass spectrometry [85].

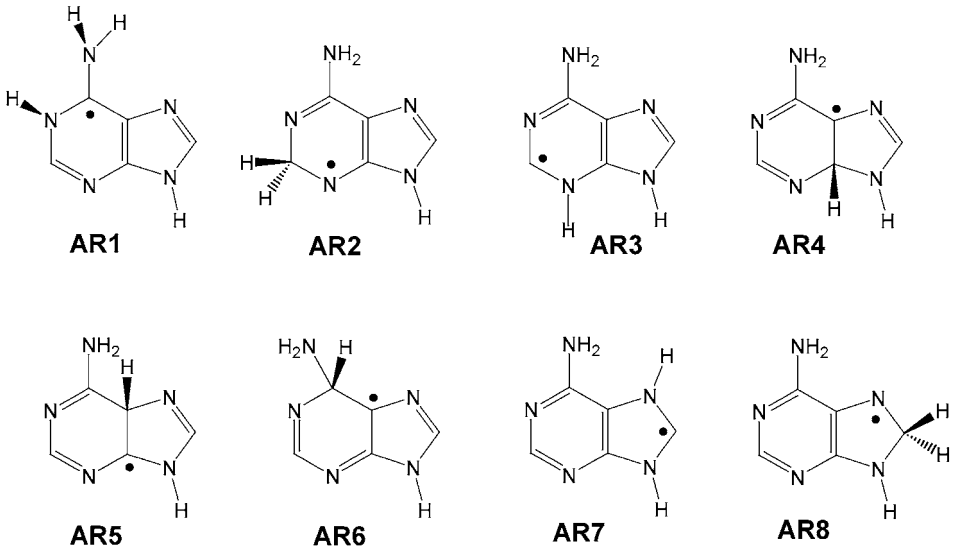

Fig. 7. Adenine radicals **AR1**–**AR8**.

4.3. Adenine

Radicals derived from adenine have been addressed by experimental and computational studies. Wetmore *et al.* [86] and Reynisson and Steenken [87] reported DFT calculations of adenine ions and the related $(A+H)^{\bullet}$ and $(A-H)^{\bullet}$ radicals. Regarding $(A+H)^{\bullet}$ radicals, the calculations agree on the $C_{(8)}$ adduct (**AR8**, Fig. 7) being the most stable isomer. This was confirmed by B3-PMP2 and CCSD(T) calculations that provided the relative energies of several $(A+H)^{\bullet}$ radicals as shown in Table 6 [88]. The $(A+H)^{\bullet}$ radicals span a range of relative enthalpies of almost 90 kJ mol^{-1}, which raises the question of their equilibration by hydrogen atom migrations around the purine ring system. This question was addressed computationally for the exothermic 1,2-H migration from $N_{(1)}$ to $C_{(2)}$ [88]. The potential energy surface was mapped in detail by B3LYP/6-31+G(d, p), but the calculations did not reveal any saddle point connecting **AR1** and **AR2** at energies below the respective transition states for hydrogen atom loss. It was therefore concluded that **AR1** cannot isomerize unimolecularly to **AR2**. Other dissociations of **AR1**, e.g., cleavages of the pyrimidine and imidazole rings, are substantially endothermic and are not likely to compete with hydrogen loss or bimolecular reactions. It should be noted that the enthalpy differences between **AR8** and the other isomers are somewhat diminished by solvation effects in the water dielectric (Table 6); nevertheless, **AR8** remains the by far most stable $(A+H)^{\bullet}$ radical that is expected to dominate at equilibrium [88]. Radical **AR1** has been specifically generated in the gas phase by femtosecond electron transfer, and its unimolecular dissociations have been studied by neutralization-reionization mass spectrometry [88].

The energetics and kinetics of H-atom additions to adenine in the gas phase were addressed by B3-PMP2 and CCSD(T) calculations including corrections for tunnel effects (Table 7). H-atom additions to adenine are notably less exothermic than those to cytosine (Table 5) and show substantially greater activation energies even for the most reactive po-

Table 6. Relative energies of adenine $(A + H)^{\bullet}$ radicals

	Relative energy[a]					
	6-311++G(2d, p)		6-311++G(3df, 2p)			
Radical	B3-PMP2	CCSD(T)[b]	B3-PMP2	CCSD(T)[b]		ΔG^{o}_{298}(aq)[c]
AR1	60	56	56	51	52[d]	36
AR2	33	31	33	31	33	29
AR3	63	65	58	58	61	34
AR4	95	86	95	84	87	73
AR5	71	64	71	63	67	58
AR6	88	79	90	82	81	–[e]
AR7	58	59	54	54	57	42
AR8	0	0	0	0	0	0

[a] Relative enthalpies in kJ mol^{-1} including B3LYP/6-31+G(d, p) zero-point vibrational energies and referring to 0 K. [b] Effective energies from basis set expansions: E[CCSD(T)/large basis set] = E[CCSD(T)/6-31G(d, p)] + E[PMP2/large basis set] − E[PMP2/6-31G(d, p)]. [c] Relative free energies in the polar dielectric (water) at 298 K. [d] Relative free energies in the gas phase at 298 K. [e] PCM calculation of the solvation free energy of radical **AR6** failed.

Table 7. Enthalpies and transition state energies for hydrogen atom additions to adenine

Position	$\Delta H_{0,\mathrm{add}}$(g)[a]	$\Delta G_{298,\mathrm{add}}$(g)[b]	$\Delta G_{298,\mathrm{add}}$(aq)[c]	E_{TS}[d]	log k_{298}[e]	log k'_{298}[f]	k'_{rel}[g]
$N_{(1)}$	−53	−30	−26	43.6	4.28	5.23	0.02
$C_{(2)}$	−73	−48	−32	37.9	5.55	6.00	0.10
$N_{(3)}$	−45	−21	−27	43.8	4.48	5.46	0.03
$C_{(4)}$	−19	6	11	57.1	2.00	2.86	0.00
$C_{(5)}$	−40	−15	−4	44.3	4.24	4.89	0.01
$C_{(6)}$	−26	−0.2	–	62.6	0.84	1.64	0.00
$N_{(7)}$	−49	−24	−20	45.5	3.93	4.91	0.01
$C_{(8)}$	−104	−82	−62	31.9	6.50	6.91	0.83

[a] Reaction enthalpies in the gas phase (0 K, kJ mol^{-1}) from effective CCSD(T)/6-311++G(3df, 2p) single-point energies and B3LYP/6-31+G(d, p) zero-point vibrational corrections. [b] Reaction free energies at 298 K in the gas phase. [c] Reaction free energies at 298 K in the water dielectric. [d] Transition state energies. [e] Rate constants at 298 K (log cm^3 mol^{-1} s^{-1}) without tunnel corrections. [f] Rate constants at 298 K (log cm^3 mol^{-1} s^{-1}) with tunnel corrections. [g] Reaction molar fractions with tunnel corrections.

sitions $C_{(8)}$ and $C_{(2)}$. Consequently, the 298 K rate constants are all $< 10^7$ mol^{-1} cm^3 s^{-1}. Position $C_{(8)}$ is calculated to involve 83% of H atom additions, with $C_{(2)}$, N(3), and $N_{(1)}$ amounting to 10, 3, and 2%, respectively [88].

4.4. Guanine

Wetmore, Boyd, and Eriksson used DFT methods to calculate the structures and hyperfine coupling constants of several putative products of radiolysis of guanine [89]. Guanine has the lowest ionization energy and redox potential of the nucleobases, and thus its radiolysis is presumed to form a significant fraction of cation-radicals, in addition to neutral intermediates formed by proton transfer. The calculations uncovered some significant discrepancies. In particular, the hyperfine coupling constants of guanine cation-radical and anion-radical did not match the assignments made in previous experimental EPR and ENDOR studies that were carried out in single crystals [90,91]. Gas-phase guanine does not have bound valence states for the extra electron, and the guanine anion radical undergoes substantial out-of-plane distortion of geometry which affects the coupling constants. However, the discrepancy did not disappear even when guanine anion-radical was artificially forced into a planar geometry to mimic its possible structure in the crystal. The discrepancy appears to have been resolved by assigning the experimental data to a neutral intermediate, a H-atom adduct to $O_{(6)}$, whose calculated coupling constants showed acceptable agreement with the experimental data form radiolysis. Interestingly, the latter isomer was calculated to be 82 kJ mol^{-1} less stable in the gas phase than the most stable H-atom adduct to $C_{(8)}$ in guanine. The relative stabilities of guanine radicals in aqueous solution have not been reported. It should be noted that the DFT calculated coupling constants for the H-atom adducts at $C_{(8)}$ and $C_{(5)}$ in guanine showed good agreement with previous experimental data and confirmed structure assignments based on those measurements.

Guanine cation-radical was calculated to retain a planar ring conformation similar to that in neutral guanine [89]. In spite of this feature, the calculated hyperfine coupling constants differed significantly from those assigned to a guanine cation radical in previous experimental studies [92]. Thus, the formation of a long-lived guanine cation-radical upon radiolysis remains controversial.

Schaefer *et al.* have reported DFT calculations of $(G - H)^{\bullet}$ radicals derived from guanine and their electron affinities using several hybrid functionals and a double-ζ basis set called DZP++ [93]. Abstraction from the guanine amino group ($N_{(10)}$) of the *syn*-hydrogen atom was found to be energetically most favorable to produce an $N_{(10)}$ aminyl radical (**GR1**, Fig. 8). The other $(G - H)^{\bullet}$ radicals reported by Schaefer *et al.*, e.g., those formed by abstraction of hydrogen atoms at $N_{(9)}$ (**GR2**), $N_{(1)}$ (**GR3**), *anti*-$N_{(10)}$ (**GR4**), and $C_{(8)}$ (**GR5**), were respectively 10, 17, 20, and 113 kJ mol^{-1} less stable than **GR1** [93].

4.5. Uracil

although uracil is an RNA nucleobase, it is linked to DNA through deamination of cytosine which is one of the most common reparable mutations. Uracil radicals have been studied in quite a detail by experiment and theory. In addition to the theoretical analysis of hyperfine coupling constants [61] relevant to radiolysis studies, $(U + H)^{\bullet}$ radicals have been generated in the gas phase by chemically specific methods and characterized by ab initio calculations [94–97].

Calculations of the relative energies of $(U + H)^{\bullet}$ radicals prefer the $C_{(5)}$–H adduct **UR1** as the most stable structure (Table 8, Fig. 9) [94]. The $C_{(6)}$–H adduct **UR2** is only slightly less stable than **UR1** and can be presumed to be present at thermal equilibrium in the gas

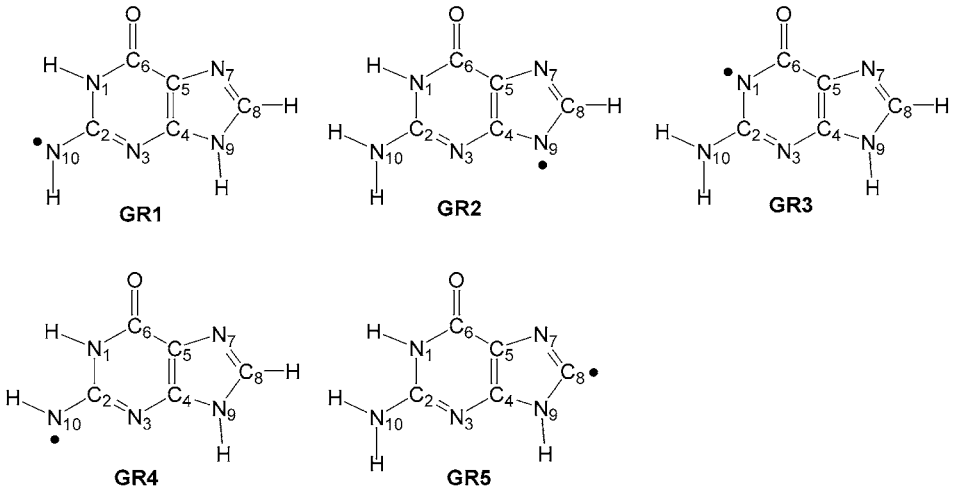

Fig. 8. Guanine $(G - H)^{\bullet}$ radicals **GR1**–**GR5**.

Table 8. Relative energies of uracil radicals

Method	Relative energy[a,b]					
	UR1	**UR2**	**UR3**	**UR4**	**UR5**	**UR6**
B3LYP/6-31+G(d, p)	0	8	41	107	41	64
B3LYP/6-311+G(3df, 2p)	0	9	34	105	42	65
PMP2/6-311+G(3df, 2p)	0	12	37	110	43	65
B3-PMP2/6-311+G(3df, 2p)[c]	0	11	35	107	42	65
QCISD(T)/6-311+G(3df, 2p)[d]	0	13	38	104	42	62
B3LYP/6-311G(2df, p)(wetmore)[e]	0	9	57	117	–	–

[a] At 0 K in units of kJ mol^{-1}. [b] From single-point energies on B3LYP/6-31+G(d, p) optimized geometries and ZPVE corrections. [c] From averaged B3LYP and PMP2 single-point energies. [d] From effective QCISD(T) energies (Ref. [94]). [e] From Ref. [61].

phase. In contrast, adducts to $O_{(4)}$ (**UR3**) and $O_{(2)}$ (**UR4**) are both substantially destabilized against **UR1** and can be expected to appear only as kinetic intermediates formed by specific chemical reactions, such as protonation of the uracil anion radical. Radicals **UR5** and **UR6**, that can be visualized as H atom adducts to the less stable uracil 2-enol tautomer, are destabilized against their respective 2-oxo-tautomers, **UR1** and **UR2**, and probably play no significant role in uracil radical chemistry.

It should be noted that the solvation free energies of $(U + H)^{\bullet}$ radicals have not been reported. With regard to the substantial effect solvation has on the related cytosine radicals (Table 4), it cannot be excluded that the ordering of relative energies might be altered in aqueous solution.

$(U + H)^{\bullet}$ radical **UR1** formally arises by hydrogen atom addition to $C_{(5)}$ or by protonation of uracil anion-radical. The calculated hyperfine coupling constants in **UR1** [61]

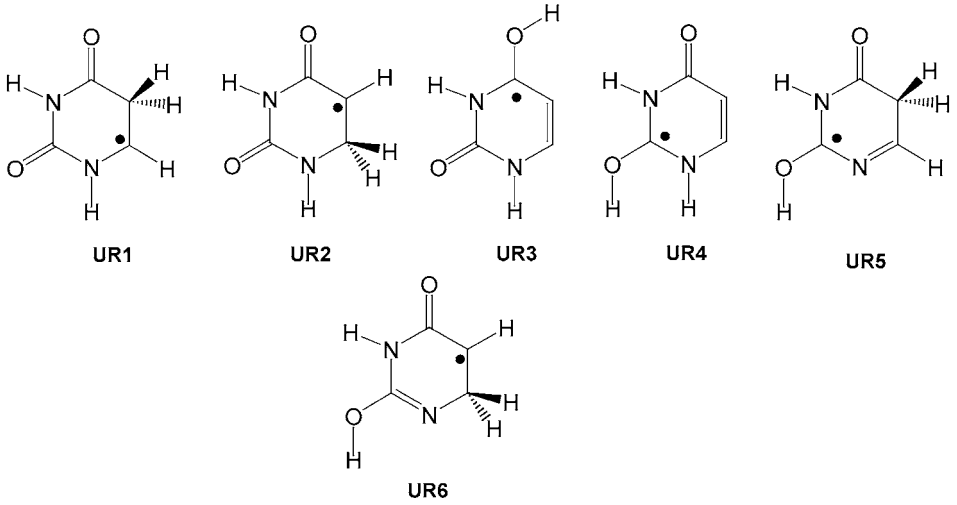

Fig. 9. Uracil $(U + H)^{\bullet}$ radicals **UR1–UR6**.

Table 9. Calculated kinetics of H atom additions to uracil

	Position			
	$C_{(5)}$	$C_{(6)}$	$O_{(2)}$	$O_{(4)}$
E_{TS}[a]				
B3-PMP2/6-311+G(2d, p)	16.8	22.5	52.0	38.0
B3-PMP2/6-311+G(2df, p)	17.0	22.8	52.2	37.9
B3-PMP2/6-311+G(3df, 2p)	15.7	21.8	51.0	36.8
QCISD(T)/6-311+G(3df, 2p)	19.0	27.1	63.5	45.4
E_{Arrh}[b]	19.8	27.7	64.1	46.2
log A[c]	12.98	12.96	12.98	13.08
log k_{298}[d]	9.52	8.11	1.74	4.98
% at 298 K[e]	96	4	0	0

[a] Transition state energies in kJ mol^{-1} for H atom additions from single-point energy calculations including B3LYP/6-31+G(d, p) zero-point energy corrections. [b] Arrhenius activation energies from effective QCISD(T)/6-311+G(3df, 2p) transition state energies. [c] Arrhenius pre-exponential factors. [d] Calculated rate constants at 298 K in log mol^{-1} cm^3 s^{-1}. [e] Fractions of H-atom additions at the indicated positions in uracil.

agree with the experimental data reported in previous radiolysis studies [98–100]. Calculations of the transition state energies for gas-phase H atom additions to uracil indicate a clear preference for addition at $C_{(5)}$ (Table 9), which is estimated to account for 96% of all adducts [94]. Thus, **UR1** is the kinetically and thermodynamically most stable $(U + H)^{\bullet}$ radical.

UR1 has also been generated by femtosecond electron transfer in the gas-phase and its dissociations were studied on the microsecond time scale. This study showed the power of

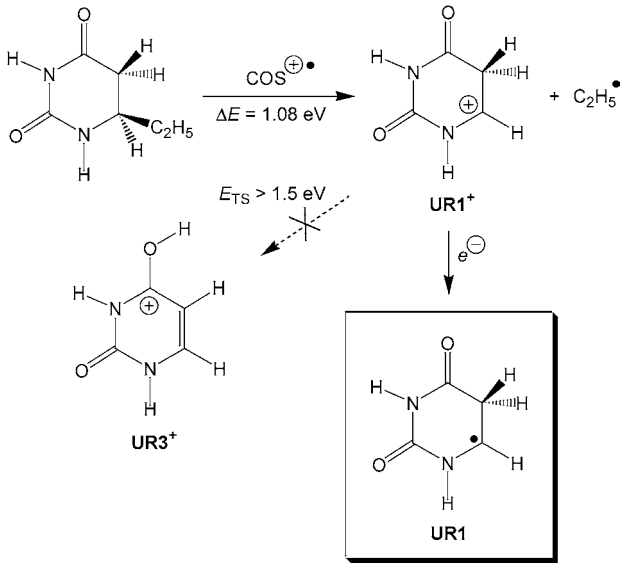

Scheme 3. Specific formation of the C_5-hydrogen atom adduct to uracil in the gas phase.

computational analysis not only in interpreting the complex chemistry of the radical dissociations, but also in planning the experiments to synthesize the radical in a chemically specific fashion in the gas phase (Scheme 3) [96]. A stable neutral precursor, 6-ethyl-5,6-dihydrouracil, was ionized by charge transfer with $COS^{+\bullet}$ to the corresponding cation-radical that dissociated specifically to produce a **UR1**$^+$ cation. The selection of the neutral molecule and the ionizing reagent was guided by ab initio calculations such as to provide sufficient energy in charge-exchange ionization to drive the dissociation which was calculated to require 10.1 eV. This was provided by $COS^{+\bullet}$ that has a 11.18 eV recombination energy. The energy excess in the dissociation (1.08 eV) is insufficient to drive an isomerization of cation **UR1**$^+$ to the much more stable ion **UR3**$^+$ that requires a 1.5 eV barrier. Reduction of **UR1**$^+$ by femtosecond electron transfer produced radical **UR1** that was characterized by neutralization–reionization mass spectrometry [96]. Radical **UR1** was found not to isomerize to **UR2**, in accordance with the calculated potential energy surface that showed that the transition state for isomerization was 35 kJ mol^{-1} above the transition state for the loss of $H_{(5)}$. Analysis of the reaction kinetics for the competitive dissociations of **UR1** using the Rice–Ramsperger–Kassel–Marcus theory and the ab initio potential energy surface indicated that rate constant for the isomerization was 10^2–10^5 smaller than that for the $H_{(5)}$ loss over a broad range of internal energies.

Detection of the less stable $O_{(4)}$ hydrogen atom adduct (**UR3**) by radiolysis of uracil appears to be uncertain. Zehner *et al.* reported hyperfine coupling constants that they assigned to **UR3** [100]. However, the experimental coupling constants differed from those calculated for **UR3** [61]. In contrast, the same computational data appear to fit the coupling constants for an unassigned radical species detected by Sagstuen *et al.* in their ENDOR study of uracil radiolysis [101].

Radical **UR3** has been unequivocally generated and characterized in the gas phase [95]. According to the computational analysis, $O_{(4)}$ is predicted to be the most basic center in

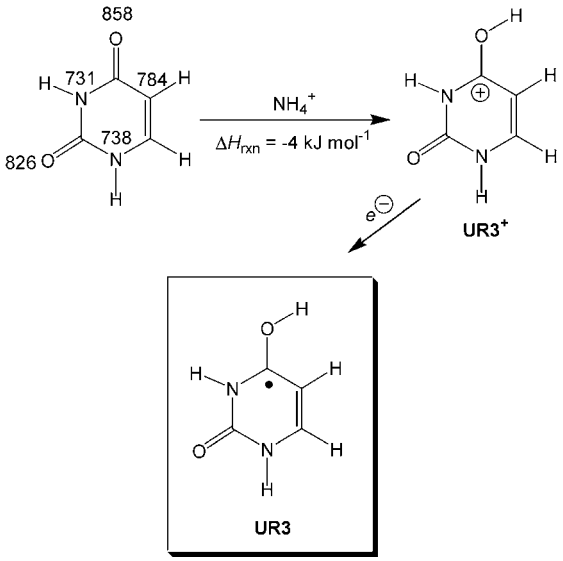

Scheme 4. Specific formation of the O_4-hydrogen atom adduct to uracil in the gas phase.

the gas-phase uracil. Accordingly, a gas-phase ion of a matching acidity (NH_4^+) was used to selectively protonate uracil at $O_{(4)}$ to produce a cation (**UR3**$^+$) that has the same bond connectivity as the target radical. Ion **UR3**$^+$ was then reduced to **UR3** by femtosecond electron transfer (Scheme 4). Loss of the newly introduced H atom from $O_{(4)}$ was calculated to be the lowest-energy dissociation of **UR3** in the gas phase, in line with the mass spectra of isotopically labeled radicals [95].

5. DEOXYRIBOSE AND RIBOSE RADICALS

In contrast to the wealth of spectroscopic data for nucleobase radicals, detection of carbohydrate radicals derived from DNA has been difficult, possibly due to multiple deoxyribose ring conformations that result in a broadening of EPR lines [102]. Carbohydrate radicals produced by H atom abstraction from 2-deoxyribose have been considered as important intermediates of strand scission in various modes of DNA damage [103,104]. Computational studies have been reported for radicals derived from 2-deoxyribofuranose and various models that incorporated small parts of the DNA structure. Since carbohydrates have sp^3 oxygen atoms, but no multiple C=C or C=O bonds, radical additions to carbohydrates are not possible and all radical products are thought to originate by nucleobase loss or H atom abstractions from 2-deoxyribose or ribose. It should be noted that H atom and alkyl radical additions to sp^3 oxygen atoms have been studied for simple alcohols and ethers and have been found to require large activation energies [105].

Miaskiewicz and Osman used Hartree–Fock calculations with the 6-31G basis set to obtain optimized geometries of radicals produced by H atom abstraction from 2,5-dideoxy-β-D-*ribo*-pentafuranosylamine (**S1**, Fig. 10) [106]. Ring conformations were optimized to correspond to the $C'_{(3)}$-*endo* (^{3}E) and $C'_{(2)}$-*endo* (^{2}E) conformations of the furanose ring

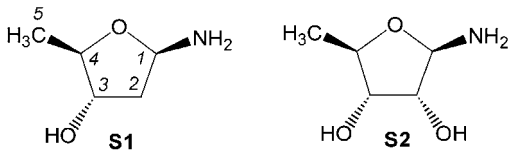

Fig. 10. Carbohydrate model molecules **S1** and **S2**.

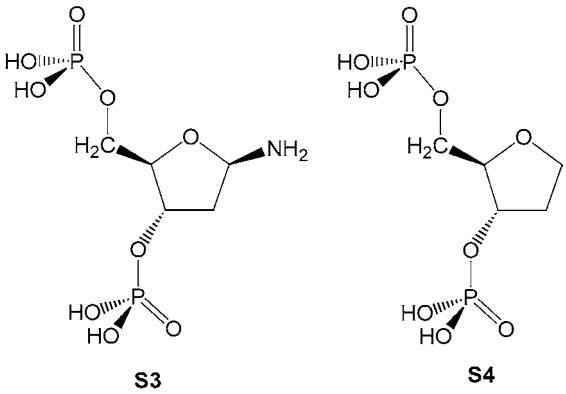

Fig. 11. Carbohydrate model molecules **S3** and **S4**.

in 2-deoxyribose. The authors noted that most of the structure parameters (bond lengths, angles, and dihedrals) calculated for **S1** were similar to those obtained from X-ray diffraction studies of nucleosides and nucleotides, thus validating their simple model. Radicals produced by H atom abstraction from $C_{(1)}$, $C_{(2)}$, $C_{(3)}$, and $C_{(4)}$ in **S1** showed a distinctive flattening of the furanose ring that was largest in the $C_{(2)}$ radical. Spin densities were also calculated and found to be mainly localized at the sp^2 carbon atoms (87–93%). Positions $C_{(1)}$, $C_{(3)}$, and $C_{(4)}$ showed 5–6% spin density delocalization to the adjacent oxygen atoms through three-electron interaction between the semioccupied carbon-based p-orbital and the oxygen lone-pairs. This caused slight pyramidization at the carbon radical center and alleviated the ring flattening. $C_{(2)}$ which has no adjacent oxygen atoms showed the highest spin density and most ring flattening.

Osman and coworkers also reported C–H bond dissociation energies (BDE) for the $C_{(2)}$, $C_{(3)}$, and $C_{(4)}$ positions in the deoxyribose model **S1** and the ribose model **S2** that were calculated from MP2/6-31G(d) single point energies [107]. **S1** and **S2** showed substantial differences in the BDE at carbon atoms having the same substitution pattern. For example, the $C_{(1)}$–H bond in **S1** was calculated to be stronger (BDE = 365 kJ mol^{-1}) than the same bond in **S2** (BDE = 342 kJ mol^{-1}). The secondary $C_{(2)}$–H bond was expectedly strongest in **S1** (BDE = 382 kJ mol^{-1}), and a substantial difference was also reported for the $C_{(4)}$–H bonds, e.g., BDE = 371 and 356 kJ mol^{-1} in **S1** and **S2**, respectively. These differences were not discussed in detail by Osman *et al.* although they noted the different ring conformations of **S1** and **S2** that may affect the BDE (*vide infra*).

Model furanose **S1** together with diphosphates **S3** and **S4** (Fig. 11) were addressed in a Hartree–Fock-level study (restricted open shell, 3-21G basis set) by Colson and

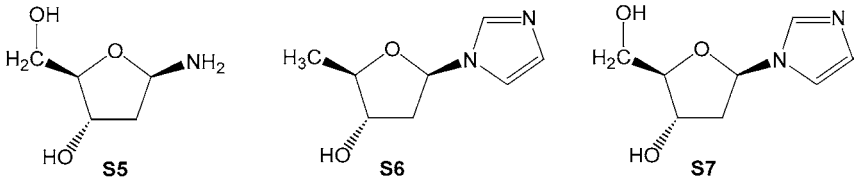

Fig. 12. Carbohydrate model molecules **S5**–**S7**.

Sevilla [108]. The BDE were reported relative to the $C_{(1)}$–H bond for each model and some profound differences were noted depending on phosphorylation at $C_{(3)}$ and the presence of other substituents on the furanose ring. The $C_{(3)}$–H bond dissociation energy was particularly sensitive to phosphorylation and showed 15–19 kJ mol^{-1} larger BDE in **S3** and **S4** than did the same bond in **S1**. The $C_{(4)}$–H bonds showed an opposite trend, but the differences were well within the expected accuracy of the HF calculations with a small basis set.

Another simple deoxyfuranose model (**S5**, Fig. 12) was used by Wetmore, Boyd, and Eriksson in a comprehensive B3LYP/6-311G(2df, p) study of radical structures, relative energies, and hyperfine coupling constants [109]. Radicals produced by H atom abstraction from $C_{(4)}$ showed a substantial ($\sim$ 14 kJ mol^{-1}) difference in stability depending on the ring conformation, while the conformer pairs of the $C_{(2)}$ and $C_{(3)}$ centered radicals were very close in energy. The oxygen-centered radicals derived from **S5** were found to be 42–54 kJ mol^{-1} less stable than the carbon-centered ones. The B3LYP relative energies of Wetmore *et al.* showed somewhat different ordering for the carbon-centered radicals than had the previous HF calculations; in particular, the $C_{(4)}$-centered radical was found to be the most stable one by B3LYP [109] as opposed to the $C_{(1)}$ radical from HF calculations [108]. The differences were ascribed to the neglect of electron correlation in the previous HF studies [109].

The adequacy of various nucleoside models in describing the conformers due to the furanose ring pseudorotation has been examined recently by Parr and Wetmore using B3LYP calculations with the 6-31G(d, p) basis set for optimization and the 6-311+G(2df, p) basis set for single-point energies [110]. These authors examined $C'_{(4)}$-radicals derived from model structures **S1**, **S5**, and the related 1′-imidazolyl derivatives **S6** and **S7** (Fig. 12). They concluded that replacing the amino group with the heterocyclic substituent resulted in significant changes in the shape of the pseudorotational potential energy surface. Model structure **S7** was found to be most representative of the conformational properties in nucleosides [110].

Radicals derived from 2-deoxyribofuranose (**S8**, Fig. 13) have been investigated in a recent comprehensive computational study that used the B3-PMP2 scheme and the 6-311++G(3df, 2p) basis set [57]. The gas-phase dissociation energies of all C–H and O–H bonds were calculated for the most stable 2-*exo* ring conformer of **S8** (Table 10). These showed very similar BDE for the $C_{(1)}$–H, $C_{(3)}$–H, $C_{(4)}$–H and $C_{(5)}$–H bonds that were in the 339–346 kJ mol^{-1} range in the gas phase. The $C_{(2)}$–H bond is notably stronger making the $C_{(2)}$ position less reactive to H atom abstraction. Interestingly, the BDE are affected to different extent by solvation in water, as calculated by employing the Polarizable Continuum Model [54]. The smallest effect of solvation was found for the $C_{(4)}$–H bond which is the weakest one in solvated **S8**. The BDE of the other bonds were found to be significantly

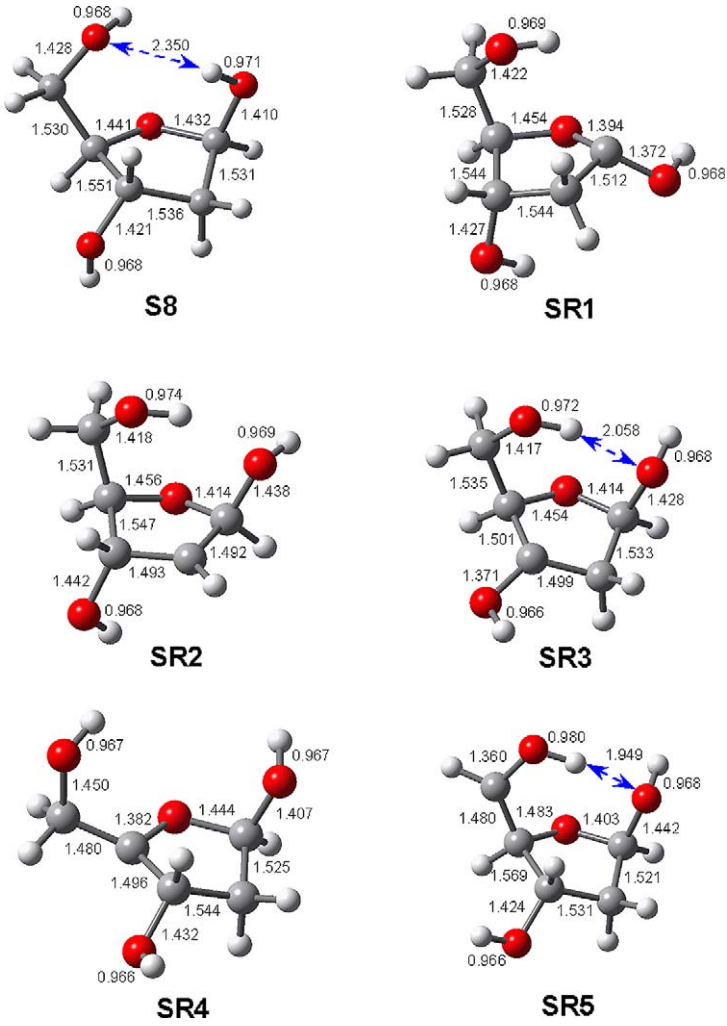

Fig. 13. B3LYP/6-31+G(d, p) optimized structures of 2-deoxyribose and its radicals. Description as in Fig. 5.

increased in water due to the less efficient solvation of the corresponding radicals when compared to **S8**. Solvent effects were also found to affect the relative stabilities ($\Delta G^{\circ}_{298,\mathrm{aq}}$) of radical conformers when compared with their analogues in the gas phase. For example, of the 2-*exo*-$C_{(4)}$-centered radicals, the 5-*endo*-OH conformer (**SR4**) is calculated to be 5 kJ mol^{-1} more stable than the 5-*exo*-OH conformer in the gas phase, presumably due to intramolecular H-bonding between the 5-OH and the ring oxygen atom in **SR4**. This order of stabilities is reversed in the water dielectric where the 5-*exo*-conformer is calculated to be 1 kJ mol^{-1} more stable [57].

The O–H bonds in **S8** were found to be substantially stronger than the C–H bonds and had BDE in the 429–435 kJ mol^{-1} range (Table 10). These are further increased by 27–

Table 10. Bond dissociation energies (kJ mol^{-1}) in 2-deoxyribofuranose $_2$E conformer **S8**[a]

	B3LYP	B3-PMP2			
Bond	6-31+G(d, p)	6-311+G(2df, p)	6-311++G(3df, 2p)	$\Delta G_{diss,g}$[b]	$\Delta G_{diss,aq}$[c]
$C_{(1)}$–H	387	382	384	346	362
$C_{(2)}$–H	399	395	397	364	383
$C_{(3)}$–H	378	392	378	343	366
$C_{(4)}$–H	378	376	379	340	349
$C_{(5)}$–H	375	370	372	339	360
$O_{(1)}$–H	414	425	429	396	423
$O_{(3)}$–H	417	429	433	400	429
$O_{(5)}$–H	415	432	435	404	440

[a] Including B3LYP/6-31+G(d, p) zero-point vibrational energies and 298 K enthalpies and referring to 298 K. [b] Free energies for bond dissociations in the gas phase at 298 K. [c] Free energies for bond dissociations in water at 298 K.

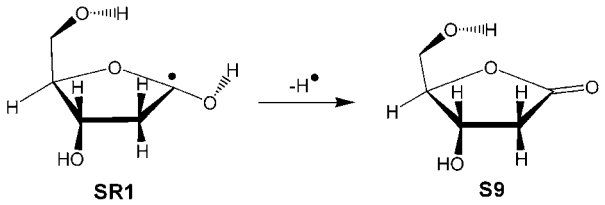

Scheme 5. Dissociation of 2-deoxyribose-1-yl radical.

36 kJ mol^{-1} in water due to the poorer solvation of the O-centered radicals relative to 2-deoxyribose [57].

Dissociation energies have also been evaluated for gas-phase carbon and oxygen-centered radicals derived from 2-deoxyribose [57]. The $C_{(1)}$-centered radical (**SR1**) is predicted to undergo a facile loss of the hydrogen atom from the glycosidic hydroxyl, which is only 37 kJ mol^{-1} endothermic forming 2-deoxyribonolactone (**S9**, Scheme 5). Ring cleavage by $C_{(4)}$–O bond dissociation in **SR1** was also considered that was analogous to the dominant dissociation of another simple carbohydrate model, 2-hydroxyoxolan-2-yl radical [111]. The lowest energy dissociation of the $C_{(3)}$-centered radical (**SR3**) was by cleavage of the adjacent $C_{(4)}$–$C_{(5)}$ bond and loss of CH_2OH that required 102 kJ mol^{-1} (Scheme 6). Note that an analogous dissociation in a DNA radical intermediate would result in a strand break. Cleavage of the $C_{(1)}$–$C_{(2)}$ bond, triggered by a $C_{(3)}$-radical, was found to be an important dissociation pathway in a model 3-hydroxyoxolan-3-yl radical [112].

The oxygen-centered radicals showed very low dissociation energies for cleavages of bonds adjacent to the radical center. For example, the $O_{(3)}$-centered radical was calculated to undergo facile ring opening by cleavage of the $C_{(3)}$–$C_{(4)}$ bond that required only 22 kJ mol^{-1} in the transition state and was overall thermoneutral when forming an open-ring intermediate [57].

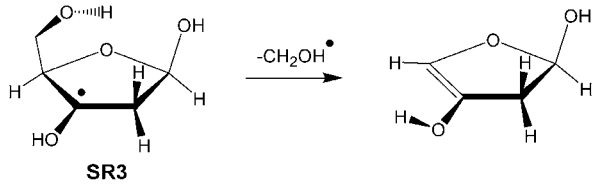

Scheme 6. Dissociation of 2-deoxyribose-3-yl radical.

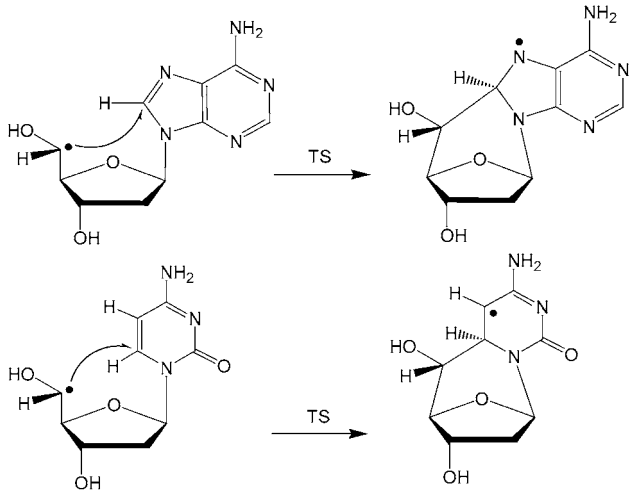

Scheme 7. Intramolecular cyclization in adenosine and cytidine 5′-yl radicals.

Zhang and Eriksson have recently reported a study of intramolecular cyclizations by attack of a deoxyribose $C'_{(5)}$-radical on $C_{(8)}$ in purine and on $C_{(6)}$ in pyrimidine nucleosides [113]. The additions were found to be 24–50 kJ mol^{-1} exoergonic when calculated with B3LYP/6-311++G(d, p) and including solvent effects by using a Polarizable Continuum Model. Interestingly, the activation energies for cyclizations producing 8,5′-*cyclo*-A, 8,5′-*cyclo*-G, 6,5′-*cyclo*-C, and 6,5′-*cyclo*-T radicals were very similar, ranging between 36–39 kJ mol^{-1} (Scheme 7).

6. CONCLUSIONS AND OUTLOOK

This review amply documents the substantial progress that has been made in computational investigations of structures, spin densities, relative stabilities, bond dissociation, and transition state energies of simple molecular systems that model radical intermediates and their reactions pertinent to DNA and RNA damage. The studies of polyatomic, yet relatively simple, model systems have revealed interesting molecular properties and chemistry that have been related to experimental results and provided valuable reference data that often have stimulated and guided new experiments. The main challenge for computational studies to be carried out in the future is to deal with radical intermediates in larger systems,

starting with nucleosides, nucleotides, and base pairs, to elucidate *intermolecular interactions* between a local damage in a nucleobase or carbohydrate moiety and the rest of the DNA segment, and also with the surrounding molecules of solvent, antioxidants, peptides, and proteins Effects on spin densities of DNA conformation and base-pairing will be of interest to aid interpretation of the often complex EPR spectra from radiolysis experiments. Accurate transition state energies for DNA radical dissociations, intra- and intermolecular hydrogen transfer, and other reactions will possibly provide reliable rate constants that will allow branching ratios to be analyzed and predicted. Including solvent effects, both through microsolvation with a limited number of solvent molecules and by using refined dielectric continuum models, will provide further insight into the DNA radical reactivity in a real-world environment. Finally, studying the reaction dynamics of fast processes, such as electron transfer, appears a challenging yet worthy goal for future computational studies of DNA damage.

ACKNOWLEDGEMENTS

Financial support of this research has been provided by the National Science Foundation (Grants CHE-0349595 for experiments and CHE-0342956 for computations). Thanks are due to Jill K. Wolken, Shetty Vivekananda, Erik A. Syrstad, Pascal Gerbaux, Minh Tho Nguyen, Xiaohong Chen, and Chunxiang Yao for their substantial contributions to the research done in the author's laboratory.

REFERENCES

[1] C. Von Sonntag, The chemistry of free-radical-mediated DNA damage, in: W.A. Glass, M.N. Varma (Eds.), *Physical and Chemical Mechanisms in Molecular Radiation Biology*, Plenum, New York, 1991, pp. 287–317.

[2] P. O'Neill, E.F. Fileden, Primary free radical processes in DNA, in: J.T. Lett, W.K. Sinclair (Eds.), *Advances in Radiation Biology*, Academic Press, San Diego, 1993, pp. 53–120.

[3] S. Steenken, Purine bases, nucleosides, and nucleotides: Aqueous solution redox chemistry and transformation reactions of their radical cations and e^- and OH adducts, *Chem. Rev.* **89** (1989) 503–520.

[4] L. Sanche, Nanoscopic aspects of radiobiological damage: Fragmentation induced by secondary low-energy electrons, *Mass Spectrom. Rev.* **21** (2002) 349–369.

[5] A.O. Colson, M.D. Sevilla, Elucidation of primary radiation damage in DNA through application of ab initio molecular orbital theory, *Int. J. Radiat. Biol.* **67** (1995) 627–645.

[6] A.O. Colson, M.D. Sevilla, Application of molecular orbital theory to the elucidation of radical processes induced by radiation damage to DNA, *Theor. Comput. Chem.* **8** (1999) 245–277.

[7] W. Kohn, A.D. Becke, R.G. Parr, Density functional theory of electronic structure, *J. Phys. Chem.* **100** (1996) 12974–12980.

[8] A.D. Becke, A new mixing of Hartree–Fock and local density-functional theories, *J. Chem. Phys.* **98** (1993) 1372–1377.

[9] A.D. Becke, Density-functional thermochemistry. III. The role of exact exchange, *J. Chem. Phys.* **98** (1993) 5648–5652.

[10] P.J. Stephens, F.J. Devlin, C.F. Chabalowski, M.J. Frisch, Ab initio calculation of vibrational absorption and circular dichroism spectra using density functional force fields, *J. Phys. Chem.* **98** (1994) 11623–11627.

[11] O. Gunnarsson, B.I. Lundquist, Exchange and correlation in atoms, molecules, and solids by the spin-density functional formalism, *Phys. Rev. B* **13** (1976) 4274–4298.

[12] C. Lee, W. Yang, R.G. Parr, Development of the Colle–Salvetti correlation-energy formula into a functional of the electron density, *Phys. Rev. B* **37** (1988) 785–789.

[13] L.A. Curtiss, C. Jones, G.W. Trucks, K. Raghavachari, J.A. Pople, Gaussian-1 theory of molecular energies for second-row compounds, *J. Chem. Phys.* **93** (1990) 2537–2545.
[14] K. Raghavachari, J.B. Anderson, Electron correlation effects in molecules, *J. Phys. Chem.* **100** (1996) 12960–12973.
[15] A.P. Scott, L. Radom, Harmonic Vibrational frequencies: An evaluation of Hartree–Fock, Møller–Plesset, quadratic configuration interaction, density functional theory, and semiempirical scale factors, *J. Phys. Chem.* **100** (1996) 16502–16513.
[16] C.J. Parkinson, P.M. Mayer, L. Radom, An assessment of theoretical procedures for the calculation of reliable radical stabilization energies, *J. Chem. Soc., Perkin Trans.* **2** (1999) 2305–2313.
[17] B. Engels, L.A. Eriksson, S. Lunell, Recent developments in configuration interaction and density functional theory calculations of radical hyperfine structure, *Adv. Quantum Chem.* **27** (1997) 297–369.
[18] R. Improta, V. Barone, Interplay of electronic, environmental, and vibrational effects in determining the hyperfine coupling constants of organic free radicals, *Chem. Rev.* **104** (2004) 1231–1253.
[19] F. Tureček, Modeling nucleobase radicals in the mass spectrometer, *J. Mass Spectrom.* **33** (1998) 779–795.
[20] M.T. Nguyen, S. Creve, L.G. Vanquickenborne, Difficulties of density functional theory in investigating addition reactions of the hydrogen atom, *J. Phys. Chem.* **100** (1996) 18422–18425.
[21] B.J. Lynch, P.L. Fast, M. Harris, D.G. Truhlar, Adiabatic connection for kinetics, *J. Phys. Chem. A* **104** (2000) 4811–4815.
[22] C. Adamo, V. Barone, Exchange functionals with improved long-range behavior and adiabatic connection methods without adjustable parameters: the mPW and mPW1PW models, *J. Chem. Phys.* **108** (1998) 664–675.
[23] F. Tureček, Proton affinity of dimethyl sulfoxide and relative stabilities of C_2H_6OS molecules and $C_2H_7OS^+$ ions. A Comparative G2(MP2) ab initio and density functional theory study, *J. Phys. Chem. A* **102** (1998) 4703–4713.
[24] V.A. Rassolov, M.A. Ratner, J.A. Pople, Electron correlation in chemical bonds, *J. Chem. Phys.* **112** (2000) 4014–4019.
[25] H.B. Schlegel, Potential energy curves using unrestricted Møller–Plesset perturbation theory with spin annihilation, *J. Chem. Phys.* **84** (1986) 4530–4534.
[26] J.K. Wolken, F. Tureček, Modeling nucleobase radicals in the gas phase. Experimental and computational study of 2-hydroxypyridinium and 2(1H)-pyridone radicals, *J. Phys. Chem. A* **103** (1999) 6268–6281.
[27] J.K. Wolken, F. Tureček, Heterocyclic radicals in the gas phase. An experimental and computational study of 3-hydroxypyridinium radicals and cations, *J. Am. Chem. Soc.* **121** (1999) 6010–6018.
[28] F. Tureček, J.K. Wolken, Dissociation energies and kinetics of aminopyrimidinium radicals by ab initio and density functional theory, *J. Phys. Chem. A* **103** (1999) 1905–1912.
[29] M. Polášek, F. Tureček, Hydrogen atom adducts to nitrobenzene. Formation of the phenylnitronic radical in the gas phase and energetics of wheland intermediates, *J. Am. Chem. Soc.* **122** (2000) 9511–9524.
[30] H. Čížek, J. Paldus, L. Šroubková, Cluster expansion analysis for delocalized systems, *Int. J. Quantum Chem.* **3** (1969) 149–167.
[31] G.D. Purvis, R.J. Bartlett, A full Coupled-cluster singles and doubles model. The inclusion of disconnected triples, *J. Chem. Phys.* **76** (1982) 1910–1918.
[32] X. Chen, E.A. Syrstad, F. Tureček, Direct observation of the forbidden hydrogen atom adduct to acetonitrile. A neutralization-reionization mass spectrometric and CCSD(T) ab initio/RRKM study, *J. Phys. Chem. A* **108** (2004) 4163–4173.
[33] D. Hegarty, M.A. Robb, Application of unitary group methods for configuration interaction calculations, *Mol. Phys.* **38** (1979) 1795–1812.
[34] M. Frisch, I.N. Ragazos, M.A. Robb, H.B. Schlegel, An evaluation of three direct MC-SCF procedures, *Chem. Phys. Lett.* **189** (1992) 524–528.
[35] X. Chen, E.A. Syrstad, P. Gerbaux, M.T. Nguyen, F. Tureček, Distonic isomers and tautomers of adenine cation radical in the gas phase and aqueous solution, *J. Phys. Chem. A* **108** (2004) 9283–9293.
[36] X. Li, L. Sanche, M.D. Sevilla, Low energy electron interactions with uracil: The energetics predicted by theory, *J. Phys. Chem. B* **108** (2004) 5472–5476.
[37] X. Li, Z. Cai, M.D. Sevilla, Investigation of proton transfer within DNA base pair anion and cation radicals by density functional theory, *J. Phys. Chem. B* **105** (2001) 10115–10123.
[38] D. Svozil, P. Jungwirth, Z. Havlas, Electron binding to nucleic acid bases. Experimental and theoretical studies. A review, *Collect. Czech. Chem. Commun.* **69** (2004) 1395–1428.
[39] R. Improta, G. Scalmani, V. Barone, Radical cations of DNA bases: Some insights on structure and fragmentation patterns by density functional methods, *Int. J. Mass Spectrom.* **201** (2000) 321–336.

[40] C. Adamo, V. Barone, Toward reliable adiabatic connection models free from adjustable parameters, *Chem. Phys. Lett.* **274** (1997) 242–250.
[41] L.A. Chewter, K. Mueller-Dethlefs, E.W. Schlag, Determination of the ionization energy of the benzene–argon complex by zero kinetic energy photoelectron spectroscopy, *Chem. Phys. Lett.* **135** (1987) 219–222.
[42] M.C.R. Cockett, Photoelectron spectroscopy without photoelectrons: Twenty years of ZEKE spectroscopy, *Chem. Soc. Rev.* **34** (2005) 935–948.
[43] M.D. Sevilla, B. Besler, A.-O. Colson, Ab initio molecular orbital calculations of DNA radical ions. 5. Scaling of calculated electron affinities and ionization potentials to experimental values, *J. Phys. Chem.* **99** (1995) 1060–1063.
[44] S.D. Wetmore, R.J. Boyd, L.A. Eriksson, Electron affinities and ionization potentials of nucleotide bases, *Chem. Phys. Lett.* **322** (2000) 129–135.
[45] R. Kobayashi, A CCSD(T) study of the relative stabilities of cytosine tautomers, *J. Phys. Chem. A* **102** (1998) 10813–10817.
[46] F. Tureček, unpublished results.
[47] V.M. Orlov, A.N. Smirnov, Ya.M. Varshavsky, Ionization potentials and electron-donor ability of nucleic acid bases and their analogues, *Tetrahedron Lett.* **1976** (1998) 4377–4378.
[48] N.S. Hush, A.S. Cheung, Ionization potentials and donor properties of nucleic acid bases and related compounds, *Chem. Phys. Lett.* **34** (1975) 11–13.
[49] J. Lin, C. Yu, S. Peng, I. Akiyama, K. Li, L.K. Lee, P.R. LeBreton, Ultraviolet photoelectron studies of the ground-state electronic structure and gas-phase tautomerism of purine and adenine, *J. Am. Chem. Soc.* **102** (1980) 4627–4631.
[50] F. Tureček, J.K. Wolken, Energetics of uracil cation-radical and anion-radical ion-molecule reactions in the gas phase, *J. Phys. Chem. A* **105** (2001) 8740–8747.
[51] C. Yu, T.J. O'Donnell, P.R. LeBreton, Ultraviolet photoelectron studies of volatile nucleoside models. Vertical ionization potential measurements of methylated uridine, thymidine, cytidine, and adenosine, *J. Phys. Chem.* **85** (1981) 3851–3855.
[52] D. Dougherty, K. Wittel, J. Meeks, S.P. McGlynn, Photoelectron spectroscopy of carbonyls. Ureas, uracils, and thymine, *J. Am. Chem. Soc.* **98** (1976) 3815–3820.
[53] V. Barone, M. Cossi, J. Tomasi, A new definition of cavities for the computation of solvation free energies by the polarizable continuum model, *J. Chem. Phys.* **107** (1997) 3210–3221.
[54] M. Cossi, G. Scalmani, N. Rega, V. Barone, New developments in the polarizable continuum model for quantum mechanical and classical calculations on molecules in solution, *J. Chem. Phys.* **117** (2002) 43–54.
[55] J. Tomasi, Quantum mechanical continuum models, *Chem. Rev.* **105** (2005) 2999–3093.
[56] M.J. Frisch, G.W. Trucks, H.B. Schlegel, G.E. Scuseria, M.A. Robb, J.R. Cheeseman, J.A. Montgomery Jr., T. Vreven, K.N. Kudin, J.C. Burant, J.M. Millam, S.S. Iyengar, J. Tomasi, V. Barone, B. Mennucci, M. Cossi, G. Scalmani, N. Rega, G.A. Petersson, H. Nakatsuji, M. Hada, M. Ehara, K. Toyota, R. Fukuda, J. Hasegawa, M. Ishida, T. Nakajima, Y. Honda, O. Kitao, H. Nakai, M. Klene, X. Li, J.E. Knox, H.P. Hratchian, J.B. Cross, C. Adamo, J. Jaramillo, R. Gomperts, R.E. Stratmann, O. Yazyev, A.J. Austin, R. Cammi, C. Pomelli, J.W. Ochterski, P.Y. Ayala, K. Morokuma, G.A. Voth, P. Salvador, J.J. Dannenberg, V.G. Zakrzewski, S. Dapprich, A.D. Daniels, M.C. Strain, O. Farkas, D.K. Malick, A.D. Rabuck, K. Raghavachari, J.B. Foresman, J.V. Ortiz, Q. Cui, A.G. Baboul, S. Clifford, J. Cioslowski, B.B. Stefanov, G. Liu, A. Liashenko, P. Piskorz, I. Komaromi, R.L. Martin, D.J. Fox, T. Keith, M.A. Al-Laham, C.Y. Peng, A. Nanayakkara, M. Challacombe, P.M.W. Gill, B. Johnson, W. Chen, M.W. Wong, C. Gonzalez, J.A. Pople, *Gaussian 03, Revision B.05*, Gaussian, Inc., Pittsburgh, PA, 2003.
[57] L.A. Vannier, C. Yao, F. Tureček, 2-deoxyribose radicals in the gas phase and aqueous solution. Transient intermediates of hydrogen atom abstraction from 2-deoxyribofuranose, *Collect. Czech. Chem. Commun.* **70** (2005) 1769–1786.
[58] J. Llano, L.A. Eriksson, First principles electrochemistry: Electrons and protons reacting as independent ions, *J. Chem. Phys.* **117** (2002) 10193–10206.
[59] J. Llano, L.A. Eriksson, First principles electrochemical study of redox events in DNA bases and chemical repair in aqueous solution, *Phys. Chem. Chem. Phys.* **6** (2004) 2426–2433.
[60] J. Llano, L.A. Eriksson, Oxidation pathways of adenine and guanine in aqueous solution from first principles electrochemistry, *Phys. Chem. Chem. Phys.* **6** (2004) 4707–4713.
[61] S.D. Wetmore, R.J. Boyd, L.A. Eriksson, Radiation products of thymine, 1-methylthymine, and uracil investigated by density functional theory, *J. Phys. Chem. B* **102** (1998) 5369–5377.
[62] L.A. Eriksson, Evaluation of the performance of non-local and hybrid density functional theory methods for π-radical hyperfine structures, *Mol. Phys.* **91** (1997) 827–833.

[63] E. Sagstuen, E.O. Hole, W.H. Nelson, D.M. Close, Radiation-induced free-radical formation in thymine derivatives: EPR/ENDOR of anhydrous thymine single crystals *x*-irradiated at 10 K, *J. Phys. Chem.* **96** (1992) 1121–1126.
[64] W.A. Bernhard, A.Z. Patrzalek, ESR characteristics of one-electron reduced thymine in monomer, oligomer, and polymer derivatives, *Radiat. Res.* **117** (1989) 379–394.
[65] E. Westhof, W. Flossmann, A. Mueller, Temperature-dependent long-range proton hyperfine coupling in pyrimidine hydrogen-addition radicals trapped in single crystals, *Mol. Phys.* **33** (1977) 1447–1455.
[66] E. Westhof, W. Flossmann, H. Zehner, A. Mueller, Formation of hydrogen-addition radicals in some pyrimidine and purine derivatives, *Faraday Discuss. Chem. Soc.* **63** (1977) 248–254.
[67] S.D. Wetmore, F. Himo, R.J. Boyd, L.A. Eriksson, Effects of ionizing radiation on crystalline cytosine monohydrate, *J. Phys. Chem. B* **102** (1998) 7484–7491.
[68] E. Sagstuen, E.O. Hole, W.H. Nelson, D.M. Close, Protonation state of radiation-produced cytosine anions and cations in the solid state: EPR/ENDOR of cytosine monohydrate single crystals *x*-irradiated at 10 K, *J. Phys. Chem.* **96** (1992) 8269–8276.
[69] D.M. Close, E. Sagstuen, E.O. Hole, W.H. Nelson, Comment on: "Effects of ionizing radiation on crystalline cytosine monohydrate", *J. Phys. Chem. B* **103** (1999) 3049–3050.
[70] S.D. Wetmore, R.J. Boyd, F. Himo, L.A. Eriksson, Reply to: "Comment on: Effects of ionizing radiation on crystalline cytosine monohydrate", *J. Phys. Chem. B* **103** (1999) 3051–3052.
[71] D.M. Close, L.A. Eriksson, E.O. Hole, E. Sagstuen, W.H. Nelson, Experimental and theoretical investigation of the mechanism of radiation-induced radical formation in hydrogen-bonded cocrystals of 1-methylcytosine and 5-fluorouracil, *J. Phys. Chem. B* **104** (2000) 9343–9350.
[72] C. Adamo, M. Heitzmann, F. Meilleur, N. Rega, G. Scalmani, A. Grand, J. Cadet, V. Barone, Interplay of intrinsic and environmental effects on the magnetic properties of free radicals issuing from H-atom addition to cytosine, *J. Am. Chem. Soc.* **123** (2001) 7113–7117.
[73] F. Tureček, C. Yao, Hydrogen atom addition to cytosine, 1-methylcytosine, and cytosine-water complexes. A computational study of a mechanistic dichotomy, *J. Phys. Chem. A* **107** (2003) 9221–9231.
[74] D.E. Holmes, R.B. Ingalls, L.S. Myers Jr., E.S.R. spectra of free radicals induced in nucleic acid purine and pyrimidine bases and selected analogues by exposure to hydrogen atoms, *Int. J. Radiat. Biol.* **13** (1967) 225–234.
[75] E. Westhof, J. Huttermann, E.S.R. of irradiated single crystals of cytosine, *Int. J. Radiat. Biol.* **24** (1973) 627–630.
[76] E. Westhof, Formation of H adduct radicals in cytosine and its derivatives, *Int. J. Radiat. Biol.* **23** (1973) 389–400.
[77] E. Westhof, W. Flossmann, A. Muller, Radical formation in salts of pyrimidines. II. Cytosine. HCl crystals, *Int. J. Radiat. Biol.* **28** (1975) 427–438.
[78] W. Flossmann, E. Westhof, A. Muller, Radical formation in salts of pyrimidines. II. Cytosine. H_2O crystals, *Int. J. Radiat. Biol.* **30** (1976) 301–315.
[79] W. Flossmann, E. Westhof, A. Muller, Light-induced displacement of hydrogen in pyrimidine H-addition radicals, *J. Chem. Phys.* **64** (1976) 1688–1691.
[80] W. Berhnard, R.A. Farley, ESR of hydrogen addition radicals in single crystals of 1-methylcytosine and 1-methyluracil, *Radiat. Res.* **66** (1976) 189–198.
[81] A. Schaefer, J. Huttermann, G. Kraft, Free radicals from polycrystalline pyrimidines and purines upon heavy ion bombardment at low temperatures: an electron spin resonance study. Radical formation in salts of pyrimidines. II. Cytosine. HCl crystals, *Int. J. Radiat. Biol.* **63** (1993) 139–149.
[82] E.O. Hole, W.H. Nelson, E. Sagstuen, D.M. Close, Electron paramagnetic resonance and electron nuclear double resonance studies of X-irradiated crystals of cytosine hydrochloride. Part I: Free radical formation at 10 K after high radiation doses, *Radiat. Res.* **149** (1998) 109–119.
[83] I.D. Podmore, M.E. Malone, M.C.R. Symons, P.M. Cullis, Factor controlling the site of protonation of the one-electron adduct of cytosine and its derivatives, *J. Chem. Soc., Faraday Trans.* **87** (1991) 3647–3652.
[84] F. Tureček, J.K. Wolken, Dissociation energies and kinetics of aminopyrimidinium radicals by ab initio and density functional theory, *J. Phys. Chem. A* **103** (1999) 1905–1912.
[85] C. Yao, M.L. Cuadrado-Peinado, M. Polášek, F. Tureček, Specific generation of 1-methylcytosine radicals in the gas phase, *Angew. Chem. Int. Ed. Engl.* **44** (2005) 6708–6711.
[86] S.D. Wetmore, R.J. Boyd, L.A. Eriksson, Theoretical investigation of adenine radicals generated in irradiated DNA components, *J. Phys. Chem. B* **102** (1998) 10602–10614.
[87] J. Reynisson, S. Steenken, One-eletron reduction of 2-aminopurine in the aqueous phase. A DFT and pulse radiolysis study, *Phys. Chem. Chem. Phys.* **7** (2005) 659–665.

[88] X. Chen, E.A. Syrstad, M.T. Nguyen, P. Gerbaux, F. Tureček, Adenine radicals in the gas phase: An experimental and computational study of hydrogen atom adducts to adenine, *J. Phys. Chem. A* **109** (2005) 8121–8132.

[89] S.D. Wetmore, R.J. Boyd, L.A. Eriksson, Comparison of experimental and calculated hyperfine coupling constants. Which radicals are formed in irradiated guanine? *J. Phys. Chem. B* **102** (1998) 9332–9343.

[90] E.O. Hole, E. Sagstuen, W.H. Nelson, D.M. Close, Environmental effects on primary radical formation in guanine: Solid-state ESR and ENDOR of guanine hydrobromide monohydrate, *Radiat. Res.* **125** (1991) 119–128.

[91] E.O. Hole, W.H. Nelson, E. Sagstuen, D.M. Close, Free radical formation in single crystals of 2′-deoxyguanosine 5′-monophosphate tetrahydrate disodium salt: An EPR/ENDOR study, *Radiat. Res.* **129** (1992) 119–138.

[92] D.M. Close, E. Sagstuen, W.H. Nelson, ESR study of the guanine cation, *J. Chem. Phys.* **82** (1985) 4386–4388.

[93] Q. Luo, S.Q. Li, Y. Xie, H.F. Schaefer, Radicals derived from guanine: Structures and energies, *Collect. Czech. Chem. Commun.* **70** (2005) 826–836.

[94] J.K. Wolken, E.A. Syrstad, S. Vivekananda, F. Tureček, Uracil radicals in the gas phase. Specific generation and energetics, *J. Am. Chem. Soc.* **123** (2001) 5804–5805.

[95] J.K. Wolken, F. Tureček, Direct observation of a hydrogen atom adduct to O-4 in uracil. Energetics and kinetics of uracil radicals, *J. Phys. Chem. A* **105** (2001) 8352–8360.

[96] E.A. Syrstad, S. Vivekananda, F. Tureček, Direct observation of a hydrogen atom adduct to C-5 in uracil. A neutralization-reionization mass spectrometric and ab initio study, *J. Phys. Chem. A* **105** (2001) 8339–8351.

[97] F. Tureček, J.K. Wolken, Energetics of uracil cation radical and anion radical ion-molecule reactions in the gas phase, *J. Phys. Chem. A* **105** (2001) 8740–8747.

[98] H.M. Novais, S. Steenken, Reactions of oxidizing radicals with 4,6-dihydroxypyrimidines as model compounds for uracil, thymine, and cytosine, *J. Phys. Chem.* **91** (1987) 426–433.

[99] J.N. Herak, C.A. McDowell, ENDOR study of long range spin interactions in molecular crystals. I. 1-Methyl uracil, *J. Chem. Phys.* **61** (1974) 1129–1135.

[100] H. Zehner, W. Flossmann, E. Westhoff, A. Müller, Electron spin resonance of irradiated single crystals of uracil, *Mol. Phys.* **32** (1976) 869–878.

[101] E. Sagstuen, E.O. Hole, W.H. Nelson, D.M. Close, Radiation damage to DNA base pairs. II. Paramagnetic resonance studies of 1-methyluracil$^{\bullet}$ 9-ethyladenine complex crystals x-irradiated at 10 K, *Radiat. Res.* **149** (1998) 120–127.

[102] D.M. Close, Where are the sugar radicals in irradiated DNA? *Radiat. Res.* **147** (1977) 663–673.

[103] W. Knapp-Pogozelski, T.D. Tullius, Oxidative strand scission of nucleic acids: Routes initiated by hydrogen abstraction from the sugar moiety, *Chem. Rev.* **98** (1998) 1089–1107.

[104] C.J. Burrows, J.G. Muller, Oxidative nucleobase modifications leading to a strand scission, *Chem. Rev.* **98** (1998) 1109–1151.

[105] F. Tureček, P.J. Reid, Metastable states of dimethyloxonium, $(CH_3)_2OH^{\bullet}$, *Int. J. Mass Spectrom.* **222** (2003) 49–61.

[106] K. Miaskiewicz, R. Osman, Theoretical study of the deoxyribose radicals formed by hydrogen abstraction, *J. Am. Chem. Soc.* **116** (1994) 232–238.

[107] N. Luo, A. Litvin, R. Osman, Theoretical studies of ribose and its radicals produced by hydrogen abstraction from ring carbons, *J. Phys. Chem. A* **103** (1999) 592–600.

[108] A.-O. Colson, M.D. Sevilla, Structure and relative stability of deoxyribose radicals in a model DNA backbone: Ab initio molecular orbital calculations, *J. Phys. Chem.* **99** (1995) 3867–3874.

[109] S.D. Wetmore, R.J. Boyd, L.A. Eriksson, A comprehensive study of sugar radicals in irradiated DNA, *J. Phys. Chem. B* **102** (1998) 7674–7686.

[110] K.D. Parr, S.D. Wetmore, The properties of DNA C'_4-centered sugar radicals: the importance of the computational model, *Chem. Phys. Lett.* **389** (2004) 75–82.

[111] S. Vivekananda, M. Sadílek, X. Chen, F. Tureček, Modeling deoxyribose radicals by neutralization–reionization mass spectrometry. Part 1. Preparation, dissociations, and energetics of 2-hydroxyoxolan-2-yl radical, neutral isomers, and cations, *J. Am. Soc. Mass Spectrom.* **15** (2004) 1055–1067.

[112] S. Vivekananda, M. Sadílek, X. Chen, L.E. Adams, F. Tureček, Modeling deoxyribose radicals by neutralization-reionization mass spectrometry. Part 2. Preparation, dissociations, and energetics of 3-hydroxyoxolan-3-yl radical and cation, *J. Am. Soc. Mass Spectrom.* **15** (2004) 1068–1079.
[113] R.B. Zhang, L.A. Eriksson, Theroretical study of the tandem cross-linkage lesion in DNA, *Chem. Phys. Lett.* **417** (2006) 303–308.

Radical Cations of the Nucleic Bases and Radiation Damage to DNA: *Ab Initio* Study

Emilie Cauët and Jacques Liévin

Service de Chimie Quantique et Photophysique, Université Libre de Bruxelles, CP 160/09, 50 Avenue F.D. Roosevelt, B-1050 Bruxelles, Belgium
E-mail: jlievin@ulb.ac.be

Abstract

This review summarizes the contribution of high level quantum chemical calculations to the investigation of some elementary reactive processes related to the radiation damage to DNA. It is focused on the biomimetic species that govern these processes at the molecular level. These species are the DNA bases, isolated or embedded in base clusters. Their cations, formed by ionization in their ground and first excited electronic states, are at the center of the present work. We present a synthetic and critical overview of the computational methods used to predict accurate ionization potentials, to correctly describe the non-bonding interactions (stacking, H-bonding and cation-π) stabilizing the studied biomimetic clusters, to characterize their excited states and to investigate the topology of the corresponding potential energy surfaces (minima, transition states, avoided crossings, conical intersections, reaction paths). All these aspects are illustrated by the recent literature and by our own research work, namely on the electron transfer occurring within a stacked dimer of guanines.

Contents

1. INTRODUCTION

The mechanism of radiation damage (RADAM) to the genetic material by ionizing radiations has been extensively studied on the macroscopic and mesoscopic scales [1,2] but it is only recently that corresponding work is carried out at the microscopic level [3–8]. Such work aims at understanding the elementary reactive processes that occur at the molecular level during the initial radiation attack and afterwards.

ADVANCES IN QUANTUM CHEMISTRY, VOLUME 52
ISSN: 0065-3276 DOI: 10.1016/S0065-3276(06)52006-4

The reactive processes depend on the nature of the radiation source (photons, electrons, ions, radioactive particles), which determine the extent of energy deposited on the genetic material and the kind of damage caused on it. Weaker sources, like infrared light, only act on the nuclear degrees of freedom and mainly enhance large amplitude intramolecular vibrations [9–16] without changing or breaking the irradiated molecule. Stronger sources, like visible and UV radiation, produce more drastic effects changing the electronic structure of the system, which is either promoted to excited states [17–27] or ionized [5,6,28]. The initial excitation is usually followed by secondary processes, like non-radiative excited states decay [7,29–36] or, in the case of ionization, electron transfer along the double helicoidal DNA strand [37–39]. The nucleobases are playing a central role in such excitation processes. Identified as the most important UV chromophores of the nucleic acids, their electronic structure is such that they can achieve fast decays to the ground state just after the initial excitation [7,29–36]. Such processes contribute so to the great photostability of DNA and RNA. The ionization process is also known to be governed by the nucleic bases [5,6,28] which can liberate one electron from their π electron clouds. Bombarding DNA with particles like electrons or ions provide more intrusive effects, the energy being sufficient for breaking bonds and operating DNA strand fragmentations [40]. Breaking is often produced by the secondary particles (electrons or ions) generated by the collisions with the primary ones. Single and double strand fragmentations have been studied experimentally as well from electron [40–46] as from ion collisions [47–50]. Fragmentation is so energetic that it is accompanied by an ionization of the products which are the molecular building blocks of DNA, i.e. isolated cations of the DNA bases or small ionized clusters of them. Given the energies involved in such fragmentations, it is likely that ions are formed as well in their ground states as in excited states, while this has not been experimentally proved.

The complexity of the elementary processes just mentioned motivates experimentalists and theoreticians to join their efforts, with as goal the application of "state-of-the-art" physico-chemical experiments and quantum chemical calculations, developed and successfully applied since a long time on small polyatomic systems, to small biomolecules in the gas phase [8,51,52]. It is a common practice now to work on the "building briks of life" (i.e. aminoacids, nucleobases and sugars, or small clusters of them) in order to deduce relevant informations on the larger biological systems to which they belong [8,51,52]. This is justified by a basic idea stating that the structure and the function of a biomolecule are related. The model systems obeying to this prescription are the so-called "biomimetic" molecules.

Most of the modern experimental techniques have been recently applied to biomimetic systems with, in the first place, all optical spectroscopy techniques covering the whole spectral range: microwave [53–56], infrared [9–16] and UV/visible [7] spectroscopies at medium and high resolution. Particle induced fragmentation experiments form another class of interesting techniques in which electron, neutrons or ions collides the biomolecules [40–50].

Theoreticians and in particular quantum chemists also participate actively to the biomimetic staff. Their role is to provide to the experimentalists guiding lines for interpreting their results. What is expected from them is to bring realistic descriptions of the Born–Oppenheimer potential energy surfaces (PES) that govern the studied reactive processes. This means that all electronic states contributing to these processes must be carefully investigated, that the geometries and relative energies of the relevant stationary points (minima and transition states) on the corresponding PES must be characterized and that reaction pathways connecting them must be rationalized. It will be stressed below that, as far as

excited states are concerned, PES crossings are of major importance, in particular the reactivity at the vicinity of avoided crossings and conical intersections where non-adiabatic couplings will selectively condition the reaction dynamics [57–60].

The task dedicated to the quantum chemist is thus far to be trivial giving the size of the molecules of interest and the properties to be calculated. The choice of methods of calculation and basis sets well adapted to the problem is thus crucial as discussed in detail below. The present paper will be focused on high level *ab initio* and density functional (DFT) studies aiming at characterizing as accurately as possible the smaller building blocks that bear the quantum information governing the elementary steps of the studied process. More approximate treatments (semi-empirical, QM/MM, ONIOM and effective Hamiltonian approaches), applied to larger parts of the biomolecules, in order to obtain a global description of the dynamics, form another research line not reviewed here (see for instance in Refs. [61,62]). Both kinds of approaches are obviously needed and are complementary. Accurate "local" quantum treatments aim indeed at providing the relevant parameters to be introduced in more global studies.

The present review will thus focus on the *ab initio* study of the particular class of biomimetic molecules related to the radiation damage. As already pointed out before, the relevant species in this framework are the DNA bases, isolated or regrouped in small clusters, neutral or positively charged. We decided to orient the present review to the ionized species only. A comprehensive review by Crespo-Hernández *et al.* [7] already covers indeed the neutral bases topic. Only few information is available in the literature for the corresponding cations whose importance in the RADAM problem justifies the present review. The ionization process itself is indeed a direct effect of radiation damage and thus merits attention. Moreover ionized DNA bases and clusters are formed in particle induced fragmentation processes and present a particular interest for interpreting the related experiments [47–49]. The role of excited states, very recently characterized for the isolated radical cations of the nucleic bases [63], will be also discussed.

As far as clusters are considered, we are facing with the problem of describing by means of *ab initio* calculations the stability of such complexes made of two or more bases connected by non-bonding interactions (Van der Waals forces and/or hydrogen bonding). As exemplified on Fig. 1 for binary clusters, two classes of such clusters emerge depending on the way the bases are connected. The bases are either paired in a Watson–Crick structure (Gua–Cyt in Fig. 1a) or in a stacked one (Ade–Gua in Fig. 1b). Both kind of cluster may be formed in fragmentation experiments. The former would correspond to the simultane-

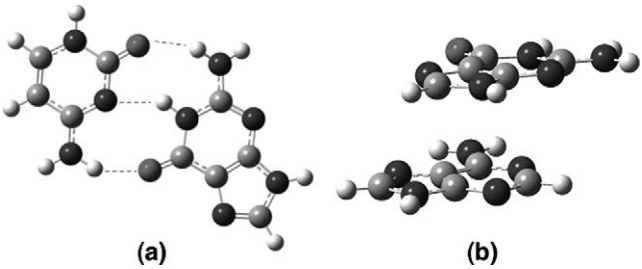

Fig. 1. Structure of base dimers: (a) Watson–Crick base pair (guanine–cytosine), (b) stacked base pair (guanine–adenine).

ous breaking of both strands of double helicoïdal DNA keeping the inter-base H-bonds preserved, while the latter would rather preserve the π–π stacking along a single DNA strand. Important efforts have been made in the literature for determining by *ab initio* calculations the stability of clusters involving stacked nucleic bases (see reviews by Šponer and coworkers [64–66]). Interactions with entities external to DNA, as for instance with the amino acid side chain of a protein binding to DNA, have also been studied [65,67,68]. New interactions are binding the protein to the DNA bases: H-bonding but also so-called cation-π interaction [69–71] occurring when the protein residues drag a positive charge, as for instance arginine, lysine, histidine, ... Let us note that the binding interface between DNA and proteins is also of concern for the RADAM problem given the role of DNA protector that the protein can play with respect to ionizing radiations [72–75].

The quantum description of intermolecular interactions within biomimetic clusters being a central problem will be reviewed in Section 4.1.

More attention will be paid in the present paper on the stacked clusters because of their particular interest in the framework of ionization. It is well known indeed [37,76] that once ionization has occur on a given nucleic base of the DNA strand, the hole just formed can be filled in by an electron from a neighbouring base. Such electron transfer is more efficient through the stacked π structure of two consecutive bases of the same DNA strand [77–79]. Hole transfer or electron transfer can then occur again and again from a base to the next through the connected stacked π electronic clouds. Electron migration at long distances along a single DNA strand has been observed experimentally and is widely studied in the literature [37–39,76]. The existence of such an "electric current" in DNA raises many questions about its biological role. Namely hypotheses about its role in the detection of damage and "initiator" of repairing mechanism have been put forward [80–82].

The electron migration process is also of interest in nanotechnologies [83–85] for potentially providing electric ropes at the nanoscale. The electron migration process opens to a very large literature [38,39] out of the scope of the present review. We would however present some preliminary results we have obtained for the electron transfer within a stacked ionized cluster of guanines.

The present paper is organized in the following way. Section 2 presents a synthetic overview of the computational methods used for investigating ionization in the framework of radiation damage, i.e. for calculating accurate ionization potentials, for taking the clusters stability properly into account and for describing ionized excited states. A critical discussion on the advantages and drawbacks of the alternative approaches (methods and basis sets) will be proposed. Section 3 is devoted to the study of isolated DNA bases with emphasis on the determination of the ionization potentials and the characterization of the excited states of the corresponding cations. The *ab initio* study of ionized clusters is then reviewed in Section 4. This section first analyzes the cluster stability in terms of competing or cooperative non-bonding interactions. It then reviews on the determination of the ionization potentials of base clusters and finally presents our preliminary results on the electron transfer within an ionized guanine cluster. Conclusion and perspectives are drawn in Section 5.

2. COMPUTATIONAL METHODS

Figure 2 proposes an overall picture of the methods of calculation to be used for dealing with biomimetic molecules in the framework of RADAM. The flowchart makes the

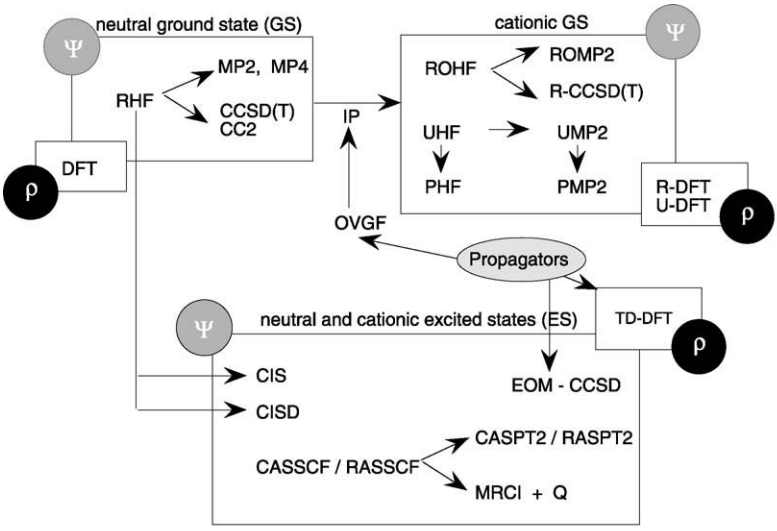

	states	E_{corr}	dispersion	properties
Mono-reference approaches:				
HF	GS	no	no	Koopmans IP
DFT	GS	yes	no	interaction energies
MP2 / CCSD(T)	GS	yes	yes	interaction energies
CIS	Singly ES	no	no	approximate excitation energies
CISD	ES	yes	yes	excitation energies
TD-DFT	Singly ES	yes	no	excitation energies
EOM - CCSD	Singly ES	yes	yes	excitation energies
Multi-reference approaches:				
CAS(RAS)SCF CAS(RAS)PT2 MRCI	ES	yes	yes	excitation energies configuration mixing conical intersections

Fig. 2. Flowchart showing the different methods of quantum chemistry used in the framework of radiation damage. The main features of the methods are summarized in the table below the graph.

methodological hierarchy appear with a separation, between wave function (Ψ) and density (ρ) functional theory (DFT) approaches, between neutral closed shell and cationic open shell species and between ground and excited states calculations. The main features of the different methods are summarized in the table below the graph showing up the methods introducing electron correlation, in particular dispersion effects, and those dedicated to ground and excited states.

Ground states can in principle be investigated by all methods when a single dominant electronic configuration can be used to describe them. This is usually the case in the vicinity of minima on the corresponding potential energy surfaces (PES). In such cases, one can

already get reasonable geometries with uncorrelated methods like Hartree–Fock, while more accurate ones are however obtained by means of MP2 second order Møller–Plesset perturbation theory [86,87] or DFT [88] theory using various hybrid functionals. The scaling of the computer time with the molecular size, in favour of DFT, explains the success of the latter approach for studying the reactivity of biomolecules [89]. MP2 is however systematically used when interaction energies of clusters are concerned, either to support DFT results, or to replace them when dispersion energy contributions are important, as in the typical case of π-stacking interactions for which DFT fails and MP2 succeeds. Recent attempts have been made for developing hybrid functionals able to tackle the stacking problem. Among them, X3LYP has been proposed for the study of Van der Waals interactions [90] but it unfortunately fails at reproducing the stacking stability [91]. Other ones, namely PWB6K, seem to give more reasonable results [92], but the intrinsic nature of the dispersion effects makes *ab initio* wave function correlated treatments more adapted to stacked systems.

MP2 is widely used in the biomolecular context because it introduces a significant part of the electron correlation at reasonable costs. Further improvements can be obtained by extending the perturbative expansion up to the fourth order MP4. Coupled-cluster theory provides another class of highly correlated methods, in particular CCSD taking single and double excitations explicitly into account [93] and CCSD(T) adding a perturbative treatment of the connected triples [94]. For computer costs reasons, MP4 and coupled-cluster theories are however limited to quite small systems. In the biomimetic context, they mostly serve as a reference level in benchmark calculations [64,68,95–100]. CC2 is an interesting alternative to CCSD [101,102] that could be more exploited in the future to deal with biomolecules. It roughly corresponds to an improved MP2 perturbation theory taking orbital relaxation arising from singles into account. Let us also mention the RI-MP2 (Resolution of Identity MP2) approach [103–105], an interesting simplified version of MP2 able to lower the computer costs by one order of magnitude seemly without significant lost of accuracy in the determination of interaction energies [106].

Going from neutral to cationic systems raises the problem of describing open shell states by either spin-restricted open shell (RO) or spin-unrestricted (U) theory. The latter alternative is widely used in the literature for reason of simplicity or code availability. The spin contamination problem, leading to an overestimation of the spin polarization, can however not be ignored, and projection techniques (PHF, PMP2, . . .) [107,108] can be used to remove it.

Unrestricted calculations are definitively not suited for determining ionization potentials (IPs). They induce indeed an unbalanced description between the neutral (restricted) and cationic (unrestricted) species and lead to underestimated values of the IPs. In the case of the DNA bases [63], the error is as large as 0.75 eV at UMP2 level, while it is less important (about 0.2 eV) with unrestricted DFT [109,110]. The latter finding probably explains why restricted DFT is rarely used in the literature. PMP2 is found to work quite well taking for proof the IP of guanine, calculated with the 6-31G(d, p) basis set, which agrees within 0.03 eV with restricted MP2, while UMP2 overestimates it by 0.47 eV [63,110]. Unrestricted coupled-cluster (UCC) methods also yield to smaller spin contamination than UMP, as a result of the infinite nature of the involved expansions [111].

Excited state calculations require adapted methods and we refer to the recent review of Serrano-Andrés [60]. The simpler approach is the CIS method [112,113] (configuration interaction of singles) consisting in a configuration interaction calculation limited to single

excitations with respect to an HF monoconfigurational wave function. It is often used as a preliminary step and gives a first very qualitative description of the low lying excited states that can be helpful for preparing more accurate treatments discussed below. CIS results must of course be used with care. They do not involve orbital optimization and do not take double excitations and thus electron correlation into account.

The partition between mono- and multi-reference wave functions merits some comments. The first is that all correlated methods based on a single configuration HF zeroth order wave function (CIS, CISD, MP2, CCSD(T), CC2, . . .) are limited to the description of the lower state of a given symmetry of the point group to which the system belongs. The second is that such a constrained zeroth order description can introduce dramatic errors in regions of the PES where configuration mixing occurs. This may happen as well on ground state (GS) or excited states (ES) surfaces when avoided crossings or conical intersections occur. This case will be addressed in Sections 3.2.2 and 4.3. Configuration mixing is rarely encountered in the close vicinity of the global or local minima on the PES except for systems exhibiting a particular electronic structure (biradicalar structure, close-lying HOMO-LUMO, . . .). Multi-reference approaches are thus imperatively required in all such cases and also for investigating higher excited states than the lowest one in a given symmetry. They are based on the application of the variational principle to a multi-configuration trial function defining the zeroth order wave function. The multi-configuration expansion can be build on a "complete active orbital space" leading to the so-called CASSCF (complete active space self consistent field) [114–116] or on a "restricted active space" introducing occupational restrictions to the CAS and leading to the corresponding RASSCF theory [117]. The definition of the complete or restricted active spaces for describing a given problem requires a particular care in the context of biomolecules. It is indeed not possible to include all valence orbitals, as it is a usual practice for small molecules. Full valence CASSCF is of course a safe approach ensuring that all strongly interacting orbitals are included in the MCSCF treatment and taking so the so-called non-dynamical correlation into account. The remaining dynamical correlation can then be introduced either by second order perturbation theory (CASPT2 or RASPT2) [118,119] or by a multireference configuration interaction (MRCI) calculation [120,121]. Both classes of methods are based on the CASSCF (RASSCF) multi-configurational zeroth order wave function from which single and double electron excitations are applied. Adaptation of such accurate approaches to biomimetic systems requires a careful definition of the active space which must be restricted to the molecular orbitals playing an "active role" in the process under study. This will be exemplified below (see Sections 3.2.2 and 4.3) in the case of the geometrical relaxation in the vicinity of a conical intersection or for the description of an electron transfer process.

Linear response theory [122] also provides interesting tools, based on propagators or Green function concepts, for investigating excited states. TD-DFT [123] and OVGF [124] methods are used in the framework of biomimetic systems [30,125]. The former is an interesting alternative to the CAS and RAS approaches for investigating singly excited states of large systems. The latter, providing accurate ionization energies at low computer costs, has been applied to the theoretical calculation of photoelectron spectra and IPs of large organic systems [126,127] and of the nucleic bases [125,128–130]. Equation-of-motion (EOM) coupled cluster methods [131,132] are also mentioned for completeness on Fig. 2, while being reserved, as all CC methods, to calibration calculations on small systems.

Biomimetic systems involve inter- and intra-molecular electronic interactions that must be described in a balance way requiring the use of appropriate basis sets. The size of the system is such that the use of extended correlation consistent polarized and augmented basis sets is proscribed except for test calculations on small model systems. Medium size singly polarized basis sets like 6-31G(d, p) or 6-311G(d, p) are often adopted because they provide, at MP2 or DFT level, and for many properties, a good compromise between accuracy and computational practability. They are however insufficient for describing the stacking stability or the electronic changes accompanying ionization. Improved and augmented medium size basis sets, specially adjusted for such properties, have been proposed in the literature [68,133]. Such advances are reviewed in Sections 3.2.1 and 4.1.

Different Quantum Chemistry packages implementing the methods of calculations described in the present section are used by the authors cited in the present review. We refer the reader to the individual papers for explicit reference to these programs. Let us cite here only those that we have actually used to perform the new calculations presented in the next sections, i.e. MOLPRO [134] for all multi-reference calculations and excited states calculations and Gaussian 03 [135] for stationary points searches.

3. ISOLATED DNA BASES

3.1. Neutral DNA bases

Single neutral DNA bases in their electronic ground states have been frequently investigated [64,67,136,137] and the non-planarity of their amino group have been noticed [136]. As mentioned before, a comprehensive review of Crespo-Hernández *et al.* [7] has already covered the neutral bases excited states topic. In parallel to the recent experimental advances for probing the excited electronic structure of the nucleobases, Kohler and co-workers [7,29], Serrano-Andrés and co-workers [32,35] and Domcke and co-workers [30,31,33,34] have carried out extensive quantum chemical studies aiming at characterizing the excited states dynamics. The electronic structure of the four nucleobases is complicated by the existence of numerous electronic states in the low-energy region. The vertical transition energies of the lowest excited singlet states of the four bases have been calculated by several authors using different quantum chemistry approaches [7]. The equilibrium geometries in the excited singlet states have been determined [138–142] and found to be non-planar. Geometry optimizations have opened a further discussion about the energetical order of the excited states indicating different state crossings and the possibility of significant non-adiabatic couplings. Attention has then been paid on the localization of conical intersections for the important role they could play in the non-radiative dynamics following photoexcitation. The potential energy surfaces of the excited singlet states of adenine and cytosine were explored by different authors who localized conical intersections connecting excited states with the ground electronic state. For adenine, Sobolewski, Domcke and co-workers [30,34] described, at the CASPT2 and TD-DFT levels, three photochemical reaction paths, each of them leading to a conical intersection between an excited surface and the potential energy surface of the ground state. For cytosine Ismail *et al.* [29] proposed, on the basis of a CASSCF study, a decay path through a conical intersection between the $n\pi^*$ and ground states. Merchán *et al.* [32] discussed, for the same molecule, a CASPT2

mechanism where a conical intersection connects the $\pi\pi^*$ state with the electronic ground state.

The major result of the above cited works has been to demonstrate theoretically the photostability of the DNA bases thanks to the existence of fast non-radiative decay channels [34].

Few theoretical results [35,143,144] have been obtained about DNA base triplet states. Nguyen *et al.* [143] have recently estimated the energy differences between the singlet and triplet states of neutral DNA bases. We refer the reader to this article for a summary of the previous calculations performed on these states.

3.2. Radical cations of DNA bases

3.2.1. Ionization potentials of the DNA bases

The determination of accurate theoretical values of the threshold energies necessary for ionizing the nucleobases is of major importance in the context of RADAM, in particular for supporting fragmentation experiments. Two different energy quantities are usually calculated, corresponding to the vertical and adiabatic ionization potentials (IP) respectively. The vertical IP corresponds to a vertical excitation occurring at the equilibrium geometry of the neutral molecule. The adiabatic IP corresponds to a vertical ionizing excitation from the equilibrium geometry of the neutral species directly followed by a relaxation to the equilibrium geometry of the cation. Both gas-phase ionization potentials have been calculated by different authors, for the four DNA bases, with comparisons to the corresponding experimental values [145–148]. Sevilla *et al.* [149] used the restricted MP2 level with a small double-ζ basis set (6-31+G(d)), while Crespo-Hernández *et al.* [110] adopted the larger 6-31++G(d, p) basis set and the UMP2/PMP2 technique. They obtained results in good agreement with experiment. Some authors [150–152] also calculated the IPs with B1LYP or B3LYP DFT but obtained systematically underestimated values resulting from the use of the unrestricted formalism. Theoretical results of IPs have also been obtained using propagator calculations in the partial third-order (P3) approximation with the 6-311G(d, p) basis set [125,128–130,153]. Let us note that attempts have been also made in several studies to examine the IPs of the bases in aqueous solution [110,152,154].

All calculations confirm the experimental findings [145–148] showing that guanine has the lowest ionization potential, followed by adenine, cytosine and thymine. The results, collected in Table 1, for the four DNA bases and for both vertical and adiabatic IPs, show that correlated calculations exhibit discrepancies ΔE as large as ± 0.6 eV with respect to the most precise experimental values. The vertical and adiabatic IPs of all DNA bases have been measured by photoelectron spectroscopy [145] (PES) and photoionization mass-spectrometry [146] (PIMS) respectively. More precise values of the adiabatic IPs have been obtained recently by Jochims *et al.* [148] for adenine and thymine using PIMS and by Choi *et al.* [147] for thymine using mass-analyzed threshold ionization (MATI). As already pointed out previously [63], the value of the vertical IP of thymine obtained by Sevilla *et al.* [149] is largely overestimated because it corresponds to ionization to the first excited state of the cation.

The need of accurate IP values for base clusters motivated us recently to analyze in detail the influence of the level of calculation on the vertical and adiabatic IPs values [63]. We

Table 1. Gas-phase vertical and adiabatic ionization potentials of guanine, adenine, cytosine and thymine (in eV) calculated at different levels of theory. Energy differences ΔE between theoretical and the corresponding most precise experimental values (in eV)

IP_{vert}								method/basis set	IP_{adia}							
Gua		Ade		Cyt		Thy			Gua		Ade		Cyt		Thy	
	ΔE		ΔE		ΔE		ΔE			ΔE		ΔE		ΔE		ΔE
7.22	1.02	7.59	0.85	9.14	−0.20	8.41	0.73	HF/6-31G(d, p)[a]	6.70	1.07	7.19	1.01	7.82	0.86	7.92	1.00
7.88	0.36	8.34	0.10	8.80	0.14	8.87	0.27	MP2/6-31G(d, p)[a]	7.42	0.35	7.94	0.26	8.49	0.19	8.60	0.32
8.29	−0.05	8.53	−0.09	9.34	−0.4	9.65	−0.51	Koopmans/6-31G(2d(0.8, 0.1), p)[a]	–	–	–	–	–	–	–	–
7.34	0.90	7.67	0.77	9.25	−0.31	8.50	0.64	HF/6-31G(2d(0.8, 0.1), p)[a]	6.83	0.94	7.28	0.92	7.92	0.76	8.01	0.91
8.21	0.03	8.63	−0.19	9.07	−0.13	9.13	0.01	MP2/6-31G(2d(0.8, 0.1), p)[a]	7.75	0.02	8.23	−0.03	8.78	−0.10	8.87	0.05
7.30	0.94	7.63	0.81	9.26	−0.32	8.47	0.67	HF/aug-ccpVDZ[a]	6.81	0.96	7.26	0.94	7.91	0.77	7.98	0.94
8.30	−0.06	8.75	−0.31	9.19	−0.25	9.23	−0.09	MP2/aug-ccpVDZ[a]	7.84	−0.07	8.33	−0.13	8.88	−0.20	8.94	−0.02
7.39	0.85	7.74	0.70	9.32	−0.38	8.56	0.58	HF/6-311++G(d, p)[a]	6.88	0.89	7.35	0.85	7.99	0.69	8.05	0.87
8.27	−0.03	8.72	−0.28	9.14	−0.2	9.20	−0.06	MP2/6-311++G(d, p)[a]	7.81	−0.04	8.31	−0.11	8.84	−0.16	8.88	0.04
7.29	0.95	7.73	0.71	8.45	0.49	8.99	0.15	HF/6-31+G(d)[b]	6.87	0.9	7.36	0.84	7.99	0.69	8.10	0.82
8.04	0.2	8.58	−0.14	8.82	0.12	10.33[h]	−1.19	MP2/6-31+G(d)[b]	7.66	0.11	8.18	0.02	8.74	−0.06	8.85	0.07
6.97	1.27	7.36	1.08	7.69	1.25	8.21	0.93	PHF/6-31++G(d, p)[c]	6.48	1.29	7.09	1.11	7.35	1.33	7.79	1.13
8.33	−0.09	8.62	−0.18	8.69	0.25	9.07	0.07	PMP2/6-31++G(d, p)[c]	7.90	−0.13	8.23	−0.03	8.78	−0.10	8.74	0.18
8.13	0.11	8.49	−0.05	8.79	0.15	9.13	0.01	OVGF-MP2/6-311G(d, p)[d]	–	–	–	–	–	–	–	–
7.65	0.59	7.99	0.45	8.35	0.59	8.72	0.42	B3LYP/6-31G(d, p)[e]	7.32	0.45	7.77	0.43	8.23	0.45	8.49	0.43
7.94	0.3	8.23	0.21	8.64	0.3	8.97	0.17	B3LYP/6-31G(2d(0.8, 0.1), p)[e]	7.61	0.16	8.02	0.18	8.52	0.16	8.74	0.18
8.02	0.22	8.33	0.11	8.74	0.2	9.05	0.09	B3LYP/6-311++G(d, p)[e]	7.69	0.08	8.11	0.09	8.63	0.05	8.81	0.11

(*continued on next page*)

Table 1. (*continued*)

IP_{vert}								method/basis set	IP_{adia}							
Gua		Ade		Cyt		Thy			Gua		Ade		Cyt		Thy	
	ΔE		ΔE		ΔE		ΔE			ΔE		ΔE		ΔE		ΔE
7.89	0.35	8.16	0.28	8.62	0.32	8.90	0.24	B1LYP/6-31+G(d, p)[f]	7.52	0.25	7.95	0.25	8.47	0.21	8.66	0.26
7.98	0.26	8.26	0.18	8.69	0.25	9.01	0.13	B3LYP/6-31++G(d, p)[g]	–	–	–	–	–	–	–	–
								Exptl	7.77 ± 0.05[j]		8.26 ± 0.05[j]		8.68 ± 0.05[j]		8.87 ± 0.05[j]	
8.24 ± 0.03[i]		8.44 ± 0.03[i]		8.94 ± 0.03[i]		9.14 ± 0.03[i]					8.20 ± 0.03[k]				8.82 ± 0.03[k]	
															8.9178 ± 0.001[l]	

[a] From Ref. [63], geometries optimized at HF/6-31G(d, p) level. [b] From Ref. [149], geometries optimized at ROHF/6-31G(d) level. [c] From Ref. [110], geometries and energies calculated at the same level. [d] From Ref. [125], geometries optimized at MP2/6-311G(d, p) level. [e] From Ref. [63], geometries optimized at B3LYP/6-31G(2d(0.8, 0.1), p) level. [f] From Ref. [150], geometries optimized at B1LYP/6-311G(d, p) level. [g] From Ref. [152], geometries and energies calculated at the same level. [h] This too large value corresponds to ionization to the first excited state [63]. [i] PES from [145]. [j] PIMS from [146]. [k] PIMS from [148]. [l] MATI from [147].

proposed the use of a medium size 6-31G(2d(0.8, α_d), p) basis set, with an optimized value of $\alpha_d = 0.1$, for predicting accurate energy differences related to ionization. A similar basis set was already proposed in a previous paper [68] for calculating interaction energies of clusters. In this context, the value of the α_d exponent was fixed to 0.2. We refer to Section 4.1 for more details on the 6-31G(2d(0.8, α_d), p) basis set and on its optimization. Let us simply tell here that it presents the advantage of describing the electronic changes accompanying ionization as well as larger polarized and/or augmented basis sets of the literature but at lower computer costs. As shown in Table 1, it significantly improves the MP2 values with respect to the standard 6-31G(d, p) basis set. The mean deviation with experiment is indeed of 0.07 and 0.25 eV for 6-31G(2d(0.8, 0.1), p) and 6-31G(d, p) respectively. Such a basis set is thus potentially interesting for investigating larger systems involving the DNA bases, like clusters of these bases (see Section 4).

3.2.2. Excited states of the radical cations of DNA bases

As explained in the introduction, the calculation of the excited states of the radical cations of DNA bases presents a great interest in the framework of RADAM. It is surprising to realize that only few efforts have been made to characterize the electronic structure of these cations. Improta *et al.* [150] have determined their equilibrium geometries by means of DFT calculations, demonstrating their planarity. The only work devoted to their excited states is, at our knowledge, our recent work [63] in which we characterized the first excited states of the cations. In that work, we determined and discussed the topology of the low-lying potential energy surfaces, showing that a conical intersection occurs, for all cations, between the ground and first excited states potential energy surfaces. For all bases, we localized, at CASSCF level, the conical intersection point connecting the ground $^2A''$ and the first $^2A'$ states at planar C_S symmetry structures. The two nuclear displacements vectors [155,156] x_1 and x_2 that define the double cone shape were determined. These two coordinates correspond to the gradient difference and non-adiabatic coupling vectors respectively. The values of their norms were calculated giving a qualitative information on the degree of adiabaticity of the system in the vicinity of the conical intersection.

As an example [63], Fig. 3 shows a 3-dimensional view of the two CASSCF adiabatic interacting states of Cyt^+ as a function of $(x_1 - x_{1e})$ and $(x_2 - x_{2e})$, x_{1e} and x_{2e} referring to the geometry at the intersection point. The normalized nuclear displacements corresponding to vectors x_1 and x_2 are also represented in the bottom panel of the figure. The case of Cyt^+ is quite different from the others because it is the only case in which the conical intersection induces a non-planar minimum on the lowest potential energy surface. We actually located two planar stationary points of $^2A''$ and $^2A'$ symmetries respectively. The former is the global minimum of the ground state surface, but the latter is a saddle point, and not a secondary minimum as in all other cationic bases. This particular topology is schematically represented in Fig. 4. On this picture, one sees the optimized stationary points (M1 and M2 for minima and S1 for saddle point) in a two-dimensional space of in-plane and out-of-plane deformations. The corresponding coordinates Q_{in} and Q_{out} hold for any possible internal displacements (or any linear combination of such displacements) conserving or not the planar structure respectively. At the conical intersection point, these Q_{in} and Q_{out} coordinates coincide with the x_1 and x_2 vectors. One of the features of this map is the symmetry of the potential energy surface with respect to the Q_{in} axis. Any displacement above and below the molecular plane is indeed isoenergetic whatever the nature of

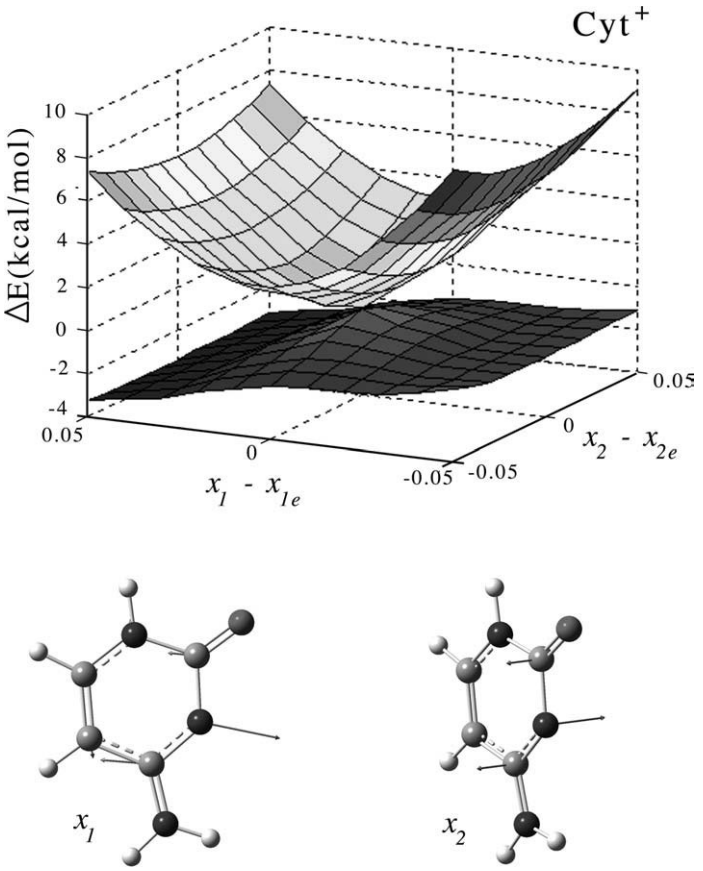

Fig. 3. 3D representation of the conical intersection between the ground and first excited states of Cyt^+, calculated at CASSCF/6-31G(d, p) level. Normalized modes of displacements corresponding to vectors x_1 and x_2 at the conical intersection point. Arrows have been multiplied by a factor of 1.5. Carbon, nitrogen, oxygen and hydrogen atoms are drawn in light grey, black, dark grey and white respectively. Adapted from Cauët *et al.* [63].

the displacement. Two stationary points have thus been found corresponding to two planar structures. An analysis of the shape of the adiabatic potential energy curves along x_1 indicates that the conical intersection point (CI) is encountered at a geometry lying between the two planar critical points. This explains the observed global topology.

The radical cations of the three other DNA bases exhibit a different situation. For Ade^+, Gua^+ and Thy^+, two planar minima have been characterized corresponding to the $^2A''$ (M1) and $^2A'$ (M2) states respectively. The topology of the conical intersection energy curve along x_1 is also different from the Cyt^+ case, with the two minima lying on the same side of the conical intersection point. Thy^+ forms a particular case with significantly weaker couplings than all other cations. This means that one could qualitatively expect a rather adiabatic behavior for this cation than for all the others.

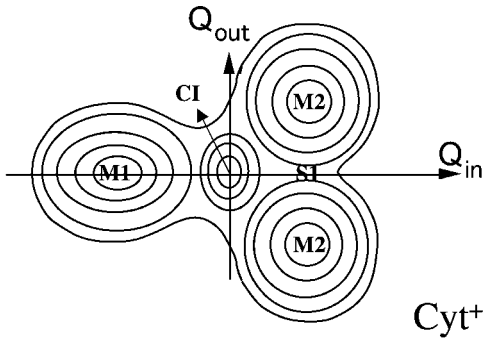

Fig. 4. Qualitative topology of the lowest potential energy surface of the radical cation of cytosine presented as an isocontour map. The coordinates Q_{in} and Q_{out} hold for any internal displacements conserving or not the planar C_s symmetry respectively. Two stationary points correspond to planar structures. The $^2A''$ stationary point (ground state) corresponds to an absolute minimum (M1). The $^2A'$ stationary point is a saddle point (S1). The second minimum (M2), corresponds to a ^2A non-planar structure. The ground state is connected to the first excited state by a conical intersection noted CI.

Table 2. Relative energies (in eV) characterizing the M1, M2 and S1 stationary points of the nucleobase cations. $\Delta E(\text{X} - \text{X}^+)$ is the energy difference between a given cation stationary point and the ground-state of the corresponding neutral system. E_{exc} is the excitation energy from the cationic ground state

	Gua^+		Ade^+		Cyt^+			Thy^+	
MP2/6-31G(2d(0.8, 0.1), p)[a]	M1	M2	M1	M2	M1	M2	S1	M1	M2
$\Delta E(\text{X} - \text{X}^+)$	7.75	9.33	8.23	8.54	8.78	9.12	9.39	8.87	9.81
$E_{\text{exc}}(\text{X}^+)$	0	1.58	0	0.31	0	0.34	0.61	0	0.94

[a] From Ref. [63], geometries optimized at HF/6-31G(d, p) level.

For all nucleobase cations, adiabatic relative energies of the stationary points have been calculated with respect to the ground state energies of the corresponding neutral systems. All MP2/6-31G(2d(0.8, 0.1), p) energy differences are presented in Table 2, together with the corresponding excitation energies E_{exc} from the ground states of the cations.

4. CLUSTERS OF DNA BASES

Clusters of DNA bases are relevant biomimetic systems for discussing the reactive processes related to RADAM. The DNA base pairing and stacking interactions, illustrated in Fig. 1, are thus to be considered and it would be desirable to extend to clusters the results obtained for the isolated DNA bases, namely the determination of ionization po-

tentials and the investigation of the excited states of the cations. Before addressing these points, we will first comment on how quantum chemical calculations can deal with the intermolecular interactions that govern the stability of such clusters.

4.1. Stability of DNA base clusters

The necessity of using extended basis sets and of including electron correlation effects for predicting the right stability of base clusters has been reported in the literature in the middle of the nineties [95,96,133,157–159]. Base clusters have been extensively studied since that time, as pointed out in reviews by Hobza, Šponer and collaborators [64–66] but also in research papers [67,68,100,106,160–173]. The computational effort resulting from the large number of interacting valence electrons (134 electrons for instance in a dimer of guanines) has motivated systematic tests for determining a level of theory combining accuracy and computational feasibility. It clearly appears that methodological needs are different for describing the hydrogen bonding maintaining bases together in a Watson–Crick arrangement (Fig. 1a) or the π–π interactions occurring in a stacked pair of bases (Fig. 1b). Most of the methods of calculations cited in Section 2 for being dedicated to ground state calculations have been tested and compared allowing a rationalization of the results obtained for a large variety of base clusters. Smaller homodimers, like those of ethylene, formamide, formamidine, benzene, pyrol, triazine, pyridine and thiophene, were also chosen for performing benchmark calculations in which MP2, MP4, CCSDT and CCSD(T) methods and various basis sets were compared [64,96–98,100,157,159,161,174–178]. The results can be summarized in the following way:

(i) Interaction energies must be corrected, in all cases, for basis set superposition errors (BSSE) by using the appropriate counterpoise approach [179]. The order of magnitude of this correction is, for instance, of 3.56 kcal/mol for a stacked dimer of guanines calculated at MP2/6-31G(2d(0.8, 0.2), p) level.

(ii) Stabilization of H-bonded base pairs mainly comes from electrostatic interactions and can therefore be described by all methods of calculation, even uncorrelated ones like HF, with medium basis sets. Electron correlation and extended basis sets are of course improving the results.

(iii) Stacked base pairs are stabilized by inter-system correlation effects corresponding to the London dispersion forces needing highly correlated approaches for being taken into account. Tsuzuki *et al.* [97] showed that MP2 tends to overestimate, by as much as 38%, the correlation energy contribution to the stacking stability as compared to CCSD(T) reference values.

Fourth order Møller–Plesset theory MP4 has also been used for calibrating the lower MP2 level [64,68,97]. In the case of the interaction energy of a stacked dimer of guanines, it has been shown [68] that the perturbation theory expansion exhibits an oscillatory behavior (-2.76, $+0.38$ and -0.68 kcal/mol for MP2, MP3 and MP4(SDQ) interaction energies respectively). The corresponding HF value being of $+6.57$ kcal/mol, one sees that, if MP2 actually overestimates the stability, it provides however the more significant stabilizing contribution (-9.3 kcal/mol). The overestimation with respect to MP4 is in this case of 28%. Note that the basis set used here is 6-31G(d(0.2)).

Another important result is that standard DFT theory fails at describing dispersion effects proscribing this family of methods for studying stacking. B3LYP/6-31G(2d(0.8, 0.2), p) predicts the wrong stability for the guanine dimer (+5.85 kcal/mol). Recently developed functionals [92], namely PWB6K, seem however to give more reasonable results. Let us also cite some semi-empirical attempts for adding dispersion energy corrections to standard DFT [164,168] and the DFT-MO Slater-GGA approach of Kurita *et al.* [162,163]. Another alternative to MP2 for large systems is the simplified RI-MP2 approach [106,169].

(iv) The basis set effect largely influences the stacking stability. The addition of diffuse polarization orbitals on the heavy atoms of the molecule is demonstrated to be deciding [64,68,95,106,133,159] and thus merits to be discussed hereby.

Extrapolation to complete basis set limit (CBS) has been investigated [98,99,106,176]. Tsuzuki *et al.* [98,99] showed that CBS limits of CCSD(T) interaction energies can economically be obtained from MP2 extrapolations. Another research line rather consists to start from the well-balanced 6-31G(d, p) medium size basis set and to augment it by additional diffuse d-polarization functions specifically optimized for describing the dispersion effects. This idea coming from the pioneering work of van Duijnevelt *et al.* [180,181] is that such additional polarization improves the multipole electric moments of the interacting monomers. This results in a better description of their polarizability and consequently of the dispersion interactions occurring between the monomers. Such improved basis sets can thus be considered as "momentum optimized" or "dispersion energy optimized" basis sets. Tsuzuki *et al.* [98,99] tested various augmented basis sets to evaluate the dispersion interactions between hydrocarbons [174]. Šponer *et al.* [133] adopted a simpler but successful approach consisting of changing the exponent of the single Gaussian d-polarization function on all second row atoms, from its standard value of $\alpha_d = 0.8$ (common to C, N and O atoms) to a lower value of $\alpha_d = 0.25$. The so-called 6-31G*(0.25) basis set has been widely used in the literature for studying stacked π–π systems [64,65,67,96,133,171,172]. An equivalent notation for 6-31G*(0.25) is 6-31G(d(0.25)) consistent with similar basis sets discussed in this work.

Wintjens *et al.* [68] revisited the problem in a study of so-called "stair motifs" [165] consisting of three interacting partners encountered at the binding interface of protein-DNA complexes: two stacked bases from the same DNA strand and an amino-acid side-chain from the binding protein. As illustrated in Fig. 5 for a cluster formed by a stacked thymine-guanine base pair in interaction with an arginine, such ternary complexes form one step of a stair and exhibit three superimposed kinds of interactions: base stacking, H-bonding and cation-π interactions. The latter, only recently characterized [69–71] for its role in the stability of DNA-protein, protein-protein and protein-ligand complexes, occurs when a positively charged moiety (the NH_2 substituant of arginine in the example of Fig. 5) approaches an aromatic π system (the lower DNA base in the example). The study of such complicated systems motivated Wintjens *et al.* [68] to adjust, at the MP2 level of theory, the α_d exponent of the 6-31G(d(α_d)) basis set in the case of the three kinds of interactions. They got the surprising result that the same value of $\alpha_d = 0.2$ was optimal for all of them. They also found that the interaction energies calculated with this adjusted basis set was close to those obtained with more extended polarized basis sets from the literature (cc-pVTZ, aug-cc-pVDZ, 6-311++G**). The same authors [68,178] also tested a further basis set improvement, noted as 6-31G(2d(0.8, 0.2), p), corresponding to the standard 6-31G** (or

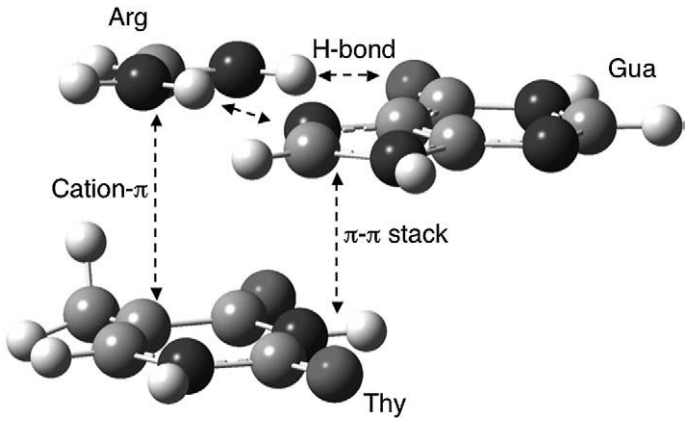

Fig. 5. Cation-π/H-bond/π–π stair motif occurring at the interface of protein–DNA complexes. The geometry is taken from a X-ray structure data base and the interacting partners are arginine, guanine and thymine. Carbon, nitrogen, oxygen and hydrogen atoms are drawn in light grey, black, dark grey and white respectively.

6-31G(d, p)) basis set in which the standard polarization $\alpha_d = 0.8$ is maintained for properly describe *intra-molecular* polarization and to which a second d-function with $\alpha_d = 0.2$ is added for improving the *inter-molecular* polarization. The latter basis set has been successfully applied for studying a large number of clusters (a few hundred) detected in high resolution data bases of biomolecular complexes [68,166,182]. The overall correlation observed between the calculated interaction energies and the frequencies of occurrence of the calculated clusters in the data bases supports the usefulness of such a theoretical approach. It is also confirmed by Hobza and Šponer [106] who assessed that MP2/6-31G(d(0.25)) provides a balanced level of theory for studying stacked and H-bonded clusters at reasonable computer costs. One can take for proof the fact that the MP2 stacking correlation energies are still overestimated but to a lower extent (10–25%) [106] than with larger basis sets (21–38%) [97]. This result probably comes from error compensations between basis set and correlation effects.

The last discussion about local interactions of DNA with proteins could probably appear as out of the scope of the present review. It is well known yet that proteins are playing the role of protectors of DNA with respect to radiation attacks [72–75]. It is thus important to investigate by means of high level *ab initio* calculations the local stability at the binding interface. The cooperativity between stacking and other occurring interactions is moreover an interesting theoretical problem tackled by different research groups like those of Šponer [65–67], Geerlings [171,172,183] and ours [165,182].

As pointed out in the introduction, we will now focus to the stacked DNA bases clusters, this choice reflecting our own research line and also the particular role played by this class of clusters in the framework of RADAM.

4.2. Ionization potentials of stacked DNA bases

Only few calculations have been performed for determining the IP values of stacked DNA bases. The results concerning pure guanine clusters are summarized in Table 3. The energy

Table 3. Calculated vertical ionization potentials of stacked guanines (in eV). The energy difference between the monomer and cluster IP values is given in parentheses

	IPvert				
	HF 6-31G(d) Koopmans		B3LYP 6-31G(d)[b]	HF 6-31G(2d(0.8, 0.2), p)[c]	MP2 6-31G(2d(0.8, 0.2), p)[c]
G	7.75[a]	7.72[b]	7.31	7.34[d]	8.07[d]
GG	7.28 (0.47)[a]	7.34 (0.38)[b]	6.64 (0.67)	6.93 (0.41)[d]	7.86 (0.21)[d]
GGG	7.07 (0.68)[a]	–	–	6.42 (0.92)	7.44 (0.63)

[a] From Ref. [184], geometries taken from X-ray structures. [b] From Ref. [185], geometries optimized with AMBER force field. [c] Geometries from a X-ray structure of 1TC3 DNA-protein complex. [d] From Ref. [63].

differences between the IPs of the clusters and the monomers are indicated. Sugiyama *et al.* [184] have computed the IPs of the N-methylated DNA base stacks by using geometries based on standard bond lengths and bond angles taken from X-ray crystal data. Vertical IPs were estimated from Koopmans' theorem from single-point calculations at the HF/6-31G(d) level. Similar results were reported by Prat *et al.* [185] from geometries optimized with the AMBER force field. The same authors also used density functional theory (B3LYP/6-31G(d)). We have recently calculated a more accurate MP2 vertical IP [63] for a stacked dimer of guanines with the 6-31G(2d(0.8, 0.2), p) basis set presented in the previous section. The geometrical structure was derived from a X-ray structure of tc3 transposase (protein code 1TC3, residues A7 and A8) taken from our previous work on stair motifs [68,165]. The IP of a trimer of guanines calculated at the same level of calculation is also given in Table 3. Some other Koopmans's calculations, not reported in Table 3, were also performed on 5- or 6-mer model sequences centered on guanines [186–188]. A direct comparison is unfortunately not possible between the different results because the authors use different molecular structures. Note that it is difficult to estimate the accuracy of the Koopmans' values subject to error compensations [63]. In addition, let us recall that B3LYP calculations do not take the dispersion attraction in a stack into account and that they systematically underestimate the IPs as a result of the unrestricted treatment. The calculations demonstrate however that the stacking interactions significantly lowers the IPs.

We propose in Fig. 6 a global energy diagram for the ionization of the guanine dimer from 1TC3. This picture, obtained at MP2/6-31G(2d(0.8, 0.2), p) level, takes into account the interaction energies ΔE of both the neutral and ionized clusters (-3.20 and -6.24 kcal/mol respectively) and the IPs of the monomer and the dimer (8.07 and 7.86 eV respectively). Note the importance of BSSE in the calculation of such interaction energies. These corrections are indeed far to be negligible and differ for the neutral and ionic species ($+3.56$ and $+5.47$ kcal/mol for GG and GG^+ respectively). One sees that the ionized dimer is stabler than the neutral one by 49%. This figure shows thus the importance of the level of calculation for determining such energy quantities. The use of MP2/6-31G(2d(0.8, 0.2), p) guarantees here a correct representation of both the stacking stability and the electronic changes accompanying ionization.

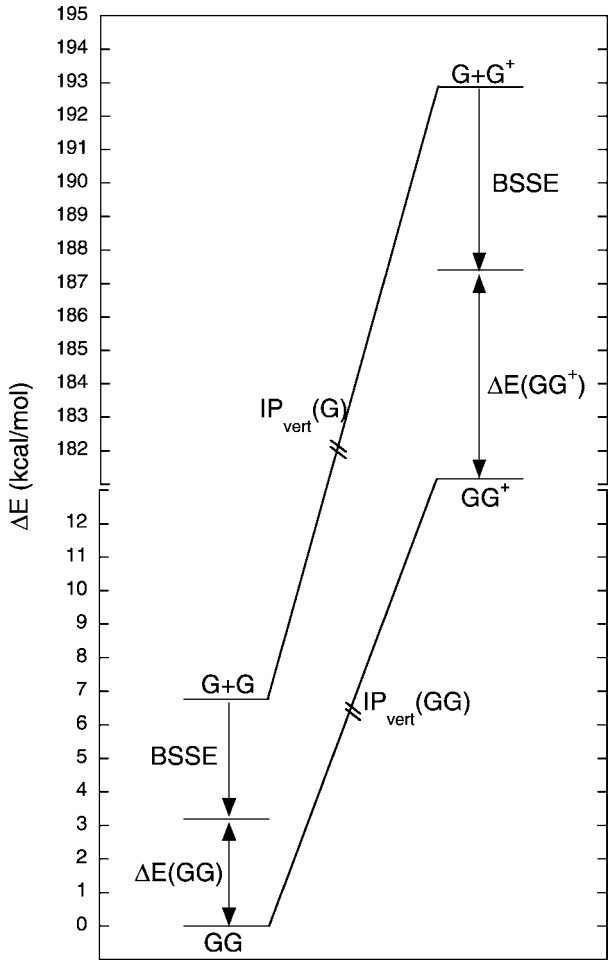

Fig. 6. Global energy diagram for the ionization of a stacked dimer of guanines obtained at MP2/6-31G(2d(0.8, 0.2), p) level of theory. The energy scale has been cut in order to represent the neutral and cationic systems on the same graph.

It is surprising to realize that only few calculated IPs are reported in the literature for stacked base clusters, probably due to the computational difficulties reported above in the description of the stacking stability.

The influence of base pairing on ionization potentials has been more widely studied. Many theoretical studies concerning the energetics of the base-pair cation radicals are available. Colson *et al.* [189] reported *ab initio* calculations on each of the DNA base-pair ions radicals. These calculations were extended to the DFT level by Hutter and Clark [190] for the GC base-pair cation radical and by Bertran *et al.* [109] and Li *et al.* [191,192] for both GC and AT base pair cations. These theoretical studies show the importance of proton transfer within the Watson–Crick base pairs for the calculations of the stability of such complexes. We refer the reader to the papers cited above for more details.

4.3. Electron transfer in a stacked cluster

In this section, we present preliminary results that we have obtained on the charge transfer process within a stacked ionized cluster of two guanines [193]. It is known that the guanine base has the lowest ionization potential among the four DNA nucleobases and that the stacking interaction of two consecutive guanine bases creates a site having an extremely low IP in duplex DNA [63,184,185]. In the charge migration process through DNA, the guanines act thus as carriers of the positive charge [194,195]. Indeed, as described in the literature [37], a guanine radical cation G_1^+ is able to oxidize a second guanine G_2. The newly formed guanine radical cation G_2^+ can then oxidize another guanine so that the positive charge is transported through DNA.

The elementary step related to the charge transfer process within a stacked guanines cluster has been studied and the role of excited states of the ionized dimer has been demonstrated.

We started from the geometry of a stacked GG pair occurring in a B-DNA strand taken from an X-ray data base. We decided to keep, for this cluster, the guanine 5′ and guanine 3′ (G5′ and G3′) labels as they are defined in the original macromolecule. A preliminary MP2 calculation at this geometry shows that the positive charge is located on G5′. Exploratory calculations have been carried out in order to properly characterize the excited states involved in the electron transfer process from G5′ to G3′. These calculations, to be detailed elsewhere [193], aimed at determining the level of theory to be adopted but also the main active nuclear degrees of freedom able to describe this transfer process.

A minimum theoretical level has been first adopted consisting in a CASSCF/MRCI calculation involving a small active space (5 electrons in 3 molecular orbitals (MOs)). A relevant active coordinate q has been selected. It corresponds to a slide of G5′ with respect to G3′, as represented on the inset of Fig. 7. The latter figure shows, in the upper panel, the relative energies of the ground and first excited states of the GG^+ dimer, calculated as a function of parameter q. The double well potential energy curve obtained for the ground state results from the configuration mixing, allowed by the multi-configurational approach that has been used. It provides a proper description of the electron transfer, as shown in the lower panel of Fig. 7, where the variation of the percentages of the positive charge located on G5′ and G3′ are plotted as a function of q in the case of the ground state.

The ground state energy curve presents two minima separated by a potential energy barrier. In one minimum, more than 66% of the positive charge is located on G5′ while, in the second, more than 64% of the positive charge is localized on the other guanine, G3′. At the avoided crossing point between the two electronic states, we observe that the positive charge is equally distributed on both bases. We demonstrate thus that the electron migration from one guanine to the other is governed by an avoided crossing occurring between the ground and first excited states of the ionized dimer.

Geometry optimizations are in progress for locating the stationary points along the reaction path describing the electron transfer from one base to the other. These calculations are performed at an improved level of theory. The RASSCF/RASPT2 approach has been chosen for that purpose, with as much as 61 electrons involved in the RASPT2 step. Full geometry optimizations were not carried out, but the more important inter-molecular active parameters have been varied: Two-dimensional slides of G5′ in the plane paral-

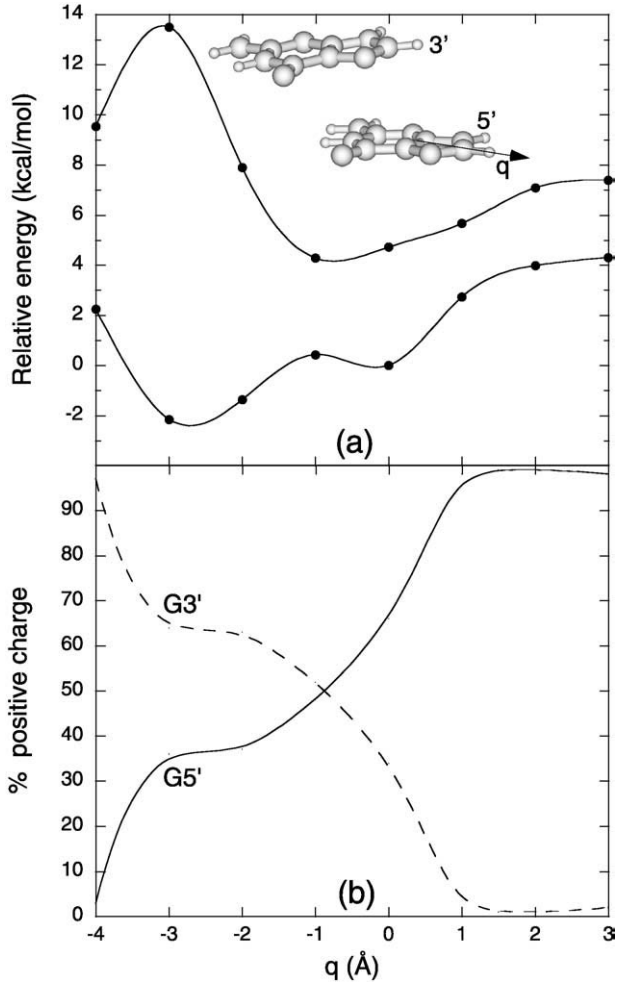

Fig. 7. (a) Relative energies (in kcal/mol) of the ground and first excited states of an ionized stacked dimer of guanines, calculated at CASSCF/MRCI level as a function of the parameter q describing a slide of guanine G5′ with respect to guanine G3′ (see inset). (b) Percentage of the positive charge located on guanine G5′ and guanine G3′ calculated from the ground state wave function as a function of the parameter q.

lel to G3′, the G5′–G3′ distance and the orientation of G5′ with respect to G3′ within its own aromatic plane (twist angle). The calculations confirm that the avoided crossing between the ground and first excited states allows the charge migration within the GG^+ cluster. It is shown in Fig. 8 that the improvement of the level of theory and the geometry relaxation induce an inversion of the energetical ordering of the two minima and an enhancement of the barrier height. Let us also note that the percentages of positive charges on G5′ and G3′ at the minimum geometries are more pure (97% and 72% respectively).

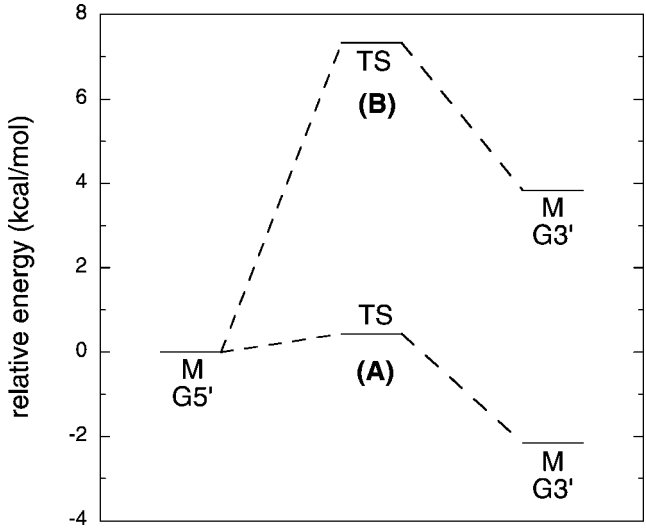

Fig. 8. Relative energies (in kcal/mol) of the stationary points (M for minimum and TS for transition state) along the reaction path describing the charge transfer in a stacked dimer of guanines. Energy profile (A) has been calculated at CASSCF/MRCI level involving 5 active electrons, from the one-dimensional curve of Fig. 7(a). Energy profile (B) has been calculated at the RASSCF/RASPT2 level with 61 correlated electrons, from a partial geometry optimization involving a two-dimensional slide of G5′ with respect to G3′, the G5′–G3′ distance and the twist angle of G5′ with respect to G3′.

5. CONCLUSION

The present review was dedicated to the *ab initio* study of elementary processes related to radiation damage to DNA focusing on the role played by positively charged DNA bases, isolated or embedded in stacked base clusters. It has been pointed out that more theoretical efforts have been made until now in the literature for characterizing the neutral species. More information on the cationic species would however be useful for interpreting many reactive processes related to DNA, in particular in the framework of radiation damage. Such information would also be worthwhile for supporting fragmentation experiments carried out in laboratory [47–49].

The present work first aimed at providing a synthetic overview on state-of-the–art computational methods to be used for studying DNA bases clusters in the framework of radiation damage. The calculation of the ionization potentials of these biomimetic species, the quantum description of the clusters stability, the characterization and the reactivity of the excited cationic states have been reviewed. The crucial role of the excited states in dynamical processes following the attack of the genetic material by ionizing radiations has been put forward. High level quantum chemistry calculations have been shown to be essential for understanding the intricate features of the involved potential energy surfaces. The existence of multiple minima, saddle points and surface crossings, and the topology of the reaction paths connecting them is expected indeed to govern the dynamics occurring on these surfaces. The important role played by avoided crossings and conical intersec-

tions has been stressed. The interest of determining reaction paths on the potential surfaces has also been exemplified by a preliminary study of the electron transfer within a cationic dimer of guanines.

The calculation of accurate values of ionization potentials and the characterization of cationic excited states for a wide variety of bases clusters would be very useful. Stacked and paired clusters should be systematically investigated, first for binary systems, but also for larger clusters.

ACKNOWLEDGEMENTS

The Communauté Française de Belgique (action de recherche concertée, ARC contract), the COST P9 Action and the Belgian National Fund for Scientific Research (I.I.S.N. contract) are acknowledged for financial support. E.C. thanks the Communauté Française de Belgique for a PhD fellowship (ARC).

REFERENCES

[1] C. von Sonntag, *The Chemical Basis for Radiation Biology*, Taylor and Francis, London, 1987.
[2] O.D. Schärer, *Angew. Chem. Int. Ed.* **42** (2003) 2946.
[3] J. Cadet, P. Vigny, in: H. Morrison (Ed.), *Bioorganic Photochemistry*, vol. 1, Wiley, New York, 1990, p. 1.
[4] J. Cadet, M. Berger, T. Douki, J.L. Ravanat, *Rev. Physiol. Biochem. Pharmacol.* **131** (1997) 1.
[5] J. Cadet, *et al.*, *Marcel Dekker Chapter* **8** (2003) 143.
[6] J. Cadet, T. Douki, D. Gasparutto, J.L. Ravanat, *Mutat. Res.* **531** (2003) 5.
[7] C.E. Crespo-Hernández, B. Cohen, P.M. Hare, B. Kohler, *Chem. Rev.* **104** (2004) 1977.
[8] Special Issues of *Eur. Phys. J. D* **20** (3) (2002);
Special Issues of *Phys. Chem. Chem. Phys.* **6** (10) (2004).
[9] F.O. Talbot, J.P. Simons, *Phys. Chem. Chem. Phys.* **4** (2002) 3562.
[10] N. Borho, M.A. Suhm, *Org. Biomol. Chem.* **1** (2003) 4351.
[11] H. Fricke, A. Gerlach, C. Unterberg, P. Rzepecki, T. Schrader, M. Gerhards, *Phys. Chem. Chem. Phys.* **6** (2004) 4636.
[12] R. Linder, M. Nispel, T. Haber, K. Kleinermanns, *Chem. Phys. Lett.* **409** (2005) 260.
[13] N. Morgner, H.-D. Barth, B. Brutschy, *Aust. J. Chem.* **59** (2005) 109.
[14] W. Chin, J.-P. Dognon, C. Canuel, F. Piuzzi, I. Dimicol, I. Compagnon, G. von Helden, G. Meijer, M. Mons, *J. Am. Chem. Soc.* **127** (2005) 1388.
[15] M. Bakker, C. Plützer, I. Hünig, G. von Helden, G. Meijer, T. Häber, K. Kleinermanns, *Chem. Phys. Chem.* **6** (2005) 120.
[16] P. Carçabal, R.A. Jockusch, I. Hünig, L. Snoek, R.T. Kroemer, B.G. Davis, D.P. Gamblin, I. Compagnon, J. Oomens, J. Simons, *J. Am. Chem. Soc.* **127** (2005) 11414.
[17] J.-M.L. Pecourt, J. Peon, B. Kohler, *J. Am. Chem. Soc.* **123** (2001) 10370.
[18] J. Peon, A.H. Zewail, *Chem. Phys. Lett.* **348** (2001) 255.
[19] T. Gustavsson, A. Sharonov, D. Markovitsi, *Chem. Phys. Lett.* **351** (2002) 195.
[20] H. Kang, K.T. Lee, B. Jung, Y.J. Ko, S.K. Kim, *J. Am. Chem. Soc.* **124** (2002) 12958.
[21] H. Kang, B. Jung, S.K. Kim, *J. Chem. Phys.* **118** (2003) 6717.
[22] R.J. Malone, A.M. Miller, B. Kohler, *Photochem. Photobiol.* **77** (2003) 158.
[23] B. Cohen, P.M. Hare, B. Kohler, *J. Am. Chem. Soc.* **125** (2003) 13594.
[24] M. Zierhut, W. Roth, I. Fischer, *Phys. Chem. Chem. Phys.* **6** (2004) 5178.
[25] S. Ullrich, T. Schultz, M.Z. Zgierski, A. Stolow, *J. Am. Chem. Soc.* **126** (2004) 2262.
[26] C. Canuel, M. Mons, F. Piuzzi, B. Tardivel, I. Dimicoli, M. Elhanine, *J. Chem. Phys.* **122** (2005) 074316.
[27] E. Samoylova, H. Lippert, S. Ullrich, I.V. Hertel, W. Radloff, T. Schultz, *J. Am. Chem. Soc.* **127** (2005) 1782.
[28] R. Kakkar, R. Garg, *J. Mol. Struct.: THEOCHEM* **620** (2003) 139.

[29] N. Ismail, L. Blancafort, M. Olivucci, B. Kohler, M.A. Robb, *J. Am. Chem. Soc.* **124** (2002) 6818.
[30] A.L. Sobolewski, W. Domcke, *Eur. Phys. J. D* **20** (2002) 369.
[31] A.L. Sobolewski, W. Domcke, C. Dedonder-Lardeux, C. Jouvet, *Phys. Chem. Chem. Phys.* **4** (2002) 1093.
[32] M. Merchán, L. Serrano-Andrès, *J. Am. Chem. Soc.* **125** (2003) 8108.
[33] S. Perun, A.L. Sobolewski, W. Domcke, *J. Am. Chem. Soc.* **127** (2005) 6257.
[34] S. Perun, A.L. Sobolewski, W. Domcke, *Chem. Phys.* **313** (2005) 107.
[35] M. Merchan, L. Serrano-Andrès, M.A. Robb, L. Blancafort, *J. Am. Chem. Soc.* **127** (2005) 1820.
[36] C. Marian, *J. Chem. Phys.* **122** (2005) 104314.
[37] B. Giese, *Annu. Rev. Biochem.* **71** (2002) 51.
[38] G.B. Schuster (Ed.), Long-Range Charge Transfer in DNA I, *Top. Curr. Chem.* **236** (2004).
[39] G.B. Schuster (Ed.), Long-Range Charge Transfer in DNA II, *Top. Curr. Chem.* **237** (2004).
[40] B. Boudaiffa, P. Cloutier, D. Hunting, M.A. Huels, L. Sanche, *Science* **287** (2000) 1658.
[41] S. Denifl, S. Ptasinska, M. Cingel, S. Matejcik, P. Scheier, T.D. Märk, *Chem. Phys. Lett.* **377** (2003) 74.
[42] S. Denifl, S. Ptasinska, M. Probst, J. Hrusak, P. Scheier, T.D. Märk, *J. Phys. Chem. A* **108** (2004) 6562.
[43] S. Ptasinska, S. Denifl, P. Scheier, T.D. Märk, *J. Chem. Phys.* **120** (2004) 8505.
[44] F. Martin, P.D. Burrow, Z. Cai, P. Cloutier, D. Hunting, L. Sanche, *Phys. Rev. Lett.* **93** (2004) 068101.
[45] H. Abdoul-Carime, S. Gohlke, E. Illenberger, *Phys. Rev. Lett.* **92** (2004) 168103.
[46] T. Solomun, E. Illenberger, *Chem. Phys. Lett.* **96** (2004) 448.
[47] J. de Vries, R. Hoekstra, R. Morgenstern, T. Schlathölter, *Eur. Phys. J. D* **24** (2003) 161.
[48] J. de Vries, R. Hoekstra, R. Morgenstern, T. Schlathölter, *Phys. Rev. Lett.* **91** (2003) 053401.
[49] T. Schlathölter, R. Hoekstra, R. Morgenstern, *Int. J. Mass Spectrom.* **233** (2004) 173.
[50] S. Lacombe, C. Le Sech, V.A. Esaulov, *Phys. Medicine Biol.* **49** (2004) N65.
[51] R. Weinkauf, J.P. Schermann, M.S. de Vries, K. Kleinermanns, *Eur. Phys. J. D* **20** (2002) 309.
[52] P.E. Barran, N.C. Polfer, D.J. Campopiano, D.J. Clarke, P.R.R. Langridge-Smith, R.J. Langley, J.R.W. Govan, A. Maxwell, J.R. Dorin, R.P. Millar, M.T. Bowers, *Int. J. Mass Spectrom.* **240** (2005) 273.
[53] S. Blanco, J.C. Lopez, J.L. Alonso, P. Otavian, W. Caminati, *J. Chem. Phys.* **119** (2003) 880.
[54] R.J. Lavrich, F.J. Lovas, D. Plusquellic, *J. Mol. Spectrosc.* **228** (2004) 251.
[55] A. Lesarri, E.J. Cocinero, J.C. Lopez, J.L. Alonso, *J. Am. Chem. Soc.* **127** (2005) 2572.
[56] A. Lesarri, R. Sanchez, E.J. Cocinero, J.C. Lopez, J.L. Alonso, *J. Am. Chem. Soc.* **127** (2005) 1295.
[57] M. Olivucci (Ed.), *Computational Photochemistry*, Elsevier, Amsterdam, 2004.
[58] W. Domcke, D.R. Yarkony, H. Köppel (Eds.), *Conical Intersections: Electronic Structure, Dynamics and Spectroscopy*, World Scientific, Singapore, 2004.
[59] L. Serrano-Andrés, M. Merchan, in: P.v.R. Schleyer, *et al.* (Eds.), *Spectroscopy: Applications Encyclopedia of Computational Chemistry*, Wiley, New York, 2004.
[60] L. Serrano-Andrés, M. Merchan, *J. Mol. Struct.: THEOCHEM* **729** (2005) 99.
[61] S. Wilson (Ed.), *Molecules in the Physico-Chemical Environment, Spectroscopy, Dynamics and Bulk Properties*, *Handbook of Molecular Physics and Quantum Chemistry*, vol. 3, Wiley, Chichester, 2002.
[62] J. Tomasi, B. Mennucci, R. Cammi, *Chem. Rev.* **105** (2005) 2999.
[63] E. Cauët, D. Dehareng, J. Liévin, *J. Phys. Chem. A* **110** (2006) 9200.
[64] P. Hobza, J. Šponer, *Chem. Rev.* **99** (1999) 3247.
[65] J. Šponer, J. Leszczynski, P. Hobza, *Biopolymers (Nucleic Acid Sci.)* **61** (2002) 3.
[66] J. Šponer, P. Hobza, *Collect. Czechoslovak Chem. Commun.* **68** (2003) 2231.
[67] J. Šponer, J. Leszczynski, P. Hobza, *J. Mol. Struct.: THEOCHEM* **573** (2001) 43.
[68] R. Wintjens, C. Biot, M. Rooman, J. Liévin, *J. Phys. Chem. A* **107** (2003) 6249.
[69] J.C. Ma, D.A. Dougherty, *Chem. Rev.* **97** (1997) 1303.
[70] H. Minoux, C. Chipot, *J. Am. Chem. Soc.* **121** (1999) 10366.
[71] R. Wintjens, J. Liévin, M. Rooman, E. Buisine, *J. Mol. Biol.* **302** (2000) 395.
[72] M. Běgusova, S. Giliberto, J. Gras, D. Sy, M. Charlier, M. Spotheim-Maurizot, *Int. J. Radiat. Biol.* **79** (2003) 385.
[73] N. Gillard, M. Běgusova, B. Castaing, M. Spotheim-Maurizot, *Radiat. Res.* **162** (2004) 566.
[74] J. Gras, D. Sy, S. Eon, M. Charlier, M. Spotheim-Maurizot, *Radiat. Phys. Chem.* **72** (2005) 271.
[75] M. Běgusova, N. Gillard, D. Sy, B. Castaing, M. Charlier, M. Spotheim-Maurizot, *Radiat. Phys. Chem.* **72** (2005) 265.
[76] E.M. Boon, J.K. Barton, *Curr. Opin. Struct. Biol.* **12** (2002) 320.
[77] S.O. Kelley, J.K. Barton, *Science* **283** (1999) 375.
[78] V. Shafirovich, A. Dourandin, W.D. Huang, N.P. Luneva, N.E. Geacintov, *Phys. Chem. Chem. Phys.* **2** (2000) 4399.

[79] F.D. Lewis, X. Zuo, J. Liu, R.T. Hayes, M.R. Wasielewski, *J. Am. Chem. Soc.* **124** (2002) 4568.
[80] S.R. Rajski, B.A. Jackson, J.K. Barton, *Mutat. Res.* **447** (2000) 49.
[81] E.M. Boon, A.L. Livingston, N.H. Chmiel, S.S. David, J.K. Barton, *Proc. Natl. Acad. Sci.* **100** (2003) 12543.
[82] E. Yavin, A.K. Boal, E.D.A. Stemp, E.M. Boon, A.L. Livingston, V.L. O'Shea, S.S. David, J.K. Barton, *Proc. Natl. Acad. Sci.* **102** (2005) 3546.
[83] H.W. Fink, C. Schönenberger, *Nature* **398** (1999) 407.
[84] D. Porath, A. Bezryadin, S. de Vries, C. Dekker, *Nature* **403** (2000) 635.
[85] D. Porath, G. Cuniberti, R. Felice, *Top. Curr. Chem.* **237** (2004) 183.
[86] C. Møller, M.S. Plesset, *Phys. Rev.* **46** (1934) 618.
[87] M. Head-Gordon, J.A. Pople, M.J. Frisch, *Chem. Phys. Lett.* **153** (1988) 503.
[88] R.G. Parr, W. Yang, *Density Functional Theory of Atoms and Molecules*, Oxford Univ. Press, Oxford, 1989.
[89] F. Ban, K.N. Rankin, J.W. Gauld, R.J. Boyd, *Theor. Chem. Acc.* **108** (2002) 1.
[90] X. Xu, W.A. Goddard III, *Proc. Natl. Acad. Sci.* **101** (2004) 2673.
[91] J. Černy, P. Hobza, *Phys. Chem. Chem. Phys.* **7** (2005) 1624.
[92] Y. Zhao, D.G. Truhlar, *Phys. Chem. Chem. Phys.* **7** (2005) 2701.
[93] R.J. Bartlett, *J. Phys. Chem.* **93** (1989) 1697.
[94] J.D. Watts, R.J. Bartlett, *Int. J. Quantum Chem. S* **27** (1993) 51.
[95] P. Hobza, J. Šponer, J. Leszczynski, *J. Phys. Chem. B* **101** (1997) 8038.
[96] J. Šponer, P. Hobza, *Chem. Phys. Lett.* **267** (1997) 263.
[97] S. Tsuzuki, T. Uchimaru, K. Matsumura, M. Mikami, K. Tanabe, *Chem. Phys. Lett.* **319** (2000) 547.
[98] S. Tsuzuki, K. Honda, T. Uchimaru, M. Mikami, K. Tanabe, *J. Am. Chem. Soc.* **124** (2002) 104.
[99] S. Tsuzuki, K. Honda, R. Azumi, *J. Am. Chem. Soc.* **124** (2002) 12200.
[100] J. Pittner, P. Hobza, *Chem. Phys. Lett.* **390** (2004) 496.
[101] O. Christiansen, H. Koch, P. Jørgensen, *Chem. Phys. Lett.* **243** (1995) 409.
[102] O. Christiansen, H. Koch, P. Jørgensen, *J. Chem. Phys.* **103** (1995) 7429.
[103] M. Feyereisen, G. Fitzgerald, A. Komornicki, *Chem. Phys. Lett.* **208** (1993) 359.
[104] O. Vahtras, J. Almlöf, M. Feyereisen, *Chem. Phys. Lett.* **213** (1993) 541.
[105] D.E. Bernholdt, R.J. Harrison, *Chem. Phys. Lett.* **250** (1996) 477.
[106] P. Hobza, J. Šponer, *J. Am. Chem. Soc.* **124** (2002) 11802.
[107] H.B. Schlegel, *J. Chem. Phys.* **84** (1986) 4530.
[108] H.B. Schlegel, *J. Phys. Chem.* **92** (1988) 3075.
[109] J. Bertran, A. Oliva, L. Rodriguez-Santiago, M. Sodupe, *J. Am. Chem. Soc.* **120** (1998) 8159.
[110] C.E. Crespo-Hernández, R. Arce, Y. Ishikawa, L. Gorb, J. Leszczynski, D.M. Close, *J. Phys. Chem. A* **108** (2004) 6373.
[111] J.P. Watts, J. Gauss, R.J. Bartlett, *J. Chem. Phys.* **98** (1993) 8718.
[112] J.B. Foresman, M. Head-Gordon, J.A. Pople, M.J. Frisch, *J. Phys. Chem.* **96** (1992) 135.
[113] F. Jensen, *Introduction to Computational Chemistry*, John Wiley & Sons, Chichester, 1999.
[114] K. Ruedenberg, L.M. Cheung, S.T. Elbert, *Int. J. Quantum Chem.* **16** (1979) 1068.
[115] B.O. Roos, *Int. J. Quantum Chem. Symp.* **175** (1980) 14.
[116] B.O. Roos, P. Taylor, P.E.M. Siegbahn, *Chem. Phys.* **48** (1980) 157.
[117] J. Olsen, B.O. Roos, P. Jorgensen, H.J.A. Jensen, *J. Chem. Phys.* **89** (1998) 2185.
[118] K. Andersson, P.-A. Malmqvist, B.O. Roos, A.J. Sadlej, K. Wolinski, *J. Phys. Chem.* **94** (1990) 5483.
[119] K. Andersson, P.-A. Malmqvist, B.O. Roos, *J. Chem. Phys.* **96** (1992) 1218.
[120] P.J. Knowles, H.J. Werner, *Chem. Phys. Lett.* **145** (1988) 514.
[121] H.J. Werner, P.J. Knowles, *J. Chem. Phys.* **89** (1988) 5803.
[122] J. Oddershede, *Adv. Chem. Phys.* **69** (1987) 201.
[123] M.E. Casida, C. Jamorski, K.C. Casida, D.R. Salahub, *J. Chem. Phys.* **108** (1998) 4439.
[124] J.V. Ortiz, V.G. Zakrzewski, O. Dolgounitcheva, in: J.-L. Calais, E. Kryachko (Eds.), *Conceptual Perspectives in Quantum Chemistry*, Kluwer Academic, Dordrecht, 1997, pp. 465–518.
[125] D.M. Close, *J. Phys. Chem. B* **107** (2003) 864.
[126] S. Knippenberg, K.L. Nixon, H. Mackenzie-Ross, M.J. Brunger, F. Wang, M.S. Deleuze, J.-P. François, D.A. Winkler, *J. Phys. Chem. A* **109** (2005) 9324.
[127] N. Kishimoto, Y. Hagihara, K. Ohno, S. Knippenberg, J.-P. François, M.S. Deleuze, *J. Phys. Chem. A* **109** (2005) 10535.
[128] O. Dolgounitcheva, V.G. Zakrzewski, J.V. Ortiz, *Int. J. Quantum Chem.* **80** (2000) 831.

[129] O. Dolgounitcheva, V.G. Zakrzewski, J.V. Ortiz, *J. Am. Chem. Soc.* **122** (2000) 12304.
[130] O. Dolgounitcheva, V.G. Zakrzewski, J.V. Ortiz, *J. Phys. Chem. A* **106** (2002) 8411.
[131] J.F. Stanton, R.J. Bartlett, *J. Chem. Phys.* **99** (1993) 5178.
[132] H. Koch, P. Jorgensen, *J. Chem. Phys.* **93** (1990) 3333.
[133] J. Šponer, J. Leszczynski, P. Hobza, *J. Phys. Chem.* **100** (1996) 5590.
[134] R.D. Amos, A. Bernhardsson, A. Berning, P. Celani, D.L. Cooper, M.J.O. Deegan, A.J. Dobbyn, F. Eckert, C. Hampel, G. Hetzer, P.J. Knowles, T. Korona, R. Lindh, A.W. Lloyd, S.J. McNicholas, F.R. Manby, W. Meyer, M.E. Mura, A. Nicklass, P. Palmieri, R. Pitzer, Rauhut, M. Schütz, U. Schumann, H. Stoll, A.J. Stone, R. Tarroni, T. Thorsteinsson, H.J. Werner, MOLPRO is a package of ab initio programs designed by H.-J. Werner and P.J. Knowles, version 2002.1.
[135] M.J. Frisch, G.W. Trucks, H.B. Schlegel, G.E. Scuseria, M.A. Robb, J.R. Cheeseman, J.A. Montgomery Jr., T. Vreven, K.N. Kudin, J.C. Burant, J.M. Millam, S.S. Iyengar, J. Tomasi, V. Barone, B. Mennucci, M. Cossi, G. Scalmani, N. Rega, G.A. Petersson, H. Nakatsuji, M. Hada, M. Ehara, K. Toyota, R. Fukuda, J. Hasegawa, M. Ishida, T. Nakajima, Y. Honda, O. Kitao, H. Nakai, M. Klene, X. Li, J.E. Knox, H.P. Hratchian, J.B. Cross, V. Bakken, C. Adamo, J. Jaramillo, R. Gomperts, R.E. Stratmann, O. Yazyev, A.J. Austin, R. Cammi, C. Pomelli, J.W. Ochterski, P.Y. Ayala, K. Morokuma, G.A. Voth, P. Salvador, J.J. Dannenberg, V.G. Zakrzewski, S. Dapprich, A.D. Daniels, M.C. Strain, O. Farkas, D.K. Malick, A.D. Rabuck, K. Raghavachari, J.B. Foresman, J.V. Ortiz, Q. Cui, A.G. Baboul, S. Clifford, J. Cioslowski, B.B. Stefanov, G. Liu, A. Liashenko, P. Piskorz, I. Komaromi, R.L. Martin, D.J. Fox, T. Keith, M.A. Al-Laham, C.Y. Peng, A. Nanayakkara, M. Challacombe, P.M.W. Gill, B. Johnson, W. Chen, M.W. Wong, C. Gonzalez, J.A. Pople, *Gaussian 03, Revision C. 02, Gaussian, Inc., Wallingford CT*, 2004.
[136] J. Šponer, P. Hobza, *J. Phys. Chem.* **98** (1994) 3161.
[137] O. Bludsky, J. Šponer, J. Leszczynski, V. Spirko, P. Hobza, *J. Chem. Phys.* **105** (1996) 11042.
[138] A. Broo, *J. Phys. Chem. A* **102** (1998) 526.
[139] M.K. Shukla, P.C. Mishra, *Chem. Phys.* **240** (1999) 319.
[140] M.K. Shukla, S.K. Mishra, A. Kumar, P.C. Mishra, *J. Comput. Chem.* **21** (2000) 826.
[141] M.K. Shukla, J. Leszczynski, *J. Phys. Chem. A* **106** (2002) 11338.
[142] H. Langer, N.L. Doltsinis, *J. Chem. Phys.* **118** (2003) 5400.
[143] M.T. Nguyen, R. Zhang, P.-C. Nam, A. Ceulemans, *J. Phys. Chem. A* **108** (2004) 6554.
[144] R. Abouaf, J. Pommier, H. Dunet, P. Quan, P.-C. Nam, M.T. Nguyen, *J. Chem. Phys.* **121** (2004) 11668.
[145] N.S. Hush, A.S. Cheung, *Chem. Phys. Lett.* **34** (1975) 11.
[146] V.M. Orlov, A.N. Smirnov, Y.M. Varshavsky, *Tetrahedron Lett.* **48** (1976) 4377.
[147] K.-W. Choi, J.-H. Lee, S.K. Kim, *J. Am. Chem. Soc.* **127** (2005) 15674.
[148] H.-W. Jochims, M. Schwell, H. Baumgärtel, S. Leach, *Chem. Phys.* **314** (2005) 263.
[149] M.D. Sevilla, B. Besler, A.O. Colson, *J. Phys. Chem.* **99** (1995) 1060.
[150] R. Improta, G. Scalmani, V. Barone, *Int. J. Mass Spectrom.* **201** (2000) 321.
[151] S.D. Wetmore, R.J. Boyd, L.A. Eriksson, *Chem. Phys. Lett.* **322** (2000) 129.
[152] D.M. Close, *J. Phys. Chem. A* **108** (2004) 10376.
[153] V. Gomzi, J.N. Herak, *J. Mol. Struct.: THEOCHEM* **683** (2004) 155.
[154] D.M. Close, C.E. Crespo-Hernández, L. Gorb, J. Leszczynski, *J. Phys. Chem. A* **110** (2006) 7485.
[155] I.N. Ragazos, M.A. Robb, F. Bernardi, M. Olivucci, *Chem. Phys. Lett.* **197** (1992) 217.
[156] M.J. Bearpark, M.A. Robb, H.B. Schlegel, *Chem. Phys. Lett.* **223** (1994) 269.
[157] P. Hobza, H.L. Selzle, E.W. Schlag, *J. Am. Chem. Soc.* **116** (1994) 3500.
[158] J. Šponer, J. Leszczynski, P. Hobza, *J. Phys. Chem.* **100** (1996) 1965.
[159] S. Tsuzuki, T. Uchimaru, M. Mikami, K. Tanabe, *Chem. Phys. Lett.* **252** (1996) 206.
[160] J. Šponer, H.A. Gabb, J. Leszczynski, P. Hobza, *Biophys. J.* **73** (1997) 76.
[161] J. Šponer, P. Hobza, *J. Phys. Chem. A* **104** (2000) 4592.
[162] N. Kurita, K. Kobayashi, *Comput. Chem.* **24** (2000) 351.
[163] N. Kurita, M. Araki, K. Nakao, K. Kobayashi, *Int. J. Quantum Chem.* **76** (2000) 677.
[164] M. Elstner, P. Hobza, T. Frauenheim, S. Suhai, E. Kaxiras, *J. Chem. Phys.* **114** (2001) 5149.
[165] M. Rooman, J. Liévin, E. Buisine, R. Wintjens, *J. Mol. Biol.* **319** (2002) 67.
[166] C. Biot, E. Buisine, J.-M. Kwasigroch, R. Wintjens, M. Rooman, *J. Biol. Chem.* **277** (2002) 40816.
[167] R.R. Toczylowski, S.M. Cybulski, *J. Phys. Chem. A* **107** (2003) 418.
[168] S. Grimme, *J. Comput. Chem.* **25** (2004) 1463.
[169] J. Šponer, P. Jurecka, P. Hobza, *J. Am. Chem. Soc.* **126** (2004) 10142.
[170] N. Kurita, V.I. Danilov, V.M. Anisimov, *Chem. Phys. Lett.* **404** (2005) 164.

[171] P. Mignon, S. Loverix, P. Geerlings, *Chem. Phys. Lett.* **401** (2005) 40.
[172] P. Mignon, S. Loverix, J. Steyaert, P. Geerlings, *Nucleic Acids Res.* **33** (2005) 1779.
[173] A. Olasz, P. Mignon, F. De Proft, T. Veszprémi, P. Geerlings, *Chem. Phys. Lett.* **407** (2005) 504.
[174] S. Tsuzuki, T. Uchimaru, M. Mikami, K. Tanabe, *J. Phys. Chem. A* **102** (1998) 2091.
[175] S. Tsuzuki, H.P. Lüthi, *J. Chem. Phys.* **114** (2001) 3949.
[176] M.O. Sinnokrot, E.F. Valeev, C.D. Sherrill, *J. Am. Chem. Soc.* **124** (2002) 10887.
[177] M.O. Sinnokrot, C.D. Sherrill, *J. Phys. Chem. A* **108** (2004) 10200.
[178] B.K. Mishra, N. Sathyamurthy, *J. Phys. Chem. A* **109** (2005) 6.
[179] S.F. Boys, F. Bernardi, *Mol. Phys.* **19** (1970) 553.
[180] J.G.C.M. van Duijneveldt-van de Rijdt, F.B. Van Duijneveldt, *J. Mol. Struct.: THEOCHEM* **89** (1982) 185.
[181] L.M.J. Kroon-Batenburg, F.B. Van Duijneveldt, *J. Mol. Struct.: THEOCHEM* **121** (1985) 185.
[182] E. Cauët, M. Rooman, R. Wintjens, J. Liévin, C. Biot, *J. Chem. Theory Comput.* **1** (2005) 472.
[183] P. Mignon, S. Loverix, F.D. Proft, P. Geerlings, *J. Phys. Chem. A* **108** (2004) 6038.
[184] H. Sugiyama, I. Saito, *J. Am. Chem. Soc.* **118** (1996) 7063.
[185] F. Prat, K.N. Houk, C.S. Foote, *J. Am. Chem. Soc.* **120** (1998) 845.
[186] I. Saito, T. Nakamura, K. Nakatani, Y. Yoshioka, K. Yamaguchi, H. Sugiyama, *J. Am. Chem. Soc.* **120** (1998) 12686.
[187] Y. Yoshioka, Y. Kitagawa, Y. Takano, K. Yamaguchi, T. Nakamura, I. Saito, *J. Am. Chem. Soc.* **121** (1999) 8712.
[188] S. Schumm, M. Prévost, D. Garcia-Fresnadillo, O. Lentzen, C. Moucheron, A. Kirsch-De Mesmaeker, *J. Phys. Chem. B* **106** (2002) 2763.
[189] A.O. Colson, B. Besler, D.M. Close, M.D. Sevilla, *J. Phys. Chem.* **96** (1992) 661.
[190] M. Hutter, T. Clark, *J. Am. Chem. Soc.* **118** (1996) 7574.
[191] X. Li, Z. Cai, M.D. Sevilla, *J. Phys. Chem. B* **105** (2001) 10115.
[192] X. Li, Z. Cai, M.D. Sevilla, *J. Phys. Chem. A* **106** (2002) 9345.
[193] E. Cauët, J. Liévin, in preparation.
[194] E. Meggers, M.E. Michel-Beyerle, B. Giese, *J. Am. Chem. Soc.* **120** (1998) 12950.
[195] J. Jortner, M. Bixon, T. Langenbacher, M.E. Michel-Beyerle, *Proc. Natl. Acad. Sci. USA* **95** (1998) 12759.

Charge Exchange and Fragmentation in Slow Collisions of He^{2+} with Water Molecules

N. Stolterfoht[1,2], R. Cabrera-Trujillo[2], R. Hellhammer[1], Z. Pešić[1], E. Deumens[2], Y. Öhrn[2] and J.R. Sabin[2]

[1] *Hahn-Meitner Institut, Glienickerstraße 100, D-14109 Berlin, Germany*
[2] *Quantum Theory Project, Departments of Physics and Chemistry, University of Florida, Gainesville, FL 32611-8435, USA*

Abstract

Cross sections for charge exchange and fragmentation in the collision system $He^{2+} + H_2O$ are investigated experimentally and theoretically at projectile energies of a few keV. Different experimental methods analyzing scattered projectiles, fragment ions and ejected photons are reviewed. Scattered and fragment ions were measured in the angular range from 25° to 135° with respect to the incident beam direction. The spectra provide evidence for the fragmentation mechanisms of Coulomb explosion and binary collisions. Emphasis is given to protons originating from collisions at large impact parameters involving the Coulomb explosion mechanism. Cross sections for proton ejections, differential in the observation angle $d\sigma/d\Omega$, are found to be anisotropic with a maximum near 90°. The theoretical investigation is carried out within the Electron–Nuclear Dynamics approach to take into account the coupling of the electrons and nuclei. The method is based on the evolution of a coherent state representation of the supermolecule wavefunction within the time-dependent variational principle. We calculate differential and total cross sections for the scattering of the projectile, charge transfer, and fragmentation of the system products. We find good agreement with the experimental data. In particular, we find that double electron capture occurs for impact parameters below 3.0 a.u. and produces full fragmentation of H_2O independent of the target orientation.

Contents

ADVANCES IN QUANTUM CHEMISTRY, VOLUME 52
ISSN: 0065-3276 DOI: 10.1016/S0065-3276(06)52007-6

1. INTRODUCTION

The interaction between multi-charged ions and molecular targets is of great interest in various research areas ranging from astrophysics, radiation damage in biological tissues, to plasma physics. In astrophysics, collisions between bare ions in the solar wind and neutral gas molecules take place in the interstellar medium [1–4]. At speeds typical for the solar wind (a few hundred km/s), electron capture by the projectile becomes the predominant process. The resulting X-ray emission [3,4] is strongly connected to stellar wind parameters, such as mass loss, wind velocities, and ion composition. These parameters are needed in the stellar evolution models. Alpha particles are one of the most abundant species in the solar wind. Consequently, collisions between He^{2+} ions and molecules play an important role in most of the scenarios where solar wind interacts with cometary atmospheres.

Recently, Greenwood *et al.* [5] reported on measurement of single and double electron capture into alpha particles from molecules relevant in cometary atmospheres. By inclusion of data from other laboratories Greenwood *et al.* [5] provided recommended cross sections for alpha particle impact whose absolute values are of relatively high accuracy. In the analysis of the cometary atmospheres, water molecules play an important role. This is due to the fact that during the approach of a comet to the sun, near-surface ice starts to sublimate, forming large clouds consisting mainly of water vapor.

Information about the interaction of alpha particles with H_2O molecules is also important for radiation damage in biological systems [6]. Since most of the energy deposited in human tissues by ion impact is absorbed by water molecules, spectra showing dissociation products of biological molecules can be interpreted by taking into account the initial interaction of the ion beam with the surrounding H_2O molecules. Hence, there is an increasing interest in fragmentation studies of the H_2O molecules. Fragments such as $OH^{\bullet}$ radicals play a dominant role in the production of single- and double-strand breaks of DNA molecules. In this context, absolute fragmentation cross sections are needed for collision systems involving water molecules.

Experimental studies of fragmentation of molecules other than H_2O have been focused on, e.g., H_2 [7–13], HD^+ [14], CO_2 [15], NO_2 [16], and CH_4 [17]. Some studies [12,13] have revealed post-collision effects by the scattered projectile, which result in an enhanced emission of fragments in the backward direction, as predicted theoretically [18,19]. Moreover, anisotropic angular distributions of the protons from fragmented H_2 have been attributed to quantum interference effects due to the identical H centres in H_2 [9] and to capture probabilities dependent of the molecular orientation [18].

In recent years, several experimental studies have been devoted to fragmentation of H_2O in collisions with singly [20–23] and multi-charged ions [24–31]. Multiple electron capture can be identified to good approximation from the energies of the detected fragment ions. Fragments originating from the Coulomb explosion (CE) of the ionized target, as well as from quasi binary collisions, have been observed. The slow fragments, whose energy does not exceed 50 eV, originate from CE of the ionized target following electron removal at intermediate impact parameters. On the other hand, violent binary collisions involving small impact parameters produce fast fragments whose energies are well determined by two-body kinematics.

From the theoretical point of view, fragmentation processes of H_2 by multi-charged ions have been investigated by means of classical Monte Carlo methods [18,19,32].

Molecular fragmentation studies using quantum theory are facing the difficulty in simultaneously treating the full coupling of the electronic and nuclear degrees of freedom. For multi-electron systems the theoretical treatments for studying molecular fragmentation are still limited. Of those, the Car–Parinello method [33], which is based on the dynamics on a single potential energy surface, has been applied to molecular fragmentation of water in ice [34]. The cleavage of HDO on OD and OH induced by double ionization by fast F^{7+} ions has been studied in a wave-packet propagation in a numerical grid [31]. Also, studies of fragmentation of DNA produced by low energy electrons, based on the electronic structure of the molecular system, has been carried out [35,36].

In the present work, processes of electron capture and fragmentation in slow collisions of He^{2+} with H_2O molecules are investigated. The purpose of this study is to compare experimental results with detailed quantum-mechanical calculations in order to gain an insight into the complex mechanisms involved in the interaction of a multi-charged ion with a water molecule. The article is structured as follows: In Section 2 we review different experimental methods and give examples of acquired spectra. In Section 3, we provide a resumé of our theoretical approach, and in Section 4 we compare experimental and theoretical results in the following order: (i) differential cross sections, (ii) total cross sections, and (iii) fragmentation. In the experimental sections primarily previous work is reviewed, whereas in the theoretical sections new results are presented.

2. EXPERIMENTAL METHODS

In the following, experimental methods from different laboratories investigating reactions in the collision system $He^{2+} + H_2O$ are reviewed. Single electron capture into $2p$ and $3p$ orbitals of helium gives rise to photon emission, which is measured using the method of photon emission spectroscopy (PES). Due to dipole selection rules, with this method it is difficult to measure electron capture into other orbitals, e.g., $1s$, $2s$, $3s$, or $3d$. The population of these states can be accessed by means of translational energy spectroscopy (TES) in which the energy loss or gain of the projectile is measured with high resolution. The capture into the $1s$ orbital liberates potential energy of the helium ion, which results in the removal of another electron from the water molecule. This transfer ionization (TI) as well as double capture (DC) leads to doubly ionized water molecules, which are likely to dissociate [37,38]. The fragmentation products are measured using the method of fragment ion spectroscopy (FIS). Thus, each experimental method has its specific merits so that combined results provide a rather broad picture of the experimental scenario.

The FIS method will be described in more detail here, since the analysis of fragment ions plays a particular role in this work. It should be noted that in the experiments two isotopes of helium were utilized. In the following, we use the notation He^{2+} when the measurements are performed with alpha particles. When the measurements are performed with helium isotopes of mass 3 we use the notation $^3He^{2+}$. We expect that the results are practically the same for different helium isotopes of equal velocities. Therefore, in the following, the projectile energy is specified in keV/amu, if not otherwise stated. The energies of the fragment ions are given in eV.

2.1. Fragment ion spectroscopy

Fragment ion spectroscopy was performed with $^3He^{2+}$ projectiles at the Ionenstrahllabor (ISL) in the Hahn–Meitner Institut (HMI), Berlin. The helium ions were extracted from a 14.5-GHz Electron Cyclotron Resonance (ECR) ion source in an energy range from 0.33 to 1.66 keV/amu (1 to 5 keV). The collision chamber used in the experiments is shown in Fig. 1. Low beam energies were achieved by means of electrostatic deceleration of the $10q$ keV ions before entering the scattering chamber, where q is the ionic charge state. The $^3He^{2+}$ ion beam was directed to a water vapor target beam ejected from an effusive jet of 1 mm inner diameter. Recoil ions resulting from fragmentation were detected by an electrostatic ion spectrometer [39,30], which consists of parallel plates in which a homogeneous electric field is produced. By varying this field, spectra representing the number of fragment ions as a function of their energy divided by the final charge state are acquired. The angular range of observation was 20°–135° with respect to the incident beam direction. The measured spectra were normalized to the ion beam collected in a Faraday cup.

In the chamber, the background pressure was of $\sim 2 \times 10^{-7}$ mbar. During the experiment, the H_2O vapor pressure was kept below 10^{-6} mbar in the chamber to achieve single collision conditions. Particular care was taken to ensure a high purity H_2O target [26]. To extract absolute cross sections, the pressure in the interaction volume has been normalized to data obtained when the chamber was filled with vapor of homogeneous pressure by moving the gas nozzle up far away from the collision center [39,30]. Fragmentation products H^+ were detected with energies larger than $\sim$ 3 eV and O^+ (or OH^+) with energies smaller than $\sim$ 3 eV. The water vapor pressure of 10^{-6} mbar was sufficiently low to avoid secondary collisions with H^+ travelling from the target region to the detector. However, the slow heavy particles O^+ and OH^+ may have still been influenced by secondary collisions, therefore the oxygen peak was not further analyzed. Fig. 2 shows a typical ion spectrum for the system $^3He^{2+} + H_2O$, in this case obtained for a detection angle of 25° at 2 keV. Two

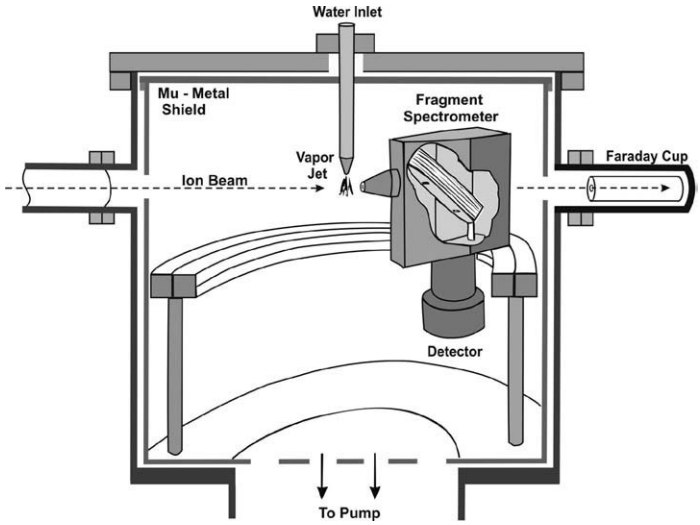

Fig. 1. Experimental chamber used in the experiments of fragment ion spectroscopy at HMI, Berlin [27,30].

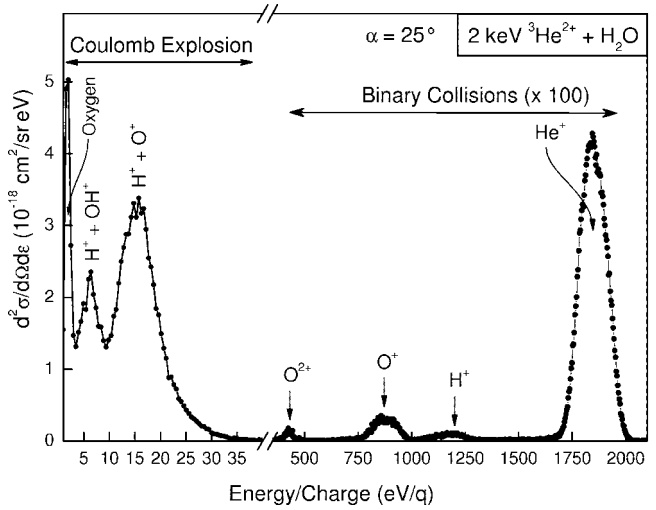

Fig. 2. Spectrum of scattered and fragment ions produced in collisions of 2 keV $^3He^{2+}$ on H_2O. Two energy regions corresponding to the processes of Coulomb explosion and binary collisions are distinguished (see text). Note that the intensity of the peaks corresponding to binary collisions was multiplied by a factor of 100. From Sobocinski *et al.* [27].

distinct peak groups are observed at forward scattered angles. The peaks located at energies lower than $\sim$ 35 eV are due to doubly-ionized water molecules produced in soft collisions, whereas the highly energetic fragments originate from quasi binary collisions [26].

The peaks located between 1 eV and $\sim$ 30 eV are interpreted to be a result of a of Coulomb explosion (CE). When two electrons from the molecule are suddenly removed by the incident ion, the residual $(H_2O)^{2+}$ molecule dissociates into charged and/or neutral particles. Then, knowing the initial separation of the atoms in the H_2O molecule, one can estimate the kinetic energies of the fragmentation products. The ejected H^+ ions give rise to the peaks labeled $H^+ + OH^+$ and $H^+ + O^+$ which correspond to the 2-body breakup of the water molecule into H^+–OH^+ and the 3-body breakup into H^+–H^0–O^+, respectively, as further discussed below.

In Fig. 2 the group of peaks located between 500 eV and 2 keV is a signature of events involving a violent collision with one of the atomic centers of the water molecule. In this case, the projectile transfers significant energy to a single atom of the H_2O molecule. The resulting fragments O^+ and H^+ and scattered $^3He^+$ projectiles are mainly detected at forward angles with relatively high kinetic energies. It is noted that the electrostatic spectrometer selects charged particles characterized by the ratio of the energy and the final charge of the detected ion. It should also be pointed out that due to the difference of masses, recoil energy of the proton is significantly larger than that of the oxygen.

2.2. Translational energy spectrometry

The results from two laboratories using translational energy spectrometry, TES, are relevant to the discussion here. At Queens University Belfast (QUB), measurements were

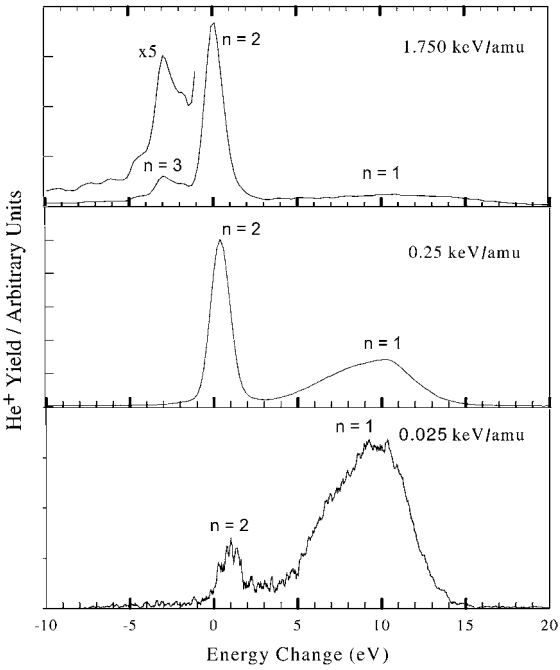

Fig. 3. Results of TES experiments for different projectile energies. The data acquired with projectile energies of 1.75 and 0.25 keV/amu originate from QUB and the 0.025 keV/amu spectrum was measured at WMU. The experimental results were combined by Sereduyk *et al.* [28].

carried out in the energy range 0.25 to 2 keV/amu while at Western Michigan University (WMU) measurements were carried out in the energy range 0.025 to 0.375 keV/amu. In the case of the QUB experiment, He^{2+} ions (i.e., alpha particles) were produced by an ECR ion source while the WMU experiment employed a recoil ion source. Full details of the spectrometers and measurement procedure used at QUB and WMU have been given in previous publications by Kearns *et al.* (2002) [40], and by Kamber *et al.* [41], respectively.

The TES method relies on careful measurements of the difference between the kinetic energy of the He^{2+} primary ion and the fast He^{+} product ion that is scattered in a cone of forward angles. The angular acceptance of the product ion energy analyzer was $\pm 3°$ for the QUB measurements and $\pm 8°$ for the WMU measurements. The energy resolution is 1 eV (FWHM).

Fig. 3 shows three representative energy change spectra from the QUB and WMU translational energy spectrometers. Analysis of the position and magnitude of the peaks in the observed energy change spectra enables identification and determination of the relative contribution of each product channel. In Fig. 3 the peaks are labeled by the principle quantum number $n = 1$, 2, and 3 of the He^{+} orbitals into which an electron is captured. Energy levels for the relevant H_2O^{+} states and their associated vibrational energy distributions were obtained from the photoelectron spectroscopy measurements of Reutt *et al.* [42], and for the H_2O^{2+} states from the photo ion–photo-ion coincidence measurements of Richardson *et al.* (1986) [43].

The TES spectra have been integrated to obtain cross sections for electron transfer as discussed further below. To determine absolute cross sections from the QUB data, the sum of the relative yields of the individual capture processes resulting in He^+ ($n = 1$), He^+ ($n = 2$) and He^+ ($n = 3$) formation were normalized to the recommended total one electron capture cross sections of Greenwood *et al.* [5]. The WMU data for He^+ ($n = 1$) and He^+ ($n = 2$) formation were determined from absolute measurements of the target pressures and detector efficiencies.

We note significant energy differences associated with the 3 peaks seen in Fig. 3. For $n = 2$ and 3, respectively, an energy loss of ~ 3 eV and a slight energy gain of $\lesssim 1$ eV is achieved. These energy shifts are equal to the corresponding Q values associated with the single-electron capture processes involved. For $n = 1$ the projectile gains a considerable energy of ~ 10 eV. This value originates from the relatively high potential energy of the incident He^{2+}. The energy of 54 eV, liberated when an electron is captured into the $n = 1$ level, is shared between the projectile and target. The energy of 44 eV, given to the target, is primarily used to remove two electrons from the H_2O molecule in a transfer-ionization process. The remaining energy of 10 eV, given to the projectile, results in an increase of its kinetic energy. Hence, the transfer-ionization process populating the $n = 1$ level is a striking example for a super-elastic collision.

2.3. Photon emission spectroscopy

Other relevant measurements, using Photon Emission Spectroscopy, PES, have been performed at KVI in Groningen. In the experiments an He^{2+} ion beam extracted from an ECR ion source was crossed with a neutral gas jet as has been reported by Lubinski *et al.* [44]. The projectile energy range was between 1.5 and 12 keV/amu. A VUV spectrometer (5–80 nm) was used to measure the photon emission spectra produced by charge exchange into the projectile. Absolute wavelength and sensitivity calibration of the VUV system was achieved by cross-reference to previous measurements on systems with well-known cross sections as described, e.g., by Hoekstra *et al.* [45]. The spectrometer is equipped with a position sensitive detector allowing for the simultaneous detection of wavelength window of approximately 20 nm.

Two representative spectra for collisions between He^{2+} and water vapor are shown in Fig. 4. The spectra are dominated by the HeII ($2p$–$1s$) line emission. Note that the HeII Lyman series is observed in second order. Therefore, the HeII ($2p$–$1s$) and HeII ($3p$–$1s$) appear at 60.4 nm and 51.2 nm, respectively. Emission from higher He^+ (np) states is detected around 48 nm. The TES spectra have been integrated to obtain cross sections for single-electron transfer into np states of He^+. They are presented further below in comparison with the results of the other laboratories.

3. THEORETICAL APPROACH

Our theoretical approach to analyze the fragmentation of water molecules by swift $^3He^{2+}$ ions is based on the application of the Time-Dependent Variational Principle to the Schrödinger equation, where the wave function is described in a coherent state representation. This method is called Electron–Nuclear Dynamics (END). As the details of the END

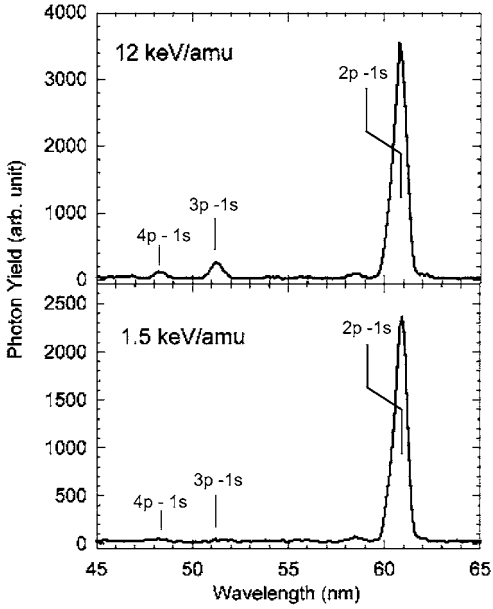

Fig. 4. Photon emission spectra produced by one-electron capture at different energies in $He^{2+}+H_2O$ collisions. The peaks are due to transitions np–$1s$ with $n = 2$, 3, and 4. The measurements are performed at KVI in Groningen. From Ref. [28].

method have been reported elsewhere [46], we give only a brief summary of the fundamental features of the theory.

The END theory [46] is based on a system wave function

$$\big|\psi(t)\big\rangle = \big|R(t),\, P(t)\big\rangle\big|z(t),\, R(t),\, P(t)\big\rangle, \tag{1}$$

characterized by a set of time-dependent parameters and a choice of basis set. The first factor on the right corresponds to the nuclear wave function

$$\big\langle X|R(t),\, P(t)\big\rangle = \prod_k \exp\left[-\frac{1}{2}\left(\frac{\mathbf{X}_k - \mathbf{R}_k}{w}\right)^2 + i\mathbf{P}_k\cdot(\mathbf{X}_k - \mathbf{R}_k)\right] \tag{2}$$

for distinguishable nuclei $\mathbf{X}_k = (X_{1k}, X_{2k}, X_{3k})$, and the time-dependent average position $\mathbf{R}_k = (R_{1k}, R_{2k}, R_{3k})$ and average momentum $\mathbf{P}_k = (P_{1k}, P_{2k}, P_{3k})$ of nucleus k. In this product, the traveling Gaussians have a common width parameter w. The second factor on the right-hand side in equation (1) corresponds to the electronic wave function (for N electrons)

$$\big\langle x\big|z(t),\, R(t),\, P(t)\big\rangle = \det\big\{\chi_i(\mathbf{x}_j)\big\}, \tag{3}$$

where the complex, non-orthogonal spin orbitals are expressed as

$$\chi_i = u_i + \sum_{j=N+1}^{K} u_j z_{ji}, \quad i = 1, 2, \ldots, N. \tag{4}$$

The atomic spin orbitals $\{u_j\}_1^K$ are represented in terms of a linear combination of traveling Gaussian basis functions of the form

$$(x - R_{1k})^l (y - R_{2k})^m (z - R_{3k})^n \exp\left[-\alpha(\mathbf{x} - \mathbf{R}_k)^2 - \frac{i}{\hbar}\mathbf{P}_k \cdot (\mathbf{x} - \mathbf{R}_k)\right], \tag{5}$$

centered on the average nuclear position $\mathbf{R}_k$ and moving with momentum $\mathbf{P}_k$. Equations (3) and (4) for the electronic wave function describe a Thouless determinant [47] with time-dependent complex Thouless coefficients $z_{ji}(t)$. Application of the time-dependent variational principle to the action produced by the quantum mechanical Lagrangian $L = \langle\psi|i\hbar\frac{\partial}{\partial t} - H|\psi\rangle/\langle\psi|\psi\rangle$, with H the system Hamiltonian combined with the Euler–Lagrange equations

$$\frac{d}{dt}\frac{\partial L}{\partial \dot{q}} = \frac{\partial L}{\partial q}, \tag{6}$$

produces the equation of motion of the dynamic variables, q, of the system. The dynamic variables q for this level of END theory are the complex Thouless coefficient z_{ph}, z^*_{ph} and the Cartesian components of the average nuclear positions and momenta R_{jk}, P_{jk}, in the limit of the width parameter $w \to 0$ (classical nuclei). In matrix form, one obtains

$$\begin{bmatrix} i\mathbf{C} & \mathbf{0} & i\mathbf{C}_R & i\mathbf{C}_P \\ \mathbf{0} & -i\mathbf{C}^* & -i\mathbf{C}^*_R & -i\mathbf{C}^*_P \\ i\mathbf{C}^\dagger_R & -i\mathbf{C}^T_R & \mathbf{C}_{RR} & -\mathbf{I} + \mathbf{C}_{RP} \\ i\mathbf{C}^\dagger_P & -i\mathbf{C}^T_P & \mathbf{I} + \mathbf{C}_{PR} & \mathbf{C}_{PP} \end{bmatrix} \begin{bmatrix} \dot{\mathbf{z}} \\ \dot{\mathbf{z}}^* \\ \dot{\mathbf{R}} \\ \dot{\mathbf{P}} \end{bmatrix} = \begin{bmatrix} \partial E/\partial \mathbf{z}^* \\ \partial E/\partial \mathbf{z} \\ \partial E/\partial \mathbf{R} \\ \partial E/\partial \mathbf{P} \end{bmatrix}, \tag{7}$$

where the dynamic metric contains the coupling elements

$$(C_{XY})_{ik;jl} = -2\,\mathrm{Im}\,\frac{\partial^2 \ln S}{\partial X_{ik}\partial Y_{jl}}\bigg|_{R'=R,\,P'=P}, \tag{8}$$

$$(C_{X_{ik}})_{ph} = (C_X)_{ph;ik} = \frac{\partial^2 \ln S}{\partial z^*_{ik}\partial X_{ik}}\bigg|_{R'=R,\,P'=P}, \tag{9}$$

$$C_{ph;qg} = \frac{\partial^2 \ln S}{\partial z^*_{ph}\partial z_{qg}}\bigg|_{R'=R,\,P'=P}, \tag{10}$$

and where

$$E = \sum_k \frac{P_k^2}{2M_k} + \frac{\langle z, R|H_{el}|R, z\rangle}{\langle z, R|R, z\rangle}, \tag{11}$$

is the total energy of the system. Here H_{el} the electronic Hamiltonian which contains the nuclear–nuclear repulsion potential energy.

In equations (7), one can discern the usual adiabatic coupling terms $\mathbf{C}_{RR}$ and nonadiabatic coupling terms $\mathbf{C}_R$.

Integration of the system of equations (7) yields trajectories of classical nuclei "dressed" with electron nuclear dynamics which in its minimal representation is implemented into the *ENDyne* program package [48].

3.1. Calculation details

The END approach requires specification of the initial conditions of the system. The target water molecule is initially placed with the oxygen atom at the origin of a Cartesian laboratory coordinate system with orientation specified by the Euler angles α, β, and γ [see Fig. 5]. The initial projectile velocity is set parallel to the z axis and directed towards the target with an impact parameter, b in the x–z plane. The $^3He^{2+}$ projectile starts 15 a.u. from the target, and the trajectory is evolved until the projectile is 120 a.u. past the target, which is the approximated time for the fragmentation to occur for a projectile energy of 5 keV. For lower energies, the propagation time was extended in accordance with the dynamics. In the case of atomic projectiles, as in this case, we need to consider the initial orientations of the target only (*vide infra*).

In order to obtain orientational averaged properties, we require to perform a target rotation over the Euler angles respect to the incoming beam. A coarse set is obtained for increments of 90° in all the three angles with a minimum number of ten independent target orientations for a molecule of C_{2v} symmetry. The ten basic target orientations place the molecular bond along the xy-, yz-, and xz-plane. In Table 1, we label these ten orientations.

In this study, the molecular target is initially in its electronic ground state ($\bar{X}^1A_1$) and equilibrium geometry, as computed in the given basis at the SCF level. The basis functions used for the atomic orbital expansion are derived from those optimized by Dunning [49, 50]. For the hydrogen atoms, the basis set consists of [$5s2p$/$5s2p$] with the addition of a diffuse s and p orbital for a better description of the long range interaction. The exponent of these orbitals follow an even-tempered sequence to avoid linear dependencies. For the

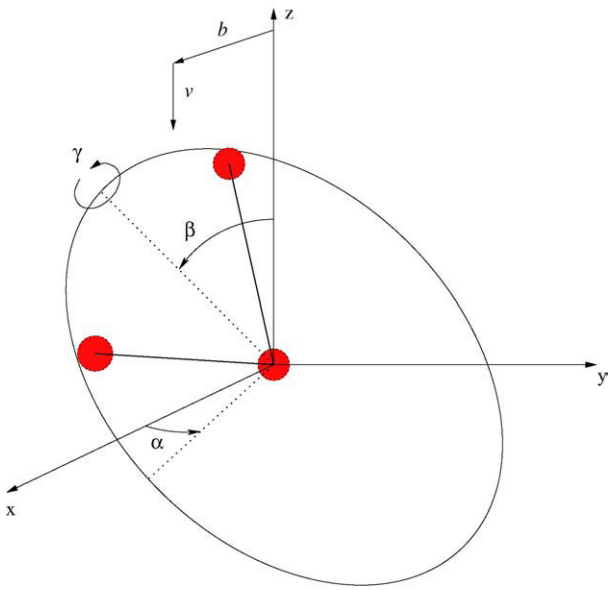

Fig. 5. Schematic representation of the space fixed molecular coordinate frame that represents the projectile and target orientations.

Table 1. Water molecule orientation in the space fixed axis system

I1	$(\alpha = 0,$	$\beta = 0,$	$\gamma = 0)$
I2	$(\alpha = 0,$	$\beta = 0,$	$\gamma = \pi/2)$
IIa1	$(\alpha = 0,$	$\beta = \pi/2,$	$\gamma = 0)$
IIa2	$(\alpha = \pi/2,$	$\beta = \pi/2,$	$\gamma = 0)$
IIa3	$(\alpha = 3\pi/2,$	$\beta = \pi/2,$	$\gamma = 0)$
IIb1	$(\alpha = 0,$	$\beta = \pi/2,$	$\gamma = \pi/2)$
IIb2	$(\alpha = \pi/2,$	$\beta = \pi/2,$	$\gamma = \pi/2)$
IIb3	$(\alpha = 3\pi/2,$	$\beta = \pi/2,$	$\gamma = \pi/2)$
III1	$(\alpha = 0,$	$\beta = \pi,$	$\gamma = 0)$
III2	$(\alpha = 0,$	$\beta = \pi,$	$\gamma = \pi/2)$

atomic oxygen we use a $[10s5p/3s2p]$ basis, and for the description of the electron capture by $^3He^{2+}$, we use a basis set consisting of $[5s2p/3s3p]$. We assign values to the impact parameter from 0.0 to 15.0 a.u. which we separate in three regions. For close collisions, from 0.0 to 4.0 a.u., we use steps of 0.1 a.u. For the intermediate region, from 4.0 to 6.0 a.u., we use steps of 0.2 a.u., and for $b > 6.0$, we use steps of 1.0. This give us 60 fully dynamic trajectories for each target orientation and projectile energy.

4. EXPERIMENTAL AND THEORETICAL RESULTS

4.1. Scattering of the projectile

In the following, we present theoretical cross sections for projectile scattering by water molecules differential with respect to the observation angle. The cross sections were calculated for various scattering angles ranging from values as small as 0.01° to values as large as 100°. The lower limit of the angular range corresponds to large impact parameters and thus soft collisions involving weak perturbations. In contrast, large scattering angles correspond to small impact parameters involving binary collisions of the projectile with a single target atom. Generally, for instrumental reasons, it is not possible to cover the whole range of scattering angles so that experimental results are available only for a restricted range. After the presentation of the theoretical results we shall describe an experiment involving small impact parameters that can be associated with binary collisions in a good approximation.

4.1.1. Differential cross sections

In soft collisions, quantum interferences become important due to collisions with different target atoms leading to the same scattering angle (analogous to rainbow and glory scattering). As a consequence of the classical description of the dynamics of the nuclei, semiclassical corrections are needed to take into account quantum interference effects. We have implemented [51] the Schiff approximation [52] for small scattering angles, to account for the quantum effects of forward scattering (long range interactions, large impact parameters).

The advantage of the Schiff approximation over some others, as for example, the eikonal, Airy or uniform approximations, is that it considers all the terms of the Born series and

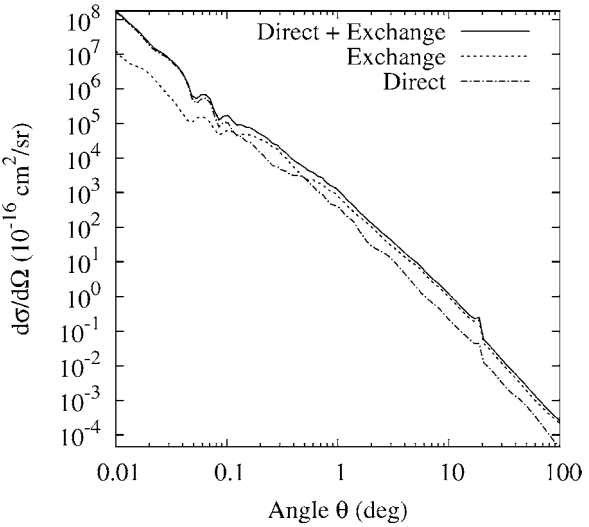

Fig. 6. Differential cross sections for scattering of 5 keV $^3He^{2+}$ from H_2O molecules. The results labeled *Direct + Exchange* include all final charge states of the projectile. The results labeled *Exchange* include the transfer of one and two electrons. The results labeled *Direct* refer to collisions without charge exchange.

treats the rainbow and glory angles in a single approach. To implement the Schiff approximation, the deflection function, $\Theta(b)$, i.e. the projectile scattering angle as a function of the impact parameter, for each orientation of the molecular target is required. We use the calculated deflection function in the Schiff approximation and average over molecular orientations [53].

In Fig. 6, we show the orientationally averaged differential scattering cross section for $^3He^{2+}$ colliding with water molecules for 5 keV as a function of the laboratory angle. For scattering up to 10°, we use the Schiff approximation, and for larger angles, we use the classical differential cross section. The results show a variation of several orders of magnitude. In the region of small scattering angles the data show wiggles, which are the results of quantum interference effects produced by effects analogous to rainbow and glory scattering.

In the same figure, we show the exchange (single + double electron capture) and the direct differential cross section as a function of the laboratory scattering angle. For scattering angles less than 1°, we note that more than one order of magnitude difference exists between the exchange and the direct cross section, showing the small probability of electron capture at large impact parameters. For larger angles, the contrary is true. For this energy, $\theta \sim 1°$ correspond to $b \sim 3$ a.u. This shows that single and double electron capture are predominant at large scattering angles or intermediate to small impact parameters.

4.1.2. Binary collisions

To allow for a comparison between the theoretical results and experimental data, we analyze quasi binary collisions. As noted, collisions for impact parameters near an atomic center, can be considered as binary collisions where the interaction between the projectile

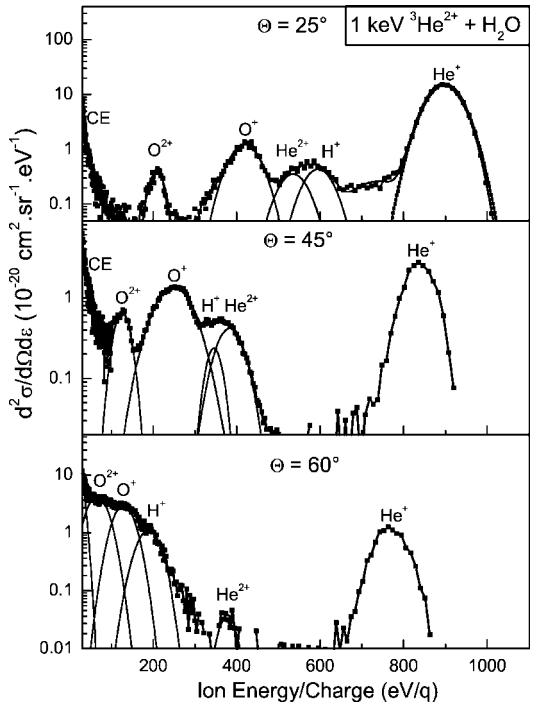

Fig. 7. Energy distributions of fragments ejected in $^3He^{2+}+H_2O$ collisions. The projectile energy is 1 keV and the observation angles are 25°, 45° and 60°. The experimental spectra are fitted by means of Gaussian curves. The spectral structures are dominated by fast helium ions scattered in binary collisions. From Sobocinski *et al.* [27].

and a single atomic particle of the molecular target dominates. Hence, violent $He^{2+}+H_2O$ collisions can be treated using the formalism of two-body kinematics. Applying the energy and momentum conservation rules for a two-body inelastic collision, one obtains the standard relation between the energy E_r of a target recoil and the observation angle θ. Similar relation are given for the energy E_p of the projectile as the function of the angle θ (e.g. [54]). Using these kinematic expressions, the peak structures in the measured spectra can be identified.

Fig. 7 shows the high-energy part of the spectra obtained at 25°, 45° and 60° for a projectile energy of 1 keV [27]. For each observation angle, the charged projectiles $^3He^+$ and $^3He^{2+}$ are detected, as well as the fragment ions O^+, O^{2+} and H^+. (We recall that neutral particles cannot be detected since the electrostatic spectrometer is sensitive only to ions.) The kinetic energies of these ions decrease with detection angle. Note that the most energetic peak always corresponds to the scattered projectiles. At 25° and 45°, the main contribution originates from $^3He^+$ ions, while at 60° the structure due to oxygen recoil ions becomes dominant.

As expected from two-body kinematics, the cross sections for scattered $^3He^{2+}$ and $^3He^+$ projectiles decrease with increasing detection angle, whereas recoil ions originating from the target (H^+, O^+, O^{2+}) are mainly emitted at larger angles (close to 60°). Cross sections for the production of singly charged ions ($^3He^+$, O^+) are significantly larger than those

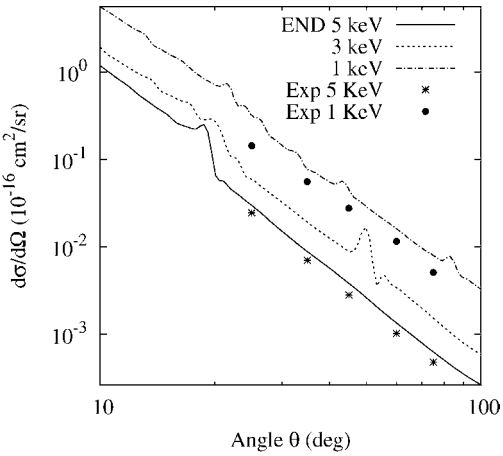

Fig. 8. Differential cross sections for scattering of $^3He^{2+}$ from H_2O molecules. The experimental data [27] contain the final projectiles $^3He^{2+}$ and $^3He^{+}$ involving zero and one-electron transfer, respectively. The theoretical results also include neutral ^3He resulting from double electron transfer into non-autoionizing states (see text).

associated with the corresponding doubly charged ions ($^3He^{2+}$, O^{2+}), i.e. by a factor of ~ 30 in the case of scattered helium ions and by a factor of ~ 5 for oxygen fragments. For angles larger than 70°, both structures due to CE and binary collisions start to overlap.

After integration of the spectra over the energy ϵ, cross sections $d\sigma_{if}/d\Omega$, differential in the observation angle, were determined from

$$\frac{d\sigma_{if}}{d\Omega} = \int \frac{d\sigma_{if}}{d\Omega\, d\varepsilon} d\varepsilon, \tag{12}$$

where i and f denotes the initial and final charge state of the ion (scattered projectile or fragment ions). In Fig. 8, the sum of measured cross sections $d\sigma_{21}/d\Omega + d\sigma_{22}/d\Omega$ for projectile scattering are compared with the theoretical results. It is seen that the experimental results are systematically lower by about 20–30% than the theoretical cross sections. These deviations lie somewhat outside the experimental uncertainties.

It should be pointed out that the theoretical cross sections contain a contribution of neutral projectiles (that cannot be observed in the experiment). Note that the 5 keV data are the same as those labeled *Direct + Exchange* in Fig. 6. We recall that the cross section $d\sigma_{22}/d\Omega$ refers to scattering where the projectile does not change its charge state (referred to as direct scattering). The cross section $d\sigma_{21}/d\Omega$ involves single capture and, in addition, contributions of double capture into autoionizing states, such as $2s\,np$. However, the contribution of double capture into non-autoionizing states (e.g., $1s\,np$) results in neutral projectiles. Hence, it is likely that the deviations between theory and experiment is explained by the missing contribution of neutral projectiles.

In any case, from the near agreement of experiment and theory in Fig. 8 we may conclude that the contribution into non-autoionizing states is not significant. Recalling the transfer-ionization process discussed above, it appears that the potential energy release due to the $1s$ capture into the projectile causes primarily the ionization and not the capture of an additional electron.

4.2. Total cross section for charge exchange

Total cross sections for charge exchange are obtained, when the differential cross sections with the label *exchange*, presented in the previous sections, are integrated over the scattering angle. It should be kept in mind that the theoretical cross sections includes mechanisms involving the capture of one and two electrons. The experiments, described in the preceding paragraph, provide differential cross sections which distinguish between the number of captured electrons. However, the angular range is limited so that total cross sections cannot be determined from this type of experiments. In this section, total cross sections are extracted from the measurements of ion and photon emission spectra, which include a summation over the full angular range of the projectile. The experiments provide additional information for single-electron capture and transfer ionization, as they determine the state into which the electron is captured. In the following, the experimental results for state selective capture are discussed first. Then, total cross sections are compared with theoretical results obtained by the END approach.

4.2.1. State selective electron capture

In Fig. 9, the state selective experimental cross sections for single-electron transitions into the $n = 2$ and $n = 3$ levels of He^+ are shown in the left-hand graph. The cross sections for transfer into the $n = 1$ level accompanied by ionization of a second electron are depicted in the right-hand graph. The data labeled DC + TI refer to cross sections including dou-

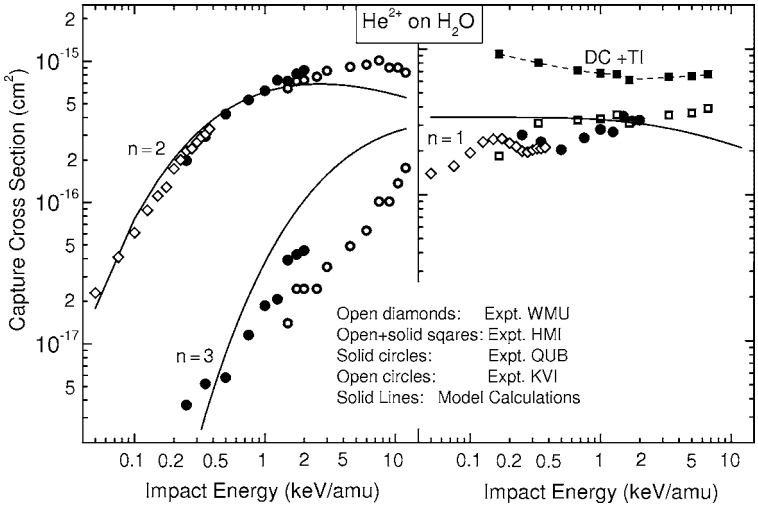

Fig. 9. Cross sections for electron capture into He^{2+} in collisions with H_2O. The left-hand graph refers to single electron transfer into $n = 2$ and 3. The right-hand graph refers to transfer-ionization populating $n = 1$. The data labeled DC + TI include double capture and transfer ionization. Open diamonds represent data from WMU, open and solid squares originate from HMI, solid circles are from QUB, and open circles are from KVI. The solid lines are estimates using the Landau–Zener model for $n = 1$ and that by Demkov for $n = 2$ and 3. The cross sections are given in Ref. [28].

ble capture and transfer ionization. The experimental data are compared with calculations performed using the well-known models by Landau–Zener [55,56] and Demkov [57] as described previously [28].

To convert the PES data for HeII($2p$–$1s$) into cross sections for the formation of He^+ ($n = 2$) the population of the $2s$ level is assumed to follow statistical rules, i.e., it is set to be proportional to the number of final states. In the overlap region of collision energies, the PES data agree well with the TES results. In the case of He^+ ($n = 3$) formation, cross sections are obtained using both the TES and PES techniques. As in the case of $n = 2$, the He^+ ($3p$–$1s$) emission cross sections have been converted into total $n = 3$ capture cross sections using statistical rules. The agreement in the overlap region is reasonable.

In the case of the capture channel resulting in He^+ ($n = 1$), the experimental results were obtained using the TES and FIS techniques. Again there is good agreement between the data from different laboratories in the region where they overlap. The FIS results, which also include information about the double capture process (see the data labeled TI + DC), will be discussed in more detail in a later section. We recall that the $n = 1$ population results from transfer-ionization where the capture into the $1s$ orbital is accompanied by an additional ionization. We emphasize that the transfer-ionization process is caused by the electron–electron interaction similarly to that for an Auger transition [28].

From Fig. 9, it is seen that the cross sections for single capture ($n = 2$ and 3) and transfer ionization ($n = 1$) involve different energy dependencies. The probabilities for mono-electronic capture into the levels $n = 2$ and 3 increase with increasing projectile energy. This is due to the fact that the transitions are produced by dynamic coupling effects initiated by the nuclear–electron interaction, which requires kinetic energy from the collision partners. On the contrary, the cross section for dielectronic transitions of transfer ionization is nearly constant. Since the dielectronic mechanism is produced by the electron–electron interaction as the Auger effect, it does not require kinetic energy from the collision partners. Rather, it loses importance when the collision time decreases, i.e., when the projectile energy increases.

The cross sections, summed over the n values, can be compared with the recommended total cross sections of Greenwood *et al.* [5]. The agreement is excellent in the region of overlap of the two sets of data. However, at energies below 0.2 keV/amu the measurements fall below the results by Greenwood *et al.* [5]. The origin of this discrepancy is not known at present. It is noted, however, that the uncertainties of the cross section data increase significantly for projectile energies below about 0.2 keV/amu.

4.3. Electron capture cross sections

From the foregoing comparison of the total cross sections from different laboratories, we are confident that the cross sections recommended by Greenwood *et al.* [5] can be used as a standard for verification of theoretical results. In the following, the total cross section for electron capture, obtained by summing the recommended data for single and double capture, are compared with equivalent results from the END approach obtained from the Mulliken population analysis [58,59]. In this analysis the electron density in a multinuclear system is partitioned for negligible overlap between atomic orbitals on different product fragments as discussed in Ref. [60].

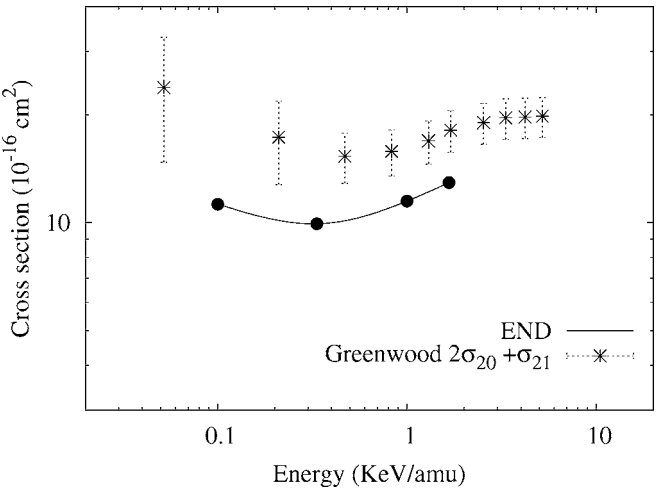

Fig. 10. Cross section sum for single and double electron capture by He^{2+} colliding with H_2O. The experimental data (crosses) are from Greenwood *et al.* [5].

For a given projectile energy, we determine the total cross section for charge exchange from

$$\sigma_{\text{exch}}(E_p) = \int n(b, E_p) b\, db\, d\phi, \tag{13}$$

where $n(b, E_p)$ is the average number of electrons in the projectile as given by the Mulliken population analysis. Thus, if P_{21} and P_{20} are the probabilities for one and two electron capture, respectively, then $n = 2P_{20} + P_{21}$ and therefore $\sigma_{\text{exch}} = 2\sigma_{20} + \sigma_{21}$.

In Fig. 10, we compare our orientationally averaged total cross section for electron capture (for one and two electrons) with the recommended experimental values of Greenwood [5] as a function of the projectile energy. We note that our results are in fair agreement with the experimental data.

4.4. Mechanisms for fragmentation

4.4.1. Fragmentation spectra

As pointed out above, two different primary processes lead to a dissociative state of the H_2O target: Double capture (DC) of electrons into the excited states such as $1s2l$ and $2l2l$ of the projectile, as well as transfer-ionization (TI) involving the transfer into the $n = 1$ level of the He^+ ion [26,28]. Both processes give rise to a doubly charged target molecule $(H_2O)^{2+}$, which is likely to dissociate into charged and/or neutral particles. Fig. 11 shows typical ion spectra for the system $^3He^{2+} + H_2O$ for an impact energy of 4 keV. The detection angles are 45°, 90°, and 135°, as indicated in the spectra. We note that these spectra were used to derive the total cross sections given in Fig. 9 (see also the data labeled DC + TI).

In this subsection we focus on the angular distribution of the proton emission. The observed peaks are primarily interpreted within the framework of a Coulomb explosion of

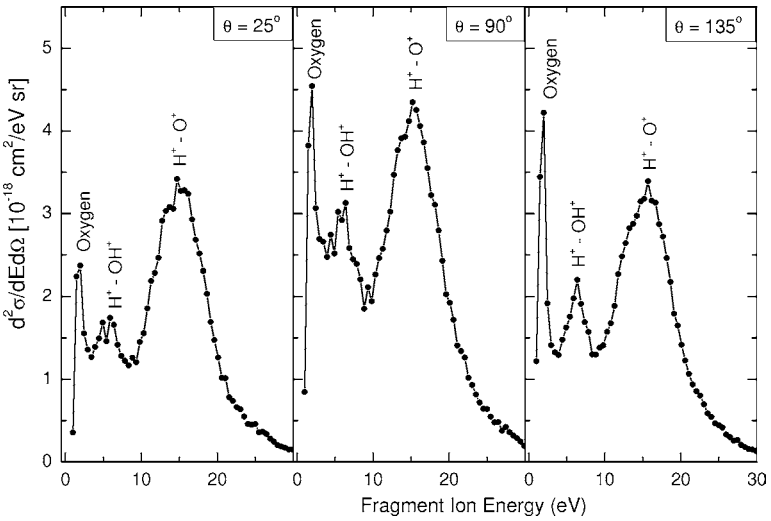

Fig. 11. Energy distributions of fragment ions ejected in 4 keV $^3He^{2+}$+H_2O collisions. Except for the peak labeled *Oxygen*, the spectra are due to the fragment product H^+. Observation angles are 25°, 90°, and 135° as indicated in the graphs. The spectra are taken from Ref. [30].

the ionized target. In addition, the spectral structures were identified using previous results from detailed coincidence measurements [29,43]. In Fig. 11 the following channels are identified as

Peak labeled Oxygen: $H_2O^{2+} \rightarrow \mathbf{O}^+ + H^+ + H^0$ or $\mathbf{OH}^+ + H^+$
Peak labeled H^+–OH^+: $H_2O^{2+} \rightarrow \mathbf{H}^+ + OH^+$ (or $\mathbf{H}^+ + H^+ + O^0$),
Peak labeled H^+–O^-: $H_2O^{2+} \rightarrow \mathbf{H}^+ + O^+ + H^0$.

The fragments contributing to each peak are in bold face and noted first. In accordance with previous studies [43], the peaks centered at 6 eV and 15 eV are attributed to H^+ fragments from the dissociation channels $H^+ + OH^+$ and $H^+ + O^+ + H^0$, respectively. The dissociation channel $H^+ + H^+ + O^0$, which also gives rise to H^+ fragments near 5 eV has been observed to be weak [43]. Double capture plus ionization, leading to H^+ fragments from the dissociation channels $H^+ + O^+ + H^+$ and $H^+ + O^{2+} + H$, have been observed at 18 eV [29] and 28 eV [26], respectively. It should be added that single capture accompanied by excitation may lead to dissociation of H_2O^{+*} ions, which results in the emission of H^+ ions with energies near 3.5 eV [29], which does not appear to be a significant fragmentation channel (Fig. 11).

4.4.2. Angular distribution of the ejected protons

Absolute cross sections, $d\sigma/d\Omega$, differential in the emission angle of the proton, were obtained from a deconvolution and integration of the spectra measured in the FIS experiments. The results for the differential cross section are shown in Fig. 12. The cross section decreases (slightly) with increasing impact energy. More important, at all energies, the protons are preferentially emitted at angles near 90°, where the cross sections are $\sim$ 50%

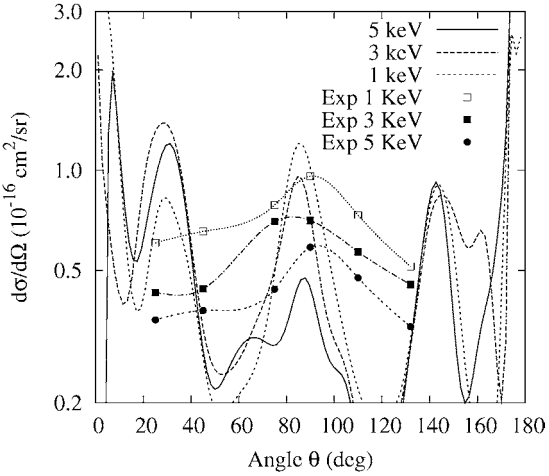

Fig. 12. H^+ fragments ejected in $^3He^{2+}+H_2O$ collisions. The projectile energies are 0.33, 1, and 1.66 keV/amu as indicated. The theoretical results are obtained with a restricted number of molecular orientations.

higher that those measured at 25° and 135°. Some mechanisms for the anisotropic proton emission such as quantum interferences and alignment effects have been considered in previous work [9,18,30]. However, at present, the origin of this anisotropic angular distribution is not fully understood.

To analyze possible mechanisms responsible for the observed angular distribution of the ejected protons we performed END calculations for the fragmentation of the water molecules. From the electron capture probabilities as a function of the impact parameter, we note that the removal of two-electrons from the water molecule is most probable for impact parameters $b \lesssim 3.0$ a.u (corresponding to scattering angles $\Theta \gtrsim 1°$ for 5 keV). Accordingly, the dissociation of the water molecule is dominant in this impact parameter range, which includes part of the CE processes and the binary collisions. By determining the scattering angle, and final kinetic energy of the fragments, we calculate the classical differential cross section for fragmentation of the H^+ from water.

The angular distribution of the H^+ fragments is shown in Fig. 12. There, we note that the H^+ are ejected perpendicular to the incoming beam due to kinematic recoil during the collision. This finding is in qualitative agreement with the experimental observation. Hence, the calculations appear to confirm the experimental observation of enhanced 90° emission of the protons. However, we also note distinct peaks in the angular distribution of H^+ at angles of $\sim 40°$ and $\sim 130°$ with respect to the projectile beam. These maxima are barely observed in the experimental results. We assume that the peaks in the theoretical results are produced by effects due to the coarse target orientation grid. The choice of the minimal set of orientations fortuitously places the OH bond at roughly 45° and 90° respect to the beam, for the dissociation of OH. A more details study with a finer orientational grid is required in order to make clear conclusion on the mechanism of dissociation of OH. This is work in progress.

5. CONCLUSIONS

We investigate charge transfer and fragmentation in collisions of doubly-charged helium with H_2O as a function of the incident energy. Information about collisions of multi-charged ions with water molecules are of great importance for several adjunct fields such as astrophysics, health physics, and biophysics. The fragmentation products from water molecules are expected to be precursors for the creation of life. On the other hand, reactive radicals originating from water fragmentation may cause single and double strand breaks of DNA molecules and, thus, destroying genetic information in living cells.

A variety of instrumental methods are reviewed demonstrating that the experiments yield a comprehensive set of data that can be used as a standard for further studies. In particular, they provide a useful tool to verify theoretical results. Quantum calculations solving the time-dependent Schrödinger equation are time consuming, since they involve the dynamics of both the electrons and nuclei. Since for multi-electron targets, quantum calculations are rare within the field of slow ion–molecule collisions, a comparison with experiment appears to be mandatory.

Using the END method, we calculated differential as well as total cross sections for the projectile scattering and charge exchange in good agreement with the experimental results. The calculations are performed with a discrete set of molecular orientations. From the agreement of the theoretical and experimental capture cross sections, we may conclude that the limited number of molecular orientations is adequate for the evaluation of the present capture cross sections. This gives confidence that the END code is a suitable tool to predict reliable cross sections for complex ion–molecule collisions relevant for astrophysical and biological systems.

Particular attention is devoted to protons ejected in fragmentation of the water molecules. Experimentally, it is found that the proton angular distribution exhibits a pronounced maximum near 90°. This observation is qualitatively confirmed by the theoretical results. However, the calculated 90° maximum is found to be more distinct than the experimental maximum. Furthermore the theory exhibits maxima at angles other than 90° which are barely seen in the measured angular distributions. This finding suggests that the theoretical reproduction of detailed experimental features require a finer grid of molecular orientations. We expect that further studies are needed to investigate the influence of the finite grid size. In particular, to obtain information about the projectile state into which the electron is captured, we plan future work by projection of the electronic wave function on specific final states.

ACKNOWLEDGEMENTS

One of us (N.S.) would like to thank Thomas Schlathölter, Bob McCullough, Ronnie Hoekstra, and Belá Sulik for very helpful communications. E.D. and Y.O. acknowledge the support of NSF grant 0513386.

REFERENCES

[1] C.M. Lisse, *et al.*, *Science* **274** (1996) 205.

[2] T.E. Cravens, *Geophys. Res. Lett.* **24** (1997) 105.
[3] V. Kharchenko, A. Dalgarno, *J. Geophys. Res.* **105** (2000) 18.
[4] J.B. Wargelin, J.J. Drake, *Astrophys. J.* **546** (2001) L57.
[5] J.B. Greenwood, R.S. Mawhorter, I. Čadež, J. Lozano, S.J. Smith, A. Chutjian, *Phys. Scr. T* **110** (2004) 358.
[6] J.E. Biaglow, in: M.A. Farhataziz, J. Rodgers (Eds.), *Radiation Chemistry: Principles and Applications*, VCH, New York, 1987, p. 527.
[7] G. Bishof, F. Linder, *Z. Phys. D* **1** (1986) 303.
[8] F.B. Yousif, B.G. Lindsay, C.J. Latimer, *J. Phys. B: At. Mol. Opt. Phys.* **21** (1988) 4157.
[9] Z. Cheng, C.L. Cocke, V. Frohne, E.Y. Kamber, J.H. McGuire, Y. Wang, *Phys. Rev. A* **47** (1993) 3923.
[10] A. Remscheid, B.A. Huber, K. Wiesmann, *Nucl. Instrum. Methods Phys. Res. Sect. B* **98** (1995) 257.
[11] F. Frémont, C. Bedouet, M. Tarisien, L. Adoui, A. Cassimi, A. Dubois, J.-Y. Chesnel, X. Husson, *J. Phys. B: At. Mol. Opt. Phys.* **33** (2000) L249.
[12] P. Sobocinski, J. Rangama, J.-Y. Chesnel, M. Tarisien, L. Adoui, A. Cassimi, X. Husson, F. Frémont, in: J. Duggan (Ed.), *Conference on Accelerators and their Application in Research and Industry, AIP Conf. Proc.* **576** (2001) 114–117.
[13] P. Sobocinski, J. Rangama, G. Laurent, L. Adoui, A. Cassimi, J.-Y. Chesnel, A. Dubois, D. Hennecart, X. Husson, F. Frémont, *J. Phys. B: At. Mol. Opt. Phys.* **35** (2002) 1353.
[14] I. Ben-Itzhak, E. Wells, K.D. Carnes, V. Krishnamurthi, O.L. Weaver, B.D. Esry, *Phys. Rev. Lett.* **85** (2000) 58.
[15] M. Tarisen, L. Adoui, F. Frémont, D. Lelièvre, L. Guillaume, J.-Y. Chesnel, H. Zhang, A. Dubois, D. Mathur, K. Sanjay, M. Krishnamurthy, A. Cassimi, *J. Phys. B: At. Mol. Opt. Phys.* **33** (2000) L11.
[16] H.O. Folkerts, R. Hoekstra, R. Morgenstern, *Phys. Rev. Lett.* **77** (1996) 3339.
[17] I. Ben-Itzhak, K.D. Carnes, D.T. Johnson, P.J. Norris, O.L. Weaver, *Phys. Rev. A* **49** (1994) 881.
[18] C.R. Feeler, C.J. Wood, R.E. Olson, *Phys. Scr.* **59** (1999) 106.
[19] C.R. Feeler, R.E. Olson, R.D. DuBois, T. Schlathölter, O. Hadjar, R. Hoeksra, R. Morgenstern, *Phys. Rev. A* **60** (1999) 2112.
[20] U. Werner, K. Beckord, J. Becker, H.O. Folkerts, H.O. Lutz, *Nucl. Instrum. Methods Phys. Res. Sect. B* **98** (1995) 385.
[21] F. Gobet, B. Farizon, M. Farizon, M.J. Gaillard, M. Carr, M. Lezius, P. Scheier, T.D. Märk, *Phys. Rev. Lett.* **86** (2004) 3751.
[22] F. Gobet, S. Eden, B.C. B, J. Tabet, B. Farizon, M. Farizon, M.J. Gaillard, M. Carr, O. S, T.D. MärkTD, P. Scheier, *Phys. Rev. A* **70** (2004) 062716.
[23] H. Luna, E.C. Montenegro, *Phys. Rev. Lett.* **94** (2005) 0043201.
[24] U. Werner, K. Beckord, J. Becker, H.O. Lutz, *Phys. Rev. Lett.* **74** (1995) 1962.
[25] O. Abu-Haija, E.Y. Kamber, S.M. Ferguson, *Nucl. Instrum. Methods Phys. Res. Sect. B* **205** (2003) 634.
[26] Z.D. Pešić, J.-Y. Chesnel, R. Hellhammer, B. Sulik, N. Stolterfoht, *J. Phys. B: At. Mol. Opt. Phys.* **37** (2004) 1405.
[27] P. Sobocinski, Z.D. Pešić, R. Hellhammer, N. Stolterfoht, B. Sulik, S. Legendre, J.-Y. Chesnel, *J. Phys. B: At. Mol. Opt. Phys.* **38** (2005) 2495.
[28] B. Sereduyk, R.W. McCullough, H. Tawara, D. Bodewits, R. Hoekstra, R. Morgenstern, N. Stolterfoht, Z.D. Pesic, P. Sobocinsk, R. Hellhammer, H.B. Gilbody, *Phys. Rev. A* **71** (2005) 022705.
[29] F. Alverado, R. Hoekstra, T. Schlathölter, *J. Phys. B: At. Mol. Opt. Phys.* **38** (2005) 4085.
[30] P. Sobocinski, Z.D. Pešić, R. Hellhammer, D. Klein, B. Sulik, J.-Y. Chesnel, N. Stolterfoht, *J. Phys. B: At. Mol. Opt. Phys.* **39** (2006) 927.
[31] A.M. Sayler, M. Leonard, K.D. Carnes, R. Cabrera-Trujillo, B.D. Esry, I. Ben-Itzhak, *J. Phys. B* **39** (2006) 1701.
[32] C.J. Wood, R.E. Olson, *Phys. Rev. A* **59** (2001) 1317.
[33] R. Car, M. Parrinello, *Phys. Rev. Lett.* **55** (1985) 2471.
[34] B. Brena, D. Nordlund, M. Odelius, H. Ogasawara, A. Nilsson, L.G.M. Pettersson, *Phys. Rev. Lett.* **93** (2004) 148302.
[35] I. Anusiewicz, J. Berdys, M. Sobczyk, P. Skurski, J. Simons, *J. Phys. Chem. A* **108** (2004) 11381.
[36] J. Berdys, P. Skurski, J. Simons, *J. Phys. Chem. B* **108** (2004) 5800.
[37] P.R. Bunker, O. Bludsky, P. Jensen, S.S. Wesolowski, T.J. Van Huis, Y. Yamaguchi, H.F. Schaefer III, *J. Mol. Spectrosc.* **198** (1999) 371.
[38] K. Nobusada, K. Tanaka, *J. Chem. Phys.* **112** (2000) 7437.
[39] N. Stolterfoht, C.C. Havener, R.A. Phaneuf, J.K. Swenson, S.M. Shafroth, *Phys. Rev. Lett.* **57** (1986) 74.

[40] D.M. Kearns, R.W. McCullough, H.B. Gilbody, *J. Phys. B: At. Mol. Opt. Phys.* **35** (2002) 4335.
[41] E.Y. Kamber, O. Abu-Haija, S.M. Ferguson, *J. Phys. B: At. Mol. Opt. Phys.* **65** (2002) 062717.
[42] J.E. Reutt, L.S. Wang, Y.T. Lee, D.Y. Shirley, *J. Chem. Phys.* **85** (1986) 6928.
[43] P.J. Richardson, J.H.D. Eland, P.G. Fournier, D.L. Cooper, *J. Chem. Phys.* **84** (1986) 3189.
[44] G. Lubinski, Z. Juhász, R. Morgenstern, R. Hoekstra, *Phys. Rev. Lett.* **86** (2001) 616.
[45] R. Hoekstra, F.J. de Heer, R. Morgenstern, *J. Phys. B: At. Mol. Opt. Phys.* **24** (1991) 4025.
[46] E. Deumens, A. Diz, R. Longo, Y. Öhrn, *Rev. Mod. Phys.* **66** (1994) 917.
[47] D.J. Thouless, *Nucl. Phys.* **21** (1960) 225.
[48] E. Deumens, T. Helgaker, A. Diz, H. Taylor, J. Oreiro, B. Mogensen, J.A. Morales, M.C. Neto, R. Cabrera-Trujillo, D. Jacquemin, *ENDyne version 2.8 Software for Electron Nuclear Dynamics, Quantum Theory Project*, University of Florida, Gainesville, FL 32611-8435, 2000.
[49] T.H. Dunning, *J. Chem. Phys.* **90** (1989) 1007.
[50] D.E. Woon, T.H. Dunning, *J. Chem. Phys.* **100** (1994) 2975.
[51] R. Cabrera-Trujillo, J.R. Sabin, Y. Öhrn, E. Deumens, *Phys. Rev. A* **61** (2000) 032719.
[52] L.I. Schiff, *Phys. Rev.* **103** (1956) 443.
[53] D. Jacquemin, J.A. Morales, E. Deumens, Y. Öhrn, *J. Chem. Phys.* **107** (1997) 6146.
[54] E.W. McDaniel, J.B.A. Mitchell, M.E. Rudd, Atomic Collisions. Heavy Particle Projectiles, Wiley, New York, 1993.
[55] C.D. Landau, *J. Phys. (Moscow)* **2** (1932) 46.
[56] C. Zener, *Proc. R. Soc. A* **137** (1932) 696.
[57] Y.N. Demkov, *Zh. Eksp. Teor. Fiz.* **49** (1963) 195.
[58] R.S. Mulliken, *J. Chem. Phys.* **23** (1955) 1833.
[59] R.S. Mulliken, *J. Chem. Phys.* **23** (1955) 1841.
[60] R. Cabrera-Trujillo, Y. Öhrn, E. Deumens, J.R. Sabin, *Phys. Rev. A* **62** (2000) 052714.

How Very Low-Energy (0.1–2 eV) Electrons Cause DNA Strand Breaks

Jack Simons

Chemistry Department, University of Utah, Salt Lake City, UT 84112, USA
E-mail: simons@chemistry.utah.edu
URL: http://simons.hec.utah.edu

Abstract

Our recent theoretical and others' experimental findings are overviewed concerning the mechanisms by which very low-energy (0.1–2 eV) free electrons attach to DNA and cause strong (ca. 4 eV) covalent bonds to break. The computational tools needed to deal with the metastable shape resonance anions that arise in these processes are discussed and illustrations of their applications to the particular case of DNA damage are provided. Our primary conclusions are that (i) attachment to base π^* orbitals in the above energy range most likely results in cleavage of sugar-phosphate C–O σ bonds, (ii) the rates of C–O bond cleavage can be as high as 10^{10} s^{-1}, and (iii) bond cleavage initiated by electron attachment to phosphate P=O π bonds is less likely involved. The experiments that motivated our theoretical work are discussed as are later experimental findings that confirm our predictions about the nature of the electron attachment event and about which bonds break when strand breaks form.

Contents

1. INTRODUCTION

In the past few years, the author's research group has been involved in [1–5] using electronic structure theory to characterize mechanisms by which electrons with kinetic energies in the 0.1 to 2 eV range attach to and subsequently fragment strong chemical bonds (e.g., having dissociation energies near 4 eV) in DNA. Our work in this area was inspired by very novel experimental findings [6] from the Sanche group in which strand breaks in dried (i.e., having only the structural water molecules intact) DNA were produced by electrons having

ADVANCES IN QUANTUM CHEMISTRY, VOLUME 52
ISSN: 0065-3276 DOI: 10.1016/S0065-3276(06)52008-8

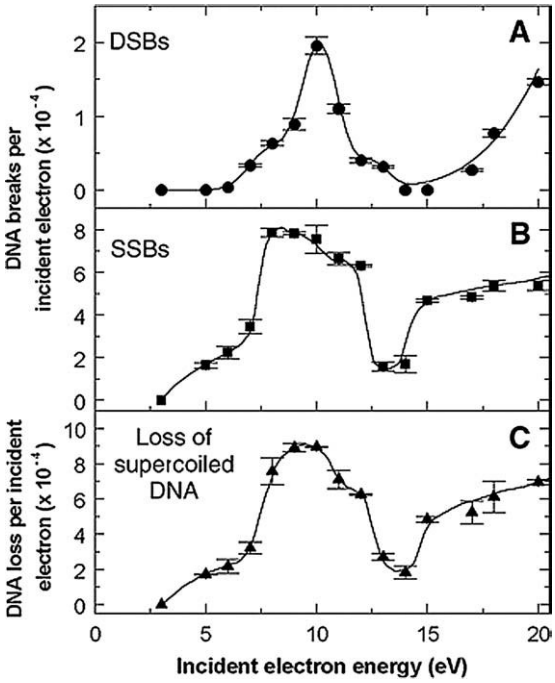

Fig. 1. The yield of single strand breaks (middle panel) per attached electron as a function of the kinetic energy of the incident electron (taken from Fig. 1 of Ref. [6]).

kinetic energies as low as 3.5 eV. The yields of single strand breaks (SSBs) were observed to depend on the energy of the incident electron in a manner (see Fig. 1) that suggested (because peaks and valleys appeared) some kind of resonant process was involved.

Based on the energies at which the peaks in the SSB plots occurred, it was suggested that the bond breaking that causes the SSB is initiated by the incident electrons attaching to the DNA bases' π^* orbitals to form core-excited resonance states (e.g., as in $e^- + \pi^2 \rightarrow \pi^1\pi^{*2}$).

However, we knew from data of the Burrow group [7] that electrons of even lower kinetic energies can attach to low-lying π^* orbitals of the bases of DNA to form shape resonance anions. In particular, the Burrow data indicated that all DNA bases have shape resonance states lying considerably below (e.g., in the 0.1–2 eV range as shown in Fig. 2) the 3.5 eV strand break threshold found in the Sanche experiments. This led us to wonder whether even lower energy electrons than used in Ref. [6] could induce strand breaks in DNA by forming shape rather than core-excited resonances.

2. WHERE DO VERY LOW-ENERGY ELECTRONS ATTACH TO DNA AND WHAT BONDS ARE BROKEN?

Knowing that shape resonances typically have shorter lifetimes (with respect to autodetachment) than core-excited resonances, we anticipated finding that although the DNA bases indeed can attach electrons at energies considerably below 3.5 eV, the shape reso-

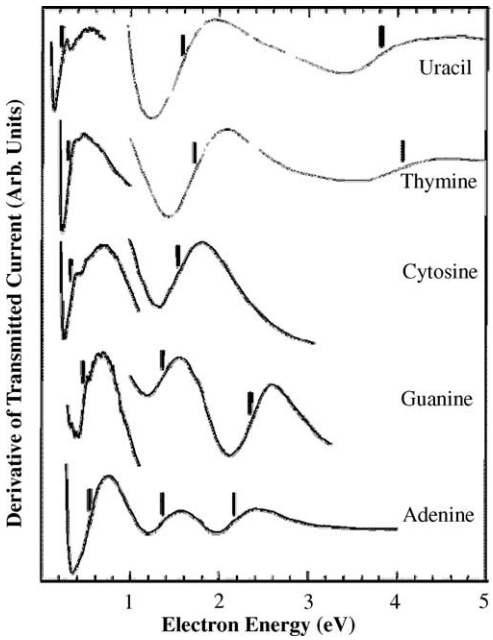

Fig. 2. The electron transmission spectra of the four DNA bases showing the energies (vertical lines) at which the low-energy π^* orbitals occur (taken from Fig. 1 of Ref. [7]).

nances thus formed decay so quickly that the yield of bond breakage is extremely low. This would be consistent with the Sanche data showing no strand break yield in the energy range where shape resonances are expected. Nevertheless, because it was clear to us from Ref. [6] that experimental limitations precluded those workers observing strand breaks at such lower energies, we decided to explore this possibility further, and our results are detailed in Refs. [1–5].

2.1. The DNA fragments studied

In each of our studies, we examined a fragment of DNA using ab initio electronic structure methods to determine which bond(s) would be most susceptible to cleavage when an electron is attached to a low-energy π^* orbital. The fragments included

a. the cytosine (C)–sugar–phosphate fragment shown in Fig. 3a,
b. an analogous fragment with cytosine replaced by thymine (T) (C and T have the lowest-lying π^* orbitals, so we began our studies with them),
c. the fragment containing three π-stacked C bases shown in Fig. 3b, and
d. the sugar–phosphate–sugar fragment shown in Fig. 3c.

We undertook the latter study because we wanted to address the relative probabilities for electron attachment to the phosphate group's P=O π^* or to a base π^* orbital.

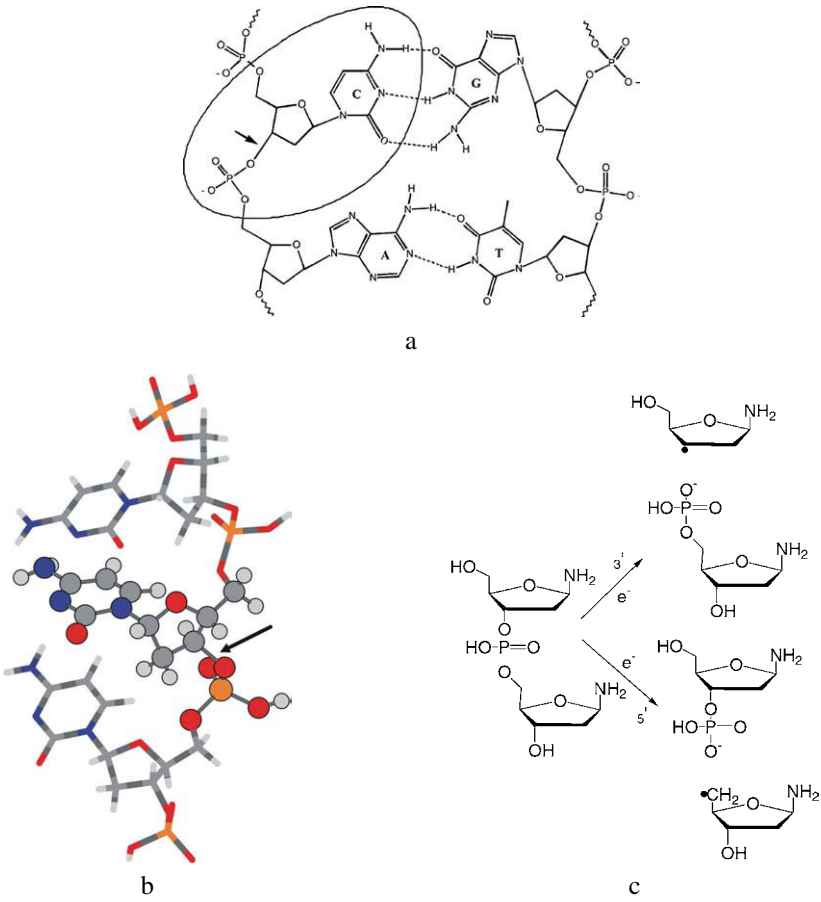

Fig. 3. DNA fragments studied in Refs. [1–5] (see text for explanation). a: taken from Ref. [1], Fig. 1; b: taken from Ref. [4], Fig. 4; c: redrawn figure from Ref. [8].

2.2. Review of our findings

The primary findings of our efforts were that:

a. Attachment of electrons in the 0.1–2 eV range (into C or T π^* orbitals) to form shape resonances can produce covalent bond cleavages.
b. A sugar-phosphate C–O σ bond is the bond whose cleavage requires surmounting the lowest barrier (i.e., in the 0.2–1 eV range, depending on the energy at which the electron attaches to the base within the Heisenberg width of the shape resonance).
c. Cleavage of a base-sugar N–C bond can also occur, but at significantly lower rates because this bond cleavage requires surmounting a larger barrier than for the sugar-phosphate C–O bond.
d. The thermodynamic driving force that causes the sugar–phosphate C–O bond to have the lowest barrier is the huge (ca. 5 eV) electron affinity of the phosphate radical generated by breaking this C–O bond.

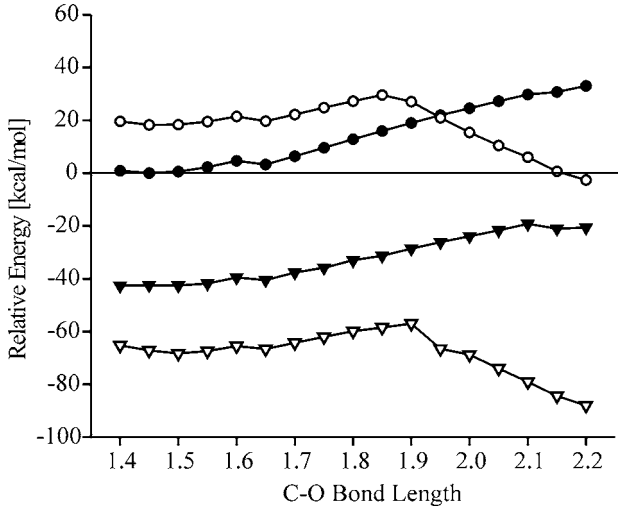

Fig. 4. Energies of neutral (filled symbols) and anionic (open symbols) cytosine-containing DNA fragment of Fig. 3a vs. C–O bond length (Å) in the absence of any solvation (top two plots) and with solvation characterized by dielectric constant $\varepsilon = 78$ (bottom two plots). Taken from Ref. [1], Fig. 2.

e. Electron attachment to the P=O π bond of the phosphate moiety requires electrons of considerably higher energy (> 2 eV) than for attachment to base π^* orbitals.
f. The fraction of C–O σ bond that cleave when an electron is attached, which is determined from the relative rates for surmounting the barrier noted above and the rates of autodetachment, can be as high as 10^{-4} for electrons in the 1 eV range.

2.3. Our proposed mechanism for sugar–phosphate C–O σ bond cleavage

To understand how electrons having kinetic energies in the 0.1–2 eV range can fragment a C–O σ bond whose dissociation energy is ca. 4 eV, we show in Fig. 4 some potential energy profiles that are characteristic of all of the findings of Refs. [1–5].

Let us focus on the top two plots in Fig. 4, which relate to the cytosine–sugar–phosphate fragment shown in Fig. 3a in the absence of any solvation (as appropriate to the experiments of Ref. [6]). The potential energy profiles appropriate to the thymine–sugar–phosphate fragment as well at the two fragments shown in Figs. 3b and 3c display similar characteristic shapes (i.e., the electron-attached state's energy rises, passes over a barrier, and then falls) although the heights of the barriers differ from fragment to fragment. The essential issue to understand is what causes these profiles to have barriers and what determines how steeply the curves fall at large R.

The data represented by the filled circles in Fig. 4 describe the variation in the energy of the neutral cytosine–sugar–phosphate unit in the absence of any attached electron as a function of the sugar–phosphate C–O bond length (R). If followed to much larger R-values, the energy of this curve approaches ca. 90 kcal mol^{-1}, which is the dissociation energy for homolytic cleavage of the C–O bond. The data represented by the open circles

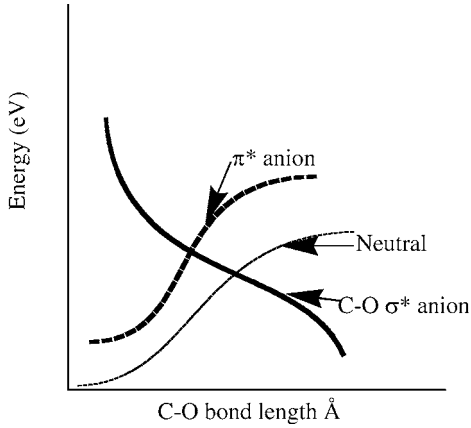

Fig. 5. Qualitative plots of the (diabatic) energies of the anion states in which the excess electron occupies the base π^* orbital and in which the electron occupies the C–O σ^* orbital as well as the variation of the energy of the neutral molecule.

in Fig. 4 describes the variation in the energy of the corresponding unit with an electron attached. Specifically, the electron has been placed into a π^* orbital of the cytosine base lying (vertically) ca. 1 eV above the energy of the neutral thus forming a metastable shape resonance.[1]

If the attached electron is forced (e.g., by constraining the orbital occupancy used in our wave function to retain its π^{*1} character) to remain in the cytosine π^* orbital, the energy of this electron-attached state would parallel that of the neutral molecule and rise by nearly 90 kcal mol^{-1} as the C–O bond cleaves. However, because our quantum wave function allows the orbital occupancy of all the electrons to be optimized, something different happens. As suggested qualitatively in Fig. 5, another anion state in which the excess electron occupies the C–O σ^* orbital also comes into play as the C–O bond is stretched.

Specifically, near the equilibrium C–O bond length, the σ^*-attached anion is much higher in energy than is the π^*-attached anion; this is why the shape resonance state at 1 eV is a base π^* state. However, as the C–O bond lengthens, its σ orbital rises in energy and its σ^* orbital decreases in energy; the latter being shown in Fig. 5. The rate at which the σ^* orbital falls as R increases is determined by the electron affinity of the phosphate radical that forms when the C–O bond breaks. At a C–O bond length near 1.9 Å (see Fig. 4), the π^{*1} and σ^{*1} anion states' diabatic energies become equal. It is near such a crossing that the configuration interaction (CI) between these two states is strongest. The resulting CI, which is automatically included in our ab initio calculation, allows the wave function to smoothly evolve from π^{*1} to σ^{*1} character as R passes through the crossing region. Again, it is important to emphasize that the reason the σ^*-attached anion's energy drops strongly as R increases lies in the very high (ca. 5 eV) electron affinity (EA) of the oxygen site of the phosphate radical. In fact, it is because the phosphate radical's EA is considerably larger than the EA of the base nitrogen-centered radical formed when a base-sugar N–C

[1] By eliminating the outgoing continuum component of the basis functions used to describe this state, we are able to force the attached electron to remain in the π^* orbital as we subsequently stretch the C–O bond to generate the open-circles data.

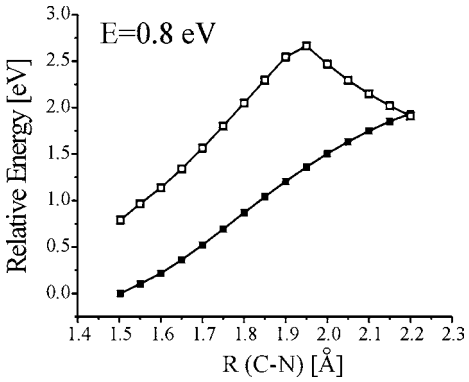

Fig. 6. Energy profile for the neutral (filled squares) and anion (open squares) thymine–sugar–phosphate unit as a function of the thymine–sugar C–N bond length (taken from Fig. 7 of Ref. [4]).

bond breaks that the barrier to sugar–phosphate C–O bond cleavage is lower than that for base-sugar N–C bond cleavage. An example of the energy profile for C–N bond cleavage in the thymine–sugar–phosphate system studied in Ref. [4] is shown in Fig. 6 for the case in which 0.8 eV electrons attach to the thymine π^* orbital.

In summary, the strand breaks we studied are generated when

a. an electron having kinetic energy appropriate to enter a low-lying π^* orbital of a DNA base strikes and enters such an orbital to form a shape resonance, after which
b. a through-bond electron transfer event occurs if the sugar–phosphate C–O σ bond is elongated (e.g., through normal vibrational motions) to near 1.9 Å allowing a barrier to be surmounted and π^*/σ^* configuration interaction to take place,
c. producing a σ^*-attached anion that promptly fragments to yield a carbon radical and a (very stable) phosphate-site anion.

The rate of the through-bond electron transfer from the base π^* to the sugar–phosphate C–O σ^* orbital was estimated by examining the avoided crossing of the π^* and σ^* anion states near the C–O bond length of 1.9 Å. The energy splitting δE was then used to compute the rate and values in the 10^{13} s^{-1} were obtained. As we show later, this through-bond transfer rate is considerably faster than the rate at which the barrier on the anion's energy surface near 1.9 Å is surmounted, so the latter is the rate-limiting event in producing SSBs.

2.4. Subsequent experimental verifications

To our pleasure, subsequent to our studies suggesting that shape resonances could induce strand breaks in DNA, new measurements [9] were carried out at even lower electron kinetic energies and strand breaks were indeed observed as Fig. 7 illustrates.

Because the DNA samples used in Refs. [6] and [9] contained all four bases, it was not possible to infer whether the electron attachment takes place at any particular base(s). However, because all four bases have their lower-energy π^* resonance states in the 0.1–2 eV range, the data strongly suggest that the strand breaks are taking place by formation of such π^* shape resonances as our earlier predictions claimed. In fact, in Ref. [9] it is

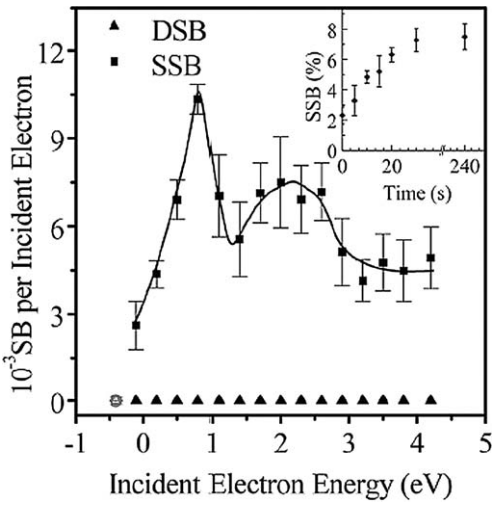

Fig. 7. Yield of DNA strand breaks as a function of electron kinetic energy showing SSBs occurring in the 0.1–2 eV range studied in Refs. [1–5] (taken from Fig. 1 of Ref. [9]).

even emphasized that the shape of the strand-break yield plot of Fig. 7 is quite similar to the known shape of the DNA bases' electron attachment cross-sections, further supporting our claim that it is to the base π^* (and not[2] phosphate P=O π^* or any σ^*) orbital that attachment occurs.

Another experimental result that supports of our proposed model (in particular of what bond is cleaved) has also recently appeared [10]. In these experiments, oligonucleotide tetramers (CGTA and GCTA) were exposed to electrons and the products of irradiation were examined by high-pressure liquid chromatography. The findings of these experiments show primarily cleavage of the phosphodiester (sugar–phosphate C–O) bond in line with our prediction. It should be noted, however, that although this is the first determination by chemical analysis of the products formed in SSBs, the electron energy used (10 eV) was higher than in our simulations. Only at such high energies could enough product be formed to permit the chemical analysis to be carried out. So, although these findings are supportive of our mechanism, it would be nice to have data from such a chemical analysis of products formed by lower-energy electrons.

3. METHODS USED TO CHARACTERIZE THE ENERGIES OF THE METASTABLE ANIONS

3.1. How the rates of bond cleavage are estimated

Before discussing the main tools we use for characterizing metastable electronic states, let us briefly specify how we estimate bond cleavage rates from the energy profiles we generate. For example, from data such as appears in Fig. 4, the rates of C–O bond cleavage

[2] It is possible that, at higher electron energies, attachment to the phosphate P=O π^* or various σ^* orbitals can occur and that SSBs can thereby be formed.

were estimated by taking the C–O vibrational frequency (ca. 10^{13} s^{-1}) and multiplying by the equilibrium Boltzmann probability

$$P = \frac{\exp(-E^*/kT)}{q} \tag{1}$$

that the bond stretches enough to reach the barrier height E^*. As noted earlier, the barrier heights found when electrons are attached to cytosine or thymine range from 0.2 to 1 eV, as a result of which the estimated $T = 298$ K (as in Ref. [6]) C–O bond cleavage rates range from 10^{10} to 10^{-4} s^{-1}. Because the autodetachment rate of a π^* shape resonance is expected to be near 10^{14} s^{-1}, and recalling that we estimated the through-bond electron transfer rates to be ca. 10^{13} s^{-1}, our bond cleavage estimates suggest that at most one in 10^4 nascent π^* anions will undergo C–O bond rupture. Moreover, because we observed that the lower barrier heights E^* occurred when the electron enters the higher-energy component of the π^* resonance, we expect the quantum yield for forming C–O bond fragmentation to be higher at such energies.

Finally, we note that, unlike the case in Refs. [6] and [9] where the DNA was dry, when significant solvation is present, the π^* anion state can be rendered electronically stable (see Fig. 4). In this case, competition between bond cleavage and electron detachment is irrelevant. Instead, transfer of the π^*-attached electron from base to base via the π-stacking framework, which is thought to occur at rates of ca. 10^{12} s^{-1} competes with the bond cleavage rates discussed above. Of course, when strong solvation is present, as it is in living organisms, the phosphate groups will not be rendered neutral by closely associated counter cations as is likely the case in Refs. [6] and [9]. An electron attached to a DNA base adjacent to a negative phosphate unit will not be able to undergo the through-bond electron transfer discussed above because this phosphate group will not provide an attractive potential to the attached electron. Instead, the attached electron likely will migrate through the π-stacking framework to another base. However, even in a solvated environment, a fraction F of the phosphate units have nearby counter cations that render them neutral. Once the attached electron reaches a base near such a neutral phosphate, it has a chance to cause a C–O bond cleavage. The result of solvation then is to reduce the rate of strand breaks from near 10^{10} s^{-1} by the fraction F.

3.2. Stabilization methods

In cases such as we are discussing in this work, the anion formed by near-vertical electron attachment to a base π^* orbital is electronically metastable, but can become electronically stable along the pathway leading to bond cleavage. An example is offered by the data shown in Fig. 4 which pertains to attaching an electron with ca. 1 eV of kinetic energy to a low-energy π^* orbital of cytosine. As the sugar–phosphate C–O bond stretches beyond the barrier at 1.9 Å, the anion potential surface drops below that of the neutral at which point the anion becomes electronically stable. Of course, in this case, at very large C–O distances, the anion lies ca. 5 eV below the neutral because of the extremely high electron affinity of the phosphate group. Although the treatment of the stable anion's Born–Oppenheimer electronic energy can be handled using conventional variational or perturbative methods with standard atomic orbital basis sets, such is not the case at geometries where the anion is electronically metastable. In the latter cases, the anion's resonance state is embedded within a continuum of states corresponding to the neutral molecule plus

a free electron. As such, a rigorous treatment of these resonance states should involve a quantum scattering approach, which, however, is not feasible for the large molecular systems studied here.

For such reasons of practical necessity, hybrid approaches such as the stabilization method [11] and the nuclear charge-scaling method [12] have proven especially useful in determining the energies (i.e., the so-called positions that represent the center of the Heisenberg broadened state) of the resonance states. Let us consider the well known N_2^{-1} shape resonance case to illustrate. Use of the stabilization method (SM) can be thought of as embedding the system of interest within a finite "box" in order to convert the continuum of states corresponding to $N_2 + e^-$ (KE) into discrete states that can be handled using more conventional methods. By then varying the size of the confining box, one can vary the energies of the discrete $N_2 + e^-$ (KE) states. By varying the box size, one of the continuum functions may have its de Broglie wavelength (and thus its KE) changed in a manner that allows this continuum function to match (in value and derivative) the valence-range portion of the N_2^- wave function. It is this combination of valence-range N_2^- and asymptotic-range continuum (properly matched in their values and derivatives) functions that corresponds to the metastable shape-resonance state, and it is the energy where significant valence components develop that provides the stabilization estimate of the state energy.

In the most conventional application of the SM, one uses a conventional atomic orbital basis set that would likely include s and p functions on each N atom, perhaps some polarization d functions and some conventional diffuse s and p orbitals on each N atom. These basis orbitals serve primarily to describe the motions of the electrons within the usual valence regions of space. To this basis, one would append an extra set of diffuse π-symmetry orbitals (because one wishes to study a $^2\Pi_u$ resonance). These orbitals could be p_π (and maybe d_π) functions centered on each nitrogen atom, or they could be d_π orbitals centered at the midpoint of the N–N bond. Either choice can be used because one only needs a basis capable of describing the long-range, $L = 2$ part of the metastable state's wave function. One usually would not add just one such function; rather several functions, each with an orbital exponent α_J that characterizes its radial extent, would be used. Let us assume, for example, that a total of K such π functions have been used.

Next, using the conventional atomic orbital basis as well as the K extra π basis functions, one carries out a calculation in which one computes many energy levels on the N_2^{-1} anion. In this calculation, one tabulates the energies of many (say M) of the electronic states of N_2^{-1}. One then scales the orbital exponents $\{\alpha_J\}$ of the K extra π basis orbitals by a factor $\eta : \alpha_J \rightarrow \eta\alpha_J$ and repeats the calculation of the energies of the M lowest energies of N_2^{-1}. This scaling causes the extra π basis orbitals to contract radially (if $\eta > 1$) or to expand radially (if $\eta < 1$). It is this basis orbital expansion and contraction that produces the expansion and contraction of the "box" discussed above. That is, one does not employ a box directly; instead, one varies the radial extent of the more diffuse basis orbitals to simulate the box variation.

If the conventional orbital basis is adequate, one finds that the extra π orbitals, whose exponents are being scaled, do not affect appreciably the energy of the neutral N_2 molecule. This can be probed by plotting the N_2 energy as a function of the scaling parameter η; if the energy varies little with η, the conventional basis is adequate. In contrast to plots of the neutral N_2 energy vs. η, plots of the energies of the M N_2^{-1} anion states show significant η-dependence as Fig. 8 illustrates.

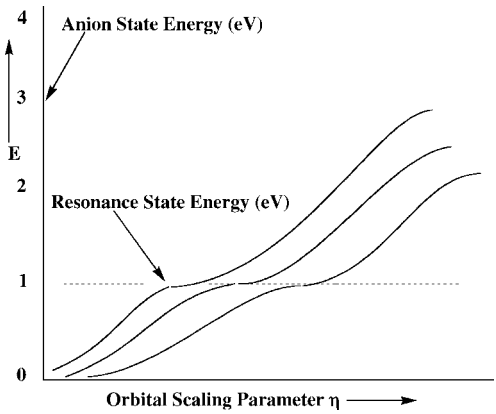

Fig. 8. Plots of the energies of several anion states vs. the orbital scaling parameter η. Note the avoided crossing of state energies near 1 eV.

We should first note that each of the plots of the energy of an anion state (relative to the neutral molecule's energy, which is independent of η) grows with increasing η. This η-dependence arises from the η-scaling of the extra diffuse π basis orbitals. Because most of the amplitude of such basis orbitals lies outside the valence region, the kinetic energy is the dominant contributor to such orbitals' energies. Because η enters into each orbital as $\exp(-\eta\alpha r^2)$, and because the kinetic energy operator involves the second derivative with respect to r, the kinetic energies of orbitals dominated by the η-scaled diffuse π basis functions vary as η^2. It is this quadratic growth with η that is shown in Fig. 8. For small η, all of the π diffuse basis functions have their amplitudes concentrated at large-r and have low kinetic energy. As η grows, these functions become more radially compact and their kinetic energies grow. For example, note the three lowest energies shown above in Fig. 8 increasing from near zero as η grows. As η further increases, one reaches a point at which two of the anion-state energies in Fig. 8 undergo an avoided crossing. At this η value, if one examines the nature of the two wave functions whose energies avoid one another, one finds that one of them contains substantial amounts of both valence and extra diffuse π function character. Just to the left of the avoided crossing, the lower-energy state contains predominantly extra diffuse π orbital character, while the higher-energy state contains largely valence π^* orbital character. In Fig. 8, other avoided crossings occur at higher η-values. For each such crossing, the lower-energy eigenfunction to the left of the avoided crossing contains predominantly extra diffuse π orbital character, while the higher-energy state contains largely valence π^* orbital character.

At any of the special values of η where two states nearly cross, the kinetic energy of the continuum state (as well as its radial size and de Broglie wavelength) are appropriate to connect properly with the valence-region state. It is such boundary condition matching of valence-range and long-range character in the wave function that the stabilization method achieves. So, at such a special η value, one can achieve a description of the shape-resonance state that correctly describes this state both in the valence region and in the large-r region. Only by tuning the energy of the large-r states using the η-scaling can one obtain this proper boundary condition matching.

If one attempts to study such metastable anion states without carrying out such a stabilization study, one is doomed to failure, even if one employs an extremely large and flexible set of diffuse basis functions. In fact, in such a large-basis calculation, one will certainly obtain a large number of anion "states" with energies lying above that of the neutral, but one will not be able to select from these states the one that is the true resonance state. Most of the states will simply be states describing an N_2 molecule with an excess electron at large-r and low KE, but, in the absence of the SM, none will offer a proper description of the metastable state.

In summary, by carrying out a series of anion-state energy calculations for several states and plotting them vs. η, one obtains a stabilization graph. By examining this graph and looking for avoided crossings, one can identify the energies at which metastable resonances occur. It is also possible to use the shapes (i.e., the magnitude of the energy splitting between the two states and the slopes of the two avoiding curves) of the avoided crossings in a stabilization graph to compute the lifetimes of the metastable states. Basically, the larger the avoided crossing energy splitting δE between the two states, the shorter is the lifetime τ of the resonance state and $\tau \approx \hbar/\delta E$.

In our studies of shape resonancesin DNA fragments, we wanted to employ such a stabilization approach. However, as can be deduced from the above discussion, such calculations require the use of quite large atomic orbital basis sets because of the need for many extra diffuse functions whose exponents must be varied. For molecules as large as the DNA fragments we studied, such calculations were simply not feasible. We therefore had to find a different way to characterize the π^* resonance states' electronic wave function. Knowing the energies (i.e., positions) of the low-lying π^* shape resonance states of all four bases from the Burrow-group experiments [7], we decided to employ atomic orbital basis sets on the DNA base to which electron attachment occurs that would generate π^* anion states at the known energies.[3] Specifically, for each of the atoms involved in the base's delocalized π-orbital framework, we scaled the orbital exponents of the most diffuse p_π basis functions by a common amount η and varied η until the energy of the π^*-attached anion (computed at the self-consistent field (SCF) level) relative to that of the neutral matched the desired energy (i.e., as from the data of Ref. [7]). Of course, we also verified that the orbital so obtained has the valence character desired by carrying out a visual inspection. For example, in Fig. 9, we show the cytosine π^* orbital we obtained for the fragment species shown in Fig. 3a; we also show how this orbital evolves as the sugar–phosphate C–O bond is elongated beyond the barrier and the electron transfers through the sugar onto the phosphate unit.

Because we included no extra diffuse basis functions, we were not able to perform true stabilization calculations. Instead, we simply scaled the radial extent of the basis to generate a π^* anion state at the energy we already knew taking care to make sure the resulting state was indeed a base π^* state. Of course, this limited approach precluded being able to estimate the lifetimes of such π^* resonances because our wave function contained only its valence-range component but no continuum component. Although such a "poor man's" stabilization approach should be improved upon in the future, it was the only route available to us at the time.

[3] Actually, because each of the π^* shape resonances have substantial Heisenberg widths, we chose to construct a range of π^* orbitals such that the electron-attached states' energies (relative to the neutral) spanned this range.

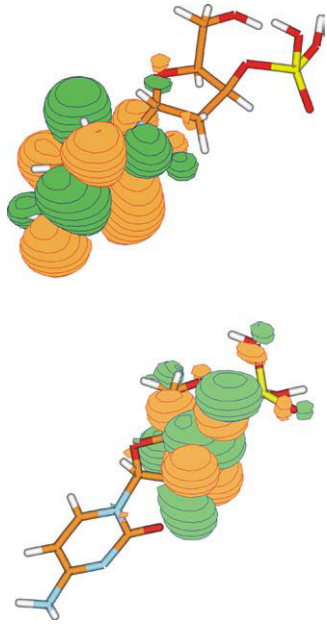

Fig. 9. Plot of the singly-occupied π^* molecular orbital of the fragment shown in Fig. 3a. On the left, this orbital is localized on the cytosine and on the right (at elongated C–O bond length), it has evolved onto the sugar and phosphate. Taken from Ref. [1], Fig. 3.

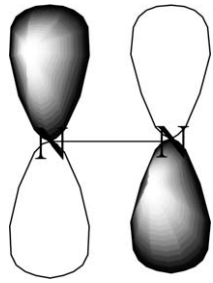

Fig. 10. The π_g^* antibonding orbital of N_2^-.

3.3. Nuclear charge scaling as applied to electron attachment to phosphate P=O π^* orbitals

To explain this technique, let us again consider the $^2\Pi_g$ shape resonance of N_2^-. Due to local valence potentials, there exists an attractive potential that the excess electron experiences while moving in the region of space defined by the π^* antibonding orbital shown in Fig. 10.

However, this potential well is not deep enough to produce a bound state for the excess electron, as a result of which N_2^- is metastable and can spontaneously decay to $N_2(X^1\Sigma_g^+) + e^-$. In contrast, the analogous $^2\Pi$ states of the isoelectronic species NO and

O_2^+ are electronically vertically stable with respect to their corresponding $^1\Sigma^+$ electron-removed species (i.e., vertically, NO lies energetically below NO^+ and O_2^+ below O_2^{2+}). A primary difference underlying this qualitative difference in the ordering of N_2^-/N_2 and the other species is the smaller nuclear charge of N compared to O.

These observations suggest a device that one can use to render metastable shape resonances stable, and thus amenable to conventional (i.e., variational and perturbative) quantum chemistry treatment, while subsequently estimating the energy (position) of the initial metastable state. Specifically, if one increments (by a (small) amount Δq) the nuclear charges of those atoms over which the shape resonance's singly occupied molecular orbital (SOMO) is delocalized,[4] one can differentially stabilize the anion relative to the neutral. If Δq is large enough, the energy of the anion (with nuclear charges increased) will lie below that of the neutral and thus both species' energies can be treated using conventional methods.

So, in the nuclear charge-scaling method, one increases certain nuclear charges by Δq and computes the energies of the neutral and anion. For values of Δq large enough to make the anion lie below the neutral, one plots the energy difference between the anion and the neutral (i.e., the excess electron binding energy). One then extrapolates this plot to $\Delta q \rightarrow 0$ to obtain an estimate of the energy of the metastable anion for the actual molecule (with $\Delta q = 0$). For anions whose energies do not lie much above the neutral (and which tend to be longer lived), one usually finds that very small fractional increments in the nuclear charges are needed. In these cases, the perturbation in the electron-nuclear attraction potential (the electrons are located at $\mathbf{r}_k$ and the nuclei at $\mathbf{R}_a$)

$$V = \sum_a \sum_k \frac{(-\Delta q)}{|\mathbf{r}_k - \mathbf{R}_a|} \tag{2}$$

introduced by replacing certain nuclear charges Z_a by $Z_a + \Delta q$, will be small. Hence, perturbation theory suggests that the shifts in the anion-neutral energy differences should vary linearly with Δq. If larger values of Δq are needed to make the anion stable, the plots in the anion-neutral energy differences can display significant quadratic (in Δq) character; in these cases, extrapolation is carried out using a second order (in Δq) polynomial but only for values of Δq where the anion is stable.

An example of the use of this nuclear charge scaling device is provided in our study of electron attachment to the P=O π^* orbital of the sugar–phosphate–sugar unit some data of which is shown in Fig. 3c. As shown in Fig. 3c, subsequent to electron attachment, either of two sugar–phosphate C–O bonds (labeled 3′ and 5′) can rupture. In Fig. 11 we show plots of the energies of the neutral and electron-attached species as functions of the C–O bond lengths for the cases in which the 3′ C–O bond is ruptured or the 5′ C–O bond breaks. For the anion, two energy curves are shown. One relates to the excess electron residing in the P=O π^* orbital and the second pertains to the excess electron being in the σ^* orbital of the C–O bond being cleaved. To obtain the data shown at C–O bond lengths where the anion

[4] It is not always necessary to place the stabilizing excess charge on the nuclei where the excess electron is localized. For example, in our study of the metastable SO_4^{2-} dianion, we increased the charge on sulfur. We made this choice because all four oxygen atoms in this species are equivalent and we did not wish to induce artificial symmetry breaking (see first references in Ref. [13]). On the other hand, when we recently studied the ground and (metastable) excited states of the O_2^- anion, we increased both oxygen atoms' charges (see second reference in Ref. [13]).

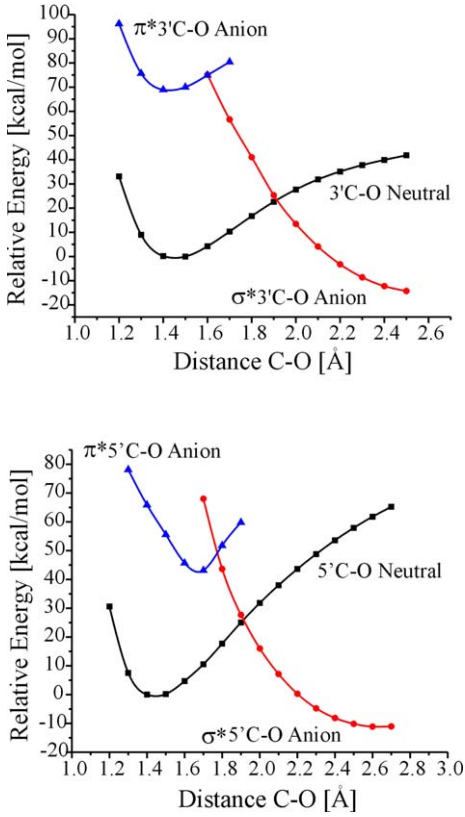

Fig. 11. Energies of the neutral, π^*-attached anion, and σ^*-attached anion as functions of the 3′ C–O (top) and 5′ C–O (bottom) C–O bond lengths. Taken from Ref. [4], Fig. 3.

curves lie above the neutral, we used the nuclear charge scaling device detailed above as we now discuss.

To illustrate the data used to extrapolate (to $\Delta q \rightarrow 0$) the anion-neutral energy plots for all values of the C–O bond lengths where the anion is metastable, we shown in Fig. 12 four such plots applying to the 3′ and 5′ cases and to the σ^* and π^* anions.

To further illustrate the utility of the nuclear charge-scaling device, we show in Fig. 13 the P=O π^* and C–O σ^* orbitals obtained when the phosphorous and oxygen nuclear charges are increased by 0.5 for the four cases whose Δq plots are shown in Fig. 12.

Before ending this section, let us return to Fig. 11 to discuss what we learned from the study relating to attaching an electron to a P=O π^* orbital. First, our data suggest that electrons in the range of 2 eV will be required to attach to such an orbital. In Ref. [9], DNA strand breaks were observed with electrons below 1 eV, so these breaks likely did not involve attachment to P=O π^* orbitals. Moreover, even when electrons of 2 eV energy or more attach to P=O π^* orbitals, evolution of this anion along the either the 3′ or 5′ C–O bond elongation to produce bond cleavage requires surmounting a barrier of ca. 1 eV (see Fig. 11 where the π^* and σ^* anion curves cross). Our earlier work showed that the barriers associated with C–O bond cleavage subsequent to base π^* orbital-attachment were much

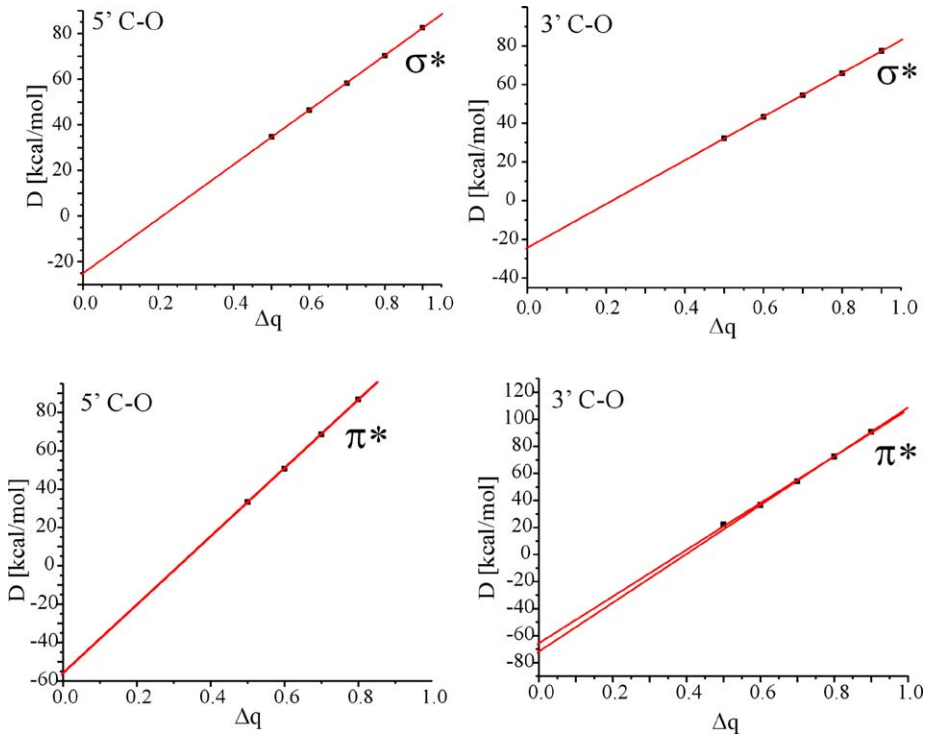

Fig. 12. SCF-level electron binding energy plots for the π^* (bottom) and σ^* (top) anions for certain values of the 3′ or 5′ C–O bond lengths at all of which the anion is metastable. Specifically, for the π^* anion $R = 1.4$ Å for the 3′ and 1.5 Å for the 5′; for the σ^* anion $R = 1.8$ Å for both the 3′ and 5′ cases. In the 3′ C–O π^* plot, displays considerable curvature, we show two linear fits to give some idea of the uncertainty. Taken from Ref. [2], Fig. 6.

lower. Therefore, we believe it unlikely that much of the strand break damage to DNA occurs by P=O π^* bond attachment when the electron has a kinetic energy in the 0.1–2 eV range.

4. SUMMARY

In this paper, we used several of our recent studies to illustrate the mechanisms by which very low-energy (0.1–2 eV) free electrons attach to DNA to cause strong (ca. 4 eV) covalent bonds to break. We also used these examples to illustrate the special tools we use for probing metastable electronic states. The primary conclusions of this body of work have been that (i) attachment to base π^* orbitals to form shape resonances in the 0.1–2 eV energy range most likely results in cleavage of sugar–phosphate C–O σ bonds, (ii) the thermodynamic driving force for this process is the large electron affinity of the phosphate unit, (iii) the rates of C–O bond cleavage can be as high as 10^{10} s^{-1} and are determined by the rate at which an energy barrier on the anion's potential surface is surmounted, (iv) bond cleavage initiated by electron attachment to phosphate P=O π bonds is less likely involved,

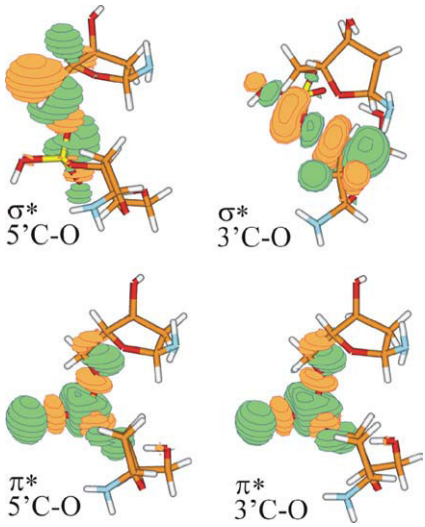

Fig. 13. The π^* and σ^* orbitals corresponding to the four cases detailed in Fig. 12 as the P and O charges are increased by 0.5. Taken from Ref. [2], Fig. 8.

and (v) the through-bond electron transfer from the base to the C–O σ bond occurs at ca. 10^{13} s^{-1} and thus is not rate-limiting. Finally, subsequent to our works in which these predictions were offered, very recent experiments have appeared in which (i) convincing evidence is given in support of our claim that 0.1–2 eV electrons attach to base π^* orbitals rather than to P=O π^* or any σ^* orbitals, and (ii) chemical analysis of the products of strand breaks shows that it is indeed primarily the sugar–phosphate C–O bond that breaks.

Before closing, it is worth noting that an excellent review appeared recently [14] covering much of the recent history of studies related to electron-induced strand breaks in DNA. In that review, work on electron-induced bond cleavage in DNA bases (where H atom elimination and base radical anion formation occurs), in base-sugar units (where cleavage of the bond connecting the base to the sugar occurs), and in sugar–phosphate units (where the sugar–phosphate C–O bond cleaves) is overviewed. In addition, the potential role of dipole-bound states in effecting the initial electron attachment is also discussed in Ref. [14].

ACKNOWLEDGEMENTS

Support of the National Science Foundation through grant CHE 0240387 is appreciated as is significant computer time provided by the Center for High Performance Computing at the University of Utah.

REFERENCES

[1] R. Barrios, P. Skurski, J. Simons, *J. Phys. Chem. B* **106** (2002) 7991–7994.
[2] J. Berdys, I. Anusiewicz, P. Skurski, J. Simons, *J. Am. Chem. Soc.* **126** (2004) 6441–6447.
[3] J. Berdys, I. Anusiewicz, P. Skurski, J. Simons, *J. Phys. Chem. A* **108** (2004) 2999–3005.

[4] I. Anusiewicz, J. Berdys, M. Sobczyk, P. Skurski, J. Simons, *J. Phys. Chem. A* **108** (2004) 11381–11387.
[5] J. Berdys, P. Skurski, J. Simons, *J. Phys. Chem. B* **108** (2004) 5800–5805.
[6] B. Boudaiffa, P. Cloutier, D. Hunting, M.A. Huels, L. Sanche, *Science* **287** (5458) (2000) 1658–1662.
[7] K. Aflatooni, G.A. Gallup, P.D. Burrow, *J. Phys. Chem. A* **102** (1998) 6205–6207.
[8] X. Li, M.D. Sevilla, L. Sanche, *J. Am. Chem. Soc.* **125** (2003) 13668–13669.
[9] F. Martin, P.D. Burrow, Z. Cai, P. Cloutier, D. Hunting, L. Sanche, *Phys. Rev. Lett.* **93** (2004) 068101.
[10] Y. Zheng, P. Cloutier, D. Hunting, L. Sanche, J.R. Wagner, *J. Am. Chem. Soc.* **127** (2005) 16592–16598.
[11] A.U. Hazi, H.S. Taylor, *Phys. Rev. A* **1** (1970) 1109–1116;
J. Simons, *J. Chem. Phys.* **75** (1981) 2465–2467;
J. Simons, Roles Played by Metastable States in Chemistry, in: *Resonances in Electron–Molecule Scattering, Van der Waals Complexes, and Reactive Chemical Dynamics*, in: *ACS Symposium Series*, vol. 263, 1984, pp. 3–16;
R.F. Frey, J. Simons, *J. Chem. Phys.* **84** (1986) 4462–4469.
[12] B. Nestmann, S.D. Peyerimhoff, *J. Phys. B* **18** (1985) 615–626;
B. Nestmann, S.D. Peyerimhoff, *J. Phys. B* **18** (1985) 4309–4319.
[13] A. Whitehead, R. Barrios, J. Simons , *J. Chem. Phys.* **116** (2002) 2848–2851;
K.M. Ervin, I. Anusiewicz, P. Skurski, J. Simons, W.C. Lineberger, *J. Phys. Chem. A* **107** (2003) 8521–8529.
[14] L. Sanche, *Eur. Phys. J. D* **35** (2005) 367–390.

Electron-Driven Molecular Processes Induced in Biological Systems by Electromagnetic and Other Ionizing Sources

I. Baccarelli[1], F.A. Gianturco[2], A. Grandi[1], R.R. Lucchese[3] and N. Sanna[1]

[1] *Supercomputing Consortium for University and Research, CASPUR, Via dei Tizii 6b, 00185 Rome, Italy*
[2] *Department of Chemistry, The University of Rome 'La Sapienza', Piazzale A. Moro 5, 00185 Rome, Italy*
[3] *Department of Chemistry, Texas A&M University, College Station, TX 77843-3255, USA*

Abstract

We describe, and analyse in some detail, a selection of the most recent theoretical and computational models which attempt to explain, at the molecular level, the dynamics of metastable negative ion formation from biological molecules in the gas-phase. Such Transient Negative Ions (TNIs) are related to the nanoscopic nuclear dynamics presiding over the occurrence of irreversible damage in the biosystems through the many possible pathways leading to dissociative attachment decay of the initial TNI. We will review the theoretical approach we adopted to study electron–molecule collision as applied to systems of biological interest. The connection between the spatial symmetry of the metastable anion and its role during the dissociative electron attachment event is also discussed and analysed through several examples.

Contents

1. INTRODUCTION

Many forms of radiation are encountered in the natural environment and are produced by modern technology [1]. A well-known category of radiation is the so-called ionizing

ADVANCES IN QUANTUM CHEMISTRY, VOLUME 52
ISSN: 0065-3276 DOI: 10.1016/S0065-3276(06)52009-X

radiation; it is particularly well studied due to its damaging effects on atoms *via* the creation of positive ions and negative electrons and the possible consequent biological harm which it may cause [2]. Ionizing radiation includes X-rays, gamma rays, alpha particles, beta particles, neutrons, and cosmic rays.

In general, most radiation forms can have both beneficial and harmful effects. All ionizing radiation, at sufficiently large exposures, can cause cancer. Many, in carefully controlled exposures, are also used for cancer therapy. In all cases, exposures to ionizing radiation have been an inevitable part of the environment and, even though unrecognized till the recent past, radiation constitutes a powerful pollutant and a significant factor in biological processes.

Human awareness of radioactivity and ionizing radiation only dates back to the beginning of the last century, after the discovery of X-rays and radioactivity and the unexpected first evidence of the harmful effects of ionizing radiation. Serious efforts to understand and control radiation exposures started in the 1920s and greatly expanded during and after World War II.

Information on the effects of radiation comes from studies of exposed groups and individuals, from animal experiments, and from studies at the cellular and molecular level. It is now well established that ionizing radiation has both prompt and delayed effects and it can also induce genetic defects.

An essential step forward in the understanding of the damaging effects of ionizing radiation on living cells took place after the discovery that the genotoxic effects, due to various DNA lesions, are not only produced by the direct impact of the initial high-energy particles (direct ionisation) [3]; such lesions might indeed be induced by the secondary species generated by the primary ionizing radiation within nanoscopic volumes along ionization tracks [4]. These species consist of excited atoms and molecules, radicals, ions and secondary low-energy electrons (LEEs). In particular LEEs, with energy between 1 and 20 eV, are the most abundant of such secondary species, and carry most of the energy of the initial fast particles. It has recently been shown [5] that reactions of such electrons, even at energies well below ionization thresholds, induce substantial yields of single- and double-strand breaks (SSBs and DSBs) in DNA, breaks which can be associated with decays of transient negative ions (TNIs) corresponding to molecular resonance states of the DNA's basic components. This fundamental finding emphasized the need to precisely understand the sequence of events subsequent to the primary irradiation which occur on the femtosecond time scale. In fact, while the primary deposition of energy is now well understood [6], the same is not true for the following events taking place at the nanoscopic level within condensed matter and caused by the secondary species. Hence, there is no well defined relationship between the initial absorbed dose and the final induced biological effects.

Under the typical cellular conditions, which correspond to those of extremely concentrated solutions, reactions occur within ultra short times and distances. Even though it was an unexpected finding, such ultra fast processes might in large part be driven by LEEs [4,7,8]: The capture of electrons to form TNIs, which subsequently decay along different fragmentation channels, is indeed a very effective means for transferring the energy of the light electron into the motions of the heavy nuclei [9]. It is then crucial to determine the yields of processes induced by the secondary electrons (SEs) colliding at energies lower than around 30 eV. On the other hand, one can disregard the possible role of secondary electrons which are being multiply scattered by the molecular network of the acqueous solute: the studies on radiation damage mechanisms, in fact, suggest [10–12] that the time scale of the slow

electron deceleration and of its solvation in the water environment after the primary ionization process is much longer than the genotoxic processes which we are considering [13]. Furthermore, the solvated electrons play a less significant role in biological damage as they primarily attack DNA bases and produce no strand breaks [4].

The study of the damaging events induced by LEEs has to include both the direct interaction of the SEs with DNA components and the indirect processes due to electron impact on the molecules surrounding the DNA in a living cell, such as water and other biomolecules. In particular, the damage of the genome strand by ionizing radiation is about one third a direct and two thirds an indirect process; almost all the indirect damage might be due to the attack on the DNA chain of the highly reactive hydroxyl radical OH^* produced in the dissociative electron attachment (DEA) processes triggered by LEEs [14].

After a brief review of the main experimental findings concerning the scattering of LEEs off biomolecules, we will summarize and discuss a theoretical approach based on the solution of the scattering equations in a single-center-expansion (SCE) frame of reference which we applied to the calculations of both the elastic cross sections and to the location of the positions and widths of the existing resonance states of the TNI. Finally, we will present our results concerning the interaction of LEEs with specific molecules of biological interest and we will draw our present conclusions in our final remarks.

2. ELECTRON-IMPACT EXPERIMENTS IN BIOLOGICAL ENVIRONMENTS: CURRENT STATE OF THE ART

We limit ourselves here to review the most important experimental results concerning the scattering of LEEs with molecules of biological interest, especially those related to the radiation damage of the DNA both in the gas and in the condensed phase.

The starting point of the experimental and theoretical radiobiological work was the identification of the mutagenic effects of ionizing radiation in terms of structural and chemical modifications of cellular DNA [4,7,15]. In the 1970s and 1980s several lines of investigation showed that the primary effect of direct radiation damage to duplex DNA was the formation of cationic and anionic radicals [16] which then participate in a chain of chemical reactions that can lead to permanent alteration of the original bases and to genetic damage. However, only in the early 1990s Sevilla and coworkers managed to assess, through an electron spin resonance (ESR) study, the relative distribution of ion radicals formed in DNA equilibrated with D_2O and γ-irradiated at 77 K [17]. Their investigation showed that the irradiation of frozen anoxic samples of DNA and polynucleotides in D_2O, prepared by use of vacuum techniques, led to the localization of positive charges on the purinic bases (and on the guanine for more than 90% of the total positive charge), and of low-energy electrons on the pyrimidinic bases, with a preference of the cytosine anion over the thymine one. The same group also investigated with the ESR technique the free radical distribution in γ-irradiated frozen samples of single stranded DNA (ssDNA) and double stranded DNA (dsDNA) [18], finding a more uniform distribution of the radical ions on the DNA bases in the ssDNA case than in the dsDNA. In hydrated dsDNA the cytosine anion is the dominant anion whereas in hydrated ssDNA a near-random distribution of the pyrimidine anions is found; such results are explained by the authors in terms of interstrand base pairing and base stacking effects. As for the cationic radicals, again the formation of the guanine cation is always favoured (both in ssDNA and in dsDNA) with respect to the

adenine one, even though the cations are again more evenly distributed between the purine bases in ssDNA than in dsDNA. The lack of the observation of substantial amounts of pyrimidine cations or purine anions is in accord with the large differences in ionization energy and electron affinities between pyrimidines and purines [19].

Restricting for the moment our attention to the nucleic acid base anions, due to the important role played in radiation-induced mutagenesis they have been the subject of numerous experimental studies, initially all in the condensed phase [20] and followed only later on by studies on the isolated DNA bases in the gas phase. They were aimed at gaining a detailed understanding of the mechanisms taking place at the molecular level.

Concerning the experiments in the condensed phase, in order to investigate the damage induced by LEEs on biological systems, particularly on DNA, experimental efforts have been devoted to isolate biomolecules as thin multilayer films in an ultra-high vacuum (UHV) where they could be bombarded with a beam of LEEs [5,12,21–23]. Such environmental conditions are necessary to avoid any LEE interaction with small surface impurities, which could modify the very damage which is being probed. In these experiments, the fragmentation of biomolecules induced by LEE bombardment can be either analysed *in situ* or outside UHV. In the former, the mass of the ions and neutral species that desorb from a multilayer film target are analysed during bombardment [12,22,23], or the products that remain in the film are characterized by X-ray photoelectron spectroscopy after bombardment [21]. If sufficient degraded material is produced, then the film target can be transported outside the UHV chamber and the products analysed by standard methods of chemical identification [24].

Recent advances in these techniques have made it possible for the first time to measure specific damage to the DNA molecule induced by LEEs. The results from bombarded plasmid-DNA samples [5] have demonstrated that LEEs can irreversibly damage the DNA backbone by producing SSB and DSB *via* fragmentation of the basic components of the molecule, including its structural water. It was also shown that DNA damage by 3–20 eV electrons, in contrast to DNA strand breaks induced by similarly energetic photons, is highly dependent on the initial kinetic energy of the incident electrons, particularly below 14 to 15 eV, with thresholds near 3 to 5 eV and intense peaks near 10 eV. Finally, the SSB and DSB peak yield values measured above 7 eV are around one to two orders of magnitude larger than those for 10 to 25 eV photons. Hence, the mechanism of DNA damage depends not only on the quantum of energy absorbed, but also on the nature of the particle that deposit the energy. The strong electron energy dependence of the DNA strand breaks observed below 14 eV was attributed to resonant electron attachment 'somewhere' within the DNA molecule (bases, deoxyribose, phosphate or hydration water), followed by localized bond rupture and subsequent reactions of the fragmentation products.

Along with the additional experiments on plasmid DNA [25], different groups have also investigated the damage induced on the DNA basic constituents, i.e. H_2O [26,27], bases [28] and sugar analogs [29], by means of various techniques aiming at interpreting the electron-stimulated desorption of anions (H^-, O^- and OH^- giving rise to the strongest signals) from thin films of linear and supercoiled DNA in the range 3–20 eV in terms of specific bond ruptures in one of the DNA components. In [25], by comparing the recorded anion desorption signals with those obtained from films of bases, amorphous ice and α-tetrahydrofuryl alcohol, the authors deduce that the main H^- desorption below 15 eV occurs mainly *via* DEA to the bases with an important contribution from the ribose ring. Moreover, they also notice that the different topologies of the DNA (linear or supercoiled),

and therefore the different physical nature of the DNA film, does not seem to affect the desorption intensity of any of the mayor anions detected, hence suggesting that the measured yields result from a local interaction (i.e. DEA to a basic constituent) not related to the long range geometrical properties of DNA. The second main signal, due to the desorption of O^-, is instead attributed to the phosphate group with the electron capture expected to occur within a π^* orbital on the O=P bond since in the vicinity of the O^- counterion the electric field may be too strong for transient anions to dissociate before autoionization. As for the third signal, the authors reason that the OH^- fragment is not likely to originate from the bases and that a portion of the signal could arise instead from reactive scattering of O^- produced at the phosphate group with the nearby sugar moiety.

Investigation of protein fragmentation by LEE impact has also been initiated in relation to DNA damage [30], since in biological cells nucleic acids interact very closely with certain proteins: some protein components are intercalated within the DNA grooves so that they interact directly with DNA bases [31,32]. After fragmentation of protein subunits by ionizing radiation, the reactive radicals produced may in turn react with a small segment of the nucleic acid and therefore may damage the DNA. Thus, understanding radiation and LEE damage to the genome also requires information on damage to proteins.

As for the gas-phase experiments on DNA bases and other relevant biomolecules, the first direct studies of the isolated DNA bases anionic radicals were limited to the investigation of the stability of the negative ions in gas phase towards the condensed phase [33–37]. Some of those studies wanted to distinguish the dipole-bound *versus* the covalent nature of the binding of the excess electron to the isolated DNA bases through either negative ion photoelectron spectroscopy (NIPS) of the anions of uracil and thymine generated via a supersonic expansion nozzle ion source [33,35,36], or a technique based on the formation of the anions in charge-exchange collisions with laser-excited Rydberg atoms [34]. The accurate measurement of electron attachment energies of the DNA bases was instead the aim of the low-energy electron transmission spectroscopy (ETS) experiments reported in [37]. The ETS technique was there employed to observe the formation of temporary anion states of uracil and all the four DNA bases upon attachment of electrons into the empty π^* molecular orbital (MO), observation that, because of the large electric dipole moments of these compounds, represented a significant experimental challenge. After directing an energy-selected electron beam through a gas cell containing a sufficient density of the target compound to partially attenuate the beam, the scattered electrons are collected at a retarding electrode following the collision region and the total transmitted current, comprising the unscattered electrons, is finally measured. A sharp dip in this current as a function of electron energy corresponds to the presence of a peak in the scattering cross section arising from the formation of a temporary anion state [37]. The ET spectra showed a common range of attachment energies into the lowest orbitals in all the 5 bases, varying from around 0.2 eV up to 4.5 eV relative to the electron 'injection' into the lowest three unoccupied π^* MOs.

The first measurement which directly pointed at elucidating the role of TNI formation in the DEA processes of DNA bases was carried out in [38]. The experiments, performed at the Berlin laboratory in a standard crossed-beam apparatus [39], demonstrated the sensitivity of specific DNA bases (thymine and cytosine) to resonant molecular dissociation even at electron energies below ionization (7.5–10 eV [40]). In particular, the authors measured the electron energy dependence for production of a great variety of anion fragments, induced by resonant attachment of subionization electrons to thymine and cytosine within

femtosecond time scales. At the lowest electron energies they also observed stable molecular anions of those bases and they finally concluded that such resonant mechanism may be related to critical damage of irradiated cellular DNA by subionizing electrons prior to thermalization.

After it became well established that the secondary low-energy electrons played a crucial role in the effective chain of reactions responsible of radiation damage (see the already mentioned work in [5]), the very last few years have witnessed a marked increase in the gas-phase experiments investigating the DEA on (isolated) biomolecules. In particular, in order to decipher possible molecular pathways leading to DNA strand breaks, different research groups started to investigate electron induced reactions in building blocks of DNA including the nucleobases [41–53], the deoxyribose molecule [54], the DNA backbone sugarlike analogue tetrahydrofuran [55], the thymidine and uridine nucleosides [56], the 5-bromouridine system [57,58].

Märk and coworkers in Innsbruck, in collaboration with Illenberger and coworkers in Berlin, employed crossed electron–molecule beams devices [59,60], consisting of an electron source, an oven and a quadrupole mass analyzer, to study the electron attachment process to the gas-phase DNA bases cytosine, thymine and uracile. They show that all nucleobases (NBs) undergo DEA at subexcitation energies (less than 3 eV) leading to dehydrogenation

$$e^- + NB \rightarrow NB^{*-} \rightarrow (NB\text{–}H)^- + H, \tag{1}$$

where NB^{*-} is the TNI of the corresponding NB and $(NB\text{–}H)^-$ is the closed shell anion formed by the ejection of a neutral hydrogen radical. The reaction is energetically driven by the appreciable electron affinity of the $(NB\text{–}H)^{\bullet}$ radicals, which is in the range between 3 and 4 eV [37,42] and it is shown to be not only bond selective [46] but also site selective [51]. Analogously, electron attachment to gas phase thymine and uracile in the energy range between 5 and 12 eV leads to bond and site selective loss of H^- [49]. The observed ion yield consist of a series of four overlapping resonances and the associated DEA reaction can be written as

$$e^- + NB \rightarrow NB^{*-} \rightarrow (NB\text{–}H) + H^-. \tag{2}$$

Each of the four resonances leads to H^- loss from one particular position, so that the DEA reaction results to be bond and site selective by properly tuning the electron energy.

The decomposition of purine nucleobases, adenine and guanine, by very low energy electrons has been instead the object of the study reported in [52]. The authors show that again the fragmentation is due to DEA involving low lying (< 3 eV) shape resonances, but also *via* core excited resonances (located near 6 eV). As observed for the pyrimidine bases, in adenine the low energy resonances exclusively lead to dehydrogenation with the excess electron remaining on the molecule. This reaction dominates DEA in the entire range 0–15 eV. On the other hand guanine behaves very different in that the loss of a neutra hydrogen is comparatively a weak process while various further decomposition reactions are observed from the low energy π^* precursor ions, implicating both single bond cleavage and more complex unimolecular decompositions associated with the excision of cyano units from the cyclic structure.

Gas-phase experiments on other molecules of biological interest have also recently carried out, such as the crossed electron–molecule beams analysis of glycine [60,61], of

alanine [62], of the formic acid dimer [63], of the conversion of aminoacids (as illustrated by the cysteine) by electrons at subexcitation energies [64], or the NIPS study of the thymine–glycine complex [65], enriching the overall understanding of the molecular mechanisms responsible of the radiation damage.

3. RECENT THEORETICAL MODELLING OF RESONANT STATES IN BIOMOLECULES

The recent experimental findings connecting the radiation damage to the interaction of secondary LEEs with DNA components and proteins provided a strong motivation to theoreticians for studying the scattering of LEEs off biomolecules, with the aim of understanding the detailed mechanisms underlying the final damaging effect of ionizing radiations. In this section we will limit ourselves to review some recent work on the modelling of the scattering of LEEs off biomolecules while in the following section we will describe the approach we have followed in our own investigation on the low-energy resonant electron attachment to molecules of biological interest.

Using *ab initio* electronic structure calculations, Simons and coworkers carried out calculations on the neutral and lowest adiabatic anion curves for species consisting of fragments of DNA consisting of a base, a deoxyribose and a phosphate group [66]. Their interest focused on the study of indirect DEA processes in which the LEE ($0.2\ \text{eV} < E < 2\ \text{eV}$) attaches to an orbital in one part of the molecule (namely a valence π^* orbital of one of DNA's bases) but a bond is subsequently broken in another part (i.e., a sugar–phosphate C–O σ^* bond); this mechanism could explain the structural damage in DNA caused by the interaction with secondary LEEs. Their quantum chemistry calculations for, e.g., the cytosine–sugar–phosphate portion of the DNA show indeed that the lower adiabatic anion state consists of a dominantly valence π^* state (i.e., with the excess electron occupying a π^* orbital of the cytosine) for R values of the C–O bond less than 1.75 Å and a dominantly σ^* state for larger R values (with the electron occupying a sugar–phosphate C–O σ^*). Hence, the electron attachment forms a π^* anion that evolves, as the C–O bond length stretches to near 1.75 Å, into a σ^* anion that then fragments to produce the very stable phosphate anion and a sugar-based carbon radical [66].

Starting from their first works, based on the electronic structure calculations of the neutral and the diabatic π^* and σ^* states (alternatively, the small-R π^* component and the large-R σ^* component of the adiabatic curves), the authors set up a theoretical model in order to eliminate much of the computational expense involved in performing such calculations [67]. The value and accuracy of the model are illustrated by studying the thymine–sugar–phosphate system, the CCC codon (with three cytosine bases) and the sugar–phosphate–sugar system. In the proposed model, the authors still calculate the energy of the neutral species and of the σ^* diabatic curve of the anion at larger R values where this anion is electronically stabler. Such curves are computed as a function the length R of the bond being considered for breakage with all other geometrical degrees of freedom relaxed to minimize the energy. As for the π^* diabatic state of the anion, they assume instead that its energy curve can be approximated, at least in a substantial neighborhood of the neutral's equilibrium bond length, by shifting the neutral's curve upward in energy by the kinetic energy E_{coll} of the incident electron for each E_{coll} lying within the Heisenberg width of the π^* state. This implies the need to know, or to compute, the position and the

width of this π^* state, for instance by a stabilization-like method [68]. The authors also assume that the σ^* curve of the anion can be extrapolated (by an appropriate exponential form) to smaller R values where the diabatic state is metastable, and that the σ^* and π^* diabatic states couple *via* a scalar (i.e., R-independent) matrix element $\langle\sigma^*|H|\pi^*\rangle = V$. Now, the lower and upper adiabatic states that arise from such coupling can be obtained as eigenvalues of a 2×2 Hamiltonian matrix. The coupling matrix elements are obtained *via* a single stabilization calculation on the lower metastable state of the anion at the value of R where the diabatic π^* and σ^* curves intersect [67].

Another theoretical research group which makes use of quantum chemistry methods to study the radiation damage problem is the group of Sommerfeld and coworkers. In their study of electron driven chemical reactions and of electronically metastable molecules, Sommerfeld and collaborators applied the *ab initio* methods they developed to the investigation of dipole-bound states, considered as doorways in DEA [69]. They previously analysed the electronic interaction between dipole-bound and valence anions of uracil and chlorouracil [70] by computing the coupling strength between the two different attachment states which, in general, show very different electronic structures with the extra electron occupying completely different regions of space. Similarly to Simons and coworkers, the coupling is obtained by fitting a diabatic model potential to a cut through the two adiabatic surfaces of the anions obtained from *ab initio* calculations. As the author discussed in Ref. [71] a reasonably balanced description of the two (very different) anionic states and of the avoided crossing structure, where the upper adiabatic state crosses the potential energy surfaces (PES) of the neutral molecule and is transferred into a resonance, can be achieved by employing the electron propagator approach. For U and UCl they employed the second-order perturbation expansion of the Green's function (ADC(2) method, Ref. [72]), whose quality turns out to be roughly comparable with MP2 calculations for the closed-shell ground states, but owing to the strong orbital relaxation of the valence states, a slight imbalance in favor of the dipole-bound states is expected.

The electron affinities as well as resonance energies associated with vertical detachment into the valence orbitals of uracil and chlorouracil are obtained and compared with the available experimental and theoretical data. In particular, the complex Siegert energies which characterize the resonance states and that cannot obviously be computed using standard bound-state quantum chemistry techniques, are obtained by means of a method [73,74] based on the ADC(2) approach combined with a complex absorbing potential [75]. The real part of the calculated Siegert energies define the adiabatic states used in the diabatization procedure and the complex parts provide the autodetachment lifetimes.

The electronic coupling of dipole-bound and valence anions was estimated to be around 43 meV for both anion pairs [70], namely about one order of magnitude smaller than the vertical energy differences of the diabatic states at their respective equilibrium structures. Hence, both U and UCl are in the weak coupling regime, though at a threshold of a valid adiabatic description; in any case, the electronic interaction makes the (vibrationally excited) dipole-bound states very efficient doorways to the valence states acting as TNIs in a DEA process. In particular, the UCl system, whose valence state lies at least 300 meV below its dipole bound state [70], contains a sufficient amount of internal energy that can be dissipated by intramolecular vibrational relaxation and that can stabilize the valence state, thereby creating a long-lived anion: this situation exemplifies the case where zero- and near zero-energy electrons may be trapped or may induce reactions by first undergoing electron capture into the dipole-bound orbital followed by intramolecular electron transfer

from the dipole-bound orbital onto the nuclear framework, the latter being allowed by its strong electronic interaction with the lowest valence state. A possible experimental evidence of the role of such coupling in free-electron attachment processes is given by the work presented in [45], where a dipole-bound state of uracil is invoked as an intermediate to explain electron-induced cleavage of a N–H bond.

Finally, by comparing the result for the electronic coupling between the two anionic states with the one obtained for the nitromethane [71] the author suggests that this order of magnitude for the electronic coupling might turn out to be typical for dipole-bound/valence state interactions.

Very recently, Tonzani and Greene [76] presented their study on LEE scattering from isolated uracile and each of the DNA bases in their equilibrium geometry, study which has been carried out with a method developed by the authors and applied so far to small molecules [77] and to other extended systems (unpublished results). Analogously to our Symmetry Adapted–Single Center Expansion (SA–SCE) method, the authors use the static exchange approximation (see Section 4.2 below) to recast the many-body problem of the interaction between the charges in a target molecule and the scattered electron into a one-body problem for the continuum electron with a nonlocal potential. Such potential is modelled as the sum of a local electrostatic contribution, the nonlocal exchange term and the equally nonlocal polarization–correlation potential. To reduce the computational task the authors use a local-density approximation for the exchange potential, which reduces it to a functional only of the local density [78], and a local parameter-free model for the correlation–polarization potential based on density-functional theory.

To describe electron scattering from a general molecule the authors employ the R-matrix method [79] which partitions space into two regions: an internal region within which all the short-range physics is confined and an outer region where only long-range interactions (such as Coulomb and dipole potentials) are important (see Ref. [79] for details).

Their results for cross sections and resonances show an overall shift of about 1.5–2 eV higher for all the computed resonances when compared to the experiments: the shift is attributed by the authors to the approximate nature of their model. However, their method seems to be capable of reproducing the observed trends of the resonance spacing, their widths and also their relative positions for different bases. Similarly to our model (see, e.g., [80]), from the nodal structure of the resonant wavefunctions, associated to the relevant TNIs, the authors try a connection with the observed breakup patterns and products.

To conclude this brief review on some selected theoretical models for the scattering of LEEs off biomolecules, we mention what has been, to the best of our knowledge, the only attempt to simulate with an euristic theoretical model the full LEE scattering from a sytylized DNA molecule. In a series of papers [81–83], Caron and Sanche propose a framework which is capable, at least qualitatively, to treat LEE scattering from large biomolecules having helical topology. The biomolecule is represented by a model of simple scatterers organized into a helical structure which is, first of all, applied to base-pair arrangements in DNA. The problem is decoupled into two parts: First, the electrons are allowed to undergo multiple scattering within the entire macromolecule and then the new (diffracted) wave function, defined by the atomic arrangement within the molecule, interacts at a specific site, where it can be captured in a resonant state. The basic equation for the asymptotic form of the total wave function for an incident plane wave in the R-matrix framework is hence modified in order to include the interference effect caused by the multiple scattering,

and the capture amplitude of an electron in a shape or core excited resonance of a basic subunit is also expressed in the multiple scattering formalism.

With their DNA model the authors are able to predict an appreciable enhancement of the elastic and resonant capture cross section at incident energies below 15 eV [81]. Even though their method is, of necessity, strongly simplified, their results may qualitatively explain the observed prominence of low-energy resonances in strand breaking of plasmid DNA.

By extending their analysis to A-type DNA as well as nonperiodic arrangements in B-type DNA [82], diffraction patterns due to base-pair spacing are found by such calculations under all conditions. The effect of geometric disorder in the bases arrangements is also investigated, showing that such disorder could be seen as due to pitch variations and to the presence of water molecules and ions within the molecule which causes a loss of coherence in the diffracted partial waves. In the discussion of the role of electron diffraction in electron attachment to the bases, leading to the formation of shape and core-excited resonances, the decay of the TNIs into dissociative-state channels produncing DNA strand breaks is described and A-type DNA is found to be much more sensitive to LEEs than B type.

Finally in [83] the authors extend the model in order to include the backbone in a static B-type DNA model, finding that the internal diffraction pattern due to base pairs is still present, but that the addition of the backbone effectively screens the base pairs by a factor of 2. On the other hand, the repeated periodic structure of the sugare–phosphate units of the backbone is not found to cause considerable diffraction features, although they find that between 2 and 5 eV electron of impact energies the localization at the phosphate unit is highly favoured. Moreover, calculation of electron capture factors at the phosphate group for electrons arriving parallel and perpendicular to the axis of DNA did not exhibit significant differences, thus suggesting that the differences observed experimentally in DNA damage due to different orientations of incoming electrons [84] are not caused by variations of the diffracted wave amplitude with angles of incidence.

4. THE PRESENT APPROACH: THE SYMMETRY ADAPTED–SINGLE CENTRE EXPANSION (SA–SCE) METHOD

The approach we follow to model the electron–molecule interaction is based on a single centre expansion of the molecular and incident electron wavefunctions about the centre of mass of the molecule. Such choice, often used in bound-state problems, was adopted in the study of electron–molecule scattering for the first time in the early 1970s [85–88] and was motivated by the semplification it induced in the formulation and solution of the scattering equations. Since then, many modifications and improvements contributed to increase the efficiency and reliability of the present computational technique [89] whose applications were extended, in the last five years, to the study of resonant DEA of LEEs to gas-phase DNA components, proteins and other molecules of biological interest.

As in the original papers quoted above, we shall assume that the electron motion occurs on a time-scale which is short compared to molecular vibrations and the Born–Oppenheimer (BO) approximation is hence considered to hold. There are of course a number of examples where this assumption breaks down [90]; for instance, within the

BO fixed nuclei (FN) approximation, in addition to the separation of electronic and molecular motions the target molecule is held at a frozen geometry during the scattering process and the total cross section is shown to diverge due to the long range of the electron–dipole interaction [91]. However, when the rotational motion of the molecule is included in the scattering problem, the averaging of the interaction potential over the rotation of the molecule removes the divergence in the total cross section [91].

In addition to working in the FN approximation, we further assume that the target molecule is adequately described by the Hartree–Fock (HF) single-determinant wavefunction associated to the ground electronic state. The asymptotic scattering state is thus given by a single Slater determinant formed by the antisymmetrized product of the HF orbitals and one additional positive energy scattering orbital. Given these assumptions, both vibrational and electronic excitation due to the electron impact are initially neglected. However, from the study of the shape resonances which may characterize the elastic scattering process and that we associate to the previously mentioned TNIs, we can still obtain relevant information on the possible fragmentation dynamics which follows the electron attachment in competition with the auto-detachment, as will be shown in Section 4.8.

In the following subsections we will outline the basic ingredients and the resulting scattering equations of the method we employ, ending with the extention of the method to include the nuclear motion and, hence, the vibrational inelastic scattering.

4.1. The SA–SCE wavefunctions and one-electron density

In our approach any three-dimensional function is expanded around a single-center taken to be the center-of-mass of the global $(N + 1)$-electron molecular structure. Hence, for instance, the one-electron bound orbitals ϕ_i of the target molecule can be expanded in a symmetry-adapted angular basis $\{X_{hl}^{p\mu}(\theta, \phi)\}$ [89]:

$$\phi_i^{p\mu}(\mathbf{r}) = \frac{1}{r} \sum_{hl} u_{hl}^{i,p\mu}(r) X_{hl}^{p\mu}(\theta, \phi), \tag{3}$$

as well as the wave function F describing the impinging electron:

$$F(\mathbf{r}) = \sum_{p\mu} F^{p\mu}(\mathbf{r}) = \frac{1}{r} \sum_{p\mu hl} F_{hl}^{p\mu}(r) X_{hl}^{p\mu}(\theta, \phi). \tag{4}$$

In equation (3) the index i labels a specific, multicenter occupied orbital which belongs to one specific irreducible representation (IR) of the point group of the molecule. The indices $(p\mu)$ label a relevant IR p and one of its components μ. The index h labels a specific basis function, for a given partial wave l, used within the μth component of the pth IR.

In the same fashion all the potential functions modelling the electron–molecule interactions will be expanded in a symmetry-adapted angular basis. The quadratures are carried out using Gauss–Legendre abscissae and weights W_α for θ and Gauss–Chebyshev abscissae and weights for ϕ, on a discrete variable radial grid.

One essential point is the construction of the symmetry-adapted spherical harmonics (SASH), X, as linear combination of spherical harmonics $Y_l^m(\theta, \phi)$ which, for a given l,

form a $(2l+1)$-dimensional basis for the IR's components of the full rotation group

$$X_{hl}^{p\mu}(\theta,\phi) = \sum_{m=-l}^{l} b_{hlm}^{p\mu} Y_l^m(\theta,\phi) \tag{5}$$

and the coefficients b can be obtained from a knowledge of the character tables for each of the IRs appearing in the specific molecular point group [92]. In the case of closed shell molecules, the Xs can be built up as linear combination of real spherical harmonics [93] which can still, by convention, labelled by the quantum numbers l and m such as [94]

$$\begin{aligned} S_{l|m|}^{+}(\theta,\phi) &= \frac{1}{\sqrt{2}}\big(Y_{lm}(\theta,\phi) + Y_{l-m}(\theta,\phi)\big), \\ S_{l|m|}^{-}(\theta,\phi) &= \frac{1}{i\sqrt{2}}\big(Y_{lm}(\theta,\phi) - Y_{l-m}(\theta,\phi)\big). \end{aligned} \tag{6}$$

In order to perform the expansion in equation (3) one needs to start from the multicentre wavefunction which describes the target molecule and then generate by quadrature each of the u_{hl}^k coefficients. We generate the bound molecular wavefunction by means of a standard quantum chemistry code, like Gaussian [95]; the explicit expression of the quadrature used to compute the u_{hl}^k coefficients for multicentre Gaussian Type Orbitals (GTOs) has been given in [96].

If the electronic state of the target molecule is described by a single Slater determinant, $\Psi(\mathbf{x}_1, \mathbf{x}_2, \ldots, \mathbf{x}_N)$, built from N occupied one-electron MOs ϕ_i, after one obtains the radial coefficients $u_{hl}^k(r)$ for each ϕ_i of equation (3), the density function with respect to the center of mass for a closed-shell electronic state can be written as

$$\rho(\mathbf{r}) = \int \big|\Psi(\mathbf{x}_1, \mathbf{x}_2, \ldots, \mathbf{x}_N)\big|^2 \, d\mathbf{x}_2 \cdots \mathbf{x}_N = 2 \times \sum_{i=1}^{n_{\mathrm{occ}}} \big|\phi_i(\mathbf{r})\big|^2, \tag{7}$$

where the factor 2 is due to the sum over spin and the i sum is over each doubly occupied orbital. Once the quantity $\rho(\mathbf{r})$ is obtained from the SCE bound-state wavefunctions $\phi_i(\mathbf{r})$, it can be expanded in terms of symmetry-adapted functions belonging to the totally symmetric (A_1) IR as

$$\rho(\mathbf{r}) = \frac{1}{r} \sum_{lm} \rho_{lm}(r) X_{lm}^{A_1}(\theta\phi) \tag{8}$$

where

$$\rho_{lm}(r) = 2 \times \sum_{i=1}^{n_{\mathrm{occ}}} \int_0^{\pi} \sin\theta \, d\theta \int_0^{2\pi} u_i(\mathbf{r}) \cdot u_i(\mathbf{r}) \, d\phi. \tag{9}$$

Notice that for the A_1 irreducible representation the SASH $X_{hl}^{A_1}$, constructed as linear combinations of real spherical harmonics S, have the expansion coefficients all singly-valued to one (that is, one value of m for each l). Thus, in this case we have only one basis function for each $|lm\rangle$ couplet, i.e. $h \equiv 1$, so the notation $X_{hl}^{A_1}$ becomes $X_{lm}^{A_1}$, the latter being a real spherical harmonic.

4.2. Fixed-nuclei scattering equations

In the FN approximation the Schrödinger equation for the electronic motion is given by

$$\hat{H}(\mathbf{r}, \mathbf{X}; \mathbf{R})\Psi(\mathbf{r}, \mathbf{X}; \mathbf{R}) = E\Psi(\mathbf{r}, \mathbf{X}; \mathbf{R}), \tag{10}$$

where $\mathbf{r}$ is the position of the continuum electron, $\mathbf{X}$ represents collectively the coordinates $\mathbf{x}_i$ $(i = 1, \ldots, N)$ of the target electrons and $\mathbf{R}$ corresponds to the set of frozen nuclear coordinates $\mathbf{R}_\gamma$ $(\gamma = 1, \ldots, M)$ of the target molecule acting as fixed parameters. The scattering Hamiltonian is given by:

$$\hat{H}(\mathbf{r}, \mathbf{X}; \mathbf{R}) = \hat{T}(\mathbf{r}) + \hat{V}(\mathbf{r}, \mathbf{X}; \mathbf{R}) + \hat{H}_{\text{target}}(\mathbf{X}; \mathbf{R}), \tag{11}$$

where $\hat{T}$ is the kinetic energy operator of the incident electron, $\hat{V}$ is the potential energy operator which describes the interaction of the electron with the target molecule and $\hat{H}_{\text{target}}$ is the electronic Hamiltonian for the target electrons. The interaction is due to the attractive and repulsive electrostatic forces among the incident electron and the charges in the molecules:

$$\hat{V}(\mathbf{r}, \mathbf{X}; \mathbf{R}) = \sum_{i=1}^{N} \frac{1}{|\mathbf{r} - \mathbf{x}_i|} - \sum_{\gamma=1}^{M} \frac{Z_\gamma}{|\mathbf{r} - \mathbf{R}_\gamma|}, \tag{12}$$

for a target molecule with N electrons and M nuclei with charge Z_γ and (fixed) positions $\mathbf{R}_\gamma$. For sake of simplicity we will drop the symbol $\mathbf{R}$, which is not associated to a set of variables in the FN approximation, in the following equations.

In a general way, by denoting with $\psi_\alpha(\mathbf{X})$ one generic eigenstate of the target Hamiltonian such that

$$\hat{H}_{\text{target}}(\mathbf{X})\psi_\alpha(\mathbf{X}) = \epsilon_\alpha \psi_\alpha(\mathbf{X}), \tag{13}$$

where ϵ_α is the electronic eigenvalue for the α asymptotic (i.e., isolated) target state, one can expand the total electronic wavefunction $\Psi(\mathbf{r}, \mathbf{X})$ in terms of the eigenstates of the target Hamiltonian:

$$\Psi(\mathbf{r}, \mathbf{X}) = \sum_{\alpha} \mathcal{A}\big\{F_\alpha(\mathbf{r})\psi_\alpha(\mathbf{X})\big\}. \tag{14}$$

In the previous equation $\mathcal{A}$ is the antisymmetrization operator which operates on the coordinates of the target electrons and of the incident electron. Inserting expression (14) into equation (10), multiplying on the left with the conjugate of one of the target eigenstates $\psi^*_\beta(\mathbf{X})$ and integrating over the target electrons degrees of freedom $\mathbf{X} \equiv \{\mathbf{x}_i\}$ leads to coupled partial integro-differential equations of the form (in a.u.)

$$\left[\frac{1}{2}\nabla^2 + (E - \epsilon_\beta)\right] F_\beta(\mathbf{r}) = \sum_{\alpha} \int \hat{V}_{\alpha\beta}(\mathbf{r}, \mathbf{r}') F_\alpha(\mathbf{r}')\, d\mathbf{r}', \tag{15}$$

where $\mathbf{r}'$ generically represents the coordinate $\mathbf{x}_i$ of one of the target electrons. The kernel of the integral operator for the potential, $V_{\alpha\beta}$, is in general a sum of diagonal (local potentials) and nondiagonal (nonlocal potentials) terms:

$$\begin{aligned}
&\hat{V}_{\alpha\beta}(\mathbf{r},\mathbf{r}')F_\alpha(\mathbf{r}') \\
&\quad = \hat{V}^{\text{loc}}_{\alpha\beta}(\mathbf{r},\mathbf{r}')F_\alpha(\mathbf{r}')\delta(\mathbf{r}-\mathbf{r}') + \hat{V}^{\text{non-loc}}_{\alpha\beta}(\mathbf{r},\mathbf{r}')F_\alpha(\mathbf{r}') \\
&\quad = \left(\int \psi^*_\beta(\mathbf{X})\hat{V}^{\text{loc}}(\mathbf{r},\mathbf{X})\psi_\alpha(\mathbf{X})\,d\mathbf{X}\right)F_\alpha(\mathbf{r}) + \hat{V}^{\text{non-loc}}_{\alpha\beta}(\mathbf{r},\mathbf{r}')F_\alpha(\mathbf{r}'),
\end{aligned} \tag{16}$$

where the nonlocal terms arise, as usual, from the evaluation of the electron–electron repulsion on a antisymmetrized wavefunction which interchanges the $\{\mathbf{x}_i\}$ and the $\mathbf{r}$ coordinates. In obtaining equation (15), we used the well-known orthonormality property of the set of the one-electron bound MOs and the orthogonality condition between the continuum wavefunction $F_\alpha(r)$ and the one-electron MOs $\phi^\alpha_j(x_j)$ defining each target eigenstate $\psi_\alpha(X)$ [89].

4.3. The static-exchange approximation

As already mentioned in the introduction to the present section, one simple approximation for the wavefunction of the target molecule is to assume it to be adequately described by a single Slater determinant. This corresponds to truncating to one state the expansion over the target states α in equation (14) such that

$$\Psi(\mathbf{r},\mathbf{X}) = F(\mathbf{r})\psi(\mathbf{X}). \tag{17}$$

This semplification leads to the static-exchange (SE) approximation for the potential in equation (15) [97] which becomes

$$\left[\frac{1}{2}\nabla^2 + (E-\epsilon)\right]F(\mathbf{r}) = \int V(\mathbf{r},\mathbf{r}')F(\mathbf{r}')\,d\mathbf{r}'. \tag{18}$$

For a target which has a closed shell electronic structure with n_{occ} doubly occupied one-electron MOs $\phi_j(\mathbf{x}_j)$ the SE potential can be written as

$$V(\mathbf{r},\mathbf{r}') = V_{\text{SE}}(\mathbf{r},\mathbf{r}') = -\sum_{\gamma=1}^{M}\frac{Z_\gamma}{|\mathbf{r}-\mathbf{R}_\gamma|} + \sum_{i=1}^{n_{\text{occ}}} 2\hat{J}_i(\mathbf{r}) - \hat{K}_i(\mathbf{r},\mathbf{r}'), \tag{19}$$

where $\hat{J}_i$ is the local repulsive static potential defined by

$$\hat{J}_i(\mathbf{r}) = \int \frac{\phi^*_i(\mathbf{r}')\phi_i(\mathbf{r}')}{|\mathbf{r}-\mathbf{r}'|}d\mathbf{r}' \tag{20}$$

and $\hat{K}_i$ is the nonlocal exchange potential operator given by

$$\hat{K}_i(\mathbf{r},\mathbf{r}')F(\mathbf{r}') = \phi_i(\mathbf{r})\int \frac{\phi^*_i(\mathbf{r}')F(\mathbf{r}')}{|\mathbf{r}-\mathbf{r}'|}d\mathbf{r}'. \tag{21}$$

The attractive interaction between the scattering electron and the positive nuclei together with the local part of the repulsive interaction with the target electrons, given by the $\hat{J}_i$ operators, define the static part of the potential in the scattering process, $\hat{V}^{\text{st}}$, which is expanded over SASHs belonging to the A_1 (total symmetric) IR as

$$\hat{V}^{\text{st}} = \sum_{lm} V^{\text{st}}_{lm}(r)X^{A_1}_{lm}(\theta,\phi). \tag{22}$$

The exchange (nonlocal) part of the electrostatic potential will be discussed into details in Section 4.5.

We can hence rewrite the equation for the electron–molecule scattering in the SE approximation (Eq. (18)) as

$$\left[-\frac{1}{2}\nabla^2 - \frac{1}{2}k^2 + \hat{V}^{\mathrm{st}}\right] F(\mathbf{r}) = \sum_{i=1}^{n_{\mathrm{occ}}} \int \hat{K}_i(\mathbf{r}, \mathbf{r}') F(\mathbf{r}')\, d\mathbf{r}', \tag{23}$$

where $k^2 = 2\,(E - \epsilon)$.

The major limitation of the SE approximation is due to the fact that if the ground electronic state of the target molecule is represented by a single Slater determinant both correlation effects and the long range target response at the incoming charged projectile, i.e. its polarization, are neglected. Additional states can be included in the description of the wavefunction in equation (17), states which can be either eigenstates of the target Hamiltonian as in equation (14) or can be chosen to be pseudo-states whose inclusion accurately reproduce the static and low-frequency polarizability of the system [98,99]. A second approach is to include the appropriate optical potential which can be computed by purely *ab initio* means [100]. An alternative approach which we have used is to include the effects of correlation and polarization through the addition of a local, energy-independent model potential $\hat{V}^{\mathrm{cp}}$ which will be described in the next subsection.

4.4. Model correlation–polarization potential

The response of the target to the incoming projectile, not included at the SE level of approximation, depends on the distance of the incoming electron, varying from a purely polarization effects at large distances up to including exchange-correlation interaction with the bound electrons within the molecular volume. The model correlation–polarization potential, $\hat{V}^{\mathrm{cp}}$, that have been implemented within a SCE treatment of polyatomic molecules is therefore distinguishing between a long-range and a short-range region of interaction. At large distances of the electron from the target electronic density the velocity of the slow electron can be considered low enough that the bound molecular electrons can respond adiabatically to the impinging projectile without a specific dependence on its local velocity. Hence, the perturbative polarization effects are dominant and the potential acquires a local analytic form, independent of the sign of its charge. As the projectile approaches the target, however, the attraction from the Coulomb core increases its local velocity and therefore strongly modifies its motion via correlation processes similar to multiple scattering effects; the ensuing potential is thus nonadiabatic on the projectile's velocity, becoming energy-dependent, and with a strong nonlocal character. The different nature of the target response to the incoming projectile in the short and long range regions shows up when comparing the scattering of electrons and positrons from molecular targets: While the asymptotic polarization potential is independent of the sign of the charge of the projectile, relevant differences appear between the behaviour of electrons and positrons approaching the target.

The overall correlation–polarization interaction can be written as

$$\hat{V}^{\mathrm{cp}}(\mathbf{r}) = \begin{cases} \hat{V}^{\mathrm{corr}}(\mathbf{r}) & \text{for } \mathbf{r} \leqslant \mathbf{r}_{\mathrm{match}}, \\ \hat{V}^{\mathrm{pol}}(\mathbf{r}) & \text{for } \mathbf{r} > \mathbf{r}_{\mathrm{match}}, \end{cases} \tag{24}$$

where the connecting spatial factor $\mathbf{r}_{\text{match}}$ is obtained by requiring the short-range V^{corr} to smoothly connect to the long-range polarization potential. Such matching can be accomplished in various ways which will be discussed below.

Starting with the short-range part of $\hat{V}^{\text{cp}}$, one possible form for the correlation potential, implemented in our SCE approach, is based on a local simulation of the short-range interaction *via* a modified Free Electron Gas (FEG) modelling in order to evaluate the correlation between the bound electrons, given as the self-consistent-field (SCF) density $\rho(\mathbf{r})$ for the target ground electronic state, and the impinging electron [101–104]. Quite generally the correlation energy E_{corr} can be written as

$$E_{\text{corr}}(\rho) = \int \rho(\mathbf{r})\epsilon_{\text{corr}}(\mathbf{r})\, d\mathbf{r} \tag{25}$$

where ϵ_{corr} is now the one-particle correlation energy at the point $\mathbf{r}$. It can be replaced by the average correlation energy of a particle within a homogeneous electron gas with density $\rho(\mathbf{r})$ and the latter correlation can now be given by a simple expression as a function of a dimensionless parameter r_s, the radius of a sphere containing one electron [105]:

$$\frac{4}{3}\pi r_s^3 a_0^3 \rho(\mathbf{r}) = 1, \tag{26}$$

finally obtaining the $\hat{V}^{\text{corr}}$ as an analytic function of the (undistorted) density of the isolated target. In our SCE approach two, very similar, functional forms derived from the FEG model (see also Section 4.5) can be used to simulate the short-range correlation effects *via* a local potential. The first one gives the expression obtained for $\hat{V}^{\text{corr}}$ in the small-r_s region (high $\rho(\mathbf{r})$) and in the high-r_s region (low-density) [102]

$$\hat{V}^{\text{corr}}(\mathbf{r}) = \begin{cases} \ln r_s(0.0311 + 0.00133 r_s) - 0.0084 r_s - 0.0584, & r_s < 1.0 \\ \frac{\gamma(1+\frac{7}{6}\beta_1 r_s^{1/2} + \frac{4}{3}\beta_2 r_s)}{(1+\beta_1 r_s^{1/2} + \beta_2 r_s)^2}, & r_s \geqslant 1.0, \end{cases} \tag{27}$$

where $\gamma = -0.1423$, $\beta_1 = 1.0529$ and $\beta_2 = 0.3334$ [102]. The second form considers instead three density regions see [103]

$$\hat{V}^{\text{corr}}(\mathbf{r}) = \begin{cases} \ln r_s(0.0311 + 0.006 r_s) - 0.015 r_s - 0.0584, & r_s \leqslant 0.7, \\ -0.07356 + 0.02224 \ln r_s, & 0.7 < r_s \leqslant 10.0, \\ -0.584 r_s^{-1} + 1.988 r_s^{-\frac{3}{2}} - 2.450 r_s^{-2} - 0.733 r_s^{-\frac{5}{2}}, & r_s > 10.0. \end{cases} \tag{28}$$

Alternatively $\hat{V}^{\text{corr}}$ can be derived from the density functional theory (DFT) expression for the correlation energy

$$\hat{V}^{\text{corr}}(\mathbf{r}) = \frac{\partial}{\partial \rho} E_{\text{corr}}\big[\rho(\mathbf{r})\big], \tag{29}$$

where E_{corr} depends on the one-electron density $\rho(\mathbf{r})$. Apart from the $\rho(\mathbf{r})$, the DFT expression for $\hat{V}^{\text{corr}}(\mathbf{r})$, which is called the LYP (Lee–Yang–Parr) correlation potential, depends on the first and second functional derivatives of $\rho(\mathbf{r})$ [106], hence requiring a further single centre expansion of the first and second functional derivatives in addition to the SCE of the bound state wavefunction [107,108]. A new formulation has been developed for the gradient and the Laplacian of a generic SCE function [109] allowing to expand the

derivatives over the same angular basis as any SCE molecular property (as the density) they are derived from. This means that also the gradient and the Laplacian of the molecular density can be expanded over the SASHs belonging to the A_1 IR (see Section 4.1) preventing the otherwise needed (very time consuming) quadrature.

Whatever the chosen model for the local correlation potential, the computed $\hat{V}^{\rm corr}$ is then expanded over the SASH of the A_1 IR as illustrated for the molecular density, see equation (8), and for the static potential $\hat{V}^{\rm st}$, see equation (22).

Concerning the long-range part of $\hat{V}^{\rm cp}$, it analytically depends on the static electrical properties of the molecules (i.e. dipole and higher moments and polarizabilities) with the general form, for a given molecular geometry **R**,

$$\hat{V}^{\rm pol}(\mathbf{r};\mathbf{R}) = \lim_{r\to\infty}\left(-\sum_{k=1}\frac{\alpha_k(\mathbf{R})}{2r^{2k+2}}\right). \tag{30}$$

In our implementation of the SCE method, $\hat{V}^{\rm pol}$ can be calculated depending on the available data (either the spherical polarizability only, or the α_0 and α_2 terms or, finally, all of the six terms defining the polarizability tensor [93]). Again, the computed $\hat{V}^{\rm pol}$, obtained as a function of the Cartesian coordinates x, y and z, is expanded over the SASH of the A_1 IR as the other potentials.

Finally, as mentioned above we need to join the short-range correlation potential to the correct asymptotic part near the molecular nuclei, where the polarization potential becomes more attractive than the local correlation interaction. For instance, one can determine the matching point $r_{\rm match}$ by first computing the SCE of both contributions and then finding the smallest r where the two radial functions for $l = 0$ intersect or, in the cases where the two $l = 0$ potentials do not intersect, the r corresponding to their closest approach [103,104]. Once located $r_{\rm match}$, a modified $\hat{V}^{\rm pol}_{\rm match}$ is then defined by

$$V^{\rm pol}_{\rm match}(\mathbf{r}) = V^{\rm pol}(\mathbf{r}) + \sum_{lm} C_{lm} r^{-\lambda} X_{lm}(\theta,\phi). \tag{31}$$

The C_{lm} coefficients are determined by making the $V^{\rm pol}_{\rm match}$ exactly equal to $\hat{V}^{\rm corr}$ at $r = r_{\rm match}$ and the exponent λ is a function of l such that: $\lambda(l) = 6, 5, 6$ for $l = 0, 1, 2$ and $\lambda(l) = l + 2$ for $l \geqslant 3$. A switching function is then used to smoothly switch between $\hat{V}^{\rm pol}_{\rm match}$ and $\hat{V}^{\rm corr}$ in the region of $r_{\rm match}$ (see [110] for details).

Alternatively, instead of selecting the lowest partial wave component one can define a matching line (along which the crossing is searched) by specifying a direction connecting the centre of mass to either a given atom or a generic x, y, z point defined in the body-fixed frame of Ref. [93].

The obtained local $V^{\rm cp}$ is added to the $V^{\rm st}$ potential of equation (23) to obtain the static-exchange-correlation–polarization (SECP) approximation for the scattering equation.

4.5. Model exchange potential

To reduce the computational task, one can replace the exact nonlocal exchange interaction with an energy-dependent local exchange potential. For this purpose one can employ the Hara FEG Exchange (HFEGE) potential [78,111] to approximate the exchange interaction by an energy-dependent local function of the electron density of the target. The actual form

of the HFEGE potential derives from two approximations in the integral exchange terms in equation (23) or in the SECP one First, the molecular electrons are treated as a free-electron gas, with a given charge density $\rho(\mathbf{r};\mathbf{R})$ associated to the electronic state of the target (initially its ground electronic state) at the fixed nuclear geometry $\mathbf{R}$. Second, the distortion due to the interaction on the continuum function is neglected and the impinging electron is treated as a plane wave. The resulting FEGE potential is then given by the following form

$$V_{\mathrm{FEGE}}^{\mathrm{ex}}(\mathbf{r}) = \frac{2}{\pi} k_F(\mathbf{r}) \left(\frac{1}{2} + \frac{1-\eta^2}{4\eta} \ln \left| \frac{1+\eta}{1-\eta} \right| \right), \tag{32}$$

where k_F is the wavevector up to the top of the Fermi surface, $k_F(\mathbf{r}) = (3\pi^2\rho(\mathbf{r}))^{1/3}$, $\eta(\mathbf{r})$ holds the ratio between the actual wavevector for the scattering electron and k_F, $\eta = k/k_F$ and the local momentum is given as

$$k(\mathbf{r}) = \left\{ 2(E_{\mathrm{coll}} + I_p) + k_F^2(\mathbf{r}) \right\}^{1/2}. \tag{33}$$

The collision energy E_{coll} is in turn given by the initial-channel energy $1/2k_0^2$ and I_p is the ionisation potential for the neutral target molecule.

The HFEGE potential is known to give fairly reliable results when compared to the (iterative) exact exchange [111,112]; however it tends to be somewhat less attractive than the true nonlocal exchange potential [113].

An alternative way to simulate the exact exchange potential with a local potential is provided by the Semi-Classical (SC) exchange potential [114–116], based on the approximation of disregarding the local momentum of the bound electrons with respect to that of the impinging projectile. This is acceptable at rather large collision energies where it is realistic to assume that electron–molecule collisions modify only slightly the velocity of the continuum electron. If one, however, wants to deal with lower collision velocities, a way of including more correctly the effects of the bound electron momenta on the velocity of the projectile is given by the Modified Semi-Classical (MSC) exchange potential [116,117], where the local velocity of the continuum particle, in a classical sense, is modified by both the existence of the static potential and by the local velocity of the bound electrons. Thus such modification is expected to correctly provide a weaker interaction at low collision energies where most of the interesting features which are typical of electron scattering from molecules are experimentally observed.

4.6. The radial SA–SCE scattering equations and the cross sections

Once all the bound and the continuum wave functions have been expanded as in equations (3) and (4), along with the potential terms which are expanded over SASHs belonging to the A_1 IR, we can derive a set of coupled radial scattering equations which will give us a way of evaluating the unknown radial coefficients for the $(N+1)$th continuum electron. In order to write such equations, we first multiply equation (18) by $X_{p'\mu'}^{l'h'}$; then, we integrate over the angular variables, thus obtaining the following expression:

$$\left[\frac{d^2}{dr^2} - \frac{l(l+1)}{r^2} + 2(E-\epsilon) \right] F_{lh}^{p\mu}(r) = 2 \sum_{l'h'} \int dr'\, V_{lh,l'h'}^{p\mu}(r,r') F_{l'h'}^{p\mu}(r'), \tag{34}$$

where E is the collision energy $E = k^2/2$ and ϵ is the electronic eigenvalue of the neutral target molecule. These equations constitute a set of coupled partial integro-differential equations, where the coupling is extended to all the (lh) channels included in the calculation. Notice that there is, instead, no coupling between different IR components $p\mu$ of F.

Now, in order to solve the previous equation one has to evaluate the exchange integrals between bound and continuum electrons, given in equation (21), which are obtained by means of an iterative-exchange procedure [118]. In practice we do not solve for the scattering functions directly but we employ the Schwinger variational method to compute the scattering matrix elements of interest [119].

Let us define a local Hamiltonian $\hat{H}_L = -\frac{1}{2}\nabla^2 + V_L$, where the $\hat{V}_L$ potential is the sum of local contributions

$$\hat{V}_L = \hat{V}^{\text{st}} + \hat{V}^{\text{pol}} + \hat{V}^{\text{model exc}}. \tag{35}$$

The scattering equations are then written in terms of a Lippmann–Schwinger equation for a potential $\hat{V}_D$ which is the difference between the $\hat{V}_L$ and the full nonlocal potential

$$\psi_p = \phi_p + \hat{G}_\alpha \hat{V}_D \psi_p, \tag{36}$$

where ϕ_p is one of the solutions of the purely local potential

$$\hat{H}_L \phi_p = E\phi_p. \tag{37}$$

The potential $\hat{V}_D$ is hence defined as

$$\hat{V}_D = \hat{V}_{\text{exact exc}} - \hat{V}_{\text{model exc}} \tag{38}$$

and the Green's function

$$(E - \hat{H}_L)\hat{G}_L = \mathbf{1}. \tag{39}$$

Using the K matrix to define the asymptotic form of the scattering solutions, we can then write the K matrix for the full potential as

$$K_{pq} = K_{pq}^{(L)} + K_{pq}^{(D)}, \tag{40}$$

where $K^{(L)}$ is the K matrix due to scattering from $\hat{V}_L$ and $K^{(D)}$ is the correction term which can be obtained from

$$K_{pq}^{(D)} = -2\langle \phi_p | \hat{V}_D | \psi_q \rangle. \tag{41}$$

The expression for the correction to the K matrix given in equation (41) can be expanded using the Born series to give

$$K_{pq}^{(D)} = -2\sum_{i=0}^{\infty} \langle \phi_p | V_D (G_L V_D)^i | \phi_q \rangle. \tag{42}$$

Using numerical techniques previously discussed [119], it is possible to compute the action of the G_L and V_D on any arbitrary function and thus to obtain all of the matrix elements given in equation (42). The convergence of this sum can be greatly enhanced by using the $[N/N]$ Padé approximants of the form [120–122]

$$K_{pq}^{(D)}[N/N] = -2 \sum_{ij=0,N-1} \langle \phi_p | V_D (G_L V_D)^i \left| \phi_q^{(i)} \right\rangle D_{ij}^{-1} \left\langle \phi_p^{(j)} \right| V_D (G_L V_D)^j | \phi_q \rangle, \tag{43}$$

where D_{ij}^{-1} is the (i, j)th element of $\hat{D}^{-1}$ which is the inverse of the matrix $\hat{D}$ with elements

$$D_{ij} = \langle \phi_p^{(i)} | \hat{V}_D (G_L V_D)^{i+j} - \hat{V}_D (G_L V_D)^{i+j-1} | \phi_q^{(j)} \rangle. \tag{44}$$

The expression for the K matrix given in equation (43) can be shown to be equivalent to the Schwinger variational expression for the K matrix with the appropriate choice for the linear variational trial functions used in the variational expression [123]. This approach for computing scattering amplitudes has been found to be very rapidly convergent with respect to the order of the Padé approximant in many applications.

The K matrix elements can then be used to evaluate total integral cross sections (rotationally summed) and further employed to generate differential cross sections (DCS) for the elastic process. Such method reduces the scattering problem to the computation, by numerical quadrature, of a series of radial integrals which are needed to evaluate the variational expressions. The resulting elastic, rotationally summed, integral cross section are produced for each IR contributing to the scattering process. The total cross section is therefore simply given as

$$\sigma_{\text{tot}}(k^2) = \sum_{p\mu} \sigma_{p\mu}^{\text{elastic}}(k^2), \tag{45}$$

where k is the wavevector corresponding to the collision energy. The individual K-matrix elements, within each $(p\mu)$, will in turn provide the total elastic differential cross section, also summed over the contributing IRs at the considered collision energy.

Finally, we briefly mention that the development of a discrete-basis-set representation of the bound and continuum orbitals in an electron–molecule scattering process suggested the use of separable approximations for handling the nonlocal exchange kernel of equation (21) [124], development which was then extended and applied to polyatomic targets [125,126]. The obtained scattering equations have been solved according to the procedure explained in the next section, generalized to the case of multichannel scattering with a separable potential [124].

4.7. Solution of the homogeneous scattering equation

In order to show the notation we will limit ourselves to present here the solution of the radial scattering equation for the continuum electron in the case of a completely local approximation for the interaction potential.

If the exchange term is approximated by a local potential we can rewrite the scattering equation in an homogeneous form to obtain the static-model-exchange correlation–polarization (SMECP) approximation for the scattering equation:

$$\left[-\frac{1}{2}\nabla^2 - \frac{1}{2}k^2 + \hat{V}^{\text{st}} + \hat{V}^{\text{cp}} + \hat{V}^{\text{model exc}} \right] F(\mathbf{r}) = 0. \tag{46}$$

We can find the solutions of this equation by a procedure introduced by Sams and Kouri [127]. Indicating by $V(\mathbf{r})$ the sum of the three local potentials $V(\mathbf{r}) = V^{\text{st}}(\mathbf{r}) + V^{\text{cp}}(\mathbf{r}) + V^{\text{model exc}}(\mathbf{r})$, the local formulation of the scattering equation (34) takes the form

$$\left[\frac{d^2}{dr^2} - \frac{l(l+1)}{r^2} + k^2 \right] F_{lh}^{p\mu}(r) = 2 \sum_{l'h'} V_{lh,l'h'}^{p\mu}(r) F_{l'h'}^{p\mu}(r), \tag{47}$$

and the potential coupling elements are given as

$$V_{lh,l'h'}(r) = \left\langle X_{lh}^{p\mu}(\hat{r}) \middle| V(\mathbf{r}) \middle| X_{l'h'}^{p\mu}(\hat{r}) \right\rangle = \int d\hat{r}\, X_{lh}^{p\mu}(\hat{r}) V(\mathbf{r}) X_{l'h'}^{p\mu}(\hat{r}). \tag{48}$$

The standard Green's function technique allows us to rewrite the previous differential equations in an integral form

$$F_{lh}^{p\mu}(r) = \delta_{lh}\, j_{l_i}(kr) + \sum_n \int_0^r dr'\, g_{l_i}(r, r') V_{lh,l'h'}(r') F_{l'h'}^{p\mu}(r). \tag{49}$$

The integral on the right-hand side of the previous equation terminates at $r' = r$ (integral equations with this property are called Volterra equations), because the regular Green's function $g_{l_i}(r, r')$ is used

$$g_l(r, r') = \frac{1}{k}\left[\hat{j}_l(kr)\hat{n}_l(kr') - \hat{n}_l(kr)\hat{j}_l(kr')\right], \tag{50}$$

where $\hat{j}_l(kr)$ and $\hat{n}_l(kr)$ are Riccati–Bessel and Riccati–Neumann functions. The numerical implementation and the methods of stabilization for integral equations (49) have been discussed for diatomics in [124] and the generalization for polyatomic system is straightforward.

4.8. Analysis of resonances: The coupled adiabatic potential model

To examine in some detail the mechanism and qualitative characteristics of low-energy, one-electron resonances we further employed a model which is simple enough to be computationally attractive but with sufficient details of the full scattering problem to reproduce the essential features of the realistic cases. Hence, to facilitate the analysis of the resonances we have used an adiabatic representation of the electron–molecule interaction potential [90]. In spite of its fairly simple implementation, in fact, such a description of single-particle resonances in polyatomic systems turns out to be very effective in linking the spatial features of the resonances with the molecular structures of the target in question.

One starts from the consideration that the standard, symmetry-adapted angular momentum eigenstates, $X_{lh}^{p\mu}$ do not form the most efficient and compact angular basis for the radially dependent electron–molecule scattering process. An alternative approach could therefore be had from diagonalizing the angular Hamiltonian at each value of the electron–molecule distance, r. The angular functions obtained in this fashion are referred to as the adiabatic angular functions $Z_k^{p\mu}(\theta, \phi, r)$ which are linear combinations of the symmetry adapted harmonics discussed before and are given by

$$Z_k^{p\mu}(\theta, \phi, r) = \sum_{lh} X_{lh}^{p\mu}(\theta, \phi) C_{lh,k}(r), \tag{51}$$

where the expansion coefficients are solutions to the matrix eigenvalue equation

$$\sum_{lh} V_{l'h',lh}(r) C_{lh,k}(r) = V_k^{\mathrm{A}}(r) C_{l'h',k}(r). \tag{52}$$

The eigenvalues $V_k^{\mathrm{A}}(r)$ then form an adiabatic radial potential for each index value k.

Solving the scattering equations using $V_k^{\mathrm{A}}(r)$ can have several advantages. First the expansion of the scattering wave function in adiabatic angular states converges more rapidly than the corresponding expansion in angular momentum eigenstates. The second advantage is that the numerical instabilities found in the solution of the standard momentum eigenfunction expansion are greatly reduced. The third advantage is that often a single radial adiabatic potential can be responsible for the appearance of a shape resonance. In such cases the adiabatic potential can be used as a qualitative guide to better understand the main features of the resonant state. The spatial extent of the resonant wave function can be determined from the well and angular momentum barrier in a given adiabatic radial potential $V_k^{\mathrm{A}}(r)$, and the physical mechanism for the resonant trapping is seen to be due to the slow rate of tunneling through the potential barrier.

The current approach to solving the radial equations is based on our earlier approach, the piecewise diabatic (PD) method [90]. We decrease the size of diabatic regions so that we essentially obtain the solution of the scattering equations for scattering from the radial adiabatic potential $V_k^{\mathrm{A}}(r)$ including all nonadiabatic kinetic energy coupling terms. We will refer to these solutions as the coupled adiabatic (CA) solutions.

A narrow and isolated resonance in a scattering process at an energy E_R and width Γ can be shown to be due to a pole in the **S** matrix analytically continued into the complex plane at an energy $E = E_R - i(\Gamma/2)$. The **S** matrix is obtained from a scattering wave function by finding a solution with the usual asymptotic form that includes the appropriate Hankel functions. It is then possible to compute directly the **S** matrix at a complex energy by computing the solution using the standard numerical procedures with a complex-valued energy and by matching the solution to the Hankel functions with the appropriate complex argument. A resonance energy in the scattering can then be located by finding the energy values for which $1/(\det \mathbf{S}) = 0$.

Once the zeros of $1/(\det \mathbf{S})$ are found in the region of interest, one can compute the single-channel scattering state at that complex energy. The corresponding radial and spatial shapes of such states can help us to relate them to the corresponding electronic and spatial features of the target molecule.

5. THE PRESENT RESULTS ON GAS-PHASE BIOMOLECULES

In this section we report the results of our quantum calculations concerning the low-energy dynamics of electrons interacting with various biosystems. In particular, we aimed at the characterization of the resonant TNIs which act as the precursor of the molecular fragmentation. The calculations are carried out at the FN level and only elastic scattering can be treated at such level of approximation. However, we will show that, from the knowledge of the spatial features of the existing shape resonances, which resemble the TNIs precursor of the fragmentation in the DEA process, we can suggest the possible pathways in the following molecular decomposition.

We do not report here our recent results on the DEA to formic acid [128] and to its dimer $(HCOOH)_2$ [63]. The formic acid constitutes together with glycine (see Section 5.2 below), one of the simplest building blocks of more complicated biosystems. For this reason both glycine and formic acid have been considered in experiments and calculations to study their behaviour under the action of secondary electrons following the ionizing radiation impact on the medium. However, the discussion on the TNIs we find in our calculations and their

relation with the observed fragmentation channels follow the same lines as in the following analysis of uracile and glycine, so that we refer the reader to the original papers [63,128].

5.1. H^- desorption from uracil via metastable electron capture and resonant precursors

In our first work on the collision of LEEs with uracil molecule [129] we focused on a specific molecular precursor to the desorption of H^- as observed to occur from room temperature thin films of pure uracil condensed on polycrystalline Pt [23]. Other gas-phase studies on this system [42,47,130] have shown at low energies a broader energy range and a wider pattern of fragmentation products which we have also examined in terms of metastable states [80] and will present below.

In such preliminar work we have treated correctly the target molecule symmetry (C_s) while increasing the symmetry of the scattered electron to D_{2h}. This technical artifice reduced the computational cost of solving the coupled channel scattering equations without substantially altering the final results (compare also with the results, discussed below, presented in Ref. [80]). We refer the reader to Ref. [129] for the computational details.

The ETS experiments carried out on uracil [37] gave evidence for the formation of short-lived anionic species of π^* character and also the presence of strong vibrational excitation of the target molecule. The more recent experiments on electron stimulated desorption of H^- from thin films of uracil condensed on polycrystalline Pt [23] indicated the presence of a strong desorption peak around 9 eV and suggested it to be mainly due to CH bond cleavage with DA decay into H^- detachment with also contributions from NH bond cleavage at lower energies [23]. Figure 1 reports the partial cross sections obtained from our

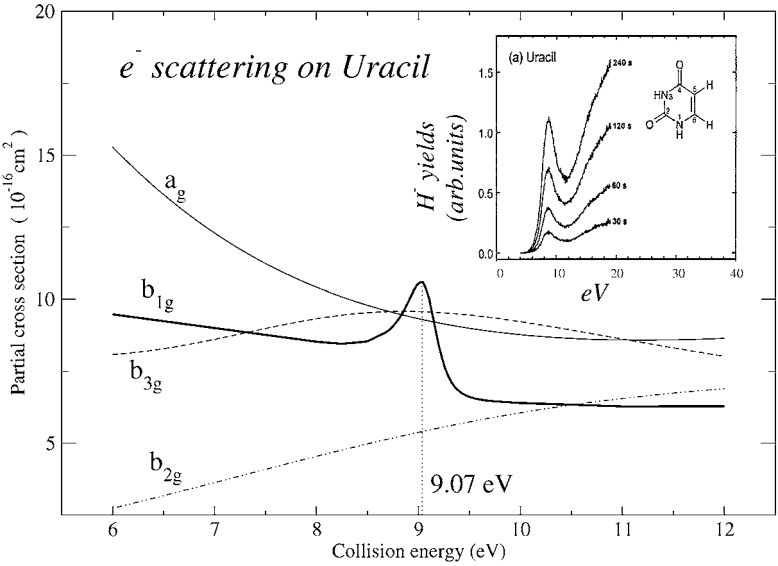

Fig. 1. Computed partial integral cross sections for electron scattering from gas-phase uracil. Inset: Experimental H^- desorption from Ref. [23].

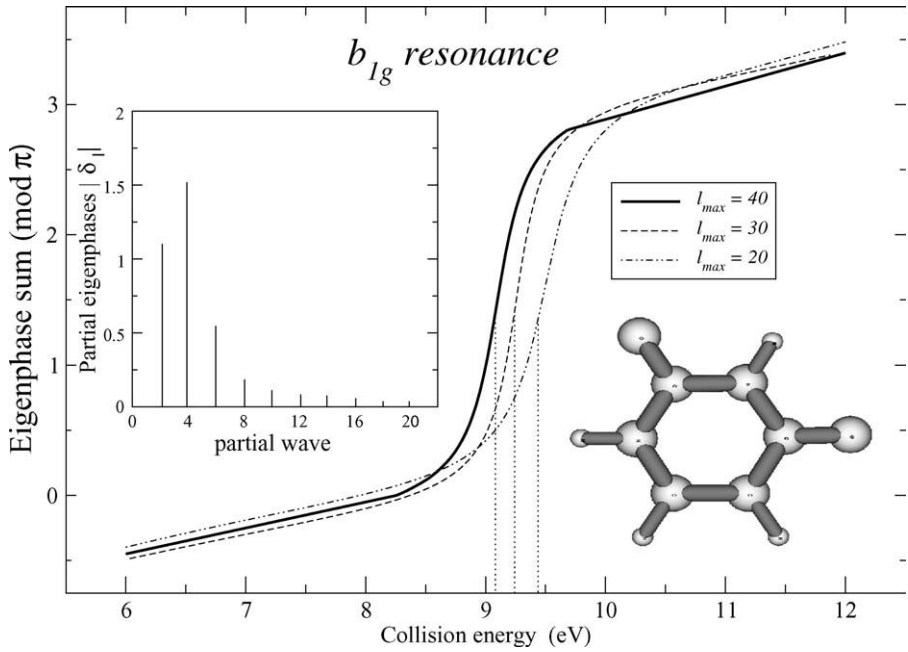

Fig. 2. Scattering eigenphase sum of b_{1g} symmetry (see text for details) as a function of collision energy and for three different partialwave expansions of the scattered electron. The inset shows the individual coefficients as a function of the partialwave contributions.

calculations for the scattering states which contribute the most to the elastic integral cross sections. The b_{1g} contribution, given by a thick line, clearly shows a marked peak centered at 9.07 eV. The inset reports the experimental results from Ref. [23], showing the chemical formula, and the atom numbering of the uracil molecule.

Figure 2 reports the computed eigenphase sum: It essentially represents the multichannel equivalent of the phaseshift of each separate partial wave appearing in a potential scattering treatment and it describes the global effects of a strongly anisotropic potential (as in our case) on the deflection and trapping of the scattered electron. The marked rise around 9 eV by about π radians points at the existence of a shape resonance since no other dynamical resonant channel can exist in the present model. We see from our calculations that the actual location of the resonance depends on the number of partial waves employed to describe the scattered electron. The three different choices in the figure are seen to shift its half-maximum location, although to increase the number of included partial waves only slightly move the energy position of the resonance and therefore does not affect much the qualitative picture extracted from calculations, while however helping in explaining the marked differences found between computed and measured width values: our lack of nuclear dynamics and of convergence saturation could provide us with only a qualitative agreement between computed and measured resonance shapes. Given the complexity of the numerics involved in solving such a huge set of equations, we felt that there was no real need to extend further the convergence study for the present model dynamics.

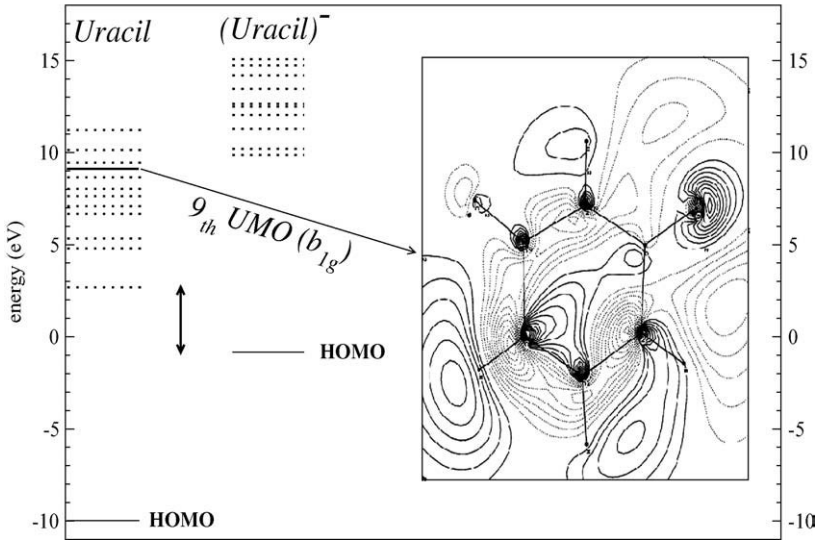

Fig. 3. Highest Occupied Molecular Orbitals (HOMO's) and virtual orbitals (UMO's) of uracil and of uracil negative ion. The map of the inset shows the excess electron density distribution for the virtual orbital selected on the left of the figure.

When the above quantity is fitted with a quadratic Wigner formula [131], the position of the resonant state is at 9.07 eV, with a width of 0.38 eV. It corresponds to a resonance lifetime about 1.25×10^{-14} s which is already about 100 times longer than the interaction time between the scattered electron and the target molecule for a direct collision at the same energy. If one further considers that the vibrational times of the several normal modes existing for the uracil molecule range between 10^{-15} and 10^{-12} s [132], then we see that the above resonant state, although decaying rather rapidly (as explained above) still lives longer than the vibrational modes associated to the CH stretching motion. Finally, the inset of Fig. 2 shows that the dominant contribution to the found TNI comes from the $l = 4$ partial wave, a feature which suggests the presence of several nodal planes in the scattered electron wavefunction.

We report in Fig. 3 our calculations for the lower-lying virtual Molecular Orbitals (MOs) obtained from SCF calculations at the equilibrium geometry of uracil (U) and for the relaxed geometry of the stable negative ion uracil$^-$ (U^-) both computed at the correct C_s symmetry. The relaxation effect caused by the stable negative ion formation is seen by the energy shift occurring between the lowest unoccupied MO (LUMO) of U and the highest occupied MO of U^- (HOMO). The location of several, metastable MOs is shown for the U system and we have highlighted the one corresponding to the location of this resonant state, remembering that the latter was indeed obtained with the U molecule kept at the undistorted geometry of its electronic ground state. That specific unoccupied MO (UMO) is the 9th in the sequence of them and indeed shows a spatial symmetry close to that of the scattering state: (b_{1g}). In order to further stress the pictorial value of this finding, we report on the right part of the figure a probability density map of that UMO over the space of the atomic nuclei of the ground state of the uracil molecule. The virtual MO clearly shows

a marked added electron density increase on the H atom attached to the C_5 atom of the uracil ring, the very one considered by experiments to be involved in the H^- desorption process [23]. It also shows that one of its nodal planes cuts across that same C–H bond, indicating clear antibonding character of the added electron density along that bond: The latter is therefore more likely to break-up during the extra electron energy release into the molecular nuclear network by following a direct decay pattern along a repulsive adiabatic potential energy 'cut' along that C–H bond. We also see that the energy involved in the rearrangement process from ground state U into ground state U^- (without zero point energy corrections) is around 3 eV, i.e. much less than the 9.0 eV available after electron trapping into the UMO shown in the figure. This means, at least qualitatively, that the TNI species formed under near-Franck–Condon conditions during the resonant scattering can release several eV of energy by electro-nuclear couplings with the molecular 'atomic' motions, thereby very likely causing the break-up effects along one of the dissociative components of the multidimensional vibrational network of the molecule.

Our calculations further show the additional electron density to be chiefly located onto one specific H atom, i.e. the one bound to the C_5 atom, and exhibiting antibonding character across that bond: they thus suggest that the extra energy of the TNI species could be preferentially funnelled into a DA channel where the C_5–H^- bond breaks up, thereby releasing the H^- fragments. One should keep in mind, however, the qualitative nature of the present model study and to understand it within the general context of the many equally qualitative discussions appearing in the experimental reports [42,45,47,130,133]. They indeed point out that at such electron energies the higher molecular electronic states are expected to be strongly coupled to the ground state and would also therefore give rise to Feshbach or core-excited resonances: The latter would then modify the observed shape resonances both in their widths and positions. Unfortunately, no explicit calculations exist as yet on the present molecule to give some quantitative support to such resonable hypothesis: We argue here that the finding of a marked, fairly long-lived, shape resonance from our nonempirical scattering calculations suggest the strong possibility that such a state would also survive when further electronic and nuclear dynamical effects were to be added to the quantum scattering and that the corresponding excess electron density over the molecule would still be guided by the existence of specific antibonding features as those shown by our calculations.

The present study has therefore shown the presence of what could be called a 'precursor' resonant state above the energy of the stable U^- formation and found it to be positioned in energy close to the experimentally observed H^- production [23]. We have further shown that this resonant TNI could be described by our simple model as due to the initial trapping of the extra electron behind the $l = 4$ centrifugal barrier and as having several nodal planes in its spatial wavefunction. The analysis of the associated MO indicates that the extra electron is chiefly located on the H atom bound to the C_5 carbon of the uracil ring and it exhibits antibonding character across that C–H bond. Hence, one can conjecture that the extra energy carried by the resonant electron, once coupled to the molecular vibrational modes, will lead to several possible DA processes and that the one causing the breaking of that C–H bond, with the ensuing release of the H^- fragment, could become favoured in the present system due to the specific density features of the resonant electron and the enviroment effects (thin films) on the molecular target.

We further analysed the location and the spatial features of the resonant TNIs in the larger energy range 0–15 eV in the work presented in [80]. By computing the poles of the

Table 1. Computed resonance positions and widths (in units of eV) for the scattering in the two IRs contributing to the present problem

Energy/eV	Width/eV	Symmetry
0.012	0.46	A'
10.37	0.87	A'
2.27	0.21	A''
3.51	0.38	A''
6.50	1.03	A''

S matrix in the PD representation discussed in Section 4.8 we found two of such poles in the A' symmetry and three poles in the A'' symmetry. Their corresponding values of positions and widths are reported in Table 1.

For all the resonances we found a clear dominance of the lower partial-wave contributions to the scattering states [80]. Indeed, by plotting the PD potential radial terms for the two symmetry components we found that for l values greater than 6 the repulsive character of the contributing centrifugal barrier effectively prevents the scattered electron from penetrating into the molecular volume [80]. However, the low symmetry of the target allows several partial waves to remain coupled and to generate strong nonadiabatic terms, shown by sharp potential discontinuities near the curve crossing locations.

Our principal aim is to use our results to make contact with the recent experimental findings from e^-–uracil scattering, showing how the three-dimensional shapes of the total scattering wave functions can guide us in selecting them as specific precursor states to the DA decay. Such precursor states are linked, in our model, to the presence of TNIs formed during the scattering process by a resonant mechanism.

Analyzing into more details the experimental findings on the LEE scattering off uracil, in addition to the already mentioned ETS experiments [37] and the study on the H^- desorption from films [23], further measurements of LEE attachment to gas-phase 5-bromouracil [134] indicated the formation of long-lived [BrU^-] parent ions near threshold, the presence of uracil–allyl [U–yl]$^-$ negative metastable with Br^- detachment from the C_5 position (at 0.14 and 6.0 eV) plus further fragmentations around 5 eV. The most recent measurements on gas-phase uracil below the threshold of electronic excitation [135] also suggest uracil decomposition with generation of a mobile hydrogen radical and the corresponding closed shell uracil fragment anion (U–H^-) at energies ranging from threshold to about 2.5 eV, indicating also large vibrational effects during the fragmentation process. Higher energy attachment peaks were also detected for fragmentations possibly caused by bond cleavage within the molecular ring and appearing with broad peaks at 6, 8 and 10 eV.

To actually perform realistic calculations of such processes would require the full dynamical coupling of the electron scattering event with the multidimensional nuclear motion on the ground electronic potential energy surface (PES) of the target electrons and also to include its possible coupling with the corresponding PESs of the lower-lying excited electronic states [132] of uracil during the nuclear evolution within the DA channels. Since such calculations are still out of reach for such large molecular systems, we have made use of the present results on resonant states and examined the spatial shapes of the scattered electron densities over the molecular nuclear network as obtained from FN dynamics calculations

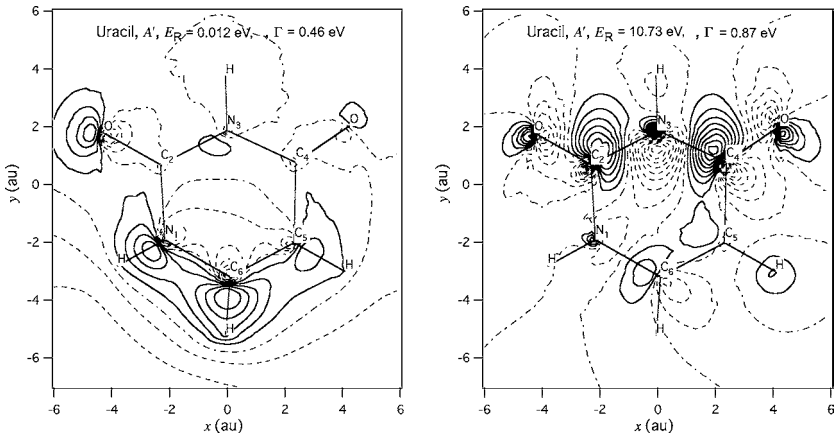

Fig. 4. Computed maps of the real parts of the resonant wave functions for the two resonant states of A′ symmetry. Changes of sign are given by solid and dotted lines. The molecular frame is also shown.

at the target molecule equilibrium geometry. The idea is therefore that of establishing a correspondence between the nodal structures of such scattering states (dominated, as they are, by a few specific values of angular momentum) and their function as precursors states of specific dissociative paths which appear in the experimental findings discussed above.

Examples of such wave function maps are shown by the two panels of Fig. 4, where we report on the left-hand side the threshold resonance wave function of A′ symmetry.

One immediately sees that the H atom bound to the nitrogen N_3 of the molecular ring exhibits very little electron density with respect to the main molecular frame, where more than 90% of the additional electron density is located. Thus, it stands to reason to expect that such a trapping resonance would provide dominant precursor state for the $[U–yl]^-$ transient anion experimentally observed at threshold in refs [23,135]: it would originate from direct H atom loss from the NH bond as the system stabilizes, possibly through internal vibrational redistribution (IVR), the allyl negative ion that leaves the extra charge on the uracil mainframe.

The resonant electron wave function mapped on the right panel of Fig. 4 shows instead the high-energy resonance of σ^*-symmetry obtained from our FN calculations around 10 eV. Here the situation is the opposite to that discussed before since we see that the H atoms bound to the main molecular frame carry very little extra charge along their bonds (as opposed to what we see on the left-hand side panel of the same figure) while the H atom bound to the C_5 carbon of the molecular ring now shows a fairly large extra electron density on it and a clear antibonding feature of its wave function that exhibits a nodal plane cutting across the C_5–H bond. This resonance may therefore be a precursor state for the TNI structure which can then cause the H^- abstraction spectrum observed around 9 eV by experiments [23,134]. We could describe it as a direct dissociating process along the stretching of that C–H bond which is affected by the nodal structure of the excess electron density in the resonant state and thus gives rise to a repulsive behavior of the PES along that bond.

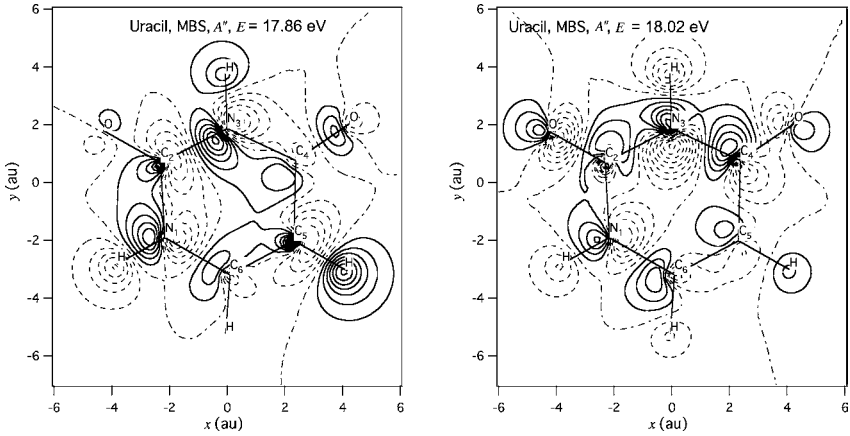

Fig. 5. Computed virtual orbitals from SCF calculations using an MBS expansion (see text). The two panels report two virtual states close to the higher energy resonance shown in Fig. 4.

Another possible description of the metastable molecular anions, albeit more qualitative, traditionally comes from analysing the structures of the virtual orbitals obtained from bound state calculations [37,132]. When the resonant states are well localized within the molecular space one can use the virtual orbitals obtained from a minimum base set (MBS) expansion to describe such resonances. It seldom occurs, however, that they turn out to have the correct energies within the continuum which is approximately mapped by the virtual MOs. A case in point for uracil is shown in Fig. 5, where we report two of the twelve A′ virtual orbitals from a MBS calculation.

The use of this small basis set filters out any description of general scattering states which comes out from larger basis set expansions, thereby obtaining resonant states (if existing) only from the more compact expansion given by the MBS choice. The present calculation produces in fact two of them with marked charge localizations on the H atom, as suggested by our resonant wave function on the right panel of Fig. 4. In fact the nodal pattern of the 18.02 eV MBS virtual state is very similar to the 10.73 eV resonance seen in Fig. 5. In spite of the similarities of the electron maps in the scattering and MBS calculations, however, the energy location is very different and varies substantially from both the experimental value and the scattering calculations. This should suggest that caution must be exercised when guessing scattering features from purely bound state calculations.

The experiments on ETS [37] further identify just above threshold two regions of resonant structures for uracil and attributed them to the presence of π^* resonances of the gaseous targets. The calculated resonant wave functions obtained in our work for that region of energy are reported in Fig. 6, where the following features can be detected:

1. both the resonances are of A″ symmetry, hence contain a symmetry reflection plane as expected from these orbital structures;
2. all resonances show large excess electron populations on the atoms and bond regions of the molecular ring structures, without any additional population on either the X–H bond or the H atoms. Thus, one could reasonably describe such precursor resonances

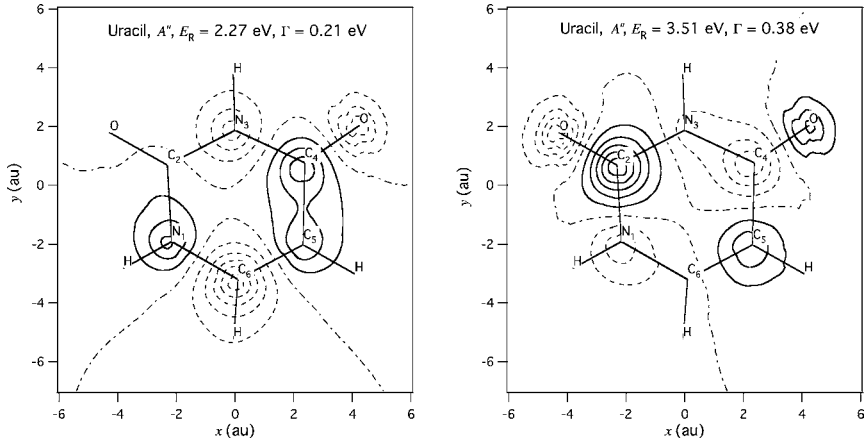

Fig. 6. Resonant wave functions for two of the resonant states of A″ symmetry. They are drawn at about adistance of 0.75 au from the molecular plane.

as likely to lead to dissociation products, as further discussed below, where the excess electron remains on the main molecular frame or on parts of it.

The location of such resonances, in fact, is qualitatively similar to those experimentally detected in [37], where two transmission features with rather broad widths were located at 1.58 and 3.83 eV, to be compared with the present computed values of 2.27, 3.51 eV. This shift is not, however, surprising since the calculations include an approximate form of exchange interaction and are performed at the geometry of the initial, neutral molecule. Furthermore, the more recent experimental data on anionic fragmentation of uracil in the gas-phase [42] indicate strong presence of the $[U–yl]^-$ ionic fragmentation (the $[U–H]^-$ ion of Ref. [23]), with a very strong peak at $\sim$ 1.0 eV and a second, broader region centered at $\sim$ 1.9 eV: Our calculations of Fig. 6 indicate the presence of two resonances that can indeed provide the FN precursor structures of that fragmentation pattern: loss of H atoms by indirect IVR stabilization of the resonant excess electron on the main molecular frame. A further higher energy A″ resonance (see Fig. 7) is located at 6.50 eV.

The wave function map reported in it clearly shows marked differences from the previous ones of the same symmetry reported in Fig. 6 and discussed above. The additional electron density is still chiefly localized on the atoms of the molecular framework; however, at odds with the map features of the two A″ resonances at lower energies discussed before, we see that this resonant state is antibonding between all six pairs of atoms that form the ring of the uracil molecule. Our present modelling, therefore, suggests here that such a TNI structure can provide a metastable precursor to fragmentation patterns that cause C–C and/or C–N bond breaking of the main molecular system beyond the simpler $[(U–yl)^-]$ formation with only H-atom loss.

A comparison with the fragmentation results of Ref. [42] seems to support the present findings: the plots at higher energies of Fig. 2 in that reference report, in fact, broad attachment cross sections around 6.50–7.00 eV (as in our calculations) which correspond to the $C_3H_2NO^-$ ion produced by the breaking of the C_5–C_6 and C_2–N_1 bonds, together with the ejection of the OCN^- residual fragment, also located in the experiments [42] around 6 eV. The further presence of another broad peak at the same energy ($\sim$ 6.5 eV) in the

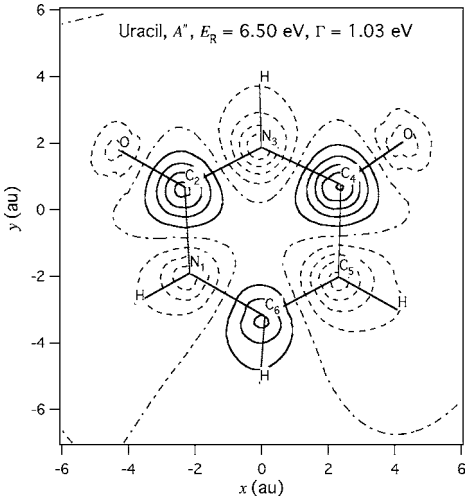

Fig. 7. Same as in Fig. 6 but for the A″ resonant state located at the highest energy position found in the calculations.

same experiments [42] lead to the detection of CN^- fragments. Following the antibonding character of the bond regions of the computed resonant state of Fig. 7, we can suggest that the same TNI of before can also undergo breaking of the C_5–C_4, C_2–N_1 bonds thereby producing CN^-, the loss of two H atoms and the larger $C_3H_2NO_2$. During the above fragmentation, however, the charge could also localize on the latter fragment that in turn can undergo further fragmentation (thanks to the antibonding feature of the C_2=O bond) with the loss of an oxygen atom and the formation of the $C_3H_2NO^-$ fragment experimentally observed at the same energy. It is interesting to note that such mechanisms of bond breaking were also suggested by the analysis of the experiments on 5-bromouracil [23].

5.2. Resonant capture of low-energy electrons by gas-phase glycine

Glycine is the simplest of the α-amino acids and therefore it has been, over the years, an important model compound in biophysics and biochemistry, providing the subject for many experimental [136–139] and theoretical [140–145] investigations. The –N–C–C–O-structure contained in glycine is an important strand of the α-amino acids, and of the proteins derived from them. The studies on the possible consequences of damaging such a building block have thus attracted a great deal of interest in recent years [60,61].

We applied the same analysis illustrated for the uracil case in the previous section to the location of TNI species from LEE scattering of gas-phase glycine [146], again looking for a structural rationalization for the fragmentation channels found in recent measurements [60]. Hence, we studied the quantum dynamics of LEEs ($E_{\text{coll}} < 15$ eV) scattered off the glycine molecule and have searched for the presence of single-particle trapped states, or shape resonances, which could give rise to TNI species in that range of energies. We have found four different resonant states of such temporary anions and established their energies and widths using molecular equilibrium geometries; we have examined the three

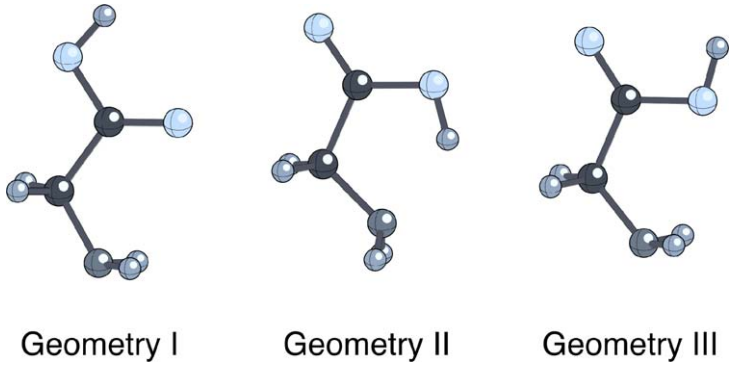

Fig. 8. 3D geometries of the lowest-energy configurations of glycine considered in this work. All geometries were obtained by global optimization [143].

Table 2. Computed energy positions and widths (both in eV) of all the metastable anionic states of glycine found in the present work. The numbering of the geometries corresponds to that of Fig. 8

Symmetry	Geometry	E_R (eV)	Γ_R (eV)
A″	I	3.14	0.23
	II	3.37	0.37
	III	2.98	0.26
A′	I	8.59	0.77
		8.73	3.82
		11.99	1.94
	II	7.47	1.68
		9.46	1.29
		13.00	1.96
	III	8.26	1.67
		8.86	1.24
		12.48	1.92

lowest energy nuclear arrangements for the isolated glycine since they are all very close to each other in terms of total energies. The experiments [60] have shown that the low-energy DEA process involves eight or nine different fragmentation channels at electron energies below 8 eV and a secondary, broad peak around 12.0 eV. The most intense peak appears at low energy and gives rise to the H abstraction process leading to the $[Gly–H]^-$ residual anion. It correlates well with our low-energy computed resonance of A″ symmetry which clearly indicates that it is a precursor state that could cause H atom release during TNI stabilization.

The bound target electrons were computed at the 6-31G(D) quality of basis set expansion [143] and three different optimized geometries were considered (see Fig. 8) since they were those located very close in energy to each other as obtained from the above calculations (typical $\Delta E \sim 7$ kJ mol^{-1}) [143] (for the computational details see [146]).

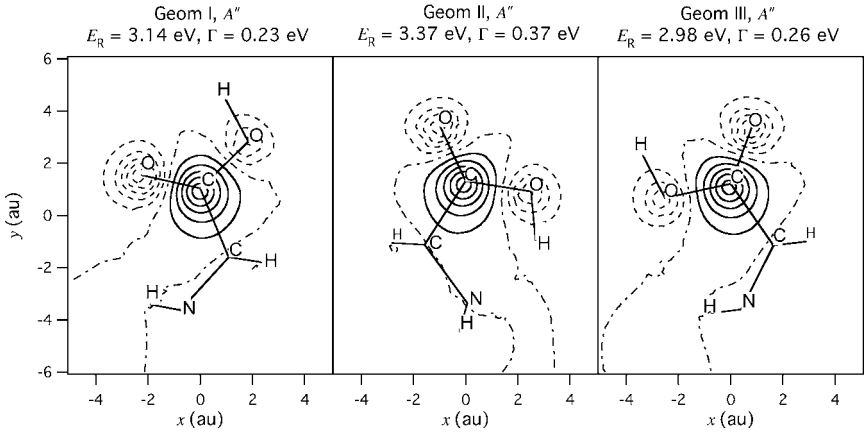

Fig. 9. The resonant wave functions of A″ symmetry found for the three glycine configurations shown in Fig. 8. The solid and dashed lines correspond to positive and negative values of the scattering wave functions. The dot-dashed lines correspond to nodes in the wave functions. For each resonant electron the position and width are given in eV. The wave functions are plotted at 0.75 au above the plane of the molecule.

As in the case of uracil, here again we found strongly coupled diabatic potentials and the location of several crossings at radial regions corresponding to the position of the molecular nuclei in one of our three chosen minimum geometries [146]. Moreover, we also saw there that with l_{max} up to 5 we are essentially describing the inner molecular region sampled by the scattered electron, although we kept in the calculations the potential curves with l_{max} up to 9 to ensure numerical convergence of our resonance features.

The locations and widths of all the resonances are given in Table 2.

A quick perusal of the data in that table shows marked similarities between the resonances produced by the three different geometries, thus suggesting that all the resonance are likely to be present for any choice of structure from the three most stable structures and therefore can be seen as being features of the glycine system rather than of any special geometry chosen for it. Furthermore, we see that the one located lowest in energy corresponds to a single resonance of A″ symmetry, i.e. one possessing a node on the molecular plane of highest symmetry, while the A″ symmetry supports three different metastable states which are located over a broad range of energies above threshold. We have therefore produced spatial maps of the TNI states described by the above resonances in order to see if their spatial features allow us to make a connection with the DEA fragmentation channels experimentally observed for this molecule in the gas phase measurements [60].

The three panels of Fig. 9 show projections on a plane containing the molecular backbone of the scattering wave function, associated with the lowest resonants state (of A″) observed from our calculations. The energy position of this resonant state is given for the three configurations at around 3 eV and with a width averaged over the three configurations of about 0.3 eV. The corresponding radial components of the scattering wave function for the same three molecular geometries are given in Fig. 10.

The present results of a narrow resonance in the low-energy region can be related to what has been experimentally found from electron-impact experiments on gas phase

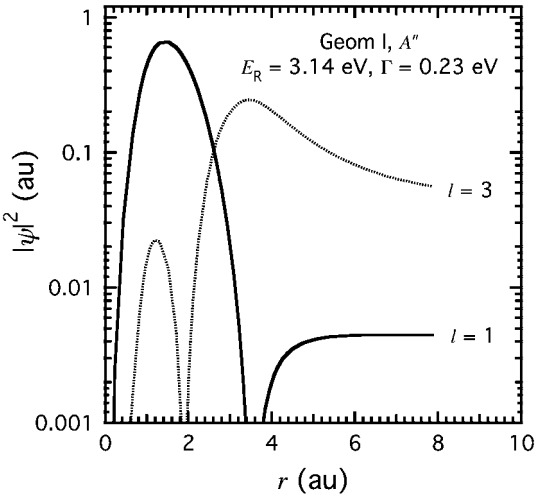

Fig. 10. Dominant partial-wave contributions (of the radial distribution functions) for the radial components of the resonant electron of A″ symmetry associated to the density map of Fig. 9 and for the geometry I of glycine.

glycine [60]. It was reported there, in fact, that two distinct fragmentation peaks appear in the 2–3 eV region: (i) one peak centered around 1.4 eV that yielded $[Gly–H]^-$ ions, i.e., negative ions with one H atom missing from the molecule and (ii) another, broader peak centered around 2 eV and associated to a negative ion with NH_3/OH detachment, i.e., to either the $CHCOOH^-$ or to the $H_2NCH_2CO^-$ negative ion fragments. Because of the approximations involved in our model calculations, we cannot expect the position of our computed resonance to exactly match the above observations, but we certainly find that our A″ resonance, given by all three geometries considered, is located between 2.7 and 3.4 eV, with an average width of about 0.3 eV. The excess electron is chiefly localized on the main molecular backbone, without any residual charge on the H atoms of the $–NH_2$, $–CH_2$ or –OH groups. It therefore seems possible that the subsequent DEA process will stabilize a molecular anion with the H atom being fragmented away to allow for the $[Gly–H]^-$ ion formation. The excess electron of the resonant state is being chiefly trapped behind the $l = 3$ barrier, as shown as an example in Fig. 10 for the I configuration and presents several marked nodal planes.

In all three configurations of Fig. 9 one sees that a nodal plane crosses the C–OH bond but not the $C–NH_2$ bond, i.e. that the former bond can take up antibonding character from the additional electron density stabilized by the resonant process, while the latter bond is not modified in the same way. The present resonance could therefore be considered a precursor state that leads to excess electron stabilization on the $H_2NCH_2CO^-$ fragment with elimination, *via* a DEA mechanism, of the –OH group. We also note that, as in the experiments, we do not find here any resonance near threshold, of either A′ or A″ symmetry, which could be construed as leading to excess electron density being localized on the H atom, thereby creating a possible precursor state for H^- detachment. The experiments, in fact, did see an H^- signal at threshold but decided it to be originating from experimental artifacts inherent to zero eV DEA detection [60]. Thus, the lack of believable H^- signal

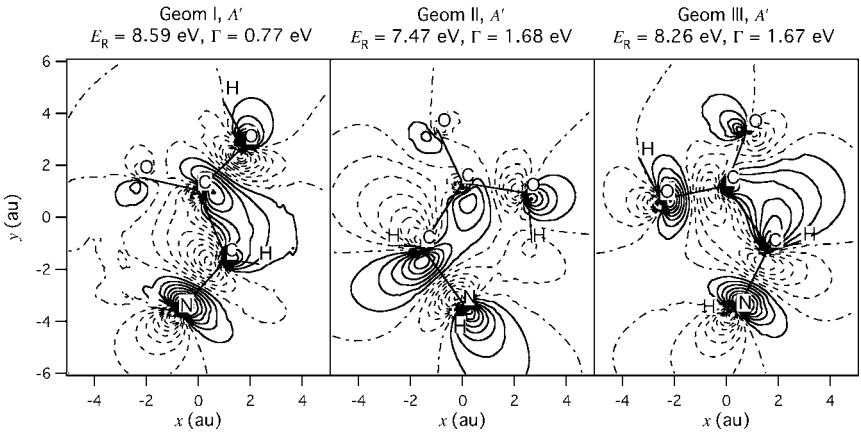

Fig. 11. The lowest resonant wave function of A′ symmetry for the three glycine configurations shown in Fig. 8. The solid and dashed lines correspond to the positive and negative values of the scattering wave functions. The dot-dashed lines correspond to nodes in the wave functions. The wave functions are plotted in the plane of the molecule.

in the experiments [61] is matched by the absence in our calculations of a possible precursor state for it. To make our analysis pictorially clearer in Fig. 10 we report the dominant angular momenta (partial waves) that contribute to the resonant electron wave function mapped in the previous Fig. 9. One clearly sees that, the scattered electron forming the metastable state is chiefly described by its $l = 3$ component on the periphery of the molecule.

This indicates that the state is trapped by the $l = 3$ angular momentum barrier. The resonant wave functions shown in Fig. 9 appear to be typical C–O π^* orbitals with some additional antibonding character between the C and the OH oxygen atom.

In the three panels reported in the Figs. 11 and 12 we show the computed TNI states of A′ symmetry that are positioned at higher energies, i.e., the first one (Fig. 11) appears located, on average, above 8.0 eV while the second resonant state (Fig. 12) is located closer to 9.0 eV. The latter resonance also exhibits a larger average width ($\sim$ 2.1 eV) than the former ($\sim$ 1.4 eV).

The experimental DEA data [60] indeed support that at energies above the appearance of the three fragments mentioned before, i.e., $[Gly–H]^-$, $[H_2C_2O_2^-]$ and $[H_4C_2NO]^-$, further fragmentation peaks are located in the region of energy between $\sim$ 6.0 and 8.0 eV, where other, smaller fragments are detected: O^-/NH_2^-, HO^-, CN^-, H_2CN^-, HCO_2^- and $H_2C_2NO^-$. The experiments also report the presence of an intense and broad fragmentation signal for O^-/NH_2^-, centered around 12.0 eV [60]. It is thus of interest to see how the two TNI states obtained in our calculations of Figs. 11 and 12 and located between 8 and 9 eV as broad resonances, can help us to rationalize some of the experimental fragmentation patterns described above. The resonant electron wave functions of Fig. 11 clearly show the presence of two nodal planes (signatures of antibonding character in the localized wave function) across the C–NH_2 bond and across the C–OH bond. They further show very little excess electron densities located over the terminal H atoms of both –OH and –NH_2 functional groups. It therefore seems reasonable to surmise that the

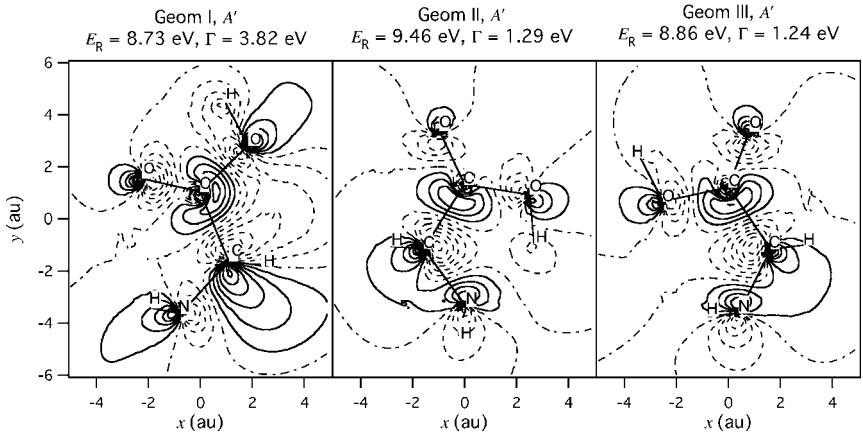

Fig. 12. Same as in Fig. 11 but for the next resonance of A′ symmetry at higher energies with respect to those of Fig. 11. The notation remains the same as in that figure.

fragmentation could occur by forming OH^- and NH_2^- fragments and that, in some of the DEA channels the fragmentation process would extend to the formation of O^- fragments.

The resonance wave functions of Fig. 12 indicate instead the antibonding character of the resonant orbital to be located across the central C–C bond indicating that the primary fragmentation of this TNI is via the breaking-up of that central bond of the molecular framework. The result of such break-up processes could produce fragments like H_2CN^- or HCO_2^-, obtained by the two primary fragments (H_4CN and HCO_2) by electron attachment on either of them followed by H losses from the carbon atom of the former fragment and due again to the lack of excess electron density on such atoms (see Fig. 12): These are indeed two prominent peaks of the fragmentation pattern experimentally observed, i.e. H_2CN^- and HCO_2^-. The former peak could also undergo H losses (as little charge is located on such atoms, see Fig. 12), to give rise to CN^- fragments as experimentally observed. Finally, after –OH detachment with excess charge left on the residual main fragment, another possible decay route of the TNI state of Fig. 12 (because of the additional nodal plane across the C–O bond) is with the larger fragment undergoing partial hydrogen abstraction processes with the formation of $(HN–CH–C=O)^-$, as experimentally observed. Thus, all observed fragments for glycine in the gas phase could be described as originating from the TNI states found in our calculations, states which can then follow different fragmentation routes and lead therefore to different final negative stable ions.

In the calculations reported by Fig. 13 we also show the spatial maps of the resonance state that we found to appear at the highest energy position, i.e. around about 12 to 13 eV. The width of this resonance also turns out to be one of the largest: An average value of about 1.94 eV. The analysis of its nodal structure indicates the antibonding character of the excess electron to be across the C–OH bond and the C–NH_2 bond. There is also another nodal plane across the central C–C bond, although without the strong density buildup on the C atoms observed in Fig. 12. The appearance of experimental peaks for OH^-/NH_2^- fragments around 12.0 eV [60] could therefore be connected with the presence of this resonant orbital that would undergo dissociative losses of the above ions at an energy higher

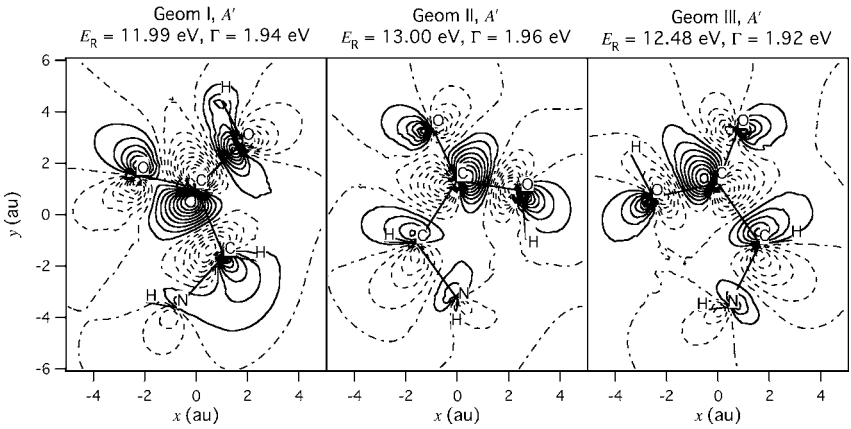

Fig. 13. Same as in Fig. 5 but for the third resonance of A′ symmetry, located at the highest energy within the rangeexamined in this work. The notation remains the same as in theother figures.

than that of the lower resonance of Fig. 11 discussed above in the context of other experimental peaks.

6. CONCLUSIONS

A full theoretical description of the DA mechanisms at the molecular level requires establishing first the structures and the locations of the resonant intermediates, possibly followed by the dynamical description of their stabilization into the different fragmentation channels that lead to different final anions. In our present treatment we have focused our analysis on the initial step of the e^-–molecule dynamics and have tried to extract from quantum scattering calculations which use a model nonempirical interaction potential and solve the correct coupled channel equations, the energy locations, the widths and the structural properties of the intermediate metastable states. In our analysis such intermediate, resonant complexes are taken to be formed first (precursor states) as single-particle, open channel resonances due to barrier trapping and thus we have not included in our model any provision for closed-channel Feshbach-type resonances. The latter resonances are also very likely to occur and to lead to core-excited shape resonance trappings coupled to our single-channel mechanisms. Our analysis does not yet include the multidimensional nuclear dynamics necessary to follow the various DEA processes, another computational extension that is not yet realistically viable with present-day computational tools when multidimensional cases are important. However, it is certainly suggestive that the different resonant states identified by our calculations can be related to essentially all the fragmentation channels experimentally observed for the various biomolecules we have studied thus far. The antibonding features revealed by the nodal characteristics of the resonant wave functions obtained here are very useful devices which indeed rationalize, albeit qualitatively, possible fragmentation patterns and can indicate our TNI structures as likely to be the precursor states for the final DEA species observed in the gas phase.

In conclusion, the complicated pathways of the electron driven chemical processes in biosystems are rationalized in our present quantum treatment of the dynamics through a two-step model. Thus, we first obtain the energy positions and widths of the existing trapping resonances and, second, we analyse their spatial features over the molecular framework in order to see the following characteristics: (i) the presence of additional electron density over specific molecular atoms and bond which will therefore be considered as strengthened by the presence of the $(N + 1)$ metastable electron, (ii) the presence of antibonding nodal planes across specific bonds which can thus suggest that the corresponding 1D cuts of the multidimensional adiabatic potential energy surfaces (real parts) along such bonds will have dissociative features, and (iii) the lack of additional electron density from the resonant orbital on specific atoms in the TNI, a fact which will suggest the likelyhood that such bound atoms may more easily break by indirect, IVR mechanisms when the excess energy of the resonant electron is released (in part or totally) into the molecular nuclear network.

One can therefore say that the use of SA–SCE approach to the calculation of resonant states in gas-phase biomolecules has been shown to be capable of providing a fairly detailed description of the corresponding molecular properties of such 'doorway' states and to allow us to form a reasonable, albeit qualitative, rationalization of the DEA patterns experimentally observed on such systems.

ACKNOWLEDGEMENTS

The financial support of the University of Rome 'La Sapienza' Research Committee, of the CASPUR Consortium computing facilities, of the European Research Network No. HPRN-CT-2002-00179 (EPIC) and of the NATO collaborative Research Grant No. PST.CLG.978702 is gratefully acknowledged. F.A.G. also acknowledges the support of the A. Von Humboldt Stiftung through a collaborative research grant with the Chemical Physics Group of the Freie Universitat Berlin (prof. E. Illenberger). We finally thank Prof. John Sabin for asking us to prepare the present review.

REFERENCES

[1] M. Eisenbud, T. Gesell, *Environmental Radioactivity: From Natural, Industrial, and Military Sources*, fourth ed., Academic Press, San Diego, 1997.
[2] W.R. Hendee, F.M. Edwards, *Health Effects of Exposure to Low-level Ionizing Radiation*, Institute of Physics Publishing, Bristol, UK, 1996.
[3] J.F. Ward, in: J.T. Lett, H. Adler (Eds.), *Advances in Radiation Biology*, fifth ed., Academic Press, New York, 1977.
[4] C. von Sonntag, *The Chemical Basis for Radiation Biology*, Taylor and Francis, London, 1987.
[5] B. Boudaïffa, P. Cloutier, D. Hunting, M.A. Huels, L. Sanche, *Science* **287** (2000) 1658.
[6] See e.g. M. Inokuti, *Rev. Mod. Phys.* **43** (1971) 297.
[7] A.F. Fuciarelli, J.D. Zimbrick (Eds.), *Radiation Damage in DNA: Structure/Function Relationship at Early Times*, Battelle, Columbus, OH, 1995.
[8] L. Sanche, *Eur. Phys. J. D* **35** (2005) 367.
[9] L. Sanche, *Scanning Microsc.* **9** (1995) 619.
[10] E.g. see: L. Sanche, *Mass. Spectrom. Rev.* **21** (2002) 349.
[11] S.M. Pimblott, J.A. LaVerne, in: A.F. Fuciarelli, J.D. Zimbrick (Eds.), *Radiation Damage in DNA: Structure/Function Relationships at Early Times*, Battelle, Columbus, OH, 1995, p. 3.

[12] H. Abdoul-Carime, P. Cloutier, L. Sanche, *Radiat. Res.* **155** (2001) 625.
[13] E.g. see: R. Laenen, T. Roth, A. Lambereau, *Phys. Rev. Lett.* **85** (2000) 50.
[14] S. Gohlke, E. Illenberger, *Europhys. News* **33** (2002) 1.
[15] O. Yamamoto, in: K. Smith (Ed.), *Aging, Carcinogenesis and Radiation Biology*, Plenum, New York, 1976.
[16] See e.g. A. Gräslund, A. Ehrenberg, A. Rupprecht, *Int. J. Radiat. Biol.* **31** (1977) 145;
M.D. Sevilla, J.B. D'Arcy, K.W. Morehouse, M.L. Englehardt, *Photochem. Photobiol.* **28** (1978) 37;
W.A. Bernhard, *J. Phys. Chem.* **93** (1989) 2187;
I. Zell, J. Hüttermann, A. Gräslund, A. Rupprecht, W. Kohnlein, *Free Radical Res. Commun.* **6** (1989) 105.
[17] M. Sevilla, D. Becker, M. Yan, S.R. Summerfield, *J. Phys. Chem.* **95** (1991) 3409.
[18] M. Yan, D. Becker, S. Summerfield, P. Renke, M. Sevilla, *J. Phys. Chem.* **96** (1992) 1983.
[19] A.-O. Colson, B. Besler, D.M. Close, M. Sevilla, *J. Phys. Chem.* **96** (1992) 661.
[20] See e.g. M.D. Sevilla, D. Becker, *Roy. Soc. Chem. Spec. Rev. Electron Spin Res.* **14** (1994);
C. von Sonntag, in: W.E. Glass, M.N. Varms (Eds.), *Physical and Chemical Mechanisms in Molecular Radiation Biology*, Plenum, New York, 1991;
S. Steenken, *Chem. Rev.* **89** (1989) 503.
[21] D.V. Klyachko, M.A. Huels, L. Sanche, *Radiat. Res.* **151** (1999) 177.
[22] H. Abdoul-Carime, P. Cloutier, L. Sanche, *Radiat. Res.* **155** (2001) 625.
[23] M.A. Herve du Penhoat, M.A. Huels, P. Cloutier, J.P. Jay-Gerin, L. Sanche, *J. Chem. Phys.* **114** (2001) 5755.
[24] B. Boudaiffa, P. Cloutier, D. Hunting, M.A. Huels, L. Sanche, *Radiat. Res.* **157** (2002) 227.
[25] X. Pan, P. Cloutier, D. Hunting, L. Sanche, *Phys. Rev. Lett.* **90** (2003) 208102.
[26] P. Rowntree, L. Parenteau, L. Sanche, *J. Chem. Phys.* **94** (1991) 8570.
[27] W.C. Simpson, M.T. Sieger, T.M. Orlando, L. Parenteau, K. Nagesha, L. Sanche, *J. Chem. Phys.* **107** (1997) 8668.
[28] H. Abdoul-Carime, P. Cloutier, L. Sanche, *Radiat. Res.* **155** (2001) 625.
[29] D. Antic, L. Parenteau, M. Lepage, L. Sanche, *J. Phys. Chem. B* **103** (1999) 6611.
[30] H. Abdoul-Carime, S. Cecchini, L. Sanche, *Radiat. Res.* **158** (2002) 23.
[31] M. Suzuki, *Nature* **344** (1990) 562.
[32] M.H. Werner, G.M. Clore, C.L. Fisher, R.J. Fisher, L. Trinh, J. Shiloach, A.M. Gronenborg, *Cell* **83** (1995) 761.
[33] J.H. Hendricks, S.A. Lyapustina, H.L. de Clercq, J.T. Snodgrass, K.H. Bowen, *J. Chem. Phys.* **104** (1996) 7788.
[34] C. Desfrançois, H. Abdoul-Carime, J.P. Schermann, *J. Chem. Phys.* **104** (1996) 7792.
[35] J.H. Hendricks, S.A. Lyapustina, H.L. de Clercq, K.H. Bowen, *J. Chem. Phys.* **108** (1998) 8.
[36] S.Y. Han, J.H. Kim, J.K. Song, S.K. Kim, *J. Chem. Phys.* **109** (1998) 9656.
[37] K. Aflatooni, G.A. Gallup, P.D. Burrow, *J. Phys. Chem. A* **102** (1998) 6205.
[38] M.A. Huels, I. Hahndorf, E. Illenberger, L. Sanche, *J. Chem. Phys.* **108** (1998) 1309.
[39] E. Illenberger, in: H. Baumgärtl, E.U. Frank, W. Grünbein (Eds.), *Gaseous Molecular Ions, Topics in Physical Chemistry*, vol. **2**, Springer, New York, 1992.
[40] A.-O. Colson, B. Besle, M. Sevilla, *J. Phys. Chem.* **96** (1992) 9787.
[41] H. Abdoul-Carime, M.A. Huels, E. Illenberger, L. Sanche, *Int. J. Mass Spectrom.* **228** (2003) 703.
[42] G. Hanel, B. Gstir, S. Denifl, P. Scheier, M. Probst, B. Farizon, M. Farizon, E. Illenberger, T.D. Märk, *Phys. Rev. Lett.* **90** (2003) 188104.
[43] R. Abouaf, J. Pommier, H. Dunet, *Int. J. Mass Spectrom.* **226** (2003) 397.
[44] F. Martin, P. Burrow, Z. Cai, P. Cloutier, D. Hunting, L. Sanche, *Phys. Rev. Lett.* **93** (2004) 068101.
[45] A.M. Scheer, K. Aflatooni, G.G. Gallup, P.D. Burrow, *Phys. Rev. Lett.* **92** (2004) 068102.
[46] H. Abdoul-Carime, S. Gohlke, E. Illenberger, *Phys. Rev. Lett.* **92** (2004) 168103.
[47] S. Denifl, S. Ptasinska, G. Hanel, B. Gstir, M. Probst, P. Scheier, T.D. Märk, *J. Chem. Phys.* **120** (2004) 6557.
[48] S. Denifl, S. Ptasinska, M. Probst, J. Hrusak, P. Scheier, T.D. Märk, *J. Phys. Chem. A* **108** (2004) 6562.
[49] S. Ptasinska, S. Denifl, V. Grill, T.D. Märk, E. Illenberger, P. Scheier, *Phys. Rev. Lett.* **95** (2005) 093201.
[50] S. Ptasinska, S. Denifl, B. Mroz, M. Probst, V. Grill, E. Illenberger, P. Scheier, T.D. Märk, *J. Chem. Phys.* **123** (2005) 124302.
[51] S. Ptasinska, S. Denifl, P. Scheier, E. Illenberger, T.D. Märk, *Angew. Chem. Int. Ed.* **44** (2005) 6941.
[52] H. Abdoul-Carime, J. Langer, M.A. Huels, E. Illenberger, *Eur. Phys. J. D* **35** (2005) 399.
[53] R. Abouaf, H. Dunet, *Eur. Phys. J. D* **35** (2005) 405.

[54] S. Ptasinska, S. Denifl, P. Scheier, T.D. Märk, *J. Chem. Phys.* **120** (2004) 8505.
[55] A.R. Milosavljević, A. Giuliani, D. Šević, M.-J. Hubin-Franskin, B.P. Marinković, *Eur. Phys. J. D* **35** (2005) 411.
[56] S. Ptasinska, P. Candori, S. Denifl, S. Yoon, V. Grill, P. Scheier, T.D. Märk, *Chem. Phys. Lett.* **409** (2005) 270.
[57] H. Abdoul-Carime, S. Gohlke, I. Petrushko, P. Limão-Vieira, N. Mason, E. Illenberger, *Chem. Phys. Lett.* **393** (2004) 442.
[58] S. Denifl, P. Candori, S. Ptasinska, P. Limão-Vieira, V. Grill, T.D. Märk, P. Scheier, *Eur. Phys. J. D* **35** (2005) 391.
[59] D. Muigg, G. Denifl, A. Stamatovic, T.D. Märk, *Chem. Phys.* **239** (1998) 409.
[60] S. Gohlke, A. Rosa, F. Brüning, M.A. Huels, E. Illenberger, *J. Chem. Phys.* **116** (2002) 10164.
[61] S. Ptasinska, S. Denifl, A. Abedi, P. Scheier, T.D. Märk, *Anal. Bioanal. Chem.* **377** (2003) 115.
[62] S. Ptasinska, S. Denifl, P. Candori, S. Matejcik, P. Scheier, T.D. Märk, *Chem. Phys. Lett.* **403** (2005) 107.
[63] F.A. Gianturco, R.R. Lucchese, J. Langer, I. Martin, M. Stano, G. Karwasz, E. Illenberger, *Eur. Phys. J. D* **35** (2005) 417.
[64] H. Abdoul-Carime, S. Gohlke, E. Illenberger, *Phys. Chem. Chem. Phys.* **6** (2004) 161.
[65] I. Dabrowska, J. Rak, M. Gutowski, J.M. Nilles, S.T. Stokes, D. Radisic, K.H. Bowen Jr., *Phys. Chem. Chem. Phys.* **6** (2004) 4351.
[66] R. Barrios, P. Skurski, J. Simons, *J. Phys. Chem. B* **106** (2002) 7991;
J. Berdys, I. Anusiewicz, P. Skurski, J. Simons, *J. Phys. Chem. A* **108** (2004) 2999;
J. Berdys, I. Anusiewicz, P. Skurski, J. Simons, *J. Am. Chem. Soc.* **126** (2004) 6441;
J. Berdys, P. Skurski, J. Simons, *J. Phys. Chem. B* **108** (2004) 5800;
I. Anusiewicz, J. Berdys, M. Sobczyk, P. Skurski, J. Simons, *J. Phys. Chem. A* **108** (2004) 11381.
[67] I. Anusiewicz, M. Sobczyk, J. Berdys-Kochanska, P. Skurski, J. Simons, *J. Phys. Chem. A* **109** (2005) 484.
[68] A.U. Hazi, H.S. Taylor, *Phys. Rev. A* **1** (1970) 1109.
[69] T. Sommerfeld, *J. Phys. Conf. Ser.* **4** (2005) 245.
[70] T. Sommerfeld, *J. Phys. Chem. A* **108** (2004) 9150.
[71] T. Sommerfeld, *Phys. Chem. Chem. Phys.* **4** (2002) 2511.
[72] J. Schirmer, L.S. Cederbaum, O. Walter, *Phys. Rev. A* **28** (1983) 1237.
[73] R. Santra, L.S. Cederbaum, *J. Chem. Phys.* **117** (2002) 5511.
[74] S. Feuerbacher, T. Sommerfeld, R. Santra, L.S. Cederbaum, *J. Chem. Phys.* **118** (2003) 6188.
[75] U.V. Riss, H.-D. Meyer, *J. Phys. B* **26** (1993) 4503.
[76] S. Tonzani, C.H. Greene, *J. Chem. Phys.* **124** (2006) 054312.
[77] S. Tonzani, C.H. Greene, *J. Chem. Phys.* **122** (2005) 014111.
[78] S. Hara, *J. Phys. Soc. Jpn.* **22** (1967) 710.
[79] C.H. Greene, A. Aymar, E. Luc-Koenig, *Rev. Mod. Phys.* **68** (1996) 1015.
[80] F.A. Gianturco, R.R. Lucchese, *J Chem. Phys.* **120** (2004) 7446.
[81] L.G. Caron, L. Sanche, *Phys. Rev. Lett.* **91** (2003) 113201.
[82] L.G. Caron, L. Sanche, *Phys. Rev. A* **70** (2004) 032719.
[83] L.G. Caron, L. Sanche, *Phys. Rev. A* **72** (2005) 032726.
[84] X. Pan, L. Sanche, *Phys. Rev. Lett.* **94** (2005) 198104.
[85] F.H.M. Faisal, *J. Phys. B: At. Mol. Opt. Phys.* **3** (1970) 636.
[86] P.G. Burke, A.L. Sinfailam, *J. Phys. B: At. Mol. Opt. Phys.* **3** (1970) 641.
[87] P.G. Burke, N. Chandra, *J. Phys. B: At. Mol. Opt. Phys.* **5** (1972) 1696.
[88] P.G. Burke, N. Chandra, F.A. Gianturco, *J. Phys. B: At. Mol. Opt. Phys.* **5** (1972) 2212.
[89] F.A. Gianturco, D.G. Thompson, A. Jain, in: W.M. Huo, F.A. Gianturco (Eds.), *Computational Methods for Electron–Molecule Collisions*, Plenum, New York, 1995.
[90] R.R. Lucchese, F.A. Gianturco, *Int. Rev. Phys. Chem.* **15** (1996) 429.
[91] W.R. Garrett, *Phys. Rev. A* **4** (1972) 2229;
See also: F.A. Gianturco, S. Meloni, P. Paioletti, N. Sanna, R.R. Lucchese, *J. Chem. Phys.* **108** (1998) 4002.
[92] M. Tinkham, *Group Theory and Quantum Mechanics*, McGraw–Hill, New York, 1964.
[93] N. Sanna, F.A. Gianturco, *Comput. Phys. Commun.* **128** (2000) 139.
[94] C.D.H. Chisholm, *Group Theoretical Techniques in Quantum Chemistry*, Academic Press, London, 1976.
[95] M.J. Frisch, G.W. Trucks, H.B. Schlegel, G.E. Scuseria, M.A. Robb, J.R. Cheeseman, J.A. Montgomery Jr., T. Vreven, K.N. Kudin, J.C. Burant, J.M. Millam, S.S. Iyengar, J. Tomasi, V. Barone, B. Mennucci, M. Cossi, G. Scalmani, N. Rega, G.A. Petersson, H. Nakatsuji, M. Hada, M. Ehara, K. Toyota, R. Fukuda,

J. Hasegawa, M. Ishida, T. Nakajima, Y. Honda, O. Kitao, H. Nakai, M. Klene, X. Li, J.E. Knox, H.P. Hratchian, J.B. Cross, V. Bakken, C. Adamo, J. Jaramillo, R. Gomperts, R.E. Stratmann, O. Yazyev, A.J. Austin, R. Cammi, C. Pomelli, J.W. Ochterski, P.Y. Ayala, K. Morokuma, G.A. Voth, P. Salvador, J.J. Dannenberg, V.G. Zakrzewski, S. Dapprich, A.D. Daniels, M.C. Strain, O. Farkas, D.K. Malick, A.D. Rabuck, K. Raghavachari, J.B. Foresman, J.V. Ortiz, Q. Cui, A.G. Baboul, S. Clifford, J. Cioslowski, B.B. Stefanov, G. Liu, A. Liashenko, P. Piskorz, I. Komaromi, R.L. Martin, D.J. Fox, T. Keith, M.A. Al-Laham, C.Y. Peng, A. Nanayakkara, M. Challacombe, P.M.W. Gill, B. Johnson, W. Chen, M.W. Wong, C. Gonzalez, J.A. Pople, *Gaussian 03, Revision C.02*, Gaussian, Inc., Wallingford, CT, 2004.

[96] F.A. Gianturco, J.A. Rodriguez-Ruiz, N. Sanna, *Phys. Rev. A* **52** (1995) 1257.
[97] N.F. Lane, *Rev. Mod. Phys.* **52** (1980) 29.
[98] P.G. Burke, J.F.B. Mitchell, *J. Phys. B: At. Mol. Opt. Phys.* **7** (1974) 665.
[99] B.I. Schneider, *Chem. Phys. Lett.* **51** (1977) 578.
[100] A. Klonover, U. Kaldor, *J. Phys. B: At. Mol. Opt. Phys.* **11** (1978) 1623.
[101] J.K. O'Connel, N.F. Lane, *Phys. Rev. A* **27** (1983) 1893.
[102] J.P. Perdew, A. Zunger, *Phys. Rev. B* **23** (1981) 5048.
[103] N.T. Padial, D.W. Norcross, *Phys. Rev. A* **29** (1984) 1742.
[104] F.A. Gianturco, A. Jain, L.C. Pantano, *J. Phys. B: At. Mol. Phys.* **20** (1987) 571.
[105] J.W. Carr Jr., A.A. Maradunin, *Phys. Rev. A* **133** (1964) 371.
[106] C. Lee, W. Yang, R.G. Parr, *Phys. Rev. B* **37** (1988) 785.
[107] F.A. Gianturco, J.A. Rodriguez-Ruiz, *J. Mol. Struct.: THEOCHEM* **260** (1992) 99.
[108] F.A. Gianturco, J.A. Rodriguez-Ruiz, *Phys. Rev. A* **47** (1993) 1075.
[109] N. Sanna, *Comput. Phys. Commun.* **132** (2000) 66.
[110] F.A. Gianturco, R.R. Lucchese, *J. Chem. Phys.* **111** (1999) 6769.
[111] S. Salvini, D.G. Thompson, *J. Phys. B: At. Mol. Opt. Phys.* **14** (1981) 3797.
[112] A. Jain, D.G. Thompson, *J. Phys. B: At. Mol. Opt. Phys.* **16** (1983) 3077;
A. Jain, D.G. Thompson, *J. Phys. B: At. Mol. Opt. Phys.* **16** (1983) 443.
[113] M.A. Morrison, L.A. Collins, *Phys. Rev. A* **23** (1981) 127.
[114] F.A. Gianturco, S. Scialla, in: P.G. Burke, J.B. West (Eds.), *Electron–Molecule Scattering and Photoionization*, Plenum, New York, 1986.
[115] L.J. Sham, V. Kohn, *Phys. Rev.* **145** (1966) 561.
[116] F.A. Gianturco, S. Scialla, *J. Phys. B: At. Mol. Phys.* **20** (1987) 3171.
[117] F.A. Gianturco, L.C. Pantano, S. Scialla, *Phys. Rev. A* **36** (1987) 557.
[118] A. Jain, F.A. Gianturco, D.G. Thompson, *J. Phys. B: At. Mol. Phys.* **24** (1991) L255.
[119] F.A. Gianturco, R.R. Lucchese, N. Sanna, A. Talamo, in: H. Ehrhardt, L.A. Morgan (Eds.), *Electron Collisions with Molecules, Clusters, and Surfaces*, Plenum Press, New York, 1994.
[120] R.R. Lucchese, *J. Chem. Phys.* **92** (1990) 4203.
[121] R.R. Lucchese, V. McKoy, *Phys. Rev. A* **42** (1990) 5357.
[122] F.A. Gianturco, R.R. Lucchese, N. Sanna, *J. Chem. Phys.* **102** (1995) 5743.
[123] J. Nuttal, *Phys. Rev.* **157** (1967) 1312.
[124] T.N. Rescigno, A.E. Orel, *Phys. Rev. A* **24** (1981) 1267;
T.N. Rescigno, A.E. Orel, *Phys. Rev. A* **24** (1982) 2402.
[125] F.A. Gianturco, T. Stoecklin, *J. Phys. B: At. Mol. Opt. Phys.* **27** (1994) 5903.
[126] R. Curik, F.A. Gianturco, N. Sanna, *J. Phys. B: At. Mol. Opt. Phys.* **33** (2000) 2705.
[127] W.M. Sams, D.J. Kouri, *J. Chem. Phys.* **51** (1969) 4809.
[128] F.A. Gianturco, R.R. Lucchese, *New J. Phys.* **6** (2004) 66.
[129] A. Grandi, F.A. Gianturco, N. Sanna, *Phys. Rev. Lett.* **93** (2004) 048103.
[130] M.-A. Hervé du Penhoat, M.A. Huels, P. Cloutier, J.-P. Jay-Gerin, L. Sanche, *Phys. Chem. Chem. Phys.* **5** (2003) 3270.
[131] E.g. see: C.J. Joachain, Quantum Collision Theory, North-Holland, Amsterdam, 1975, Chapter 3.
[132] J. Lorentzon, M.P. Fülscher, B.O. Roos, *J. Am. Chem. Soc.* **117** (1995) 9265.
[133] H. Abdoul-Carime, M.A. Huels, E. Illenberg, L. Sanche, *J. Am. Chem. Soc.* **123** (2001) 5354.
[134] H. Abdoul-Carime, M.A. Huels, L. Sanche, F. Bruening, E. Illenberg, *J. Chem. Phys.* **113** (2000) 2517.
[135] G. Hanel, B. Gstir, T. Fiegele, F. Hagelberg, K. Baker, P. Scheier, A. Snegurky, T.D. Märk, *J. Chem. Phys.* **116** (2002) 2456.
[136] L. Schaefer, H.L. Sellers, F.J. Lovas, R.D. Suenram, *J. Am. Chem. Soc.* **102** (1980) 6566.
[137] R.D. Suenram, F.J. Lovas, *J. Am. Chem. Soc.* **102** (1980) 7180.

[138] R.D. Brown, P.D. Godfrey, J.W.V. Storey, M.P. Bassez, *J. Chem. Soc. Chem. Comm.* **547** (1978).
[139] P.H. Cannington, N.S. Ham, *J. Electron Spectrosc. Rel. Phenom.* **32** (1983) 139.
[140] L.L. Shipman, R.E. Christoffersen, *Theor. Chim. Acta* **31** (1973) 75.
[141] Y.-C. Tse, M.D. Newton, S. Vishveshwara, J.A. Pople, *J. Am. Chem. Soc.* **100** (1978) 4329.
[142] J.H. Jensen, M.S. Gordon, *J. Am. Chem. Soc.* **113** (1991) 7917.
[143] K. Aflatooni, B. Hitt, G.A. Gallup, P.D. Burrow, *J. Chem. Phys.* **115** (2001) 6489.
[144] R.A.J. O'Hair, S. Blanksby, M. Styles, J.H. Bowie, *Int. J. Mass Spectrom.* **182–183** (1999) 203.
[145] M. Gutowski, P. Skurski, J. Simons, *J. Am. Chem. Soc.* **122** (2000) 10159.
[146] F.A. Gianturco, R.R. Lucchese, *J. Phys. Chem. A* **34** (2004) 7056.

Electron Attachment to DNA Base Complexes

Abraham F. Jalbout and Ludwik Adamowicz

Department of Chemistry, The University of Arizona, Tucson, AZ 85721, USA
E-mail: ajalbout@u.arizona.edu; ludwik@u.arizona.edu

Abstract

In this work we present a review of our groups recent work of our group and that of others related to *ab initio* studies involving DNA base dimers and complexes. We present recent calculations, as well as some relevant experimental investigations concerning excess electron attachment to these systems. In addition to covalent-bound electron attachment, we discuss formation of dipole-bound anions, solvated electron systems, and the experimental–theoretical comparisons that are currently available. Finally, we will discuss possible future avenues of research in this area.

Contents

1. OVERVIEW

The attachment of excess electrons to DNA bases has significant biological consequences. Excess electrons may appear in biological systems as a result of primary and secondary reactions caused by ionizing radiation. The general effect behind biological reactions involving excess electrons has to do with the ionization of molecular fragments of biomolecules. The mechanism, by which the presence of excess electrons causes damages to human cells and therefore tissues, is by transformations that accompany ionization of components of larger molecular complexes or molecular frameworks (i.e. DNA).

Ionized radiation that is absorbed under normal conditions by human tissue usually has enough energy to remove electrons from molecular fragments of cells and tissues. If some electrons that are involved in the formation of molecular bonds in the tissue are removed, it may then lead to molecular complexes coming apart and causing damage at the molecular level. This process has been viewed as a general model for radiation damage to chromosomes and other biological systems [1,2]. Chromosomes are the most critical part of the

ADVANCES IN QUANTUM CHEMISTRY, VOLUME 52
ISSN: 0065-3276 DOI: 10.1016/S0065-3276(06)52010-6

cell because they contain the genetic information required for the cell to perform its function, as well as for reproductive purposes. Therefore, if the chromosomes are affected by ionizing radiation, significant negative consequences to life functions may occur.

The discussion of the general problem of the effects of radiation on DNA at the molecular level can benefit form a review of the recent literature concerning both theoretical and experimental works on the subject. In studies of the radiation effects on DNA an array of different experimental and theoretical approaches have been used. For example, in recent works atomic force microscopy (AFM) has been added as a tool to study the radiation effects on DNA. In the AFM studies it has been found that with that method it is possible to investigate the radiation effects of one molecule in a larger DNA molecular framework [3,4]. The AFM work has lead to interesting findings into the mechanistic changes associated with radiative damage to DNA. They studied the mechanisms associated with the replacement of certain DNA bases and their effects on the structure.

In addition, to studying the effects of the radiation damage to DNA as a whole, molecular complexes involving two or more nucleic acid bases that are fragments of DNA can be studied for structural effects related to the damage and to the damage resistance. For example, Pezeshk [5] recently proposed that thiols may act as radioprotectors in DNA chains by either protecting or repairing damage to DNA induced by radiation effects and electron transfer. It has even been proposed that certain DNA bases (i.e. thymine) may be excised from DNA by radiolysis mechanisms [6]. Repair of DNA has also been proposed in other studies [7], where cellular effects and molecular initiation have been discussed as potential avenues for the repair processes.

There are several types of molecules (in addition to DNA bases) that are involved in the radiolysis processes of biosystems. It has been shown that damage induced by electrons to the DNA (or RNA) strands may start preferentially at the ribose backbone. The damaged deoxyribose, which is a key intermediate in producing strand breaks, are the most severe form of lesions in the radiation damage to DNA and lead subsequently to cell death [8]. The effect of DNA fragmentation [9] resulting from exposure to various radiation sources [10, 11] has also been studied and its mechanism explained at the molecular level. The physical basis and implications to medicine of this and related processes [12] have recently been discussed in relation to the theoretical fundamentals in chemical and physical research [13]. The synchrony between physical science and direct medical applications has a foundation in DNA photochemistry.

This brings us to the goal of this work. We have previously reviewed excess electron attachment to DNA bases [14], but there has been much advancement in this area over the last few years since that paper was published and a new review describing the recent developments can be useful. Since the advent of the theoretical analysis of DNA bases began [15], several categories of calculations have been undertaken. We will begin by discussing the recent advancements in DNA studies with relation to photochemical reactions, and then we will characterize various forms of bound anionic states that result from attachment of excess electrons to DNA. After this we will discuss the future implications of our current studies.

2. INTRODUCTION

It is the common notion of biochemists to perceive double helical DNA as a target for molecular recognition. The physical chemistry of the interaction of DNA molecules with excess

electrons is especially important in order to obtain an understanding of the charge transfer that occurs in these and other biologically-important molecular frameworks [16–18].

A very interesting aspect of DNA photochemistry is its ability to undergo charge transfer. There are two separate types of electron transfer: oxidative [19–24] electron transfer and reductive electron transfer. Although, the precise mechanisms of these charge-transfer processes remain unclear, they are very important to the overall study of biological functions. As we mentioned, the effects of radiation, including ultra-violet (UV) radiation, on living cells can cause adverse changes to the living tissue in the biological organism. We can summarize these effects to DNA as structural damage leading to the breakage of phosphodiester bonds and single-strands, as well as double strand breaks. In addition, we can classify damage according to a change in the information caused by the chemical modifications of individual DNA bases.

Reactions involving DNA and, in particular, its bases are also of interest in the study of their radiative properties. It has been reported, for example, that the repair of thymine dimers can be triggered by oxidative reactions [24–27], or by reductive pathways [28]. In addition to this, charge transfer in DNA can act to potentially protect genes against mutation [29]. It was shown that guanine is especially involved in mutations during the replication phase of DNA by becoming oxidized to heterocycles. From these studies, it has been shown that genes that posses a larger concentration of guanine–cytosine (G:C) bases can act as sinks for positive charge. Since these bases are generally located outside the framework of the encoding region, mutations will occur outside of these regions. To this end, experimental and theoretical studies of GGG selectivity have also been reported [30]. In these studies these phenomena were quantified in orbital terms that show that the electron density of the excess electron is localized between the guanine and cytosine molecules. Therefore, if this is in fact true, the quinine–cytosine can act as molecular traps for electron density.

In addition, there has been much interest in the electrical conductivity of DNA, due to its unique structure that permits a compact stack of π-electrons that are potentially associated with this effect [31,32]. In addition to these effects, biological applications have also been proposed. Simons and co-workers [33] have suggested that DNA base stacking may have a direct effect on single-strand breaking (SSB). These effects are induced by low energy electrons that attach to π^*-orbitals (i.e. via covalent anion formation). There is yet another possible future application of dealing with the DNA structures and the DNA electron transfer. The principles of electron conductivity via base stacking can be used in the design of sensor applications [34] and other materials. It has also been proposed that the interactions between stacked base pairs may even act as a conduction band pathway for charge separation [35].

The exact quantification of the stability of excess electrons in molecules can be characterized by the vertical detachment energy (VDE), and the adiabatic electron affinity (AEA). VDE is the amount of energy required to remove an electron from the anion at its equilibrium geometry. The VDE value is sometimes referred to as the first vertical ionization potential of the anion. The AEA on the other hand is the difference in energy between an anion species and its neutral counterpart (both at their respective equilibrium geometries). Positive values of AEA suggest stability towards ionization, and a negative value tells us that there is instability in the anion formation, relative to the neutral system at its equilibrium structure. A positive AEA value would therefore suggest entrapment of the electron in the molecule, which can then act to influence chemical reactions involving electron trans-

fer. The phenomenon of entrapment has macroscale applications when dealing with the DNA molecule as a whole, but the fundamental microscale aspect of this process must first be understood.

In the study [35] Huang proposed that the photoreactivity of DNA could be directly correlated to the number of cross-links formed as a result of mutations (i.e. via free radicals). Huang also described structural changes occurring as a results of stacked DNA permutations, in which cytosine has a crucial role in the process. This is an interesting finding, since cytosine has been shown to be involved in many crucial electron attachment roles, as will be described later. The quantification of these ionizing defects has been proposed by others [36,37], and has been well documented in the literature. Other studies relate anions in terms of effects of damage to DNA using various forms of commonly studied biological molecules [38–42].

There are many effects that can result from damage to DNA and are directly related to the presence of excess electrons. A prerequisite to the study of these effects is characterization of stationary anionic states that DNA fragments, particularly nucleic acid base complexes, can form with excess electrons.

This review is devoted to the discussion of types of anions produced by excess electron addition to complexes involving DNA bases. There are two commonly know ntypes of anions that can result from electron addition to closed-shell molecules. These are covalent anions and dipole-bound (DB) anions. In a covalent anionic state, the excess electron occupies a valence molecular orbital and its density is tightly distributed at and around the molecular framework of the molecule or complex. In the DB case, the electron is weakly bound and occupies a very diffuse σ-type orbital. The density of a DB electron is mainly distributed outside the molecular framework of the system. There are criteria as to whether or not a dipole-bound anion can form, but it is a general rule that a dipole moment of the system in question has to be $2.5D$ or greater in order to allow formation of a DB anion [43–47]. The two forms of anions, covalent and dipole-bound have been extensively discussed in the literature, and have been the topic of many recent scientific reports. There is however a third form of a molecular complex anion besides the covalent anion and the DB anion. This third form has been identified by our group as “an anion with an internally suspended electron” or AISE for short. In an anion of this type the excess electron density is located between two molecular dipoles. Examples of the three types of anions mentioned above are shown in Fig. 1. The plots shown in the figure depict the orbitals occupied by the excess electrons in the three types of anions.

In this work we will describe electron attachment properties of various DNA base complexes. We will review our recent computational studies of anions of these complexes and dimers, as well as future prospects in the field of DNA anion photochemistry and radiation chemistry.

3. EXPERIMENTAL METHODS

Many years of theoretical, as well as experimental research, have still lead to discrepancies in the electron affinities for DNA bases. In the study of molecular anions, two common methods used include negative ion photoelectron spectroscopy (PES) [48,49] and Rydberg electron transfer (RET) [50] spectroscopy. PES experiments are generally done by crossing a mass-selected beam of negative ions with a fixed frequency laser beam, and then

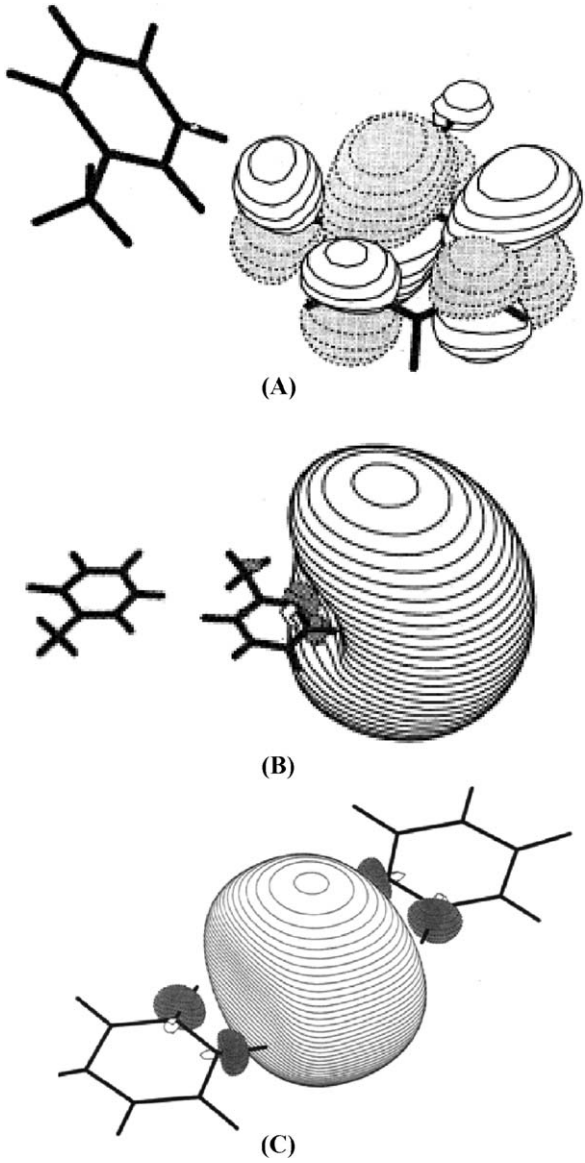

Fig. 1. Example of the three anionic states, in which we present the covalent anion of the thymine dimer (A) the dipole bound anion of the thymine dimer (B) as well as the AISE of the uracil dimer (C). The thymine dimer HOMO's are taken from Ref. [55] and the uracil dimer HOMO from Ref. [88].

analyzing of the photodetached electrons. The RET experiments are performed by first considering a pulsed beam of molecules seeded in helium that crosses a pulsed supersonic beam of Rydberg-excited Xe atoms. The excited Rydberg electrons are then transferred to the molecule of interest. The determination of the dipole-bound electron affinities then

relies upon the observed anion formation rate as a function of the quantum number n of the Rydberg electrons [51]. An empirical relation was derived to compute the electron affinity as: EA $= 23/n_{\max}^{2.8}$. The RET method is good for dipole-bound anion detection, but not covalent-bound anions. This has to do with the well-noted fact [52] that the EA values for covalent-bound anions cannot be computed from the RET spectra since the presence of covalent anions corresponds to a background shift in the n values.

4. THEORETICAL METHODS

Most of our theoretical calculations for anions involving nucleic acid bases have been performed with the GAUSSIAN [53] set of packages (GAUSSIAN03 is the most recent), and the HOMO's have been visualized with the MOLDEN software package [54]. However, other programs have also been used. For calculations of neutral and covalent anion structures, no special basis sets need to be employed provided that standard diffuse orbitals are included in the basis. It is typical to employ *ab initio* methods since density functional theory (DFT) methods usually overestimate the energy per electron and thus the electron affinity. This is perhaps due to lack of parameterization in these calculations to correctly describe systems with different number of electrons [55, references therein].

Our geometry optimizations of dipole-bound anions involving nucleic acid bases have generally been performed using a basis set consisting of the standard 6-31++G** or aug-cc-pvdz basis augmented with six diffuse Gaussian sp-shells with exponents equal to 0.01, 0.002, 0.0004, 0.00008, 0.000016, and 0.000032, and a p-shell with exponent 0.036. These additional orbitals are placed at the hydrogen atom located closest to the direction of the molecular dipole and near the location of the positive pole of the dipole. By using Gaussians with very small exponents in the basis, we not only are able to describe the very diffuse state of a dipole-bound electron, but we also allow the excess electron to escape from the system if this would lower the system energy. In general, it is important to carry out the calculation for the anion in such a way that allows not only localization of the excess electron at the molecule but also enables electron detachment from the system. In this way there is less chance to converge the calculation to a spurious anionic state that confines the excess electron to the molecule by virtue of the orbital basis being too spatially localized. The 6-31++G** basis set augmented with diffuse sp-shells will be denoted as 6-31++G**X in the discussion that follows. Such a basis has been used in calculations of both dipole bound anions and "anions with internally suspended electrons" (AISE) for a multitude of cases. Tables 1, 2 show the VDE values for some of the dimer and complexed systems, which will be discussed in the next sections.

5. COVALENT BOUND ANIONS

The covalent anions of DNA bases has been extensively studied and reviewed in the literature. We will begin by discussing the uracil and thymine systems. For the uracil anion there are a variety of experimental and theoretical electron affinity (EA) and vertical detachment energy (VDE) values available [56]. The covalent bound anion of uracil has an experimentally determined value of 0.75 eV for the EA as reported by Wentworth [57]. This value was refined to 0.80 eV by cyclic voltammetry studies conducted by the same group [58,59].

Table 1. Some dimer and solvated DNA base VDE values (eV), for the most stable covalent and dipole-bound anions are presented in this table

System	Theory method	Covalent anion	Dipole-bound anion	Ref.
Uracil $(H_2O)_3$	UMP2/6-31++G*// UHF/6-31+G**	1.48	0.013	[62]
Uracil dimer	UMP2/6-31++G*// UHF/6-31+G**	0.176		[60]
Uracil dimer (stacked)	UMP2/6-31++G*	0.25		[61]
Uracil trimer (stacked)	UMP2/6-31++G*	0.048		[61]
Uracil–thymine	UMP2/6-31++G*// UHF/6-31+G**	0.28		[63]
Adenine–imidazole	UMP2/6-31++G**X		0.0896	[81]
[a] Adenine (H_2O)	UMP2/6-31++G**X	0.016		[80]
[a] Adenine $(H_2O)_2$	UMP2/6-31++G**X		0.090	[80]
[a] Adenine $(H_2O)_3$	UMP2/6-31++G**X		0.003	[80]
[b] Adenine (H_2O)	UMP2/aug-cc-pVDZ	0.09		[69]
[b] Adenine $(H_2O)_2$	UMP2/aug-cc-pVDZ	0.50		[69]
[b] Adenine $(H_2O)_3$	UMP2/aug-cc-pVDZ	0.94		[69]
[b] Adenine $(H_2O)_4$	UMP2/aug-cc-pVDZ	1.25		[69]
Adenine (CH_3OH)	UMP2/6-31++G*// UHF/6-31+G**		0.011	[67]
Adenine $(CH_3OH)_2$	UMP2/6-31++G*// UHF/6-31+G**		0.058	[67]
Adenine $(CH_3OH)_3$	UMP2/6-31++G*// UHF/6-31+G**	0.020	0.001	[67]
Thymine dimer	UMP2/6-31++G**X	0.028	0.098	[66]
Guanine–cytosine	UMP2/6-31++G**X	0.750	0.0950	[55]

[a] From Ref. [81] for which the dipole-bound anions were computed.

[b] From Ref. [69] for which the covalent-bound anions were computed.

The theoretical values for the electron binding energy of the uracil anion, as well as other DNA base molecules, have all been calculated to be negative [14,16] when computed with both *ab initio* and DFT methods using the standard basis sets. MP2 results, which are generally the method of choice for the computation of electron affinities of larger molecular systems, provide AEA values of −0.25 eV for uracil, −0.30 eV for thymine, −0.46 eV for cytosine −0.75 eV for guanine, and −1.19 eV for adenine. The B3LYP values are not consistent as has been shown by several theoretical studies. For uracil, for example, they vary from −0.4 eV at the B3LYP/-6311G (2df, p) to 0.20 at the B3LYP/D95V+D [14]. However, these values cannot be trusted, and any experimental correlations are generally only coincidental.

Table 2. Some dimer and complexed VDE values (eV), for the most stable AISE anions are presented in this table. Experimental values for $(HF)_3$ are shown in parenthesis and the two configurations considered are plotted in Fig. 6

System	Theory method	AISE VDE	Ref.
$(HF)_3$ A	CCSD(T)/aug-cc-pVTZ	0.24 (0.21)	[82]
$(HF)_3$ B	CCSD(T)/aug-cc-pVTZ	0.43 (0.44)	[82]
$(OH_2(\cdots FH{\cdot}e{\cdot}FH\cdots)_4)$	MP2/6-31++G**X	4.8	[83]
Uracil (HF)	MP4/6-31++G**X// MP2/6-31++G**X	0.28	[84]
Uracil (H_2O)	MP4/6-31++G**X// MP2/6-31++G**X	0.24	[84]
Uracil $(HF)_2$	MP2/6-31++G**X	0.71	[85]
Uracil $(H_2O)_2$	MP2/6-31++G**X	0.45	[86]
Uracil–He	MP4/6-31++G**X// MP2/6-31++G**X	0.059	[87]
Uracil–Ne	MP4/6-31++G**X// MP2/6-31++G**X	0.059	[87]
Uracil–uracil	MP2/6-31++G**X	0.47	[88]
Uracil–glycine	MP2/6-31++G**X	0.16	[89]
Uracil–adenine	MP2/6-31++G**X	0.36	[90]
Thymine–adenine	MP2/6-31++G**X	0.20	[91]
Cytosine–guanine	MP2/6-31++G**X	0.40	[92]

Although these results suggest that individual DNA base molecules, such as uracil, do not form stable covalent anion states, their complexes do. In our original studies on the effect of water on anion formation with uracil, we computed that the covalent and dipole-bound anions states should co-exist [57]. Our calculations on the uracil dimer show that the excess electron is localized on one of the uracil rings and causes out of plane distortions in that ring [60]. At the UMP2/6-31++G**//UHF/6-31++G** level of theory we obtained a value of 0.176 eV for the electron affinity of the covalently bound anion of this complex. This value suggests that the anions are marginally stable, but since the AEA is positive, the covalent anion should be observed experimentally. In the dimer complex the majority of the excess electron density lies exclusively on one of the uracil molecules the other molecule plays a spectator role and stabilizes the excess electron on the first uracil by the solvation interaction. This effect has been shown to be a common characteristic among DNA base complex anions.

In a more recent study on stacked uracil dimer and trimer systems [61], we have found that the covalent anion systems also have the HOMO density primarily localized on only one of the uracil molecules. The adiabatic detachment energy calculated at the MP2/6-31++G** level of theory was found to be 0.25 eV for the stacked dimer covalent anion, and 0.048 eV for the trimer anion. The scenario for the formation of anions by stacking uracils is more realistically feasible in the frameworks of the DNA molecules, where the stacked systems occur naturally. The orbitals occupied by the excess electrons in the dimer and trimer stacked uracil anions are shown in Fig. 2.

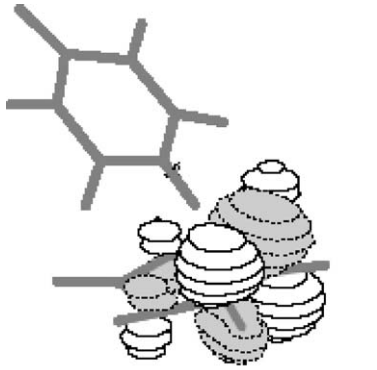

(A)

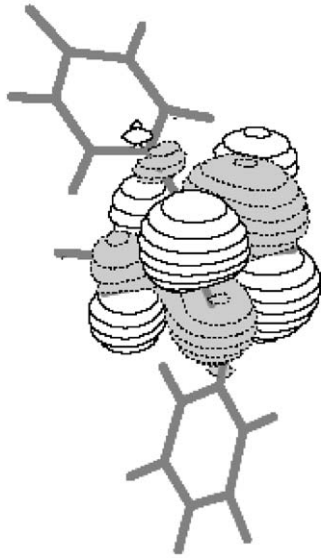

(B)

Fig. 2. Dimer (A) and trimer (B) uracil HOMO plots taken from Ref. [61], plotted at a counter level of 0.05 bohr$^{-3/2}$.

Our work on the uracil water clusters ($U(H_2O)_3$) also revealed that this complex and related complexes are in fact adiabatically unstable towards electron attachment by -0.11 at the MP2/aug-cc-pVDZ level of theory [62]. This complex was selected for the investigation due to the fact that it had recently been experimentally investigated and found to exist in a covalently bound state. Our single point vertical detachment energy (VDE) calculations did reveal a stability of 1.48 eV relative to electron detachment. The relatively large magnitude of the VDE value shows that the anion formed corresponds to a covalent-bound state. Interestingly, the comparison of the equilibrium geometries of the neutral and anionic $U(H_2O)_3$ systems and the HOMO plot for the anion suggest that the water molecules re-

arrange themselves around the uracil molecule when an excess electron attaches to increase penetration of the excess-electron density by the hydrogen atoms of the water molecules. Since the hydrogens have partial positive charge such penetration enhances the stability of the anion. Thus, the water molecules in the $U(H_2O)_3$ anion act as solvating spectators allowing the excess electron to become more localized, thereby reducing the energy of the system. From our calculations we showed that the $U(H_2O)_3$ system could also form stable dipole-bound anions. These anions will be discussed in the next section.

Other complexes of uracil have been studied also. In the uracil–thymine dimer [63] there were similarities in the physical and structural properties of the complex to that of the uracil dimer. As it is known the primary difference between the uracil and thymine molecule is the methyl group that is located at the C5 position of thymine. It was found that the dimer anion can coexists as a mixture of two structures. The first can be described as the $U{\cdot}T^-$ system and the second as the $T^-{\cdot}U$ system. In a way similar to the uracil dimer anion, the excess electron in the two uracil–thymine anions is localized on a single molecular unit (i.e. either on thymine or uracil). In both anions the ring of the unit with the excess electron was noticeably distorted from planarity, which is typical for these types of anion structures.

The general trend in DNA base dimer anions is that the excess electron density is generally located exclusively on one of the molecular rings and the second molecule plays a spectator role stabilizing the excess electron via electrostatic interaction. Our calculations have verified this effect both numerically and visually through HOMO plots. The dimer of uracil and thymine was found to be stable with an MP2 VDE value of 0.87 eV and 0.71 eV for the $T^-{\cdot}U$ and $U{\cdot}T^-$, respectively. Interestingly, our calculations revealed that the $T^-{\cdot}U$ is 1.4 kcal/mol less stable than the $U{\cdot}T^-$ dimer. This effect probably has to do with the increased electron affinity of uracil relative to thymine, which is verified both experimentally and theoretically. Although, the electron affinities of the monomers of uracil and thymine are both negative, together they form a stable anion complex.

As for the other nucleic acid bases, we have considered the electron affinities of cytosine, guanine, and adenine in addition to their complexes. We will begin by discussing adenine due to its relevance with thymine complexation, which we have previously described in the above discussion. The adenine–thymine complex is what is referred to as a traditional Watson–Crick type base pair [64,65], and forms strong hydrogen bonds holding it together. The molecular anion of this complex exhibits a puckered distortion of the thymine ring in the dimer relative to the neutral monomer which is planar. This is in agreement with the previously described structures of the anions of the uracil–water complex and the uracil–uracil dimer (stacked and hydrogen bonded), as well as with the anion of the uracil–thymine dimer. In the adenine–thymine dimer anion we also observed a difference in the orientation of the intermolecular hydrogen bonds in comparison with the neutral counterpart. Upon electron detachment from the adenine–thymine dimer anion two of the hydrogen bonds shorten and the last hydrogen bond elongates leading to a noticeable difference in the configuration. The anion of the adenine–thymine dimer while vertically stable is not adiabatically stable, with the adiabatic electron detachment energy of -0.403 eV. We therefore concluded from our calculations that this structure cannot strongly trap excess electrons in a covalent anion state.

We will now discuss anions of thymine complexes. In previous studies we have investigated the thymine dimer (T–T) through theoretical calculations [66]. There is, of course, a large similarity in this structure to the uracil–thymine dimer anion as we already discussed above, the major distinction being the methylation at the C5 site of the thymine ring. For the

covalent anion of this system we observed that the most stable configuration is a structure with a nearly perpendicular orientation of the two rings, which resembles the uracil–uracil and uracil–thymine dimer anion geometries. We computed an MP2/6-31+G** adiabatic detachment energies (ADE) of 0.27 eV for one configuration of the dimer and 0.28 eV for the second configuration. The difference has to do with the fact that they have slightly different bonding patterns, in addition to the effect of the methyl group on thymine. At the DFT/B3LYP-6-31++G** level we obtain values of 0.69 eV for both configurations, suggesting an almost three-fold increase stability. The DFT level, however, was unable to differentiate the two systems, yielding equal energies for both configurations of the T–T dimer anion. On the other hand, the MP2 level result yielded a difference of 0.01 eV, thereby, energetically distinguishing the two isomers.

From a structural point of view, we observed that the excess electronic density in the T–T dimer was exclusively located on one of the thymine molecules and an out of plane distortion of that thymine also occurred. The comparison of the DFT and MP2 electron binding energies suggested to us that the DFT method significantly overestimates the binding energies, and the MP2 underestimates these values. It is possible that a higher order electron correlation method (i.e. QCISD, CCSD, etc.) needs to be apply to obtain a more realistic value which as we expect should lie somewhere in between the MP2 and DFT results, although most likely significantly closer to the MP2 value. Overall, we came to the conclusion that this dimer does form a stable covalent anion.

We will now discuss the ability of various adenine complexes to attach excess electrons. In previous work, the issue of solvation on the adenine structure by methanol has been studied [67]. In that study we related our calculations on the previously reported Rydberg electron transfer spectroscopy (RET) experiments on this system [68]. After an analysis of the adenine–methanol $A{\cdot}M_n$ ($n = 1$–3) complexes we found that only when three methanol molecules are involved do we obtain a stable covalent anion of the complex. The VDE value for the $A{\cdot}M_3$ anion was predicted to be 0.02 eV suggesting some level of stability of this system towards electron detachment. The other complexes ($A{\cdot}M_n$, $n = 1$–2) do form dipole-bound anions that are metastable, however, the presence of covalent anions was not computed to being a relevantly plausible mechanism for electron attachment to these tow systems.

In addition to methanol, adenine solvated by water can also form a stable covalent anion [69]. It was experimentally verified by Periquet *et al*. [68] that the adenine–water anion is formed by electron addition to the neutral cluster. We calculated structures for adenine–$(H_2O)_n$ ($n = 1$–4), and found that the VDE were all positive of which the adenine–$(H_2O)_4$ anion had the highest value of 1.25 eV (see Table 1). In addition, the latter complex was the only one that had marginally positive adiabatic detachment energy (ADE) of 0.04 eV. From a structural perspective, we showed that the excess electron localizes more on the five-member ring of adenine rather than on its six-member ring. The presence of the excess electron on the five-member ring results in off-plane deformations of some hydrogens connected to the atoms forming the ring.

Lastly, we will discuss the cytosine in relation to the possibility of covalent anion formation of complexes of this system. For the cytosine monomer we observed some interesting trends. The first study that we performed on the cytosine anion [31] included an analysis of the amino-oxo and amino-hydroxy tautomers. The experimental photoelectron spectroscopy study of Weinkauf *et al*. [65] suggested that there was a sharp peak at 0.085 eV and a weak band at 0.230 eV. Our best approximation was 0.058 eV for the first peak, which

corresponds to the amino-oxo form, and 0.022 eV as well as 0.006 eV for the two rotamers of the amino-hydroxy molecules corresponding, perhaps, to the second band. However, from our calculations we found that only the amino-oxo covalent anion is vertically stable with a VDE of around 0.102 eV, and the other forms are unstable.

When cytosine is complexed with other molecules we also observe stable anions. For the cytosine–guanine system [55] we examined two forms of the covalent anions, the Watson–Crick configuration as well as the reversed Watson–Crick base pair. For the first case, we obtain a VDE value of 0.565 eV and the adiabatic electron affinity (AEA) of −0.056 eV. For the reversed Watson–Crick molecule we observed a value of 0.750 eV for the VDE and −0.177 eV for the AEA. Interestingly, the DFT-B3LYP/6-31++G** (6d) calculations resulted in a positive AEA of 0.391 eV, which is much different than the *ab initio* results. From this study we came to the conclusion that including higher order correlation effects in the calculations may perhaps lead to a positive AEA rendering the covalent anion of the complex both vertically and adiabatically stable.

In addition to solvated forms of DNA base anions and anions of DNA base self-dimers other molecular complex anions have also been investigated. In a recent study, positive AEA values for 2′-deoxyribonucleosides in DNA were obtained [70]. There calculations resulted in positive VDE values, suggesting that complexation yields metastable anions for these species. Other studies on DNA complexes with acrylamide [71] also result in positive VDE values, thereby suggesting increased stability for this and related complex anions.

Potential avenues of future theoretical investigation on covalent anions of DNA bases can be in relation to the recent experimental work of Liu *et al*. [72], in which microsolvated dianions were observed. They proposed that various anions exist in covalent states, where the internal proton transfer occurs from the sugar to the adenine anion in efforts to stabilize the dianion. This results in a short-lived dianion product, which was recorded via collisions of sodium vapor with nucleotide anions in a mass spectrometry experiment. These results are yet to be theoretically computed to provide a physical analysis of the system.

6. DIPOLE-BOUND ANIONS

In this section we will discuss the ability of DNA bases and their complexes to form stable dipole-bound anions. Many of the systems described here are similar to those discussed above, since many anions can exist in multiple states (i.e. covalent, dipole-bound, AISE).

We will begin by discussing dipole-bound anions of uracil and its complexes. From earlier studies in our group, we predicted the stability of the uracil dipole-bound anion [73,74]. These preliminary results were obtained using HF/3-21G calculations and involved some additional very diffuse basis functions. We placed the diffuse functions in a point separated by 1 Å from the molecular framework. The AEA was found to be 0.086 eV. Later a similar approach yielded the value of 0.088 eV for AEA of thymine. This value was later refined [75] by higher-level MP2/6-31++G**X calculations to yield an AEA for the dipole-bound anion of uracil of 0.047 eV and 0.032 eV for thymine. This lead to a difference of around 50% for these two molecules resulting from the improved calculations and was used to illustrate how sensitive the AEA results for dipole-bound anions are to the level of theory and to the basis set used.

We also have investigated the effect of methylation on uracil [76]. We found that the difference is around 25 eV between uracil and N,N-dimethylated uracil, which is one of

the forms that methylated uracil can exist. Later we investigated the effects of solvation on the dipole-bound anion of uracil. In that study [77] we computed that the uracil–$(H_2O)_3$ did in fact have a positive UMP2/6-31+G**X//UHF/6-31++G**X AEA of 0.013 eV, which was in relative agreement to the experimental results. The AEA of the covalent anion of the uracil–$(H_2O)_2$ complex did not have a positive value, in fact, as we described before, it was marginally negative. While solvation appeared to only marginally stabilize the uracil–$(H_2O)_2$ anion in a dipole-bound state, the dipole-bound anion of the uracil dimer was shown to be stable [60]. We calculated that the highest value of the electron affinity for the hydrogen-bonded uracil dimer to be 0.132 eV (for the lowest energy structure).

Next, we will consider the very similar structure of thymine. As we mentioned above, thymine has similar properties to uracil and can also attach electrons in a weakly bound diffuse state. Tautomarization of thymine can lead to various changes in the dipole-bound anion formation. The lowest energy tautomer of thymine is the di-oxo form. We calculated that the electron affinity of the 4-hydroxy tautomer is in fact 0.006 eV lower than the most stabe di-oxo form, despite the fact that the LUMO of the di-oxo form is larger than of the latter structure.

The thymine dimer dipole-bound anion has been investigated in our recent studies [66]. The calculations suggested that the lowest energy structure yielded an electron affinity of 0.098 eV corresponding to this dipole-bound anion state. We predicted that a dipole bound anion was in fact quite stable for this molecular complex.

In this section we will also discuss the dipole-bound anions of cytosine and its complexes. In our previous work the dipole-bound anions of cytosine have been reported [31]. In the study we explored the formation of stable dipole-bound anions of amino-oxo form as well as the two rotamers of the amino-hydroxy form. Our most accurate predictions of the AEA using the MP4/MP2 approach (employing the 6-31++G**X basis set) were 0.055 eV for the amino-oxo, and 0.003 eV and 0.016 eV for the rotamers of the amino-hydroxy form.

Thymine can also form metastable anion complexes with other DNA bases, such as guanine. While we predicted that the covalent anion of the guanine–thymine complex had a negative adiabatic electron affinity, the dipole bound anion state of the guanine–thymine dimer had a positive MP2/6-31++G**X value of 0.095 eV, suggesting that this molecular complex is in fact stable towards electron attachment, if the electron occupies a diffuse σ-orbital. We also predicted that majority of the excess electron density lies near the cytosine molecule. Due to a relatively large dipole moment of the complex, we believe that attachment of an excess electron should first occur through a dipole-bound anion state, which we described in the calculations. A covalent anion could form later, even if at a low rate as a result of intramolecular electron-transfer and a structural transformation. The HOMO plot for the dipole-bound anion of this system is shown in Fig. 3.

There are not many theoretical studies of guanine complexes, other than the monomer study of its electron affinity [78]. In the next section, we will discuss the ability of guanine to form AISE anion systems. We did consider the ability of four tautomers of guanine to form dipole-bound states with an excess electron (those with sufficiently high dipoles to bind an excess electron via a diffuse state). The only structures that resulted in a stable dipole bound anions were the oxo-amino N(9)H teutomer with an AEA of 0.034 eV and the hydroxy-amino N(9)H tautomer with an AEA of 0.00037 eV.

Finally we will discuss the dipole bound anions of adenine and its complexes. Adenine has several stable dipole-bound anions of its tautomers [79]. As it is known, the thermody-

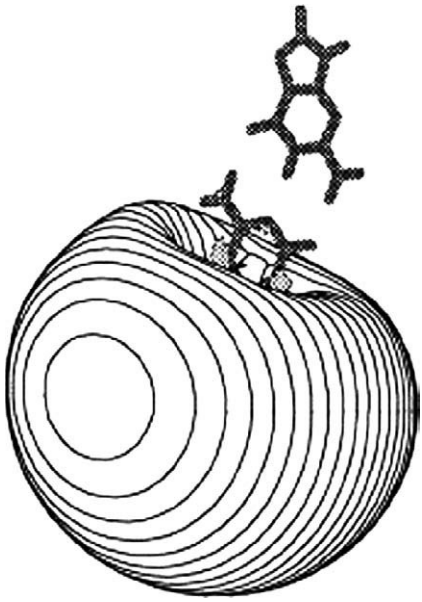

Fig. 3. HOMO plots of the dipole-bound anion of the cytosine–guanine system from Ref. [55] plotted at the counter level of 0.02 bohr$^{-3/2}$.

namic equilibrium of adenine depends on the environment. This system exists as a mixture of the N(9)H, N(3)H, and N(7)H tautomers, all of which are relatively stable. While the N(9)H tautomer is the lowest in energy, it has an electron affinity of nearly zero for the dipole-bound state. This is due to a small dipole moment of this system predicted to be only 2.52D in the calculations. The N(7)H structure is higher in energy by 7.46 kcal/mol than the N(9)H tautomer, but it has a more stable dipole-bound anion with an AEA value of 0.122 eV. This is due to a larger dipole moment of this form being 7.02D as predicted in the calculations. The other structures lack a dipole high enough to bind an excess electron in stable dipole-bound diffuse anionic states.

Next we consider the possibility of adenine forming dipole-bound anions when complexed with water [80], methanol [67] and imidazole [81]. For the first case, we considered dipole-bound anions of the adenine–$(H_2O)_n$ ($n = 1$–3) complexes. While, we have already discussed covalent anion formation for these adenine–water clusters, we will now consider the dipole bound anions. When $n = 1$ we located three similar structures of the complex, but found that only one complex can form a stable dipole-bound anion, with an MP2/6-31++G**X AEA of 0.016 eV. When $n = 2$ we have located nine structures on the potential energy surface of which six of them had sufficiently high enough dipole moments to attach an excess electron in a dipole-bound state. The highest AEA value obtained for one of the structures was 0.09 eV. This structure had no neutral counterpart, but it was interesting since the dipole moments of the adenine and the two waters were aligned (to maximize the dipole moment) to allow for maximum stabilization of the excess electron in a dipole-bound state. When the electron in this configuration was removed it converged to a structure of the neutral complex that was significantly different from the structure of

the anion. For the trimer complex, the MP2 AEA for the dipole-bound anion was only 0.003 eV due the small dipole moment of the system.

In our next study we considered the adenine–methanol anions. The calculations were performed for the adenine–$(CH_3OH)_n$ ($n = 1$–3) complexes. We suggested that dipole-bound anion formation with $n = 1, 2$ is possible, but not when $n = 3$, as previously alluded to. For $n = 1$, we obtained three stable structures on the dipole-bound anion potential energy surface. The highest dipole moment obtained for one of structures was $3.93D$ leading to a dipole-bound MP2/6-31+G**X AEA of 0.0114 eV. When the adenine complex involving two methanol molecules were considered we obtained nine stable structures (as with the adenine–$(H_2O)_2$ system), but only two structures yielded stable dipole-bound anions. The highest MP2/6-31+G**X AEA was at 0.06 eV for these structures, which made the anions only marginally stable. The experimental data suggests that it takes two water molecules not three as in the case of methanol to form a stable covalent anion.

Finally, we studied the possibility of dipole-bound electron attachment to the adenine–imidazole complex. We identified nine structures, of which seven formed dipole-bound anions. The highest value of the AEA was an MP2/6-31+G**X//UHF/6-31+G**X value of 0.09 eV for a configuration in which the electron was located by the imidazole and away from the adenine molecule. We predicted that the RET spectrum should be able to distinguish the different structures, due to their substantial energy and dipole differences.

7. AISE SYSTEMS

We now present the results of our studies on a novel type of the anionic state. This type of anion attachment is referred to as "anions with internally suspended electrons" or AISE for short, as we have mentioned above. These structures can possibly be formed in two steps. First, a dipole-bound anion is formed by one of the subunits of the complex. Then, the second subunit (or the remaining subunits, if there is more than one of them) attaches to the dipole-bound electron on its opposite end from the end where the first unit is connected. Thus in this system, the excess electron is suspended between the two closed shell molecular fragments.

Our first study in relation to the phenomenon of the formation of AISE's was a joint experimental theoretical study [82] on the HF trimer anion. In this study we benchmarked our findings that revealed a novel metastable anion system where the electron was trapped between the HF molecules. In a later study [83] we computed a structure in which identified a tweezer like $\cdots$FH·e·HF$\cdots$ system. In this system we predicted that a water-mediated tweezer ($OH_2(\cdots FH{\cdot}e{\cdot}FH\cdots)_4$) yielded a VDE of 4.8 eV, which made the anion quite stable (see Fig. 4).

The AISE formation has also been recently investigated for systems involving nucleic acid bases. The focus of these works has been to describe the effects of dimerization with solvent molecules or other DNA bases that trap excess electrons in AISE-type states. In a recent study on uracil–solvent complexes [84] we considered AISE's formed by the uracil–water and uracil–HF systems. The presence of the electron facilitated a weak-bonding pattern between the two closed-shell fragments of these systems, very different to previously considered anions of the uracil–water and uracil–HF complexes. In the AISE structures, the excess electrons exists inside the cluster and not on its surface, like in the dipole-bound anions. The AISE interaction is in some ways is similar to a hydrogen bond,

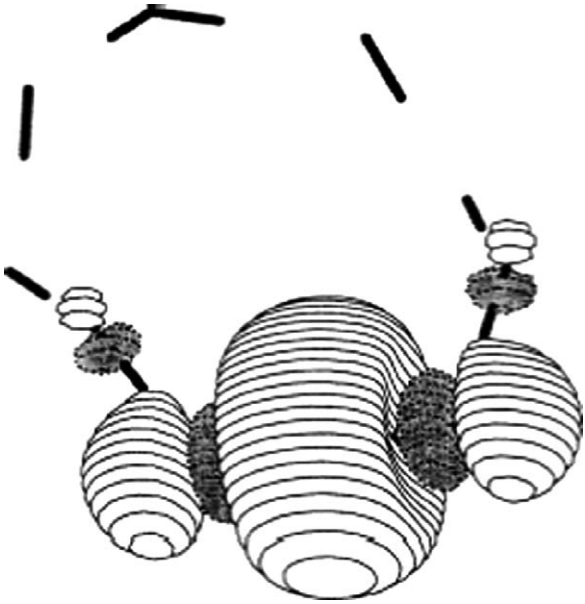

Fig. 4. The orbital occupied in the $OH_2(\cdots(FH)_4)_2{\cdot}e$ anion by the excess electron, computed at the UMP2/6-31++G**X level of theory taken from Ref. [83].

and has thus been also labeled as an e-bond by us and other workers in the field. For the uracil–water system we obtained an MP4/6-31++G**X//MP2/6-31++G**X VDE value of 0.24 eV, and 0.28 eV for the uracil–HF system. Since the uracil molecule has a sufficient dipole moment and forms a stable dipole-bound anion, it can capture an excess electron in a bound diffuse state. This electron can interact with a water or HF molecule to form an AISE, by binding it to the uracil. The VDE's for such species are substantially higher for than for traditional dipole-bound anions, due to their higher stability. Although, neither exact structure of an AISE nor the mechanism of its formation has been experimentally determined, we believe that under specific experimental conditions AISE's may form for the uracil–water and uracil–HF complexes.

We next examined the stability of an internally suspended excess electron in a uracil molecule paired with two HF molecules [85]. In that work we identified 5 uracil–$(HF)_2$ structures that formed stable AISE systems. The most stable structures were those with the general arrangement uracil–HF$\cdots$e$\cdots$HF. In the uracil–HF$\cdots$e$\cdots$HF structure both HF's are in direct contact with the excess electron and the electron has no direct contact with the uracil molecule. The dipole moment of a HF molecule on one side of the excess electron and the dipole moment of the uracil–HF dimer on the other side interact with the electron stabilizing it between the two species. This results in an increase of the VDE value. Similarly we explored the potential of uracil and two water molecules to form a stable AISE system. For this molecular complex, we obtained a VDE value of 0.45 eV, which is substantially lower than that for the most stable uracil–HF$\cdots$e$\cdots$HF AISE, that had a VDE of around 0.71 eV.

We also explored the possibility of the uracil–NGA (NGA = He, Ne) system to form stable AISE systems [86]. From this study we found that the uracil–He and uracil–Ne

AISE systems both had MP4//MP2 VDE values of 0.059 eV, suggesting a weak attractive interaction via the excess electron between the uracil and the noble gas atom (NGA) in the complex. Interestingly, the uracil–NGA (NGA = He, Ne) AISEs have relatively high VDE values considering the fact that the two systems in the complex were separated by a distance of nearly 20 Å, and yet still were connected by an excess electron to form a metastable bound state. Thus we concluded that noble gas atoms may solvate a dipole-bound excess electron in the uracil anion. Our calculations revealed that the localization of a noble gas atom near a dipole-bound electron requires formation of a local hole in its density that reduces the overlap of the extra electron with the electrons of the noble gas atom. Such a hole has to be formed to reduce the strong repulsion between the noble gas atom and the excess electron.

Now that we have discussed the uracil AISE complexes with small molecules and atoms, we will discuss their self-complexation [88], as well as complexes with glycine [89], adenine [90], and their corresponding AISE states that result from excess electron addition to these systems. As the first case we studied the ability of uracil to form an e-bonded dimer complex. In that work we found that a AISE can be formed and that it was metastable with respect to an adiabatic electron detachment, but vertically stable. We calculated the MP2 VDE of the uracil dimer AISE to be 0.47 eV, which is quite high, revealing that two uracil molecules can be effectively connected by an excess electron. This result showed that it would take a considerable amount of energy to dissociate the system into products (i.e. a neutral uracil molecule and a uracil dipole-bound anion) and that the stability of the AISE uracil dimer complex is rather high.

We next explored the possibility of uracil to attach to glycine via an e-bond. We found that the uracil–glycine AISE has the VDE of 0.163 eV. In our AISE calculations, we performed an optimization of the neutral complex starting the optimization with the geometry of the AISE. In all cases such calculations have been attempted, they showed that the removal of the excess electron from an AISE caused a significant structural change in the complex. This is due to highly unstable state in which the two closed-shell fragments find themselves after the electron removal with their dipoles directly facing each other. Our calculations suggested that the uracil–glycine AISE may be formed by a gas-phase collision between a uracil dipole-bound anion and a glycine molecule (as long as the excess intermolecular vibrational energy is removed from the system allowing the e-bonded anion to cool).

Finally, we studied the possibility of the uracil–adenine system to form an AISE. For this system we considered two isomers, which yielded an MP2 VDE value of 0.36 eV for both structures. Both structures are rather stable similarly to the other uracil AISE complexes [88].

In other calculations we have shown that the thymine–adenine also forms a stable AISE system [91]. We obtained two similar AISE structures with VDE values of about 0.20 eV. In both structures the thymine molecule was separated from the adenine molecule by over 7.2 Å. The positive and quite large VDE value suggests that the thymine–adenine AISEs are in fact stable.

Similarly, we have recently calculated the cytosine–guanine AISE system [92] which was also shown to be relatively stable towards electron detachment. For this molecule we predicted that the cytosine and guanine molecules form an almost perpendicular geometrical arrangement with the electron suspended in the middle. The MP2 VDE value of this system is 0.40 eV, which is similar to that obtained for the uracil dimer system. The e-bond

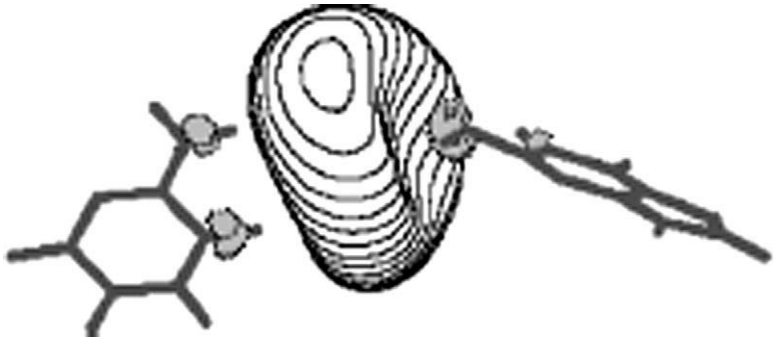

Fig. 5. HOMO plot of the cytosine–guanine AISE system taken from [61] plotted at the counter level of 0.05 bohr$^{-3/2}$.

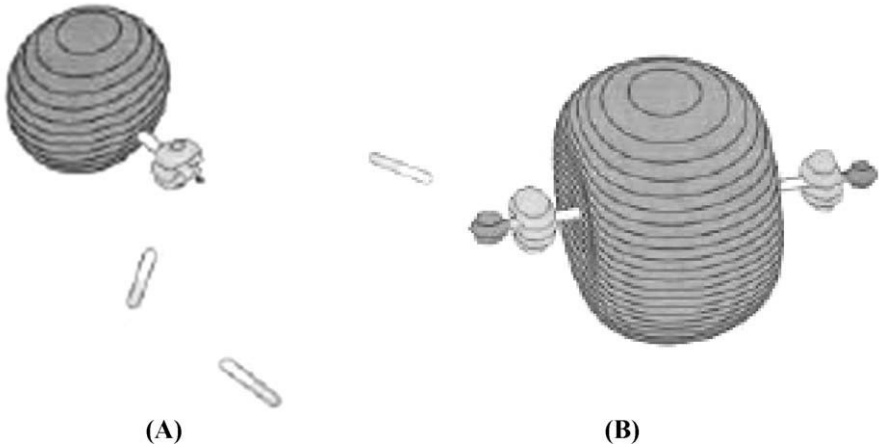

Fig. 6. The zz-$(HF)_3$ anion (A), and the $(2+1)$-$(HF)_3$ anion (B) from Ref. [82] and referenced to in Table 2.

formed in the cytosine–guanine AISE is shown in Fig. 5 where the HOMO occupied by the excess electron is depicted.

It should be stressed that in all AISE structures involving DNA bases found in our calculations the systems only represent local minima on the potential energy surfaces for the respective anions. Table 2 summarizes the VDE values for the most stable AISEs and lists the corresponding references. We should also mention that the purpose of the AISE studies has not been to explore the whole potential energy surface of the anion of the complex, but rather to ponder on the possibility of the two closed-shell systems forming the complex to bind through an excess electron. We believe that formation of these e-bonds may add new structural elements to the DNA helix when excess electrons penetrate it. The AISE formation, since it immobilizes excess electrons, creates yet an additional form of electron trapping and may contribute to the effects related to damage to DNA by radiation and/or photochemical processes.

8. SUMMARY AND FUTURE DIRECTIONS

In this work we have examined various forms of excess electron attachment to DNA bases. We examined the DNA base monomer covalent, as well as dipole-bound anion stability. In addition, the recent works in the area of the formation of DNA base dimer anions and solvated anions have also been discussed. Apart from discussing the formation of conventional covalent and dipole-bound anions, we also described the most recently characterized novel form of the anions that occurs via an intermolecular suspension of an electron. The latter was identified as "anions with internally suspended electrons" or AISE's for short. These were shown to be metastable kinetically formed products that are weakly bound similar to a hydrogen bond. Future studies will include searching for other novel forms of bonding where excess electrons are involved and electron entrapment. Another future avenue of research is investigation of anions formed by DNA stacked systems [33,61,93–100]. Since these stacked systems are dominantly present in DNA they need to be considered in relation to develop a realistic physical picture of electron attachment in DNA.

We have also shown that the anions of DNA base dimers can in many cases significantly differ in terms of their structures from their neutral counterparts. Electron addition may favor some conformations, which are less stable or even unstable as neutral complexes. Identifying stable anions first (as in the AISE cases) in the calculations usually helps to locate the neutral counterparts along the potential energy surface. For certain classes of anions we have not attempted to locate the global minima on their respective potential energy surfaces, but we have concentrated on such conformations that can facilitate optimal conditions for the formation of stable stationary states of excess electrons.

The possibility of DNA base complexes to stabilize excess charge is very important to the overall life of the organism. If molecular electron traps are formed, they can act to reduce or even eliminate the effects that free radicals and electrons have in living organisms. As we mentioned, radiation and certain photochemical reactions can have an adverse effect on DNA by yielding excess electrons and other charged species that can act to damage DNA, by causing mutations. Therefore, existence of low energy anion complexes that act to stabilize and control an otherwise uncontrollable situation by acting as sinks for extra charge is a desirable effect in biological systems.

We hope that this review will be a general reference for those wishing to pursue theoretical and experimental studies in this area.

ACKNOWLEDGEMENTS

We would like to thank the University of Arizona for valuable resources.

REFERENCES

[1] C. Von Sonntag, *The Chemical Basis of Radiation Biology*, Taylor & Francis, Philadelphia, PA, 1987.
[2] D. Becker, M. Sevilla, in: J.T. Lett, W.K. Sincair (Eds.), *The Chemical Consequences of Radiation Damage to DNA*, *Advances in Radiation Biology*, vol. 17, Academic Press, San Diego, CA, 1999.
[3] S. Boichot, M. Fromm, S. Cunniffe, P. O'Neill, J.C. Labrune, A. Chambaudet, E. Delain, E. Le Cam, *Radiat. Prot. Dosimet.* **99** (2002) 121.
[4] A.C. Rabon, D.T. Miller, T.E. Shannon, D.W. Jokisch, *Health Phys.* **84** (6) (2003) s151.

[5] A. Pezeshk, *Life Sci.* **74** (19) (2004) 2423.
[6] H. Abdoul-Carime, S. Gohlke, E. Fischbach, J. Scheike, E. Illenberger, *Chem. Phys. Lett.* **387** (2004) 267.
[7] H. Willers, J. Dahm-Daphi, S.N. Powell, *Br. J. Cancer* **90** (2004) 1297.
[8] S. Ptasinska, S. Denifl, P. Scheier, T.D. Mark, *J. Chem. Phys.* **120** (2004) 8505.
[9] W. Friedland, M. Dingfelder, P. Jacob, H.G. Paretzke, *Radiat. Phys. Chem.* **72** (2005) 279.
[10] E. Tsoulou, C.A. Alfas, E.G. Sideris, *Radiat. Res.* **163** (2005) 90.
[11] W. Friedland, M. Dingfelder, P. Jacob, H.G. Paretzke, *Radiat. Phys. Chem.* **72** (2005) 279.
[12] A.F. Jalbout, *J. Biomed. Biotech.* **3** (2003) 212.
[13] A.C. Elitzur, *Electron. J. Math. Phys. Sci.* **1** (2002) 8.
[14] D.M.A. Smith, L. Adamowicz, in: J. Kalcher (Ed.), *Theoretical Prospect of Negative Ions*, Res. Signpost, Kerale, 2002, p. 139.
[15] S. Steenken, *Chem. Rev.* **89** (1989) 503.
[16] D. Svozil, P. Jungwirth, Z. Havlas, *Collect. Czech. Chem. Commun.* **69** (2004) 1395.
[17] M. Volobuyev, L. Adamowicz, *J. Phys. Chem. B* **109** (2005) 1048.
[18] D.M.A. Smith, L. Adamowicz, *J. Phys. Chem. B* **105** (2001) 9345.
[19] H. Kasai, Z. Yamaizumi, M. Berger, J. Cadet, *J. Am. Chem. Soc.* **114** (1992) 9692.
[20] F. Lewis, R. Letsinger, M. Wasielewski, *Acc. Chem. Res.* **34** (2001) 159.
[21] M. O'Neill, H. Becker, C. Wan, J. Barton, A. Zewail, *Angew. Chem. Int. Ed.* **42** (2003) 5896.
[22] F. Lewis, J. Liu, X. Zou, R. Hayes, M. Wasielewski, *J. Am. Chem. Soc.* **125** (2003) 4850.
[23] J. Jortner, M. Bixon, T. Langenbacher, M. Michel-Beyerle, *Proc. Natl. Acad. Sci. USA* **95** (1998) 12759.
[24] P. Henderson, D. Jones, G. Hampikian, Y. Kan, G. Schuster, *Proc. Natl. Acad. Sci. USA* **96** (1999) 8353.
[25] P. Dandliker, R. Holmlin, J. Barton, *Science* **275** (1997) 1465.
[26] P. Dandliker, M. Nunez, J. Barton, *Biochemistry* **37** (1998) 6491.
[27] D. Vici, D. Odom, M. Nunez, D. Gianolio, L. McLaughlin, J. Barton, *J. Am. Chem. Soc.* **122** (2000) 8603.
[28] T. Carell, *Angew. Chem. Int. Ed. Engl.* **34** (1995) 2491.
[29] A. Heller, *Faraday Discuss. Chem. Soc.* **1** (2000).
[30] Y. Yoshioka, Y. Kitagawa, Y. Takano, Y. Yu, T. Nakamara, I. Saito, *J. Am. Chem. Soc.* **121** (1999) 8712.
[31] D.M.A. Smith, A.F. Jalbout, J. Smets, L. Adamowicz, *Chem. Phys.* **260** (2000) 45.
[32] N.A. Oyler, L. Adamowicz, *Chem. Phys. Lett.* **219** (1994) 223.
[33] I. Anusiewicz, J. Berdys, M. Sobczyk, P. Skurski, J. Simons, *J. Phys. Chem. A* **108** (2004) 11381.
[34] D.M. Eley, D.I. Spivey, *Trans. Faraday Soc.* **58** (1962) 411.
[35] H. Huang, *J. Theor. Biol.* **87** (1980) 585.
[36] V.G. Petin, V.P. Komarov, *Rad. Env. Biophys.* **20** (1982) 79.
[37] L. Sanche, *Eur. J. Phys. D* **35** (2005) 367.
[38] R. Huo, J. Gu, Y. Xie, Y. Yaoming, H.F. Schaefer, *J. Phys. Chem. B* **109** (2005) 22053.
[39] A. Martinez, *J. Chem. Phys.* **123** (2005) 24311.
[40] D. Radisic, K.H. Bowen Jr., I. Dabkowska, P. Storoniak, J. Rak, M. Gutowski, *J. Am. Chem. Soc.* **127** (2005) 6443.
[41] J. Simons, K. Jordan, *Chem. Rev.* **87** (1987) 535.
[42] J. Simons, *Chem. Phys. Lett.* **5** (2002) 55.
[43] C. Desfrançois, H. Abdoul-Carime, N. Khelifa, J. Schermann, *Phys. Rev. Lett.* **73** (1994) 2436.
[44] C. Desfrançois, H. Abdoul-Carime, N. Khelifa, J. Schermann, *Europhys. Lett.* **26** (1994) 25.
[45] C. Desfrançois, H. Abdoul-Carime, J. Schermann, *J. Chem. Phys.* **104** (1996) 7792.
[46] H.O. Crawford, *Proc. R. Soc. London* **91** (1967) 279.
[47] H.O. Crawford, A. Dalgarno, *Chem. Phys. Lett.* **1** (1967) 23.
[48] M.T. Bowers (Ed.), *Gas Phase Ion Chemistry: Ions and Light*, Academic Press, San Diego, CA, 1984.
[49] J.P. Majer (Ed.), *Ion and Cluster Ion Spectroscopy and Structure*, Elsevier, Amsterdam, 1989.
[50] C. Desfrançois, S. Carles, J. Schermann, *Chem. Rev.* **100** (2000) 3943.
[51] S. Carles, C.D. Desfrançois, J.P. Schermann, A.F. Jalbout, L. Adamowicz, *Chem. Phys. Lett.* **334** (2001) 374.
[52] F. Dunning, *J. Phys. B: At. Mol. Opt. Phys.* **28** (1995) 1645.
[53] M.J. Frisch, *et al.*, GAUSSIAN03, *Revision B.05, Gaussian*, Pittsburgh, PA, 2003.
[54] G. Schaftenaar, J.H. Noordik, *J. Comput.-Aided Mol. Des.* **14** (2000) 123.
[55] J. Smets, A.F. Jalbout, L. Adamowicz, *Chem. Phys. Lett.* **342** (2001) 342.
[56] E. Chen, E. Chen, N. Sane, *Biochem. Biophys. Res. Commun.* **171** (1990) 97.
[57] J. Wiley, J. Robinson, S. Ehdaie, E. Chen, E. Chen, W. Wentworth, *Biochem. Biophys. Res. Commun.* **180** (1991) 841.

[58] E. Chen, J. Wiley, C. Batten, W. Wentworth, *J. Phys. Chem.* **98** (1994) 88.
[59] J.H. Hendricks, S.A. Lyapustima, H.L. de Clercq, K.H. Bowen Jr., *J. Chem. Phys.* **108** (1998) 8.
[60] D.M.A. Smith, J. Smets, L. Adamowicz, *J. Phys. Chem. A* **103** (1999) 5784.
[61] A.F. Jalbout, L. Adamowicz, *Chem. Phys. Lett.*, in press, CPLETT-05-2448.
[62] J. Smets, D.M.A. Smith, Y. Elkadi, L. Adamowicz, *J. Phys. Chem. A* **101** (1997) 9152.
[63] D.M.A. Smith, J. Smets, L. Adamowicz, *J. Phys. Chem. A* **103** (1999) 4309.
[64] J.D. Watson, F.H.C. Crick, *Nature* **171** (1953) 964.
[65] J. Schiedt, R. Weinkauf, D. Neumark, E. Schalg, *Chem. Phys.* **239** (1998) 511.
[66] A.F. Jalbout, J. Smets, L. Adamowicz, *Chem. Phys.* **273** (2001) 51.
[67] A.F. Jalbout, L. Adamowicz, *J. Mol. Struct.* **605** (2002) 93.
[68] V. Periquet, A. Moreau, S. Carles, J.P. Schermann, C. Desfrançois, *J. Electron Spectrosc. Relat. Phenom.* **106** (2000) 141.
[69] M.L. Nugent, L. Adamowicz, *Mol. Phys.* **103** (2005) 1467.
[70] N.A. Richardson, J. Gu, S. Wang, Y. Xie, H.F. Shaefer III, *J. Am. Chem. Soc.* **126** (2004) 4404.
[71] C. Carra, N. Iordanova, S. Hammes-Schiffer, *J. Phys. Chem. B* **106** (2002) 8415.
[72] B. Liu, S. Tomita, J. Rangama, P. Hvelplund, N. Preben, B. Steen, *Chem. Phys. Chem.* **4** (2003) 1341.
[73] N. Oyler, L. Adamowicz, *J. Phys. Chem.* **97** (1993) 11122.
[74] N. Oyler, L. Adamowicz, *Chem. Phys. Lett.* **219** (1994) 223.
[75] C. Desfrançois, H. Aboul-Carime, S. Carles, V. Periquet, J.P. Schermann, D. Smith, L. Adamowicz, *J. Chem. Phys.* **110** (1999) 11876.
[76] D.M.A. Smith, J. Smets, Y. Elkadi, L. Adamowicz, *J. Phys. Chem. A* **101** (1997) 8123.
[77] J. Smets, D.M.A. Smith, Y. Elkadi, L. Adamowicz, *J. Phys. Chem. A* **101** (1997) 9152.
[78] G.H. Roehrig, N.A. Oyler, L. Adamowicz, *Chem. Phys. Lett.* **225** (1994) 265.
[79] G.H. Roehrig, N.A. Oyler, L. Adamowicz, *J. Phys. Chem.* **99** (1995) 14285.
[80] A.F. Jalbout, L. Adamowicz, *J. Phys. Chem. A* **105** (2001) 1033.
[81] A.F. Jalbout, L. Adamowicz, *J. Phys. Chem. A* **105** (2001) 1071.
[82] M. Gutowski, C.S. Hall, L. Adamowicz, J. Hendricks, H. De Clercq, S. Lyapustina, J. Nilles, S. Xu, K. Bowen, *Phys. Rev. Lett.* **88** (2002) 143001.
[83] A.F. Jalbout, C.A. Morgado, L. Adamowicz, *Chem. Phys. Lett.* **383** (2004) 317.
[84] A.F. Jalbout, C.S. Hall-Black, L. Adamowicz, *Chem. Phys. Lett.* **354** (2002) 128.
[85] C.A. Morgado, K.Y. Pichugin, L. Adamowicz, *Chem. Phys. Lett.* **389** (2004) 19.
[86] C.A. Morgado, K.Y. Pichugin, L. Adamowicz, *Phys. Chem. Chem. Phys.* **6** (2004) 2758.
[87] C.S. Hall, L. Adamowicz, *Mol. Phys.* **100** (2002) 3469.
[88] C.S. Hall, L. Adamowicz, *J. Phys. Chem. A* **106** (2002) 6099.
[89] A.F. Jalbout, K.Y. Pichugin, L. Adamowicz, *Eur. J. Phys. D* **26** (2003) 197.
[90] S. Stepanian, A.F. Jalbout, C.S. Hall, L. Adamowicz, *J. Phys. Chem. A* **107** (2003) 7911.
[91] A.F. Jalbout, K.Y. Pichugin, L. Adamowicz, *Chem. Phys. Lett.* **376** (2003) 799.
[92] A.F. Jalbout, L. Adamowicz, *Chem. Phys. Lett.*, CPLETT-05-2450, in press.
[93] R. Barrios, P. Skurski, J. Simons, *J. Phys. Chem. B* **106** (2002) 7991.
[94] H. Abdoul-Carime, P. Cloutier, L. Sanche, *Radiat. Res.* **155** (2001) 625.
[95] K. Aflatooni, G.A. Gallup, P.D. Burrow, *J. Phys. Chem. A* **102** (1998) 6205.
[96] J. Stubbe, J.W. Kozarich, *Chem. Rev.* **87** (1987) 1107.
[97] L. Giloni, M. Takeshita, F. Johnson, C. Iden, A.P. Grollman, *J. Biol. Chem.* **236** (1984) 8608.
[98] J.R. Ditchfield, W.J. Hehre, J.A. Pople, *J. Chem. Phys.* **54** (1971) 724.
[99] J. Florian, J. Leszcynski, *J. Am. Chem. Soc.* **118** (1996) 3010.
[100] A.F. Jalbout, L. Adamowicz, Mol. Phys., in press.

Accelerating Multiple Scattering of Electrons by Ion Impact: Contribution to Molecular Fragmentation and Radiation Damages

Béla Sulik and Károly Tőkési

Institute of Nuclear Research of the Hungarian Academy of Sciences, H-4001 Debrecen, Hungary
E-mail: sulik@atomki.hu

Abstract

Secondary electrons play an important role in transferring energy from swift, heavy charged particles to matter. Such electrons, when formed in biological tissues by high energy particle impact, significantly contribute to the fragmentation of small molecules and to single- and double-strand brakes in DNA. Knowledge about differential spectra of electrons emitted in collisions of decelerating swift ions is of vital importance for estimating ion impact radiation damages. In this work, we focus our interest to a specific ionization mechanism, the so-called Fermi-shuttle type acceleration. We show that this process can produce a significant enhancement in the emission of high energy secondary electrons. After a brief history of the study of Fermi-shuttle acceleration mechanisms in atomic collisions, we present the results of recent systematic experimental studies and follow the way of identifying and analyzing the multiple scattering components by the help of classical trajectory Monte-Carlo (CTMC) calculations. We think that this specific ionization mechanism can play a significant role in high-energy electron emission, and may contribute to radiation damages in biological tissues.

Contents

1. INTRODUCTION

Interactions of swift heavy ions with matter yield a large variety of collision events [1–4]. At high (a few tens of MeV/u or higher) impact energies, the dominant process is ionization on both the projectile and the target sides. Accordingly, in a sequence of collisions in dense materials, the projectile ions become highly charged at these energies. For non-bare projectiles, dielectronic interactions between projectile and target electrons often play a significant role in this energy range. After loosing kinetic energy, excitation comes into play, and charge transfer channels open gradually. The decelerated projectile ions carry more electrons, and often get excited. Ionization remains an important electron emission

ADVANCES IN QUANTUM CHEMISTRY, VOLUME 52
ISSN: 0065-3276 DOI: 10.1016/S0065-3276(06)52011-8

channel but autoionization and Auger transitions also contribute to the spectra of the emitted electrons. Free electron production is an important contribution to the energy transfer from ions to matter, in the entire energy range during the deceleration of the ions, down to their stopping. From practical aspects, the most interesting impact energy region is where the energy transfer per unit length shows a sharp maximum. This is the peak of the maximum energy deposition before the ion stops, usually referred to as the Bragg peak [5].

Radiation damage is an irreversible modification of crystal or molecular structure by energetic impact (in our case the impact of an ion). In the following, we focus our attention to molecules, where the most frequent result of an energetic collision is fragmentation. These considerations have some relevance in astrophysical applications and plasma physics too [6]. A molecule can be fragmented in direct ion–molecule collisions or due to the impact of secondary particles (electrons, photons or molecular fragments) emitted in the direct collisions. Note, that not all the particle-emitting direct collisions lead to molecular fragmentations, therefore the yield of secondary processes might be eventually higher than that of the direct fragmentation events.

A direct binary process is, e.g., when the incoming ion hits one of the nuclei of the molecule, and transfers a large part of its kinetic energy to it [7]. This process becomes significant only at very low ion-impact energies, in the so-called nuclear stopping region. More significant direct fragmentation processes start with electronic transitions, i.e., the transfer of electrons from the target to the projectile, or with target ionization. When electrons are removed from the molecule, the repulsive forces between its positive and/or polarized cores may result in a Coulomb explosion [8].

Among the secondary particles emitted in direct collisions, secondary electrons are responsible for a large fraction of further fragmentation events. This was understood rather early, when the interest was focused on radiation damages in biological tissues in connection with developments in cancer therapy [9,10]. The important role of these electrons in the primary molecular steps towards radiation damage has now widely been recognized [11]. The majority of the secondary electrons are ballistic electrons, with energies of a few tens of eV. Via inelastic collisions, these low energy electrons initiate further ionization and excitation processes. They create neutral radicals, ions and electrons. At low energies they may be captured at particular molecular sites or trapped as solvated electrons. As a result, they can efficiently induce single and double strand breaks in supercoiled DNA [12]. In this low energy range, resonant processes may enhance molecular dissociation enormously. Electrons at even subexcitation energy (0–4 eV) are able to effectively induce single strand breaks in DNA [13].

From the point of view of radiation induced damages, the higher energy part of the secondary electron spectrum is also very important [14,15]. The yield of double-strand breaks induced by electrons in the DNA shows a maximum at energies of a few hundred eV. Accordingly, these fast secondary electrons are most effective to segment the DNA molecule [14]. Such high energy electrons may create inner shell vacancies, and the subsequent Auger cascades produce both electrons and multiple charged ions. In this way, ionization clusters can be formed in small volumes, comparable to the size of small DNA segments [14]. In addition, it has also been pointed out by Scully *et al.* [15], that the fragmentation cross section of water molecules by electron impact has a broad maximum between 50 and 300 eV electron energies. For illustration, the production cross section of different fragments is shown in Fig. 1. The charged (indicated in Fig. 1), neutral and neutralized fragments, like free OH radicals, are largely responsible for DNA strand

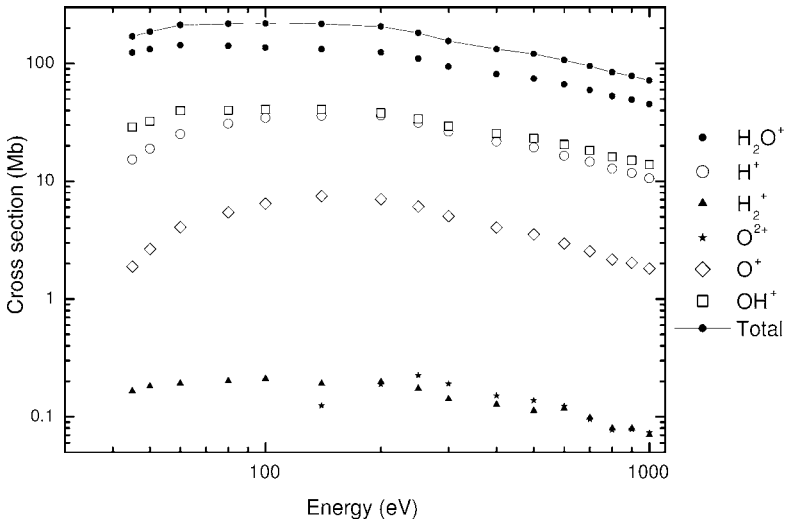

Fig. 1. Fragment production cross sections for electron impact ionization of H_2O [15] (1 Mb = 10^{-18} cm^2).

brakes [12]. In conclusion, few hundred eV electrons can be considered as important damaging agents. The contribution of these fast electrons to radiation damages is determined by their relative intensity, which depends on the charge state and the actual energy of the bombarding ion species. The angular and energy distribution of the emitted electrons strongly varies along the ion-path as its velocity decreases down to zero, but, in general, the relative intensity of such few-hundred-eV electrons is typically much smaller than that of the ballistic electrons. Accurate knowledge of the amount and the distribution of the emitted electrons is especially important in the region of the Bragg peak, at the end of the ion trajectory, where the largest part of the ion-energy is deposited.

In the present work, we demonstrate that an unexpectedly large amount of high-energy (few hundred eV) electrons can be emitted relatively close to the Bragg peak. The considered mechanism of fast electron emission is the so-called Fermi-shuttle acceleration in atomic collisions [16–20], where the electron is scattered forward and backward by the incoming heavy projectile ion and the target core before being ejected. In the following we introduce the concept, and provide a short history of the study of the Fermi-shuttle acceleration mechanisms. Then we present the results of recent systematic experimental studies and follow the way of identifying and analyzing the multiple scattering components by the help of classical trajectory Monte-Carlo (CTMC) calculations. We show that this specific ionization mechanism can play a significant role in high-energy electron emission, and may remarkably contribute to radiation damages in biological tissues. In this paper, atomic units ($\hbar = e = m_e = 1$) are used.

2. FAST ELECTRON EMISSION AND FERMI-SHUTTLE ACCELERATION

Detailed information about atomic collision processes can be gained by studying differential spectra of the emitted electrons, or from multiple differential coincidence studies.

Electron emission spectra are usually doubly differential (in energy and polar observation angle). Characteristic structures in these spectra can be associated with different collision mechanisms [1,3]. Sharp lines are due to autoionization of multiple excited states created by excitation, electron transfer or inner-shell vacancy production. For fast collisions, characteristic structures can also be identified in the continuous part of the electron spectra. The ionization of the target atoms by fast ions (with impact velocity V) is dominated by the emission of low energy electrons maximizing the cross section in the so-called soft-collision region. The ionization of dressed projectile ions provides the electron loss (EL) peak, centered at or close to the cusp energy, $T = V^2/2$, at all observation angles in the laboratory frame (note that T is the kinetic energy of an electron moving with the projectile velocity). Close collisions between the projectile ion and the active target electron form the binary encounter (BE) peak at forward observation angles $\theta < 90°$, with the approximate mean energy $E_{\mathrm{BE}}(\theta) = 4V^2\cos^2(\theta)$. The mean electron velocity of the BE peak at zero degree is $2V$, so the BE electron energy is about four times larger than that of the EL peak. The high-energy tail of the BE peak is determined by the target Compton profile [3,21]. No other structures are expected in the electron spectra at energies above the BE peak in first order theories.

Experimentally, significant enhancement of electron emission yields was observed in some ion–atom collision systems far above the BE energies, as early as in 1979 [22]. Later, in a few ion-solid collision experiments, high energy electron emission yields have been found by orders of magnitudes larger than any theoretical predictions [4,18,23–30]. One of the candidates to explain the enhancement of the yield of fast electrons is the so-called Fermi-shuttle acceleration. Originally, Fermi [31] had proposed the mechanism as a possible origin of energetic cosmic rays. Weak but giant magnetic fields, moving in outer space, can accelerate charged particles to extremely high energies in long sequences of reflections. Similarly, a light electron can be scattered forward and backward by heavy target atom(s) and an incoming heavy projectile ion. Due to the repeated collisions, the electron can be accelerated to relatively high energies. At first sight, our intuition does not predict long sequences with these microscopic, spherically symmetric "paddles" (or "bats") [32–35].

With heavy atomic centers ($M/m_e \gg 1$), the kinematics of such a game is rather simple. The velocity of the liberated electron is increased by approximately $2V$, in every 180° elastic scattering with the incoming projectile, while only the direction of the electronic motion is changed by scatterings on the target field. In Ref. [19], we introduced the shorthand P and T to denote the electron-projectile and electron-target scatterings, respectively. With this notation, the BE process, i.e., target ionization by a binary collision of a target electron with the *field of the projectile*, is denoted by P. Projectile ionization due to a binary collision of a projectile electron with the *field of the target* is denoted by T. If the first P scattering of the electron e.g., is followed by a second scattering on the target field, it is called a P–T process. Notations like P–T–P, or T–P–T–P–T refer to longer sequences. Let n be the number of encounters between the electron and the projectile. Target ionization sequences always start with a P process, and emit electrons up to the velocity $2nV$ in both forward and backward directions relative to the projectile motion. For projectile ionization sequences (starting with T), the final velocity is $(2n + 1)V$. In Fig. 2, we show a set of "snapshots" for a P–T–P process [20].

We note here that the above mechanism has fundamental importance, even if its yield is small. Ionization is one of the most important phenomena related to the Coulomb three-body problem. These fast electrons are ejected in particular ionization processes, which

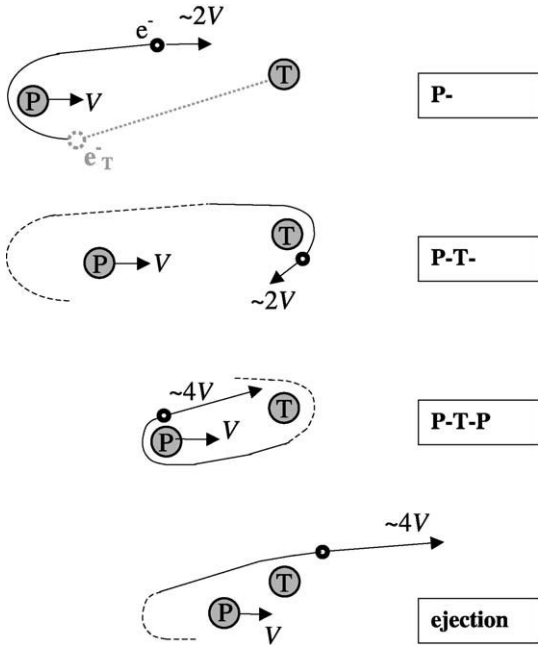

Fig. 2. A classical scenario of a P–T–P scattering sequence in "snapshots". The starting step is a binary collision between the heavy projectile ion and the active target electron, i.e., a P process [20].

can be associated with specific three-body states. Moreover, as a source of a long-range secondary particle radiation, the Fermi-acceleration process may gain importance in ion-matter interactions in general. It might be relevant not only in radiation effect in biological tissues, but in many other fields like astrophysics, plasma physics, analytical methods, or ion-beam technologies.

3. FIRST EXPERIMENTAL INDICATIONS—TWO STEP PROCESSES

The series of observations of multiple scattered "hot" electrons in atomic collisions started at low collision energies. Enhanced forward and backward emission of relatively very fast ($3V < v_e < 7V$) electrons was already reported by Stolterfoht and Schneider in 1979, in collisions of 50–400 keV O^+ ions with Ar atoms [22]. They observed intensity maxima in the spectra, shifting to higher electron energies with increasing projectile energies [22]. Our recent CTMC calculations (see below) confirmed the significant role of accelerating multiple scattering in their collision systems.

Surprisingly high-energy electrons have been observed in collisions of slow (few keV) He^+ and Ar^+ ions with solid targets by Baragiola and coworkers [24]. They found the striking result that some of the emitted electrons can gain kinetic energies up to 40% of the CM energy of the colliding atomic cores. For explanation, a Fermi-shuttle type acceleration process with an electron scattered many times by the two approaching atomic centers

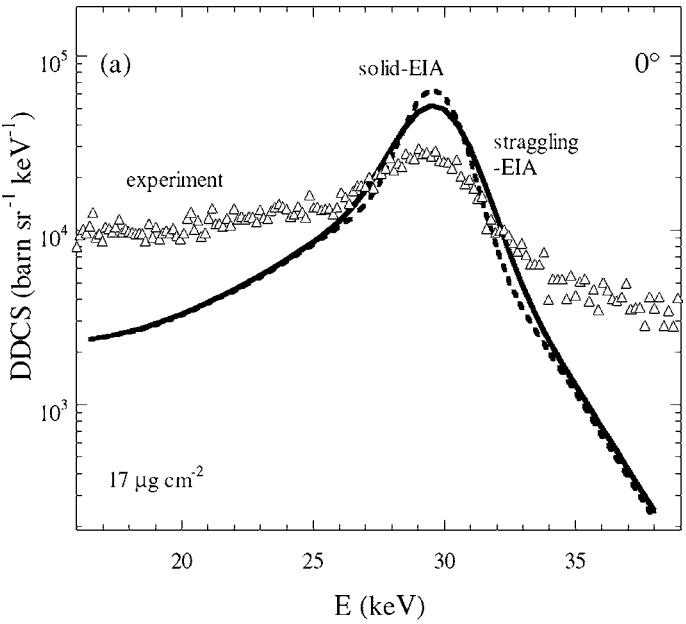

Fig. 3. Doubly differential electron emission cross section for 13.6 MeV/u Ar^{18+} impinging on a C foil of 17 μg/cm^2 in the BE region at 0° observation angle [27]. The solid line is a calculation performed in the Electron Impact Approximation (EIA), including energy straggling and electron transport effects [25]. Both the flattening of the BE peak and the order-of magnitude larger experimental cross sections at the highest measured energies is typical for this type of experiments. From Ref. [20].

(i.e., a long sequence of P–T–P–T. . . collisions) was considered by Sigmund [35], and this model was further refined later [36,37].

The ion-solid measurements reported at higher ion energies, in the 1–100 MeV/u impact energy range [4,18,23,25–30,38–40], were primarily focused on the study of the BE peak region. In many cases [4,18,23,25,26,29,30], strong indication has been found for an order of magnitude enhancement above the BE peak in the electron yields compared to single electron scattering theories [25,30]. A typical example is shown in Fig. 3, for the impact of 13.6 MeV/u Ar^{18+} ions on a relatively thin (17 μg/cm^2) C foil [27]. The forward electron emission cross section above (and below) the BE peak is significantly larger than the theoretical prediction. The strong enhancement at the high energy tail of the BE peak is typical for many of such experiments (e.g., [4,23,25–28]).

The Fermi-shuttle acceleration mechanism explained the high-velocity tail of the in the spectra of electrons emitted to forward angles in fast 45 MeV/u Ni^{28+} + Au (foil) collisions (Lanzano *et al.* [18,29]). A Monte Carlo simulation, based on a two-step collision sequence, convincingly reproduced the high energy tail of the spectra above the BE peak. More recently, Lanzano *et al.* [30] performed a systematic study for the dependence of the extra electron yield on the target atomic number Z in collisions of 23 MeV/u Au^{36+} ions with cc. 90 μg/cm^2 C, Ni, Ag and Au foil targets, and found that the normalized yield of the high energy tail, relative to the BE intensity, increased with the target atomic number.

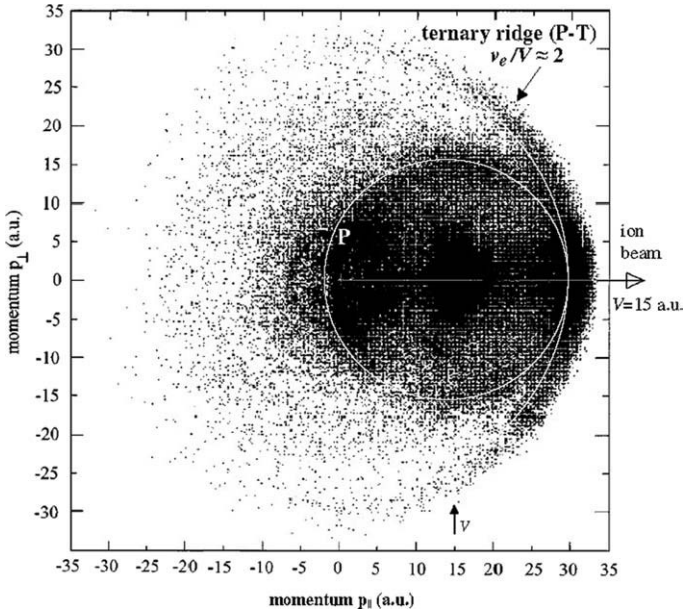

Fig. 4. Two-dimensional final state momentum distribution for electrons emitted in collisions of 5.88 MeV/u U^{29+} with C_3F_8 [17]. The abscissa and the ordinate show the electron momentum components parallel and perpendicular to the projectile velocity vector, respectively. We take the scatter plot from Ref. [17], and indicate both the binary ridge (P), and the ternary ridge (P–T) by white circles. From Ref. [20].

They identified the main contribution of the tails with an accelerating T–P scattering sequence, in which backscattered convoy electrons collide with the incoming projectile ion in a second step.

In ion-solid experiments, single collisions are rare events. Due to the high density of the scattering centers in condensed matter, multiple electron scattering sequences may be significantly more likely, if more than one target center can play role in the process. In most cases, however, only an average of different processes can be observed, and even the remaining structures are shadowed by solid state effects. Usually, an observed enhancement alone cannot provide a clear evidence for multiple scattering processes.

To investigate the mechanism in more details, it was more promising to proceed with thin gaseous targets. In clean two-center P–T–P–. . . sequences, one might expect observable structures, but also very small cross sections. In such two center ion–atom collisions the first experimental evidence was provided by Suarez *et al.* [16,41] in the ionization of neutral hydrogen projectiles by single collisions with He targets at 20–50 keV impact energies. They observed an enhanced intensity in the electron spectrum in the forward direction at approximately $3V$. This structure was identified as due to the T–P process. Following the above breakthrough, the corresponding P–T double scattering effect in the ionization of the target was first identified by Bechtold *et al.* [17] at the surprisingly high energy of 5.9 MeV/u of the U^{29+} projectile. Here, the observed signature of double scattering was a peak in the electron spectra appearing at the electron velocity $2V$. For heavier atomic

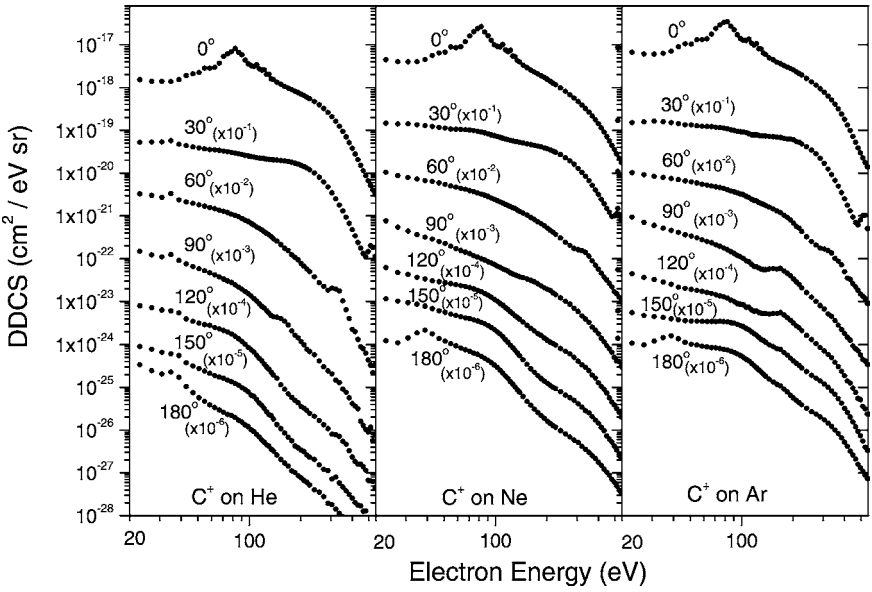

Fig. 5. Double differential electron emission spectra from the collisions of 150 keV/u C^+ ions with inert gas targets. For graphical reasons, the spectra taken at different observation angles are divided by the powers of ten. The order of magnitude enhancement at backward angles with increasing target atomic number is clearly seen from the left to the right panels [43].

and molecular targets, this $2V$ peak was clearly observable in the 0°–130° angular region, forming a "ternary ridge" in the scatter plot [17,42]. Results for the C_3F_8 molecular target [17] are shown in Fig. 4.

The characteristic binary (P) and ternary (P–T) ridges are also indicated in the two-dimensional momentum distribution, which is a descriptive way to visualize kinematical relations. Note that for electrons, the momentum and velocity values are identical in atomic units. Accordingly, elastic scattering or emission of the light electrons by the heavy centers of the target and the projectile is represented by circles centered at the $0, 0$ and the $V, 0$ points, respectively.

Since the ternary ridge has been found to be relatively weak at the backward direction (close to 180°) one could not expect an observable triple or higher order scattering in this high projectile velocity region.

The first indication for possible longer sequences was provided by Sulik and coworkers [43,44]. In intermediate velocity (150 keV/u) ion-inert gas collisions, they found a strong enhancement peaked at backward observation angles. The results are summarized in Fig. 5 [43]. While the zero-degree cross sections increase only a factor of about three from He to Ar, the backward yield at 180° observation angle increases more than a factor of twenty at 300 eV electron energy.

This signature of a strong second scattering of the electron by the target core towards the incoming projectile was the starting point to find evidence for longer scattering se-

quences (P–T–P and P–T–P–T) in single ion-atom collisions. These experimental studies are presented in Section 5 of the present work.

4. THEORETICAL CONSIDERATIONS

Although the picture outlined above looks completely classical, the first theoretical evidence for Fermi-shuttle acceleration of electrons in atomic collisions was found by Wang *et al.* [34], who applied a pure quantum mechanical model with zero-range potentials for two-center collisions. For the ionization of the target atom by a heavy charged projectile with impact velocity V, the model had predicted peaks in the spectrum of the emitted electrons at velocities $2V, 4V, 6V, \ldots$ in both forward (0°) and backward (180°) directions.

In collision of atomic systems, Fermi-shuttle mechanism—namely that cluster impact accelerated deuterons could gain a significant amount of kinetic energy—was also considered as a possible way to ignite cold fusion [32,33]. It was shown, that multiple collision sequences lead to an exponential tail in the deuteron energy spectrum [32,33]. However, the calculated probabilities for generating fusion events were by several orders of magnitudes too small compared to the reported experimental data [47]. We note here that the exponential tail refers to consecutive independent elastic scattering events. First, this assumption was also extended to the case of multiple scattered electrons [35]. The importance of the attractive potential in multiple electron scattering was realized by Jakas [36,37], who introduced the concept of trapping. He showed, that in the screened fields of the approaching atomic cores, the electron could be trapped into slowly changing closed—molecular like—orbits, up to many turns around the two heavy centers. Though the scattering events still were considered as independent, Jakas [36] recognized that a closed orbit for the active electron could be created due to the fact that the scattering angle in the screened field of an ionic core can be larger than in the Coulomb field of its bare nucleus. Jakas showed that multi-turn orbits could not be formed by independent scatterings on two Coulomb centers with Z/r type potentials [36,37].

The importance of the electronically screened core fields in atomic collisions has been widely recognized. In fast collisions, ionization of loosely bound electrons can be considered as a scattering of quasi-free electrons by the field of the ionizing partner (see, e.g., in [3,25,26,48–56]). Diffraction patterns characteristic for free electron scattering by non-Coulomb fields have been observed in both target ionization by screened projectiles [49–52] and projectile ionization [53–56]. It is also generally assumed that such diffraction phenomena play a significant role in the formation of Fermi-shuttle scattering sequences, since they may enhance the probability of forward–backward focusing [17,19,36,37,42–46,59,60].

At high projectile velocities, one might consider the Fermi-shuttle ionization process as a set of independent core–electron collisions. In such cases, the backscattering of the electrons within a narrow cone around 180° is a necessary condition of forming longer sequences. Therefore, one can define the effective area of an "ionic core paddle" as roughly proportional to the cross section for 180° elastic electron scattering by the core [46]. In a first approximation, it is proportional to the square of the atomic number Z^2 [19,42]. Accordingly, one might expect that the probability of longer sequences very strongly increases with increasing atomic number of both the projectile and the target. For separating

and identifying the structures originating from the different orders of the multiple scattering processes, the relevant quantity is the observability. For a P–T–P process on the "background" of a single scattering P process, e.g., the observability can be characterized by the ratio $\sigma_{\mathrm{P-T-P}}/\sigma_{\mathrm{P}}$. For order of magnitude estimations, one can consider this ratio proportional with Z^2_{proj} [19]. Due to dispersion, however, the elastic electron scattering cross section at 180° can be either smaller or larger than the Rutherford cross section for the bare nucleus. By selecting an appropriate pair of collision partners and an optimum collision velocity, both the relevant cross sections and the observability ratios can be strongly enhanced compared to the case of bare Z/r type core potentials [19,42–46].

The above picture of a sequence of independent collisions should be completely changed at the low energy limit, where the ion energy is small, but large enough to Fermi-accelerate the ejected electrons. This is clearly the field of quantum calculations. In these slow, but still non-adiabatic ion–atom collisions, Fermi-shuttle acceleration can be considered as a development of specific molecular orbitals, i.e., it can be identified with a promotion mechanism, sometimes denoted as S-promotion (super-promotion) [57,58]. This region is a challenge for both experiments, and quantum calculations for the experimentally available collision systems.

The ion impact energy range, where the electron backscattering sequence cannot be considered as a set of independent events, is not limited to the very slow, almost adiabatic collisions. Except the case of very fast collisions, the electron orbits in the field of two attractive heavy centers (with screened Coulomb fields), which move against each other. The electron feels both fields, similarly to an electron in a diatomic molecule. However, it also gains energy in every "turn" from the moving projectile ion. There is a wide impact energy region, where the cross section of Fermi acceleration may significantly increase compared to that of a sequence of independent scattering events.

A general theory for such collisions should be extremely complicated. A second order, analytic quantum mechanical model calculation with exponentially screened potentials [59] has explained the main features of the P–T process. It was also shown that a partial account for the P–T process could be provided even within a 1st-Born calculation, where the final state was represented by a solution of the Schrödinger equation on a realistic screened potential [59]. Moreover, the application of an impulse approximation for the latter case provided a reasonable description of the P–T process [60] compared to the experimental results of Bechthold *et al.* [17]. Finally, it is interesting to note that the solution of the Dirac equation in the momentum space in the nearly relativistic (100 MeV/u) impact energy region also provided Fermi-shuttle like double scatering patterns in the calculated spectra of the ejected electrons [61]. For treating longer sequences however, up till now, only the classical trajectory Monte Carlo method have been applied.

4.1. Classical trajectory Monte-Carlo calculations

The classical trajectory Monte Carlo (CTMC) method treats the atomic collisions in a non-perturbative manner. Classical equations of motions are solved numerically with randomly selected initial conditions [62–65]. The method has successfully been used for a wide range of atomic collision systems [66–68], among others, in many Fermi-shuttle acceleration cases [18,19,29,30,42–46,69]. One of the main advantages of the CTMC method is that the three-body interaction is exactly taken into account during the collision at a classical

level. We note that many body effects can also be treated by CTMC beyond the perturbation treatment in certain approximations [68].

Since the Fermi-shuttle acceleration process is associated with a complicated classical trajectory of the scattered electron, a natural theoretical approach is the use of the classical and non-perturbative CTMC method as a first attempt to account for the experimental findings. We will see later that the analysis of the individual CTMC trajectories can provide somewhat more, namely the classification and identification of multiple electron scattering events.

In the present work the CTMC simulations have always been performed in the three-body approximation, i.e., the many-electron target was replaced by an effective one-electron atom and the projectile ion was taken into account as a screened nucleus [70,71]. Therefore in our CTMC model the three particles are the projectile ion (P), one atomic active target electron (e), and the remaining target ion core (T). Both projectile and target cores may include nucleus and electrons. The three "particles" are characterized by their masses and the interaction potentials between them. We note that this model is the classical analogue of the quantum-mechanical effective single-electron treatment of atomic collisions [63]. For the interaction of the electron with the screened ionic cores, we used a central model potential developed by Green [72], which is based on Hartree–Fock calculations. The potential can be written (by introducing the r dependent effective charge Z^{eff}) as:

$$V(r) = q\frac{Z-(N-1)[1-\Omega^{-1}(r)]}{r} = q\frac{Z^{\mathrm{eff}}(r)}{r}, \tag{1}$$

where Z is the nuclear charge, N is the total number of electrons in the atom or ion, r is the distance between the nucleus and the test charge q, and

$$\Omega(r) = \frac{\eta}{\xi}\left(e^{r\xi}-1\right)+1. \tag{2}$$

The potential parameters ξ and η can be obtained in such a way that they minimize the energy for a given atom or ion. This type of potential has further advantages, because it has a correct asymptotic form for both small (Eq. (3)) and large (Eq. (4)) values of r.

$$\lim_{r\to 0} Z^{\mathrm{eff}}(r) = Z, \tag{3}$$

$$\lim_{r\to \infty} Z^{\mathrm{eff}}(r) = Z-(N-1). \tag{4}$$

This potential was originally developed for describing the electronic ground states of neutral atoms. Accordingly, most of the tabulated parameters ξ and η have been published for the singly charged ionic cores of the elements, but there exist tables of ξ and η values also for doubly (and some multiply) charged ionic cores [73]. If the projectile is singly or doubly charged, both the projectile field and the singly charged target core can be characterized by the above model potentials. The Lagrangian for the three particles can be written as:

$$L = L_K - L_V, \tag{5}$$

where

$$L_K = \frac{1}{2}m_P\dot{\vec{r}}_P^{\,2} + \frac{1}{2}m_e\dot{\vec{r}}_e^{\,2} + \frac{1}{2}m_T\dot{\vec{r}}_T^{\,2}, \tag{6}$$

and

$$L_V = \frac{Z_P^{\text{eff}}(|\vec{r}_P - \vec{r}_e|)Z_e}{|\vec{r}_P - \vec{r}_e|} + \frac{Z_P^{\text{eff}}(|\vec{r}_P - \vec{r}_T|)Z_T^{\text{eff}}(|\vec{r}_P - \vec{r}_T|)}{|\vec{r}_P - \vec{r}_T|} + \frac{Z_e Z_T^{\text{eff}}(|\vec{r}_e - \vec{r}_T|)}{|\vec{r}_e - \vec{r}_T|}. \tag{7}$$

$\vec{r}$, Z and m are the position vector, the charge ($Z_e = -1$) and the mass of the denoted particle, respectively. We note that the second term is an approximate, but applicable representation of the core–core interaction. At small internuclear distances, it tends to the accurate nucleus–nucleus interaction term, which usually does not alter atomic cross sections significantly (except at very small impact velocities). The equations of motion can be calculated as:

$$\frac{d}{dt}\frac{\partial L}{\partial \dot{q}_i} = \frac{\partial L}{\partial q_i} \quad (i = P, e, T). \tag{8}$$

Introducing the relative position vectors $\vec{A} = \vec{r}_e - \vec{r}_T$, $\vec{B} = \vec{r}_T - \vec{r}_P$, and $\vec{C} = \vec{r}_P - \vec{r}_e$, in such a way that $\vec{A} + \vec{B} + \vec{C} = \vec{0}$, we can write

$$m_P \ddot{\vec{r}}_P = -\frac{1}{B^2} f(B, Z_T, Z_P)\vec{B} + \frac{Z_e}{C^2}\left(\frac{Z_P(C)}{C} - \frac{\partial Z_P(C)}{\partial C}\right)\vec{C}, \tag{9}$$

$$m_e \ddot{\vec{r}}_e = \frac{Z_e}{A^2}\left(\frac{Z_T(A)}{A} - \frac{\partial Z_T(A)}{\partial A}\right)\vec{A} - \frac{Z_e}{C^2}\left(\frac{Z_P(C)}{C} - \frac{\partial Z_P(C)}{\partial C}\right)\vec{C}, \tag{10}$$

$$m_T \ddot{\vec{r}}_T = -\frac{Z_e}{A^2}\left(\frac{Z_T(A)}{A} - \frac{\partial Z_T(A)}{\partial A}\right)\vec{A} + \frac{1}{B^2} f(B, Z_T, Z_P)\vec{B}, \tag{11}$$

where

$$f(B, Z_T, Z_P) = \frac{Z_P(B)Z_T(B)}{B} - Z_P(B)\frac{\partial Z_T(B)}{\partial B} - Z_T(B)\frac{\partial Z_P(B)}{\partial B}, \tag{12}$$

$$Z_T(r) = Z_T - (N_T - 1)\left[1 - \frac{1}{\Omega_T(r)}\right], \tag{13}$$

$$\Omega_T(r) = \frac{\eta_T}{\xi_T}\left(e^{r\xi_T} - 1\right) + 1, \tag{14}$$

$$\frac{\partial Z_T(r)}{\partial r} = \frac{(1 - N_T)\eta_T e^{r\xi_T}}{\Omega_T^2(r)}, \tag{15}$$

$$\eta_T = \eta_T^{(0)} + \eta_T^{(1)}(Z_T - N_T), \tag{16}$$

$$\xi_T = \xi_T^{(0)} + \xi_T^{(1)}(Z_T - N_T). \tag{17}$$

Here the subscript T stands for the target. In the same way, we can get the corresponding formulas for the projectile:

$$Z_P(r) = Z_P - N_P\left[1 - \frac{1}{\Omega_P(r)}\right], \tag{18}$$

$$\Omega_P(r) = \frac{\eta_P}{\xi_P}\left(e^{r\xi_P} - 1\right) + 1, \tag{19}$$

$$\frac{\partial Z_P(r)}{\partial r} = -\frac{N_P \eta_P e^{r\xi_P}}{\Omega_P^2(r)}, \tag{20}$$

$$\eta_P = \eta_P^{(0)} + \eta_P^{(1)}(Z_P - N_P - 1), \tag{21}$$

$$\xi_P = \xi_P^{(0)} + \xi_P^{(1)}(Z_P - N_P - 1). \tag{22}$$

Garvey *et al.* [73] tabulated the parameters $\eta_X^{(0)}$, $\eta_X^{(1)}$, $\xi_X^{(0)}$, $\xi_X^{(1)}$ ($X = P$ or T) for a wide range of N and Z. After some elementary calculus, Eqs. (9)–(11) reduce to the following two formulas:

$$\begin{aligned}\ddot{\vec{A}} = &\left[\left(\frac{1}{m_e}\right)\frac{Z_e}{C^2}\left(\frac{Z_P(C)}{C} - \frac{\partial Z_P(C)}{\partial C}\right)\right.\\ &\left. + \left(\frac{1}{m_e} + \frac{1}{m_T}\right)\frac{Z_e}{A^2}\left(\frac{Z_T(A)}{A} - \frac{\partial Z_T(A)}{\partial A}\right)\right]\vec{A}\\ &+ \left[\left(\frac{1}{m_e}\right)\frac{Z_e}{C^2}\left(\frac{Z_P(C)}{C} - \frac{\partial Z_P(C)}{\partial C}\right) - \left(\frac{1}{m_T}\right)\frac{1}{B^2}f(B, Z_T, Z_P)\right]\vec{B},\end{aligned} \tag{23}$$

$$\begin{aligned}\ddot{\vec{B}} = &\left[\left(\frac{1}{m_P}\right)\frac{Z_e}{C^2}\left(\frac{Z_P(C)}{C} - \frac{\partial Z_P(C)}{\partial C}\right) - \left(\frac{1}{m_T}\right)\frac{Z_e}{A^2}\left(\frac{Z_T(A)}{A} - \frac{\partial Z_T(A)}{\partial A}\right)\right]\vec{A}\\ &+ \left[\left(\frac{1}{m_P}\right)\frac{Z_e}{C^2}\left(\frac{Z_P(C)}{C} - \frac{\partial Z_P(C)}{\partial C}\right)\right.\\ &\left. + \left(\frac{1}{m_P} + \frac{1}{m_T}\right)\frac{1}{B^2}f(B, Z_T, Z_P)\right]\vec{B}.\end{aligned} \tag{24}$$

These differential equations are integrated with respect to time (as independent variable) by the standard Runge–Kutta method. The randomly selected initial conditions are: (i) the impact parameter of the projectile with respect to the target atom, (ii) the position and velocity vectors of the target electron moving in classical orbits (in the Coulombic case, e.g., Kepler orbits). The initial conditions of the individual collisions are chosen at sufficiently large internuclear separations, where the interaction between the projectile and the target constituents is negligible. The initial state of the target is characterized by a microcanonical ensemble constrained to the binding energy of the given shell.

For our present non-Coulombic systems, the random selection of the position and velocity vectors of the target electron has been performed according to the general method of Reinhold and Falcon [74], and the classical interval equivalents of the orbital quantum numbers of Becker and MacKellar [75] have been applied. Since the (pure or partially screened) Coulomb interaction has a long range character, the equations of motion have to be integrated over 10^5 a.u. For saving computer time, the integration was skipped for the non-analyzed class of events [76]. First, we integrated the equations of motion as far as the real exit channel was observed (excitation, ionization, and charge transfer). From this point we continued the integration only when the exit channel was ionization. For the ionization channel the final energy and the scattering angles (polar (θ) and azimuth (ϕ)) of the projectile and the ionized electron were recorded. These parameters were calculated at large internuclear separation.

The total and double differential cross sections were computed by the following formulas:

$$\sigma = \frac{2\pi b_{\max}}{T_N}\sum_j b_j^{(i)}, \tag{25}$$

$$\frac{d^2\sigma}{dE\,d\Omega} = \frac{2\pi b_{\max}}{T_N \Delta E \Delta\Omega}\sum_j b_j^{(i)}. \tag{26}$$

The statistical uncertainty of the cross section is given by

$$\Delta\sigma = \sigma\left(\frac{T_N - T_N^{(i)}}{T_N T_N^{(i)}}\right)^{1/2}. \tag{27}$$

In equations (25)–(27) T_N is the total number of trajectories calculated for impact parameters less than $b_{\max}$, $T_N^{(i)}$ is the number of trajectories that satisfy the criteria for ionization, and $b_j^{(i)}$ is the actual impact parameter for the trajectory corresponding to the ionization process under consideration in the energy interval ΔE and the emission angle interval $\Delta\Omega$ of the electron.

We should emphasis here that classical and quantum mechanical elastic scattering of electrons by screened cores provide usually rather different angular distribution patterns. Therefore, one might expect only a qualitative agreement between experiment and CTMC results for multiple electron-scattering in general. At high impact velocities, however, classical and quantum scattering patterns around 180° became rather similar [42]. Moreover, in the case of more turns at lower impact velocities, the unrealistically sharp classical patterns are probably washed out by statistical averaging, so CTMC might provide realistic results again. However, there is no general answer for the region of applicability of CTMC. The first steps of a systematic experimental and theoretical study in that direction will be shown below.

An important advantage of the CTMC calculations is that many details of the classical scenario of multiple scattering can be conveniently analyzed within this framework. For illustration, we demonstrate the "3-dimensional" trajectories of all the three particles in a P–T–P–T collision in Fig. 6. In this particular case, both projectile-electron encounters are clearly seen.

For the analysis of a large number of trajectories, we need a quick procedure to classify the different events. For this purpose, we extracted specific information from the complicated trajectories similar to that of Fig. 6. For example, the z-coordinates and the energies of the particles as a function of the collision time can be analyzed much faster than the full trajectories.

In such an analysis, we can test some of our intuitive pictures too. They tell us, for example, that multiple scattering sequences are more likely to be formed in small impact parameter collisions. This picture has indeed been confirmed by CTMC calculations. In general, the analysis of the calculated CTMC trajectories makes it possible to study the classical initial phase space regions belonging to certain classes of multiple scattering events. Let us consider, for example the initial phase space for higher orders of multiple scattering. The forward–backward mean electron velocities $2V$, $4V$, $6V$, etc., correspond to a start with a target electron initially "at rest". Since a backscattering event needs a finite time, the length of possible sequences is limited for such electrons. If, however, an electron initially moves fast towards the projectile, this electron keeps moving faster during the whole "ping-pong game", while the ion velocity will be the same. Therefore, the high-momentum tail of the initial state distribution (Compton profile) could be favored, and a shift of the observed mean velocity to higher values can be expected for longer sequences. This was confirmed by both experiments and CTMC calculations [19,20]. Of course, in such analyses one always should keep in mind the limitations of a classical model for atomic systems.

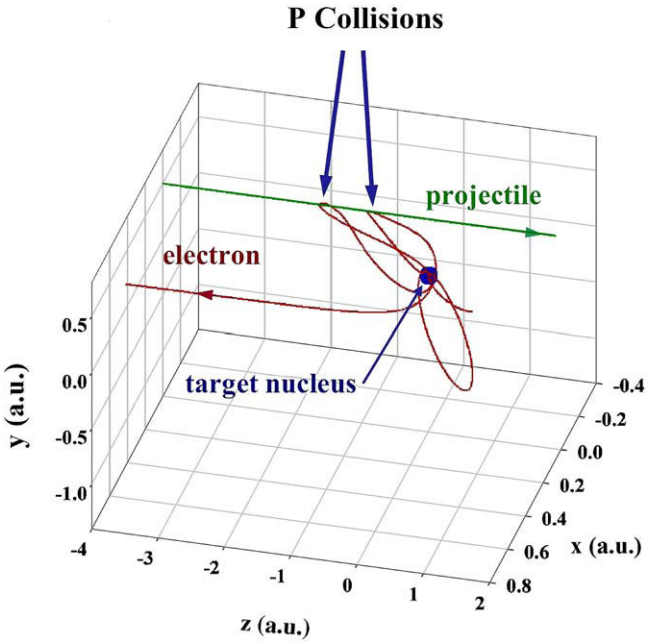

Fig. 6. A sample CTMC event for a P–T–P–T scattering sequence in a 150 keV/u $C^+ + Xe$ collision. The projectile and electron trajectories clearly show two consecutive close P collisions between the active target electron and the incoming projectile ion.

5. HIGHER ORDER ELECTRON SCATTERING SEQUENCES

In the following, we would like to provide a brief overview about the experimental studies of longer electron scattering sequences. These are mostly, but not exclusively our results. In all the treated cases, double differential cross sections for electron emission have been measured.

The first set of measurements has been performed with intermediate velocity projectile ions, and led us to the separation and identification of triple (P–T–P) and quadruple (P–T–P–T) multiple scattering contributions to electron emission [19,43–46]. Here the spectra were taken for electron energies of 20–3400 eV and for observation angles $\theta = 0$–$180°$. In the measurements, performed at ATOMKI, Debrecen, beams of He^+ and C^+ ions with 150- and 233-keV/u energies were directed onto He, Ne, Ar and Xe gas jet targets. The electron spectra were collected simultaneously in 13 angular channels with a triple-pass electrostatic spectrometer [77].

As already shown in Fig. 5, at first we observed a strong enhancement of the electron yield in the 150–500 eV energy region (around $2V$) at 180° observation angle in 150 keV/u $C^+ + He$, Ne and Ar collisions, and identified it as a signature of the P–T process [43,44]. The intensity of the observed shoulder strongly increases with the target atomic number, and it exhibits a maximum at 180°. Therefore, we concluded that a third scattering should be likely in this intermediate ion-impact velocity region (~ 2.5 au). To find an appropriate collision system, we searched for efficient backscattering cores by calculating the 180° elastic electron-scattering cross sections for different projectile and target cores for a few

projectile velocities, and in the entire electron impact velocity region relevant for the multiple scattering sequences. Finally, 150- and 233-keV/u carbon ions had been selected as projectiles, and xenon atom as a relatively heavy inert gas target with a high electron backscattering cross section in the velocity range concerned. We also collected data for an independent reference system (233-keV/u $He^+ + Xe$) where, according to the calculations, no significant multiple scattering contributions were expected [19].

In order to identify the signatures of multiple scattering in the double differential electron spectra, we needed to separate them from the single scattering contributions. To estimate the latter components, reference spectra were taken with He^+ projectile, where only a negligible P–T–P contribution had been expected compared to the C^+ impact. Since we got an excellent agreement between the He^+ reference spectra and auxiliary 1st-Born calculations (even the calculated subshell effects were observed in the experimental data), the theoretical 1st-Born spectra were used to represent the single scattering target ionization contributions [19].

We also performed CTMC calculations for the ionization of both the projectile (all shells) and the target ($4d$, $5s$, $5p$ shells). A kinematical analysis of the multiple scattering yields clearly proved the presence of both the triple (P–T–P), and quadruple (P–T–P–T) electron scattering in $C^+ + Xe$ collisions at both impact energies. For illustration, the 150 keV/u $C^+ + Xe$ results for the forward P–T–P scattering contribution are shown in Fig. 7. Both the measured and the calculated cross sections are averaged over an angular region of a forward cone, $0° \leqslant \theta \leqslant 60°$, and compared to each other in Fig. 7a. The strongest deviation between experiment and 1st-Born theory is a wide peak-like enhancement in the experimental data centered at about 1150 eV. It is just the expected mean energy of the P–T–P scattered electrons in the considered forward cone ($\sim 4V$). In contrary to the 1st-Born prediction, the results of the CTMC calculations, which are expected to account for multiple scattering, are in an almost perfect agreement with the experimental data. We note that the total experimental uncertainty for the integrated data of Fig. 7a is typically 30–40%.

For finer details, we enlarged the multiple scattering contributions by removing the strong energy variations of the cross sections in both the experimental and CTMC data. Both data sets have been normalized to the single scattering reference cross sections by dividing them with the 1st-Born results calculated for the target. The ratios are presented in Fig. 7b.

The experimental peak, centered around $4V$, clearly shows that the P–T–P scattering structure is significant. Moreover, experimental and CTMC data exhibit the same structure. It is also seen that the statistics of the CTMC data is poorer than that for the experiment. The slight difference between experiment and theory for the $4V$ peak can be due to the fact that not all the target shells were calculated. The larger CTMC peak at $2V$ probably reflects the approximate character of the classical treatment of potential scattering at lower electron velocities.

In general, multiple scattering yields have strictly followed the expected kinematical patterns in the energy and angular spectra at both projectile energies. This is clearly demonstrated by the contour plot of Fig. 8 [19], where the displayed quantity is the ratio of experiment and the 1st-Born results calculated for the target (see the Exp./1st-Born ratio of Fig. 7b). To visualize the kinematical relations, the data are shown in the normalized velocity space [16] (see also Fig. 4), where all the velocity components are divided by the

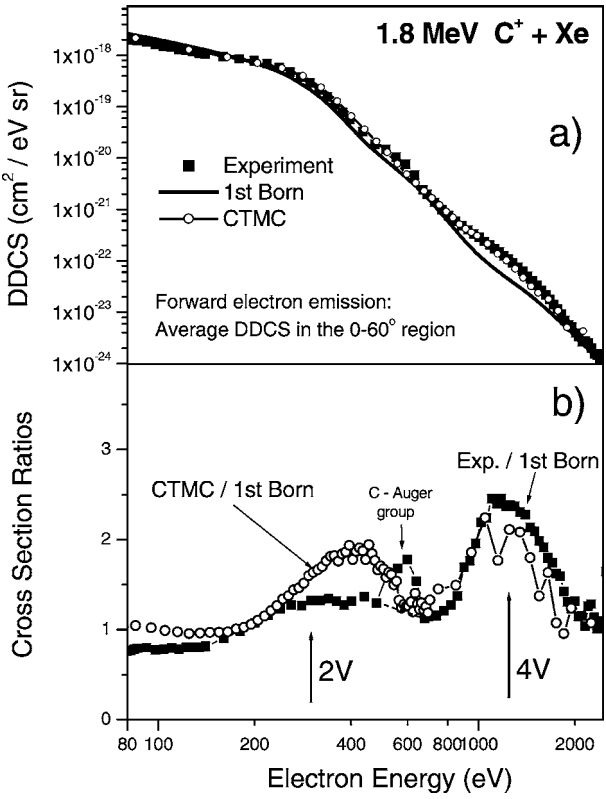

Fig. 7. The signatures of P–T–P scattering in the electron spectra in intermediate velocity 150 keV/u $C^+ + Xe$ collisions [19]: (a) measured and calculated double differential electron emission cross sections averaged over the forward (0°–60°) cone, (b) comparison of the averaged experimental and the CTMC cross sections, both divided by the 1st-Born data.

projectile velocity. Both the P–T–P and the P–T–P–T patterns are clearly seen in the ratio, especially at forward and backward directions, as expected.

From the analysis of the extra yields above the "background" of the 1st-Born results, we extracted the intensities belonging to the consecutive backscattering events in the multiple scattering sequence.

We found that almost 3% of the double scattered P–T electrons (emitted into the 120°–180° backward scattering cone) were scattered in a subsequent P process into the 0°–60° forward scattering cone, forming the P–T–P ridge. Moreover, around 7% of these P–T–P electrons was scattered again backward in the next T process [19]. This increasing fraction of the higher order scattering steps indicates the presence of a trapping mechanism [19]. Since the CTMC calculations provided very similar ratios, we carefully analyzed the few hundred calculated CTMC trajectories with electron energies belonging to the $4V$ peak. Clearly independent scattering events could be identified only in a few cases. The development of the classical electron trajectories was more molecular-like. Nevertheless, following the energy and momentum values for the (classically orbiting) electron as a function of the

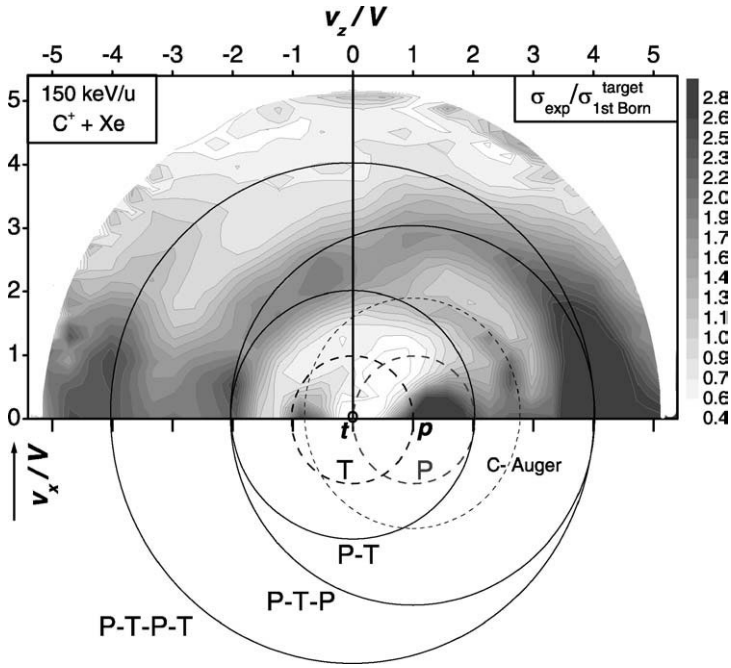

Fig. 8. Contour plot for the ratio of experiment and 1st-Born target ionization theory for 150 keV/u $C^+ + Xe$ collisions. The normalized electron velocity components v_z/V and v_x/V are parallel and perpendicular to the beam direction, respectively. From Ref. [19].

collision time, typical patterns could be identified for triple and quadruple scattering events. For the studied $C^+ + Xe$ collision system, we have got the result that at least 97% of the "CTMC events" belonging to the $4V$ peak in Fig. 7b, were due to (calculated) P–T–P scattering [19]. The 97% was a value "after background subtraction". It corresponded to 70% of all the CTMC electrons emitted in the forward (0°–60°) cone, and in the energy window of 1100–1500 eV.

Later we refined the method, by following the z-coordinate of the moving electron too. In this way now, we are able to identify multiple scattering events safely. The more accurate analysis of the above xenon CTMC data resulted in a value of 80% for the P–T–P events out of 146 CTMC trajectories for the forward cone. The corresponding ratio is 78% (out of 59 trajectories) for the P–T–P–T events in the backward (120°–180°) cone. In summary, we have got the result that the contribution of triple and quadruple scattering was *negligible to the total cross section*, but in the energy region where it appeared, it was the *dominant contribution* to the electron emission. This finding naturally pointed into the direction of lower impact velocities where larger multiple scattering contributions at lower electron energies seem to be likely.

Moreover, in fast single collisions, one cannot expect scattering sequences longer than the P–T–P–T quadruple scattering, with observable intensities. When searching for higher-order scattering sequences, lower projectile velocities seemed to be definitely more advantageous. Low impact energy measurements have been performed at the beamline of an electron cyclotron resonance (ECR) ion source at the IonenStrahlLabor (ISL) of Hahn–

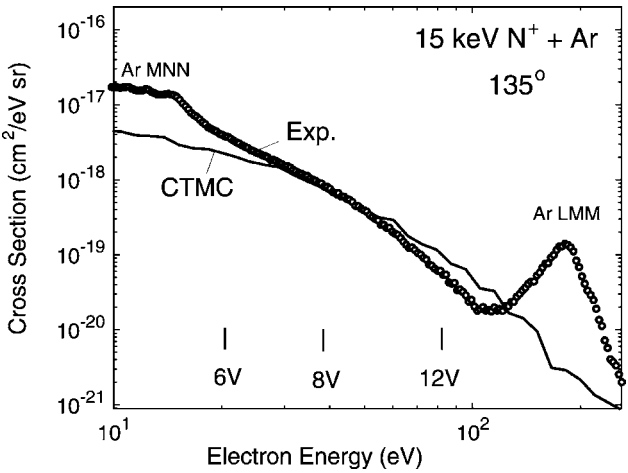

Fig. 9. Doubly differential cross section for electron emission at 135° observation angle in 15 keV $N^+ + Ar$ collisions. Line: CTMC calculations for the L and M shells of argon and the L shell of nitrogen. Circles: Experiment [43] normalized to theory at 40 eV. Multiples of the projectile velocity are indicated. From Ref. [78].

Meitner Institute Berlin, where Ar gas targets have been bombarded by few-tens-of-keV low charge state light ions [20]. Considerable yields of emitted electrons have been measured up to few hundred eV energies. A typical spectrum is shown in Fig. 9 for the collisions of singly charged 15 keV N^+ ions with Ar atoms.

The advantage of single charged ion impact in slow collisions lies in the fact that no projectile excited states are produced by double or multiple electron transfer processes. Practically, only target Auger lines disturb the continuous spectra of the emitted electrons, which are significantly simpler than those produced by the impact of doubly charged ions. In the studied $N^+ + Ar$ collisions, a forward–backward enhancement in the normalized spectra was found in the energy range belonging to the $6V$–$14V$ electron velocity range (not shown). This was an indication for the existence of longer (6–14) multiple scattering sequences.

The spectrum of the electrons emitted at 135° observation angle is shown in Fig. 9. Auger structures, like the Ar LMM Auger group centered around 180 eV, and the Ar MNN group below 16 eV are clearly seen in the spectrum. It is interesting to note that the 135° spectrum is almost identical with the 90° spectrum everywhere, except in the 20–120 eV (6–14V) energy range, where it shows a definite ($\sim 20\%$) enhancement compared to the 90° data [20]. Since no structure appeared in this energy range, we considered this fact as an indication for overlapping multiple scattering (nV) contributions.

For understanding this low energy collision system, we performed CTMC calculations for both projectile and target ionization. Since our measured electron emission cross sections are not absolute, only the relative energy and angular dependence of the calculated and measured data could be studied. Accordingly, the experimental data shown in Fig. 9, are normalized to the CTMC theory at 40 eV.

Our CTMC calculations [78] reproduced quite well the main features of the experimental spectra [43]. The observed forward–backward enhancement and their asymmetry were

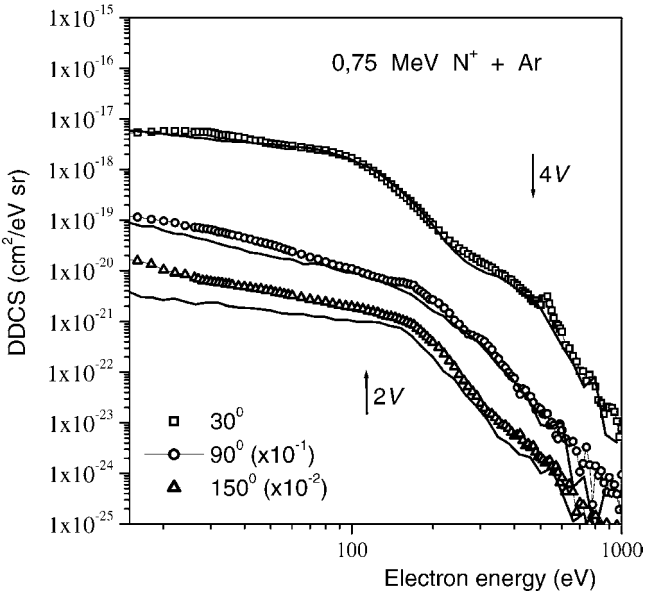

Fig. 10. Double differential cross section for electron emission at 30°, 90° and 150° in 750 keV $N^+ + Ar$ collisions as a function of the ejected electron energy [79,80]. Symbols: Experimental data, lines: CTMC results for the ionization of the target.

correctly accounted for (not shown). However, the energy dependence of the spectra was only qualitatively reproduced, as seen in Fig. 9. The CTMC results seem to overestimate the high energy tail of the electron spectra. The really striking feature of the CTMC calculations, however, is that they literally show the same number of turns in the multiple scattering sequences as predicted by the multiples of the projectile velocity, indicated in Fig. 9 (e.g., $8V$ corresponds to a P–T–P–T–P–T–P–T scattering!), at least up to 100 eV. Moreover, almost all CTMC electron emission "events" above 10 eV fall into the multiple scattering category. If true, this means that accelerating multiple scattering can dominate electron emission at low ion impact energies. We are going to perform absolute cross section measurements to verify this strange theoretical expectation in this low impact energy range.

We also performed CTMC calculations for the cross section ratios of the collision systems of Ref. [22] (50–400 keV $O^+ + Ar$), and found convincing agreement with them. It became clear that this somewhat higher impact energy region (5–50 keV/u) is ideal in the sense that one might expect distinct structures and large multiple scattering yields in the same collision. Therefore, we performed a set of experiments with different collision systems in this energy region (50–100 keV/u N^+ and N_2^+ ions on N_2, Ne and Ar targets) at the beam-line of the 5 MV Van de Graaff accelerator in ATOMKI, Debrecen by using the same experimental setup as for Ref. [19]. We determined absolute cross sections, and, for most of the collision systems, CTMC calculations have been accomplished for target ionization.

At this point, the surprise was that experiment and CTMC provided a quantitative agreement at forward angles. This is clearly seen in Fig. 10, for a typical collision system. One

can find significant differences between experiment and target ionization theory only at low electron energies and backward angles. We expect that future calculations for the projectile ionization contribution will remove these discrepancies.

A random sampling based analysis of the CTMC trajectories has shown that more than 60% of the analyzed events belonged to P–T–P, P–T–P–T or higher order scattering events above 250 eV electron energy [80]. This corresponds to cca. 4.5% of the total electron emission [80]. We note that if P–T scattering is included, the above 60% ratio becomes higher it is >80% of (CTMC) electrons above 200 eV are emitted in multiple scattering.

Though this is still below 10% of the total electron emission cross section, we recall that this contribution can play an important role in the fragmentation of molecules, e.g., in the case of ion impact in biological tissues. It is also worth noting that the above two sets of experiments ([20] and [79,80]) indicate that in slow collisions Fermi-acceleration may even dominate the total electron emission. More experimental efforts and alternative theoretical attempts are needed to clarify the role of different electron emission mechanisms in slow ion–atom and ion–molecule collisions.

6. CONCLUSIONS AND OUTLOOK

In the present work, we considered the role of secondary electrons in the fragmentation of molecules, and in radiation damages of biological tissues. Special emphasis was taken to the importance of fast electrons. Most of the work is devoted to the analysis of a specific electron emission mechanism, namely the ionization by Fermi-shuttle type accelerating multiple scattering. A brief overview of the experimental findings and theoretical methods connected to Fermi-shuttle type acceleration of the ejected electrons in atomic collisions has been provided. It was found that accelerating multiple scattering of the ejected electrons has a practical importance in the interaction of ions stopped in condensed matter or liquid. However, for finding clear evidence for the process, and studying it quantitatively, ion-atom collision experiments under single-collision conditions had to be performed.

In our first ion–gas collision studies, we have found evidence for double (P–T), triple (P–T–P) and quadruple (P–T–P–T) electron scattering sequences between the projectile and the target in single collisions of ions with atoms, in the impact velocity range of 2.5–3 au. In more recent measurements, we have got a strong indication that longer, 6–12-fold scattering sequences are present at lower (0.3–1 au) projectile velocities. Finally, we found an intermediate velocity range (1.5–1.8 au), where the identification of the different scattering sequences by their kinematical patterns is straightforward, where theory and experiments show a quantitative agreement, and the contribution of the Fermi-shuttle mechanism is important.

On the basis of the above results, we continue searching for large yields of Fermi-accelerated high energy electrons. Such findings may attract both fundamental and practical interest. In recent collision studies, Fermi-acceleration process is more and more considered as possible explanation of unexpectedly large yields of high energy electrons [81–84], even in high impact energy, 6–10 MeV/u $He^{2+} + H_2O$ collisions [81,82]. A systematic study has been performed by Rothard and coworkers [85] to find empirical scaling rules for this process in fast ion-solid collisions. In the 14–95 MeV/u impact energy range, they found that the yield of the Fermi shuttle accelerated electrons emitted from solids is proportional to $Z_p^2 Z_T^2 / V^3$ in a good approximation [85]. Accelerating multiple scattering

has been recently considered as a possible explanation of small, but observable oscillating structures in slow collisions of He ions with He atoms [86]. Finally, it has also been shown recently, that the reflection of electrons by atomic cores may play a significant role even if the accelerating force is completely independent, e.g., a periodic force provided by electromagnetic radiation [87]. Atoms of a large cluster may play ping-pong games with the photo-ionized electrons, and a fraction of those games can be more or less synchronized with the frequency of the laser radiation. This way, some electrons can be accelerated up to a few keV kinetic energy, and induce energetic X-ray emission from the clusters. Atomic cores seem to play essential role in trapping electrons, and participate in "strange" accelerating effects. In such effects, a few electrons can gain unexpectedly high energies, similarly to those small water droplets, which fly up to the ceiling in the commonly known phenomenon of splashing.

ACKNOWLEDGEMENTS

We are indebted to all our coworkers in studying multiple electron scattering phenomena, especially Dénes Berényi for initiating these studies, and Nico Stolterfoht for the efficient collaboration and many enlightening discussions. We thank to László Sarkadi and Ákos Kövér for the critical reading of the manuscript. We acknowledge support from the Hungarian Scientific Research Fund (OTKA, Grant No. T046905). In part, this work was also supported by the COST P9 Action of the European Union ("Radiation Damage in Biomolecular Systems"), and by the grant "Bolyai" from the Hungarian Academy of Sciences.

REFERENCES

[1] M.E. Rudd, J.H. Macek, *Case Stud. At. Phys.* **3** (1976) 47–136.
[2] R.A. Baragiola (Ed.), *Ionization of Solids by Heavy Particles*, *NATO ASI Series B: Physics*, vol. 306, Plenum, New York, 1993.
[3] N. Stolterfoht, R.D. DuBois, R.D. Rivarola, *Electron Emission in Heavy Ion–Atom Collisions*, Springer, Berlin, 1997.
[4] H. Rothard, *Nucl. Instrum. Methods B* **146** (1998) 1.
[5] Z. Deng, I. Bald, E. Illenberger, M.A. Huels, *Phys. Rev. Lett.* **95** (2005) 153201.
[6] R.A. Baragiola, C.L. Atteberry, C.A. Dukes, M. Fama, B.D. Teolis, *Nucl. Instrum. Methods B* **193** (2002) 720.
[7] P. Sobocinski, Z.D. Pesic, R. Hellhammer, N. Stolterfoht, B. Sulik, S. Legendre, J.-Y. Chesnel, *J. Phys. B* **38** (2006) 1.
[8] Z.D. Pesic, J.-Y. Chesnel, R. Hellhammer, B. Sulik, N. Stolterfoht, *J. Phys. B* **37** (2004) 1405.
[9] G. Kraft, M. Krämer, *Adv. Radiat. Biol.* **17** (1993) 1.
[10] M. Scholz, G. Kraft, *Radiat. Prot. Dosimet.* **52** (1994) 29.
[11] G.P. Collins, *Sci. Am.* **289** (3) (2003) 26.
[12] B. Boudaïffa, P. Cloutier, D. Hunting, M.A. Huels, L. Sanche, *Science* **287** (2000) 1658.
[13] H. Abdoul-Carime, S. Gohlke, E. Illenberger, *Phys. Rev. Lett.* **92** (2004) 168103.
[14] W. Friedland, P. Jacob, H.G. Paretzke, T. Stork, *Radiat. Res.* **150** (1998) 170.
[15] S.W.J. Scully, V. Senthil, J.A. Wyer, E.C. Montenegro, M.B. Shah, in: F.D. Colavecchia *et al.* (Eds.), *Abstracts of Contributed Papers*, in: *ICPEAC 2005, 24th International Conference on Photonic Electronic and Atomic Collisions Rosario*, Argentina, 20–26 July, 2005, p. 324.
[16] S. Suarez, R.O. Barrachina, W. Meckbach, *Phys. Rev. Lett.* **77** (1996) 474.
[17] U. Bechthold, S. Hagmann, J. Ullrich, B. Bathelt, A. Bohris, R. Moshammer, U. Ramm, C. Bhalla, G. Kraft, H. Schmidt-Böcking, *Phys. Rev. Lett.* **79** (1997) 2034.

[18] G. Lanzanò, E. De Filippo, D. Mahboub, H. Rothard, S. Aiello, A. Anzalone, S. Cavallaro, A. Elanique, E. Geraci, M. Geraci, F. Giustolisi, A. Pagano, G. Politi, *Phys. Rev. Lett.* **83** (1999) 4518.
[19] B. Sulik, Cs. Koncz, K. Tőkési, A. Orbán, D. Berényi, *Phys. Rev. Lett.* **88** (2002) 073201.
[20] B. Sulik, N. Stolterfoht, R. Hellhammer, Z. Pesic, Cs. Koncz, K. Tőkési, D. Berényi, *Nucl. Instrum. Methods B* **212** (2003) 32.
[21] D.H. Lee, P. Richard, T.J.M. Zouros, J.M. Sanders, J.L. Shinpaugh, H. Hidmi, *Phys. Rev. A* **41** (1990) 4816.
[22] N. Stolterfoht, D. Schneider, *IEEE Trans. Nucl. Sci.* **26** (1979) 1130.
[23] Y. Yamazaki, K. Komaki, T. Azuma, K. Kuroki, K. Kawatsura, Y. Kanai, T. Kambara, M. Ohura, Y. Awaya, *RIKEN Accel. Prog. Rep.* **24** (1990) 54;
Y. Yamazaki, K. Komaki, T. Azuma, K. Kuroki, K. Kawatsura, Y. Kanai, T. Kambara, M. Ohura, Y. Awaya, *RIKEN Accel. Prog. Rep.* **26** (1992) 66.
[24] R.A. Baragiola, E.V. Alonso, A. Oliva, A. Bonnano, F. Xu, *Phys. Rev. A* **45** (1992) 5286.
[25] H. Rothard, D.H. Jakubassa-Amundsen, A. Billebaud, *J. Phys. B* **31** (1998) 1563.
[26] D.H. Jakubassa-Amundsen, H. Rothard, *Phys. Rev. A* **60** (1999) 385.
[27] H. Rothard, G. Lanzano, D.H. Jakubassa-Amundsen, E. De Filippo, D. Mahoub, *J. Phys. B* **34** (2001) 3261.
[28] G. Lanzanò, E. De Filippo, S. Aiello, M. Geraci, A. Pagano, S. Cavallaro, F. Lo Piano, E.C. Pollacco, C. Volant, S. Vuillier, *et al.*, *Phys. Rev. A* **58** (1998) 3634.
[29] G. Lanzanò, E. De Filippo, D. Mahboub, H. Rothard, S. Aiello, A. Anzalone, S. Cavallaro, A. Elanique, E. Geraci, M. Geraci, F. Giustolisi, A. Pagano, G. Politi, *Phys. Rev. A* **63** (2001) 032702.
[30] G. Lanzanò, A. Anzalone, N. Arena, E. De Filippo, M. Geraci, D.F. Giustolisi, A. Pagano, H. Rothard, C. Volant, *Nucl. Instrum. Methods B* **209** (2003) 212.
[31] E. Fermi, *Phys. Rev.* **75** (1949) 1169.
[32] M. Hautala, Z. Pan, P. Sigmund, *Phys. Rev. A* **44** (1991) 7428.
[33] J. Burgdörfer, J. Wang, R.H. Ritchie, *Phys. Scr.* **44** (1991) 391.
[34] J. Wang, J. Burgdörfer, A. Bárány, *Phys. Rev. A* **43** (1991) 4036.
[35] P. Sigmund, in: R.A. Baragiola (Ed.), *Ionization of Solids by Heavy Particles*, *NATO ASI Series B: Physics*, vol. 306, Plenum, New York, 1993, p. 59.
[36] M.M. Jakas, *Phys. Rev. A* **52** (1995) 866.
[37] M.M. Jakas, *Nucl. Instrum. Methods B* **111** (1996) 255.
[38] D. Schneider, G. Schiwietz, D. DeWitt, *Phys. Rev. A* **47** (1993) 3945.
[39] B.B. DePaola, Y. Kanai, P. Richard, Y. Nakai, T. Kambara, T.M. Kojima, Y. Awaya, *J. Phys. B* **28** (1995) 4283.
[40] K. Kimura, T. Kishi, M. Mannami, *Nucl. Instrum. Methods B* **90** (1994) 282.
[41] S. Suarez, R.O. Barrachina, A.D. Gonzalez, W. Meckbach, *Nucl. Instrum. Methods B* **124** (1997) 358.
[42] C.O. Reinhold, D.R. Schulz, U. Bechtold, G. Kraft, S. Hagmann, H. Schmidt-Böcking, *Phys. Rev. A* **58** (1998) 2671.
[43] B. Sulik, Cs. Konc, K. Tőkési, Á. Kövér, S. Ricz, Gy. Víkor, J.-Y. Chesnel, N. Stolterfoht, D. Berényi, *Nucl. Instrum. Methods B* **154** (1999) 281.
[44] B. Sulik, Á. Kövér, S. Ricz, Cs. Konc, K. Tőkési, Gy. Víkor, J.-Y. Chesnel, N. Stolterfoht, D. Berényi, *Phys. Scr. T* **80** (1999) 338.
[45] B. Sulik, K. Tőkési, Cs. Konc, Á. Kövér, S. Ricz, A. Orbán, N. Stolterfoht, J.-Y. Chesnel, D. Berényi, *Phys. Scr. T* **92** (2001) 463.
[46] B. Sulik, Cs. Konc, K. Tőkési, A. Orbán, Á. Kövér, S. Ricz, N. Stolterfoht, R. Hellhammer, J.-Y. Chesnel, P. Richard, H. Tawara, H. Aliabadi, D. Berényi, Multiple electron scattering in ion–atom collisions: Fermi-shuttle acceleration in ionization, *AIP Conf. Proc.* **652** (2003) 195.
[47] R.J. Beuhler, G. Friedlander, L. Friedman, *Phys. Rev. Lett.* **53** (1989) 1292.
[48] J. Wang, C.O. Reinhold, J. Burgdörfer, *Phys. Rev. A* **44** (1991) 7243.
[49] P. Richard, D.H. Lee, T.J.M. Zouros, J.M. Sanders, J.L. Sinpaugh, *J. Phys. B* **23** (1990) L213.
[50] C.O. Reinhold, D.R. Schulz, R.E. Olson, C. Kelbch, R. Koch, H. Schmidt-Böcking, *Phys. Rev. Lett.* **66** (1991) 1842.
[51] H.I. Hidmi, P. Richard, J.M. Sanders, H. Schöne, J.P. Giese, D.H. Lee, T.J.M. Zouros, S.L. Varghese, *Phys. Rev. A* **48** (1993) 4421.
[52] T.J.M. Zouros, K.L. Wong, S. Grabbe, H.I. Hidmi, P. Richard, E.C. Montenegro, J.M. Sanders, C. Liao, S. Hagmann, C.P. Bhalla, *Phys. Rev. A* **53** (1996) 2272.
[53] Á. Kövér, D. Varga, Gy. Szabó, D. Berényi, I. Kádár, S. Ricz, G. Hock, *J. Phys. B* **16** (1983) 1017.
[54] Á. Kövér, Gy. Szabó, L. Gulyás, K. Tőkési, D. Berényi, O. Heil, K.O. Groeneveld, *J. Phys. B* **21** (1988) 3231.

[55] M. Kuzel, *et al.*, *Phys. Rev. Lett.* **71** (1993) 2879.
[56] M. Kuzel, R.D. DuBois, R. Maier, O. Heil, D.H. Jakubassa-Amundsen, M.W. Lucas, K.O. Groeneveld, *J. Phys. B* **27** (1994) 1993.
[57] S.Yu. Ovchinnikov, J.H. Macek, *Phys. Rev. Lett.* **75** (1995) 2474.
[58] S.Yu. Ovchinnikov, J.H. Macek, *Nucl. Instrum. Methods B* **154** (1999) 41.
[59] Cs. Koncz, B. Sulik, *J. Phys. B* **32** (1999) 5009.
[60] Cs. Koncz, *J. Phys. B* **34** (2001) 3879.
[61] D.C. Ionescu, A. Belkacem, *Eur. Phys. J. D* **18** (2002) 301.
[62] R. Abrines, I.C. Percival, *Proc. Phys. Soc. (London)* **88** (1966) 861.
[63] R.E. Olson, A. Salop, *Phys. Rev. A* **16** (1977) 531.
[64] K. Tőkési, G. Hock, *Nucl. Instrum. Methods Phys. Res. B* **86** (1994) 201.
[65] K. Tőkési, G. Hock, *J. Phys. B* **29** (1996) 119.
[66] C.O. Reinhold, J. Burgdörfer, *Phys. Rev. A* **55** (1997) 450.
[67] C.O. Reinhold, J. Burgdörfer, *J. Phys. B* **26** (1993) 3101.
[68] J.S. Cohen, *Phys. Rev. A* **51** (1995) 266.
[69] R.A. Sparrow, R.E. Olson, D. Schneider, *J. Phys. B* **28** (1995) 3427.
[70] K. Tőkési, Á. Kövér, *Nucl. Instrum. Methods Phys. Res. B* **154** (1999) 259.
[71] K. Tőkési, Á. Kövér, *J. Phys. B* **33** (2000) 3067–3077.
[72] A.E.S. Green, *Adv. Quantum Chem.* **7** (1973) 221.
[73] R.H. Garvey, C.H. Jackman, A.E.S. Green, *Phys. Rev. A* **12** (1975) 1144.
[74] C.O. Reinhold, C.A. Falcon, *Phys. Rev. A* **33** (1986) 3859.
[75] R.L. Becker, A.D. MacKellar, *J. Phys. B* **17** (1984) 3923.
[76] K. Tőkési, T. Mukoyama, *Bull. Inst. Chem. Res. Kyoto Univ.* **72** (1994) 62.
[77] D. Varga, I. Kádár, S. Ricz, J. Végh, Á. Kövér, B. Sulik, D. Berényi, *Nucl. Instrum. Methods A* **313** (1992) 163.
[78] K. Tőkési, B. Sulik, N. Stolterfoht, *Nucl. Instrum. Methods B* **233** (2005) 187.
[79] T. Ricsóka, Gy. Víkor, Sz. Nagy, K. Tőkési, Z. Berényi, B. Paripás, N. Stolterfoht, B. Sulik, *Nucl. Instrum. Methods B.* **235** (2005) 397.
[80] B. Sulik, K. Tőkési, N. Stolterfoht, T. Ricsóka, Gy. Víkor, Sz. Nagy, Z. Berényi, R. Hellhammer, Z. Pesic, D. Berényi, *Radiat. Phys. Chem.* (2006), in press.
[81] D. Oshawa, Y. Sato, Y. Okada, V.P. Shevelko, F. Soga, *Phys. Lett. A* **342** (2005) 168.
[82] D. Oshawa, Y. Sato, Y. Okada, V.P. Shevelko, F. Soga, *Phys. Rev. A* **72** (2005) 062710.
[83] H. Rothard, *Nucl. Instrum. Methods B* **225** (2004) 27.
[84] G. Lanzano, E. De Filippo, H. Rothard, C. Volant, A. Anzalone, N. Arena, M. Geraci, F. Giustolisi, A. Pagano, *Nucl. Instrum. Methods B* **233** (2005) 31.
[85] H. Rothard, G. Lanzano, E. De Filippo, C. Volant, *Nucl. Instrum. Methods B* **230** (2005) 419.
[86] F. Frémont, A. Hajaji, A. Naja, C. Leclercq, J. Soret, J.A. Tanis, B. Sulik, J.-Y. Chesnel, *Phys. Rev. A* **72** (2005) 050704.
[87] C. Deiss, N. Rohringer, J. Burgdörfer, E. Lamour, C. Prigent, J.P. Rozet, D. Vernhet, *Phys. Rev. Lett.* **96** (2006) 013203.

Total Electron Stopping Powers and CSDA-Ranges from 20 eV to 10 MeV Electron Energies for Components of DNA and RNA

A. Akar[1], H. Gümüş[1] and N.T. Okumuşoğlu[2]

[1] *Department of Physics, Faculty of Arts and Sciences, Ondokuz Mayıs University, Samsun 55139, Turkey*
[2] *Department of Physics, Rize Faculty of Arts and Sciences, Karadeniz Technical University, Rize 53100, Turkey*

Abstract

An appropriate formula for the total stopping power of electrons of initial kinetic energy from 20 eV to 10 MeV in some biological materials is presented. The continuous slowing down approximation-range (CSDA-range) from the total stopping power is also made. The collisional stopping power formula is evaluated using Generalized Oscillator Strength (GOS) model and exchange correction on the inelastic differential cross section (IDCS) given by [M. Inokuti, *Rev. Mod. Phys.* **43** (1971) 297–347] and the radiative stopping power formula is calculated from the bremsstrahlung differential cross section (DCS) given by [H.W. Koch, J.W. Motz, *Rev. Mod. Phys.* **31** (4) (1959) 920–955]. Calculation of the total stopping powers (SPs) and CSDA-range for biological compounds: $C_5H_5N_5$ (adenine), $C_5H_5N_5O$ (guanine), $C_4H_5N_3O$ (cytosine), $C_5H_6N_2O_2$ (thymine), $C_4H_4N_2O_2$ (uracil), C_4H_8O (tetrahydrofuran), $C_4H_8O_2$ (3-hydroxytetrahydrofuran), $C_5H_{10}O_2$ (α-tetrahydrofurfuryl alcohol), H_3PO_4 (phosphoric acid), $C_{19}H_{26}N_8O_{13}P_2$ (thymine–adenine–DNA) have been introduced for incident electrons in the 20 eV–10 MeV energy range. The calculated results have been compared with experimental data, PENELOPE program results and other theoretical results. The calculated results of total stopping power and CSDA-ranges for electrons in energy range from 20 eV to 10 MeV are found to be in good agreement to within 8% with available data.

Contents

1. INTRODUCTION

It is important to understand the effects on biological materials of charged particles for some medicine fields such as nuclear medicine, radiation dosimetry and radiotherapy. The total stopping power for electrons can be given as a combination of the collision and radiative types of interactions. Collision energy losses include losses due to ionization and excitation of the atoms and radiative losses contain to bremsstrahlung emission. The Inelastic Differential Cross Section (IDCS) for collision losses is calculated from the generalized oscillator strength model defined by the electronic configuration, ionization energies of the various electron shells of the target atoms and the mean excitation energy, I. Radiative losses are described on the basis of the Bethe–Heitler approximation.

ADVANCES IN QUANTUM CHEMISTRY, VOLUME 52
ISSN: 0065-3276 DOI: 10.1016/S0065-3276(06)52012-X

When radiation passes through tissue, a proportion of the energy is absorbed, leading to the formation of radicals that can cause damage to a variety of cell processes, and in particular to DNA (deoxyribonucleic acid) and RNA (ribonucleic acid). Radiation can therefore lead to a whole spectrum of DNA damage, ranging from chromosome breaks and translocations to point mutations. If the damage is sufficiently severe, it can cause cell death through interference with the cell—this usually requires a dose of several hundred gray. With smaller doses, those cells that die do so in mitosis or just afterward, either at the first mitosis or, with lower doses, after the second or occasionally the third mitosis. Thus, understanding of some of the mechanisms by which radiation induces changes in DNA, RNA and living cells and the consequences of those changes is important to all who use radiation or study its effects.

In recent years, as mentioned above, because of the importance of knowledge of the energy loss of electrons, in Ref. [3] calculated inelastic stopping power, the inelastic mean free path and the CSDA-range in DNA (thymine–adenine or cytosine–guanine) for low and intermediate energy ranges. These calculations were also studied for liquid water, guanine and organic molecules in the energy range 20 eV to 10 keV [4,5]. In addition [6] calculated cross sections for electron scattering from components of DNA and RNA. Till now only few total stopping power and CSDA-range for electron interaction, including low and intermediate energy electrons with DNA and RNA bases can be found in the literature. Recently, we have presented the collision stopping power, the inelastic mean free path and the CSDA-range for electron collision from DNA bases (adenine, guanine, thymine and cytosine) with Generalized Oscillator Strength (GOS) model [7,8].

The aim of the present study, considering the bremsstrahlung stopping power for electron energies above 300 keV, is to calculate the total stopping power and the CSDA-range for electron scattering from molecules, which are similar to those found in the backbone of DNA and RNA. The SPs and CSDA ranges for ten important biological compounds $C_5H_5N_5$ (adenine), $C_5H_5N_5O$ (guanine), $C_4H_5N_3O$ (cytosine), $C_5H_6N_2O_2$ (thymine), $C_4H_4N_2O_2$ (uracil), C_4H_8O (tetrahydrofuran), $C_4H_8O_2$ (3-hydroxytetrahydrofuran), $C_5H_{10}O_2$ (α-tetrahydrofurfuryl alcohol), H_3PO_4 (phosphoric acid), $C_{19}H_{26}N_8O_{13}P_2$ (thymine–adenine–DNA) have been calculated.

2. THEORY

The theoretical approachs applied for the collision stopping power and CSDA-range in the present work are the same as those used in our previous calculation. Thus, a short description of the methods and procedures for the collision stopping power is given. In addition, the bremsstrahlung stopping power has been described below paragraphs.

Consider an electrons having mass m and charge $-e$, moving with velocity v. The Inelastic Differential Cross Section (IDCS) obtained from the first Born approximation is given by [1] as

$$\frac{d^2\sigma}{dQ\,dW} = \chi \frac{1}{WQ} \frac{df(Q,W)}{dW}, \tag{1}$$

where $\chi = 2\pi e^4/mc^2\beta^2$, W is energy loss and Q is the recoil energy given as

$$Q = q^2/2m = 2E - W - 2\sqrt{E(E-W)}\cos\theta. \tag{2}$$

Here E is the kinetic energy of incident particle. The IDCS can be written as follows [9]:

$$\sigma^n = \int_0^{W_{\max}} dW\, W^n \int_{Q_-}^{Q_+} dQ \frac{d^2\sigma}{dQ\, dW}. \tag{3}$$

The kinematically allowed recoil energies lie in the interval $Q_- < Q < Q_+$. Recoil energy, Q_-, is given in [10] as mentioned in [11] as follows:

$$Q_-(E, W) = \sqrt{\frac{W^2}{\beta^2} + \left(mc^2\right)^2} - mc^2. \tag{4}$$

The inelastic stopping power S_{in} is giving as follows:

$$S_{\text{in}} = N\sigma^{(1)}, \tag{5}$$

where $\sigma^{(1)}$ is the stopping cross section. The function $\frac{df(Q,W)}{dW}$ is the GOS. The GOS satisfies the Bethe sum rule [1]:

$$\frac{1}{Z}\int_0^{\infty} \frac{df(Q, W)}{dW} dW = 1 \quad \text{or} \quad \sum_{i=1}^{M} f_i = Z, \tag{6}$$

where Z is the number of electrons per atom or molecule. The GOS, also known as the Bethe surface, is given in [12] as

$$\frac{df(Q, W)}{dW} \equiv \sum_{i=1}^{M} f_i F(W_i; Q, W), \tag{7}$$

where M, f_i and W_i are the number of shells, oscillator strengths for the ith shell of the target atom and ith shell resonance energies, respectively. Each oscillator may be considered as the total spectrum of excitations of electrons belonging to a shell. The excitation spectrum $F(W_i; Q, W)$ has been suggested in [12] to be written as

$$F(W_i; Q, W) = \delta(W - W_i)\theta(W_i - Q) + \delta(W - Q)\theta(Q - W_i), \tag{8}$$

where $\delta(x)$ is the Dirac delta function and $\theta(x)$ is a step function ($\theta(x) = 0$ if $x < 0$ and $\theta(x) = 1$ if $x \geqslant 0$).

The bremsstrahlung DCS, known as the Bethe–Heitler approximation, without screening correction and found using the relativistic Born approximation for radiative losses are given in [2] as

$$d\sigma_k = \frac{4Z^2 r_0^2}{137}\frac{dk}{k}\left[1 + \left(\frac{E}{E_0}\right)^2 - \frac{2}{3}\frac{E}{E_0}\right]\left[\ln\left(\frac{2E_0 E}{k}\right) - \frac{1}{2}\right], \tag{9}$$

where k, E_0 and E are energy of the emitted photon, initial and final total energy of the electron in a collision in m_0c^2, respectively.

$$S_{\text{brem}} = N\int_{k_{\min}}^{k_{\max}} k\frac{d\sigma}{dk} dk, \tag{10}$$

where k, energy of the emitted photon, takes between 0 and E_0 energy values. The total stopping power is given with following expressions:

$$S(E) = S_{\text{in}}(E) + S_{\text{brem}}, \tag{11}$$

where S_{brem} is the bremsstrahlung stopping power. The total stopping powers of compounds are calculated from Bragg's addition rule [13] as follows,

$$\frac{S(E)}{\rho}(\text{compound}) = w_1\left[\frac{S(E)}{\rho}\right]_1 + w_2\left[\frac{S(E)}{\rho}\right]_2 + \cdots = \sum_i w_i\left[\frac{S(E)}{\rho}\right]_i, \tag{12}$$

where $w_1, w_2, \ldots$ are the atomic fractions of elements (1), (2), ... and so on.

The CSDA-range is given with following expression

$$R(E) = \int_T^0 \big(S(E)\big)^{-1}\, dE. \tag{13}$$

The CSDA-ranges of compounds are evaluated from trapezoidal rule using the stopping powers calculated through Bragg's sum rule

$$R_{\text{compound}}(E) = \int_T^0 \big(S_{\text{compound}}(E)\big)^{-1}\, dE. \tag{14}$$

3. CALCULATED RESULTS AND DISCUSSION

The calculated total SPs and the CSDA-ranges for $C_5H_5N_5$ (adenine), $C_5H_5N_5O$ (guanine), $C_4H_5N_3O$ (cytosine), $C_5H_6N_2O_2$ (thymine), $C_4H_4N_2O_2$ (uracil), C_4H_8O (tetrahydrofuran), $C_4H_8O_2$ (3-hydroxytetrahydrofuran), $C_5H_{10}O_2$ (α-tetrahydrofurfuryl alcohol), H_3PO_4 (phosphoric acid), $C_{19}H_{26}N_8O_{13}P_2$ (thymine–adenine–DNA) are given Tables 1 and 2 and Figs. 1–4.

Figure 1 shows the total stopping power in guanine for the energy range 20–10 MeV. The total SP results obtained from this study have been compared with the Monte Carlo

Table 1. SPs (MeV cm^2/g) for 1—$C_5H_5N_5$ (adenine), 2—$C_5H_5N_5O$ (guanine), 3—$C_4H_5N_3O$ (cytosine), 4—$C_5H_6N_2O_2$ (thymine), 5—$C_4H_4N_2O_2$ (uracil), 6—$C_{19}H_{26}N_8O_{13}P_2$ (thymine–adenine), 7—C_4H_8O (tetrahydrofuran), 8—$C_4H_8O_2$ (3-hydroxytetrahydrofuran), 9—$C_5H_{10}O_2$ (α-tetrahydrofurfuryl alcohol), 10—H_3PO_4 (phosphoric acid)

E (eV)	1	2	3	4	5	6	7	8	9	10
20	34.789	31.104	42.318	44.739	33.557	39.929	104.33	85.364	92.071	28.781
30	60.358	53.965	73.421	77.621	58.222	69.277	181.01	148.10	159.74	49.934
40	166.79	149.14	178.65	193.10	160.88	175.24	350.86	287.10	309.63	99.071
50	309.02	276.30	290.02	273.81	244.23	237.54	397.56	325.33	350.85	108.81
60	346.99	327.98	344.59	340.57	316.64	311.61	451.66	400.01	418.27	220.82
70	364.78	347.95	363.46	359.96	338.10	331.37	462.42	415.78	432.27	245.21
80	371.23	356.29	370.83	367.83	347.79	340.03	462.68	420.39	435.34	258.79
90	371.18	357.82	371.51	368.96	350.47	342.10	457.18	418.59	432.24	265.57
100	367.38	355.35	368.28	366.12	348.97	340.24	448.58	413.15	425.68	268.04
200	292.99	287.24	295.74	295.26	285.18	276.94	346.04	326.51	333.43	230.87
300	237.24	233.56	240.01	239.97	232.68	227.02	277.44	263.79	268.63	195.60

(*continued on next page*)

Table 1. (*continued*)

E (eV)	1	2	3	4	5	6	7	8	9	10
400	199.98	197.30	202.55	202.66	196.90	193.17	232.69	222.12	225.87	170.55
500	173.57	171.47	175.93	176.11	171.32	168.74	201.32	192.66	195.73	151.42
600	153.86	152.13	156.03	156.24	152.11	150.27	178.06	170.69	173.30	136.43
700	138.54	137.08	140.55	140.77	137.14	135.79	160.07	153.64	155.92	124.38
800	128.31	126.83	130.12	130.55	127.08	125.85	148.76	142.50	144.72	114.47
900	118.63	117.48	120.61	121.30	118.17	117.23	138.06	132.54	134.50	107.52
1E3	111.76	110.63	113.37	113.76	110.	109.94	128.78	123.73	125.52	100.84
2E3	70.023	69.425	70.983	71.255	69.677	69.146	79.694	76.905	77.894	64.174
3E3	52.330	51.919	53.028	53.232	52.119	51.738	59.213	57.253	57.948	48.235
4E3	42.293	41.978	42.847	43.011	42.142	41.841	47.686.	46.162	46.703	39.109
5E3	35.745	35.489	36.209	36.348	35.632	35.406	40.209	38.956	39.401	33.213
6E3	31.108	30.892	31.508	31.629	31.017	30.834	34.932	33.863	34.243	28.988
7E3	27.634	27.446	27.987	28.094	27.558	27.406	30.988	30.054	30.385	25.810
8E3	24.925	24.759	25.242	25.338	24.861	24.732	27.918	27.088	27.383	23.327
9E3	22.752	22.603	23.040	23.128	22.697	22.584	25.461	24.712	24.978	21.327
1E4	20.964	20.829	21.228	21.309	20.916	20.816	23.441	22.757	23.000	19.675
2E4	12.215	12.143	12.365	12.412	12.195	12.152	13.597	13.221	13.354	11.556
3E4	8.9383	8.8874	9.0475	9.0819	8.9262	8.9007	9.9311	9.6625	9.7579	8.4863
4E4	7.1944	7.1545	7.2820	7.3100	7.1864	7.1686	7.9853	7.7725	7.8481	6.8457
5E4	6.0965	6.0638	6.1701	6.1934	6.0908	6.0771	6.7551	6.5788	6.6414	5.8132
6E4	5.3463	5.3181	5.4105	5.4310	5.3418	5.3308	5.9194	5.7663	5.8207	5.1036
7E4	4.7988	4.7737	4.8566	4.8751	4.7953	4.7865	5.3125	5.1757	5.2243	4.5858
8E4	4.3792	4.3567	4.4319	4.4492	4.3769	4.3694	4.8456	4.7218	4.7657	4.1886
9E4	4.0495	4.0287	4.0982	4.1142	4.0474	4.0409	4.4807	4.3662	4.4069	3.8750
1E5	3.7815	3.7621	3.8267	3.8413	3.7792	3.7736	4.1817	4.0754	4.1132	3.6203
2E5	2.5367	2.5244	2.5665	2.5761	2.5358	2.5331	2.7977	2.7289	2.7534	2.4366
3E5	2.1440	2.1345	2.1693	2.1776	2.1447	2.1460	2.3596	2.3067	2.3238	2.0763
4E5	1.9459	1.9378	1.9691	1.9767	1.9473	1.9503	2.1397	2.0936	2.1080	1.8931
5E4	1.8348	1.8277	1.8566	1.8636	1.8367	1.8410	2.0135	1.9723	1.9846	1.7928
6E5	1.7700	1.7634	1.7905	1.7969	1.7717	1.7769	1.9380	1.9000	1.9109	1.7349
7E5	1.7293	1.7233	1.7502	1.7573	1.7326	1.7393	1.8961	1.8596	1.8698	1.7024
8E5	1.7011	1.6958	1.7221	1.7293	1.7055	1.7139	1.8638	1.8295	1.8387	1.6833
9E5	1.6872	1.6819	1.7075	1.7143	1.6911	1.7001	1.8456	1.8123	1.8210	1.6719
1E6	1.6768	1.6720	1.6973	1.7044	1.6817	1.6920	1.8329	1.8013	1.8092	1.6689
2E6	1.7224	1.7204	1.7438	1.7516	1.7320	1.7537	1.8670	1.8436	1.8478	1.7676
3E6	1.8323	1.8329	1.8554	1.8637	1.8461	1.8792	1.9711	1.9536	1.9554	1.9282
4E6	1.9511	1.9541	1.9761	1.9852	1.9694	2.0141	2.0863	2.0739	2.0737	2.0978
5E6	2.0723	2.0777	2.0992	2.1091	2.0951	2.1516	2.2042	2.1967	2.1947	2.2703
6E6	2.1940	2.2019	2.2229	2.2337	2.2214	2.2898	2.3225	2.3199	2.3162	2.4437
7E6	2.3158	2.3262	2.3467	2.3583	2.3478	2.4281	2.4408	2.4431	2.4376	2.6175
8E6	2.4375	2.4503	2.4703	2.4828	2.4741	2.5664	2.5590	2.5661	2.5590	2.7915
9E6	2.5590	2.5744	2.5939	2.6072	2.6003	2.7046	2.6770	2.6890	2.6802	2.9657
1E7	2.6805	2.6984	2.7173	2.7315	2.7265	2.8429	2.7948	2.8117	2.8012	3.1400

Table 2. CSDA-ranges (μg/cm^2) for 1—$C_5H_5N_5$ (adenine), 2—$C_5H_5N_5O$ (guanine), 3—$C_4H_5N_3O$ (cytosine), 4—$C_5H_6N_2O_2$ (thymine), 5—$C_4H_4N_2O_2$ (uracil), 6—$C_{19}H_{26}N_8O_{13}P_2$ (thymine–adenine), 7—C_4H_8O (tetrahydrofuran), 8—$C_4H_8O_2$ (3-hydroxytetrahydrofuran), 9—$C_5H_{10}O_2$ (α-tetrahydrofurfuryl alcohol), 10—H_3PO_4 (phosphoric acid)

E (eV)	1	2	3	4	5	6	7	8	9	10
30	0.20459	0.22882	0.16819	0.15909	0.21209	0.17825	0.068219	0.08336	0.07730	0.24729
40	0.31244	0.34945	0.26063	0.24588	0.32391	0.27006	0.108925	0.13310	0.12343	0.37137
50	0.35155	0.39319	0.30075	0.28689	0.37079	0.31676	0.135441	0.16550	0.15347	0.46688
60	0.38186	0.42571	0.33161	0.31840	0.40511	0.35163	0.158464	0.19204	0.17865	0.52214
70	0.40987	0.45520	0.35977	0.34685	0.43555	0.38263	0.180290	0.21648	0.20210	0.56489
80	0.43700	0.48354	0.38695	0.37428	0.46465	0.41236	0.201880	0.24036	0.22512	0.60447
90	0.46391	0.51151	0.41387	0.40139	0.49325	0.44164	0.223607	0.26417	0.24815	0.64255
100	0.49097	0.53954	0.44088	0.42858	0.52183	0.47093	0.245679	0.28820	0.27145	0.67999
200	0.79485	0.85101	0.74271	0.73137	0.83678	0.79482	0.500000	0.56005	0.53684	1.0763
300	1.1762	1.2391	1.1201	1.0904	1.2269	1.1960	0.824820	0.90271	0.87300	1.5514
400	1.6372	1.7067	1.5754	1.5643	1.6958	1.7578	0.22011	1.3175	1.2806	2.1014
500	2.1755	2.2519	2.1066	2.0951	2.2418	2.3111	1.68350	1.8022	1.7576	2.7249
600	2.7887	2.8723	2.7114	2.6991	2.8625	2.6032	2.21282	2.3547	2.3017	3.4217
700	3.4747	3.5659	3.3878	3.3745	3.5559	3.6130	2.80610	2.9731	2.9110	4.1902
800	4.2219	4.3218	4.1246	4.1092	4.3107	4.3940	3.45083	3.6459	3.5737	5.0291
900	5.0332	5.1424	4.9244	4.9061	5.1292	5.1500	4.15027	4.3760	4.2927	5.9363
1E3	5.9021	6.0201	5.7801	5.7579	6.0031	6.0314	4.90077	5.1573	5.0628	6.8972
2E3	17.575	17.801	17.292	17.227	17.744	17.868	15.1079	15.751	15.517	19.705
3E3	34.299	34.662	33.794	33.665	34.543	34.792	29.8519	31.010	30.590	37.893
4E3	55.696	56.224	54.911	54.702	56.021	56.426	48.7986	50.590	49.943	61.065
5E3	81.522	82.238	80.404	80.098	81.932	82.513	71.7316	74.267	73.352	88.923
6E3	111.59	112.52	110.09	109.67	112.09	112.86	98.4891	101.87	100.65	121.23
7E3	145.77	146.94	143.83	143.28	146.36	147.33	128.947	133.28	131.71	157.87

(*continued on next page*)

Table 2. (*continued*)

E (eV)	1	2	3	4	5	6	7	8	9	10
8E3	183.93	185.35	181.51	180.82	184.63	185.79	162.996	168.38	166.43	198.68
9E3	0.225.97	227.67	223.03	222.18	226.77	228.16	200.550	207.07	204.72	243.57
1E4	271.80	273.81	268.29	267.27	272.71	274.32	241.523	249.27	246.48	292.43
2E4	923.94	929.97	912.42	908.95	926.08	930.28	826.334	851.01	842.15	983.82
3E4	1895.3	0.191e4	0.187e4	0.186e4	0.189e4	0.191e4	0.1699e4	0.175e4	0.173e4	0.201e4
4E4	3151.8	0.317e4	0.311e4	0.311e4	0.315e4	0.316e4	0.2832e4	0.291e4	0.288e4	0.333e4
5E4	4668.5	0.469e4	0.461e4	0.459e4	0.467e4	0.468e4	0.4198e4	0.432e4	0.427e4	0.492e4
6E4	6424.6	0.646e4	0.635e4	0.632e4	0.643e4	0.645e4	0.5784e4	0.594e4	0.588e4	0.676e4
7E4	0.840e4	0.845e4	0.830e4	0.826e4	0.841e4	0.844e4	0.7570e4	0.778e4	0.770e4	0.883e4
8E4	0.106e5	0.106e5	0.105e5	0.104e5	0.106e5	0.106e5	0.9544e4	0.980e4	0.971e4	0.111e5
9E4	0.129e5	0.130e5	0.128e5	0.127e5	0.129e5	0.130e5	0.1169e5	0.120e5	0.118e5	0.136e5
1E5	0.155e5	0.156e5	0.153e5	0.153e5	0.155e5	0.156e5	0.1401e5	0.144e5	0.142e5	0.163e5
2E5	0.490e5	0.493e5	0.484e5	0.482e5	0.490e5	0.491e5	0.4433e5	0.455e5	0.451e5	0.512e5
3E5	0.926e5	0.931e5	0.915e5	0.912e5	0.926e5	0.927e5	0.8387e5	0.860e5	0.852e5	0.965e5
4E5	0.142e6	0.142e6	0.140e6	0.139e6	0.142e6	0.142e6	0.1286e6	0.132e6	0.131e6	0.147e6
5E4	0.195e6	0.196e6	0.192e6	0.192e6	0.195e6	0.195e6	0.1769e6	0.181e6	0.179e6	0.201e6
6E5	0.251e6	0.252e6	0.247e6	0.246e6	0.250e6	0.250e6	0.2275e6	0.233e6	0.231e6	0.258e6
7E5	0.308e6	0.309e6	0.304e6	0.303e6	0.307e6	0.307e6	0.2798e6	0.286e6	0.284e6	0.316e6
8E5	0.366e6	0.368e6	0.362e6	0.360e6	0.366e6	0.365e6	0.3331e6	0.341e6	0.338e6	0.375e6
9E5	0.425e6	0.427e6	0.420e6	0.418e6	0.42462	0.424e6	0.3870e6	0.396e6	0.393e6	0.435e6
1E6	0.485e6	0.486e6	0.479e6	0.476e6	0.48393	0.482e61	0.4414e6	0.451e6	0.448e6	0.495e6
2E6	1.07e6	1.08e6	1.06e6	1.06e6	1.07e6	0.06e6	0.9859e6	1.01e6	0.999e6	1.08e6
3E6	1.64e6	1.64e6	1.62e6	1.61e6	1.6335	1.62e6	1.507e6	1.53e6	1.53e6	1.62e6
4E6	2.16e6	2.17e6	2.14e6	2.13e6	2.16e6	2.13e62	2.001e6	2.03e6	2.02e6	2.12e6

(*continued on next page*)

Table 2. (*continued*)

E (eV)	1	2	3	4	5	6	7	8	9	10
5E6	2.66e6	2.67e6	2.63e6	2.62e6	2.65e6	0.61e6	2.467e6	2.50e6	2.49e6	2.57e6
6E6	3.14e6	3.14e6	3.09e6	3.08e6	3.11e6	3.06e6	2.909e6	2.95e6	2.93e6	3.00e6
7E6	3.57e6	3.57e6	3.53e6	3.52e6	3.55e6	3.48e6	3.328e6	3.37e6	3.35e6	3.39e6
8E6	3.99e6	3.99e6	3.95e6	3.93e6	3.96e6	3.88e6	3.729e6	3.77e6	3.75e6	3.76e6
9E6	4.40e6	4.39e6	4.34e6	4.3246	4.36e6	4.26e6	4.111e6	4.15e6	4.14e6	4.11e6
1E7	4.78e6	4.77e6	4.72e6	4.6993	4.73e6	4.62e6	4.477e6	4.5156	4.50e6	4.44e6

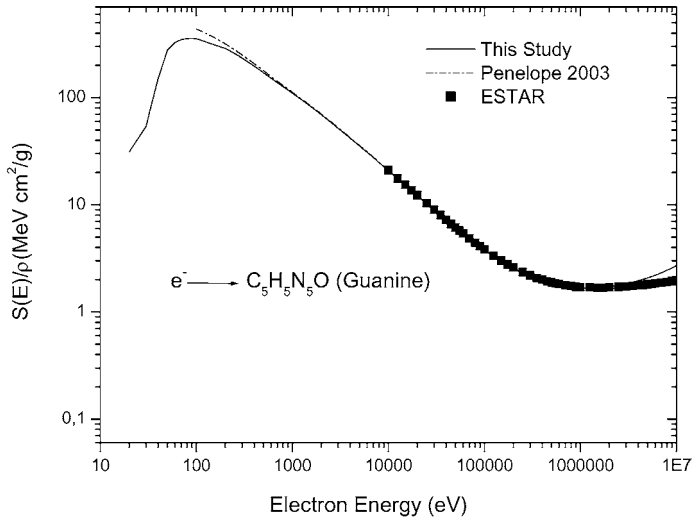

Fig. 1. Total stopping power $S(E)$ for incident electron energies, in guanine. —: present study; –·–: results calculated from PENELOPE program [14]; ■: data from the ESTAR program [15] (Nist database, 2003).

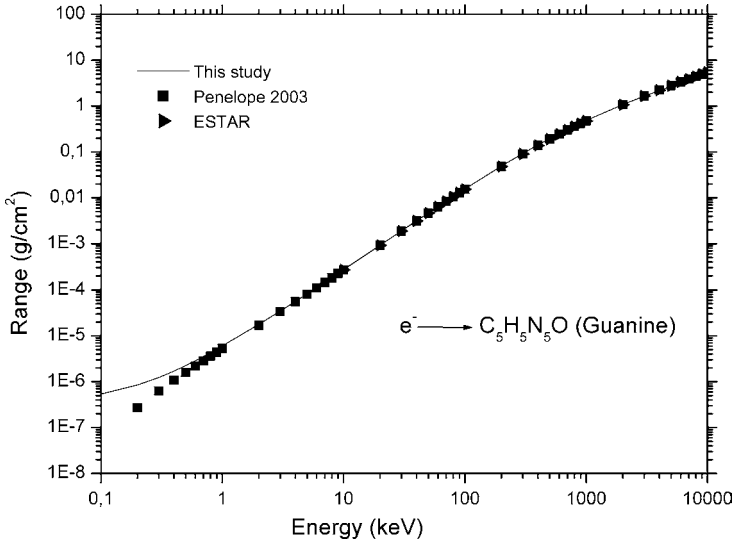

Fig. 2. The CSDA-range for incident electron energies, in guanine. —: present study; ■: results calculated from PENELOPE program [14]; ▶: data from the ESTAR program [15] (Nist database, 2003).

code PENELOPE [14] for the energy ranges 100 eV–1 MeV, 100 eV–5 MeV and 100 eV–10 MeV and the ESTAR program results (NIST database, 2003) for incident electron

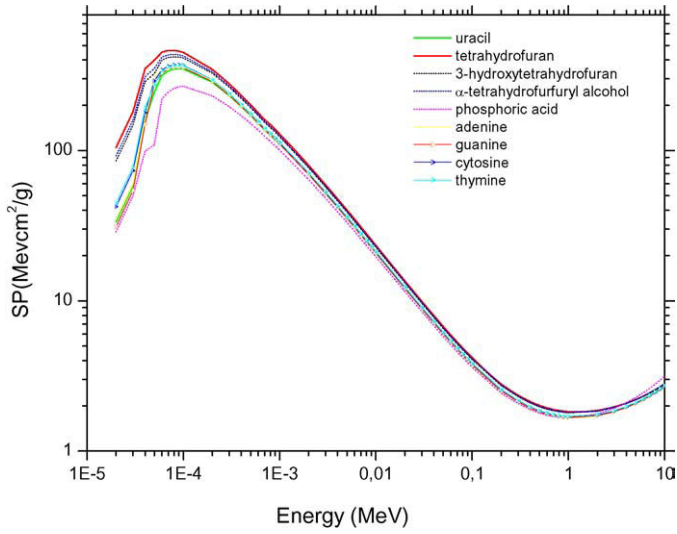

Fig. 3. Comparison of total SPs for incident electron energies, in uracil, tetrahydrofuran, 3-hydroxytetrahydrofuran, α-tetrahydrofurfuryl alcohol, phosphoric acid, adenine, guanine, cytosine and thymine.

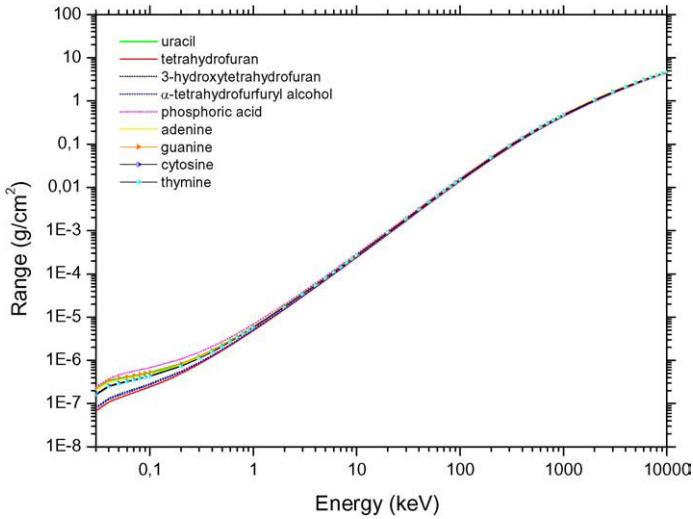

Fig. 4. Comparison of the CSDA-ranges for incident electron energies, in uracil, tetrahydrofuran, 3-hydroxytetrahydrofuran, α-tetrahydrofurfuryl alcohol, phosphoric acid, adenine, guanine, cytosine and thymine.

energies 10 keV–10 MeV. The total SP results are in good agreement to within 2%, 3%, 7% and 8%, respectively.

In Fig. 2, the CSDA-range results of this study for guanine have been compared with the PENELOPE [14] for the energy ranges 500 eV–1 MeV, 500 eV–5 MeV and 500 eV–10 MeV and the ESTAR program results (NIST database, 2003) for incident electron energies 10 keV–10 MeV. The results obtained in this study are found to be in agreement to within 6%, 6%, 6% and 3%, respectively.

Figures 3 and 4 show comparisons between the total stopping power and the CSDA-range values for incident electrons components of DNA and RNA in the 20 eV–10 MeV energy range. All total stopping power of components of DNA and RNA versus energy curves exhibit maximum around 100 eV and minima around 1 MeV.

4. CONCLUDING REMARKS

In this work, inelastic stopping power values for electrons in biological materials have been calculated with the GOS model. Total stopping power is evaluated from equation (11). The calculated results of total stopping power for electrons in biological molecules are found to be in good agreement with theoretical data. The presented total electron stopping powers and the CSDA-ranges results, considering the bremsstrahlung stopping power for electron energies above 300 keV, for biological compounds, $C_5H_5N_5$ (adenine), $C_5H_5N_5O$ (guanine), $C_4H_5N_3O$ (cytosine), $C_5H_6N_2O_2$ (thymine), $C_4H_4N_2O_2$ (uracil), C_4H_8O (tetrahydrofuran), $C_4H_8O_2$ (3-hydroxytetrahydrofuran), $C_5H_{10}O_2$ (α-tetrahydrofurfuryl alcohol), H_3PO_4 (phosphoric acid), $C_{19}H_{26}N_8O_{13}P_2$ (thymine–adenine–DNA) have been introduced for incident electrons in the 20 eV–10 MeV energy range. The presented total electron stopping power and the CSDA-ranges calculations should be useful in understanding of radiation damage and dose calculations for biological materials such as components of DNA and RNA.

REFERENCES

[1] M. Inokuti, Inelastic collisions of fast charged particles with atoms and molecules: The Bethe theory revisited, *Rev. Mod. Phys.* **43** (1971) 297–347.
[2] H.W. Koch, J.W. Motz, Bremsstrahlung cross-section formulas and related data, *Rev. Mod. Phys.* **31** (4) (1959) 920–955.
[3] J. Verne, M.S. Pimblott, Electron energy-loss distributions in solid, dry DNA, *Radiat. Res.* **141** (1995) 208–215.
[4] Z. Tan, Y. Xia, M. Zhao, X. Liu, F. Li, B. Huang, Y. Ji, *Nucl. Instrum. Methods Phys. Res. B* **222** (2004) 27–43.
[5] A. Akkerman, E. Akkerman, Characteristics of electron inelastic interactions in organic compounds and water over the energy range 20–10 000 eV, *J. Appl. Phys.* **86** (1999) 5809–5816.
[6] P. Mozejko, L. Sanche, Cross sections for electron scattering from selected components of DNA and RNA, *Radiat. Phys. Chem.* **73** (2005) 77–84.
[7] A. Akar, H. Gümüş, Electron stopping power in biological compounds for low and intermediate energies with the generalized oscillator strength (GOS) model, *Radiat. Phys. Chem.* **73** (2005) 196–203.
[8] A. Akar, H. Gümüş, N.T. Okumuşoğlu, Electron inelastic mean free path formula and CSDA-range calculation in biological compounds for low and intermediate energies, *Appl. Radiat. Isot.* **64** (2006) 543–550.
[9] J.M. Fernández-Varea, Monte Carlo simulation of the inelastic scattering of electrons and positrons using optical-data models, *Radiat. Phys. Chem.* **53** (1998) 235–245.
[10] U. Fano, Penetration of protons, alpha particles and mesons, *Annu. Rev. Nucl. Sci.* **13** (1963) 1–6.
[11] M. Inokuti, Inelastic collisions of fast charged particles with atoms and molecules: The Bethe theory revisited, *Rev. Mod. Phys.* **50** (1978) 23–35.

[12] D. Liljequist, Simple generalized oscillator strength density model applied to the simulation of keV electron-energy-loss distributions, *J. Appl. Phys.* **57** (1985) 657–665.
[13] W.H. Bragg, R. Kleeman, On the alpha particles of radium and their loss of range in passing through various atoms and molecules, *Philos. Mag.* **10** (1905) 318–340.
[14] F. Salvat, J.M. Fernández-Varea, E. Acosta, J. Sempau, *PENELOPE A Code System for Monte Carlo Simulation of Electron and Photon Transport NEA*, Data Bank, France, 2003.
[15] ESTAR, 2003. Stopping Power and Range Tables for Electron. Data available from http://physics.nist.gov/PhysRefData/Star/Text/ESTAR.html.

The Influence of Stopping Powers upon Dosimetry for Radiation Therapy with Energetic Ions

Helmut Paul[1], Oksana Geithner[2] and Oliver Jäkel[2]

[1]*Institut für Experimentalphysik, Atom- und Oberflächenphysik, Johannes-Kepler-Universität, Altenbergerstrasse 69, A-4040 Linz, Austria*
[2]*Department of Medical Physics, German Cancer Research Center (DKFZ), D-69120 Heidelberg, Germany*

Abstract

Following a recent recommendation from the International Atomic Energy Agency (IAEA), air filled ionization chambers (calibrated in terms of absorbed dose to water) should be used for the dosimetry in radiation therapy with fast ions. According to IAEA, the main source of uncertainty in the dose determination is resulting from the stopping power ratio water to air, which is introduced in order to convert the dose measured in the air cavity to the dose to water, which is used as the standard reference medium. We show that our knowledge of suitable stopping power data is very limited, but that the dependence of the stopping power ratio on the mean ionization energies I_{water} and I_{air} is dominating this quantity over a large energy range. We discuss the I-values used in ICRU Reports 37, 49, and 73, and we show how the various choices affect the ratio of stopping powers and the stopping power ratio. In doing so, we also investigate a choice of I-values differing from the ICRU recommendations. The stopping power ratio is calculated as the fluence-weighted average ratio of stopping powers using the Monte Carlo program SHIELD-HIT v2, for primary carbon ions at 50 and 400 MeV/nucleon, including the effect of secondary fragments produced by nuclear reactions.

Using a single set of I-values for all primary and secondary particles, we find that the stopping power ratio hardly differs from the simple ratio of stopping powers for C ions over a large energy range. Compared to an earlier result [O. Geithner *et al.*, *Phys. Med. Biol.* **51** (2006) 2279] there are some minor differences, arising from a combination of different I-values from different stopping power tables (ICRU 49 for protons and alphas, ICRU 73 for the heavier ions).

For the very low energy region, which is important for dosimetrical measurements close to the Bragg peak, the simple ratio of stopping powers is no longer valid. When using a consistent set of I-values it is shown that the deviation of the stopping power ratio (including nuclear fragmentation) from the recommendation of IAEA is very small at high energies, but increases up to 3% in the stopping region.

Concerning future investigations, we think it is worthwhile to reanalyze the various sources of I-values taking into account not only stopping power data but also precision range measurements, since the calculated ranges critically depend on the selected I-value.

Contents

ADVANCES IN QUANTUM CHEMISTRY, VOLUME 52
ISSN: 0065-3276 DOI: 10.1016/S0065-3276(06)52013-1

1. INTRODUCTION

The idea of using highly energetic ion beams for radiotherapy dates back to the year 1946, when R.R. Wilson in a seminal paper argued, that the properties of charged particle beams would be of great advantage in radiation therapy [1]. In 2004, radiotherapy with proton beams celebrated its 50th anniversary and between 1954 and 2004 nearly 40 000 patients have been treated with protons. Heavier ions were first used for radiotherapy in 1957 and until today around 4500 patients received treatments mainly with helium, carbon and neon ions [2].

Within the last decade, ion radiotherapy and especially carbon ion therapy has gained increasing interest: nearly half of all patients treated with ions received a carbon ion treatment within the last 10 years. Worldwide, there are currently 3 facilities treating patients with carbon ions, two of them in Japan within a clinical setting and one in Germany within a research facility. Two more ion radiotherapy facilities are currently under construction in Heidelberg, Germany and Pavia, Italy and a third one in Austria has been approved recently. All these new facilities will provide proton and carbon beams in a hospital environment. In Heidelberg, helium and oxygen ions will also be available for radiotherapy.

The main rationale for the use of fast ions in radiotherapy is the strong increase of their energy loss (and consequently of the deposited dose) with penetration depth up to the maximum range (the so-called Bragg peak) and the rapid dose fall-off behind the peak. These properties allow the application of large doses to deeply seated tumours, while sparing the surrounding normal tissue to a hitherto unknown extent (see, e.g., [3]). Compared to protons and helium ions, carbon ions have an additional advantage because of their increased relative biological effectiveness in the Bragg peak as compared to the entrance region, which is due to a strong increase of the ionization density. Also, they show less lateral scattering and smaller range straggling than protons. On the other hand, nuclear fragmentation of a carbon beam will lead to a certain dose also beyond the Bragg peak.

Proton radiotherapy nowadays is a well established method in the management of cancer diseases, even though its availability is still limited to few specialized centres. Although very encouraging clinical results have been achieved with radiotherapy using ions heavier than protons, the role of these ions in cancer therapy has yet to be evaluated in the upcoming clinical centres.

Due to the increasing use of ion beams in radiotherapy, the accurate determination of the dose delivered to the patient by ion beams becomes more and more relevant. The commonly recommended method of clinical dosimetry in radiotherapy (including ion beams) is to use air-filled ionization chambers calibrated in absorbed dose to water in a well know radiation quality (mostly Cobalt-60). This method was also proposed by the International Atomic Energy Agency (IAEA) in their Technical Report Series TRS-398 [4], which today is the most advanced international standard for clinical dosimetry. Since there are currently no primary standardization laboratories for ion beams, it is recommended by TRS-398 that a calculated beam quality correction factor is used to derive the absorbed dose to water in

an ion beam from the measurements done with a chamber calibrated in a different beam quality.[1] One of the key quantities entering this calculation is the stopping power ratio[2] water to air for the ion and energy under investigation. This stopping power ratio relates the dose to air measured in the chamber to the dose to water, which is the standard reference material for clinical dosimetry.

Using this method, the relative standard uncertainty of the calculated quality correction factor for carbon ions (to which the dose is directly proportional) was estimated in TRS-398 to be close to 3% (as compared to 2% for protons). The major source of this uncertainty comes from the uncertainty of the stopping power ratio for carbon which amounts to 2% (as compared to about 1% for protons). In contrast, the combined standard uncertainty of the quality correction factor for high energy photon beams, as used in conventional radiotherapy, is estimated to be 1%. This threefold increased uncertainty in the dose determination for ion beams as compared to conventional radiotherapy illustrates the need for improvement in ion dosimetry and especially in the knowledge of the stopping power ratios.

In a recent publication [5] the stopping power ratios for a carbon ion beam in water were calculated, using particle spectra obtained by a Monte Carlo simulation of the ion transport in water together with the most recent state-of-the-art stopping power data published by ICRU. The aim of this publication was to investigate possible variations of the stopping power ratio with energy and depth in water in order to reduce the uncertainty connected to the currently suggested value in TRS-398. In the present contribution we would rather like to focus on the uncertainty connected with the I values used in the stopping power data obtained from different sources.

2. STOPPING POWER

2.1. Definition

Linear stopping power[3] $S = -(dE/ds)_{\mathrm{av}}$, where E is the particle energy and s is the path length, is defined as the average rate at which charged particles lose energy along the track, averaged over many particles. Here, we shall mostly use the mass stopping power S/ρ, since this quantity does not depend on the density ρ of the material, to first order. Stopping power can be subdivided into several components [6]:

- Electronic stopping power (also called collision stopping power [7]) due to the transfer of energy to bound target or projectile electrons;
- Radiative stopping power due to the emission of bremsstrahlung quanta in Coulomb collisions;
- "Nuclear" stopping power due to the transfer of energy to entire nuclei or atoms in elastic Coulomb collisions;

[1] The beam quality (or radiation quality) is connected to the energy spectrum of the particles in a radiation field. Various quantitative measures for the beam quality can be used in order to distinguish beams with different dosimetrical properties.

[2] The stopping power ratio is defined here as a fluence weighted ratio of stopping powers averaged over the complete particle spectrum including secondary particles produced in nuclear fragmentation reactions (see Section 4.2).

[3] Also called "stopping force" according to P. Sigmund's suggestion.

- Energy losses due to truly nuclear interactions.

The restricted collision stopping power [8] or linear energy transfer L_Δ [9] is the mean energy loss per unit path length involving energy transfers smaller than some chosen cut-off energy Δ. This quantity is meant to describe, approximately, the energy absorbed in the vicinity of the particle track.

Since stopping power depends primarily on the velocity v of the projectile, it is usually tabulated as a function of *specific energy* E/A_1, where A_1 is the mass number of the projectile. For the ion energies considered here, radiative and "nuclear" stopping[4] can be neglected.

The energy range of carbon ions, which is relevant for radiotherapy is between 50 MeV/nucleon and 450 MeV/nucleon. In principle lower energies are important for the stopping region of the ions (e.g. at 10 MeV/nucleon the residual range of carbon ions is below 1 mm), e.g. to describe the effect of a beam stopping in an ionization chamber. This low energy range, however, will be excluded from our analysis. In the above mentioned clinical energy range, and for stopping power ratios, it is sufficient [10] to approximate the stopping power by the simplest non-relativistic Bethe expression[5] for point-charge particles [11,12]

$$\frac{S}{\rho} = \frac{4\pi r_e^2 mc^2}{\beta^2}\frac{1}{u}\frac{Z_1^2 Z_2}{A_2} \times \ln\left(\frac{2mv^2}{I}\right), \tag{1}$$

where m is the mass and r_e the classical radius of the electron, $\beta = v/c$, u is the atomic mass unit, Z_1 is the charge number of the projectile, Z_2 is the charge number and A_2 the mass number of the target atom, and I is the mean ionization potential of the material. For a mixture or, assuming Bragg's rule, for a compound, we have [12]

$$\ln I = \left(\sum w_j \frac{Z_{2j}}{A_{2j}} \ln I_j\right) \Big/ \left\langle\frac{Z_2}{A_2}\right\rangle, \tag{2}$$

where

$$\left\langle\frac{Z_2}{A_2}\right\rangle = \sum w_j \frac{Z_{2j}}{A_{2j}}, \tag{3}$$

w_j is the fraction by weight and index j refers to the jth constituent.

2.2. Experimental data, and available tables and computer codes

Experimental data for the stopping of ions in matter have been compiled and graphically presented by Ziegler [13] and by Paul [14]. An extended table of published tables and codes has been published in [16]. Among these, the SRIM code [13], the MSTAR code [14] and MSTAR table [17], and the PASS table [16] stand out as being recent, generally available, and suitable for many ions and targets. These codes and tables have been compared statistically with experimental data in [16] and in [10]. Briefly, for light and medium heavy ions, it was found that MSTAR and SRIM describe the data about equally well, while the PASS table is less reliable in many cases.

[4] For C ions in water at 4 MeV/nucleon (range 0.1 mm), e.g., "nuclear" stopping is less than 0.1%.

[5] Though not good enough for calculating the stopping power itself, at high energy this expression is good enough for ratios, due to cancelling corrections.

For protons and alpha particles, the codes and tables PSTAR, ASTAR [12,18] and SRIM [13] are available. In a statistical comparison [19], it was found that these codes describe the data better than other (older) codes, with SRIM being slightly better than PSTAR/ASTAR.

Unfortunately, there are [14] practically no experimental data for air and water[6] up to the energies of therapeutic interest. For air, the highest specific energies available are 0.5 MeV/nucleon (Li ions), 2 MeV/nucleon (He ions), and 3 MeV/nucleon (H ions). For water, this is 0.1 MeV/nucleon (Li ions) and 1.9 MeV/nucleon (He ions). For nitrogen targets, somewhat higher energies are available: 10 MeV/nucleon (C ions), 83 MeV/nucleon (O ions), and 56 MeV/nucleon (Ar ions).

One of the latter cases, experimental stopping data for Ar ions in nitrogen, can be seen in [14]. At low energies, the data agree well only with the SRIM [13] curve. With increasing energy, the agreement becomes better and better. Fig. 1 shows these data, normalized to the MSTAR [14] curve. The normalized SRIM [13], PASS [16] and BEST[7] [20] curves are also shown. Evidently, the agreement between the data above 28 MeV/nucleon [21] and the BEST and MSTAR curves is excellent; it is slightly worse for SRIM and PASS.

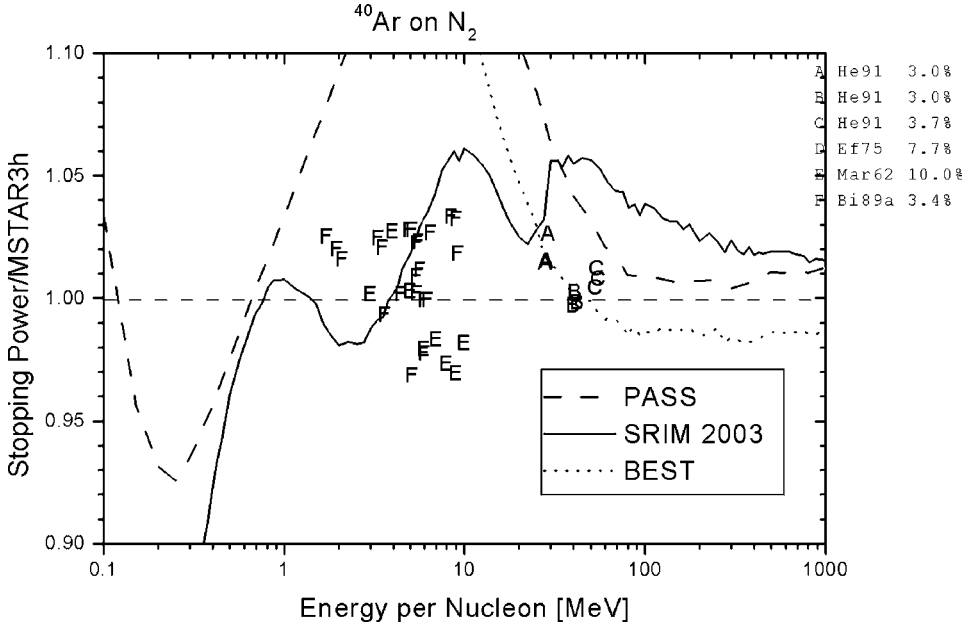

Fig. 1. The stopping power of nitrogen gas for Ar ions, as measured by Mar62 [31], Ef75 [30], Bi89a [33], and He91 [21], normalized to MSTAR v. 3(h) [14], compared to the codes BEST [20], SRIM 2003 [13], and PASS [16]. Measured points are shown by letters.

[6] In this paper, "water" always means liquid water.

[7] Bethe stopping power code including shell, Barkas, Bloch and density effect corrections, for point particles. This code has been used for the preparation of the high energy part of the tables in ICRU 49 [12], with the I values given there in Tables 1.1 and 1.2.

Table 1. Mean normalized difference $\Delta \pm \sigma$ (in %) between experimental stopping power data for C, O, Ne, S, Cl, and Ar ions in nitrogen, and the tables listed

E/A_1 (MeV) Experimental references	1–10.1 Mar62 [31], Pi68 [32], Bi89a [33]	10.1–100 Bi89a [33], He91 [21]
No. of points	83	18
MSTAR [14]	1.8 ± 0.3	0.6 ± 0.3
SRIM 2003_26 [13]	-0.5 ± 0.4	-1.7 ± 0.7
PASS, ICRU 73 [16]	-9.8 ± 0.5	-2.6 ± 0.4
BEST [20]	-44 ± 4	1.1 ± 0.3

This comparison can also be carried out numerically using the analysis program "Judge" [22]. For certain projectiles and for a certain target, and for every data point, the normalized difference $\delta = 100 \times (S_{\text{exp}} - S_{\text{table}})/S_{\text{exp}}$ is calculated. In every range of specific energy E/A_1 with n experimental points, the mean normalized difference $\Delta = \langle\delta\rangle$ and its standard deviation[8] $\sigma = \sqrt{(\langle\delta^2\rangle - \langle\delta\rangle^2)/(n-1)}$ are determined. Here, $\langle\,\rangle$ signifies an unweighted average, S_{exp} is an experimental stopping power value taken from the large data collection [14], and S_{table} the corresponding value from a particular stopping power table or program.

Corresponding numerical results, for C, O, Ne, S, Cl and Ar ions in nitrogen, are shown in Table 1. Here again, one sees the beautiful agreement between the data of the Bimbot group [21,33] above 12 MeV/nucleon and the BEST and MSTAR tables. Considering that the stated accuracy of the Bimbot and Herault data is between 3 and 4.2%, it is remarkable that the standard deviations of the single values[9] found here are all smaller than 3%. Starting from MSTAR and BEST,[10] the agreement gets slightly worse for PASS and SRIM.

3. *I* VALUES FOR WATER AND AIR

As we have seen before [10], for the calculation of stopping power ratios at therapeutically relevant energies, it is the I values that matter most. A thorough discussion and compilation of I values has been given in 1984 by M.J. Berger *et al.* in ICRU Report 37 [8] for the stopping of electrons. The same list of I values has been published again in ICRU Report 49, where it was used for protons and alphas. The discussion has been brought up to date in 1995, again by Berger [6]. Briefly, one can obtain I values from experimental data by

1. analyzing stopping power and range data for protons, deuterons, and alpha particles;
2. analyzing oscillator strength distributions for gases;
3. analyzing the dielectric response function for condensed media.

For some atomic gases, ab initio calculations have also been done.

[8] It should be noted that in our earlier statistical comparisons, we did not divide by $(n-1)$, i.e., we used the standard deviation of the single values. Here we use the standard deviation of the average.

[9] I.e., if the factor $(n-1)$ is omitted from σ.

[10] It gets much worse, of course, toward lower energy, since BEST assumes ions without electrons.

Table 2. Three sets of I values to be discussed

	I_{water} (eV)	I_{air} (eV)
Set A (ICRU 37/49)	75 ± 3	85.7
Set B (ICRU 73)	67.2	82.8
Set C (suggested here)	80.8 ± 2	88.8 ± 3

Table 3. Sources of I values for nitrogen gas used in ICRU 37, with newer additions. S. . .stopping power; OSD. . .oscillator strength distributions

I (eV)	Reference [15]	Method
88 ± 9	By55	S, 4.45 MeV p
79 ± 7	Mar62	S, 4–40 MeV alphas
76 ± 9	Sw70	S, 0.4–3.4 p
86.7	Bs79	S, 0.04–1 MeV p
83.5	Ba83a	S, 0.066–0.8 MeV p
86.0[a] ± 3	Sm99a	S, 4–11.5 MeV p
82.1	Dalgarno 67 [34]	Semi-empirical OSD
81.84 ± 0.95	Zeiss 77 [35,36]	Semi-empirical OSD
82.0 ± 2	Chosen value (ICRU 37 and 49), based on OSD	
78.5	Chosen value (ICRU 73), based on OSD	
86 ± 3	Suggested value, this work, based on Sm99a	

[a] Average of two values with different shell corrections.

In the following, we discuss the I values of water and air in view of present knowledge. We are aware of the fact that the I-values proposed in the ICRU 37/49 and ICRU 73 Reports have been chosen after a very careful analysis of all available data. Nevertheless, according to our considerations presented below, we think that it is justified to consider also I values which deviate from the recommendation of ICRU. In the following, we shall introduce three sets of I values, see Table 2: Set A which corresponds to the values of ICRU 37/49, set B which corresponds to the choice of ICRU 73, and set C which corresponds to values suggested here, on the basis of what will be discussed below. We shall then show how the choice of these sets affects stopping power ratios.

3.1. I values for air

We first consider nitrogen. Table 3 shows the experimental values used in ICRU Report 37, with more recent data added. Figure 2a shows the experimental stopping powers compared to three codes: BEST,[11] ICRU 49 and SRIM. To make small differences visible, Fig. 2b

[11] The BEST curve (valid above 500 keV) is identical to the ICRU 49 curve in this energy range.

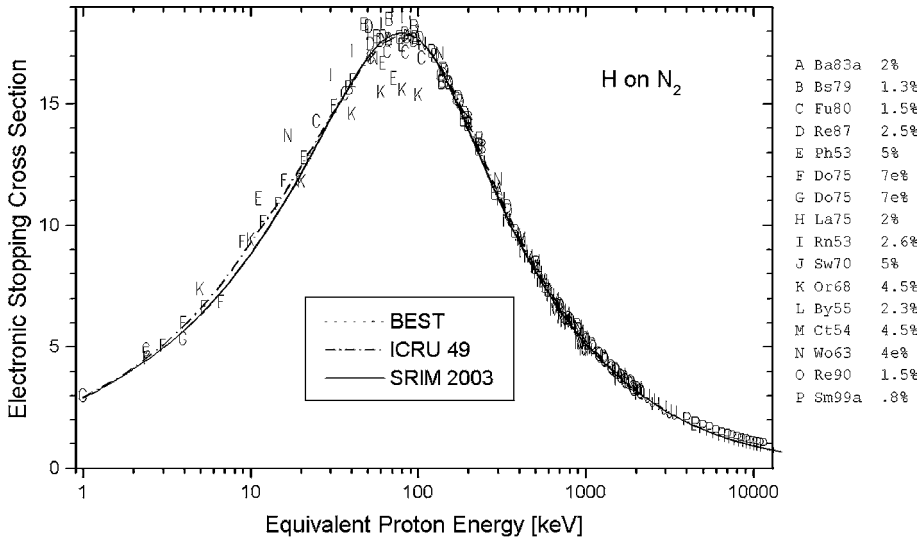

(a)

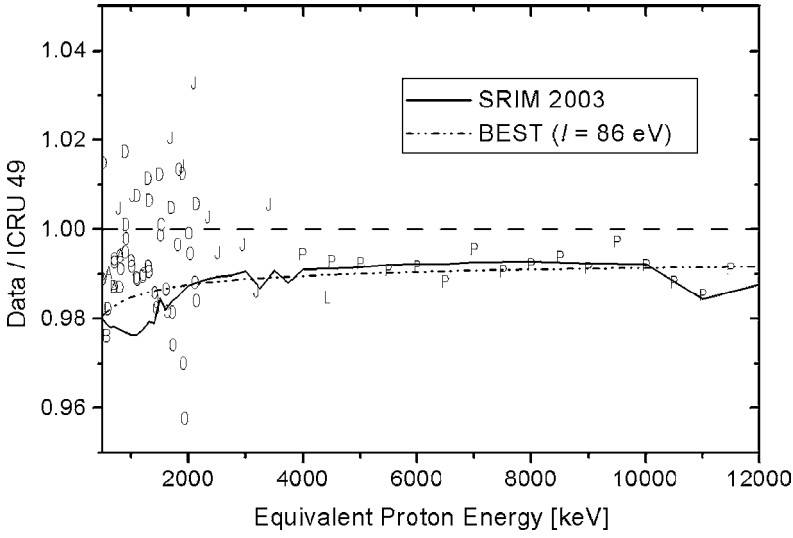

(b)

Fig. 2. a: Electronic stopping cross section of nitrogen gas for protons, in 10^{-15} eV cm^2/atom, vs. energy, compared to BEST [20], ICRU 49 [12], and SRIM 2003 [13]. The graph is taken from [14], where the references to experimental papers are also given [15]. b: Like part a, but normalized by the ICRU 49 curve (which is identical to BEST with $I = 82$ eV). The BEST curve with $I = 86$ eV is also shown.

shows the same data again (above 500 keV), but normalized by BEST (with $I = 82$ eV, the value from ICRU Report 49).

Here, the Shiomi data (Sm99a) from Nara Womens' University stand out as going to rather high energy, i.e., to a region where higher order corrections to the Bethe equation

Table 4. Sources of I values for oxygen gas used in ICRU 37, with newer additions. S. . .stopping power; OSD. . .oscillator strength distributions

I (eV)	Reference [15]	Method
95 ± 8	By55	S, 4.45 MeV p
90 ± 10	Sw70	S, 0.4–3.4 MeV p
102.1	Bs79	S, 0.04–1 MeV p
96.0	Ba83a	S, 0.066–0.8 MeV p
96.7 ± 3[a]	Sm99a	S, 4–13 MeV p
95.02 ± 0.95	Zeiss 77 [35,36]	Semi-empirical OSD
95.0 ± 2	Chosen value (ICRU 37 and 49), based on OSD	
94.6	Chosen value (ICRU 73), based on OSD	

[a] Average of two values with different shell corrections.

become rather unimportant. Indeed, the group from that university has made many stopping power measurements with high accuracy[12] at high energy over recent years, and these results will certainly influence our choice of I values. In this case, their stopping values are clearly below the values of ICRU 49, as seen in Fig. 2b, and hence their suggested value ($I = 86$ eV) is higher than that assumed in ICRU 49, see Table 3.

Since the BEST curve with $I = 86$ eV follows the experimental data more closely, a value $I = 86$ eV may be more appropriate for nitrogen, although this is a change barely outside the stated errors.

For oxygen, no change appears necessary. As Table 4 shows, the results by Sm99a again suggest a somewhat higher I value than that given in ICRU 49. But because of the small difference and the stated uncertainties, a different value does not seem to be justified.

For air,[13] there are, unfortunately, no high-energy high-precision measurements like for nitrogen and oxygen. In ICRU 37, the I value of air ($I_{\text{air}} = 85.7$ eV) is calculated from the I values of the components, using the additivity rule, equation (2). If we use this rule, take the I values for the components of air from ICRU 37 and change only the value for nitrogen from $I_{\text{N}} = 82$ eV to $I_{\text{N}} = 86$ eV, we obtain $I_{\text{air}} = 88.8$ eV. I values for air are shown in Table 5.

3.2. I values for water

Table 6 shows the experimental values used in ICRU Report 37 [8] and, in addition, two newer values: The experimental value by Bichsel *et al.* [27,28] obtained by measuring Bragg ionization curves with 70 MeV protons, and the semi-empirical dielectric response result by Dingfelder *et al.* [41]. It is remarkable that these two more recent results agree very well. We therefore included a value of $I_{\text{water}} = 80.8 \pm 2$ eV in set C.

Additional information about the reliability of the Bichsel results (see also Berger's discussions in footnote 2 of ICRU Report 49 [12] and in [6]) can be obtained from Table 7,

[12] There has been a long-standing discrepancy at a high level of accuracy between proton stopping power results of the Nara group and of the Danish group (see [19]). Eventually, the two groups agreed for Al. But for Ag and Au targets, a 1% discrepancy remains.

[13] Dry air, near sea level.

Table 5. I values for air, obtained from the values for constituents, using equation (2)

I (eV)	Reference
85.7	ICRU 37, 49
82.8	ICRU 73
88.8 ± 3	This work

Table 6. Sources of I values for water used in ICRU 37, with newer additions. R. . .range; S. . .stopping power; DRF. . .dielectric response function; OSD. . .oscillator strength distributions

I (eV)	Reference	Method
75.4 ± 1.9[a]	Thompson 52 [37]	R, 340–200 MeV p, assuming $I_{Cu} = 322$ eV
74.6 ± 2.7[a]	Nordin 79 [38]	S, 60 MeV p
79.7 ± 2	Bichsel 92 [27,28]	Ionization curves, 70 MeV p
75	Ritchie 78 [39]	Dielectric response function
75.4	Ashley 82 [40]	Dielectric response function
81.8	Dingfelder 98 [41]	Dielectric response function
75.0 ± 3	Chosen value (ICRU 37 and 49), based on all the data available in 1984	
67.2	Chosen value (ICRU 73), based on OSD	
80.8 ± 2	Suggested value, this work, based on Bichsel and Dingfelder	

[a] The data were analyzed by Berger (ICRU 37).

Table 7. I values for solid elements according to ICRU 49 [12], and experimental values due to BH92 [27] and Sk91 [42,23], and evaluated using Bichsel's shell corrections. The BH92 results are based on $I_{Al} = 166$ eV. In the last columns to the right, the I values are normalized in various ways

Element	ICRU 49	Sk91	BH92	Sk91 / ICRU 49	BH92 / ICRU 49	Sk91 / BH92
Al	166	168.7 ± 4.5	[166]	1.016	[1.000]	
Ti	233	242.2 ± 6.2	242	1.039	1.039	1.001
Cu	322	337.2 ± 8.2	339	1.047	1.053	0.995
Mo	424	452 ± 11	440	1.066	1.038	1.027
Ag	470	494 ± 12	489	1.051	1.040	1.010
Sn	488	491 ± 12	508	1.006	1.041	0.966
Ta	718	758 ± 17	736	1.056	1.025	1.030
Pb	823	827 ± 19	816	1.005	0.991	1.013

where other results from the same Bichsel paper, measured with the same apparatus, are compared to transmission results measured by the Nara University group [42,23] with protons of 55, 65 and 73 MeV, and to the values from ICRU 49. One can see that in almost all cases the Bichsel and the Sakamoto results are a few percent higher than the numbers from ICRU 49, and that the results from Bichsel and Sakamoto agree within 2%, on the average. This makes the Bichsel result for water even more plausible.

For completeness, it should also be mentioned, that a value of 77 eV for I_{water} was derived by Krämer *et al.* [24] from precision measurements of carbon ion Bragg curves in water. The mentioned value of 77 eV best reproduced the position of the Bragg peak using an empirical model for the nuclear fragmentation and adding the various contributions of all fragments to the total energy loss of the primary carbon ions.

4. STOPPING POWER RATIOS FOR DOSIMETRY

4.1. Ratios of stopping powers

To convert the absorbed dose in air determined by means of an air ionisation chamber to the dose in water, the first approximation—within the framework of cavity theory—is to use the ratio of stopping powers

$$\frac{(S(E)/\rho)_{\text{water}}}{(S(E)/\rho)_{\text{air}}} \tag{4}$$

where $(S(E)/\rho)_m$ denotes the mass stopping power of medium m evaluated at the energy E. Since we have almost no suitable experimental values, as mentioned above, we must rely on theory. In doing so, it is the mean ionization potential I of the substance that matters most. This can be seen as follows [10]:

Using equations (1) and (3), the ratio of stopping powers water/air becomes, approximately,

$$\frac{(S/\rho)_{\text{water}}}{(S/\rho)_{\text{air}}} = \frac{(Z_2/A_2)_{\text{water}}}{(Z_2/A_2)_{\text{air}}} \frac{\ln(2mv^2/I_{\text{water}})}{\ln(2mv^2/I_{\text{air}})} = \frac{0.5551}{0.4992} \frac{\ln(2mv^2/I_{\text{water}})}{\ln(2mv^2/I_{\text{air}})}. \tag{5}$$

In Fig. 3, the ratio of stopping powers is shown for protons, as taken from SRIM, ICRU Report 49, BEST,[14] and calculated using equation (5). The ICRU 49 and BEST curves are identical, since the high energy part of the ICRU 49 table has been produced using BEST. But we also see that the curve based on the approximation equation (5) differs very little from BEST (by less than 0.001 above 10 MeV). Evidently, the higher order corrections nearly cancel.

Clearly, the differences between the curves in Fig. 3 are essentially due to differences in I values. Table 8 shows the various I values used, and their ratio. The SRIM values, where Bragg's rule is used above 2 MeV/nucleon, are calculated from SRIM\Data\SCOEF03.dat [13,25] using equation (2). The PASS values,[15] were calculated [26] using equation (3.24) and Table 6.2 of ICRU Report 73 [16] (for water) and taken from Table 3.1 of ICRU Report 73 [16] (for nitrogen), respectively. The PASS values are also shown in this table to make

[14] Using the built-in data file for target properties.

[15] Actually, the I values shown here for PASS are not used directly, since PASS calculates the contributions to the stopping power shell by shell.

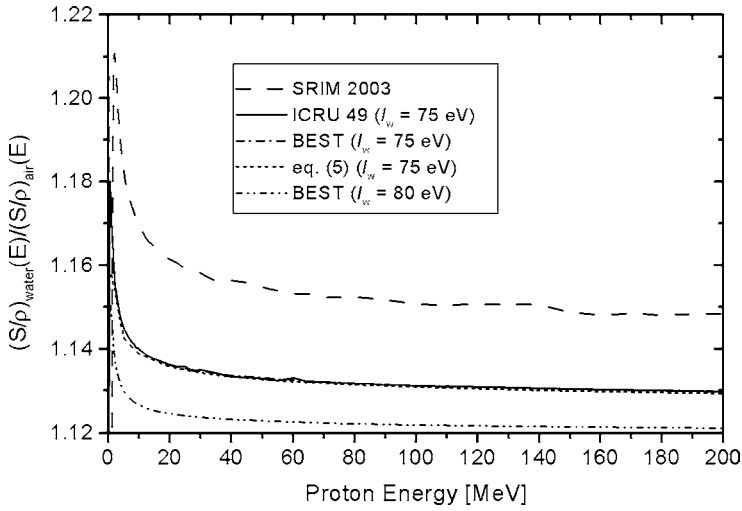

Fig. 3. The ratio of stopping powers water/air for protons, versus energy, using BEST [20], ICRU 49 [12], SRIM 2003 [13], and equation (5). The BEST curve is shown using both $I_{\text{water}} = 75$ eV and $I_{\text{water}} = 80$ eV for water. SRIM uses $I_{\text{water}} = 69.7$ eV and $I_{\text{air}} = 91.0$ eV. For all other curves, $I_{\text{air}} = 85.7$ eV.

Table 8. The I values for water and air (in eV) used by the various tables or programs

Table or program	I value for water	I value for air	$I_{\text{air}}/I_{\text{water}}$
SRIM 2003 (p, α) [13]	69.7	91.0	1.301
PASS, ICRU 73 [16]	67.2	82.8	1.232
ICRU 49 [12]	75 ± 3	85.7	1.143

the difference between the values of ICRU 49 and ICRU 73 apparent, which may not be obvious to the casual reader of ICRU 73. Fig. 3 also shows a curve for $I_{\text{water}} = 80$ eV, calculated using BEST,[16] which corresponds to the newer value measured by Bichsel and Hiraoka [27,28] (see Section 3.2). Generally, the vertical sequence of the curves in Fig. 3 follows the sequence of ratios $I_{\text{air}}/I_{\text{water}}$, as one would expect.

We now consider carbon ions. Fig. 4 shows the ratio of stopping powers for carbon ions, versus energy, using BEST [20], ICRU 73 [16], SRIM 2003 [13], MSTAR [14], and equation (5). The BEST curve is shown using both, the I values suggested by ICRU 49, and the values suggested here (set C). The sequence of the curves is seen to correspond to the sequence of ratios $I_{\text{air}}/I_{\text{water}}$, like in Fig. 3, with the highest curve (SRIM) corresponding to $I_{\text{air}}/I_{\text{water}} = 1.3$, and the lowest curve to $I_{\text{air}}/I_{\text{water}} = 1.1$. Starting from the lowest curve based on set C, the calculations with MSTAR, PASS and SRIM are progressively deviating from this curve. Remarkably, this sequence is similar to what we should have expected on the basis of our comparison with experimental values for nitrogen gas (Fig. 1 and Table 1 above). In Fig. 5, the same values are plotted as in Fig. 4, but now versus range

[16] It is an advantage of the BEST code that one change the I value, if necessary.

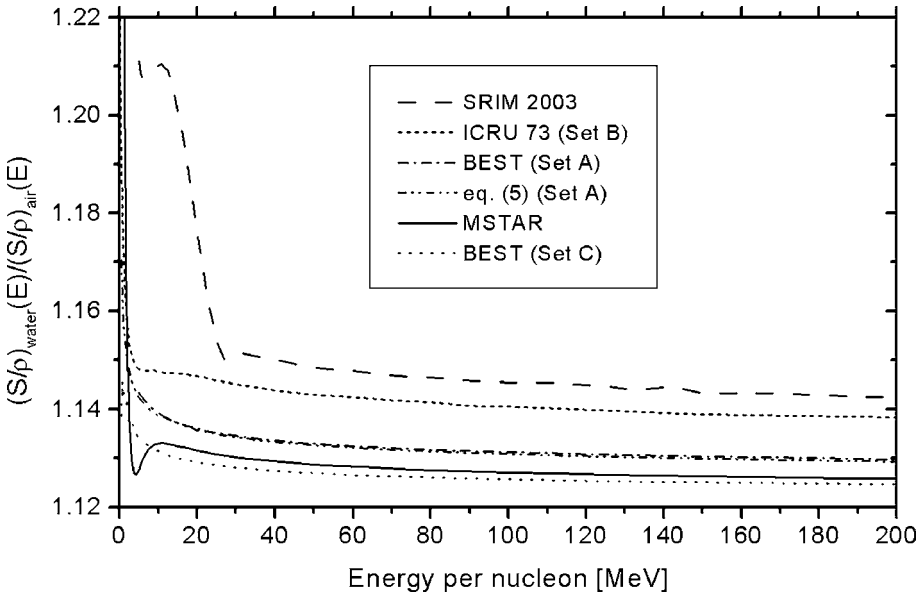

Fig. 4. The ratio of stopping powers water/air for carbon ions, versus energy, using BEST [20], ICRU 73 [16], SRIM 2003 [13], MSTAR [14], and equation (5). The BEST curve is shown using both, with the I values suggested by ICRU 49, and with the values suggested here. For SRIM and ICRU 73, the I values are as given in Table 8.

in water. The constant value $s_{\text{water,air}} = 1.13 \pm 0.02$ adopted for heavy ion beams in TRS 398 [4] is also shown. Fig. 6 shows the same values versus depth in water, for the particular case of a C beam of 400 MeV/nucleon ($R_E = 27$ cm). The values shown are limited to $E/A \geqslant 5$ MeV/nucleon (i.e., $R \geqslant 0.013$ cm); all the curves except for SRIM are within $s_{\text{water,air}} = 1.13 \pm 0.02$.

4.2. Stopping power ratios

To obtain a more accurate correspondence between the measurement in air and its application to water, it is necessary to use Monte Carlo calculations to take into account all physical processes, especially the effect of secondary fragments produced by nuclear reactions (see, e.g., [5] and [29]). One defines the 'stopping power ratio' [4] (as opposed to the simple ratio of stopping powers defined in equation (4) above), i.e., the fluence-weighted average ratio of stopping powers

$$s_{\text{water,air}} = \frac{\sum_i \int_0^\infty \Phi_{E,i,\text{water}} (S_i(E)/\rho)_{\text{water}}\, dE}{\sum_i \int_0^\infty \Phi_{E,i,\text{water}} (S_i(E)/\rho)_{\text{air}}\, dE}, \tag{6}$$

where $S_i(E)/\rho$ is the mass stopping power for a (primary or secondary) particle i with energy E in water or air, and $\Phi_{E,i,\text{water}}$ is the particle spectrum differential in energy, at a particular depth in water, for particles of type i.

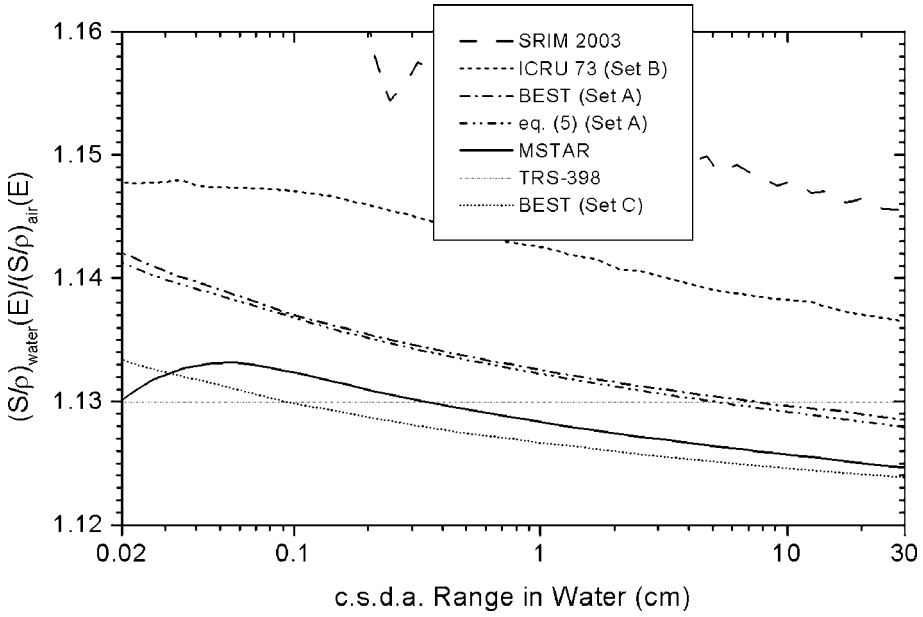

Fig. 5. Like Fig. 4, but versus range in water. The constant from TRS 398 [4] is also indicated.

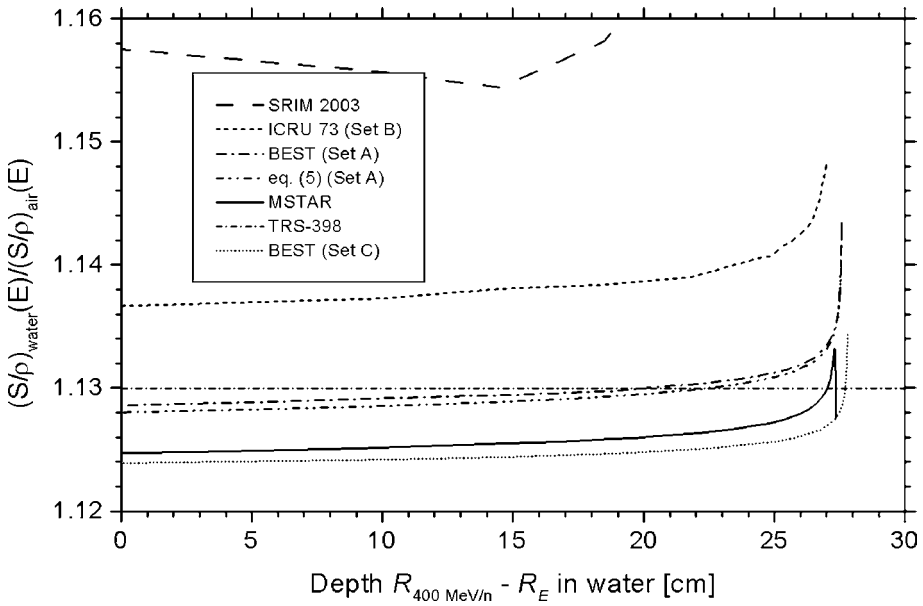

Fig. 6. The ratio of stopping powers water/air for C ions of 400 MeV/nucleon like Fig. 4, but versus depth in water. The values shown are limited to $E/A \geqslant 5$ MeV/nucleon, corresponding to $R \geqslant 0.013$ cm, since the ratios become unreliable at lower energies.

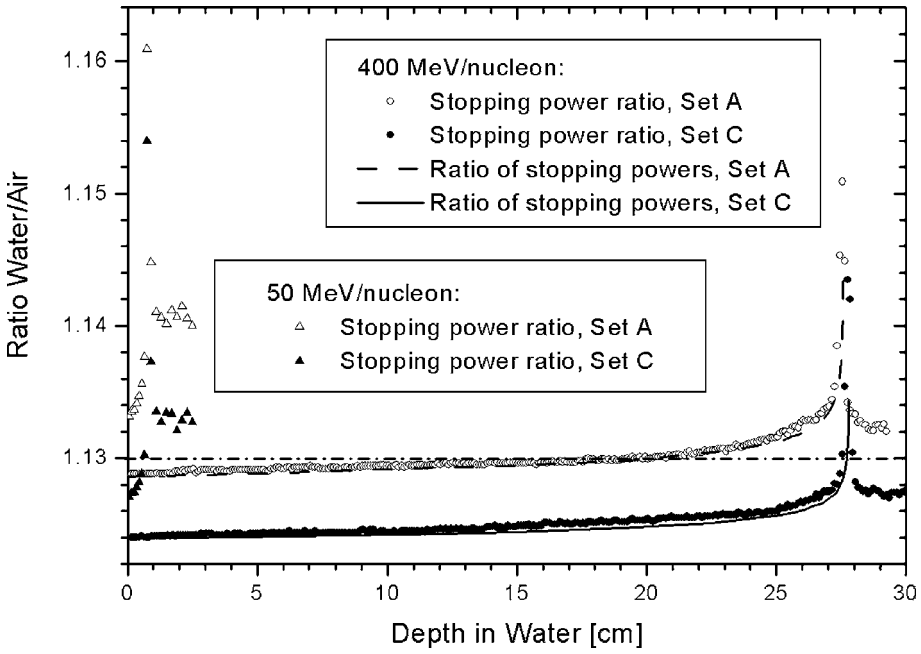

Fig. 7. Stopping power ratios, obtained by Monte Carlo calculation, compared to ratios of stopping powers according to equation (5), for carbon ions of 400 MeV/nucleon, for two assumptions about I values: set A and set C. Curves based on set B would lie higher than those for set A. The ranges are: 27.59 cm (set A), and 27.81 cm (set C). Monte Carlo calculations for 50 MeV/nucleon are also shown.

By way of example, Fig. 7 shows calculations carried out using Monte Carlo code SHIELD-HIT v2 [5] for carbon ions for two assumptions about I values (set A and set C). The spectra of primary and secondary particles differential in energy, $\Phi_{E,i,\mathrm{water}}$, were obtained from the transport of a monoenergetic pencil beam of two different initial energies, 50 and 400 MeV/nucleon, in a water cylinder (20 cm diameter $\times$ 30 cm length). The cylindrical geometry was divided into 300 equal slices of 0.1 cm thickness. These calculations used stopping powers for H, He, Li, Be, B, and C nuclei obtained from BEST [20] for high energies. At low energies (below 0.5 to 5 MeV/nucleon, depending on Z_1), where BEST is wrong since it assumes point nuclei, MSTAR was used instead. For 400 MeV/nucleon, the Monte Carlo results fit well into the range 1.13 ± 0.02 suggested by TRS-398 [4], but for 50 MeV/nucleon, the ratio goes up to 1.16. Fig. 7 also shows simple ratios of stopping powers calculated according to equation (4) for the 400 MeV/nucleon case.

5. DISCUSSION

When comparing the results shown in Fig. 7 for 400 MeV/nucleon with the previous findings in Fig. 5 of [5], which have been obtained with the same code SHIELD-HIT v2, a number of differences can be observed: the curves in Ref. [5] are slightly higher than in

the present Fig. 7 (about 0.5% for set A and about 1% for set C), and they appear concave rather than monotonely rising as in Fig. 7. The only difference in the two results is the set of stopping power data that have been used. To obtain the data shown in Fig. 7, a consistent set of I values (set A or C, respectively) has been used for all the ions, while the calculations in [5] were done using state-of-the-art stopping powers, i.e., ICRU 49 for protons and alphas, and ICRU 73 for the heavier ions. As we see now, this corresponds to a mixture of sets A and B. As Fig. 4 shows, the stopping power ratio is higher for set B than for set A. This fact alone would have made the curves in [5] higher than they are here. But the important contribution of protons and alphas to the energy deposition [5] has lowered the stopping power ratio again, and it has produced the concave shape of the curves in [5].

The other new result in Fig. 7 is the near identity of stopping power ratio and ratio of stopping powers for 400 MeV/nucleon, except at and beyond the Bragg peak (where the ratio of stopping powers is not valid as pointed out above). Evidently, for a large part of the range, it does not matter to the energy deposition whether it is due to a primary or to a secondary particle, if the I values are the same. The differences observed in Fig. 5 of Ref. [5] are obviously due to the different I values used in ICRU 73 and ICRU 49.

Concerning the choice of I values, we think that set C yields more consistent results for the stopping power ratio, as compared to sets A and B, but clearly a more detailed analysis is needed here. In particular, more precision measurements of the stopping power of water would be very helpful.

There is, however, another aspect of the choice of I values, which was not analyzed here: while there is consistency of the stopping power data when using the I values of set C, there might be an inconsistency when looking at the precise position of the Bragg peak of particles (or in other words the total range of the ions). Fig. 7 shows that a change from set A to set C changes the range by 2.3 mm. A change of the I value for water from 67.2 eV (set B) to 80.8 eV (set C) would therefore result in a drastic shift of the Bragg peak by nearly 6 mm. This is in clear disagreement to the result obtained in Fig. 2 of Ref. [5], where an excellent agreement of the Bragg peak position with measured data was achieved using the ICRU 73 stopping power data for ions. In this respect, the influence of the proton and helium fragments (and thus of the data from ICRU 49) can be neglected, as the Bragg peak position is determined by the carbon ions alone.

Finally, the changes of the stopping power ratio at very low energies should be considered. These are important in order to obtain dosimetrical correction factors for measurements with plane parallel ion chambers close to the Bragg peak, as was shown in Ref. [5]. It was pointed out already, that the BEST code does not yield good results for the stopping region of the particles. Therefore, as mentioned above, the MSTAR data were used for the low energy region in the simulations done with SHIELD-HIT v2 and shown in Fig. 7. The simple ratio of stopping powers for the primary ion will not lead to reliable results in the region close to the Bragg peak, because obviously the contribution of nuclear fragments is essential here. At 400 MeV/nucleon, the variation in the stopping power ratio seen in Fig. 7 is about 2% over the total penetration depth for both sets of I-values and is thus in agreement with the findings in Ref. [5].

6. CONCLUSIONS

Considering the importance of the stopping powers of water and air for the dosimetry in radiation therapy using fast ions, we have re-analyzed the choice of I values of ICRU Reports

37 and 49. On the basis of newer results, we think that it is justified to consider I values for both water and air, which are significantly increased compared to the recommendations of ICRU 49. It is noteworthy that the change of I values suggested in the recent ICRU Report 73 goes in the opposite direction. In any case, for a physically meaningful calculation of stopping power ratios, it would be very important to have stopping power tables with a single consistent value I_{water} for the whole range of ions from protons up to Ar. When changes of the I values are discussed, also the resulting Bragg peak positions of the ions have to be compared to precision measurements, since they critically depend on the I values.

We have found that the stopping power ratio, i.e., the fluence-weighted average stopping power ratio water/air, for C ions of 400 MeV/nucleon, is within the limits suggested by TRS-398. It is hardly different from the simple ratio of stopping powers water/air, and this in turn can be calculated to a very good approximation using the lowest order Bethe formula, over most of the energy range. For the very low energy region, which is important for dosimetrical measurements close to the Bragg peak, this may no longer be true and additional work should be put into accurate calculations down to the 1 MeV/nucleon region including Monte Carlo simulations of the nuclear fragmentation effects. At 50 MeV/nucleon, the stopping power ratio at the Bragg peak is somewhat outside the limits of TRS-398, as found already in Ref. [5].

ACKNOWLEDGEMENT

One of the authors (H.P.) is grateful for important help from N. Sakamoto, J. Ziegler, and P. Sigmund. All of the authors acknowledge helpful discussions with P. Andreo.

REFERENCES

[1] R.R. Wilson, *Radiology* **45** (1946) 487.
[2] J. Sisterson, *Nucl. Instrum. Methods B* **241** (2005) 713.
[3] G. Kraft, *Prog. Part. Nucl. Phys.* **45** (2000) S473–S544;
G. Kraft, *Prog. Part. Nucl. Phys.* **46** (2001) 1.
[4] P. Andreo, D.T. Burns, K. Hohlfeld, M.S. Huq, T. Kanai, F. Laitano, V.G. Smythe, S. Vynckier, Absorbed Dose Determination in External Beam Radiotherapy: An International Code of Practice for Dosimetry Based on Standards of absorbed Dose to Water, Tech. Report Series No. 398, International Atomic Energy Agency, Vienna, 2000.
[5] O. Geithner, P. Andreo, N. Sobolevsky, G. Hartmann, O. Jäkel, *Phys. Med. Biol.* **51** (2006) 2279.
[6] M.J. Berger, H. Paul, *Stopping Powers, Ranges, and Straggling*, Chapter 7 of *Atomic and molecular data for radiotherapy and radiation research*, IAEA-TECDOC-799, International Atomic Energy Agency, Vienna, 1995.
[7] ICRU Report 33, International Commission on Radiation Units and Measurements, Bethesda, MD, USA, 1980.
[8] ICRU Report 37, International Commission on Radiation Units and Measurements, Bethesda, MD, USA, 1984.
[9] ICRU Report 16, International Commission on Radiation Units and Measurements, Bethesda, MD, USA, 1970.
[10] H. Paul, *Nucl. Instrum. Methods B* **247** (2006) 166.
[11] H. Bethe, *Ann. Phys.* **5** (1930) 325.
[12] ICRU Report 49, International Commission on Radiation Units and Measurements, Bethesda, MD, USA, 1993.
[13] J. Ziegler, available from http://www.srim.org.

[14] H. Paul, Stopping power for light ions, available from http://www-nds.iaea.or.at/stoppinggraphs/.
[15] See "list of all data references" in [14].
[16] ICRU Report 73 International Commission on Radiation Units and Measurements, *J. ICRU* **5** (1) (2005).
[17] H. Paul, A. Schinner, *At. Data Nucl. Data Tables* **85** (2003) 377.
[18] NISTIR 4999, available from http://physics.nist.gov/PhysRefData/Star/Text/contents.html.
[19] H. Paul, A. Schinner, *Nucl. Instrum. Methods B* **227** (2005) 461.
[20] M. Berger, H. Bichsel, BE(the) ST(opping) code BEST. Personal communication from M. Berger to H. Paul (1993).
[21] J. Herault, R. Bimbot, H. Gauvin, B. Kubica, R. Anne, G. Bastin, F. Hubert, *Nucl. Instrum. Methods B* **61** (1991) 156.
[22] H. Paul, A. Schinner, *Nucl. Instrum. Methods B* **179** (2001) 299.
[23] N. Sakamoto, personal communication to H. Paul (2006).
[24] M. Krämer, O. Jäkel, T. Haberer, G. Kraft, D. Schardt, U. Weber, *Phys. Med. Biol.* **45** (2000) 3299.
[25] J. Ziegler, personal communication to H. Paul (2005).
[26] P. Sigmund, personal communication to H. Paul (2005).
[27] H. Bichsel, T. Hiraoka, *Nucl. Instrum. Methods B* **66** (1992) 345.
[28] H. Bichsel, T. Hiraoka, K. Omata, *Rad. Res.* **153** (2000) 208.
[29] K. Amako, *et al.*, GEANT4 Collaboration, *Nucl. Phys. B (Proc. Suppl.)* **150** (2006) 44.
[30] B. Efken, D. Hahn, D. Hilscher, G. Wustefeld, *Nucl. Instrum. Methods* **129** (1975) 219.
[31] E.W. Martin, L.C. Northcliffe, *Phys. Rev.* **128** (1962) 1166.
[32] T.E. Pierce, M. Blann, *Phys. Rev.* **173** (1968) 390.
[33] R. Bimbot, C. Cabot, D. Gardes, H. Gauvin, R. Hingmann, I. Orliange, L. de Reilhac, F. Hubert, *Nucl. Instrum. Methods B* **44** (1989) 1.
[34] A. Dalgarno, T. Degges, D.A. Williams, *Proc. Phys. Soc. (London)* **92** (1967) 291.
[35] G.D. Zeiss, W.J. Meath, J.C.F. MacDonald, D.J. Dawson, *Can. J. Phys.* **55** (1977) 2080.
[36] G.D. Zeiss, W.J. Meath, J.C.F. MacDonald, D.J. Dawson, *Radiat. Res.* **70** (1977) 284.
[37] T.J. Thompson, Report UCRL-1910, University of California Radiation Lab., Berkeley, CA, USA, 1952.
[38] J.A. Nordin, R.M. Henkelman, *Phys. Med. Biol.* **24** (1979) 781.
[39] R.H. Ritchie, W. Brandt, *Phys. Rev. A* **17** (1978) 2102.
[40] J.C. Ashley, *Radiat. Res.* **89** (1982) 25.
[41] M. Dingfelder, D. Hantke, M. Inokuti, H.G. Paretzke, *Radiat. Phys. Chem.* **53** (1998) 1.
[42] N. Sakamoto, H. Ogawa, M. Mannami, K. Kimura, Y. Susuki, M. Hasegawa, I. Hatayama, T. Noro, H. Ikegami, *Rad. Effects Defects Sol.* **117** (1991) 193.

Subject Index

C

D

I

K

L

M

N

S

T